

# **Numerical Modelling of a Counter-Current Spray Drying Tower**

**Muzammil Ali**

Submitted in accordance with the requirements for the degree of  
Doctor of Philosophy

The University of Leeds  
Institute of Particle Science and Engineering  
School of Chemical and Process Engineering

March 2014



The candidate confirms that the work submitted is his own, except where work which has formed part of jointly authored publications has been included. The contribution of the candidate and the other authors to this work has been explicitly indicated below. The candidate confirms that appropriate credit has been given within the thesis where reference has been made to the work of others.

The work in Chapter 5 of the thesis has appeared in publication as follows:

A one-dimensional plug-flow model of a counter-current spray drying tower. *Chem. Eng. Res. Des.*, 2014, Ali, M., Mahmud, T., Heggs, P. J., Ghadiri, M., Djurdjevic, D., Ahmadian, H., Martin de Juan, L., Amador, C. and Bayly, A.

I was responsible for the write-up of the paper, development of mathematical model of the counter-current spray drying tower, development of the algorithm for solving the model, application of the mathematical model using MATLAB (2010) and generating the results.

The contributions of other authors were of supervision nature: Mahmud, T., Heggs, P. J., Ghadiri, M., Djurdjevic, D., Ahmadian, H. and Bayly, A.: Critical review of the work and gave suggestions to improve the article. Martin de Juan, L.: Measured the data used for model validation, critically reviewed the work and gave suggestions. Amador, C.: Measured the data used in the model.

The work in Chapter 6 of the thesis has appeared in publication as follows:

Heat losses from a pilot-scale counter-current spray drying tower. *13th UK Heat Transfer Conference UKHTC2013*, 2-3 Sept. 2013, Imperial College London, UK, Ali, M., Mahmud, T., Heggs, P. J., Ghadiri, M., Davidson, A., Ahmadian, H., Martin de Juan, L., Djurdjevic, D. and Bayly, A.

The paper is based on my own modelling work on of heat-loss through the tower, developing user-defined functions, simulation of the spray drying tower and generating the results. I was also responsible for write-up of the paper.

The contributions of other authors were: Mahmud, T., Heggs, P. J., Ghadiri, M., Ahmadian, H., Djurdjevic, D. and Bayly, A.: Critical review of the work and gave suggestions to improve the article. Martin de Juan, L. and Davidson, A.: Measured the data used for model validation.

The work in Chapter 7 of the thesis has appeared in publication as follows:

CFD modelling of a counter-current spray drying tower. *8th International Conference on Multiphase Flow ICMF 2013*, 26-31 May 2013, Jeju, South Korea, Ali, M., Mahmud, T., Heggs, P. J., Ghadiri, M., Francia, V., Ahmadian, H., Martin de Juan, L., Djurdjevic, D. and Bayly, A.

I was responsible for the write-up of the paper, modelling of heat-loss through the tower, developing user-defined functions, simulation of the spray drying tower and generating the results.

The contributions of other authors: Mahmud, T., Heggs, P. J., Ghadiri, M., Djurdjevic, D., and Bayly, A. were to critically review the work and they gave me suggestions on how to improve the article. Further, Francia, V., Martin de Juan, L. and Ahmadian, H. provided data used for model validation and a review of the work and suggestions.

The work in Chapter 7 (Section 7.2.12) of the thesis has appeared in the publication as follows:

CFD simulation of a counter-current spray drying tower with stochastic treatment of particle-wall collision. *7th World Congress on Particle Technology*, 19-22 May 2014, Beijing, China, Ali, M., Mahmud, T., Heggs, P. J., Ghadiri, M., Bayly, A., Ahmadian, H. and Martin de Juan, L.

I was responsible for the write-up of the paper and development and application of the rough-wall collision model, simulation of the tower and generating the results.

The contributions of other authors: Mahmud, T., Heggs, P. J., Ghadiri, M. and Bayly, A. were to critically review the work and they gave me suggestions on how to improve the article. Further, Martin de Juan, L. and Ahmadian, H. provided data used for model validation.

This copy has been supplied on the understanding that it is copyright material and that no quotation from the thesis may be published without proper acknowledgement.

## **Acknowledgements**

All praise belongs to Allah, the most gracious and the most merciful, for his constant blessings. Thereafter, I would like to thank my supervisors Dr. Tariq Mahmud, Prof. Peter John Heggs and Prof. Mojtaba Ghadiri for the critical review of my work during the weekly project meetings, throughout my PhD period. Dr. Tariq Mahmud's constructive critical review enabled me to broaden my thoughts and to exceed my potential. I am very grateful to Prof. Peter Heggs for taking great interest in my project, providing me guidance and reviewing my modelling work that helped in the improvement of the models predictions. I am thankful to Prof. Mojtaba Ghadiri for critically reviewing my work and for the arrangements he made with P&G for the funding of my project and for the maintenance costs.

I would like to especially thank Prof. Andrew Bayly for being very active in my project. His constant interest and guidance in my project led to significant improvement in my work. I am very thankful to Dr. Luis Martin de Juan and Dr. Hossein Ahmadian for always being prompt in the review of my work and for sharing the data collected from the pilot-plant to compare with the model predictions. I am thankful to Dr. Dusan Djurdjevic for providing me guidance especially in the early stages of my research work and to Dr. Boon Ho Ng for giving a tutorial on using user-defined functions. I am grateful to Mr. Victor Francia for sharing his data on the velocity profiles and to Ms. Anne Davidson for measuring the gas temperature profiles collected from the pilot-plant spray drying tower to validate the model predictions.

I would like to acknowledge the financial support by P&G and the University of Leeds. I am thankful to Mr. Zayeed Alam from P&G for his support. Finally I am especially thankful to my parents for their persistent love and encouragement throughout my time in Leeds.

## **Abstract**

Spray drying of atomised solutions or slurries is one of the most common methods for the production of a wide variety of particulate products in the chemical, food, personal care products and pharmaceutical industries. The modelling of a spray drying process for the manufacture of detergent powder in a counter-current tower is carried out using two different approaches: a simple one-dimensional multiphase plug-flow modelling and a more rigorous CFD modelling approach. Both approaches are coupled with an existing semi-empirical slurry droplet drying model. The plug-flow model considers heat, mass and momentum transfer between the polydispersed droplets/particles and gas phase, along the tower height. In the CFD model, based on the Eulerian-Lagrangian method, the three-dimensional turbulent swirling gas flow is fully coupled with the droplets/particles motion along with particle-wall interactions via the heat, mass and momentum exchanges. The simulation results are compared with the experimental data collected from a large scale pilot-plant spray drying tower and a reasonable agreement with the measured powder outlet temperature, moisture content, and exhaust gas temperature is obtained, considering the complexity of the process and the accuracy of the measured data. The plug-flow model gives similar qualitative trends compared to the CFD model and can be a useful supplement for quick determination of operating conditions for pilot-plant trials that would enable more extensive and accurate optimisation of the process. The more computationally expensive CFD model can be used for tackling operational and product quality issues including wall deposition and thermal degradation. The gas flow and temperature profiles, and droplet/particle trajectories obtained from the CFD modelling results are used to propose a zonal modelling approach to model spray tower in a computationally efficient manner. This approach can be used to develop models for process optimisation of counter-current spray drying towers, as reliably as the CFD model.

## List of Contents

Acknowledgements .....	iii
Abstract .....	iv
List of Contents .....	v
List of Figures .....	x
List of Tables.....	xviii
Nomenclature .....	xx
Abbreviations .....	xxvi
1. INTRODUCTION .....	1
1.1 Background and Motivation for Research.....	1
1.2 Aims and Objectives.....	3
1.3 Structure of the Thesis .....	5
1.4 Thesis Map.....	7
2. SPRAY DRYING FUNDAMENTALS .....	8
2.1 Spray Drying Process.....	8
2.1.1 Advantages and Disadvantages of Spray Drying.....	8
2.2 Atomisation.....	10
2.3 Types of Spray Dryers .....	14
2.4 Spray-Air Contact in Spray Drying Towers .....	17
2.5 Wall Deposition in Spray Dryers.....	18
2.6 Thermal Efficiency of Spray Dryers.....	20
2.7 Applications of Spray Drying Process.....	21
2.7.1 Spray Drying in the Food Industry .....	21
2.7.2 Spray Drying in the Pharmaceutical Industry .....	22
2.7.3 Spray Drying in the Detergent Industry .....	22
2.8 Detergent Powder Characteristics.....	23
2.8.1 Bulk Density .....	23
2.8.2 Particle Size Distribution .....	23
2.8.3 Moisture Content.....	24
2.8.4 Powder Flowability .....	24
3. LITERATURE REVIEW .....	25
3.1 Introduction.....	25
3.2 Theory of Drying .....	25
3.3 Droplet Drying in Spray Drying Towers .....	26
3.4 Single Droplet Drying.....	28

3.4.1	Effect of High Mass Flux on Droplet/Particle Heat Transfer .....	35
3.4.2	Effect of Radiation Heat Transfer.....	36
3.5	Particle Morphologies.....	36
3.6	Detergent Slurry Composition.....	40
3.7	Modelling Approaches for Spray Drying Towers .....	41
3.8	Plug-Flow Models for Spray Drying .....	42
3.9	CFD Modelling.....	44
3.9.1	Conservation Equations for the Fluid Flow.....	45
3.10	Turbulence Modelling .....	46
3.10.1	Standard $k-\varepsilon$ Model.....	47
3.10.2	RNG $k-\varepsilon$ Model.....	48
3.10.3	Realizable $k-\varepsilon$ Model .....	49
3.10.4	Shear Stress Transport (SST) Model .....	50
3.10.5	Reynolds Stress Transport Model.....	51
3.10.6	Modelling of Flow Near the Wall.....	55
3.10.7	Modelling of Temperature Near the Wall .....	57
3.10.8	Scalar Transport Equations.....	58
3.11	Modelling of the Discrete Phase.....	59
3.11.1	Drag Force on Droplets/Particles.....	60
3.11.2	Effect of Mass Transfer on the Drag Coefficient .....	62
3.11.3	Particle-Wall Interaction.....	62
3.11.4	Turbulent Dispersion of Droplets/Particles .....	63
3.12	Coupling between the Discrete and Continuous Phases.....	64
3.12.1	Evaluation of Source Terms .....	67
3.13	Importance of Gas Velocity Profiles in CFD Modelling of Spray Drying Towers.....	68
3.14	Experimental Study of Gas Flow profiles in the Spray Drying Tower .....	68
3.15	CFD Modelling of Gas Flow in Counter-Current Spray Drying Towers.....	72
3.16	CFD Modelling of Spray Drying Process.....	74
3.17	Experimental Studies on Spray Drying Process in Counter-Current Towers	77
3.18	Conclusions.....	78
4.	COLLECTION OF EXPERIMENTAL DATA .....	80
4.1	Introduction.....	80
4.2	Spray drying process in the IPP unit.....	80
4.3	Geometry of the Tower.....	83
4.4	Characterisation of Dried Detergent Powder.....	84

4.4.1	Measurement of Powder Size Distribution .....	84
4.4.2	Measurement of Moisture Content.....	84
4.4.3	Measurement of Bulk Density .....	85
4.4.4	Measurement of Envelope Density .....	85
4.4.5	Measurement of Cake Strength.....	86
4.5	Droplet Size Distribution Measurement .....	86
4.6	Data from the IPP Spray Drying Tower .....	87
4.6.1	Measurement of velocity profiles inside the spray drying tower.....	87
4.6.2	Measurement of temperature profiles inside the spray drying tower.....	88
5.	PLUG-FLOW MODELLING OF SPRAY DRYING TOWER.....	90
5.1	Introduction.....	90
5.2	Droplet/Particle Drying Model .....	90
5.2.1	Droplet/Particle Drying Mechanism .....	90
5.2.2	Drying Model Assumptions .....	91
5.2.3	Governing Equations.....	92
5.3	Spray Drying Tower Model.....	96
5.3.1	Assumptions Incorporated in the Spray Drying Tower Model.....	96
5.3.2	Governing Equations.....	97
5.3.3	Droplets Initial Velocity.....	101
5.3.4	Boundary Conditions .....	101
5.3.5	Solution Methodology.....	101
5.4	Size Distribution of Droplets .....	103
5.5	Simulation Results .....	104
5.5.1	Solution Dependency on the Number of Increments .....	107
5.5.2	Solution Dependency on Cut Sizes .....	108
5.5.3	Simulation Results and Discussion .....	110
5.5.4	Influence of Initial Droplet Size Distribution on the Simulation Results .....	125
5.5.5	Solution Dependency on the Number of Increments .....	127
5.5.6	Solution Dependency on the Number of Discrete Sizes .....	128
5.6	Conclusions.....	137
6.	SINGLE PHASE CFD MODELLING .....	139
6.1	Isothermal Single Phase CFD Modelling .....	139
6.1.1	Numerical Solution Method.....	140
6.1.2	Boundary Conditions .....	140
6.1.3	Mesh Independency Test .....	141
6.1.4	Numerical Discretisation Scheme .....	146

6.1.5	Transient vs Steady State.....	149
6.1.6	Selection of Turbulence Model .....	156
6.1.7	Results and Discussion of the RST Model .....	159
6.1.8	Effect of Surface Roughness .....	163
6.1.9	Effect of Pressure Strain Term in the RST Model Prediction and a Discussion of Final Results.....	166
6.1.10	Conclusions .....	176
6.2	CFD Modelling of Non-Isothermal Single Phase Flows .....	178
6.2.1	Modelling of Heat Loss From the Wall.....	178
6.2.2	Numerical Solution Method .....	180
6.2.3	Boundary Condition Specifications.....	181
6.2.4	Simulation Cases .....	181
6.2.5	Simulation Convergence.....	182
6.2.6	Simulation Results for Case 1.....	183
6.2.7	Case 2 .....	189
6.2.8	Case 3 .....	190
6.2.9	Analysis of Experimental Data.....	190
6.2.10	Case 4 .....	196
6.2.11	Conclusions .....	202
7.	MULTIPHASE CFD MODELLING .....	203
7.1	Study of Particle Flow under Isothermal Flow Condition.....	203
7.1.1	Numerical Solution Method and Boundary Conditions .....	204
7.1.2	Conclusions .....	218
7.2	CFD Simulation of Spray Drying Process.....	219
7.2.1	Drying Gas Composition and its Physical Properties.....	220
7.2.2	Initial Size Distribution of Droplets .....	221
7.2.3	Initial Velocity of Droplets.....	221
7.2.4	Droplet Drying Kinetics .....	222
7.2.5	Modelling of Particle-Wall Interaction and Particle Motion .....	223
7.2.6	Boundary Conditions.....	223
7.2.7	Numerical Solution Method for the Continuous Phase .....	224
7.2.8	Convergence Criteria.....	224
7.2.9	Simulation Results and Discussion.....	230
7.2.10	Study of the Influence of Non-Spherical Drag Law .....	245
7.2.11	Study of the Influence of Initial Droplet Size Distribution .....	248
7.2.12	Modelling of Rough-Wall Collision Model .....	254
7.2.13	Simulation Results With Rough Wall Collision Model .....	257

7.2.14	Conclusions.....	265
8.	MODELLING OF A SPRAY DRYING TOWER WITH TWO NOZZLES	268
8.1	Introduction.....	268
8.2	Plug-Flow Modelling with Two Nozzles.....	268
8.3	CFD Modelling with Two Nozzles.....	274
8.4	Conclusions.....	289
9.	ZONAL MODELLING OF SPRAY DRYING TOWER .....	290
9.1	Introduction.....	290
9.2	Description of a Zonal Model.....	290
9.2.1	Zone 1 (Entrained Particles Zone) .....	292
9.2.2	Zone 2 (Spray Zone) .....	295
9.2.3	Zone 3 (Annular Plug-Flow Zone) and Zone 4 (Hot Core Zone) .....	297
9.2.4	Zone 5 (CSTR Zone).....	302
9.2.5	Solution Methodology.....	303
9.2.6	Simulation Results .....	305
9.3	Conclusions.....	311
10.	CONCLUSIONS AND RECOMMENDATIONS .....	312
10.1	Conclusions.....	312
10.1.1	Plug-Flow Modelling .....	312
10.1.2	Single Phase CFD Modelling.....	314
10.1.3	Multiphase CFD Modelling .....	315
10.1.4	Zonal Modelling.....	318
10.1.5	Summary of Modelling Approaches .....	319
10.2	Recommendations for Future Work .....	319
	REFERENCES.....	323
	APPENDIX – I.....	343
	APPENDIX – II .....	358
	APPENDIX – III.....	364

## List of Figures

Figure – 2.1: Schematic of spray drying process shown in stages. (Adapted from Masters, 1972).	10
Figure – 2.2: Schematic of a pressure swirl nozzle atomiser.	11
Figure – 2.3: Droplet population profiles in solid cone and hollow cone spray patterns.	12
Figure – 2.4: Schematic of a rotary atomiser (adapted from Masters, 1985).	13
Figure – 2.5: Schematic of a two-fluid atomiser (adapted from Masters, 1985).	13
Figure – 2.6: Schematic diagrams of spray dryers: (a) Co-current flow; (b) Counter-current flow; (c) Mixed flow.	16
Figure – 3.1: Equilibrium moisture curve (Adapted from Masters, 1985).	26
Figure – 3.2: Typical droplet drying temperature curve in a spray dryer (Adapted from Handscomb <i>et al.</i> , 2009a).	27
Figure – 3.3: Typical characteristic drying curve.	31
Figure – 3.4: Mechanisms of droplet drying in the second stage of drying process.	34
Figure – 3.5: Scanning electron microscope images of spray dried particles. (a): Porous ceramic particle (source: Effting <i>et al.</i> , 2010), (b): Hollow detergent particle (Martin de Juan, 2012).	35
Figure – 3.6: Particles with different morphologies: (a): Co-dried egg and skim milk powder (skin forming structure), (b): Yoghurt powder (skin forming structure), (c): Trisodium orthophosphate (crystalline structure), (d): Organic UV brightener (crystalline structure), (e): Lead Chromate (agglomerate structure), (f): Ferrite (agglomerate structure). (Source: Walton and Mumford, 1999a).	38
Figure – 3.7: Schematic of different particle morphologies resulting from spray drying (Source: Handscomb <i>et al.</i> , 2009a).	40
Figure – 3.8: Detergent slurry composition in different phases.	41
Figure – 3.9: Droplet/particle wall impact.	63
Figure – 3.10: Flow chart for PSI-Cell computational scheme (adapted from Crowe, 1977).	66
Figure – 4.1: Process flow diagram of detergent slurry spray drying.	81
Figure – 4.2: Collection of dried powder at the bottom of the tower.	82
Figure – 4.3: Separation of entrained fine powder from exhaust gas.	83
Figure – 4.4: Schematic of the spray drying tower.	83
Figure – 4.5: Schematic of a porous particle.	85
Figure – 4.6: Cylinder and piston arrangement in GeoPyc device.	86
Figure – 4.7: Measurement of powder cake strength.	86
Figure – 4.8: Schematic of the atomisation rig.	87

Figure – 4.9: Temperature measurement probe (a): thermocouple mounted on the rod, (b) direction of thermocouple facing the gas flow, (c), (d) and (e): Temperature measurement probe after the run with droplets/particles (Martin de Juan, 2012). .....	89
Figure – 5.1: Four stages of drying of a slurry droplet. ....	91
Figure – 5.2: Counter-current spray drying tower schematic. ....	96
Figure – 5.3: Control volume inside the spray tower. ....	102
Figure – 5.4: Logic flow diagram of the solution algorithm. ....	103
Figure – 5.5: Particle size distribution plot on a cumulative mass basis. ....	105
Figure – 5.6: Plot of Error (difference in predicted and actual gas inlet temperature) v/s Iteration. ....	109
Figure – 5.7: Residence time distribution of particles. ....	110
Figure – 5.8: Velocity profile of droplets/particles of different sizes. ....	111
Figure – 5.9: Temperature profile of droplets/particles of different sizes. ....	112
Figure – 5.10: Heat transfer coefficient profile of droplets/particles of different sizes. ....	113
Figure – 5.11: Mass transfer coefficient profile of droplets/particles of different sizes. ....	114
Figure – 5.12: Moisture profiles of droplets/particles of different sizes along the dimensionless tower height. ....	115
Figure – 5.13: Drying rate of droplets/particles of different sizes along the dimensionless tower height. ....	116
Figure – 5.14: Particle and gas temperatures, slurry boiling point and corresponding drying rate along the dimensionless height for a 400 $\mu\text{m}$ size particle. ....	117
Figure – 5.15: Particle and gas temperatures, slurry boiling point and the temperature difference along the dimensionless height for a 400 $\mu\text{m}$ size particle. ....	117
Figure – 5.16: Density of droplets/particles of different sizes along the dimensionless tower height. ....	118
Figure – 5.17: Specific heat of droplets/particles of different sizes along the dimensionless tower height. ....	118
Figure – 5.18: Outlet temperatures and moisture contents as a function of size. ....	119
Figure – 5.19: Normalised gas velocity along the tower height. ....	119
Figure – 5.20: Heat flux through the column wall v/s dimensionless height. ....	120
Figure – 5.21: Corrected heat transfer coefficient v/s dimensionless height. ....	121
Figure – 5.22: Corrected particle velocity v/s dimensionless height. ....	121
Figure – 5.23: Size distribution of atomised droplets and spray dried powder cumulative mass basis. ....	125
Figure – 5.24: Residence time of particles of different sizes for plug-flow Case 1. ....	129
Figure – 5.25: Temperature profiles of droplets/particles and hot gas for plug-flow Case 1. ....	130

Figure – 5.26: Particle exit temperature and moisture content for plug-flow Case 1...	131
Figure – 5.27: Residence time of particles of different sizes for plug-flow Case 2.....	131
Figure – 5.28: Temperature profiles of droplets/particles and hot gas for plug-flow Case 2.....	132
Figure – 5.29: Particle exit temperature and moisture content for plug-flow Case 2...	133
Figure – 5.30: Heat Flux through the column wall to the surrounding.....	134
Figure – 6.1 (a): Meshing of spray drying tower: (i) Mesh-1, (ii) Mesh-2, (iii) Mesh-3.	142
Figure – 6.1 (b): Cross-sectional view of the mesh: (a) Mesh 1, (b) Mesh 2, (c) Mesh 3.	143
Figure – 6.2: Convergence residuals: (a) Mesh-1, (b) Mesh-2, (c) Mesh-3 .....	144
Figure – 6.3: Cross-sectional axial velocity profiles.....	145
Figure – 6.4: Cross-sectional tangential velocity profiles.....	146
Figure – 6.5: Convergence residuals for discretisation scheme. (a) FOU; (b) SOU; (c) QUICK .....	148
Figure – 6.6: Cross-sectional axial velocity profiles computed using different discretisation schemes .....	149
Figure – 6.7: Convergence residuals for steady state solution. (a) Standard $k-\varepsilon$ turbulence model; (b) RST model.....	151
Figure – 6.8: Steady v/s transient simulation axial velocity comparison using standard $k-\varepsilon$ model. ....	152
Figure – 6.9: Tangential velocity comparison for steady v/s transient case using standard $k-\varepsilon$ model. ....	153
Figure – 6.10: Steady v/s transient simulation axial velocity comparison using the RST model.....	154
Figure – 6.11: Tangential velocity comparison for steady v/s transient case using RST model.....	155
Figure – 6.12: Comparison of axial velocity profiles using different turbulence models and with experimental data by Francia (2011).....	157
Figure – 6.13: Comparison of tangential velocity profiles computed using different turbulence models with experimental data by Francia (2011). ....	158
Figure – 6.14: Contours of magnitude of mean velocity components. ....	160
Figure – 6.15: Path lines of air velocity coloured by tangential velocity component (m/s) in the bottom conical region.....	161
Figure – 6.16: Contour plot of turbulent intensity. ....	162
Figure – 6.17: Cross-sectional view of mean velocity magnitude contours at various dimensionless heights and at different times. ....	163
Figure – 6.18: Tangential velocity profiles predicted using smooth and rough wall assumption and a comparison with experimental data by Francia (2011). ....	165

Figure – 6.19: Axial velocity profiles predicted using smooth and rough wall assumption and a comparison with experimental data by Francia (2011).	166
Figure – 6.20: Axial velocity profiles computed using LRR and SSG pressure strain models and a comparison with experimental data by Francia (2011).	167
Figure – 6.21: Predicted pressure variation along the dimensionless radius at various dimensionless heights using the LRR-RST model.	168
Figure – 6.22: Tangential velocity profiles computed using LRR and SSG pressure strain models and a comparison with experimental data by Francia (2011).	170
Figure – 6.23: Radial velocity profiles computed using LRR and SSG pressure strain models and a comparison with experimental data by Francia (2011).	172
Figure – 6.24: Swirl number as a function of dimensionless height.	173
Figure – 6.25: Turbulent intensity computed using LRR and SSG pressure strain models and compared with measurements by Francia (2011).	174
Figure – 6.26: Plots of normalised turbulent normal stresses computed using the LRR-RST model.	176
Figure – 6.27: Thermal resistances considered in the calculation of heat loss.	179
Figure – 6.28: Convergence residuals for non-isothermal Case 1.	183
Figure – 6.29: Convergence history of weighted averaged axial and tangential velocities.	183
Figure – 6.30: Temperature profiles at different axial locations, a comparison of non-isothermal cases with experimental data.	185
Figure – 6.31: Contours of the predicted gas temperature profiles inside the spray drying tower.	186
Figure – 6.32: Predicted axial velocity profiles at various axial locations (Case 1).	187
Figure – 6.33: Predicted tangential velocity profiles at various heights (Case 1).	188
Figure – 6.34: Predicted inside film coefficient along the dimensionless height (Case 1).	189
Figure – 6.35: Heat flux along the dimensionless tower height.	195
Figure – 6.36: Heat transfer coefficient and swirl number along the dimensionless tower height (Case 3).	196
Figure – 6.37: The effect of turbulent Prandtl number in predicting temperature profiles (using Case 4 conditions).	198
Figure – 6.38: Temperature profiles at different axial locations, a comparison of non-isothermal cases with different wall roughness with experimental data.	201
Figure – 7.1: Residuals of convergence for isothermal Case 1.	206
Figure – 7.2: Area weighted average tangential and axial velocity profiles during the simulation run for isothermal Case 1.	207
Figure – 7.3: Particle trajectories of different sizes in the spray drying tower coloured by diameter ( $C_r = 1.0$ ).	208

Figure – 7.4: Forces acting on a particle in the bottom conical region of the tower. ...	208
Figure – 7.5: Particle trajectories of different sizes coloured by diameter ( $C_r = 0.4$ )...	209
Figure – 7.6: Comparison of single phase and multiphase axial velocity profiles. ....	210
Figure – 7.7: Comparison of single phase and multiphase tangential velocity profiles.	211
Figure – 7.8: Swirl number comparison along the tower height.....	212
Figure – 7.9: Contour plot of air velocity magnitude. ....	213
Figure – 7.10: Vector plot of air velocity magnitude near the nozzle. ....	214
Figure – 7.11: Contour plot of turbulent intensity. ....	214
Figure – 7.12: Residence time of particles collected from the bottom of the tower. ....	215
Figure – 7.13: Size distribution of particles collected from the bottom. ....	216
Figure – 7.14: Size distribution of particles collected from the top of the tower. ....	217
Figure – 7.15: Mean axial velocity profiles of the air at different heights. ....	217
Figure – 7.16: Residuals for Case 1. ....	226
Figure – 7.17: Residuals for Case 2. ....	226
Figure – 7.18: Exhaust gas temperature v/s iteration for Case 1. ....	226
Figure – 7.19: Exhaust gas temperature vs iterations for Case 2.....	227
Figure – 7.20: Area weighted average axial and tangential velocities v/s iteration for Case 1.....	227
Figure – 7.21: Area weighted average axial and tangential velocity profiles for Case 2.	228
Figure – 7.22: Overall enthalpy balance schematic. ....	229
Figure – 7.23: Droplet/particle tracks coloured by diameter. ....	231
Figure – 7.24: Size distribution of particles exiting from the bottom (a) and top (b) of the tower (Case 2). ....	232
Figure – 7.25: Residence times of particles collected from the bottom outlet.....	233
Figure – 7.26: Gas velocity distributions coloured by velocity magnitude. ....	234
Figure – 7.27: Vector plot of air velocity magnitude near the nozzle. ....	235
Figure – 7.28: Mean axial and tangential velocity profiles computed from Case 1 and 2.	236
Figure – 7.29: Swirl number along the tower height. ....	237
Figure – 7.30: Gas turbulence intensity distributions. ....	238
Figure – 7.31: Discrete phase concentration for Case 2. ....	239
Figure – 7.32: Gas temperature and moisture distributions. ....	240
Figure – 7.33: Heat flux along the dimensionless tower height.....	241
Figure – 7.34: Particle exit temperature and moisture content at the bottom outlet. ....	243
Figure – 7.35: Particle exit density at the bottom outlet. ....	243

Figure – 7.36: Temperature profile and dimensionless moisture profile of a 700 $\mu\text{m}$ particle size.....	244
Figure – 7.37: Comparison of heat flux through the column wall.....	245
Figure – 7.38: Residence time of particles collected from the tower bottom. ....	246
Figure – 7.39: Residence time of particles collected from the tower bottom. ....	247
Figure – 7.40: Contours of gas temperature distribution. ....	250
Figure – 7.41: Predicted gas temperature profiles compared with measurements by Martin de Juan (2012). ....	251
Figure – 7.42: Predicted residence times of different particle sizes. ....	252
Figure – 7.43: Particle exit temperature and moisture content at the bottom outlet. ....	253
Figure – 7.44: Particle-rough wall collision.....	255
Figure – 7.45: Particle-rough wall collision model algorithm. ....	258
Figure – 7.46: Particle trajectories coloured by diameter. ....	259
Figure – 7.47: Discrete phase concentration at different dimensionless heights. ....	260
Figure – 7.48: Trajectories of particles of different sizes coloured by velocity. ....	261
Figure – 7.49: Trajectories of particles of different sizes coloured by post-wall collision angles.....	262
Figure – 7.50: Residence time of particles of different sizes.....	263
Figure – 7.51: Gas temperature distributions.....	264
Figure – 7.52: Exit temperature and normalised moisture fraction of particles.....	265
Figure – 8.1: Logic flow diagram of the algorithm for the plug-flow model with two nozzles.....	269
Figure – 8.2: Cumulative droplet and particle size distribution.....	271
Figure – 8.3: Residence time of particles of different sizes for plug-flow Case 3.....	271
Figure – 8.4: Final temperature and moisture content of particles of different sizes for plug-flow Case 3. ....	272
Figure – 8.5: Temperature profiles of gas and particles injected from nozzle 1.....	273
Figure – 8.6: Temperature profiles of gas and particles injected from nozzle 2.....	273
Figure – 8.7: Residence time of particles of different sizes for plug-flow Case 4.....	274
Figure – 8.8: Gas velocity distribution coloured by magnitude of velocity components.....	276
Figure – 8.9: Swirl number along the dimensionless tower height (Case 8). ....	277
Figure – 8.10: Gas velocity vectors coloured by velocity magnitude (Case 8). ....	277
Figure – 8.11: Gas velocity distribution coloured by magnitude of velocity components.....	278
Figure – 8.12: Gas temperature distributions.....	279
Figure – 8.13: Gas temperature profile comparison for Cases 8 and 9.....	281
Figure – 8.14: Gas temperature near the wall along the dimensionless tower height... ..	282

Figure – 8.15: Residence time of particles of different sizes for CFD Case 8.....	282
Figure – 8.16: Residence time of particles at the tower bottom. ....	283
Figure – 8.17: Final temperature and moisture content of particles of different sizes for CFD Case 8. ....	284
Figure – 8.18: Moisture fraction profile of 800 $\mu\text{m}$ particle size for Case 8. ....	285
Figure – 8.19: Temperature of particles at the tower bottom.....	286
Figure – 8.20: Moisture of particles at the tower bottom.....	286
Figure – 8.21: Gas temperature profiles along the tower axis. ....	287
Figure – 9.1: Zones for numerical modelling of spray drying tower.....	291
Figure – 9.2: Variables in zonal modelling.....	292
Figure – 9.3: Gas temperature profile along the above the spray nozzle.....	293
Figure – 9.4: Gas temperature in the centreline of the tower along the dimensionless height.....	294
Figure – 9.5: Discrete phase concentration along the radius of the tower above the nozzle. ....	294
Figure – 9.6: Gas temperature along the radius of the tower in the spray zone.....	296
Figure – 9.7: Gas mass flow along the radius of the tower in the spray zone. ....	296
Figure – 9.8: Radial profiles of discrete phase concentration in the cylindrical region of the tower.....	298
Figure – 9.9: Radial temperature profiles of gas in the cylindrical region of the tower.....	299
Figure – 9.10: Cup mixing temperature along the tower height in the cylindrical region of the tower. ....	299
Figure – 9.11: Radial profile of gas mass flow at different heights.....	300
Figure – 9.12: Residence time of particles in the cylindrical region. ....	301
Figure – 9.13: Residence time of particles in the conical region of the tower.....	303
Figure – 9.14: Solution algorithm for zonal modelling. ....	304
Figure – 9.15: Gas temperature profile along the dimensionless tower height in different zones using ZM 1 approach. ....	306
Figure – 9.16: Gas temperature profile along the dimensionless tower height in different zones using ZM 2 approach. ....	306
Figure – 9.17: Particle exit temperature obtained from different models.....	308
Figure – 9.18: Exit normalised moisture content of particles. ....	309
Figure – 9.19: Particles residence times obtained from different models.....	310
Figure – A1.1.1: Overall mass balance on an element of unit volume in a spray tower.....	344
Figure – A1.4.1: Energy balance on a single droplet/particle.....	350
Figure – A1.7.1: Momentum balance on a single droplet/particle.....	357

Figure – A2.2.1: Measured and corrected gas temperatures inside the spray drying tower..... 363

## List of Tables

Table – 2.1: A typical size distribution of a detergent powder (Masters, 1985).....	24
Table – 3.1: Detergent slurry composition (Griffith <i>et al.</i> , 2008).....	40
Table – 5.1: Input operating conditions for Base Case (Martin de Juan, 2011). ....	106
Table – 5.2: Discrete droplet size distribution .....	107
Table – 5.3: Solution dependency on the number of increments for Base Case.....	108
Table – 5.4: Solution dependency on the number of discrete droplet sizes.....	109
Table – 5.5: Comparison of simulation results and pilot-plant data. ....	122
Table – 5.6: Input operating conditions (Martin de Juan, 2012).....	126
Table – 5.7: Solution dependency on the number of increments.....	127
Table – 5.8: Solution dependency on the number of discrete sizes. ....	128
Table – 5.9: Surface drying time and residence time of different particle sizes.....	135
Table – 5.10: Simulation results and measured data.....	136
Table – 6.1: Under relaxation factors.....	140
Table – 6.2: Boundary conditions used in isothermal simulation cases. ....	140
Table – 6.3: Meshes used for grid independency test. ....	142
Table – 6.4: Under relaxation factors used with the RST turbulence model .....	150
Table – 6.5: Spray tower operating conditions for non-isothermal run (without slurry spray by Martin de Juan, 2012).....	178
Table – 6.6: Wall conditions for the calculation of heat loss.....	179
Table – 6.7: Boundary Conditions used in the simulation of Case 1 to 4.....	182
Table – 6.8: Heat flux calculated using the first method .....	192
Table – 6.9: Heat losses calculated using the second method .....	194
Table – 6.10: A comparison of measured (Martin de Juan, 2012) and predicted exhaust gas temperatures.....	199
Table – 6.11: Spray drying tower operating conditions under non-isothermal condition (Ahmadian, 2013). ....	200
Table – 7.1: Input parameters for studying particle flow under isothermal (constant temperature with no heat and mass transfer) condition. ....	205
Table – 7.2: Summary of modelling conditions in the CFD simulation cases.....	220
Table – 7.3: Specified composition of drying gas at the inlet of the spray tower.....	221
Table – 7.4: Initial and boundary condition specifications (Martin de Juan, 2011). ....	224
Table – 7.5: The under-relaxation factors used in the simulation and the level of residuals specified and at converged solution.....	225
Table – 7.6: Mass balance on the discrete phase. ....	228

Table – 7.7: Overall enthalpy balance. ....	229
Table – 7.8: Comparison of simulation results with experiment. ....	248
Table – 7.9: Mass balance on the discrete phase. ....	249
Table – 7.10: Comparison of simulation results with experiment. ....	254
Table – 7.11: Comparison of CFD simulation results with experimental data. ....	265
Table – 8.1: Input operating conditions for two nozzle configuration (Martin de Juan, 2012). ....	270
Table – 8.2: Mass balance on the discrete phase for CFD simulations. ....	275
Table – 8.3: Simulation results and experimental measurements. ....	288
Table – 9.1: Residence time of particles in the cylindrical region of the tower. ....	301
Table – 9.2: Residence time of particles in the conical region of the tower. ....	302
Table – 9.3: Average results from the CFD, zonal and plug-flow models. ....	311
Table – A2.1.1: Data used for calculation of corrected gas temperature at inlet gas duct. ....	359
Table – A2.2.2: Data used for calculation of corrected gas temperature at exhaust gas duct. ....	362

## Nomenclature

$A$	surface area	$m^2$
$B$	empirical constant for log-law of the wall	
$B'$	transfer number	
$C_D$	drag coefficient	
$C_{v,s}$	surface vapour concentration	$kg/m^3$
$C_{v,sat}$	saturated vapour concentration	$kg/m^3$
$C_{v,\infty}$	vapour concentration in the bulk	$kg/m^3$
$C_L$	empirical constant for discrete random walk model	
$C_{l,s}$	moisture concentration at the surface	$kg/m^3$
$C_{l,i}$	initial moisture concentration	$kg/m^3$
$C_\mu$	turbulence model constant	
$C_{\varepsilon 1}$	turbulence model constant	
$C_r$	restitution coefficient	
$C_s$	roughness constant	
$c_p$	specific heat	$J/kgK$
$d$	diameter	$m$
$d_m$	size constant	$m$
$d_w$	normal distance to wall	$m$
$d_{32}$	Sauter mean diameter	$m$
$D_{AW}$	diffusion coefficient of water into the air	$m^2/s$
$D_H$	hydraulic diameter	$m$
$D_R$	drying rate	$kg/s$
$D_{WS}$	diffusion coefficient of water in the slurry	$m^2/s$
$D_{T,i}$	thermal diffusion coefficient	$m^2/s$
$D_{\phi,m}$	mass diffusion coefficient	$m^2/s$
$E$	empirical constant for log-law of the wall	
$\Delta E_v$	correction factor for apparent activation energy	$J/kmol$
$\Delta E_{v,\infty}$	equilibrium activation energy	$J/kmol$
$\vec{F}$	source term for momentum transfer	$kg/m^2s^2$

$\vec{F}_a$	buoyancy force	N
$\vec{F}_b$	body force	N
$\vec{F}_d$	drag force	N
$\vec{F}_N$	normal contact force	N
$g$	acceleration due to gravity	$\text{m}^2/\text{s}$
$G$	mass flux	$\text{kg}/\text{m}^2\text{s}$
$G_k$	mean velocity gradients generated turbulence kinetic energy	$\text{kg}/\text{ms}^3$
$h_1, h_2$	height of roughness at first, second impact	
$h_g$	gas specific enthalpy	J/kg
$h_p$	droplet/particle specific enthalpy	J/kg
$h_{fg}$	latent heat of vapourisation of moisture	J/kg
$H$	specific humidity	
$I_t$	turbulence intensity	%
$\bar{J}_\phi$	diffusion flux	$\text{kg}/\text{m}^2\text{s}$
$k$	turbulence kinetic energy	$\text{m}^2/\text{s}^2$
$k_c$	mass transfer coefficient	m/s
$k_s^+$	dimensionless sand grain roughness height	
$k_s$	sand grain roughness height	m
$K$	partition coefficient	
$l_s$	length between two successive roughness heights	m
$l$	eddy length scale	m
$\dot{m}'_p$	mass flow of parcel	kg/s
$\dot{m}_p$	mass flow of a droplet/particle in a parcel	kg/s
$m_i$	mass flux based on tower cross-sectional area	$\text{kg}/\text{m}^2\text{s}$
$M$	mass	kg
$\dot{M}$	mass flow	kg/s
$M_w$	molecular weight	g/mol
N	number of moles	
$\hat{N}_D$	mass flux in the first stage of drying	$\text{kg}/\text{m}^2\text{s}$
$N_D$	mass flux in the second stage of drying	$\text{kg}/\text{m}^2\text{s}$

$n$	number per unit time	1/s
$n_i, n_j, n_k$	components of unit vector normal to the wall	
$p$	pressure	Pa
$Pr_t$	turbulent Prandtl number	
$\dot{Q}_{slurry}$	measured slurry volumetric flow rate	m <sup>3</sup> /s
$\dot{Q}$	heat loss	W
$\dot{q}$	heat flux	W/m <sup>2</sup>
$R$	radius of column	m
$R_\varepsilon$	additional term in turbulence dissipation rate for swirl modification	kg/m <sup>2</sup> s <sup>4</sup>
$R_g$	gas constant	J/molK
$r$	radius	m
$r_c$	air core radius	m
$r_o$	nozzle orifice radius	m
$\bar{S}_m$	continuity equation source term	kg/m <sup>3</sup> s
$\bar{S}_\phi$	energy transport equation source term	kg/m <sup>3</sup> s
$S_{rp}$	surface area of an irregular particle	m <sup>2</sup>
$S_{sp}$	surface area of a sphere	m <sup>2</sup>
$Sc_t$	turbulent Schmidt number	
$t$	time	s
$t_{sd}$	surface drying time	s
$T$	temperature	K
$\tilde{T}$	mass weighted average temperature	K
$T^*$	dimensionless near-wall temperature	
$T_L$	eddy interaction time	s
$u$	velocity	m/s
$u_s$	distribution parameter	
$\bar{u}_i, \bar{u}_j$	mean velocity components	m/s
$\tilde{u}$	velocity at the inlet of a control volume	m/s
$u'$	fluctuating velocity component	m/s
$u_\tau$	friction velocity	m/s

$U$	overall heat transfer coefficient	$\text{W/m}^2\text{K}$
$\bar{U}$	mean velocity	$\text{m/s}$
$U_{ref}$	reference velocity	$\text{m/s}$
$\bar{U}_c$	mean velocity magnitude at $y^* = y_T^*$	$\text{m/s}$
$V$	volume	$\text{m}^3$
$w_c$	critical moisture fraction	
$w_{eq}$	equilibrium moisture fraction	
$w_l$	moisture fraction	
$\tilde{w}_i$	mass weighted average moisture fraction	
$x_i, x_j$	coordinate axis	
$y$	distance from wall	$\text{m}$
$y^* / y^+$	dimensionless distance from wall	
$y_T^*$	thermal sub-layer thickness	
$Y_i$	mole fraction	
$Y_d$	cumulative weight fraction oversize	
$z$	vertical distance	$\text{m}$
$Z$	total tower height	$\text{m}$
<b>Greek Letters</b>		
$\alpha$	heat transfer coefficient	$\text{W/m}^2\text{K}$
$\alpha_s$	swirl constant	
$\varepsilon$	turbulence dissipation rate	$\text{m}^2/\text{s}^3$
$\varepsilon_{ij}$	turbulence dissipation rate tensor	$\text{m}^2/\text{s}^4$
$\varepsilon_m$	emissivity	
$\rho$	density	$\text{kg/m}^3$
$\eta_{overall}$	overall adiabatic thermal efficiency	
$\kappa$	von Kármán constant (=0.4187)	
$\tau_p$	particle response time	$\text{s}$
$\tau_F$	fluid response time	$\text{s}$
$\tau_w$	wall shear stress	$\text{Pa}$
$\lambda$	thermal conductivity	$\text{W/mK}$
$\mu$	viscosity	$\text{kg/ms}$

$\mu_t$	turbulence viscosity	kg/ms
$\delta$	thickness	m
$\sigma$	Stefan-Boltzmann constant	W/m <sup>2</sup> K <sup>4</sup>
$\sigma_k$	turbulent Prandtl number for $k$ equation	
$\sigma_\varepsilon$	turbulent Prandtl number for $\varepsilon$ equation	
$\sigma_\omega$	turbulent Prandtl number for $\omega$ equation	
$\hat{\phi}$	characteristic moisture content	
$\phi$	mass fraction, gas enthalpy	
$\phi_s$	sphericity	
$\psi$	fractionality coefficient	
$\omega$	specific turbulence dissipation rate	m <sup>2</sup> /s <sup>3</sup>
$\theta$	angle	degree
$\theta_{wp}$	particle-wall impact angle	degree
$\theta_{pi}$	particle inclination angle	degree
$\theta_{pr}$	particle rebound angle	degree
$\Omega_{ij}$	mean rate of rotation tensor	1/s
$\Omega$	swirl number	
$\zeta$	normal/Gaussian distributed random number	
$\zeta'$	uniformly distributed random number	

## Subscripts

<i>amb</i>	ambient
<i>boil</i>	boiling
<i>cell</i>	of the computational cell
<i>cg</i>	cold gas
<i>corr</i>	corrected
<i>D</i>	of the tower
<i>dep</i>	of the deposit
<i>drop</i>	of the droplet
<i>eff</i>	effective
<i>gas</i>	of the drying gas
<i>init</i>	initial value
<i>in</i>	inlet value

<i>ins</i>	of the insulation
<i>l</i>	of the liquid
<i>out</i>	outlet value
<i>p</i>	of the droplet/particle
<i>pore</i>	of the pore
<i>r</i>	in the radial direction
<i>rad</i>	radiation
<i>ref</i>	reference
<i>s</i>	of the solid
<i>sat</i>	at saturation
<i>slurry</i>	of the slurry
<i>solid</i>	of the solid
<i>term</i>	terminal
<i>vap</i>	of the vapours
<i>w</i>	of the wall
<i>water</i>	of water
<i>x</i>	axial component
<i>z</i>	in the z direction
$\theta$	tangential component
<i>0</i>	at the tower top
<i>Z</i>	at the tower bottom

## Dimensionless Constants

Nu	$\text{Nu} = \frac{\alpha d_p}{\lambda_{gas}}$	Nusselt number
Pe	$\text{Pe} = \frac{Lu}{D_{WS}}$	Peclet number
Pr	$\text{Pr} = \frac{\mu_{gas} c_{p, gas}}{\lambda_{gas}}$	Prandtl number
Re	$\text{Re} = \frac{\rho_{gas} d_p  u_p - u_{gas} }{\mu_{gas}}$	Reynolds number
Sc	$\text{Sc} = \frac{\mu_{gas}}{\rho_{gas} D_{AW}}$	Schmidt number
Sh	$\text{Sh} = \frac{k_c d_p}{D_{AW}}$	Sherwood number

St	$St = \frac{\tau_p}{\tau_F}$	Stokes number
----	------------------------------	---------------

## **Abbreviations**

3D	Three Dimensional
CDC	Characteristic Drying Curve
CFD	Computational Fluid Dynamics
CSTR	Continuous Stirred Tank Reactor
DEM	Discrete Element Method
FOU	First Order Upwind
IPP	Integrated Pilot-Plant
LAS	Linear Alkyl Sulfonate
LES	Large Eddy Simulation
LDA	Laser Doppler Anemometry
LRR	Launder, Reece and Rhodi (linear pressure strain model)
P&G	Procter and Gamble
PISO	Pressure Implicit with Splitting of Operators
PIV	Particle Image Velocimetry
PRESTO	Pressure Staggering Option
PSD	Particle Size Distribution
QUICK	Quadratic Upstream Interpolation for Convective Kinetics
RANS	Reynolds Averaged Navier-Stokes
REA	Reaction Engineering Approach
RNG	Re-Normalisation Group
RST	Reynolds Stress Turbulence
RTD	Residence Time Distribution
SOU	Second Order Upwind
SSG	Speziale, Sarkar and Gatski (quadratic pressure-strain model)
SST	Shear Stress Transport
UDF	User-Defined Function
VLES	Very Large Eddy Simulation
ZM 1	Zonal Modelling Methodology 1
ZM 2	Zonal Modelling Methodology 2

# **1. INTRODUCTION**

## **1.1 Background and Motivation for Research**

Spray drying is one of the oldest and the most common unit operations used in the manufacture of food, chemical, pharmaceutical, household and personal care particulate products (Masters, 1972). The earliest patented spray dryer design dates back to 1914 (Masters, 1984). The commercial production of food and chemicals using the spray drying process started during the Second World War (Masters, 1972; Patel *et al.*, 2009; Cal and Sollohub, 2009). The process involves drying of a solution or slurry into dry particles by a hot gas. The hot gas is typically atmospheric air, heated to the required temperature. Spray drying is carried out in a spray drying tower, in which the feed is atomised into small droplets. The atomised droplets come in contact with a hot air flow and exchange heat, mass and momentum. Moisture leaves the droplets and solid particles are formed. It is applicable to drying of both heat sensitive as well as thermally stable products. The contact between the droplets/particles and a hot gas is either co-current or counter-current. The co-current spray drying towers are suitable for drying of heat sensitive materials such as food and pharmaceutical products. The counter-current spray drying towers are thermally more efficient than co-current towers as they are capable of utilising heat more efficiently due to the counter-current contact between the two phases (Masters, 1984). Counter-current spray drying towers are used for the manufacture of thermally stable products; the most common example is the detergent powder, which is the focus of this study. Spray drying is preferred over other drying unit operations (such as rotary dryers, fluidized bed dryers, spouted bed dryers, belt dryers, etc.) for producing dry powders of required characteristics due to its advantage of converting pumpable feed (solution/slurry) into a powder form in a single, continuous unit operation and the resulting particles are typically fairly spherical. Due to these advantages, spray drying is considered as one of the most important industrial drying system (Masters, 1984).

It is highly desirable to have optimised design parameters (such as the tower diameter and height, type of spray nozzle and angle of air inlet nozzles/swirl vane) and operating conditions (such as feed temperature, moisture content, pressure and mass flow, drying gas temperature and mass flow, and arrangement of nozzles for the case of multi-nozzle tower) in a spray drying tower for stable and efficient tower operation and to produce

powders of required characteristics such as bulk density, morphology, flowability, size distribution and moisture content. Despite being a prevalent drying technology, the design of spray drying towers and process optimisation rely heavily on the past operating experience of the operator and the experimental data from laboratory and pilot-scale plants (Marshall and Seltzer, 1950b; Masters, 1968, 1972; Bahu, 1992; Langrish and Fletcher, 2003; Xin, and Mujumdar, 2009). This is because of the complexity of the spray drying process as it involves simultaneous heat, mass and momentum transfer between billions of droplets/particles of a wide range of sizes and the drying gas with a complex, three-dimensional, turbulent and swirling flow pattern. Furthermore, coalescence of droplets, agglomeration and breakage of particles, droplets/particles deposition on the wall and re-entrainment of deposited material back into the gas flow makes the prediction of the spray dryer design and operating parameters even more challenging. A wide range of inter-dependent operating variables are involved in the spray drying process that can be varied to optimise the process (Oakley, 2004; Cal and Sollohub, 2009). These include drying gas temperature and flow rate, nozzle arrangement (in the case of multiple nozzles), feed temperature, flow rate and pressure and feed solid concentration. All of these affect the dried powder characteristics including powder size distribution, morphology, flowability, moisture content and bulk density. The performance of a spray dryer is stable only within a narrow range of operating variables (Nath and Satpathy, 1998; Zbicinski *et al.*, 2004). To study the influence of these operating variables on dried powder characteristics, laboratory and pilot-scale experimental trials are carried out and optimised operating parameters are determined. These experimental trials are expensive, time consuming and it is not possible to study the effect of major design modifications in the tower for optimum performance. The scale-up of spray drying towers is challenging and relies heavily on the experience of the designer (Masters, 1995). The use of dimensionless groups, in the scale-up is of limited use as it is not possible to ensure dynamic similarity between small and large drying chambers due to a wide range of length and velocity scales inside the spray dryer including chamber diameter, atomiser dimensions, droplet diameters and velocities of gas and droplets/particles (Arnason and Crowe, 1980; Oakley, 1994; Langrish, 2007).

Mathematical modelling of spray drying towers can reduce the design and process optimisation time and costs. The complexity of interacting transport processes in a spray drying tower, as mentioned above, poses challenges to spray drying modelling. Many of the modelling efforts made in the past used over-simplified assumptions (Parti and

Palancz, 1974; Katta and Gauvin, 1975; Gauvin *et al.*, 1975; Keey and Pham, 1976; Topar, 1980; Montazer-Rahmati and Ghafele-Bashi, 2007). These simple modelling approaches (mainly assuming plug-flow of the gas phase) ignored the interaction of the droplets/particles with complex aerodynamics of the drying gas, droplets/particles and wall interactions, and inter-particle interactions. Therefore, the existing simple models find limited use in the determination of optimum design and operating conditions.

In recent decades, the modelling of spray drying towers using Computational Fluid Dynamics (CFD) has gained attention. A number of studies have been published which have shown the potential of CFD in predicting the spray dryer performance by modelling the complex interactions between the droplets/particles with gas, inter-droplet/particle interactions and particle-wall interactions. However, the focus of these studies has been on the modelling of co-current spray drying towers. The CFD studies on the counter-current towers are scarce.

A study of the complex interactions between the droplets/particles with the drying gas and the droplet/particle-wall interactions along with the transport processes between the discrete phase (droplets/particles) and the continuous phase (drying gas) using CFD can improve our understanding of the spray drying processes in counter-current spray drying towers. This will result in a more efficient design and operation of such drying towers and improved product qualities. However, multi-phase CFD models have a disadvantage of being computationally expensive; therefore this approach is not yet feasible for routine use by industries to determine optimised parameters for spray drying operations. A simplified approach is required to model counter-current spray drying processes, capturing all the important features of the process that can have an impact on the predictability of the spray dried powder characteristics. The improved understanding of the spray drying process obtained via CFD simulations can be used to develop a numerical model using a simplified approach, capturing important processes occurring within the spray drying tower. Such a model can be used expediently for the determination of optimised operating parameters for an efficient spray drying operation and product quality improvement.

## **1.2 Aims and Objectives**

The overall aim of this project is to improve the understanding of the spray drying process for the manufacture of detergent powders in a counter-current spray drying tower using CFD modelling, thereby setting up a CFD modelling methodology for these

towers. Furthermore, to propose a methodology for the development of a numerical model using a simplified approach which can be used routinely to predict the performance of counter-current spray drying towers in a computationally efficient manner. The data collected by other researchers in a counter-current pilot-plant spray drying tower, called integrated pilot-plant (IPP), installed at Procter and Gamble (P&G) Research Centres in Newcastle, UK, is used for the validation of modelling results.

The CFD modelling of this IPP spray drying tower is carried out considering heat and mass transfer between the droplets/particles and the drying gas using an existing semi-empirical detergent slurry droplet drying model developed by Hecht (2012). In addition, the momentum coupling between the two phases and particle-wall interactions as well as heat losses from the spray drying tower are also studied using the CFD model. The experimental data, including input/output parameters from the pilot-plant spray tower as well as flow and temperature profiles collected from inside the tower by the P&G research team is used for validation of CFD modelling results. A simplified plug-flow approach is also used to develop a model which considers one-dimensional flow of the discrete phase and the drying gas coupled with heat, mass and particulate phase momentum transfer. This model is validated against the pilot-plant data (IPP tower in Newcastle) and also compared with CFD modelling results. The detailed information about the droplet drying kinetics in the spray drying tower obtained from the CFD modelling results is used to propose a simplified numerical modelling approach utilising the simplicity of the plug-flow model for capturing important processes in the spray tower. This can then be used to determine optimised operating conditions for the spray drying process in a computationally efficient manner.

The specific aims and objectives of the project are outlined below:

- (a) To develop a plug-flow model for a counter-current spray drying tower for quick estimation of the influence of operating parameters on the properties of spray dried powder and validate the modelling results with the experimental data obtained in the IPP spray drying tower.
- (b) To carry out CFD modelling of single-phase, isothermal turbulent swirling flows in the IPP tower to select a suitable mesh size, numerical discretisation scheme and turbulence model to reproduce the measured velocity profiles in the tower. It is important to have a good prediction of the gas flow profiles for a reliable estimation of dried powder characteristics.

- (c) To carry out single-phase non-isothermal CFD modelling of the spray drying tower to study the heat loss from the spray drying tower to the ambient and validate the temperature predictions with the experimental data.
- (d) To carry out multiphase CFD modelling of the spray drying tower considering heat, mass and momentum transfer between the gas and the discrete phase, droplet/particle wall interactions and heat loss from the tower to study the spray drying process for the manufacture of detergent powders.
- (e) Compare the results of the plug-flow and multiphase CFD model with experimental data using single nozzle slurry spray as well as two nozzles at two different heights.
- (f) Propose a simplified zonal modelling approach for predicting the performance of spray drying towers without requiring large computational resources. This will be based on the CFD and plug-flow modelling results.

### **1.3 Structure of the Thesis**

The contents of this thesis are outlined below:

In Chapter 2, a general spray drying process is described along with the description of the major components of the spray drying process operation. The advantages and disadvantages of the spray drying process are presented. The applications of spray drying in various industries are discussed with particular focus on the spray drying in the detergent manufacturing industry.

In Chapter 3, a review of existing models available for the prediction of the drying rate of the droplets in a spray drying process is presented. A literature review on the development that has been made in spray drying modelling is carried out.

In Chapter 4, the spray drying process in the IPP spray drying tower of P&G in Newcastle is described along with measurements and tests carried out by other researchers at P&G for dried powder characterisation. A brief description of the measurement of the data taken from inside the IPP tower (including gas velocity and temperature profiles) is given in this chapter. This data is used for validation of model predictions.

In Chapter 5, a plug-flow model of spray drying in a counter-current spray tower as well as the semi-empirical slurry droplet drying model (Hecht, 2012) used to predict the

droplet drying rate is described. The results of the plug-flow model are compared with the experimental data collected from the IPP tower.

In Chapter 6, single phase CFD simulations of the IPP spray drying tower is carried out to determine a suitable mesh size, numerical scheme and turbulence model for predicting the gas velocity profiles. The results are compared with the measured velocity profiles at various axial locations. The simulation is further extended by considering non-isothermal conditions with incorporated heat losses through the insulated tower wall. The predicted temperature profiles at different axial locations are compared with the experimental data.

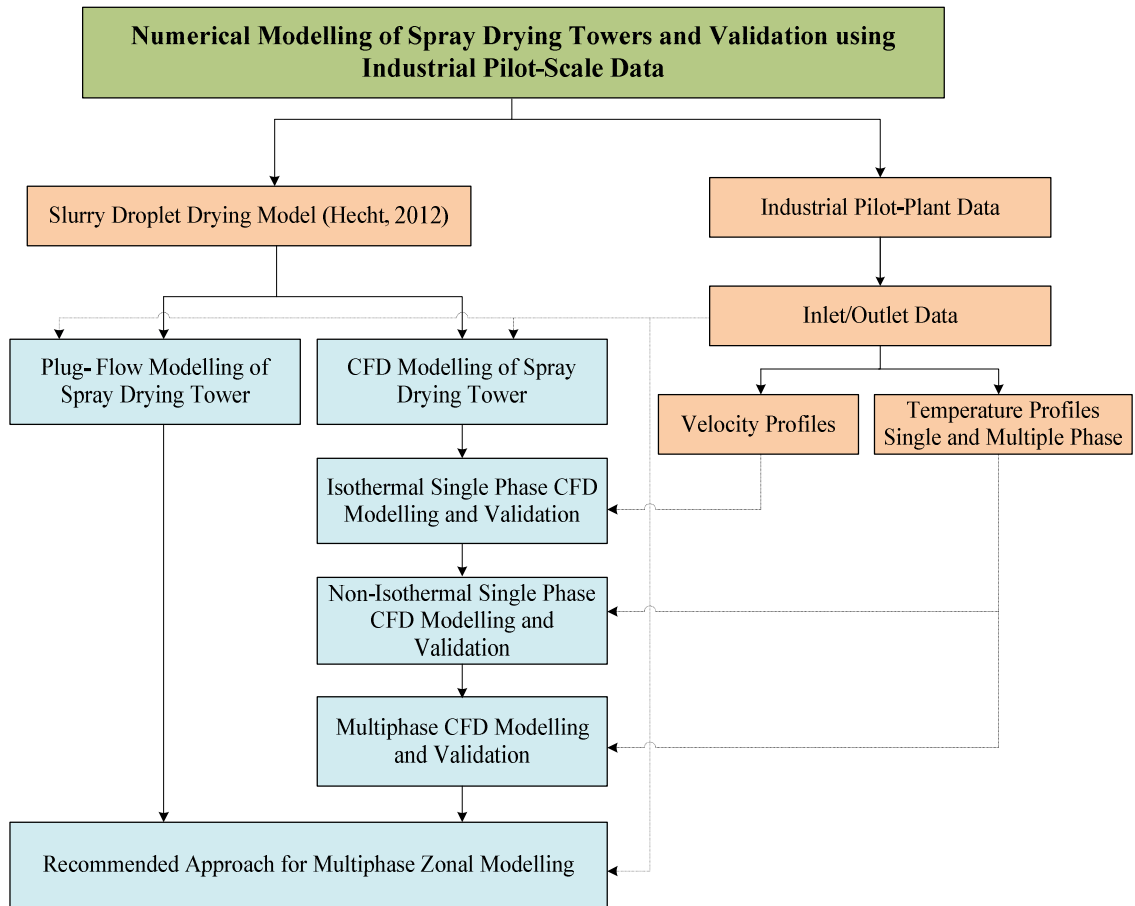
In Chapter 7, CFD modelling of the detergent spray drying process is carried out considering heat, mass and momentum transfer between the discrete (droplets/particles) and continuous (drying gas) phases. The slurry is sprayed using a single centrally located hollow-cone nozzle. The results of CFD model are compared with the experimental data including output data (powder temperature, powder moisture content and exhaust air temperature) and temperature profiles of gas phase inside the spray drying tower (where available) as well as with the plug-flow modelling results. The sensitivity of various parameters including initial droplet size distribution, droplet injection velocity, drag coefficient and particle-wall interaction on the simulation results is also studied.

In Chapter 8, the plug-flow and CFD approaches are applied to modelling of the spray drying process with slurry sprayed using two single, centrally located hollow-cone nozzles at different heights. The modelling results are validated with experimental data.

In Chapter 9, recommendations are made for dividing the tower into various zones (comprising plug-flow and CSTR) to develop a zonal model based on the CFD predicted gas flow pattern and droplet/particle trajectories.

Chapter 10 concludes the research work findings and recommendations are made for future work.

## 1.4 Thesis Map



## **2. SPRAY DRYING FUNDAMENTALS**

### **2.1 Spray Drying Process**

The process of spray drying can be divided into three distinct stages as shown schematically in Figure 2.1 (Masters, 1972). The first stage involves preparation of feed consisting of a solution or slurry in a mixer. It is then pumped to an atomiser, which atomises the solution or slurry into fine droplets inside a spray drying tower. In the second stage, the fine droplets come in contact with a hot gas stream flowing either co-current or counter-current to the droplets, the moisture in the droplets is evaporated and dried particles are formed. In the final stage, the dried powder is separated from the gas stream. This is typically done using a cyclone separator. The wet gas containing evaporated moisture is removed either from the system (open cycle operation) or it is recycled back to the dryer after scrubbing operation to remove the moisture (closed cycle operation). Closed cycle operation is typically used when it is required to prevent the contact of O<sub>2</sub> with the powder to avoid oxidation or when a flammable solvent system is involved; hence the drying gas in this case is not air. Open cycle operation is by far the most widely used configuration (Masters, 1985). Process steps involved in spray drying are depicted in Figure 2.1.

#### **2.1.1 Advantages and Disadvantages of Spray Drying**

Spray drying operation has the following advantages and disadvantages as listed by Masters (1985) and Marshall and Seltzer (1950a):

1. Certain product properties and quality attributes can be effectively controlled and varied by spray drying, including product density within a given range by varying the operating parameters. Particle size distribution can be frequently varied in a given range by varying the operating conditions.
2. Particle shape resulting from spray drying approximates a sphere either hollow or solid depending on feed properties and operating conditions.
3. It is frequently possible to preserve the quality of a product and prevent it from thermal degradation.
4. It is particularly suitable for large volume production as the cost per unit mass of product decreases with increasing product volume compared to other dryer types.
5. The material is dried in a single unit operation, thus reducing the cost of maintenance.

6. A wide range of dryer designs are available, with selection of a suitable dryer design, and product specification are readily met for drying both thermally stable and heat sensitive products.
7. Spray dryers can be designed to any individual capacity requirement.
8. Spray dryers can handle inflammable organic solvent-based feedstocks, powders which can potentially form explosive mixture, drying of toxic materials and drying of feedstocks that require handling in aseptic/hygienic conditions.

Despite these advantages, spray drying also has some disadvantages. Some of these are inherent in the spray drying operation while some are due to the lack of knowledge of the spray drying operation. The disadvantages of spray drying are listed below:

1. It involves a higher initial investment than other types of continuous dryers. Since the spray drying units are physically larger per unit mass of powder output than other types of dryers.
2. Spray drying towers have relatively poor thermal efficiency compared to other dryer types due to the large volume of the tower required to produce relatively smaller amount of product.
3. The exhaust gas from the spray dryer contains a large amount of low-grade waste heat and it is expensive to utilise this heat in a heat exchanger since the equipment must handle powder-laden air.
4. Spray drying towers have larger evaporative loads compared to other dryer types due to the requirement of pumpable liquid as feed.
5. Sometimes a low bulk density product is produced when a high bulk density product is required.
6. A spray dryer designed for fine powder production in general cannot produce coarse powder if required.

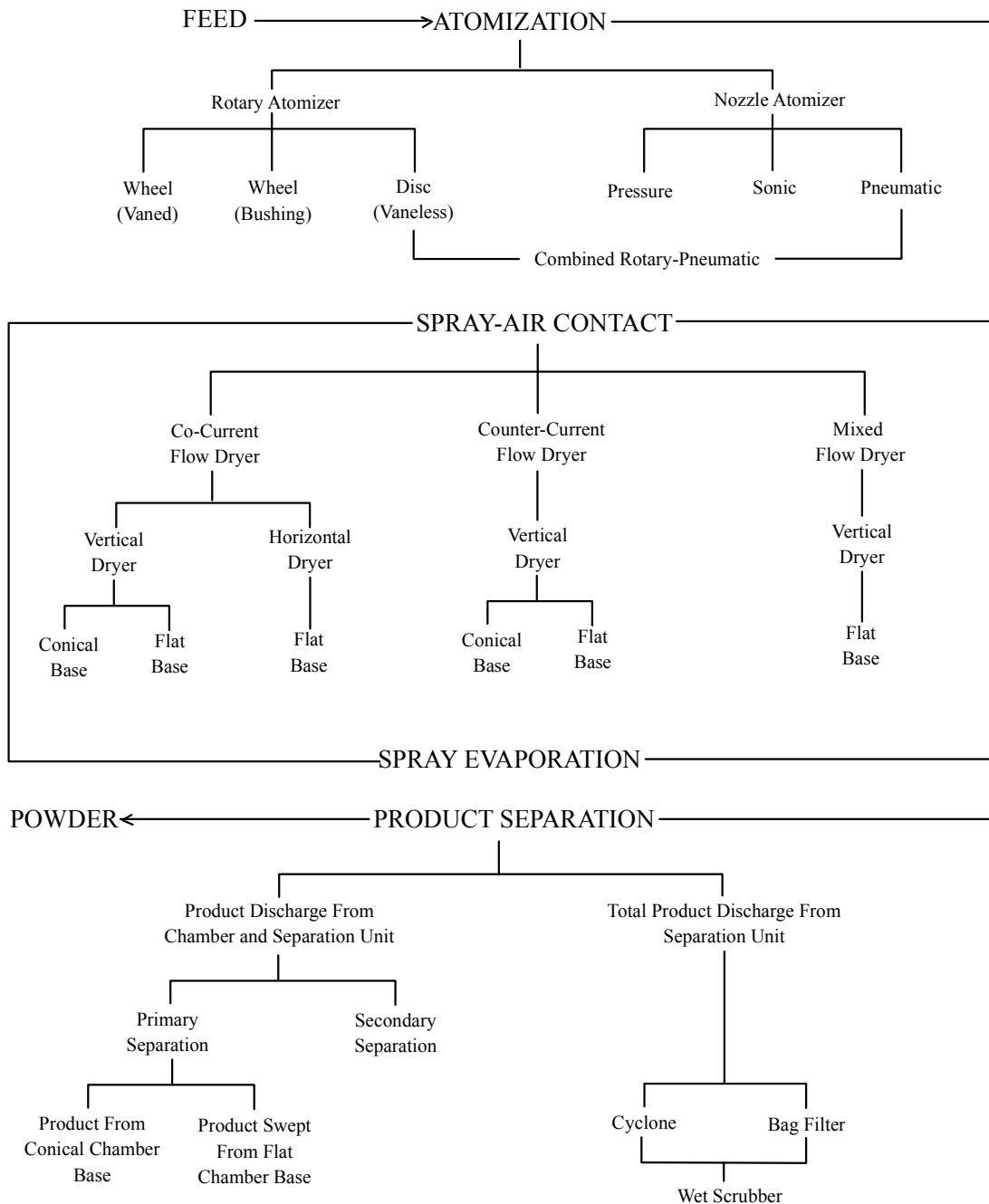


Figure – 2.1: Schematic of spray drying process shown in stages. (Adapted from Masters, 1972).

## 2.2 Atomisation

Atomisation is carried out inside the spray drying tower by means of an atomiser to convert a liquid or slurry feed into small droplets. The size distribution of the particles is controlled by the size distribution of the droplets produced in atomisation. The breakup of pumpable feed into small droplets requires energy. Atomisers used in spray drying towers include rotary nozzle (utilisation of centrifugal energy), pressure swirl nozzle (utilisation of pressure energy) and pneumatic (two-fluid) nozzle atomisers

(utilisation of kinetic energy). The choice of an atomiser is dependent on both the nature of feed, feed flow, type of spray tower and the required powder characteristics (Masters, 1985).

In a pressure swirl nozzle atomiser, the liquid is pumped into a swirl chamber at a high pressure and discharged through an orifice (Figure 2.2). The choice of an orifice size is dependent on the liquid flow and the required size distribution of the dried powder. To produce finer particles, a higher nozzle pressure is required. The most commonly used spray patterns in pressure nozzle atomisers are hollow cone and solid cone sprays (Figure 2.3). The hollow cone spray has an air-core at the centre of the orifice which is formed due to the tangential entry of the feed into the swirl chamber. This results in a hollow cone pattern of the spray droplets. In the solid-cone sprays, the droplets are distributed fairly uniformly throughout the spray. The size distribution in the hollow cone spray is more homogeneous compared to the solid cone spray (Masters, 1985).

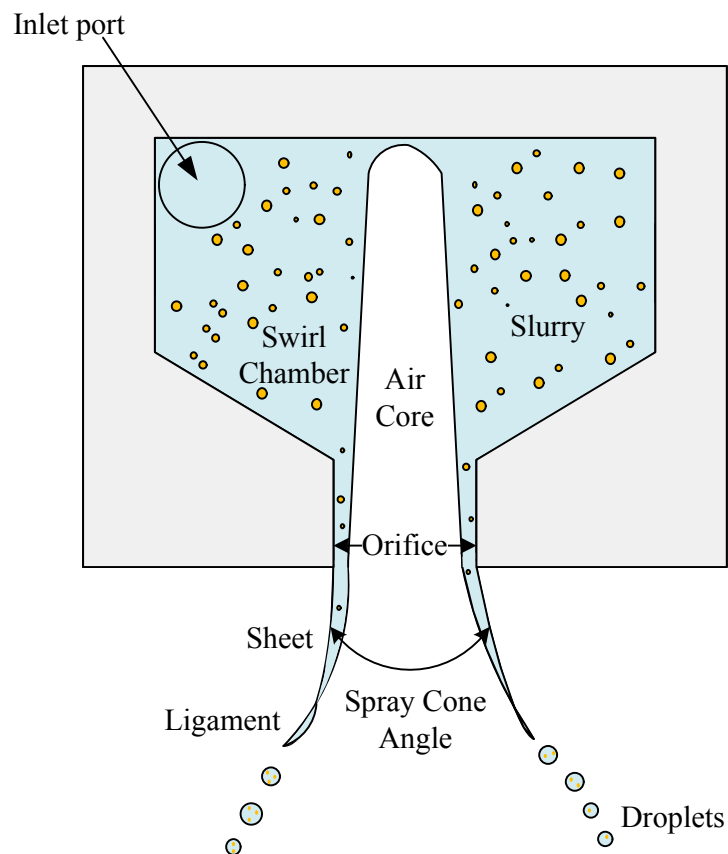


Figure – 2.2: Schematic of a pressure swirl nozzle atomiser.

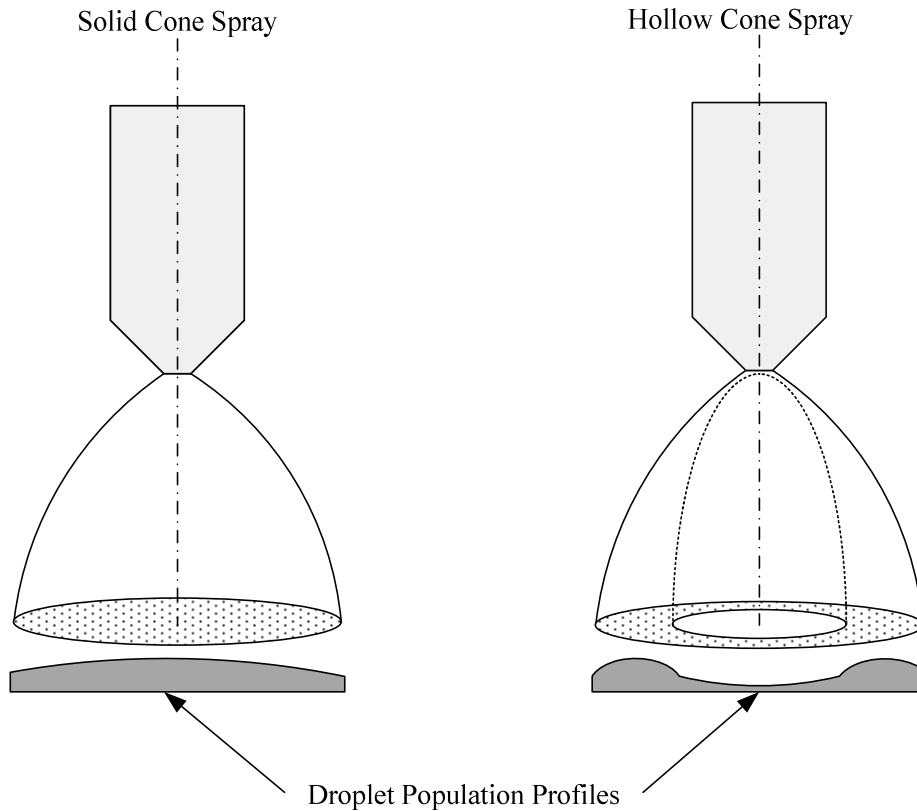


Figure – 2.3: Droplet population profiles in solid cone and hollow cone spray patterns.

Rotary atomisers are used to produce a fine to medium-coarse product. It is also called a rotary wheel or centrifugal atomiser. In a rotary atomiser, a spinning disc is used to accelerate the liquid or slurry feed to a high speed. The high relative speed between the liquid or slurry film and the surrounding air at the edge of the wheel causes the liquid to form small droplets. The liquid or slurry leaves the outer edge of the disc radially into the hot air stream as a flat cloud of droplets. The major factor affecting the particle size of the liquid or slurry droplets is the wheel tip speed. For finer particles, the centrifugal atomiser is spun at a high speed. A wide variety of spray characteristics can be obtained for a given feed by variation in feed rate, atomiser speed and design of atomiser. Rotary atomisers are capable of handling varying loads (Masters, 1972). A drawback of rotary atomiser is that it throws the droplets radially outwards, hence a larger chamber diameter is required to ensure that the droplets do not impinge on the wall (Oakley, 1997), hence it is not suitable for a drying chamber with a small diameter (typically in counter-current spray towers), it is also unsuitable for a highly viscous slurry feed. Figure 2.4 is a schematic of a rotary atomiser.

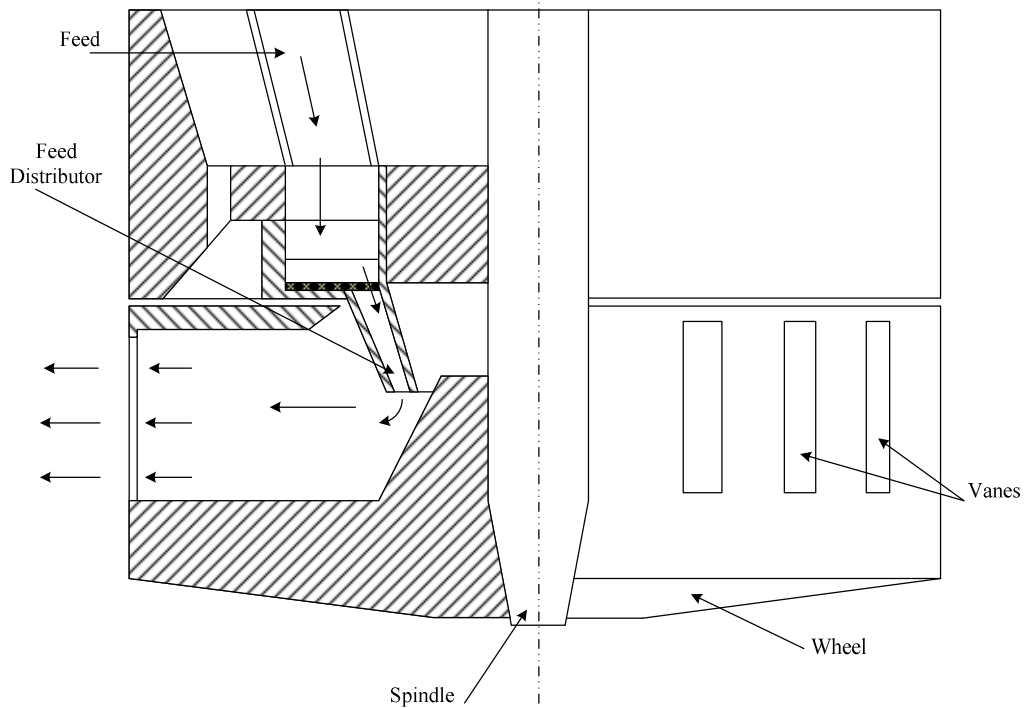


Figure – 2.4: Schematic of a rotary atomiser (adapted from Masters, 1985).

In two-fluid nozzle atomisers, the feed is impacted with high velocity air/gas, which creates high frictional forces over liquid surfaces causing liquid disintegration into spray droplets (Masters, 1985). Two-fluid nozzle atomisers are suitable for a low feed mass flow because at high liquid mass flow, the air/gas cannot penetrate the thick liquid jet and atomisation is incomplete, resulting in a wide range of droplet size distribution. Figure 2.5 is schematic of a two-fluid nozzle atomiser.

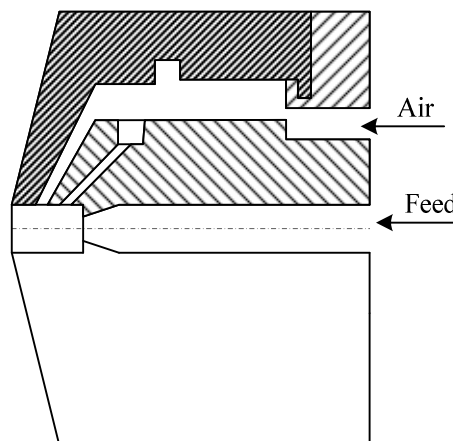


Figure – 2.5: Schematic of a two-fluid atomiser (adapted from Masters, 1985).

The Sauter mean droplet diameter is widely used to characterise the distribution of spray droplets, it is given by (Masters, 1985):

$$d_{32} = \frac{\sum_{j=1}^J n_j d_{p,i}^3}{\sum_{j=1}^J n_j d_{p,i}^2} \quad (2.1)$$

### 2.3 Types of Spray Dryers

With respect to contact between the droplets/particles and the hot gas, spray dryers are classified as co-current, counter-current and mixed-flow dryers. With respect to the height to diameter ratio, the spray drying towers are classified as short-form and tall-form. The short-form spray drying towers have a height to diameter ratio less than 3 (Masters, 1972). The choice of spray drying tower is based primarily on the properties of material being dried. Figure 2.6 is a schematic of co-current, counter-current and mixed flow dryers.

In co-current spray dryers (Figure 2.6 (a)), the feed and the gas flow in the same direction. They are suitable for heat sensitive products, e.g., in food and pharmaceutical industry. When feed is introduced into the drying tower, it contains a lot of moisture so the heat is utilised in evaporation of moisture from the droplets and prevents the droplets from getting exposed to high gas temperature. As the particles reach the bottom, the gas becomes much cooler as most of the heat of the gas has been given up at the top in evaporating the moisture. So a low temperature condition prevails at most of the tower height (Masters, 1972). This configuration enables particles to have a lower residence time which is important to ensure the stability of heat sensitive products. In these towers, typically, the gas is introduced from the top via a swirl vane that induces swirl in the gas flow inside the tower. The dried powder and drying gas both exit from the bottom of the tower and particles are typically separated from the exhaust gas using a cyclone separator. In these towers, short-form configuration is more common.

In counter-current spray dryers (Figure 2.6 (b)), the droplets enter the tower from the top, while the hot gas is introduced near the bottom exit of the tower. The atomised droplets come in contact with a relatively cold gas. Moisture evaporation from the droplets takes place and is soon transformed into wet particles as it goes down due to gravity. The particles at the bottom of spray tower come in contact with the hot gas. At this point, since most of the moisture from the particles is evaporated, it results in a

rapid rise in the temperature of the particles. Hence this configuration is suitable for thermally stable products like detergents and ceramics. The dried powder is collected from the bottom while the exhaust gas leaving the tower contains entrained fine powder, which is typically separated using a cyclone separator. This configuration offers better heat utilisation compared to co-current spray dryers and enables particles to have a maximum residence time (Masters, 1972). In counter-current spray drying towers, the gas is typically introduced via multiple inlet nozzles at the bottom of the tower. These can be inclined tangentially, which imparts swirl to the gas flow (Masters, 1985). The counter-current spray drying towers are typically tall-form.

In the mixed-type configuration (Figure 2.6 (c)), the particles moving upwards through the drying chamber exhibit both co-current and counter-current flow to the hot gas. The spray nozzle is located at the bottom (hence the slurry is sprayed in the upward direction) while the gas enters the tower from the top. The droplets first come in counter-current contact with the hot gas. The particles soon start moving downward due to gravity and become co-current with the gas. The dried powder leaves with the exhaust gas and is typically separated using a cyclone separator. This configuration offers maximum residence time for a given tower height. This type of spray dryer configuration is suitable for thermally stable products (Masters, 1972). The use of co-current and counter-current spray drying towers is more common in industries compared to mixed-flow configuration.

The spray dryers can also have a fluid bed integrated into the chamber base to promote agglomeration, the powder is then discharged into an externally-mounted vibrated fluid bed for powder cooling. This type of arrangement is used for semi-instant skim milk. For dryers with a conical base at the bottom, vibrating fluidized beds are mounted outside the chamber base. In these types it is ensured that the powder leaving the tower base is sufficiently wet to promote agglomeration through self-adhesion of particles. The powder is discharged to a first fluidized bed for completion of drying and agglomeration and then onto a second fluidized bed for powder cooling (Masters, 1985).

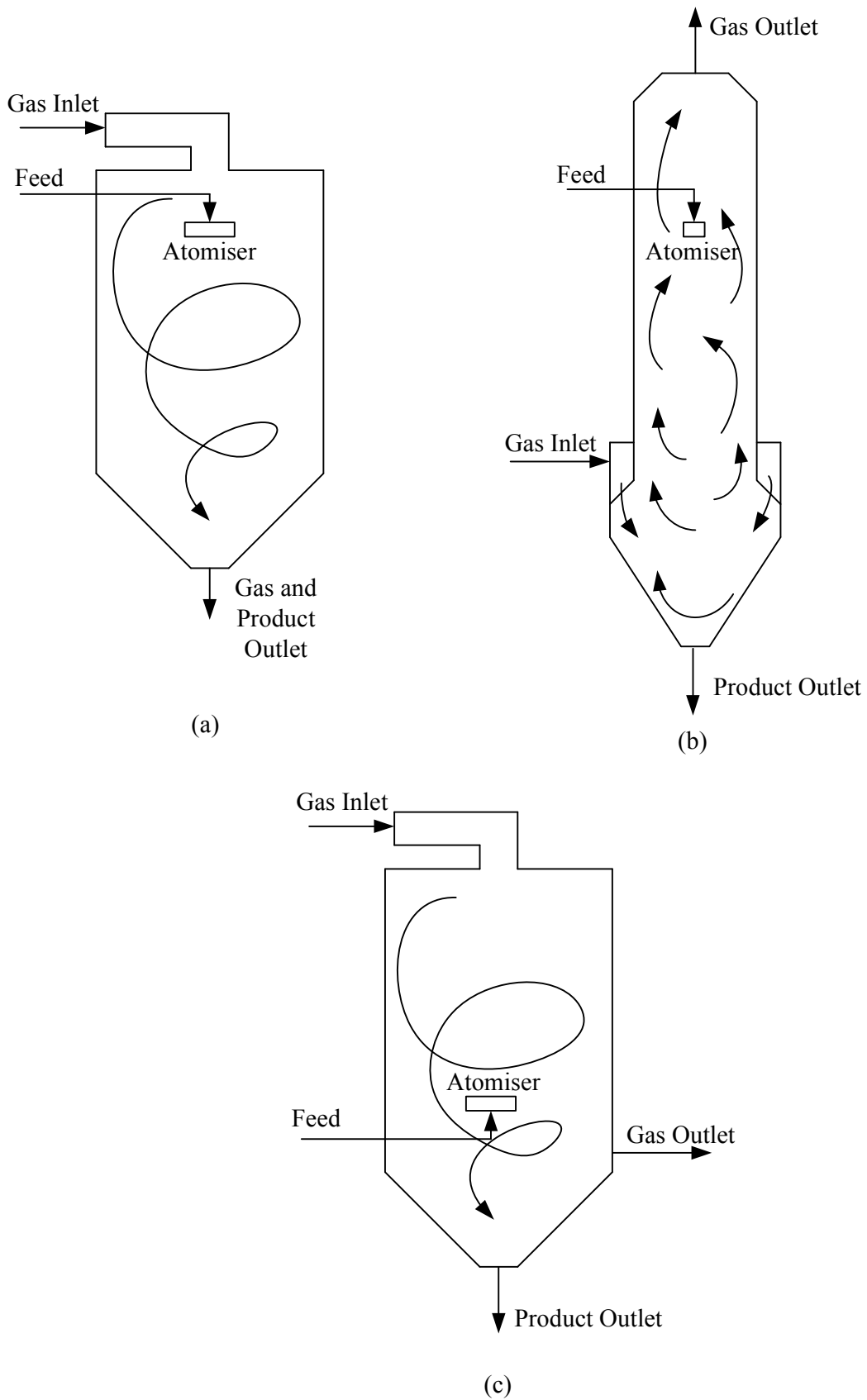


Figure – 2.6: Schematic diagrams of spray dryers: (a) Co-current flow; (b) Counter-current flow; (c) Mixed flow

## 2.4 Spray-Air Contact in Spray Drying Towers

In both co-current and counter-current spray drying towers, typically a swirl is induced in the gas to improve thermal efficiency of the spray tower. It also helps in stabilising the gas flow patterns which leads to steady tower operation and minimised deposition on the wall (Langrish and Zbicinski, 1994; Huntington, 2004; Fletcher *et al.*, 2003; Langrish and Fletcher, 2003; Wawrzyniak *et al.*, 2012a; Harvie *et al.*, 2001). However, in some cases, in both co-current and counter-current spray towers, the gas is introduced into the tower without swirl in which case, a high instability in the gas flow patterns has been reported (Southwell and Langrish, 2000; Wawrzyniak *et al.*, 2012a; Wawrzyniak *et al.*, 2012b).

In co-current spray drying towers with the swirling flow, the gas is typically introduced via a swirl vane at an angle that induces swirl in the gas flow inside the tower (Kieviet, 1997; Langrish *et al.*, 2004). The gas flow consists of a faster flowing central core surrounded by a slower recirculating gas flow due to sudden expansion of the gas in the drying tower. The intensity of the swirl depends on the angle of air inlet swirl vanes. If the vane angle is sufficiently large, then vortex breakdown (abrupt change in vortex structure) may also occur (Langrish *et al.* 1993; Kieviet, 1997), resulting in back mixing of the gas flow. The rotation of the rotary atomiser also induces swirl in the gas flow (Woo *et al.*, 2012) and it can be large enough to cause vortex breakdown. Studies on spray drying in co-current towers have shown that back mixing is generally avoided, because it results in dried particles coming in contact with the hot gas that promotes thermal degradation (Southwell and Langrish, 2001). Highly swirling flow in spray dryers also leads to greater deposition rate (Ozmen and Langrish, 2003, 2005). The co-current spray drying towers due to a larger diameter have fairly unstable gas flow patterns both with and without swirl, because there is a large unconstrained space for the drying gas jet to give time-dependent oscillations (Langrish and Fletcher, 2001; Lebarbier *et al.*, 2001). In co-current spray drying towers, smaller particles typically have shorter residence time because these particles remain in the faster moving gas core in the central region of the tower due to smaller momentum, while the larger particles are able to reach closer to the wall where the gas velocity is relatively smaller (Fletcher *et al.*, 2003; Saleh, 2010).

In counter-current spray drying towers, the gas enters via a number of tangential-entry inlet nozzles at the bottom of the tower that imparts swirl to the gas flow (Place *et al.*,

1959; Harvie *et al.*, 2001; Sharma, 1990; Bayly *et al.*, 2004). Due to restricted space (height to diameter ratio greater than 3), the central core flow is stable, resulting in a steady gas flow (Fletcher *et al.*, 2003). In counter-current spray drying towers, the back mixing resulting from the vortex breakdown is desirable as it improves the thermal efficiency of the spray tower operation because it reduces the temperature gradient along the tower axis and increases the contact time of the particles with the drying gas. Smaller particles in counter-current towers, as they fall down and move counter-current to the gas flow, have greater residence time compared to larger particles, because smaller particles exhibit greater influence of drag force due to smaller momentum. Since smaller particles have a larger residence time and greater heat and mass transfer coefficients, these particles may lose all free moisture before they exit the tower and may get exposed to high inlet gas temperature which may result in thermal degradation. Previous experimental and CFD modelling studies of gas flow patterns in counter-current spray drying towers are reviewed in Section 3.14 and 3.15, respectively.

## **2.5 Wall Deposition in Spray Dryers**

Wall deposition is the particle build-up on the walls of the spray dryers due to the adhesion of particles on initially clean walls. Subsequent layers of particles eventually become attached to the wall during the operation (Langrish and Fletcher, 2001; Langrish, 2007). The primary adhesive forces responsible for wall deposition are liquid bridge forces, which depend on the composition of the feed (Booyani *et al.*, 2004), Van der Waals forces and electrostatic forces. Some materials also exhibit sticky nature under a certain range of temperature called sticky point temperature. On the other hand, particles may be removed by the gas flow past the wall. The primary forces responsible for re-entrainment of the particles are the drag force, the lift force and the impact force (Hanus and Langrish, 2007). The shear stress created from the gas flow past the wall will also contribute to re-entrainment of the particles, eventually a dynamic equilibrium is established between the deposited and the re-entrained particles (Masuda and Matsusaka, 1997). Kieviet (1997) noted that wall deposition plays a major role in determining the residence time of particles in co-current spray drying towers. Wall deposition should be avoided as the deposited material may eventually dry, overheat and degrade before falling and mixing with the dried powder, thus affecting the dried product quality (Harvie *et al.* 2001). A thick layer of deposits on the wall may also change the air flow profiles which would affect the spray dryer performance. Wall deposition is promoted by highly unsteady gas flow pattern in co-current spray drying

towers (Fletcher *et al.*, 2003; Langrish and Fletcher, 2003). This unsteady flow pattern may also promote wall deposition in counter-current spray dryers (Wawrzyniak *et al.*, 2012a). Counter-current spray towers exhibit considerable wall build-up (Marshall and Seltzer, 1950b), which may be due to the fact that these towers typically have high degree of swirl in the gas flow which allows particles to move close to the wall and have more frequent particle-wall collision and promoting deposition. The counter-current spray towers are also typically tall-form, i.e., having more restricted space compared to co-current towers adding more possibility of particle-wall collision resulting in deposition. Wall deposition may also occur during start-up and shutdown when the system is out of equilibrium (Huntington, 2004).

The effect of wall surface properties including surface roughness, wall temperature, surface energy and dielectric properties on wall deposition were experimentally studied by Woo *et al.* (2008b). It was found that a surface with a higher roughness produced a larger deposition flux. Higher temperatures tend to promote deposition on the wall, lower surface energy material tends to inhibit deposition and dielectric material tends to promote deposition on the wall. The study showed that in addition to the material being spray dried, the wall surface properties can also influence deposition on the wall.

In a study carried out by Hassal (2011), the characteristics of the deposits on the wall were studied in the IPP spray drying tower, which is used for CFD modelling in this study. The deposits were a maximum close to the spray nozzle due to the particles being more wet at this location. The deposits were a minimum close to the drying gas inlets because as the particles become dry the tendency to stick to the wall decreases, the higher velocity in the bottom region due to higher gas temperature also hampered the deposition of particles. Typically, 2.5-9% of the material was deposited on the wall. Various parameters influencing the deposition rate were also studied including initial slurry moisture content, slurry composition, dried powder moisture content, size distribution of dried powder, and dried powder outlet temperature. It was found that an increase in initial slurry moisture content and the amount of surfactant in the slurry increased the deposition rate. The deposition rate was also found to be greater when the dried powder had a greater final moisture content, a higher mean particle size and a lower powder outlet temperature.

The deposits on the wall also pose safety issues as the deposited material may be exposed to a high temperature for a prolonged period of time that may result in

combustion, causing a fire inside the spray drying tower. Therefore the spray drying tower needs to be inspected for material build-up on the wall and cleaned periodically, which requires shutting down the plant, which contributes to the production costs (Masters, 1985). It is therefore highly desirable to have minimised deposition rate in a spray drying operation for a safe, efficient and stable operation.

## **2.6 Thermal Efficiency of Spray Dryers**

It is desirable to have spray dryers operated at the highest possible thermal efficiency. The thermal efficiency of spray dryers can be represented in terms of an overall adiabatic thermal efficiency defined as the fraction of total heat supplied to the dryer used in evaporation process. It can be approximated using the following relation (Masters, 1985):

$$\eta_{overall} = \left( \frac{T_{gas,in} - T_{gas,out}}{T_{gas,in} - T_{amb}} \right) \times 100 \quad (2.2)$$

Spray dryers, like other industrial dryers, consume large amounts of energy, typically 3-20 GJ per tonne of water evaporated (Baker and McKenzie, 2005) and are often operated inefficiently (Al-Mansour *et al.*, 2011). Baker and McKenzie (2005) analysed 32 industrial spray dryers in the UK chemical, food and ceramic industries using their adiabatic dryer model and estimated that around 29% of the energy supplied to these dryers was wasted. The thermal efficiency of spray dryers decreases with decreasing capacity of dryers. Spray dryers with a capacity of <1 t/h typically consume 4-5 times more energy in evaporating a unit mass of moisture (Baker and McKenzie, 2005). A thermally efficient spray drying operation can reduce the operating cost by reducing fuel consumption and become more environmentally friendly. The thermal efficiency can be improved by minimising heat losses to the surroundings. From equation (2.1), it can be realised that the thermal efficiency of spray dryers can be increased by increasing the temperature of the drying gas and by operating the dryer at a minimum possible exhaust gas temperature. However, this would also require operating the drying tower at a higher feed rate, which can lead to more wall deposition (Masters, 1985). Operating the spray tower at higher inlet gas temperature may also make the product more susceptible to thermal degradation and increase the heat loss from the tower.

## **2.7 Applications of Spray Drying Process**

The process of spray drying is used in a wide range of industries including food, household and personal care products and pharmaceutical. It can be designed to fit any required capacity ranging from a few kilograms per hour to tens of tonnes per hour. The feed can be in the form of slurry, solution, paste or melt. Despite its disadvantage of having a low thermal efficiency because a large volumetric flow of air is required for drying relatively smaller amount of feed, it is considered as an ideal unit operation for drying and particle formation due to unique product characteristics (Mujumdar, 1987). Spray drying process offers a fair degree of precision and control over characteristics of the product like bulk density, particle size, volatile retention and residual solvent. It combines drying and particle formation in a single, continuous, unit operation. Applications of spray drying process include detergent, ceramic, pesticide, fertilizer, dyestuff, pigment, milk products, fruits, vegetables, egg products, fish products, antibiotics, enzymes, vaccines, plasma and many others (Masters, 1985). Recently, spray drying has been used to produce nanoparticles in laboratory scale equipment (Arpagaus, 2012; Khan *et al.*, 2012).

The main drivers for developments in spray drying technology include (Masters, 2004):

- (i) Reduction of excessive undesirable deposition of powder on the tower wall.
- (ii) Meeting changing market requirements regarding powder specifications.
- (iii) Reduction in the cost of production of powder.
- (iv) Meeting the ever more stringent health, safety and environmental protection constraints.

### **2.7.1 Spray Drying in the Food Industry**

Spray drying is used for drying and particle formation of food products including milk, beverages, flavouring compounds, fruits, vegetables, corn products, sugar products and wheat gluten. Food products are heat sensitive, so spray drying of food products is generally carried out in the co-current spray dryers. In the spray drying of food products, flavour and aroma retention is of primary importance. It is also required that drying does not affect the nutritional content of food. To prevent the loss of flavours and aroma, most of the food products are dried with edible gums plus carbohydrate that form a solid edible film at the surface of the particle on the formation of solid shell during drying (Masters, 1972). The deposition of particles on the wall is highly

undesirable as this may lead to unhygienic conditions resulting from microbial growth in the deposits (Masters and Masters, 2006).

### **2.7.2 Spray Drying in the Pharmaceutical Industry**

Spray drying technology is widely applied in pharmaceutical field. Spray dried products in the pharmaceutical industry include antibiotics, enzymes, yeasts, vaccines and plasma. In pharmaceutical products, narrow particle size distribution, good flowability, low friability, improved compressibility, low bulk density, high solubility and reduced moisture content is important. Most of these products are high value compounds and are produced in small quantities. Therefore, in selecting a spray dryer type, energy conservation is of secondary importance (Mujumdar, 1987). The particle size of spray dried products is very small for tablet production; hence spray drying is typically followed by granulation.

### **2.7.3 Spray Drying in the Detergent Industry**

Detergent powder is one of the best know examples of spray dried products (Marshall and Seltzer, 1950a; Masters, 1985; Oakley, 1997). The commercial production of spray-dried detergent powders started in the early 1930s (Chaloud *et al.*, 1957; Huntington, 2004). Since then, although a number of other products forms have been introduced including tablets, liquid detergents, gels and pouches, but the detergent powders continue to dominate the laundry market (Rahse and Dicoi, 2001). Detergent powders offer significant advantages over the other forms of detergents as they contain relatively larger proportions of inorganic materials, such as water hardness removers, alkalinity sources and bleaches, which tend to be cheaper. Owing to their low moisture content, it is easier to include a range of more complex materials such as bleach and enzymes and keep them stable for a longer period of time. Additionally, the powdered form also has an advantage of being consistent in formulation, while in the liquid forms, phase separation can occur (Bayly *et al.*, 2009).

The global soap and detergent manufacturing industry includes about 700 companies with a combined annual revenue of over £10 billion, with Procter and Gamble, Unilever and Dial among the detergent manufacturing companies having the major market share (First research, 2008). The laundry detergent accounts for 40% of this revenue. In order to maintain this market share, the large companies are faced by competition to produce cheaper detergent powder with improved quality. This requires continuous

improvement in the product formulation and efficient production via spray drying without compromising operational health and safety, and environmental protection regulations.

For the manufacture of detergent powder, counter-current spray drying towers are preferred (Masters, 1985; Oakley, 1997). The counter-current spray drying towers have an advantage of being more thermally efficient compared to co-current spray drying towers. The key quality measures of the spray dried detergent powder include: bulk density, particle size distribution and moisture content (Huntington, 2004).

## **2.8 Detergent Powder Characteristics**

### **2.8.1 Bulk Density**

The bulk density is an important powder characteristic as many of the detergent packing operations use volume fill rather than weight fill. The consumer also measures the detergent powder in terms of volume for use in washing machine. The bulk density of detergent powder is typically maintained in the range of 350 to 900 kg/m<sup>3</sup> (Bayly, 2013). The bulk density of the spray dried powder is influenced by the extent of inflation of the particles due to expansion of air and moisture vapour inside the particle during drying (termed as puffing). Thus the amount of air introduced into the slurry before atomisation is the primary controlling factor. The operating conditions inside the tower also facilitate the extent of puffing. Typically, an increase in drying gas inlet temperature and gas flow result in lower bulk density powder (Chu *et al.*, 1951; Chaloud *et al.*, 1957). The initial slurry composition also influences the bulk density of the dried powder (NIIR, 2013). Detergent powder shows a marked increase in bulk density with increase in feed solid concentration (Marshall and Seltzer, 1950b). An increase in feed temperature also tends to increase the bulk density (Marshall and Seltzer, 1950b).

### **2.8.2 Particle Size Distribution**

Particle size distribution is an important characteristic of the detergent powder. Powder size must not be too coarse that it is slow in dissolution and must not be too fine to give a dusty appearance (Huntington, 2004). Powder size distribution also influences its flowability (Walton and Mumford, 1999a). A typical size distribution of a detergent powder is listed in Table 2.1.

Table – 2.1: A typical size distribution of a detergent powder (Masters, 1985).

Size Range ( $\mu\text{m}$ )	Weight (%)
>1500 $\mu\text{m}$	2-3%
>500 $\mu\text{m}$	10-20%
>250 $\mu\text{m}$	50-75%
>120 $\mu\text{m}$	85-90%
>60 $\mu\text{m}$	95-100%

The size distribution of the dried powder is mainly a result of the degree of agglomeration in the spray drying tower. This is dictated primarily by the gas temperature in the atomisation zone, which is controlled by varying the distance from hot gas inlets (Piatowski and Zbicinski, 2007). A high gas temperature in the atomisation zone inhibits the agglomeration. Hence the mean particle size in this case is smaller (Piatowski and Zbicinski, 2007). Furthermore, the spray angle and the initial injection velocity and size distribution of the droplets are also important in influencing the final powder size distribution (Langrish and Zbicinski, 1994).

### 2.8.3 Moisture Content

The final moisture content of the dried powder should be such that it forms a free flowing powder. If the moisture in the dried powder is high, then the powder may form a cake, which will cause difficulty in handling. Very low moisture content in the spray dried powder is also avoided as the moisture-free powder may get over-heated upon exposure to a high gas temperature at the bottom. This over-heating may cause thermal degradation of the surfactant which affects the performance of detergent powder. Typically, an increase in the air temperature and the air flow result in a more dried powder. Powder packing, bulk density and colour density of the powder is also affected by dried powder moisture content (Walton, 2000).

### 2.8.4 Powder Flowability

It is required that the spray dried powder should be free flowing to avoid issues in handling and packing of the powder. Powder flowability is influenced by particle size, size distribution, shape, moisture content and hygroscopic nature of powder (Walton and Mumford, 1999a).

### **3. LITERATURE REVIEW**

#### **3.1 Introduction**

In this chapter a literature review of single droplet drying models used for modelling drying kinetics is presented followed by a review of various approaches used in the modelling of spray drying towers. Experimental investigation of counter-current spray drying towers and Computational Fluid Dynamics (CFD) work carried out for the modelling of counter-current spray drying towers is also presented.

#### **3.2 Theory of Drying**

Drying is the removal of moisture from a body to yield a dry solid. During drying, energy is transferred from the heating source which evaporates the moisture (Mujumdar, 1987). Materials containing moisture can be classified as hygroscopic and non-hygroscopic. The moisture in a hygroscopic material is present in two forms: bound moisture and unbound moisture (Masters, 1985). The bound moisture exerts an equilibrium vapour pressure less than pure water at the same temperature (see Figure 3.1). Examples of bound moisture include water contained in very small capillaries in a porous solid, adsorbed at the surface or chemically combined with the solids. Unbound moisture includes water that is in excess of the bound moisture. Unbound moisture exerts an equilibrium vapour pressure equal to that of pure water at the same temperature. In a non-hygroscopic material, all water is present as unbound moisture (Masters, 1985). Examples of hygroscopic materials include salts, metal oxides and many polymers. Examples of non-hygroscopic materials include crushed stones, plastic pellets, etc. (Keey, 1978).

The drying of solids is divided into two periods, namely the constant rate period and the falling rate period. In the constant rate period, all the unbound moisture from the material is removed and the drying rate proceeds at a fairly constant rate. In this stage, the partial pressure of vapour at the surface is equal to the saturation vapour pressure. The first stage of drying continues as long as the rate of diffusion of moisture to the surface maintains saturated conditions at the surface. Once all the unbound moisture has been removed, the partial pressure of vapour at the surface falls and the drying rate decreases, this is called the falling rate period. The moisture content at which transformation from the constant rate period to the falling rate period occurs is termed

as the critical moisture content. The drying continues to take place in the falling rate period until the equilibrium moisture content is reached. The equilibrium moisture is the moisture which is in equilibrium with the partial pressure of water vapour of the surroundings.

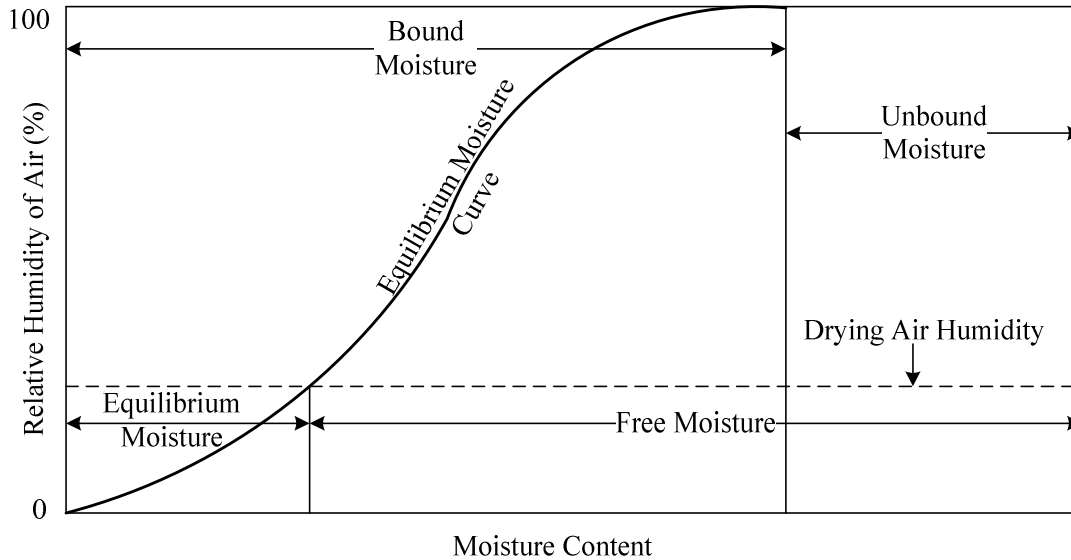


Figure – 3.1: Equilibrium moisture curve (Adapted from Masters, 1985).

### 3.3 Droplet Drying in Spray Drying Towers

The drying of droplets in spray drying towers involves simultaneous heat, mass and momentum transfer. When the droplets are injected from the atomiser, the droplets come in contact with the drying gas, and heat is transferred from the gas to the droplet via convection. The heat transferred to the droplet is converted to latent heat during moisture evaporation. The velocity of the droplets leaving the atomiser is significantly greater than the surrounding gas, hence the momentum transfer between the droplets and the drying gas also take place. Figure 3.2 is a plot of typical temperature profile of a droplet containing dissolved/suspended solids. Due to the evaporation of moisture from the droplet surface, the temperature of the droplet reaches the wet bulb temperature (A-B in Figure 3.2), and once the droplet is at the wet bulb temperature, the drying proceeds at a nearly constant rate and the temperature of the droplet remains fairly constant (B-C in Figure 3.2). There will be a slight increase in the temperature of droplets containing dissolved solids (B-C' in Figure 3.2), as the presence of dissolved solids will lower the vapour pressure and hence the mass transfer rate, causing the droplet temperature to rise above the wet bulb temperature. Due to the evaporation of moisture, the droplet surface is soon covered by a layer of solids and the droplet is

transformed into a particle. The moisture content at which the droplet transformation to a particle takes place is called the critical moisture content.

Once the critical moisture content is reached, the drying rate falls as the moisture removal from the surface is limited by the diffusion of moisture from the inside of the particle to the surface (Masters, 1985). Due to the reduced drying rate, most of the heat transported to the droplet from the gas contributes to increasing the temperature of the particle and the particle temperature rises rapidly (C-D in Figure 3.2). If the drying gas temperature is greater than the boiling point of the moisture, the vapourisation of moisture will take place at the boiling point. At this point, all heat will be used up in vaporisation of moisture from the particle and the particle temperature will remain at the boiling point. There will be an increase in the boiling point due to the presence of solids (D-E in Figure 3.2). Once all the free moisture has been removed, the temperature of the particle will again begin to rise as heat transferred to the dried particle results in changing the particle temperature (E-F in Figure 3.2), the rise in particle temperature continues until it reaches the drying gas temperature.

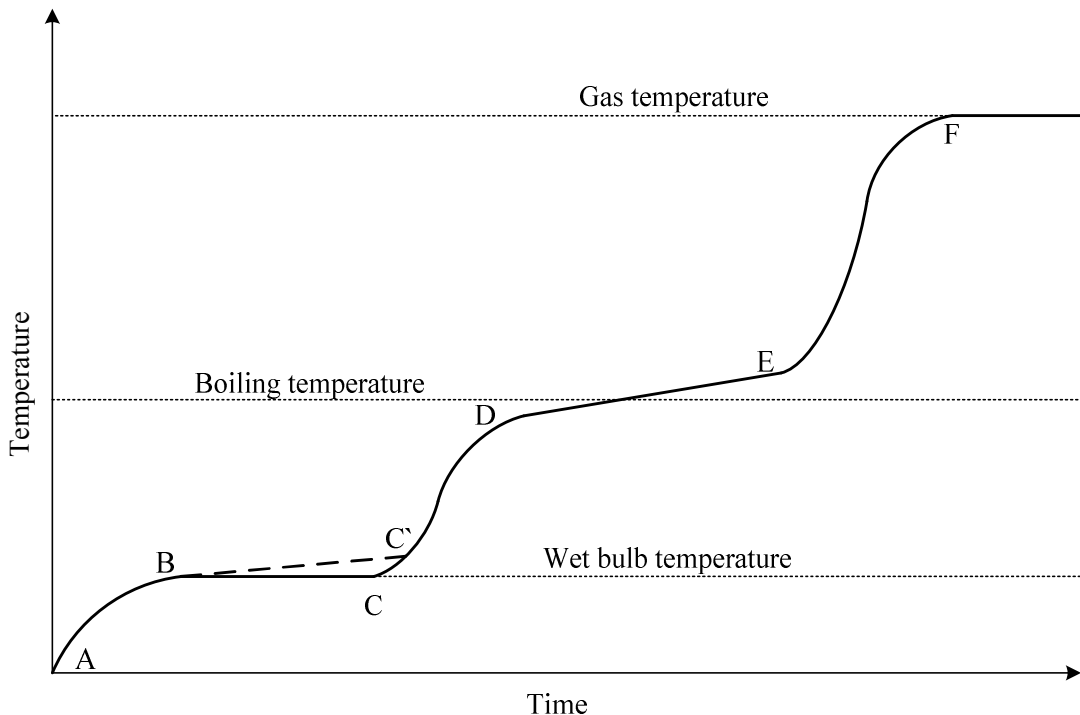


Figure – 3.2: Typical droplet drying temperature curve in a spray dryer (Adapted from Handscomb *et al.*, 2009a).

### 3.4 Single Droplet Drying

The modelling of spray drying towers requires information about the drying kinetics of a single droplet. The complexity of the spray drying process makes it impracticable to study heat, mass and momentum transfer from individual droplets in a spray drying tower. Therefore, single droplet drying experiments are used. The single droplet drying experiments provide useful information about the drying kinetics and morphological changes that occur during drying. In a single droplet drying experiment, the droplet is suspended in a flowing stream of drying gas using either a filament or it is levitated in a gas stream. The gas stream is typically atmospheric air, heated using a heater. The resulting changes in size and shape are monitored along with the temperature and concentration of the exit gas stream. Many researchers (Ranz and Marshall, 1952; Charlesworth and Marshall, 1960; Trommelen and Crosby, 1970; Sano and Keey, 1982; Furuta *et al.*, 1983; Cheong *et al.*, 1986; Nešić and Vodnik, 1991; Hassan and Mumford, 1993; Sunkel and King, 1993; Yamamoto and Sano, 1994; Hecht and King, 2000a; Lin and Gentry, 2003; Lin and Chen, 2002, 2004; Chen and Lin, 2005; Al-Mubarak *et al.*, 2010) have studied the drying behaviour of a single droplet experimentally, among which Ranz and Marshall (1952) were one of the first to investigate the drying of a droplet containing dissolved and suspended solids. The droplet of about 1 mm diameter was suspended from a filament in a hot air stream and the rate of heat and mass transfer were recorded. For the droplets containing dissolved solids, they concluded that before the formation of a solid structure, the solvent evaporated at a constant rate and the solution was saturated throughout the droplet. The evaporation rate was less than that for a pure solvent. For the droplets containing suspended solids, the presence of solid particles did not lower the vapour pressure significantly; hence, the initial evaporation rate corresponded to that of pure solvent. After the formation of a solid structure, the falling rate period began and the temperature of the particle rose continually.

Based on the experimental data, the correlations for calculating Nusselt (Nu) and Sherwood (Sh) numbers were proposed by Ranz and Marshall (1952) (equation (3.1) and (3.2)), which were applicable to the droplet Reynolds number in the range of 0 to 1000, which covers the laminar (Stokes) and transition regimes for spherical bodies. For Prandtl and Schmidt numbers, the range of applicability is in between 0 to 250. The equations do not take into account the effect of sensible heat carried away by the

vapours diffusing out from the surface of the droplet/particles, which in high mass transfer rates may be significant. The droplets were suspended using a filament, but in the actual spray drying tower, the droplets may rotate, which may appreciably change the rates of heat and mass transfer. The droplets/particles are spherical, however, in spray drying towers, the particles may deform due to morphological changes during drying as well as due to agglomeration/breakage of the particles, which may also change the heat and mass transfer rates from the surface of the particle. Despite these simplifying assumptions, these correlations predict Nu and Sh numbers with a fairly good accuracy for a wide range of Re numbers and are widely used in calculating heat and mass transfer for evaporating droplets/particles (Masters, 1985):

$$\text{Nu} = 2.0 + 0.6 \text{Re}^{0.5} \text{Pr}^{1/3} \quad (3.1)$$

$$\text{Sh} = 2.0 + 0.6 \text{Re}^{0.5} \text{Sc}^{1/3} \quad (3.2)$$

Many researchers cited above have carried out further single droplet drying experiments for various solutions and slurry droplets. These experiments revealed that the drying behaviour depended strongly on the morphological development, which in turn depended primarily on the composition of the droplet. The droplet drying experiment work has led to the development of single droplet drying models.

The models of droplet drying have been categorised into the following by Mezhericher *et al.* (2010b):

1. Models based on the semi-empirical approach that utilise the concept of a characteristic drying curve (CDC) (Keey and Pham, 1976; Fyhr and Kemp, 1998; Langrish and Kockel, 2001; Harvie *et al.*, 2002; Jannot *et al.*, 2004; Huang *et al.* 2004b; Chen and Lin, 2005).
2. Drying models based on the reaction engineering approach (REA) (Chen and Xie, 1997; Chen *et al.*, 2001; Chen and Lin, 2004; 2005; Patel and Chen, 2005; Lin and Chen, 2006; 2007; Putranto and Chen, 2012).
3. Models that describe the process of drying by using the continuity, momentum, energy and species conservation equations called deterministic drying models (Audu and Jeffreys, 1975; Sano and Keey, 1982; Cheong *et al.*, 1986; Nešić and Vodnik, 1991; Elperin and Krasovitov, 1995; Hecht and King, 2000b; Kadja and

Bergeles, 2003; Farid, 2003; Mezhericher *et al.*, 2007, 2008a; Handscomb *et al.*, 2009b; Al-Mubarak *et al.*, 2010).

The semi-empirical CDC models have an advantage of being cheap in computational resources because they are represented by a small set of empirical equations. The temperature distribution inside the droplet/particle is ignored in these models (Biot number assumed to be small). The drying rate is typically divided into two periods, the constant rate period and the falling rate period. In the constant rate period, it is assumed that the resistance to mass transfer lies in the vapour boundary layer and the mass flux ( $\hat{N}_D$ ) is proportional to the difference in the concentration of moisture vapours at the droplet surface and in the bulk, which is given by:

$$\hat{N}_D = k_c(C_{v,s} - C_{v,\infty}) \quad (3.3)$$

The droplet diameter is allowed to decrease due to evaporation of moisture from the surface. The relative drying rate ( $f$ ) is then defined as:

$$f(\hat{\phi}) = \frac{N_D}{\hat{N}_D} \quad (3.4)$$

where  $N_D$  is the mass flux in the second stage of drying.  $f$  is a function of the characteristic moisture content ( $\hat{\phi}$ ), which is given by:

$$\hat{\phi} = \frac{w_l - w_{eq}}{w_c - w_{eq}} \quad (3.5)$$

where  $w_l$  is the particle moisture fraction,  $w_{eq}$  is the equilibrium moisture fraction and  $w_c$  is the critical moisture fraction. The critical moisture fraction is defined as the moisture fraction when a solid crust covers the surface of the particle and drying rate becomes dependent on the internal diffusion of moisture to the surface, resulting in the onset of the falling rate.

The mass flux in the second stage (falling rate) is then given by:

$$N_D = f(\hat{\phi})k_c(C_{v,s} - C_{v,\infty}) \quad (3.6)$$

$f$  is determined from the characteristic drying rate curve that characterises the drying rate of a given material. The value of  $f$  is 1 at the critical moisture content and becomes zero at the equilibrium moisture content.  $C_{v,s}$  is calculated by assuming that the droplet surface is saturated with water vapour. The characteristic drying rate curve is obtained from a droplet drying experiment. Figure 3.3 is a plot of a typical characteristic drying curve. The particle diameter is fixed during the falling rate period.

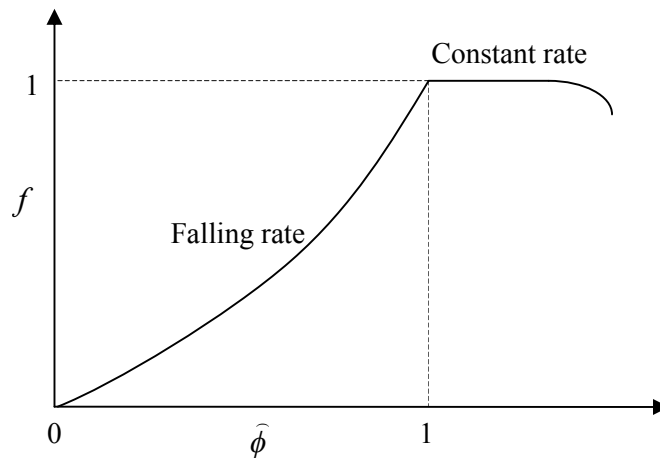


Figure – 3.3: Typical characteristic drying curve.

A limitation of this model is that it does not perform well in conditions different from those used in the experimental investigation (Fyhr and Kemp, 1998; Mezhericher *et al.*, 2010b). The critical moisture content is considered to be a constant. However, it may vary with the surrounding gas conditions encountered by the droplet. Initial droplet moisture content also influences the critical moisture content (Zbicinski and Li, 2006). In the droplet drying experiment, the suspended droplet size is typically greater than the droplet size distribution resulting from the atomiser, but the same critical moisture content is used for all droplet sizes. The critical moisture content may be different for different droplet sizes. Additionally, this approach cannot model the morphological changes that occur during particle drying.

In the REA approach, it is assumed that moisture evaporation is an activation process and requires overcoming an energy barrier. The REA models require a good knowledge of drying behaviour of the materials because the REA approach requires an empirical correlation connecting the partial vapour concentration over the droplet/particle surface

and the average moisture content. This empirical correlation is determined experimentally for each material whose drying behaviour is modelled at different moistures. The droplet/particle surface vapour concentration is related to the saturation water vapour concentration ( $C_{v,sat}$ ) as follows (Chen and Xie, 1997):

$$C_{v,s} = \psi C_{v,sat}(T_p) \quad (3.7)$$

where  $T_p$  is the droplet/particle temperature.

$\psi$  is a fractionality coefficient depending upon the moisture content at the interface. It is in effect, the relative humidity at the interface of the droplet/particle and the drying air.  $\psi$  is expressed as follows (Chen and Xie, 1997):

$$\psi = \frac{C_{v,s}}{C_{v,sat}} = \exp\left(-\frac{\Delta E_v}{R_g T_p}\right) \quad (3.8)$$

$\Delta E_v$  is a correction factor for the apparent activation energy for drying. Equation (3.8) approaches unity when the droplet surface is saturated with water vapour, hence  $\Delta E_v$  is zero in that case.  $\Delta E_v$  is given by:

$$\Delta E_v = -R_g T_p \ln\left(\frac{C_{v,s}}{C_{v,sat}}\right) \quad (3.9)$$

Combining equation (3.7), (3.8) and putting in equation (3.3) gives the required mass flux.

$$\hat{N} = k_c (C_{v,sat} \exp\left(-\frac{\Delta E_v}{R_g T_p}\right) - C_{v,\infty}) \quad (3.10)$$

The plot of  $\Delta E_v$  v/s moisture content is considered as the characteristic of a material being dried under the given conditions. For droplets under different drying conditions, a

characteristic functional relationship is obtained from the following equation (Chen and Xie, 1997):

$$\frac{\Delta E_v}{\Delta E_{v,\infty}} = f(w_l - w_{eq}) \quad (3.11)$$

where  $\Delta E_{v,\infty}$  is the equilibrium activation energy, which represents the maximum  $\Delta E_v$  at relative humidity and temperature of the drying gas.

The temperature distribution inside the droplet/particle is neglected. The advantage of this model is that it is relatively cheap in terms of computational resources and does not require the critical moisture content, which may vary with the operating conditions as well as the droplet size.

The REA modelling is a relatively new approach, applied mainly in predicting the drying rate of food products, and has demonstrated a better agreement with experimental data compared to the CDC model (Chen and Lin, 2004; Patel and Chen, 2005; Woo *et al.*, 2008a). Due to low computing requirement, the CDC and REA approaches have been used in the CFD models for studying drying kinetics of droplets in spray drying towers. In both the REA and CDC models, the agglomeration and deposition of particles on the wall must also be treated empirically since they depend on the surface concentration, which is not resolved in these models.

In the deterministic drying models, the drying of droplets containing dissolved or suspended solids has commonly been divided into two distinct stages. In the first stage, the liquid evaporates from the surface at a fairly constant rate. The size of the droplet reduces due to moisture evaporation. The second stage begins when a solid crust covers the surface of the droplet. The drying rate in this stage becomes entirely dependent on the internal diffusion of moisture to the surface. Hecht and King (2000b) introduced a third stage which occurs when the particle temperature reaches the boiling point of slurry. The drying rate in this stage is controlled by the rate of heat transfer to the particle. It should be noted that in spray drying particles with a wide range of morphologies can be produced which have been described by various phenomenological models (see review in Charlesworth and Marshall, 1960; Walton and Mumford, 1999b).

Two mechanisms of droplet drying process have been proposed for the development of deterministic drying models herein referred to as Type 1 and Type 2 models are given below:

1. Droplet with a dry solid crust (Audu and Jeffreys, 1975; Cheong *et al.*, 1986; Nešić and Vodnik, 1991; Elperin and Krasovtsov, 1995; Kadja and Bergeles, 2003; Farid, 2003; Dalmaz *et al.*, 2007; Mezhericher *et al.*, 2007, 2008a; Handscomb *et al.*, 2009b, Al-Mubarak *et al.*, 2010).
2. Droplet with a pliable crust and a bubble (Sano and Keey, 1982; Hecht and King, 2000b; Handscomb *et al.*, 2009b).

The modelling approaches based on these two mechanisms differ in the second stage of drying process. In the Type 1 model, it is assumed that a rigid porous crust is formed and the outer diameter of the particle remains constant. The evaporation only occurs at the interface between the crust and the wet core. The evaporated vapour then diffuses through the porous solid crust to its outer surface. The thickness of the crust increases as solid is deposited on the crust core interface due to evaporation of moisture (Figure 3.4a). The wet core continues to shrink until all the moisture is evaporated resulting in a dry porous particle as depicted in Figure 3.5a. In the Type 2 model (Figure 3.4b), after the formation of a pliable solid crust, the moisture diffuses to the outer surface of the particle from where it evaporates throughout the drying process. An increase in temperature of the particle causes vapourisation of solvent within the wet core. It is assumed that a single, centrally located saturated vapour bubble expands due to vapourisation of the solvent. This causes the particle to inflate. An arbitrary maximum particle size is specified in order to limit the expansion of the particle. The evaporation of the solvent takes place from the surface of the particle throughout the drying period (Figure 3.4b). This approach explains the formation of dry hollow particles (Figure 3.5b).

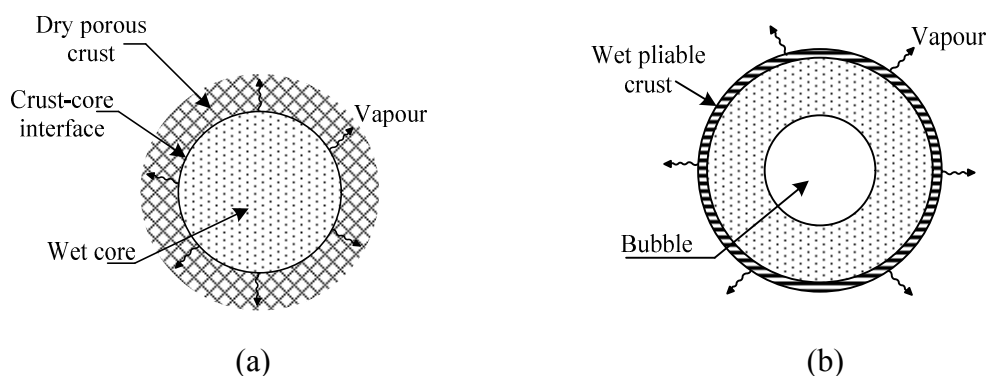


Figure – 3.4: Mechanisms of droplet drying in the second stage of drying process.

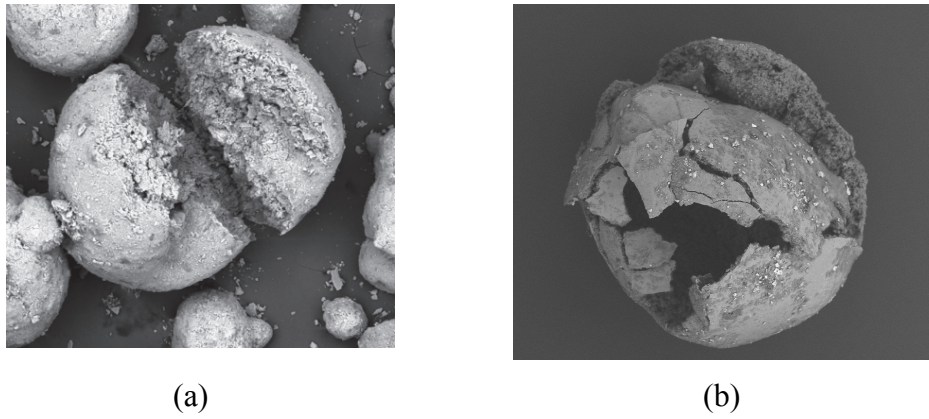


Figure – 3.5: Scanning electron microscope images of spray dried particles. (a): Porous ceramic particle (source: Effting *et al.*, 2010), (b): Hollow detergent particle (Martin de Juan, 2012).

In the deterministic drying models, the process of drying is represented by a set of differential equations with corresponding initial and boundary conditions. The solution of these equations is complicated because of reduction in diameter in the first stage of drying and the receding interface between the core and the solid crust in the second stage of droplet drying for Type 1 models and increase in particle diameter due to the bubble expansion in Type 2 models. These models have a disadvantage of being computationally expensive, but since the concentration gradient inside the particle is resolved in these models, therefore it is possible to model agglomeration and wall deposition based on the surface moisture content. The only three-dimensional CFD model reported in the literature which has utilised the Type 2 model for spray drying process is by Verdurmen (2004). In the Type 1 model however, since a dry porous crust is assumed (free from liquid moisture), therefore it may not be possible in the Type 1 model to predict agglomeration and deposition of particles on the wall after the formation of a solid crust.

The deterministic models require knowledge of many parameters like thermal diffusivity, mass diffusivity, particle porosity, critical moisture content etc. under different conditions of moisture and temperature, which are often difficult to find, hence experimental investigation is often required (Fyhr and Kemp, 1998; Mezhericher *et al.*, 2010b).

#### **3.4.1 Effect of High Mass Flux on Droplet/Particle Heat Transfer**

When the mass transfer rate from the surface of the droplet/particle to the bulk is large, then it can significantly alter the heat transfer coefficient, hence a modification to the

correlation used for Nu is required. A correction for Nusselt number ( $Nu_{corr}$ ) for high mass transfer rates was proposed by Spalding (1953), which is given by:

$$Nu_{corr}/Nu = 1/B' \ln(1+B') \quad (3.12)$$

where  $B'$  is the Spalding number (also called transfer number), which for the non-volatile, evaporating droplets/particles is given by:

$$B' = c_{p,vap} (T_{gas} - T_p)/h_{fg} \quad (3.13)$$

### 3.4.2 Effect of Radiation Heat Transfer

When the drying gas temperature is large, the effect of radiation may be significant. In that case, the effective heat transfer coefficient is given as:

$$\alpha_{eff} = \alpha + \alpha_{rad} \quad (3.14)$$

where

$\alpha$  is the convective heat transfer coefficient, calculated from equation (3.1)

$\alpha_{rad}$  is the radiative heat transfer coefficient, given by:

$$\alpha_{rad} = 4\sigma\epsilon_m T_p^3 \quad (3.15)$$

## 3.5 Particle Morphologies

Charlesworth and Marshall (1960) reported observations of different particle morphologies observed during single droplet drying experiments of different aqueous solutions under different initial solute concentrations and at different drying air temperatures. The different morphologies that occurred during drying and final appearance of the particles were dependent on the initial solute concentration, solution type and the drying air temperature. Walton and Mumford (1999b) carried out single droplet drying experiments to study particle morphology during drying of various solutions, slurries and colloidal suspensions by varying the initial solids/solute

concentration and temperature. The chemical and physical properties of the material being dried influenced its drying behaviour and physical properties. Three distinct types of dried particle morphologies were identified; they were defined structurally as skin forming, crystalline and agglomerate. Skin forming material is defined as a particle composed of a continuous non-liquid phase which is polymeric or sub-microcrystalline in nature (Walton, 2000). The nature of skin forming material allowed multiple cycles of inflation and collapse during drying. The ruptures on the skin surface occurred during inflation and collapse were quickly sealed. Final particle structure of these materials was either partially hollow with nearly spherical shape or a shrivelled and deformed structure depending on the nature of the material, feed concentration and drying temperature (see Figure 3.6 (a) and (b)). Materials which formed a skin-forming structure included sodium silicate solution, sodium dodecyl sulphate solution, semi-instant skimmed milk suspension, potassium nitrate solution, gelatine solution, yoghurt and co-dried egg/skimmed milk suspension. The commercially spray-dried skin forming materials show features such as particle inflation, particle collapse/shrivelling, blowholes and cratering, particles with cracks and fissures, vacuolation, particles which are hollow and particles which are solid with some vacuolation (Walton, 2000).

Crystalline material (Figure 3.6 (c) and (d)) is defined as a composition of large individual crystal nuclei bound together by a continuous microcrystalline phase (Walton, 2000). Materials which formed a crystalline structure included solutions of ammonium dihydrogen orthophosphate, sodium chloride, sodium carbonate, trisodium orthophosphate, zinc sulphate, sodium pyrophosphate, sodium benzoate, sodium formate and ethylenediaminetetra-acetic  $2\text{Na}^+$ . The crystal size and shape varied with the type of material being dried. Crystalline particles formed in commercial spray-drying process in contrast to skin forming materials exhibit only a limited range of morphological features, e.g., particles with cracks and fissures with occasional cratering, particles with blowholes and particles which are hollow (Walton, 2000).

Agglomerate solid morphology (Figure 3.6 (e) and (f)) is defined as a composition of individual grains of solids bound together by sub-micron solid particles (Walton, 2000). In this case, the dried particles exhibited a high degree of sphericity with either solid or hollow structure as the droplet containing suspended solids simply decreased in size until most of the bulk moisture has been removed (Walton and Mumford, 1999b). Particle blowholes and craters were uncommon in agglomerates. The wall structure was

thicker in a hollow agglomerate structure. Materials which formed an agglomerate structure included suspension of silica and colloidal carbon.

Particle morphologies produced from a combination of skin forming and crystalline materials are complex. A detergent particle is one of the examples of a multi-component mixture. The influence of level of feed aeration and drying temperature on the final particle morphology of detergent particles was studied by Walton and Mumford (1999b). All dried detergent particles showed a smooth surface with a highly porous interior. In some cases, the vacuoles were so large that the particle could be regarded as hollow despite a very little particle size inflation (less than 10%) was observed at various drying temperatures. A number of reasons can be responsible for hollow particle formation. According to Masters (1985), the following main reasons contribute to hollow particle formation:

- (i) Due to rapid formation of solid surface layer, semi-imperious to vapour flow causing puffing or ballooning of the particle due to the pressure of vapourised moisture trapped within the particle.
- (ii) Due to increased rate of moisture evaporation compared to the rate of diffusion of solids back into the core.
- (iii) The capillary action may draw liquid and solids to the surface, leaving void at the centre of the droplet.
- (iv) The entrainment of air in the feed or during atomisation can cause hollow particles during drying of a droplet.

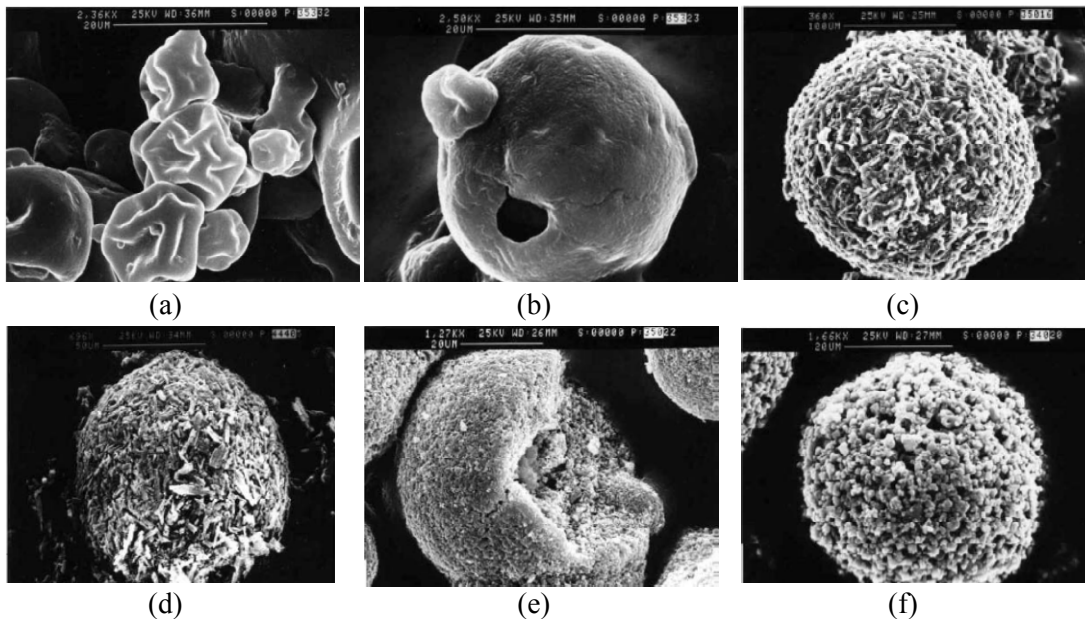


Figure – 3.6: Particles with different morphologies: (a): Co-dried egg and skim milk powder (skin forming structure), (b): Yoghurt powder (skin forming structure), (c):

Trisodium orthophosphate (crystalline structure), (d): Organic UV brightener (crystalline structure), (e): Lead Chromate (agglomerate structure), (f): Ferrite (agglomerate structure). (Source: Walton and Mumford, 1999a).

Dlouhy and Gauvin (1960) carried out experimental investigation in a co-current spray tower to study drying kinetics of various feed materials and found that the effect of operating variables on the properties of the spray-dried particles was dependent on the type of material being dried. For materials which formed crystalline structure, the effect of inlet air temperature on particle density was not so significant whereas for skin forming materials the effect of inlet air temperature showed pronounced effect on dried powder density. Figure 3.7 depicts some of the particle morphologies that may result from drying of droplets containing suspended or dissolved solids.

Theoretical explanation of the formation of dried particles of different morphologies is based on Peclet number ( $Pe$ ), defined as the ratio between the rate of advection and the rate of diffusion of solute. For low  $Pe$ , the diffusion motion of the solutes is fast compared to the receding droplet surface velocity. The droplet shrinks and the solutes migrate to the centre until a solid structure is formed at the surface. This results in formation of dense solid particles with fairly spherical shape (Vehring, 2008; Vicente *et al.*, 2013). For high  $Pe$ , the surface evaporation rate is faster and results in rapid formation of dried solid layer at the surface. In such case, the particles can be hollow, shrivelled or wrinkled (Vehring, 2008; Vicente *et al.*, 2013). Vicente *et al.* (2013) carried out experimental investigation to study the influence of initial droplet size, initial concentration of solute and drying gas temperature on dried particle morphology and it was concluded that the final particle morphology can be changed by varying these parameters to produce dried powder of required characteristics.

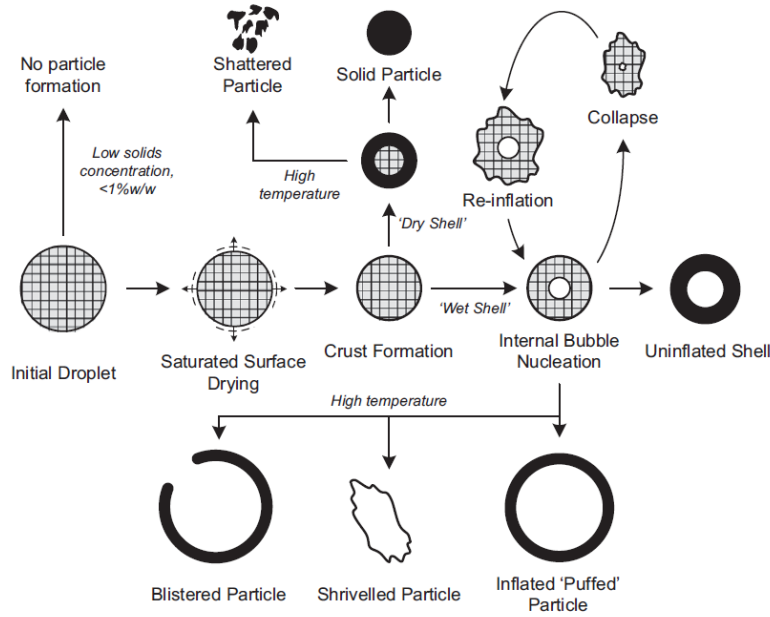


Figure – 3.7: Schematic of different particle morphologies resulting from spray drying  
(Source: Handscomb *et al.*, 2009a).

### 3.6 Detergent Slurry Composition

The morphological development and hence the drying behaviour and final powder characteristics depends on the composition of the slurry. From an operational point of view, it is advantageous to have as high initial solids concentration in the slurry as possible (Walton and Mumford, 1999a). A few percentage increase in the level of solids adds up to a significant economical benefit in the overall process of producing spray dried detergents (Bentley and Waddill, 1973). Detergent slurry typically contains a high solid concentration. The major detergent slurry components include surfactant, water and conditioning agents (water hardness removers and alkalinity sources). The exact composition of the detergent slurry is a commercially guarded secret. A typical detergent slurry composition is given by Griffith *et al.* (2008) and is listed in Table 3.1.

Table – 3.1: Detergent slurry composition (Griffith *et al.*, 2008).

Component	Weight %
Linear Alkyl Sulfonate (LAS)	9
Water	29
Acusol polymer	3
Sodium sulfate	35
Zeolite	24

Griffith (2008) reported that the detergent slurry comprises three phases, namely, the neat phase, the lye phase and the solid phase. The neat and lye phases form the continuous phase of the slurry. The composition of each phase is given in Figure 3.8 (Griffith, 2008):

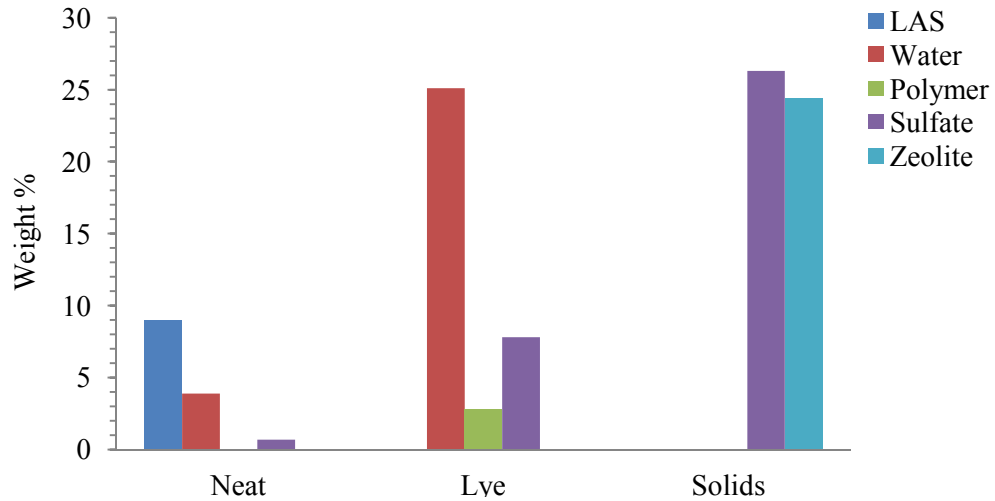


Figure – 3.8: Detergent slurry composition in different phases.

### 3.7 Modelling Approaches for Spray Drying Towers

The aim of modelling spray drying towers is to predict spray dried powder characteristics upon changing the operating and design conditions so that the operation of the tower can be optimised and to troubleshoot operational and product quality issues. For this purpose, the single droplet drying model (discussed in Section 3.4) needs to be coupled with the various transfer mechanisms occurring within the gas phase of the spray tower, i.e., momentum, heat and mass transfer. Various approaches have been used for the modelling of spray drying towers, which can be categorised in terms of geometry as being zero-dimensional (lumped parameter models), one-dimensional, two-dimensional and three-dimensional. The zero-dimensional models are based on overall mass and energy balance between the drying gas and the droplets/particles at the feed and hot gas inlet and outlet and do not require any information about the dryer design parameters, i.e., drying tower height and diameter. In the one-dimensional models, plug-flow of the gas flow and the movement of the discrete phase are considered in one-dimension only. They are also called plug-flow models. In the two-dimensional models, the gas phase and the discrete phase vary in the axial and in the radial coordinates. In the three-dimensional models, the gas and the discrete phases are allowed to vary in the axial, radial as well as in the tangential coordinates. The two-dimensional and three-dimensional models fall under the category

of CFD models and a suitable turbulence model is used to solve the gas phase turbulence.

### **3.8 Plug-Flow Models for Spray Drying**

The plug-flow models are one of the simplest of the spray drying models that provide information about important droplet/particle parameters like temperature, moisture content etc. along the tower height. The properties of the drying gas are allowed to vary in the axial direction. Complete mixing in the radial direction and no back mixing are assumed. They offer a quick estimation of the performance of the spray drying towers with varying design and operating parameters and can be used as an aid for design and optimisation of spray drying towers. A disadvantage of this approach is that it is unable to capture the complex interactions between the discrete phase (droplets/particles) and the continuous phase (drying gas) due to coalescence, agglomeration, deposition on the wall and re-entrainment of deposited particles into the gas.

Parti and Palancz (1974) developed a mathematical model for particle drying in both co-current and counter-current spray drying towers that considered mono-sized particles, uniformly dispersed over the cross-section of the spray drying tower. The droplet/particle and air velocities were one-dimensional and parallel to the axis of the dryer. The temperature and humidity of air were allowed to vary axially. The drying model considered shrinking of the droplet due to evaporation of moisture. The diameter was kept constant once it reached the critical moisture content. The heat loss from the column was neglected. The model was not validated with the experimental data. Topar (1980) extended the model proposed by Parti and Palancz (1974) by adding droplet size distribution. The model results were presented for a co-current spray drying tower. It was concluded that in the model with a single droplet size representing the mean diameter, the particles were dried out in a much shorter time. No validation with the experimental data was reported.

Montazer-Rahmati and Ghafele-Bashi (2007) proposed a mathematical model for a counter-current spray drying of detergent slurry droplets. The model assumed plug-flow of the particles and the gas phase. The droplet/particle size distribution was represented through a fixed mean diameter. The drying of the particles was carried using a deterministic drying model proposed by Kadja and Bergeles (2003). The heat loss from the column was neglected. A unique feature of their model was the entrainment of finer particles by the exit gas stream. The fines were 6-8% of the dried product leaving the

tower. The exchange of particles from the downward moving particle stream to the upward moving particle stream took place when particles of a certain fraction of the distribution in the downward moving particle stream reached their terminal velocity. The model was compared with experimental data collected from an industrial-scale counter-current spray drying tower and an agreement within 10% was observed in terms of exhaust gas temperature, dried powder moisture content and dried powder temperature.

Recently, Pinto *et al.* (2014) presented a plug-flow model for a co-current spray drying tower considering droplets of varying sizes. CDC model was used to study droplet drying. Several scenarios were simulated to determine boundary values of drying achieved, including consideration of only constant drying rate period without and with droplet shrinkage due to evaporation, only falling rate period with and without shrinkage. The results showed that the constant drying rate consideration results in lower final moisture content, similarly if the droplet shrinkage is not considered, then the drying rate is faster as the heat transfer to large, hollow non-shrinking droplets is greater compared to the shrinking droplets. The model results showed that the average moisture content of the particles exiting from the tower is dependent on the initial droplet size as well as on the residence times.

Another class of one-dimensional models include those which allow variation of the droplets/particles parameters along the height and relaxing the assumption of plug-flow. These models are called Quasi one-dimensional models. Keey and Pham (1976) developed a numerical model for a co-current spray drying tower by dividing into two zones, namely the spray zone and the plug-flow zone. The spray zone, considered variations in the cross-section of the droplets/particles parameters, but the drying gas properties remain constant over the cross-section. In the plug-flow zone, the parameters of the droplets/particles as well as the drying gas were varied only in the axial direction. The model was applied to the drying of skim milk slurry. The model considered droplets of varying sizes. In the droplet drying model (CDC model), after the formation of a solid crust, the drying was approximated using the drying rate curve for skim milk proposed by Trommelen and Crosby (1970). The influence of high mass transfer rate on heat transfer was corrected using a blowing correction factor (Eisenklam *et al.*, 1967). The turbulence effects were taken into account by adding the turbulent velocity to the mean air velocity. The effect of turbulence and radiation was found to be negligible. The strongest influence on the simulation predictions was found for the drying air flow

rates, inlet air temperature and the inlet solids concentration in the feed. The predicted average moisture content was compared with experimental data and the difference between predicted and measured value was within 0.4%.

Katta and Gauvin (1975) used a similar approach to predict droplet trajectories in the nozzle zone (defined by the region traversed by rapidly decelerating droplets up to the point where the droplets get freely entrained by the drying gas) and the free-entrainment zone (where the droplets are freely conveyed by the drying gas) in a laboratory scale co-current spray drying tower and to predict the drying rate of calcium lignosulfate solution. In both zones, the trajectories of the droplets/particles were determined by the equation of motion representing the axial, radial and tangential velocity components. The axial, radial and tangential components of the gas phase were determined using empirical equations. The model was also used to determine the maximum evaporative capacity of the drying chamber which was limited by the condition that the largest particle hitting the wall must be completely dry. The model results were compared with the experimental observations and a reasonable accuracy was obtained. Gauvin *et al.* (1975) applied this model for the determination of maximum capacity of a laboratory scale co-current spray drying chamber using water droplets under given operating parameters. Maximum capacity of the drying chamber was limited by the condition that the largest droplet must be evaporated completely before hitting the wall.

Arnanson and Crowe (1980) compared the performance of one-dimensional and quasi one-dimensional model against experimental data measured by Manning and Gauvin (1960) for the evaporation of pure water droplets in a co-current spray drying tower. The quasi one-dimensional model gave a better prediction compared to one-dimensional model which tend to overpredict the evaporation rate.

### **3.9 CFD Modelling**

In the past two decades, the use of CFD (Computational Fluid Dynamics) has developed very rapidly. The advancement in computing power in the recent decades at lower costs has made it possible to carry out modelling of three-dimensional (3D) flow inside complex geometries of industrial scale equipment. There is a substantial scope of CFD technique in the modelling of spray drying towers including design and troubleshooting of operational problems due to the potential of CFD to predict complex 3D turbulent gas flow patterns and interacting dispersed phase which is encountered in spray drying towers.

The most commonly used commercial CFD software is Fluent (Fluent, 2009), which is used to carry out CFD simulation of the spray drying tower in this study. Fluent is an unstructured mesh solver and uses the finite volume method for the discretisation of the governing equations (given in Section 3.9.1) using a turbulence model (discussed in Section 3.10) in the computational domain to give a set of algebraic equations. The solution of the algebraic equations is then carried out using an iterative method (Versteeg and Malalasekera, 1995).

### **3.9.1 Conservation Equations for the Fluid Flow**

The modelling of turbulent fluid flow involves numerical solution of the conservation equations for the transport of mass and momentum. The conservation equation for the mass transport is given by the continuity equation. The momentum conservation equation is given by the Navier-Stokes equation. In a three-dimensional turbulent flow, the velocity components fluctuate randomly in all directions, even in a steady state condition. In the instantaneous Navier-Stokes equations, no special treatment is required for the numerical modelling of turbulent flows, but in order to capture the smallest scale of the random fluctuations (Kolmogorov length scale), a very fine mesh is required for a numerical solution. Additionally, the time scale used for integration of solution in time must be small enough to capture the fastest fluctuating motion (Kolmogorov time scale). The number of cells required for three-dimensional resolution scales of the order of  $Re^{9/4}$  (Peyret, 1996). The method of numerically solving the Navier-Stokes equation without any special treatment is called Direct Numerical Simulation (DNS). This method is impractical for simulating turbulent flows in large geometries with high Reynolds numbers due to the limitation of the available computational resources. A solution to this lies in solving the time-averaged form of the Navier-Stokes equations, which are derived by splitting the randomly fluctuating instantaneous velocity into time-average and fluctuating (about the mean) quantity. The method of solving the turbulent fluid flow based on the averaged, also referred to as the Reynolds averaged, form of the Navier-Stokes equations is called the RANS method. Another approach for modelling turbulence is the large eddy simulation (LES), where the small scale eddies are modelled using RANS method and the large scale eddies are numerically resolved. The velocities are decomposed into the modelled and filtered components. The size of the filter is determined by the mesh size. The filtered Navier-Stokes equations resolve the largest scales of fluid motion. The LES modelling approach is computationally expensive compared to RANS modelling approach. An acceptable level of agreement

between the simulated and measured velocity profiles has been shown by Bayly *et al.* (2004) in a laboratory-scale counter-current spray drying tower using RANS modelling hence it may be applicable for modelling of air flow in the IPP tower used in this study. Therefore for CFD modelling of this tower, RANS approach has been selected. This approach also has an advantage of using steady-state approximation and is less computationally expensive compared to LES modelling.

The time-averaged continuity equation in the Cartesian tensor notation can be written as:

$$\frac{\partial}{\partial t}(\rho) + \frac{\partial}{\partial x_i}(\rho \bar{u}_i) = \bar{S}_m \quad (3.16)$$

$\bar{S}_m$  in equation (3.16) is the source term arising from the exchange of mass.

The time-averaged Navier-Stokes equation in Cartesian tensor notation can be expressed as:

$$\begin{aligned} \frac{\partial}{\partial t}(\rho \bar{u}_i) + \frac{\partial}{\partial x_i}(\rho \bar{u}_i \bar{u}_j) = \frac{\partial}{\partial x_i} \left( \mu \left( \frac{\partial \bar{u}_i}{\partial x_j} + \frac{\partial \bar{u}_j}{\partial x_i} \right) \right) - \frac{\partial p}{\partial x_j} \\ + \frac{\partial}{\partial x_i}(-\rho \overline{u_i u_j}) + \vec{F}_b + \vec{F} \end{aligned} \quad (3.17)$$

The term  $-\rho \overline{u_i u_j}$  in equation (3.17) is called the Reynolds stresses (also called turbulent stresses) and results from averaging of the Navier-Stokes equation and requires additional modelling.

### **3.10 Turbulence Modelling**

Various turbulence models are available to model the Reynolds stresses that appear in equation (3.17). The simplest turbulence models used in this study are based on the eddy-viscosity concept proposed by Bousinesq in 1877, in which the Reynolds stress term is replaced by the product of the turbulent viscosity (which is a property of the fluid flow) and the mean velocity gradients. While more complex models are based on solving the transport equation for the turbulent stresses. The modelling of turbulent swirling flows using CFD poses a challenge due to anisotropic turbulent stresses in such

flows (Chang and Dhir, 1994), additionally the presence of secondary flow (recirculating flow) may also occur depending on swirl intensity (Kioth, 1991), which should be predicted by the turbulence model.

### 3.10.1 Standard $k$ - $\varepsilon$ Model

The standard  $k$ - $\varepsilon$  model proposed by Launder and Spalding (1972) is based on the eddy-viscosity (turbulent viscosity) concept. The term  $k$  represents the turbulence kinetic energy and the term  $\varepsilon$  represents the turbulence dissipation rate. In this model, the differential transport equations for  $k$  and  $\varepsilon$  are solved to determine the eddy viscosity. The model assumes isotropy of the Reynolds stresses. The turbulent viscosity has the following form:

$$\mu_t = \rho C_\mu \frac{k^2}{\varepsilon} \quad (3.18)$$

The transport equation for  $k$  for incompressible flow is given by:

$$\frac{\partial}{\partial t}(\rho k) + \frac{\partial}{\partial x_i}(\rho \bar{u}_i k) = \frac{\partial}{\partial x_i} \left( \left( \mu + \frac{\mu_t}{\sigma_k} \right) \frac{\partial k}{\partial x_i} \right) + G_k - \rho \varepsilon \quad (3.19)$$

where  $G_k$  is the generation of the turbulence kinetic energy due to mean velocity gradients, given by:

$$G_k = \rho \overline{u_i u_j} \frac{\partial \bar{u}_i}{\partial x_j} \quad (3.20)$$

$G_k$  is evaluated using the following equation:

$$G_k = \mu_t \left( 0.707 \left( \frac{\partial \bar{u}_j}{\partial x_i} + \frac{\partial \bar{u}_i}{\partial x_j} \right) \right)^2 \quad (3.21)$$

The dissipation rate  $\varepsilon$  is computed with the following transport equation:

$$\frac{\partial}{\partial t}(\rho\varepsilon) + \frac{\partial}{\partial x_i}(\rho\bar{u}_i\varepsilon) = \frac{\partial}{\partial x_i} \left( \left( \mu + \frac{\mu_t}{\sigma_\varepsilon} \right) \frac{\partial \varepsilon}{\partial x_i} \right) + C_{\varepsilon 1} \frac{\varepsilon}{k} G_k - C_{\varepsilon 2} \rho \frac{\varepsilon^2}{k} \quad (3.22)$$

where  $\sigma_k$  and  $\sigma_\varepsilon$  are turbulent Prandtl numbers for  $k$  and  $\varepsilon$  equations with values 1.0 and 1.3, respectively.  $C_{\varepsilon 1}$ ,  $C_{\varepsilon 2}$  and  $C_\mu$  are model constants with values 1.44, 1.92 and 0.09, respectively (Launder and Spalding, 1974).

The standard  $k$ - $\varepsilon$  model is one of the most widely used turbulence models due to its simplicity and applicability in modelling a range of turbulent flows. A disadvantage of this model is that it does not give satisfactory results for flows involving swirl, rotation, streamline curvature and splitting of the streamlines. It is mainly due to the eddy viscosity concept used by this model, which assumes the Reynolds stresses to be isotropic. The shortcomings of the  $k$ - $\varepsilon$  model in predicting the flows involving swirl have been detailed by various researchers (Chen and Lin, 1999; German and Mahmud, 2005; Jakirlić *et al.*, 2002; Jones and Pascau, 1989; Hoekstra *et al.*, 1999; Hogg and Leschziner, 1989; Leschziner, 1990; Leschziner and Kobayashi, 1988; Shamami and Birouk, 2008; Talbi *et al.*, 2011; Xia *et al.*, 1998).

### 3.10.2 RNG $k$ - $\varepsilon$ Model

The RNG  $k$ - $\varepsilon$  model is derived from instantaneous Navier-Stokes equations using a mathematical technique called Renormalization group method (Choudhury, 1993). The model is similar in form to the standard  $k$ - $\varepsilon$  model, but it contains modification in the dissipation equation for better prediction of flows with swirl and flows involving splitting of the streamlines. It also contains an additional equation for the turbulent viscosity modification due to swirl to take into account the non-isotropy of the Reynolds stresses in swirling flow. The additional term in the  $\varepsilon$  equation is:

$$R_\varepsilon = \frac{C_\mu \rho \hat{\eta}^3 (1 - \hat{\eta} / \hat{\eta}_o)}{1 + \hat{\beta} \hat{\eta}^3} \frac{\varepsilon^2}{k} \quad (3.23)$$

where

$$\hat{\eta} = Sk / \varepsilon \quad (3.24)$$

$$\hat{\eta}_o = 4.38 \text{ and } \hat{\beta} = 0.012$$

$$S = 0.707 \left( \frac{\partial \bar{u}_i}{\partial x_j} - \frac{\partial \bar{u}_j}{\partial x_i} \right) \quad (3.25)$$

The effect of swirl on turbulent viscosity is given by:

$$\mu_t = \mu_{t0} f \left( \alpha_s, \Omega, \frac{k}{\varepsilon} \right) \quad (3.26)$$

where  $\alpha_s$  is a swirl constant, taken as 0.07 for mildly swirling flows (Fluent, 2009),  $\Omega$  is the characteristic swirl number given by equation (3.73).  $\mu_{t0}$  is the value of turbulent viscosity without swirl modification. The model constants  $C_{\varepsilon 1}$ ,  $C_{\varepsilon 2}$ ,  $C_\mu$ ,  $\sigma_k$  and  $\sigma_\varepsilon$  have the following values respectively: 1.42, 1.68, 0.085, 0.7179, 0.7179. Details of RNG  $k$ - $\varepsilon$  model can be found in Choudhury (1993).

The RNG  $k$ - $\varepsilon$  model works well for high Reynolds number flows as well as flows in the transition region and gives improved prediction for flows involving swirl in comparison to the standard  $k$ - $\varepsilon$  model (Bakker, 2002). A comparison of standard and RNG  $k$ - $\varepsilon$  models for recirculating flow by Papageorgakis and Assanis (1999) showed that the RNG  $k$ - $\varepsilon$  model predicts less dissipative behaviour, which enables it to better predict the recirculation length compared to the standard  $k$ - $\varepsilon$  model. Xia *et al.* (1998) compared the prediction of both the standard  $k$ - $\varepsilon$  and RNG  $k$ - $\varepsilon$  models for strongly swirling flow (inlet swirl number of 1.68, defined using equation 3.73) and found very little improvement in the prediction of the central toroidal recirculation zone connected with the central reverse zone; however both models failed to correctly predict the size of central recirculation zone. Escue and Chui (2010) compared the prediction of RNG  $k$ - $\varepsilon$  model and Reynolds Stress Transport (RST) turbulence model against experimental data for moderate and highly swirling flows with swirl number ranging from 0.25 to 2.0. The RNG  $k$ - $\varepsilon$  model showed better predictions with moderately swirling flows, while RST model showed superior predictions for highly swirling flows.

### 3.10.3 Realizable $k$ - $\varepsilon$ Model

In the Realizable  $k$ - $\varepsilon$  model the term realizable means that the model meets certain mathematical constraints on the normal stresses, consistent with the physics of the turbulent flows (Fluent, 2009). It eliminates the possibility of unrealistic values of normal stresses from occurring in highly strained flows. For the estimation of turbulent viscosity, equation (3.18) is used but instead of keeping  $C_\mu$  a constant, it is treated as a variable. The variable form of  $C_\mu$  is a function of the local strain rate and rotation of the fluid.

$$C_\mu = \frac{1}{A_o + A_s \frac{kU^*}{\varepsilon}} \quad (3.27)$$

where  $A_o = 4.04$  and  $A_s = \sqrt{6} \cos\phi$  (model constants) and  $U^*$  is a function of strain rate and rate of rotation of fluid tensor given by equations (3.40) and (3.41) respectively.

The realizable  $k$ - $\varepsilon$  model uses different source and sink terms for eddy dissipation in the transport equation. Details of this model can be found in Shih *et al.* (1995). The model constants  $C_{\varepsilon 2}$ ,  $\sigma_k$  and  $\sigma_\varepsilon$  have following values respectively: 1.90, 1.0 and 1.2. The modified equation for  $\varepsilon$  and  $\mu_t$  makes this model superior to other  $k$ - $\varepsilon$  models (Bakker, 2002). The model gave improved predictions for low to mildly swirling flows ( $\Omega = 0.25$ ) compared to the standard  $k$ - $\varepsilon$  model (Shih *et al.*, 1995). Recently, Rudolf (2012) carried out numerical validation of highly swirling flows in a converging-diverging nozzle using Realizable  $k$ - $\varepsilon$  model and found that this model is not suitable for predicting highly swirling flows as it gave a severely underpredicted peak value of the Rankine vortex profile and overpredicted the size of the forced vortex region.

#### **3.10.4 Shear Stress Transport (SST) Model**

The SST model combines the eddy viscosity based model  $k$ - $\omega$ , applied to the near wall region and the standard  $k$ - $\varepsilon$  model in the region away from the walls. The model was proposed by Menter (1994). The transport equation for  $\omega$  is given by (Fluent, 2009):

$$\begin{aligned} \frac{\partial}{\partial t}(\rho\omega) + \frac{\partial}{\partial x_i}(\rho\bar{u}_i\omega) = \frac{\partial}{\partial x_i} \left( \left( \mu + \frac{\mu_t}{\sigma_\omega} \right) \frac{\partial \omega}{\partial x_i} \right) \\ + 2(1-F_1)\rho\sigma_{\omega,k-\varepsilon} \frac{1}{\omega} \frac{\partial k}{\partial x_i} + \hat{\alpha} \frac{\omega}{k} P_k - \beta\rho\omega^2 \end{aligned} \quad (3.28)$$

where  $F_1$  is a blending function (for near-wall calculation using  $k-\omega$  model) calculated using the expression given by Menter (1994). The model constants are (Fluent, 2009):

$$\sigma_{k1} = 1.176; \sigma_{\omega1} = 2.0; \sigma_{k2} = 1.0; \sigma_{\omega2} = 1.168; a_1 = 0.31; \beta_{i,1} = 0.075; \beta_{i,2} = 0.0828$$

Yaras and Grosvenor (2003) compared the prediction of the SST model with experimental data in a strongly swirling confined flow and concluded that the SST model predicts excessive radial diffusive transport of turbulence. Lu *et al.* (2008) compared the prediction of the SST model with standard  $k-\varepsilon$  model and Realizable  $k-\varepsilon$  model in a swirl flow combustor and concluded that the SST model gives slight improvement in predicting strong velocity variation and accompanying reverse flow.

### 3.10.5 Reynolds Stress Transport Model

The Reynolds stress transport (RST) model is based on the partial differential equations for the transport of Reynolds stresses (Launder *et al.*, 1975). In the RST model, the shear stresses are anisotropic, hence it is capable of giving better predictions compared to isotropic eddy-viscosity based models in flows involving streamline curvature and swirl. The improved prediction of the RST model in such flows compared to the eddy-viscosity based models has been shown by many researchers (Leschziner and Kobayashi, 1988; Hogg and Leschziner, 1989; Jones and Pascau, 1989; Leschziner, 1990; Xia *et al.*, 1998; Chen and Lin, 1999; Hoekstra *et al.*, 1999; Jakirlić *et al.*, 2002; German and Mahmud, 2005; Shamami and Birouk, 2008; Talbi *et al.*, 2011). The general form of the Reynolds stress transport equation is given as (Fluent, 2009):

$$\underbrace{\frac{\partial}{\partial t}(\rho \overline{u_i u_j})}_{\text{Time rate of change}} + \underbrace{\frac{\partial}{\partial x_i}(\rho \overline{u_k} \overline{u_i u_j})}_{C_j \text{ Convective transport}} = \underbrace{P_{ij}}_{\text{Stress Production}} + \underbrace{D_{Tij}}_{\text{Turbulent Diffusion}} + \underbrace{\phi_{ij}}_{\text{Pressure strain}} - \underbrace{\varepsilon_{ij}}_{\text{Dissipation}} + \underbrace{F_{ij}}_{\text{Body forces}} \quad (3.29)$$

The stress production terms  $P_{ij}$ ,  $F_{ij}$  and the convection terms are exact, whereas, the remaining terms are modelled. The turbulence dissipation due to viscous action is assumed to be isotropic, the dissipation tensor,  $\varepsilon_{ij}$  is given by:

$$\varepsilon_{ij} = \frac{2}{3} \delta_{ij} \varepsilon \quad (3.30)$$

where  $\delta_{ij}=1$ , if  $i=j$  and 0, if  $i \neq j$ .

The dissipation rate  $\varepsilon$  is computed using equation (3.22). The model constants in equation (3.22) are assigned the following standard values proposed by Launder and Spalding (1974):  $C_\mu=0.09$ ,  $C_{\varepsilon 1}=1.44$ ,  $C_{\varepsilon 2}=1.92$ ,  $\sigma_\varepsilon=1.3$

The production term  $P_{ij}$  in equation (3.29) can be expressed as:

$$P_{ij} = -\rho \left( \overline{u_i u_k} \frac{\partial \overline{u_j}}{\partial x_k} + \overline{u_j u_k} \frac{\partial \overline{u_i}}{\partial x_k} \right) \quad (3.31)$$

The diffusion term  $D_{Tij}$  is modelled by a scalar turbulent diffusivity (Lien and Leschziner, 1994). It is given by:

$$D_{Tij} = -\frac{\partial}{\partial x_k} \left( \frac{\mu_t}{\sigma_k} \frac{\partial \overline{u_i u_j}}{\partial x_k} \right) \quad (3.32)$$

The term  $F_{ij}$  represents additional stress production due to system rotation, and is given by:

$$F_{ij} = -2\rho\Omega_k \left( \overline{u_j u_m} \varepsilon_{ikm} + \overline{u_i u_m} \varepsilon_{jkm} \right) \quad (3.33)$$

It has been shown by various researchers (Leschziner, 1990; Lu and Semiao, 2003; Nikjooy and Mongia, 1991; Speziale *et al.*, 1991; Younis *et al.*, 2009) that the ability of the RST model in predicting the flow fields depends largely on the modelling of the pressure strain redistribution term ( $\phi_{ij}$ ) given in equation (3.29). Although the isotropic eddy viscosity assumption for turbulence dissipation term also impacts the quality of the prediction of the RST model, for highly swirling flows, the predictions are more sensitive to the modelling of the pressure strain term (Lu and Semiao, 2003). The different versions of RST models used in this study differ in the modelling of  $\phi_{ij}$ . In the first model of pressure strain term proposed by Launder *et al.*, (1975) (hereafter referred to as LRR model), the term ( $\phi_{ij}$ ) is modelled using a linear approximation. The pressure strain redistribution term is modelled as the sum of the “slow” pressure strain term ( $\phi_{ij,1}$ ), the “rapid” pressure strain term ( $\phi_{ij,2}$ ), and the “wall reflection” term ( $\phi_{ij,w}$ ). The pressure strain redistribution term ( $\phi_{ij}$ ) can be written as:

$$\phi_{ij} = \phi_{ij,1} + \phi_{ij,2} + \phi_{ij,w} \quad (3.34)$$

The slow pressure strain term  $\phi_{ij,1}$ , which is also known as the return to isotropy term, takes into account the effects of pressure on the Reynolds stresses. It is given by:

$$\phi_{ij,1} = -C_{\phi 1} \rho \frac{\varepsilon}{k} \left( \overline{u_i u_j} - \frac{2}{3} \delta_{ij} k \right) \quad (3.35)$$

The rapid pressure strain term  $\phi_{ij,2}$ , which is also known as turbulence-mean flow interaction term, takes into account the effect of mean flow on the Reynolds stresses. It is given by (Launder, 1989):

$$\phi_{ij,2} = -C_{\phi 2} \left( P_{ij} + F_{ij} - C_{ij} - \frac{2}{3} \delta_{ij} \left( \frac{1}{2} P_{kk} - \frac{1}{2} C_{kk} \right) \right) \quad (3.36)$$

The wall reflection term  $\phi_{ij,w}$  takes into account the near wall effects on the Reynolds stresses (Gibson and Launder, 1978). It tends to damp the normal stress perpendicular to the wall and enhances the normal stress parallel to the wall. It is given by:

$$\begin{aligned} \phi_{ij,w} = & -C'_{\phi 1} \frac{\varepsilon}{k} \left( \overline{u_k u_m} n_k n_m \delta_{ij} - \frac{3}{2} \overline{u_i u_k} n_j n_k - \frac{3}{2} \overline{u_j u_k} n_i n_k \right) \frac{C_{\mu}^{3/4} k^{3/2}}{\kappa \varepsilon d_w} \\ & - C'_{\phi 2} \frac{\varepsilon}{k} \left( \phi_{km,2} n_k n_m \delta_{ij} - \frac{3}{2} \phi_{ik,2} n_j n_k - \frac{3}{2} \phi_{jk,2} n_i n_k \right) \frac{C_{\mu}^{3/4} k^{3/2}}{\kappa \varepsilon d_w} \end{aligned} \quad (3.37)$$

The model constants in equations (3.35), (3.36) and (3.37) are assigned the following values proposed by Gibson and Launder (1978):  $C_{\phi 1}=1.8$ ,  $C_{\phi 2}=0.60$ ,  $C'_{\phi 1}=0.5$ ,  $C'_{\phi 2}=0.3$

In the second model proposed by Speziale *et al.* (1991) (hereafter referred to as SSG model),  $\phi_{ij}$  is quadratic and does not require special treatment near the wall. The pressure strain redistribution term is given by:

$$\begin{aligned} \phi_{ij} = & -(C''_{\phi 1} \rho \varepsilon + C^*_{\phi 1} P) b_{ij} + C''_{\phi 2} \rho \varepsilon \left( b_{ik} b_{kj} - \frac{1}{3} b_{mn}^2 \delta_{ij} \right) + (C''_{\phi 3} - C^*_{\phi 3} \sqrt{b_{ij} b_{ij}}) \rho k S_{ij} \\ & + C''_{\phi 4} \rho k \left( b_{ik} S_{jk} + b_{jk} S_{ik} - \frac{2}{3} b_{mn} S_{mn} \delta_{ij} \right) + C''_{\phi 5} \rho k (b_{ik} \Omega_{jk} + b_{jk} \Omega_{ik}) \end{aligned} \quad (3.38)$$

where  $b_{ij}$  is the Reynolds stress anisotropy tensor, defined as:

$$b_{ij} = \left( \frac{-\rho \overline{u_i u_j} + \frac{2}{3} \rho k \delta_{ij}}{2 \rho k} \right) \quad (3.39)$$

The mean strain rate,  $S_{ij}$  is defined as:

$$S_{ij} = \frac{1}{2} \left( \frac{\partial \overline{u_j}}{\partial x_i} + \frac{\partial \overline{u_i}}{\partial x_j} \right) \quad (3.40)$$

The mean rate of rotation tensor  $\Omega_{ij}$  is defined as:

$$\Omega_{ij} = \frac{1}{2} \left( \frac{\partial \bar{u}_i}{\partial x_j} + \frac{\partial \bar{u}_j}{\partial x_i} \right) \quad (3.41)$$

The following constants are used (Speziale *et al.*, 1991):

$$C_{\phi_1}'' = 3.4, C_{\phi_1}^* = 1.8, C_{\phi_2}'' = 4.2, C_{\phi_3}'' = 0.8, C_{\phi_3}^* = 1.3, C_{\phi_4}'' = 1.25, C_{\phi_5}'' = 0.4$$

A comparison of the LRR and SSG model predictions with the experimental data for strongly swirling flows in a pipe was carried out by Chen and Lin (1999). It was found that for a swirl number of 2.25 (defined using equation 3.73); both the LRR and SSG RST models gave equally good agreement with the experimental data. But at a swirl number of 0.85, the LRR model gave a relatively flat axial velocity profile compared to the measurement which showed a lower velocity near the centre and a higher velocity towards the wall. Ko *et al.* (2006) studied the performance of both of these models in a cylindrical hydrocyclone for a swirl number of 8.1. The swirl number was based on the ratio of mass flow through the hydrocyclone and the inlet cross-sectional area. It was concluded that the SSG model gave an overall better prediction compared to the LRR model.

### **3.10.6 Modelling of Flow Near the Wall**

The modelling of flow near the wall is carried out using wall functions (Fluent, 2009). In a region close to the wall ( $0 \leq y^+ \leq 5$ ), the flow is influenced by the viscous stresses and does not depend on the free stream parameters. The mean velocity close to the wall (referred to as the viscous sub-layer) is given by law of the wall (Fluent, 2009):

$$u^+ = \frac{\bar{U}}{u_\tau} = f\left(\frac{\rho u_\tau y}{\mu}\right) = f(y^+) \quad (3.42)$$

where  $u^+$  and  $y^+$  are the dimensionless groups. The mean velocity  $\bar{U}$  is given by:

$$\bar{U} = \frac{\tau_w y}{\mu} \quad (3.43)$$

where  $\tau_w$  in equation (3.43) is the wall shear stress, and  $u_\tau$  in equation (3.42) is the friction velocity given by:

$$u_\tau = \sqrt{\frac{\tau_w}{\rho}} \quad (3.44)$$

Further away from the wall ( $30 \leq y^+ \leq 500$ ), both viscous and turbulent stresses dominate the flow (this layer referred to as log-law layer). The velocity distribution in this region is given by a log-law:

$$u^+ = \frac{1}{\kappa} \ln y^+ + B = \frac{1}{\kappa} \ln(Ey^+) \quad (3.45)$$

The above equation is valid for smooth surfaces when  $B = 5.5$  (or  $E=9.8$ ) for all turbulent flows (Versteeg and Malalasekera, 1995).  $\kappa$  is von Kármán constant. The inner wall of a spray drying tower investigated has a layer of deposits on the wall which causes significant surface roughness. A study was carried out by Kaya *et al.* (2011) to see the effect of surface roughness on swirling flow in a tangential inlet cyclone separator using CFD simulations with near-wall flow modelled using log-law of the wall modified for surface roughness. A considerable reduction in the tangential velocity was attributed to the surface roughness. The modification of log-law of the wall (equation 3.45) for rough surfaces is based on the experiments for flow in rough circular pipes with inner surface covered by tightly packed sand grains was given by Cebeci and Bradshaw (1977). These experiments indicated that the mean velocity distribution near the rough surface (in log-law of the wall region) has the same slope as that in equation (3.45), but it has a different intercept. The shift in the intercept  $\Delta B$  is a function of the dimensionless sand grain roughness height  $k_s^+$  given by:

$$k_s^+ = \frac{\rho k_s u_\tau}{\mu} \quad (3.46)$$

where  $k_s$  is the sand grain roughness height.

The logarithmic law for the rough surface wall is given by (Cebeci and Bradshaw, 1977):

$$u^+ = \frac{1}{\kappa} \ln y^+ + B - \Delta B(k_s^+) \quad (3.47)$$

The relation between  $\Delta B$  and  $k_s^+$  has been determined empirically from various types of roughness geometry. Three regimes are distinguished, namely, aerodynamically smooth ( $0 \leq k_s^+ \leq 5$ ), transitional ( $5 \leq k_s^+ \leq 70$ ) and fully rough regime ( $k_s^+ \geq 70$ ) (Schlichting, 1979). The surface is considered as hydrodynamically smooth when the roughness height is below the viscous sub layer. The fully rough flow condition exists when the roughness elements are so large that sublayer is completely eliminated and the flow can be considered to be independent of the molecular viscosity. In the fully rough regime,  $\Delta B$  is given by (Fluent, 2009):

$$\Delta B = \frac{1}{\kappa} \ln(1 + C_s k_s^+) \quad (3.48)$$

where  $C_s$  is a roughness constant and depends on the type of roughness. For a pipe with the inner surface tightly packed with sand grain roughness a  $C_s$  value of 0.5 is recommended (Fluent, 2009), whereas for the surface roughness that departs from a uniform sand grain roughness, a higher value of  $C_s$  varying from 0.5 ~ 1.0 can be used (Fluent, 2009).

### **3.10.7 Modelling of Temperature Near the Wall**

The modelling of temperature near the wall/deposit surface is carried out using a log-law representation for thermal boundary layer, which is given as follows (Viegas *et al.*, 1985):

$$T^* = \frac{(T_{dep} - T_p) \rho c_p k_p^{1/2}}{\dot{q}} = \begin{cases} \Pr y^* + \frac{1}{2} \rho \Pr \frac{C_\mu^{1/4} k_p^{1/2}}{\dot{q}} \bar{U}_p^2 & (y^* < y_T^*) \\ \Pr_t \left[ \frac{1}{\kappa} \ln(Ey^*) + D \right] + \\ \frac{1}{2} \rho \frac{C_\mu^{1/4} k_p^{1/2}}{\dot{q}} \{ \Pr_t U_p^2 + (\Pr - \Pr_t) \bar{U}_c^2 \} & (y^* > y_T^*) \end{cases} \quad (3.49)$$

where  $T_p$ ,  $\bar{U}_p$  and  $k_p$  are temperature, mean velocity and turbulence kinetic energy at near-wall node respectively, and  $D$  is given by:

$$D = 3.15 \Pr^{0.695} \left( \frac{1}{E'} - \frac{1}{E} \right)^{0.359} + \left( \frac{E'}{E} \right)^{0.6} \left[ 9.24 \left[ \left( \frac{\Pr}{\Pr_t} \right)^{3/4} - 1 \right] \left[ 1 + 0.28 \exp^{-0.007 \Pr / \Pr_t} \right] \right] \quad (3.50)$$

For the temperature at the surface of the wall/deposit, equation (3.49) reduces to:

$$T_{dep} = \frac{1}{2} \frac{\Pr C_\mu^{1/4} U_p^2}{c_p} + T_p \quad (3.51)$$

The inside film coefficient  $\alpha_i$  for post-processing is calculated by Fluent using the following equation (Fluent, 2009):

$$\alpha_i = \frac{\dot{q}}{(T_w - T_p)} \quad (3.52)$$

### 3.10.8 Scalar Transport Equations

The transport of scalar including enthalpy and species is modelled using the scalar transport equation, which is given by:

$$\frac{\partial}{\partial x_i} (\rho \bar{u}_i \bar{\phi}) = - \frac{\partial}{\partial x_i} (\bar{J}_\phi) + \bar{S}_\phi \quad (3.53)$$

$\bar{S}_\phi$  in equation (3.53) is the source term representing the species mass fraction added to the continuous phase from the discrete phase in the species transport equation and gas-particle heat transfer rate in the enthalpy transport equation.

The variable  $\bar{\phi}$  represents the mass fraction of species and gas enthalpy.  $\bar{J}_\phi$  represents the corresponding diffusion fluxes for turbulent flow which are modelled using the gradient-diffusion approach, given by:

$$\bar{J}_\phi = - \left( \frac{\mu_t}{\sigma_t} \right) \frac{\partial \phi_i}{\partial x_i} - \frac{D_{T,i}}{T} \frac{\partial T}{\partial x_i} \quad (3.54)$$

In the above equation,  $\sigma_t$  represents turbulent Prandtl number ( $Pr_t$ ) in case of enthalpy transport and turbulent Schmidt number ( $Sc_t$ ) in case of species transport equation.

The gas enthalpy is related to the enthalpy of components using the following equation:

$$h_g = \sum_{i=1}^N Y_i h_{g,i} \quad (3.55)$$

In the non-isothermal simulation runs (Section 6.2 in Chapter 6), the density of the gas is considered to be a function of temperature and composition of the gas and is calculated using the ideal gas law, given by:

$$\rho_g = \frac{p \sum_{i=1}^N M_{w,i} Y_i}{R_g T_g} \quad (3.56)$$

### **3.11 Modelling of the Discrete Phase**

The discrete phase is modelled using the Lagrangian approach. The trajectories of the droplets/particles are calculated by solving the equation of motion for each droplet/particle, which is given by:

$$\frac{d\vec{u}_p}{dt} = \vec{F}_d(\vec{u} - \vec{u}_p) + \frac{g(\rho_p - \rho)}{\rho_p} \quad (3.57)$$

The first term on the right hand side is the drag force per unit mass, the second term represents the gravity and buoyancy force per unit mass. The drag force is given by:

$$\vec{F}_d = \frac{18\mu}{\rho_p d_p^2} \frac{C_D \text{Re}}{24} \quad (3.58)$$

where Re is the particle Reynolds number based on the relative velocity of the particle, given by:

$$\text{Re} = \frac{\rho d_p |\vec{u}_p - \vec{u}|}{\mu} \quad (3.59)$$

$C_D$  in equation (3.58) is the drag coefficient discussed in Section 3.11.1.

A number of other forces also act on a particle inside the spray drying tower including the Basset (history) force, shear and rotation induced lift force, thermophoretic and Brownian forces. The Basset force occurs due to the delay in development of the boundary layer as the relative velocity changes with time (Crowe *et al.*, 1998), which in this study is not taken into account. Similarly shear and rotation induced lift forces are also neglected in the present study. Thermophoretic force (arising due to the temperature gradient in the continuous phase) and Brownian force (arising due to molecular motion) are neglected in this study as they are negligible for the size range of droplets/particles considered (varying from 50  $\mu\text{m}$  to 2300  $\mu\text{m}$ ).

### 3.11.1 Drag Force on Droplets/Particles

When droplets/particles move in an air flow, they experience a retarding force called drag. The magnitude of this force is dependent on the density, shape and cross-sectional area of the droplet/particle, which is represented using a dimensionless quantity called a drag coefficient. A large number of drag coefficient correlations exist for a wide range of shapes and for a range of Reynolds numbers. In the existing CFD simulations of spray towers, the droplets and particles are assumed to be smooth and spherical

throughout, and the drag coefficient correlation for spherical bodies proposed by Morsi and Alexander (1972) is commonly used.

$$C_D = a_1 + \frac{a_2}{\text{Re}} + \frac{a_3}{\text{Re}^2} \quad (3.60)$$

where  $a_1$ ,  $a_2$  and  $a_3$  are constants which depend on the particle Reynolds number and is applicable for particles Reynolds numbers ranging from 0 to 50000.

The droplets may deform as they move in the air flow field and in addition, the evaporation from the droplet surface and shear induced internal recirculation of the liquid inside the droplet may change the drag force acting on the droplets. Equation (3.61) and (3.62) are the drag coefficient for burning fuel droplets (involving a high rate of mass transfer which may modify the flow around the droplet) for a range of Reynolds numbers reported by Williams (1976):

$$\text{For } \text{Re} < 80, C_D = 27\text{Re}^{-0.84} \quad (3.61)$$

$$\text{For } 80 < \text{Re} < 10000, C_D = 0.271\text{Re}^{0.217} \quad (3.62)$$

The particles may also change shape due to agglomeration as well as morphological changes that occur during drying. Therefore the correlation given by equation (3.60) may not be applicable if the particles become non-spherical. The particles experience higher drag as they become non-spherical (Pettyjohn and Christiansen, 1948). Hence the residence time of the non-spherical particles will be greater. Wadell (1934) introduced the concept of particle sphericity ( $\phi_s$ ) to account for change in surface area due to deviation of a particle shape from a sphere. It is defined as the ratio of surface area of the sphere having the same volume as that of particle and the surface area of the particle.

$$\phi_s = \frac{A_{\text{sphere}}}{A_p} \quad (3.63)$$

The drag coefficient correlation proposed by Haider and Levenspiel (1989) for non-spherical particles valid for particle Re ranging from 0.1 to 100000, and is given by:

$$C_D = \frac{24}{\text{Re}} \left( 1 + b_1 \text{Re}^{b_2} \right) + \frac{b_3 \text{Re}}{b_4 + \text{Re}} \quad (3.64)$$

where:

$$\begin{aligned} b_1 &= \exp(2.3288 - 6.4581\phi_s + 2.4486\phi_s^2) \\ b_2 &= 0.0964 + 0.5565\phi_s \\ b_3 &= \exp(4.905 - 13.8944\phi_s + 18.4222\phi_s^2 - 10.2599\phi_s^3) \\ b_4 &= \exp(1.4681 + 12.2584\phi_s - 20.7322\phi_s^2 + 15.8855\phi_s^3) \end{aligned} \quad (3.65)$$

To the best of author's knowledge, no reported modelling work of spray drying towers has considered drag coefficient for non-spherical particles. The size and shape of particles can change during drying due to agglomeration and morphological changes which is difficult to predict.

### **3.11.2 Effect of Mass Transfer on the Drag Coefficient**

The drag coefficient of the drying particles is affected by the mass transfer from the surface. Eisenklam *et al.* (1967) found that the evaporation of volatiles from the burning fuel droplet affected the drag coefficient according to the following correlation:

$$C'_D = \frac{C_{D_0}}{1 + B'} \quad (3.66)$$

where

$C_{D_0}$  is the drag coefficient with no mass transfer, and

$B'$  is the transfer number given by equation (3.13).

Equation (3.66) may be applied as a correction factor to equation (3.60) to account for change in drag coefficient due to evaporation of moisture from the surface.

### **3.11.3 Particle-Wall Interaction**

When a droplet/particle hits the wall, it can bounce back with a velocity either equal to or less than the impact velocity (Figure 3.9). The particle-wall interaction can be modelled using the reflect boundary condition in Fluent (2009). This is given by the restitution coefficient which is defined as the ratio between the velocity after impact

with the wall and the velocity before impact. Hence the value of restitution coefficient can be in the range of 0 to 1.

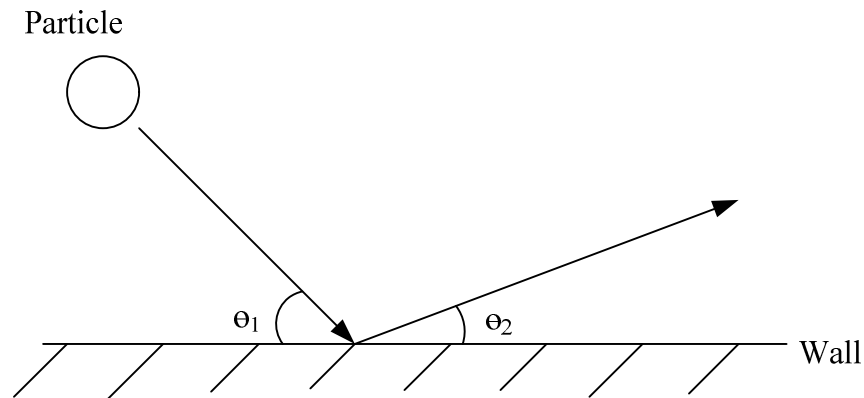


Figure – 3.9: Droplet/particle wall impact.

The restitution coefficient has two components: the normal restitution and the tangential restitution coefficients. The normal restitution coefficient defines the momentum in the direction normal to the wall that is retained after impact with the wall. The tangential restitution coefficient defines the momentum in the direction tangent to the wall retained by the particle after impact. A number of factors can influence the normal and tangential restitution coefficients including the surface and bulk characteristics of the impacting particle, particle shape, impact angle, impact velocity (Hassal, 2011) as well as the roughness of impacting surface (Sommerfeld, 1992; Huber and Sommerfeld, 1998; Sommerfeld and Huber, 1999). It can also depend on the moisture content of the impacting particle.

#### **3.11.4 Turbulent Dispersion of Droplets/Particles**

The degree of dispersion is characterised by the Stokes number, which is defined as the ratio between the particle response time and the characteristic time scale.

$$St = \frac{\tau_p}{\tau_F} \quad (3.67)$$

where  $\tau_p$  is the particle response time, i.e., the time taken by the particle to respond to change in the surrounding flow field and  $\tau_F$  is the characteristic time of the flow field, which is defined as the ratio between the characteristic length of the flow field and the flow velocity.

If  $St \ll 1$ , then the response time of particles is much less than the characteristic time associated with the fluid flow, hence the particles will have sufficient time to respond to changes in the flow field and the particle will follow the fluid motion. Whereas, if  $St \gg 1$ , the particles will move independently within the fluid (Crowe *et al.*, 1998).

The velocity experienced by the droplets/particles in a turbulent flow field is the sum of the mean velocity component and the fluctuating velocity component. The effect of the fluctuating velocity component of gas on the droplets/particles dispersion is taken into account using the discrete random walk model (Fluent, 2009), in which the discrete phase is assumed to interact with a succession of eddies. The interaction with each eddy lasts until the particle residence time in the computational cell exceeds the eddy crossing time or the eddy lifetime. The fluctuating velocity components are sampled by assuming a Gaussian probability distribution and are given by:

$$u_i' = \zeta \sqrt{u_i'^2} \quad (3.68)$$

where  $\zeta$  is the normally distributed random number. During the eddy interaction, the fluctuating velocity is kept constant for a certain time interval. This time interval is given by:

$$T_L = C_L \frac{k}{\varepsilon} \quad (3.69)$$

where  $C_L$  is a constant determined empirically. In the RST model, its value is 0.30 (Fluent, 2009).

### **3.12 Coupling between the Discrete and Continuous Phases**

The coupling between the drying gas (continuous phase) and the droplets/particles (dispersed phase) can be achieved using either the Eulerian-Eulerian and Eulerian-Lagrangian approaches. In the Eulerian-Eulerian approach, both the gas phase and the dispersed are treated as continuum by solving the time-averaged transport equations and each computational cell contains a certain fraction of the continuous and the dispersed phases. This approach has a disadvantage of being highly computationally expensive in modelling poly-dispersed flows, because each of the particle size classes will require an

additional set of transport equations. In spray drying towers, the droplets/particles consist of varying sizes, therefore a large number of transport equations will be required to represent the range of droplets/particles, hence this approach is not feasible in the modelling of spray drying towers.

In the Eulerian-Lagrangian approach, the gas phase is treated as a continuum by solving the time-averaged continuity and Navier-Stokes equations (Eulerian reference frame) for the fluid flow. Typically, the discrete phase in spray drying tower comprises billions of droplets/particles. Tracking of each individual droplet/particle in this case is highly computationally expensive. Therefore, the motion of droplet/particle is solved by tracking a number of parcels through the calculated flow field of the continuous phase by solving the droplet/particle equation of motion, this is termed as Lagrangian reference frame (Nijdam *et al.*, 2003). Each parcel in the Lagrangian reference frame represents a number of droplets/particles having the same size, position and velocity. Hence each parcel contains a certain fraction of the total mass flow of the discrete phase. The trajectories of parcels are computed by integrating the equation of motion (equation 3.57). These individual parcels are tracked through the flow domain until the parcels exit the domain. Each individual droplet/particle in a parcel exhibits the same heat, mass and momentum transfer. The source terms for the continuous phase resulting from heat, mass and momentum transfer to the parcel in a cell is the sum of heat, mass and momentum transfer to all the droplets/particles in that parcel respectively. Increasing the number of parcels decreases the mass fraction of the discrete phase in that parcel, but it also increases the computational time. Hence a preliminary CFD investigation of the influence of number of parcels on the results is necessary to select a suitable number of parcels to represent the discrete phase.

A parcel is treated as a point in the computational space and does not occupy any volume in the computational cell. Hence the Eulerian-Lagrangian approach is not suitable for dense discrete phase flows. This approach is computationally cheaper compared to the Eulerian-Eulerian approach for modelling poly-dispersed flows. It also provides history of each tracked parcel inside the flow domain. Because of these advantages, in the existing CFD modelling studies of spray drying towers, the coupling of heat, mass and momentum transfer between the continuous and the dispersed phase has been carried out using the Eulerian-Lagrangian approach utilising the Particle-Source-In-Cell (PSI-Cell) model developed by Crowe *et al.* (1977), Crowe (1980).

In the PSI-Cell model, the calculation of multiphase simulation is started by solving the gas phase only. Using the gas phase flow field and temperature, the droplets/particle trajectories and associated heat and mass transfer are calculated. The mass, momentum and energy source terms resulting from the interaction of the discrete and continuous phases in each cell are determined. The gas phase equations are solved again along with the calculated source terms. The resulting updated gas flow field and temperature is then used to calculate the new droplets/particle trajectories as well as associated heat and mass transfer resulting in new source terms for the gas phase equations. The iterative calculations are repeated until a suitable level of tolerance is achieved in the overall heat and mass balance. Figure 3.10 is a flow chart of the PSI-Cell scheme.

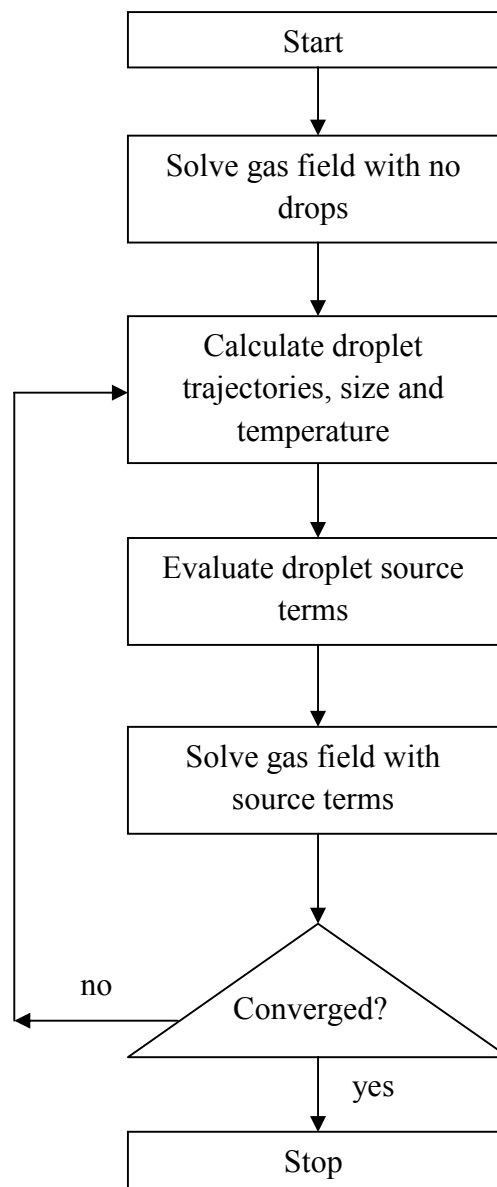


Figure – 3.10: Flow chart for PSI-Cell computational scheme (adapted from Crowe, 1977).

### 3.12.1 Evaluation of Source Terms

The source terms that appear in the governing equations for the continuous phase result from the exchange of heat, mass and momentum transfer between the discrete and the continuous phases in each cell when two-way coupling is considered. The source term resulting from momentum transfer between the two phases in a computational cell is included in the Navier-Stokes equation (given by equation 3.17) and is evaluated by the following equation:

$$\vec{F} = \sum_{i=1}^n \left[ \left( \frac{18\mu C_{D,i} \text{Re}}{24\rho_{p,i} d_{p,i}^2} (\vec{u}_{p,i} - \vec{u}) + \vec{g} \right) \dot{m}'_{p,i} \Delta t_i \right] / V_{cell} \quad (3.70)$$

where  $n$  is the total number of parcels passing through the computational cell.

The source term for the continuous phase resulting from heat transfer between the two phases in a computational cell is included in the scalar transport equation (given by equation 3.53) and is evaluated using the following equation:

$$\bar{S}_{\phi,h} = \sum_{i=1}^n \left[ \begin{aligned} & (\dot{m}'_{p,i,in} - \dot{m}'_{p,i,out}) h_{vap} - \dot{m}'_{p,i,out} \int_{T_{ref}}^{T_{p,i,out}} c_{p,p,i} dT_{p,i} \\ & + \dot{m}'_{p,i,in} \int_{T_{ref}}^{T_{p,i,in}} c_{p,p,i} dT_{p,i} \end{aligned} \right] / V_{cell} \quad (3.71)$$

The source term arising from the exchange of mass between the two phases in a computational cell is included in the continuity equation (given by equation 3.16), and in the species transport equation (given by equation 3.53), which is evaluated using the following equation:

$$\bar{S}_m = \sum_{i=1}^n \left[ \frac{\Delta \dot{m}_{p,i}}{\dot{m}_{p,i,in}} \dot{m}'_{p,i,in} \right] / V_{cell} \quad (3.72)$$

The source terms for the heat, mass and momentum exchange are updated after each continuous phase iteration by multiplying with a suitable under-relaxation factor.

### **3.13 Importance of Gas Velocity Profiles in CFD Modelling of Spray Drying Towers**

CFD modelling of spray drying towers requires modelling of the gas flow patterns using a suitable turbulence model and once a satisfactory validation of the fluid velocity profiles using the turbulence model is achieved, the drying with the discrete phase is considered using a suitable level of coupling between the discrete and the continuous phases. The modelling of turbulent flow inside a spray drying tower is challenging due to the presence of highly complex gas flow patterns resulting from a three-dimensional and swirling flow. The gas flow patterns affect the droplet and particle trajectories and consequently drying rates, coalescence/agglomeration, temperatures and residence times, which in turn influence the quality of the dried powder, for example, powder size distribution, average dried powder moisture content, powder colour and the level of thermal degradation. It also influences the stability of drying operation by affecting the deposition rate of particles on the wall. The understanding of gas flow patterns is therefore extremely important in the design and optimisation of spray drying towers. Information about the gas velocity profiles in a spray drying tower can be obtained by experimental investigation using a velocity measurement instrument, which in the presence of droplets/particles is very difficult due to the possibility of sticking of droplets and wet particles with the measurement instrument. Alternatively, by carrying out CFD modelling which is more convenient, but a proper validation of predicted velocity profiles is required to gain confidence in the CFD model predictions. A review of previous experimental studies carried out to study gas velocity profiles in counter-current spray drying towers is given in Section 3.14. A review of CFD modelling work carried out to model gas velocity profiles and its validation with measured velocity profiles in these spray towers is given in Section 3.15.

### **3.14 Experimental Study of Gas Flow profiles in the Spray Drying Tower**

The counter-current spray drying tower involves three dimensional, turbulent and swirling flow of the gas. The swirl is induced due to the tangential entry of the gas at the bottom of the tower, as shown schematically in Figure 2.5 (b). The gas flow profiles in a counter-current spray tower were first measured by Chaloud *et al.* (1957) in which the tangential velocity profile showed the presence of a combined (Rankine) vortex and the magnitude of the axial velocity was maximum at the central axis of the tower with a

gradual decay away from the central axis. However, it was not mentioned how the measurement was taken. The Rankine vortex can be divided into three regions, namely the core, annular and the near-wall region (Kioth, 1991). The core region is dominated by a forced vortex. The flow inside the forced vortex is rotational flow. In the forced vortex region, the flow is stabilised due to a suitable pressure gradient and turbulence is suppressed. The annular region is dominated by the free vortex. The flow inside the free vortex is irrotational, unstable and highly turbulent. The turbulent stresses in this region are highly anisotropic (Chang and Dhir, 1994). In the near-wall region, the wall effects become important and a sharp decrease in the tangential velocity occurs. The advantage of such a flow is that it stabilizes the gas flow pattern in a spray tower. It has been shown by many researchers that the swirling flow also improves the inter-phase heat (Chang and Dhir, 1995) and mass transfer rates (Shoukry and Shemll, 1985; Javed *et al.*, 2006). In a spray drying tower, the presence of a highly swirling flow enhances the heat and mass transfer between the droplets/particles and gas due to high shear flow and increased relative velocity between the droplets/particles and drying gas (Chaloud *et al.*, 1957). The strength of swirl in the flow is usually characterised by a dimensionless swirl number, which is defined as the ratio of the angular momentum flux and the axial momentum flux and is given by (Yajnik and Subbaiah, 1973):

$$\Omega = \frac{\int_0^R \bar{u}_x \bar{u}_\theta r^2 dr}{R \int_0^R \bar{u}_x^2 r dr} \quad (3.73)$$

Flow at a swirl number greater than 0.5 is considered as highly swirling flow and in such flows, vortex breakdown occurs resulting in the formation of a reverse flow zone (Kioth, 1991). Many researchers have carried out experiments to study the gas flow patterns in counter-current spray towers varying from industrial scale having height (H) of 24 m, with diameter (D) of 6 m (H/D = 4.0) to laboratory scale having a height of 4.2 m and diameter of 1.2 m (H/D = 3.5). In earlier studies (Place *et al.*, 1959; Paris *et al.*, 1971; Ade-John and Jeffreys, 1978; Sharma, 1990), tracer concentration measurement and flow visualisation techniques were used to identify gas flow patterns. One of the earliest reported data among such studies was given by Place *et al.* (1959), who used helium as a tracer to study gas flow patterns and residence time distribution of air. The tower studied was an industrial-scale counter-current tower, having a height of 15 m (cylindrical section) and a diameter of 6.4 m. The contours of exit times of 50% of the

injected tracer were plotted. The tracer injection experiment provided useful information about the gas flow patterns in the spray tower. The gas flow patterns were found to be highly unstable. Three zones were identified in the tower along the cross-section, based on the gas-flow patterns, i.e., the inner, intermediate and the outer zone (near the wall). In the inner and outer zones, the flow was in the upward direction, while a slow moving or even downward flow was observed in the intermediate zone. This reverse flow in the intermediate zone was the main mechanism of back mixing and was believed to be beneficial for spray dryer performance as it gives uniformity in the temperature along the tower height.

Paris *et al.* (1971) also used helium as a tracer in the air flow in an industrial-scale counter-current spray drying to identify different flow zones. The tower used was relatively large in height, having a height of 24 m and a diameter of 6 m. Place *et al.* (1959) and Paris *et al.* (1971) used the measured residence time data to develop a model for the prediction of residence time distribution (RTD) in the spray drying tower by approximating sequences of well-mixed and plug-flow zones in different regions of the spray tower. In both studies, the measurements were made without the spray of feed. Reay (1988) highlighted the disadvantages of this approach, which includes the requirement of accurate measurement of the RTD data, the method being incapable of designing new towers and the inability to assess the effect of varying chamber geometry or operating conditions on the RTDs. In addition to these disadvantages, the presence of droplets/particles and temperature profiles may also influence the air flow profiles. Ade-John and Jeffreys (1978) conducted experiments using a tracer to investigate different zones of two phase air-water droplets flows in a laboratory-scale, transparent walled spray drying tower having a height of 4.2 m and a diameter of 1.2 m, considering the interaction of air with water droplets. Four zones were identified: an intensely turbulent zone near the air inlets, a turbulent zone near the spray nozzle, a cylindrical plug-flow zone in between these two zones and an air bypass zone near the wall that existed throughout the height of the tower. Sharma (1990) used the flow visualisation technique to study the gas flow patterns in the same spray drying tower used by Ade-John and Jeffreys (1978) with and without the presence of a water spray by varying the angle of tangential-entry gas inlets. The gas flow patterns were made visible by the use of smoke as a tracer. The gas flow pattern and stability of the flow was found to be dependent on the horizontal and radial angles of the gas inlet nozzles. A strongly swirling gas core

was observed in the tower with a stable gas flow when both the horizontal and radial angles were  $25^\circ$ .

The first reported quantitative measurements of gas velocity profiles in a counter-current spray drying tower were made by Bayly *et al.* (2004). The measurement of axial and tangential velocity components of the ambient gas flow were taken in the same spray tower which was previously studied by Ade-John and Jeffreys (1978) and later by Sharma (1990) using laser doppler anemometry technique at a series of axial locations. The radial and horizontal gas inlet angles were  $25^\circ$ . The tangential velocity component was an order of magnitude greater than the axial velocity component. The tangential velocity profiles showed the presence of a Rankine vortex that persisted throughout the tower height. The axial velocity profiles showed reverse flow (negative axial velocity) in the annular region of the tower that persisted through most of the tower height. The magnitude of negative axial velocity reduced along the tower height. The quantitative measurement of gas velocity profiles in an industrial-scale counter-current spray drying tower was recently done by Wawrzyniak *et al.* (2012a). The tower studied had a diameter of 6 m and a height of 36 m. The measurement of magnitude of velocity components at two axial locations was presented which was measured using a pitot tube. The gas flow was found to be highly unsteady, which was reported to be due to the construction of the gas inlets. The gas inlets did not have tangential entry hence no swirl was imparted to the gas flow. The measured data by Bayly *et al.* (2004) and Wawrzyniak *et al.* (2012a) was used to verify CFD model predictions of the gas flow by these authors, which is discussed in the next section.

These experimental studies have revealed that the flow in a counter-current spray dryer involves turbulent, swirling, complex flow patterns with back mixing and bypass regions shown by both qualitative and velocity measurement techniques. The only comprehensive quantitative measurement of velocity components is done by Bayly *et al.* (2004) for a laboratory-scale spray tower, which shows that the tangential velocity profiles contains a Rankine vortex and is an order of magnitude higher than the axial velocity component. Also, the negative axial velocity indicates a vortex breakdown. The existing studies have not reported turbulence data which may be useful for validation of a turbulence model used in the CFD study for flow modelling.

### **3.15 CFD Modelling of Gas Flow in Counter-Current Spray Drying Towers**

The modelling of turbulent gas flow inside a spray drying tower is challenging due to the presence of highly complex gas flow patterns resulting from three-dimensional and swirling flows, as revealed by the previous experimental studies cited above. The gas flow patterns in counter-current spray drying towers have been investigated using CFD by a few researchers in the past. Harvie *et al.* (2001) used single phase, three-dimensional CFD simulations with a very large eddy simulation (VLES) approach to study the gas flow patterns in the laboratory-scale counter-current spray drying tower which was previously studied experimentally by Sharma (1990). In the VLES approach the computational mesh is chosen to be fine enough to resolve the significant flow features and a turbulence model is used to represent the dissipative scale, which in this case was  $k-\varepsilon$  model (Harvie *et al.*, 2001). They investigated the effect of varying horizontal and radial angles of the inlet gas nozzles on the gas flow pattern. The simulation results showed that the gas velocity profiles were highly dependent on the radial and horizontal angles of the gas inlet nozzles. The most stable (time invariant) gas flow patterns were observed at a radial and horizontal angle of  $25^\circ$ , which confirmed the findings by Sharma (1990). The predicted tangential velocity profiles showed the presence of a forced vortex inside the cylindrical section of the tower. A good qualitative agreement between the predicted flow patterns and that observed by Sharma (1990) was also observed. No quantitative comparison of CFD simulation results was made by Harvie *et al.* (2001).

Bayly *et al.* (2004) studied gas flow profiles in the same spray dryer which Sharma (1990) studied experimentally, using single phase, three-dimensional CFD modelling with a Reynolds stress transport (RST) model. The simulation results were compared with the experimental data measured using an LDA technique at a series of axial locations (see Section 3.14). A good quantitative agreement was observed between the measured and simulated mean axial and tangential velocity profiles. In contrast to the simulation results reported by Harvie *et al.* (2001) in the tangential velocity profiles measured and predicted by Bayly *et al.* (2004), a Rankine vortex was observed in the cylindrical section of the tower with a peak value in the tangential velocity profile moving towards the centre as the gas flows in the upward direction. The study of Bayly *et al.* (2004) also showed that the axial and tangential velocity components differ by an order of magnitude (in both measurement and predictions); hence the comparison of

observed flow patterns by Sharma (1990) with CFD predicted flow patterns study by Harvie *et al.* (2001) to validate the CFD model predictions may not be a valid approach.

Recently, Wawrzyniak *et al.* (2012a) carried out single phase CFD modelling of an industrial counter-current spray drying tower, which they also studied experimentally as mentioned above in Section 3.14. The predicted gas velocity magnitude using the RST model was compared with the experimentally measured data at two axial locations. A fairly good agreement between the experimental data and modelling results was observed, considering the unsteadiness in the flow which was reported to be due to the construction of gas inlets as a result of which no swirl was induced in the gas flow at the entry. However, a comparison of individual velocity components was not presented as they were not measured. Wawrzyniak *et al.* (2012a) also studied the effect of varying the horizontal angle of the gas inlet nozzles on the stability (steadiness) of gas flow patterns using CFD simulation. It was found that the most stable gas flow patterns were observed at gas inlet nozzle angles of  $20^\circ$  and  $30^\circ$ . This confirmed the findings by other researchers (Sharma, 1990; Harvie *et al.*, 2001) that the stability of the gas flow patterns depends on the degree of swirl, which is dependent on the angles of the tangential-entry gas inlets.

The limited numerical simulations have revealed that the CFD models are capable of reproducing qualitatively the observed flow profiles in laboratory scale spray drying tower and quantitatively using the RST model. It has been shown via CFD modelling that the gas flow pattern depends significantly on the angle of the gas inlet nozzles and become stable when the gas inlet nozzle angles are between  $20^\circ$  to  $30^\circ$ . The tangential velocity component is the dominant component in the spray drying tower with an order of magnitude higher than the axial velocity component. There is a lack of comprehensive quantitative validation of the turbulence models with experimental data for large scale counter-current spray drying towers. The pilot-plant and industrial scale spray drying towers have a layer of deposits on the wall due to sticking of the wet particles and droplets on the wall. This results in a rough surface at the wall and an increased frictional resistance. The role of wall roughness due to wall deposits in altering the velocity profiles is not evaluated in the existing simulations. This layer of deposits provides additional frictional resistance to the swirling flow and this result in a faster decay of swirl along the height (Francia *et al.*, 2013). Hence the effect of wall roughness on the modelling of gas flow in the tower also needs to be evaluated.

Additionally, no comparison has been made between the measured and predicted fluctuating velocity components.

### **3.16 CFD Modelling of Spray Drying Process**

Most of the previous CFD modelling work on spray drying process is focused on the co-current spray drying towers (Livesley *et al.*, 1992; Oakley and Bahu, 1993; Langrish and Zbicinski, 1994; Zbicinski, 1995; Kieviet, 1997; Southwell *et al.*, 1999; Straatsma *et al.*, 1999; Harvie *et al.*, 2002; Huang *et al.*, 2003a, 2003b, 2004a, 2004b, 2006; Verdurmen *et al.*, 2004; Li and Zbicinski, 2005; Kota and Langrish, 2007; Anandharamakrishnan *et al.*, 2010; Saleh, 2010; Mezhericher *et al.*, 2008b, 2009, 2010a, 2012a, 2012b; Jin and Chen, 2009, 2010; Sadripour *et al.*, 2012). In these studies, the continuous phase is treated as Eulerian while the discrete phase (droplets and particles) is treated as Lagrangian. The coupling between the two phases is done using the Particle-Source-in-Cell (PSI-Cell) model of Crowe *et al.* (1977). It was found that the turbulence model, droplet drying kinetics model, initial atomisation parameters and turbulent particle dispersion were crucial parameters that influenced the accuracy of CFD modelling results.

These studies have demonstrated the potential of CFD for improving the design and operation of co-current spray drying towers to produce better product quality. It is found that the stability of gas flow patterns have an impact on wall deposits (Langrish and Zbicinski, 1994) and the uniformity of dried product characteristics. The swirl flow improves the stability of gas flow, however, a disadvantage of swirl in co-current spray towers is that it increases the residence time of particles which may cause over drying as well as conveying the particles towards a higher gas temperature region, causing thermal degradation (Harvie *et al.*, 2002). Studies have also been carried out to check the dryer performance using different nozzle types (Huang *et al.*, 2006; Anandharamakrishnan *et al.*, 2010) and also by changing the inlet angle of swirl vane to change the level of swirl of the drying gas (Langrish and Zbicinski, 1994). CFD simulation has also been used to evaluate alternate chamber geometries including conical, hour-glass and lantern shaped drying chambers (Huang *et al.*, 2003b). CFD simulations have been carried out to predict agglomeration (Verdurmen *et al.*, 2004) and deposition of particles on the wall (Jin and Chen, 2010; Sadripour, 2012) and has shown a good deposition trend compared to experimental data. A review of CFD modelling of spray drying in co-current towers is given by Kuriakose and Anandharamakrishnan

(2010), Jamaledine and Ray (2010), Langrish (2007), Norton and Sun (2006), Langrish and Fletcher (2003), Langrish and Fletcher (2001).

Spray drying in a counter-current tower is a poorly understood process (Zbicinski and Piatkowski, 2009). Less attention has been given to the experimental and modelling work to gain a good understanding of the counter-current spray drying process. According to Zbicinski and Piatkowski (2009), complicated hydrodynamics of the continuous and discrete phases, intensive agglomeration, less availability of counter-current spray towers and difficulty in gathering reliable data for model validation are the major factors limiting the research work on the counter-current spray drying towers. Counter-current spray drying towers offer better heat utilisation compared to the co-current spray drying towers. A better understanding of drying kinetics in these towers would enable the operating issues pertinent to counter-current spray drying towers, including high wall deposits, high agglomeration and product thermal degradation to be controlled by making modifications in the operating parameters and in the tower design. This may also enable a wider range of products to be dried using counter-current spray towers.

Crowe (1983) applied the PSI-Cell model in a 2-D counter-current spray tower simulation. The diameter and height of the tower were 1 m and 4 m, respectively. The gas flow was modelled using the  $k-\varepsilon$  turbulence model. It was concluded that the heat, mass and momentum coupling between the discrete and the continuous phases has a significant influence on the results. The model was not validated by experimental data. Livesley *et al.* (1992) used the same approach for 2D and 3D CFD modelling of a pilot-scale counter-current spray tower having a height and diameter of 9 m and 1.8 m, respectively. The turbulence was modelled using the  $k-\varepsilon$  model. The dispersion of the particles due to turbulence was included in the simulation. The mean droplet/particle size across the radius was compared with the measurement at 0.3 m below the atomiser for water droplets and at 1.3 m for a zeolite slurry. The spread of the mean size of the water droplets over the radius was slightly underpredicted which was attributed to the shortcomings in the turbulence model used. For the case in which a zeolite slurry was used, the agreement between the measured mean droplet/particle size across the radius and the prediction was poor. Because the model did not account for coalescence and agglomeration, the mean droplet/particle sizes along the radius were underpredicted. The predicted gas temperature profiles in the spray drying tower were highly asymmetric in the bottom region of the tower, but became symmetric near the top

outlet. The predicted temperature profiles were not validated by experiment. The hot gas inlet angles were not reported in the study, which significantly impacts the velocity profiles in the spray tower (Sharma 1990; Harvie *et al.*, 2001 and Wawrzyniak *et al.*, 2012a). It is also not mentioned how the droplet/particle and wall interaction were modelled which can significantly affect the residence time of the discrete phase as reported by Kieviet (1997) for a co-current spray tower. This study indicated the potential of the CFD technique in modelling spray drying processes in a counter-current tower and highlighted the importance of accurate modelling of the gas flow using a reliable turbulence model and the need for inclusion of agglomeration.

Zbicinski and Zietara (2004) carried out a 2D, axisymmetric, steady-state simulation of a counter-current spray drying tower using an aqueous solution of maltodextrin as the feed. The coalescence/agglomeration process was included in the CFD model using a non-physical collision model for droplets and particles based on a stochastic approach for determining the probability of collisions (Sommerfeld, 2001). However, the detail of the droplet/particle and wall interaction was not given. The results of measured temperature and humidity profiles of the gas and moisture content of particles were compared with the predictions at various axial locations. Overall a good agreement was observed, but at some axial locations, significant discrepancy was seen; this was attributed to measurement errors.

Recently, Wawrzyniak *et al.* (2012b) developed a novel approach for CFD modelling of heat and mass transfer in an industrial counter-current spray drying tower having a height of 37 m and a diameter of 6 m. The modelling approach was based on a negative heat source term which reflects the energy necessary for evaporation of moisture from the discrete phase. This approach required estimation of the total power consumption during the drying process and the determination of a power density distribution function in the dryer. The energy source term in the energy transport equation was used as a negative heat source term in the gas phase reflecting the energy transport in vapourising the moisture content from the discrete phase without requiring the need to include drying kinetics of the discrete phase in the CFD model. This negative energy source term was obtained from the heat and mass balances of the tower under operation using the measured temperature data. Hence this approach required the accurate determination of temperatures across the radius and along the height, from which a volumetric map of the energy used for evaporation of moisture inside the dryer was formulated using a probability function. The determination of the gas temperatures in the spray drying

tower posed difficulties due to the presence of droplets/particles as well as the highly transient nature of the gas flow in the spray tower. Some artificial limits to the predicted temperatures were imposed in the model to prevent uncontrolled gas temperatures either to rise or fall to unrealistic values during the iterations. The determination of accurate temperature profiles in spray drying towers is difficult due to the presence of wet particles in the gas phase and in some cases the transient behaviour of gas phase also makes the measurements less reliable. Another disadvantage of this approach is that it requires experimental trials for the determination of the volumetric energy source term: hence reliance on experimental trials is not eliminated using this approach.

The existing work on CFD modelling of counter-current spray drying towers has shown the potential of modelling the complex interacting transport processes inside the spray drying tower. However, there are still many gaps in the spray drying process modelling including comprehensive validation of the turbulence models used to simulate gas flow profiles in a spray drying tower, consideration of drying kinetics of droplets/particles in three-dimensional gas flow with coupled heat, mass and momentum transfer along with particle-wall interactions. Investigation of the role of initial specified droplet size distribution and velocity on the final dried powder parameters has not been investigated in the earlier studies. The final residence times of particles and moisture content as a function of sizes also needs to be evaluated and compared with experimental data, the influence of change in size/shape of the particle on the heat and mass transfer coefficients as well as on the drag force is also remains unexplored. In addition, the influence of inter droplets/particle collisions as well as particle-wall interactions including wall deposition and re-entrainment of the wall deposits as well as breakage of particles due to these interactions in the CFD modelling of spray drying tower also needs to be evaluated.

### **3.17 Experimental Studies on Spray Drying Process in Counter-Current Towers**

Experimental studies provide useful information about the behaviour of the droplets/particles and the drying gas in a spray drying tower. The experimental data can also be used for the validation of spray drying process models. A limited number of experimental studies have been carried out to study drying kinetics in counter-current spray drying towers. Piatowski and Zbicinski (2007) conducted experiments in a counter-current spray drying tower using a solution of maltodextrin (50% w/w) as a

feed to investigate the effect of gas temperatures near the atomisation zone on the agglomeration by varying the height of a single centrally located pneumatic nozzle. The tower studied had a height of 9 m and a diameter of 0.5 m. The hot gas was injected via fins with adjustable angles that induced swirl in the flow. It was found that this parameter has a significant influence on agglomeration. The percentage of larger particles ( $>150\ \mu\text{m}$ ) collected from the bottom of the tower increased with a larger distance between the gas inlet and the nozzle. The increase in distance between the gas inlets and the atomiser resulted in a lower temperature near the atomisation zone which promoted the agglomeration process, while a higher gas temperature near the atomisation zone (achieved by decreasing the distance between the gas inlets and the nozzle) hampered the agglomeration process due to rapid moisture evaporation near the atomisation zone. Hence agglomeration happens when the colliding particles have a greater moisture content. The morphology of the spray dried particle was also reported. In the drying conditions which resulted in minimum agglomeration, the particles were in the form of combined spheres. In the case of severe agglomeration, the particles were of more uniform spherical structure. Zbicnski and Piatkowski (2009) later studied the extent of deposition on the wall in the same spray tower by changing the feed pressure to the atomiser, which changed the size distribution of the atomised droplets. The deposition of droplets/particles on the walls was found to be more severe for coarse atomisation (larger droplets). The axial velocity of the droplets/particles was found to be dependent on the gas velocity except in the vicinity of the atomiser. The effect of atomiser height on the level of agglomeration was also investigated. It was found that at a lower height (close to the gas inlet), the level of agglomeration was significantly smaller. Above the nozzle, the smaller particles were freely entrained with the drying gas to the top receiver. The temperature distributions of the gas with and without the presence of the spray were also reported. In the presence of spray, the temperature profiles of the gas were less uniform. It was found that the slurry flow rate, nozzle location and inlet gas temperature are the most decisive factors that control size distribution and density of the dried powder.

### **3.18 Conclusions**

A review of droplet drying models used in the modelling of spray drying process is presented. The droplet drying models are either based on a semi-empirical approach or a theoretical approach. The low computing requirement of semi-empirical models make them suitable for studying drying kinetics using CFD modelling of spray drying

process. Two most common approaches used in the modelling of spray drying towers are the plug-flow approach and the CFD approach. The one-dimensional (plug-flow) models give quick estimations of the effect of the operating parameters on the dried powder characteristics, but are unable to model complex processes including particle-wall interactions and the resulting wall deposition/re-entrainment and droplet/particle-particle interactions. The CFD models are computationally expensive, however, in these models it is possible to capture complex interactions between the discrete and the continuous phases, and to identify and troubleshoot problems pertaining to the dryer performance, for example excessive or insufficient level of agglomeration and wall deposition, and optimisation of the tower operation and design. Most of the modelling work on spray drying towers has been focused on co-current spray drying towers. The modelling work on counter-current spray drying towers is scarce. Very limited experimental work has been reported on the study of drying process in a counter-current spray drying tower. There is a need to carry out modelling work on counter-current spray drying towers considering the interactions between the discrete and continuous phases to develop a better understanding of the drying kinetics in these towers, which would help in developing more efficient and optimised operation of spray drying towers, more reliable prediction of dried powder characteristics as well as in troubleshooting the operating problems.

## **4. COLLECTION OF EXPERIMENTAL DATA**

### **4.1 Introduction**

The counter-current spray drying tower which was used to collect data for the validation of modelling results in this study is a pilot-plant tower, called integrated pilot-plant (IPP), at P&G research centre in Newcastle, UK. The data is collected by other researchers in P&G research centre. This spray drying tower is a scaled-down version of typical commercial spray drying towers used by P&G to manufacture detergent powder. It is used to evaluate the effect of operating conditions on the quality of the detergent powder (determined by measuring spray dried powder moisture content, bulk density and size distribution) using different detergent slurry formulations and hence to optimise the operating parameters to assist in the determination of optimised operating parameters in the commercial spray drying units. This spray tower has a single centrally located hollow-cone pressure nozzle atomiser installed at different heights. The spray drying process can be carried out using a single as well as multiple nozzles at different heights during the operation. The commercial spray drying units have similar height but have a larger diameter due to greater capacity. The slurry in commercial spray drying towers is sprayed using a ring of nozzles at various heights.

### **4.2 Spray drying process in the IPP unit**

In the spray drying process studied, the feed is a detergent slurry. The slurry is a mixture of zeolite, surfactant, water and additives. Typical initial moisture fraction of the slurry is in the range of 0.25-0.35 w/w wet basis. The slurry is prepared in mixing tanks in a batch wise manner, which is then fed to a crutcher (mixer), which acts as a holding tank for the continuous supply of feed. The slurry from the crutcher is fed to a hollow cone pressure nozzle atomiser at a pressure of about 60-75 bar inside the IPP spray drying tower. This is done using a series of low-pressure and high pressure pumps. The height of the atomiser can be adjusted, this will primarily have an impact on the residence time of the particles. The slurry can also be sprayed using two nozzles at different heights in the tower. The slurry is atomised into small droplets in the spray drying tower. Figure 4.1 is a process flow diagram of the spray drying process in the IPP.

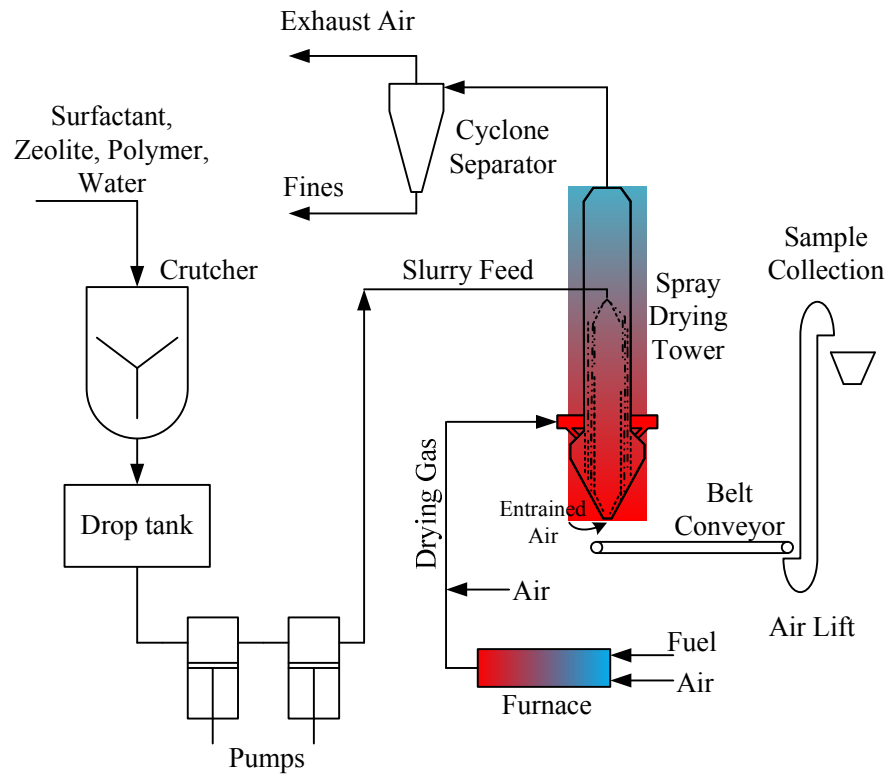


Figure – 4.1: Process flow diagram of detergent slurry spray drying.

The hot gas used as the drying medium is composed of atmospheric air and flue gas. The atmospheric air is injected into a direct fired furnace via an air blower. Methane is used as fuel gas for the furnace. The air is heated up to the required temperature (typically 200 to 300°C). The resulting hot gas is a mixture of air, CO<sub>2</sub> and H<sub>2</sub>O vapours. The hot gas goes into the distribution ring. The gas is distributed around the ring and goes into the gas inlet nozzles. The gas inlet nozzles are mounted tangentially to the spray drying tower at an angle. The tangential entry of gas gives swirl to the hot gas flowing counter-current to the droplets/particles. The hot gas inlet temperature is measured using a *k-type* thermocouple (comprising chromel-alumel alloys) in a duct that supplies drying gas to the distribution ring. The contact of the gas with droplets and particles results in removal of moisture. The dried particles fall into a belt conveyor at the bottom of the tower inside a semi enclosed chamber. The temperature of the dried powder is measured at the belt conveyor using an infrared probe a few meters away from the location of the particle exit from the tower. The dried powder is then lifted up using an air lift and collected in a storage tank, from where the sample of powder is collected for the measurement of moisture content, bulk density and cake strength testing. The operating pressure inside the spray drying tower is slightly below atmospheric (-300 Pa at the outlet) using an induced draft fan. Due to lower operating

pressure, some amount of atmospheric air gets entrained into the tower from the open ends at the sides of the enclosure around the belt conveyor (see Figure 4.2). This amount of cold air results in cooling of the dried particles exiting from the bottom.

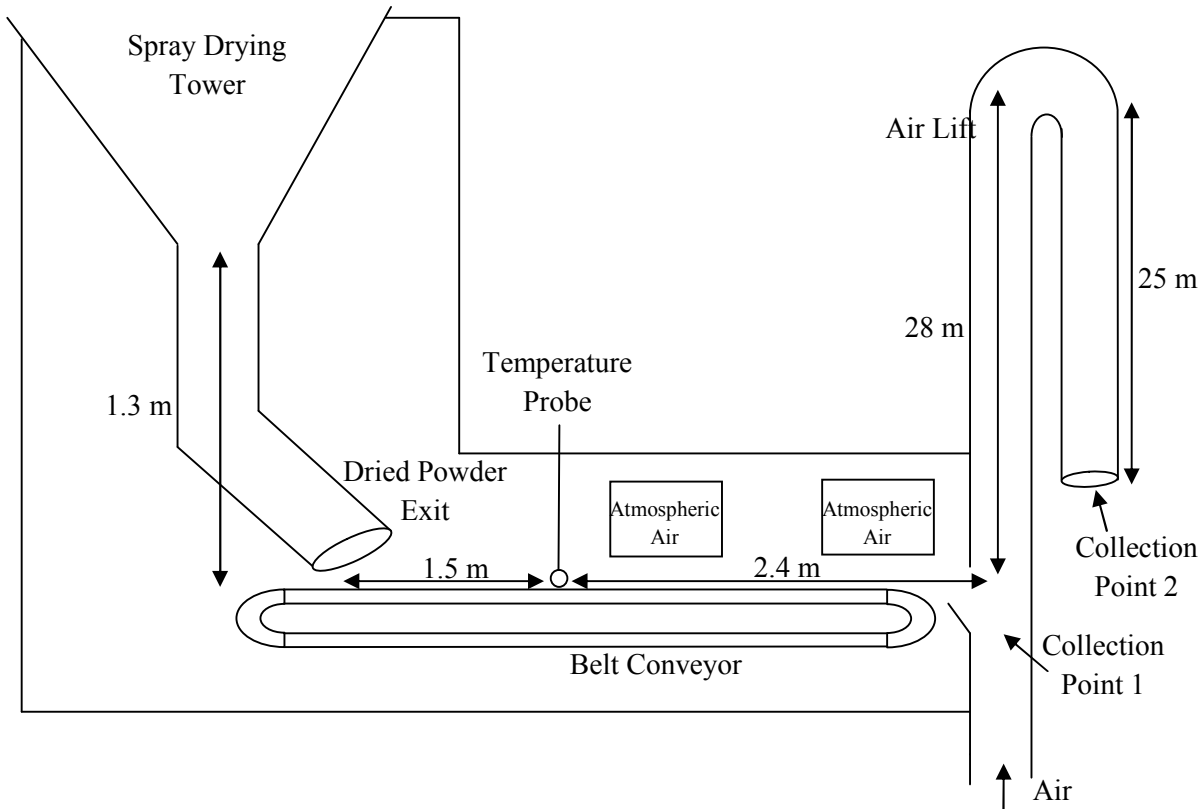


Figure – 4.2: Collection of dried powder at the bottom of the tower.

Fine particles (typically  $<150\ \mu\text{m}$ ) get entrained by the exhaust gas exiting from the top of the spray drying tower. Fine particles need to be separated before the gas can be released into the atmosphere. To separate fine particles from the exhaust gas stream, the gas goes into a cyclone separator. The fines are collected from the bottom of the cyclone separator (see Figure 4.3). The exhaust gas stream is then released to the atmosphere. The exhaust gas stream temperature is measured at the inlet header of the cyclone separator using a *k-type* thermocouple.

The spray drying tower is insulated using fibre glass insulation. Electrical trace heating is also provided between the insulation and the wall of the tower, which ensures that the inside temperature of insulation does not fall below ( $60^\circ\text{C}$ ) when the tower is not in operation to avoid delay in the tower start-up. The inside walls of the spray drying tower during a spray drying run are covered by a layer of deposits. Therefore, the wall of the tower is usually cleaned using a brushing assembly before a new run is started.

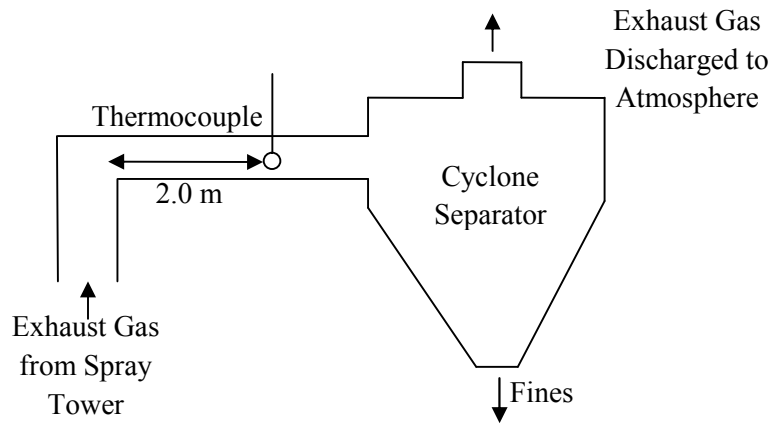


Figure – 4.3: Separation of entrained fine powder from exhaust gas.

### 4.3 Geometry of the Tower

Figure 4.4 is a schematic of the spray drying tower. It is a long-form counter-current spray tower which is characterised by height to diameter ratio greater than 3. It consists of a cylindrical section and the bottom conical section. The gas enters the tower tangentially into the bottom conical section via gas inlet nozzles which are inclined at an angle both horizontal and radial. The horizontal angle ( $\beta$ ) is the angle which the gas inlets make with the horizontal axis (Figure 4.4 (b)). The radial angle ( $\theta$ ) is the angle between the gas inlet nozzle and line normal to the tangent of the dryer circumference (Figure 4.4 (c)). This tangential entry of the gas imparts swirl to the flow. The gas leaves the tower via a vortex finder at the top. Due to confidentiality reasons the geometrical dimensions are not shown.

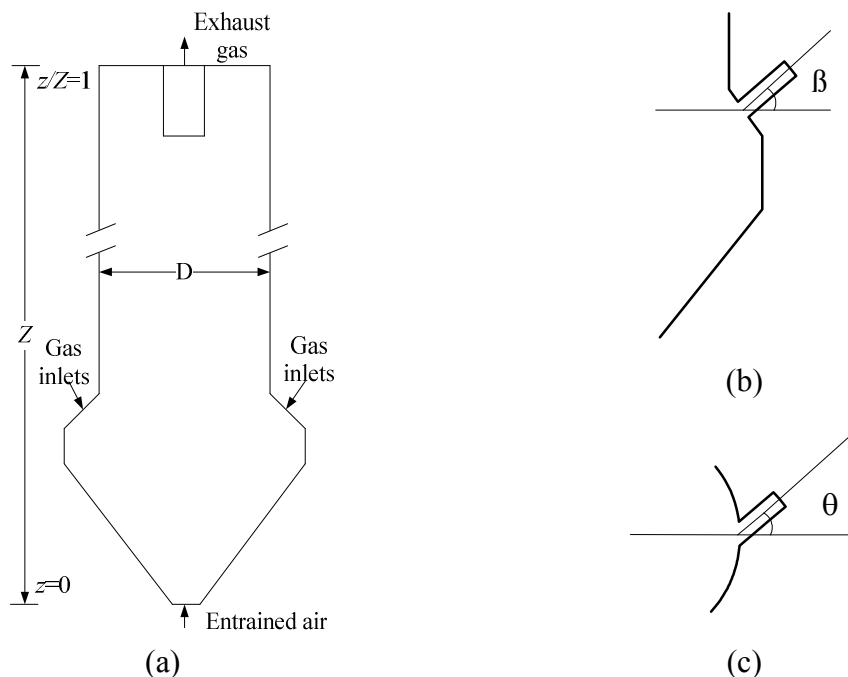


Figure – 4.4: Schematic of the spray drying tower.

## **4.4 Characterisation of Dried Detergent Powder**

The measurement of spray dried powder characteristics is carried out by researchers at P&G using a sample of spray dried powder in a laboratory at P&G, Newcastle Technical Centres. The tests include measurement of size distribution of dried powder, average moisture content, measurement of bulk density and cake strength.

### **4.4.1 Measurement of Powder Size Distribution**

Dried powder collected from a spray drying tower consists of a range of particle sizes. A number of factors impact the size distribution of the dried powder including coalescence, agglomeration and re-entrainment of deposited particles during spray drying. The spray dried powder should neither contain too much fines ( $<150\ \mu\text{m}$ ) nor it should contain an excessive amount of coarse particles ( $>1000\ \mu\text{m}$ ). Powder containing excessive amount of fine particles causes dust formation (Djurdjevic, 2010). On the other hand, excessively coarse powder affects the dissolution rate (Ahmadian, 2012). Typically the mass mean diameter of dried powder should be between  $300\ \mu\text{m}$  to  $600\ \mu\text{m}$ . The measurement of dried powder size distribution is carried out by sieving. Typically 10 sieve sizes (ranging from  $150\ \mu\text{m}$  to  $3350\ \mu\text{m}$ ) are used to classify particles of different sizes (Martin de Juan, 2011). The separated fractions are then weighed to determine the powder mass mean diameter.

### **4.4.2 Measurement of Moisture Content**

The moisture content is another important characteristic of the spray dried powder. The dried powder moisture content is affected by the drying conditions in the spray drying tower as well as the slurry formulation. The target moisture content in the dried powder is typically 2.0 to 3.0% by weight (wet basis). If the exit moisture content of the dried powder is below this limit, it indicates exposure of powder to a high temperature, resulting in thermal degradation of powder and affects its performance. Moisture content higher than 3% is also avoided as it results in the formation of cake, thereby affecting powder flowability. Moisture content of dried powder sample collected from the tower (as depicted in Figure 4.2) is measured using gravimetric analysis. A sample of 2 gm of powder is placed in a heater for 5 minutes at  $160\ ^\circ\text{C}$ , the sample is then again weighed. The resulting weight loss is the amount of moisture present in the dried powder sample (Martin de Juan, 2011).

#### 4.4.3 Measurement of Bulk Density

Bulk density of dried powder affects the amount required for mixing with additives including perfume and optic brighteners before packing as well as final packaging of powder because powder is consumed by the end user in terms of volume. The bulk density of powder is primarily affected by inflation (puffing) of particles during drying, which is controlled by varying the amount of air injected in the slurry feed line. The conditions inside the tower also influence the extent of inflation of particles. The bulk density of powder is measured by putting the sample of powder into a container of known volume and measuring the sample weight. The ratio between sample weight and volume is the bulk density of powder.

#### 4.4.4 Measurement of Envelope Density

Envelope density ( $\rho_{envelop}$ ) refers to the density of a single particle including the volume of internal and external pores. For the comparison of density of particles predicted by the models, envelope density is used. It is defined as the mass occupied by a single particle divided by total volume of a single particle including pore volume (see Figure 4.5). It is given by:

$$\rho_{envelop} = \frac{M_{solid}}{V_{pore} + V_{solid}} \quad (4.1)$$

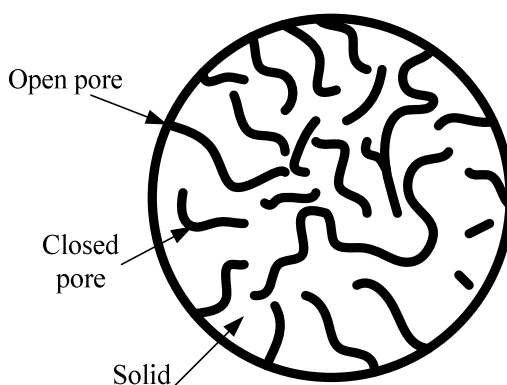


Figure – 4.5: Schematic of a porous particle.

The envelope density is measured using a GeoPyc device (Micromeritics, 2013). The equipment consists of a piston and cylinder arrangement (see Figure 4.6) in which a sample of powder is poured along with a commercial fluid that occupies the remaining volume in the cylinder. A force is then applied to the piston, so that the fluid occupies

the inter-particle voids in the sample. The density of sample is then calculated from the displacement of piston for a known applied force.

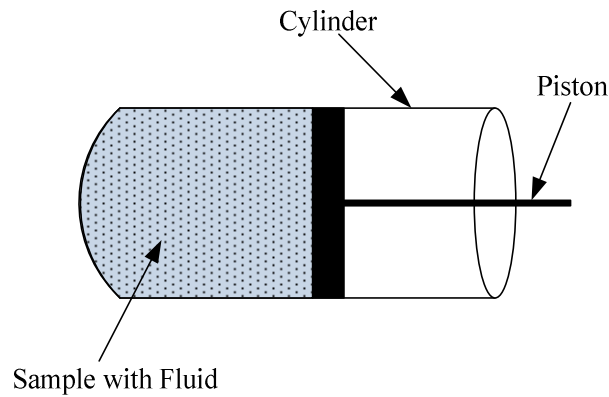


Figure – 4.6: Cylinder and piston arrangement in GeoPyc device.

#### **4.4.5 Measurement of Cake Strength**

Cake strength is important in determining flowability of the dried powder as it impacts the handling of powder. To measure the cake strength, the powder sample is compressed to form cake in a die. The cake is subjected to unconfined load until the cake fractures. The load at which deformation occurs in the cake gives a measure of powder flowability.

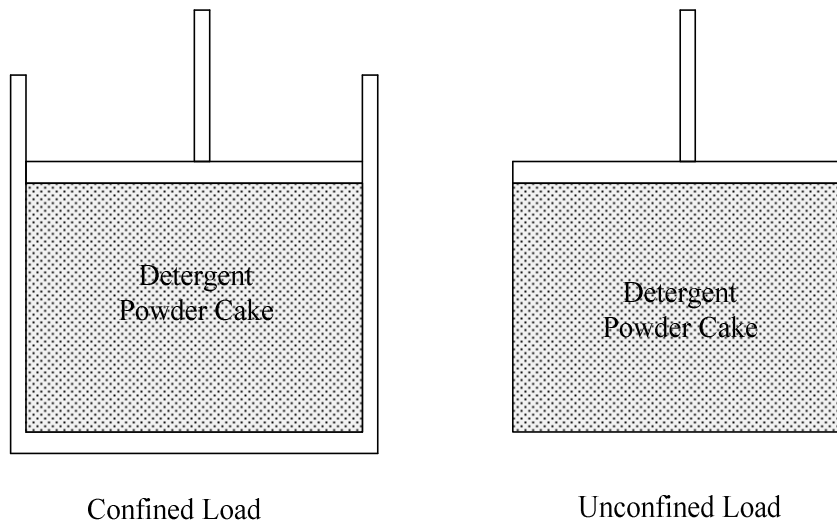


Figure – 4.7: Measurement of powder cake strength.

### **4.5 Droplet Size Distribution Measurement**

The measurement of size distribution of droplets resulting from atomisation of liquid slurry feed is carried out by Martin de Juan (2012) in an assembly developed in-house by P&G, called the atomisation rig depicted in Figure 4.8. The slurry is atomised in the

atomisation rig at the required pressure using a hollow-cone pressure nozzle atomiser. The resulting size distribution of droplets in the spray is measured using laser diffraction in Malvern Spraytec Analyser (Malvern, 2013) which records the angular intensity of scattered laser beam as the spray passes through it. The scattering pattern is then analysed using Malvern RTSizer to yield a size distribution. Typically, size distribution of the sprayed droplets range from 10  $\mu\text{m}$  to 1000  $\mu\text{m}$ . The spray angle can also be measured by taking a photograph of the spray using a camera installed in the atomisation rig.

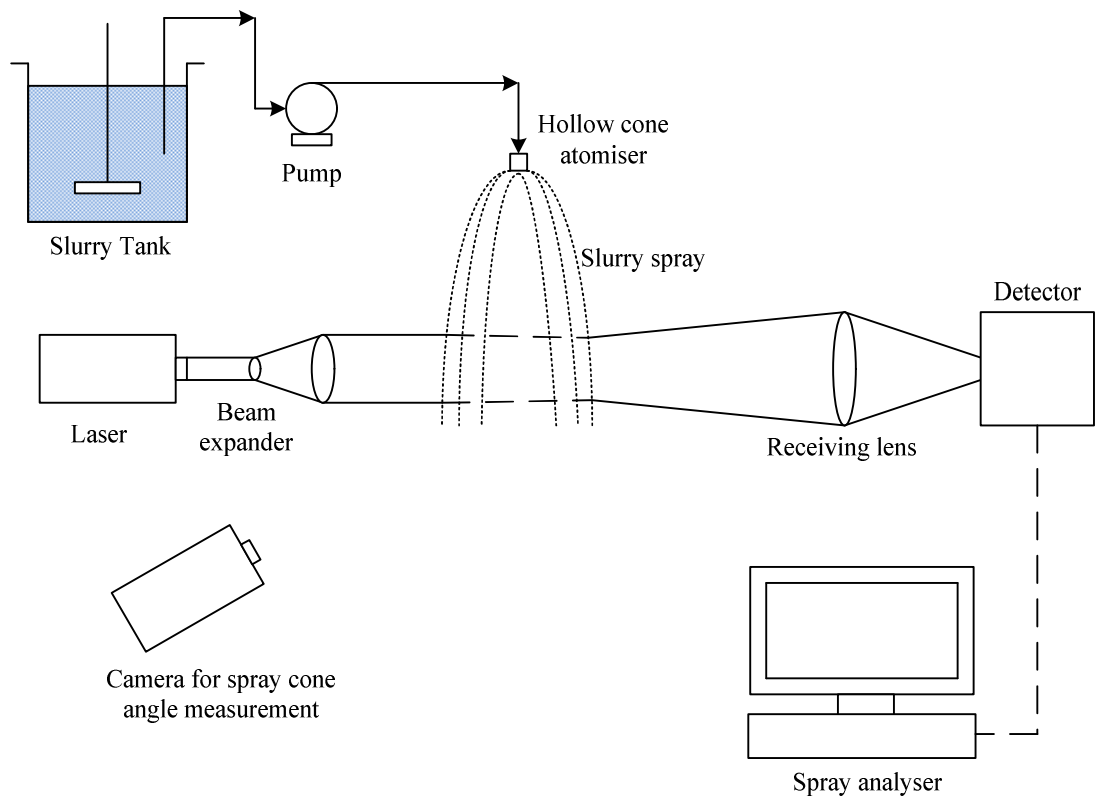


Figure – 4.8: Schematic of the atomisation rig.

## **4.6 Data from the IPP Spray Drying Tower**

The data measured inside the tower was used to validate the model predictions. The data used for validation of models in this thesis include velocity components (axial, radial and tangential) inside the spray drying tower and temperature measurements of gas at various axial locations.

### **4.6.1 Measurement of velocity profiles inside the spray drying tower**

The velocity profiles inside the spray drying tower were measured by Francia (2011). Measurements were taken using sonic velocity anemometer for air flow at ambient

temperature (8°C) without the spray. The variation of axial, tangential and radial velocity components along the radius were measured at five axial locations within the cylindrical region inside the spray drying tower. At each axial location, the data was taken at 11 points along the radius. Due to the construction of the anemometer, measurements very close to the wall could not be taken as the access was limited by the equipment inaccessibility. The measured time-averaged data is used to validate the turbulence models used for reproducing the velocity profiles in the spray drying tower. Additionally the measured turbulence intensity data is also used to validate the CFD model predictions. The tower used for velocity profiles measurement contained a layer of deposits on the wall, which adds to the wall surface roughness. A comparison of velocity profiles predicted by CFD using various turbulence models and the measurements are given in Chapter 6.

#### **4.6.2 Measurement of temperature profiles inside the spray drying tower**

Temperature profiles of the gas phase were measured by Martin de Juan (2012), Davidson (2012) and Ahmadian (2013) inside the spray drying tower with and without the spray. The temperature measurements were taken using *k-type* thermocouples which were placed in a temperature measurement probe developed to measure the gas temperature along the radius of the tower (Figure 4.9 (a)). The temperature probe consisted of seven thermocouples which measured the temperature of drying gas along the radius. The temperature probe diameter was 10 mm while the diameter of the thermocouples was 1 mm. The temperature probe was aligned inside the tower so that the thermocouples face the direction of gas flow (see Figure 4.9 (b)). The temperature measurements were taken at various axial locations in the cylindrical region of the tower. A comparison of time-averaged gas temperature measurements and predicted temperatures inside the tower without the spray is given in Chapter 6. The measured time-averaged gas temperature profiles with the spray and its comparison with predicted gas temperature profiles is given in Chapter 7. Due to the presence of droplets/particles in that case, at the end of the trial, the temperature probes were inspected for possible deposition of particles on the thermocouples. Most of the powder was deposited on the upper side of the probe which prevented particles from depositing on the thermocouples, although some deposition on the thermocouple was also observed. Figure 4.9 (c), (d) and (e) are photographs of thermocouples taken out at the end of an experimental run which clearly show some deposition on the thermocouples, which affected the accuracy of measured gas temperatures in the presence of droplets/particles.

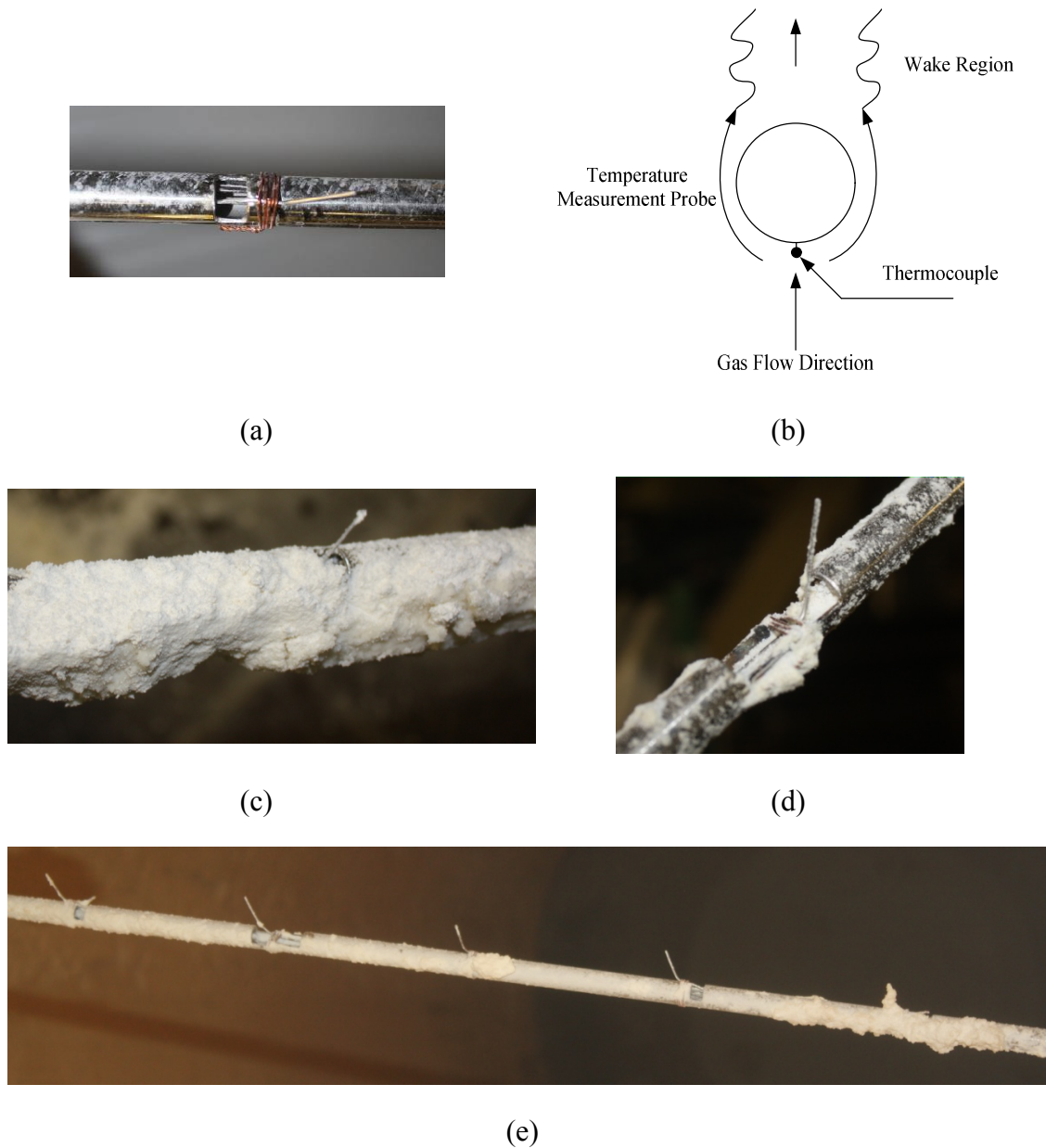


Figure – 4.9: Temperature measurement probe (a): thermocouple mounted on the rod, (b) direction of thermocouple facing the gas flow, (c), (d) and (e): Temperature measurement probe after the run with droplets/particles (Martin de Juan, 2012).

Two sets of data were taken by Martin de Juan, referred to as Martin de Juan (2011) and Martin de Juan (2012). The data measured in 2011 included measurement of input parameters and outlet values of the IPP spray drying tower run, which are listed in Tables 5.1, 5.5, 7.4, 7.8 and 7.11. The data measured in 2012 was more extensive and included gas temperature profiles inside the IPP tower without and with the spray of droplets, depicted in Figures 6.30 and 7.41, respectively. Additionally, the measurement of input parameters and outlet values of the IPP spray drying tower runs were also carried out, which are listed in Tables 5.6, 5.10, 6.5, 7.10, 8.1 and 8.3.

## **5. PLUG-FLOW MODELLING OF SPRAY DRYING TOWER**

### **5.1 Introduction**

In this chapter, a mathematical model for a counter-current spray drying tower is developed using the plug-flow modelling approach to evaluate the suitability of this approach in modelling the spray drying process. A semi-empirical single droplet drying model developed in-house by P&G (Hecht, 2012) is used to model the drying kinetics to droplets of a range of sizes. The semi-empirical model is based on the full numerical model proposed by Hecht and King (2000b). The plug-flow model considers axial variation of temperature, density, viscosity and humidity of the hot gas and simulates drying of droplets/particles of a range of sizes. The model is validated against data from the IPP spray drying tower.

### **5.2 Droplet/Particle Drying Model**

The spray drying of droplets of detergent slurry consisting of an aqueous solution containing insoluble solid particles is addressed. The droplet/particle drying model is applied to each particle size. Major components of the detergent slurry include a surfactant, a polymer, a binding agent dissolved in water and a softening agent as solid particles. The exact composition of the slurry cannot be provided because of the confidentiality reasons, however it is very similar to the detergent slurry studied by Griffith *et al.* (2008) and Handscomb *et al.* (2009b). The components of that slurry along with soluble and insoluble compounds are given in Section 3.6 in Chapter 3. The model based on Hecht and King (2000b) has been selected for describing the drying rate of the detergent slurry in a counter-current spray drying tower as it explains the formation of hollow particles (see Figure 3.5 (b) in Section 3.4), which is observed in the dried detergent particles.

#### **5.2.1 Droplet/Particle Drying Mechanism**

The drying process illustrated in Figure 5.1 consists of four stages. In the first stage (A-C), the initial heating/cooling of droplets to the wet bulb temperature takes place as the moisture evaporates from the surface of the droplet. The size of droplet also decreases due to the evaporation of water in this stage. The second stage (C-D) begins when the water in the droplet is insufficient to maintain a saturated condition at the droplet

surface, thus causing a solid crust to form at the surface. The particle temperature begins to rise rapidly in this stage. The third stage (D-F) starts when the particle temperature is equal to the boiling point of the slurry. The particle inflates in this stage due to internal vapourisation of moisture in a saturated vapour bubble. Drying continues after maximum inflation of the particle until the moisture reaches equilibrium. In the fourth stage, the particle temperature reaches the gas temperature and the equilibrium moisture in the particle changes accordingly.

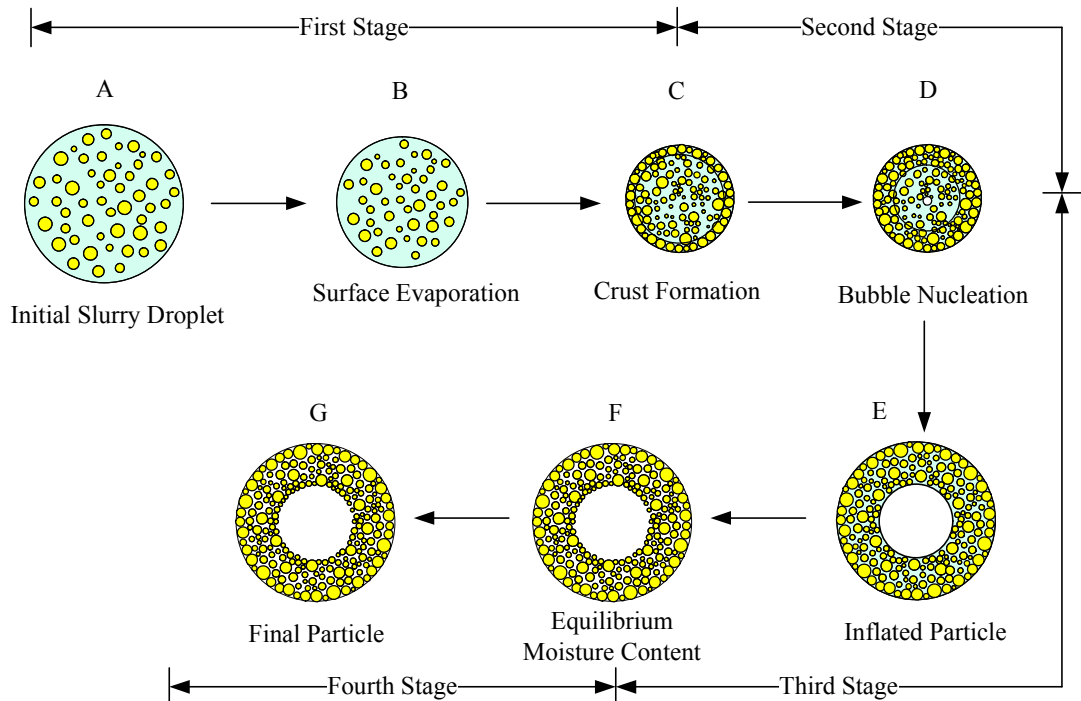


Figure – 5.1: Four stages of drying of a slurry droplet.

### **5.2.2 Drying Model Assumptions**

The following assumptions are applicable to the single droplet/particle drying model used in this study:

1. There are no temperature/concentration gradients within the droplet/particle. Since the droplets/particles are very small (ranging from 50  $\mu\text{m}$  to 2300  $\mu\text{m}$ ), the variation of temperature within the droplet can be neglected (Biot number is small  $< 0.1$ ).
2. Internal circulation inside the slurry droplet is neglected. The droplet sizes are relatively small and the presence of solid particles inside the droplet hampers internal circulation of the liquid.
3. The droplets and the resulting particles remain spherical throughout the tower. The shape of the particles may undergo changes due to morphological development

during drying, agglomeration, particle-wall interaction and breakage of the particles. The simulation of droplets/particles with non-spherical symmetry involves excessive complexity, which may not be worth the additional effort at this stage.

4. It is assumed that drying continues to take place in the third stage until all the moisture is evaporated from the particle, since modelling particle drying in the fourth stage requires a water isotherm for the detergent as a function of temperature, which is not available. Therefore, in the fourth stage, only sensible heat transfer takes place from the gas to the particle until the particle temperature is equal to the gas temperature.
5. To account for particle inflation in the third stage due to internal vapourisation of moisture, the size of the particle is increased to the initial diameter of the droplet. This results in a change in particle density. The choice of the maximum size of the inflated particle is based on the measured density of dried powder.
6. The density and specific heat of the slurry, and the diffusivity of vapours into the bulk remain constant.

### 5.2.3 Governing Equations

The change in temperature of the droplet/particle as a function of vertical distance can be calculated by the following energy balance:

$$\underbrace{M_p c_{p,drop} \tilde{u}_p \frac{dT_p}{dz}}_{\text{Heat absorbed by the droplet/particle}} = \underbrace{\alpha_p A_p (T_{gas} - T_p)}_{\text{Heat input to the droplet/particle by convection}} + \underbrace{h_{fg} \frac{dM_l}{dt}}_{\text{Heat consumed in vapourizing the moisture}} \quad (5.1)$$

The heat transfer coefficient,  $\alpha_p$ , in equation (5.1) is calculated from the Ranz and Marshall (1952) correlation (equation 3.1).

The moisture content in the droplet is calculated using the equation proposed by Hecht and King (2000b):

$$\tilde{u}_p \frac{dw_l}{dz} = \frac{(1 - w_l)^2}{M_{solid}} \frac{dM_l}{dt} \quad (5.2)$$

The change in droplet radius due to evaporation of liquid in the first stage of drying (see Figure 5.1) is given by:

$$\tilde{u}_p \frac{dr_p}{dz} = \frac{dM_l}{4\pi\rho_l r_p^2 dt} \quad (5.3)$$

In the first stage of drying, the evaporation of moisture from the surface of the droplet depends upon the surface vapour concentration and the vapour concentration in the bulk. The initial slurry droplet drying rate is given by:

$$\frac{dM_l}{dt} = -4\pi r_p^2 k_c (C_{v,s} - C_{v,\infty}) \quad (5.4)$$

The surface vapour concentration ( $C_{v,s}$ ) in equation (5.4) is calculated by assuming the partial pressure of vapours at the surface to be in equilibrium with the liquid phase, it is given by:

$$C_{v,s} = \frac{P_{sat,vap} N_{vap}}{1000 \times R_g T_p} \quad (5.5)$$

The saturated vapour concentration is calculated using Antoine's equation (Perry and Green, 1997).

$k_c$  in equation (5.4) is the mass transfer coefficient, and is calculated from the Ranz and Marshall (1952) correlation (equation (3.2)).

The transformation of the first stage of drying to the second stage takes place when a layer of solids covers the surface of the droplet. The time for the surface to become dry is approximated by solving the diffusion equation in planar coordinates system for diffusion in a semi-infinite slab. The analytical solution is given by Crank (1975) and for the surface concentration it becomes:

$$\frac{(C_{l,s} - C_{l,i})}{(C_{l,\infty} - C_{l,i})} = 1 - \exp\left(-\left(\frac{K k_c}{D_{ws}}\right)^2 D_{ws} t\right) \operatorname{erfc}\left(\left(\frac{K k_c}{D_{ws}}\right) \sqrt{D_{ws} t}\right) \quad (5.6)$$

where  $\text{erfc}$  is the complementary error function and  $K$  is the partition coefficient, given by:

$$K = \frac{C_v}{C_s} \cong \frac{H \rho_{gas}}{w_{l,initial} \rho_{slurry}} \quad (5.7)$$

Equation (5.6) is simplified by introducing the following dimensionless parameter:

$$B = K k_c \sqrt{\frac{t}{D_{ws}}} \quad (5.8)$$

Equation (5.6) now becomes:

$$\frac{(C_{l,s} - C_{l,i})}{(C_{l,\infty} - C_{l,i})} = 1 - \exp(B^2) \text{erfc}(B) \quad (5.9)$$

The surface drying time ( $t_{sd}$ ) is taken as the time for  $C_{l,s}$  to reduce to a value corresponding to 90% of the equilibrium moisture content (Hecht, 2012). Thus, equation (5.9) becomes:

$$\exp(B^2) \text{erfc}(B) = 0.1 \quad (5.10)$$

The solution of equation (5.10) using trial and error results in:

$$B = 5.5 \quad (5.11)$$

From equations (5.8) and (5.11),  $t_{sd}$  is given by:

$$t_{sd} = D_{ws} \left( \frac{5.5}{K k_c} \right)^2 \quad (5.12)$$

Once the surface is dry (step C in Figure 5.1), the drying rate becomes dependent on the internal diffusion of moisture to the surface. Hecht (2012) developed an algebraic equation for this step by fitting results from a full numerical model for droplet drying

previously developed by Hecht and King (2000b). The drying rate for this stage is given by:

$$\frac{dM_l}{dt} = -10^6 r_p \exp \left[ -A \left( \frac{t - t_{sd}}{10^6 r_p} \right)^B - C \right] \quad (5.13)$$

where A, B and C are constants for the exponential curve fit with values of 18.9, 0.2 and 17.7, respectively.

Puffing (particle inflation) starts at the beginning of stage 3, when the particle temperature is equal to the boiling point of the slurry (step D in Figure 5.1). To take into account the inflation of particles in this stage, the diameter of the particle is changed to the initial droplet diameter. During the puffing stage, the drying process is controlled by the external heat transfer from the gas to the particle. As the particle dries, the boiling temperature of the slurry increases. The drying rate is obtained by a simple energy balance on a particle, with the boiling temperature of the slurry represented as a function of moisture content:

$$\frac{dM_l}{dt} = - \frac{\alpha_p 4\pi \left( \frac{d_p}{2} \right)^2 (T_{gas} - T_p)}{h_{fg} - (w_s c_{p,s} + w_l c_{p,l}) w_s \frac{dT_{boil}}{dw_l}} \quad (5.14)$$

The relationship between the boiling point of the detergent slurry and moisture content was determined experimentally by Amador (2012) and is given by:

$$T_{boil} = \exp \left( \frac{276.25}{23.68 + 100 w_l} - 6.6 \right) + 373.15 \quad (5.15)$$

### 5.3 Spray Drying Tower Model

The model of the spray drying tower illustrated in Figure 5.2 is taken to be a vertical cylinder with a uniform cross-sectional area. In the actual tower, the hot gas enters the bottom enlarged region of the tower by a number of inlets. The tower is operated at slightly below atmospheric pressure which causes entrainment of air from the bottom exit of the tower. In the model, an enthalpy balance is used to obtain the inlet hot gas temperature (adiabatic mixing of hot gas and cold entrained air streams) and the gas velocity is also a combination of the two streams. This hot gas flows counter-currently to the droplet/particles. The mass flow, humidity, density and temperature of gas are allowed to vary in the axial direction by dividing the tower height into a number of equal increments, because the resulting differential equations need to be discretised and solved using a finite difference method. In each increment, the heat and mass transfer between the two phases and the particulate phase momentum transfer are solved.

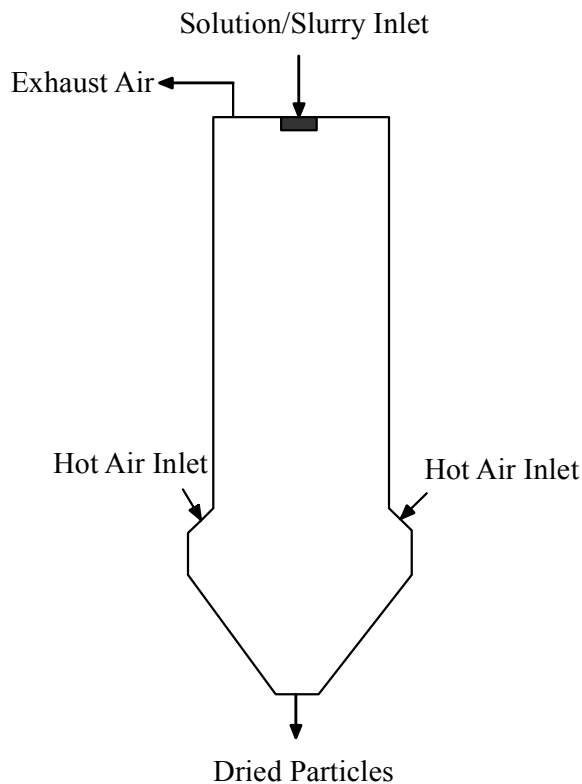


Figure – 5.2: Counter-current spray drying tower schematic.

#### 5.3.1 Assumptions Incorporated in the Spray Drying Tower Model

1. The flow of hot gas in a spray drying tower involves complex three-dimensional swirling flow. However, for simplicity, the radial and angular velocities of the hot gas and droplets/particles are assumed to be zero.

2. Hot gas is assumed to follow the ideal gas law. The spray drying tower operates at atmospheric pressure and medium temperature (200-400°C).
3. Heat transfer by radiation is neglected as it only becomes significant at very high temperatures.
4. The droplets/particles are uniformly dispersed over the cross section of the tower with no interaction between them. In actual spray drying towers, interaction between the droplets/particles takes place, which may result in change in size of the droplets/particles. The modelling of particle-particle and particle-wall interactions inside the spray drying tower is not included due to the complexities involved.
5. The minimum velocity of the particles is limited to the terminal falling velocity of the particles. Although particles of diameter up to 200  $\mu\text{m}$  get entrained with the gas and exit from the top, but this amount is only 3% by mass of the dried powder collected from the bottom. Hence the entrainment of particles is not considered. In the actual spray drying tower, the particles move close to the wall where the gas velocity is almost zero. This leads to smaller particles exiting from the bottom which would otherwise get entrained in the gas stream.

### 5.3.2 Governing Equations

An energy balance on the gas phase results in the following equation for the variation of the gas temperature:

$$\underbrace{\dot{M}_{gas} c_{p, gas} \frac{dT_{gas}}{dz}}_{\text{Heat transfer from the air to the droplets}} = \underbrace{\sum_{j=1}^J \alpha_j A_{p_j} (T_{p_j} - T_{gas}) \cdot \frac{n_j}{\tilde{u}_{p,j}}}_{\text{Total heat input to the droplets by convection}} - \underbrace{\sum_{j=1}^J \left( \frac{dM_l}{dt} \right)_j c_{p, vap} (T_{p_j} - T_{gas}) \cdot \frac{n_j}{\tilde{u}_{p,j}}}_{\text{Sensible heat to the evaporated vapours}} \quad (5.16)$$

$$+ \underbrace{2\pi r_i U (T_{amb} - T_{gas})}_{\text{Heat loss to the environment}}$$

where  $j$  is the identifier for each discrete size.  $J$  is the total number of discrete sizes. The number of droplets or particles ( $n_j$ ) for each discrete size in a control volume per unit time is given by:

$$n_j = \frac{\dot{M}_{slurry,j}}{M_{p_j}} \quad (5.17)$$

For the calculation of heat loss to the environment, a constant thickness of column wall and insulation is assumed. The overall heat transfer coefficient ( $U$ ) in equation (5.16) is calculated along the column height and is given by:

$$\frac{1}{U} = \frac{1}{\alpha_D} + \frac{r_i \ln\left(\frac{r_i + \delta_w}{r_i}\right)}{\lambda_w} + \frac{r_i \ln\left(\frac{r_i + \delta_w + \delta_{ins}}{r_i + \delta_w}\right)}{\lambda_{ins}} + \frac{r_i}{\alpha_{amb}(r_i + \delta_w + \delta_{ins})} \quad (5.18)$$

where  $r_i$  is the inside radius of the column, measured from the centre to the column wall.

The Nusselt number used for calculation of the inside film coefficient ( $\alpha_D$ ) is given by (Kreith, 1973):

$$\text{Nu}_D = 0.023 \text{Re}_D^{0.8} \text{Pr}^{0.33} \quad (5.19)$$

Equation (5.19) is applicable to fully developed turbulent flow in a circular duct ( $\text{Re} > 4000$ ), typical value of gas  $\text{Re}$  in the cylindrical region is  $2 \times 10^5$ . The change in mass flow of the gas is given by the following equation:

$$\underbrace{\frac{d\dot{M}_{gas}}{dz}}_{\text{Change in mass flow of gas}} = \underbrace{\sum_{j=1}^J \frac{-n_j}{\tilde{u}_{p,j}} \left( \frac{dM_l}{dt} \right)_j}_{\text{Change in mass of droplets/particles}} \quad (5.20)$$

The droplet/particle velocity for each particle size is calculated from the equation of motion:

$$\underbrace{M_p \tilde{u}_p \frac{dv_p}{dz}}_{\text{Change in droplet/particle momentum}} = \underbrace{M_p \mathbf{g}}_{\text{droplet/particle weight}} + \underbrace{\bar{F}_a}_{\text{Bouyancy force}} + \underbrace{\bar{F}_d}_{\text{Drag force}} \quad (5.21)$$

The buoyancy force ( $\vec{F}_a$ ) is given by:

$$\vec{F}_a = -M_p g \left( \frac{\rho_{gas}}{\rho_p} \right) \vec{i} \quad (5.22)$$

The drag force ( $\vec{F}_d$ ) in equation (5.21) is given by:

$$\vec{F}_d = -\frac{1}{2} \rho_{gas} \pi r_p^2 C_D |u_p - u_{gas}| (u_p - u_{gas}) \quad (5.23)$$

The Reynolds number based on the relative velocity is given by:

$$Re = \frac{\rho_{gas} d_p |u_p - u_{gas}|}{\mu_{gas}} \quad (5.24)$$

The drag coefficient for the droplets is calculated using correlations proposed by Williams (1976), which was measured for burning oil droplets and is given by equation (3.61) and (3.62). The drag coefficient for the particles is calculated using correlations proposed by Morsi and Alexander (1972) which is applicable to smooth spherical particles, given by equation (3.60). The minimum velocity of the particle is limited to the particle terminal velocity to avoid negative velocity values for the particles and is given by:

$$u_{p,term} = \sqrt{\frac{4gd_p(\rho_p - \rho_{air})}{3C_D\rho_{air}}} \quad (5.25)$$

The density of the hot gas as a function of temperature is calculated by the ideal gas law:

$$\rho_{gas} = \frac{p N_{gas}}{1000 \times R_g T_{gas}} \quad (5.26)$$

The viscosity of gas is considered as a function of gas temperature and is calculated using the following relationship obtained from air viscosity data in Perry and Green (1997):

$$\mu_{gas} = 10^{-5} (0.0036 T_{gas} - 6 \times 10^{-7} T_{gas}^2 + 1.8626) \quad (5.27)$$

The mass weighted average particle temperature at the outlet is calculated using the following equation:

$$\tilde{T}_p = \frac{\sum_{j=1}^J M_{p,z,j} T_{p,z,j}}{\sum_{j=1}^J M_{p,z,j}} \quad (5.28)$$

The mass weighted average particle moisture content at the outlet is calculated using the following equation:

$$\tilde{w}_l = \frac{\sum_{j=1}^J M_{p,z,j} w_{l,z,j}}{\sum_{j=1}^J M_{p,z,j}} \quad (5.29)$$

The temperature of the gas stream going into the tower is calculated using the following equation:

$$T_{gas} = \frac{\dot{M}_{gas,hot} c_{p,gas,hot} T_{gas,hot} + \dot{M}_{gas,cold} c_{p,gas,cold} T_{gas,cold}}{\dot{M}_{gas,hot} c_{p,gas,hot} + \dot{M}_{gas,cold} c_{p,gas,cold}} \quad (5.30)$$

A derivation of generalised form of the equations representing the heat and mass transfer between the droplets/particles and the gas in the plug-flow model are given in Appendix I.

### 5.3.3 Droplets Initial Velocity

The slurry is atomised using a hollow-cone pressure nozzle atomiser. The initial velocity is assumed to be same for all the droplet sizes and is calculated using the following equation:

$$u_p = \frac{\dot{Q}_{slurry}}{\pi(r_o^2 - r_c^2)\cos\left(\frac{\theta}{2}\right)} \quad (5.31)$$

The above equation requires the radius of the air core ( $r_c$ ) and spray cone injection angle ( $\theta$ ). The injection angle is taken to be  $40^\circ$  based on the vendor provided data and the radius of the nozzle  $r_o$  is  $1.38 \times 10^{-3}$  m. The air core radius is taken from the data reported by Nelson and Stevens (1961).

### 5.3.4 Boundary Conditions

At  $z = 0$  (at the top of the tower corresponding to droplet inlet), the following boundary conditions are applicable:

$$T_p = T_{p,0}, u_p = u_{p,0}, w_l = w_{l,0}, d_p = d_{p,0}, \dot{M}_{gas} = \dot{M}_{gas,0}, T_{gas} = T_{gas,0} \text{ and} \\ u_{gas} = u_{gas,0} \quad (5.32)$$

At  $z = Z$  (at the bottom of the tower corresponding to the gas inlet), the following boundary conditions apply:

$$T_{gas} = T_{gas,Z} \text{ and } u_{gas} = u_{gas,Z} \quad (5.33)$$

### 5.3.5 Solution Methodology

The spray tower is divided into a number of equal sized increments of length  $\Delta z$  to solve the differential equations using a finite difference method. The differential equations (5.1, 5.2, 5.3, and 5.21) are discretised using a forward difference approximation; whereas equations (5.16 and 5.20) are discretised using a backward difference approximation. In equation (5.1), the mass, drying rate, heat transfer coefficient, specific heat and velocity of each particle size are considered to be constant within the

increment. The counter-current particle-gas flow arrangement and unknown exit conditions of the gas (at  $z = 0$ ) and particles (at  $z = Z$ ), necessitate an iterative technique to obtain the numerical solution, thus converting the boundary value problem to an initial value problem. The starting point of the calculation is at the top of the tower ( $z = 0$ ) where the slurry is sprayed (see Figure 5.3). The initial values of the outlet gas temperature and mass flow are required in order to solve the discretised equations for the first iteration. These values are estimated based on the overall energy balance assuming that the particles outlet temperatures are equal to the inlet gas temperature and moisture fraction of the particles is zero. The calculated gas temperature at the bottom of the tower ( $z = Z$ ) is compared with the known value of inlet gas temperature. The initial estimated value of the outlet gas temperature is then adjusted, based on the difference between the calculated value and the known value of inlet gas temperature. The outlet gas moisture content is also adjusted, based on the moisture content of the dried particles. The calculation is repeated until specified values of tolerances of 0.5 K between the calculated and known gas inlet temperatures as well as a 1% difference between the outlet mass flow of the gas for two successive iterations are obtained. The solution methodology is implemented in the computer software package MATLAB (2010). Figure 5.4 is the logic flow diagram of the algorithm for the numerical solution of the full model.

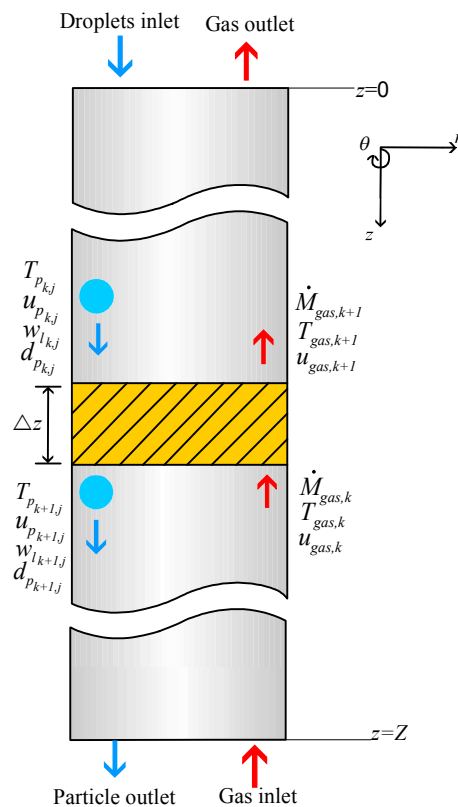


Figure – 5.3: Control volume inside the spray tower.

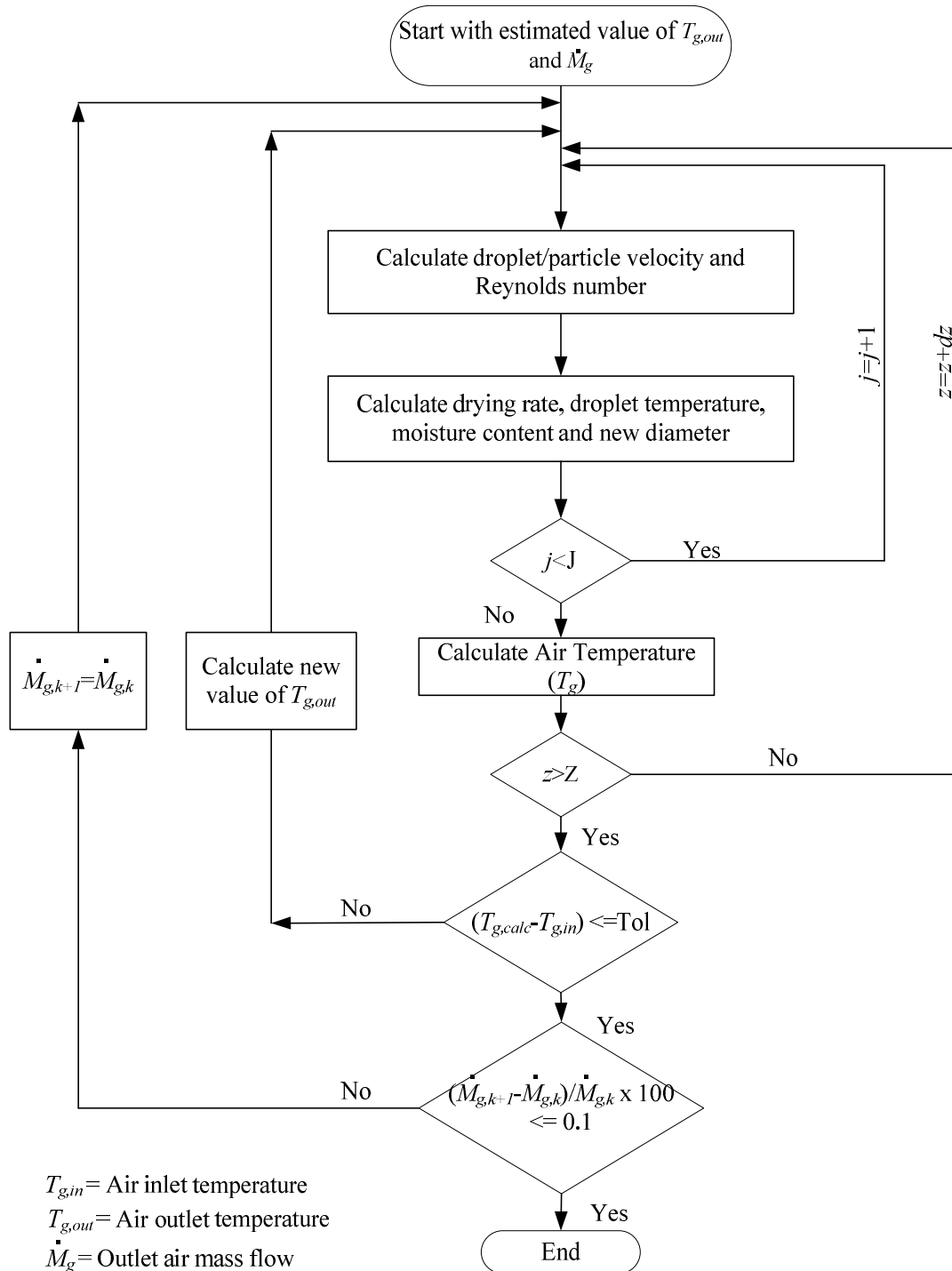


Figure – 5.4: Logic flow diagram of the solution algorithm.

#### 5.4 Size Distribution of Droplets

The spray drying process starts from a distribution of droplets resulting from the atomisation of feed using an atomiser. The estimation of initial size distribution may be important in predicting the overall performance of the spray drying tower. In this study, the measured size distribution of the slurry droplets as well as the measured size

distribution of the dried powder is used as the initial size distribution by considering various cases. The cumulative size distribution curve of the sprayed droplets in the simulation is represented by using a Rosin-Rammler fit (Rosin and Rammler, 1933) given by equation (5.34).

$$Y_d = \exp\left\{-\left(d_p/d_m\right)^{u_s}\right\} \quad (5.34)$$

## 5.5 Simulation Results

The plug-flow model is used to simulate spray drying of a detergent slurry to predict detergent powder characteristics in the IPP spray tower. It is important to first investigate the influence of grid size ( $\Delta z$ ) on the simulation results. Similarly it is also important to investigate the effect of number of cut sizes which are used to represent droplet/particle size distribution on the simulation results. Increase in the number of discrete sizes used to represent the size distribution should result in a more accurate representation of how the size distribution affects the predicted results of the simulations, but there will be corresponding increase in the run times per simulation. The input operating conditions are taken from the pilot-plant for checking numerical accuracy and suitable number of cut sizes, which are listed in Table 5.1 (Martin de Juan, 2011). This case is referred to as the Base Case. The droplets initial velocity is calculated using equation (5.31). The simulation results are later compared with the experimental data to establish the validity of this model.

An experimentally measured dried powder size distribution resulting from the above listed operating conditions from the spray tower is used in this investigation as the initial droplet size distribution. The range of sizes is from 100  $\mu\text{m}$  to 2300  $\mu\text{m}$ . The measurement of the particle size distribution was carried out by P&G (Martin de Juan, 2011) using 10 sieve sizes (see Section 4.4.1). Figure 5.5 is the particle size distribution showing cumulative mass fraction oversize as a function of sieve size. A Rosin-Rammler distribution using equation (5.34) is fitted to experimentally measured data for dried particles (shown by a continuous curve). The best curve fit is obtained using a size constant ( $d_m$ ) of 750  $\mu\text{m}$  with a distribution parameter ( $u_s$ ) of 1.35.

The continuous function represented in Figure 5.5 cannot be used in the simulations and so the size distribution will be a number of particles of equal size cuts. For instance, a size cut of 100  $\mu\text{m}$  results in 23 discrete particle sizes: starting at 100  $\mu\text{m}$  in intervals of

100  $\mu\text{m}$  up to 2300  $\mu\text{m}$ . Each particle size will be considered in parallel during the calculations. The particle size in each of the 23 discrete samples, the percentage by weight, the surface area of each size and the area density are listed in Table 5.2. The particle size of 300  $\mu\text{m}$  has the greatest wt% (9.84 %) followed by size of 400  $\mu\text{m}$ . The smallest particle size of 100  $\mu\text{m}$  has the largest number of particles (not shown due to confidentiality reasons), which have the lowest surface area, but by far the greatest specific surface area.

Each of these droplets/particle sizes will have very different experiences within the spray tower and it is imperative in any simulation to accommodate the size distribution. In addition, it will be important to investigate how the number of discrete sizes (bins) representing the particle size distribution affects the predicted performance of the spray tower.

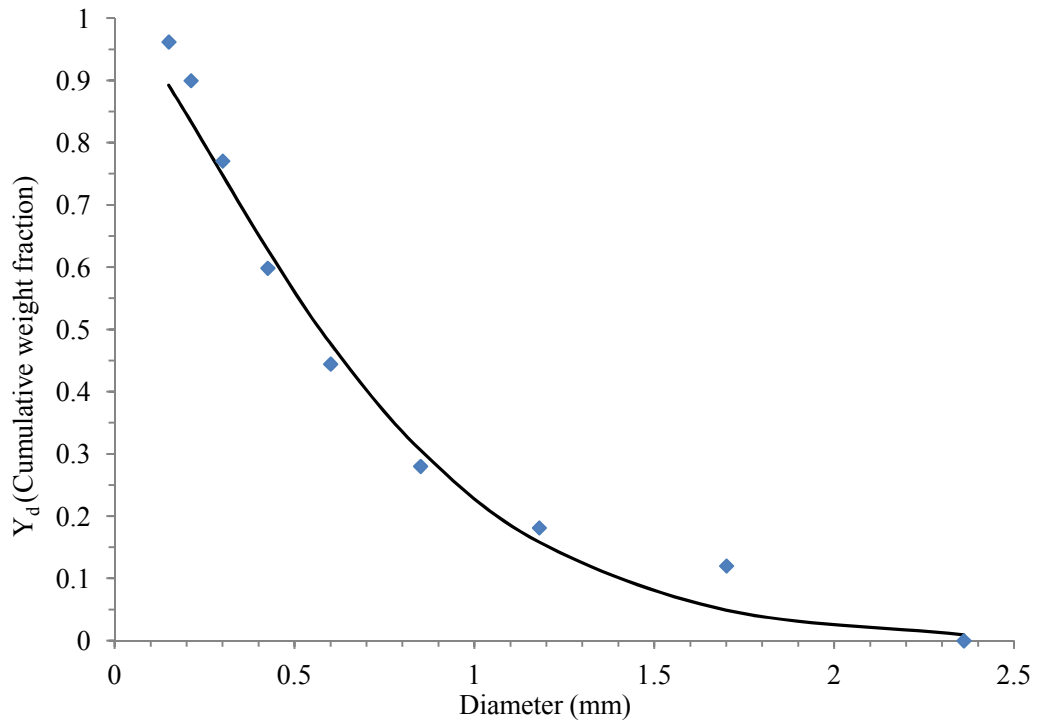


Figure – 5.5: Particle size distribution plot on a cumulative mass basis.

Table – 5.1: Input operating conditions for Base Case (Martin de Juan, 2011).

Droplet Properties		
Slurry inlet temperature $T_{p,o}$	358	K
Slurry mass flux $\dot{M}_{slurry} / A_{tower}$	0.21	kg/m <sup>2</sup> s
Specific heat of dried particle $c_{p,solid}$	1500	J/kg K
Specific heat of solvent $c_{p,water}$	4180	J/kg K
Specific heat of vapours $c_{p,vapours}$	1900	J/kg K
Density of slurry $\rho_{slurry}$	1200	kg/m <sup>3</sup>
Latent heat of vapourisation $h_{fg}$	2260000	J/kg
Diffusion coefficient of water in slurry $D_{WS}$	$3.0 \times 10^{-11}$	m <sup>2</sup> /s
Diffusion coefficient of water vapour into air $D_{AW}$	$2.6 \times 10^{-5}$	m <sup>2</sup> /s
Gas Properties		
Hot gas temperature $T_{gas,hot}$	563	K
Hot gas mass flux $\dot{M}_{gas,hot} / A_{tower}$	0.92	kg/m <sup>2</sup> s
Gas pressure $p$	101325	Pa
Gas thermal conductivity $\lambda_{gas}$	$3.0 \times 10^{-2}$	W/mK
Entrained air mass flux $\dot{M}_{gas,cold} / A_{tower}$	0.046	kg/m <sup>2</sup> s
Entrained air temperature $T_{gas,cold}$	293	K
Specific heat of air $c_{p,air}$	1006.4	J/kg K
Ambient temperature $T_{amb}$	293	K
Column Wall		
Metal wall thickness $\delta_w$	0.006	m
Metal wall thermal conductivity $\lambda_w$	18.8	W/mK
Insulation thickness $\delta_{ins}$	0.105	m
Insulation thermal conductivity $\lambda_{ins}$	0.04	W/mK

Table – 5.2: Discrete droplet size distribution

Size $\mu\text{m}$	Weight %	Surface Area ( $\text{m}^2$ ) $\times 10^8$	Specific surface Area ( $\text{m}^2/\text{m}^3$ ) $\times 10^{-3}$
100	6.44	3.14	59.97
200	9.18	12.56	29.98
300	9.84	28.26	19.99
400	9.73	50.24	14.99
500	9.20	78.50	11.99
600	8.45	113.04	9.99
700	7.59	153.86	8.57
800	6.69	200.96	7.50
900	5.82	254.34	6.66
1000	5.00	314.00	6.00
1100	4.24	379.94	5.45
1200	3.56	452.16	5.00
1300	2.97	530.66	4.61
1400	2.45	615.44	4.28
1500	2.01	706.50	4.00
1600	1.64	803.84	3.75
1700	1.32	907.46	3.53
1800	1.06	1017.36	3.33
1900	0.85	1133.54	3.16
2000	0.67	1256.00	3.00
2100	0.53	1384.74	2.86
2200	0.42	1519.76	2.73
2300	0.33	1661.06	2.61
Total	100		

### 5.5.1 Solution Dependency on the Number of Increments

The solution was investigated for numerical accuracy by changing the number of increments ( $\Delta z$ ) used for the representation of total tower height. A size cut of 100  $\mu\text{m}$  with 23 discrete sizes is used for this investigation. In Table 5.3 the variation of calculated values of the outlet mass weighted average particle temperature, moisture

content and gas temperature as well as the inlet air temperature are listed for total number of increments of 1500, 3000, 6000 and 12000. The simulation diverged when the total increments were reduced below 1500. The sensitivity of the results on the number of grid sizes (Table 5.3) is very small and the corresponding increase in run time is also negligible. Hence any number of increments in the above range can be used. For this case, 6000 increments have been used to represent the total tower height.

Figure 5.6 is a plot of the convergence of the error between the calculated and known inlet air temperature against the iteration number for the simulation with 6000 grids. The solution for this run reaches the required tolerance limit (0.5 K) in 7 iterations.

Table – 5.3: Solution dependency on the number of increments for Base Case.

S. No.	No. of increments	No. of iterations	Particle average outlet temperature (K)	Particle average moisture % (w/w)	Outlet air temperature (K)	Inlet air temperature (K)	Run time (minutes)
1	1500	6	482.19	5.89	396.26	550.29	0.3
2	3000	6	482.21	5.89	396.39	550.29	0.6
3	6000	7	482.20	5.88	396.46	550.29	1.7
4	12000	6	482.20	5.88	396.49	550.29	3.3

### **5.5.2 Solution Dependency on Cut Sizes**

The size distribution of the droplets/particles in Figure 5.5 is represented by a number of discrete sizes. Increase in the number of discrete sizes used to represent the size distribution should result in a more accurate representation of the size distribution and can affect the predicted results of the simulations, but there will be a corresponding increase in the run times per simulation. Table 5.4 lists simulated values of the average particle outlet temperature and moisture content, and the gas outlet temperature for increasing the number of discrete sizes. The number of discrete sizes slightly influences the simulation results. An increase in the average particle moisture content and outlet gas temperature is observed with increase in number of discrete droplet sizes; however its influence on the particle average outlet temperature is negligible. The predictions using 23 discrete sizes are very close to the predictions using 92 discrete sizes. Hence a size cut of 25  $\mu\text{m}$  is sufficient for this investigation.

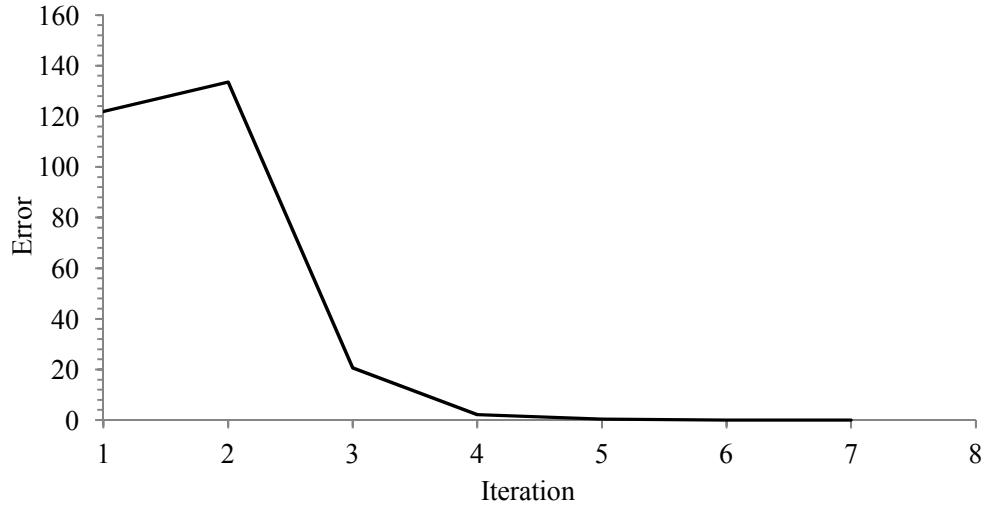


Figure – 5.6: Plot of Error (difference in predicted and actual gas inlet temperature) v/s Iteration.

Table – 5.4: Solution dependency on the number of discrete droplet sizes.

S. No.	Discrete droplet sizes	Size cut ( $\mu\text{m}$ )	Particle average outlet temperature (K)	Particle average moisture content % (w/w)	Outlet air temperature (K)	Run Time (minutes)
1	23	100	482.20	5.88	396.46	1.7
2	46	50	481.03	5.99	399.93	3.05
3	92	25	480.45	6.03	401.82	6.2

An overall enthalpy balance error is 0.43% for the simulation run number 1 in Table 5.4, which is based on these predicted outlet values and the inlet conditions and is given by the following expression:

$$100 \times [(E_1 + E_2) - (E_3 + E_4 + E_5)] / (E_1 + E_2) \quad (5.35)$$

where  $E$  is the enthalpy of a stream and the subscripts 1, 2, 3, 4 and 5 refer to the streams of the gas inlet, the slurry inlet, the gas outlet, the particles outlet and heat loss, respectively, and is given by:

$$E_1 = \dot{M}_{gas,Z} c_{p,gas} T_{gas,Z} \quad (5.36)$$

$$E_2 = \dot{M}_{slurry} \left( (1 - w_{l,0}) c_{p,slurry} + w_{l,0} c_{p,water} \right) T_{p,0} \quad (5.37)$$

$$E_3 = \dot{M}_{gas,Z} c_{p,gas} T_{gas,Z} + (\dot{M}_{gas,0} - \dot{M}_{gas,Z}) (c_{p,water} \times 373.15 + h_{fg} + c_{p,vap} (T_{gas,0} - 373.15)) \quad (5.38)$$

$$E_4 = (\dot{M}_{slurry} - (\dot{M}_{gas,0} - \dot{M}_{gas,Z})) ((1 - \tilde{w}_{l,Z}) c_{p,slurry} + \tilde{w}_{l,Z} c_{p,water}) \tilde{T}_{p,Z} \quad (5.39)$$

$$E_5 = \sum_{j=1}^N 2\pi r_i U_j (T_{amb} - T_{gas,j}) \Delta z \quad (5.40)$$

Similarly, the overall mass balance error is 0.25%.

### 5.5.3 Simulation Results and Discussion

All the results presented here are based on the simulation case with 6000 increments and a size cut of 25  $\mu\text{m}$ . The profiles are presented and discussed for the particle residence times, temperatures, moisture contents, drying rates and velocities for selected particle sizes. Also the plots of profiles of the gas temperature, gas velocity and wall heat flux are presented and discussed below.

Figure 5.7 is a plot of residence time of particles of different sizes in the tower ranging from 100  $\mu\text{m}$  to 2300  $\mu\text{m}$ . The smaller particles (up to 300  $\mu\text{m}$ ) have significantly greater residence times compared to the larger particles. The difference in the residence times of very large particles is very small (1300  $\mu\text{m}$  and greater). On the contrary, the difference in the residence times of the smaller particles vary significantly with particle sizes. The residence time distribution plot shows an exponential decline with increasing particle sizes.

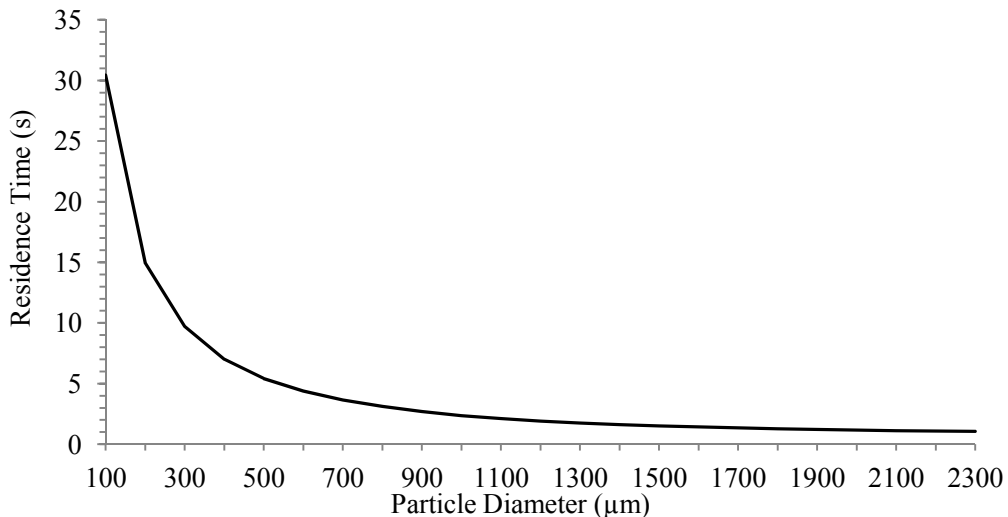


Figure – 5.7: Residence time distribution of particles.

Figure 5.8 is a plot of normalised velocity profiles of a selected number of sizes: 100  $\mu\text{m}$ , 400  $\mu\text{m}$ , 800  $\mu\text{m}$ , 1000  $\mu\text{m}$ , 1500  $\mu\text{m}$  and 2300  $\mu\text{m}$ , along the dimensionless tower height, where 0 represents the nozzle location (where droplets are sprayed) and 1 is the bottom outlet. The initial velocity of all the injected droplets is the same. Smaller particles lose the initial velocity quicker compared to larger particles because smaller particles have smaller weight and hence smaller inertia and a greater influence of drag force, therefore deceleration of smaller particles occurs more rapidly as they move downwards. The minimum velocity of the particles is set to the terminal falling velocity based on stationary gas velocity as explained in the model assumptions. This is an appropriate assumption considering the fact that the particles move close to the wall and the gas velocity near the wall is approaching zero, as found in the CFD investigation (Chapter 7). Therefore when the particles reach their terminal falling velocity, they continue to fall at this terminal velocity. Smaller particles have a smaller terminal falling velocity compared to the larger particles. Hence the overall result is that smaller particles have greater residence times compared to larger particles, which is observed in Figure 5.7.

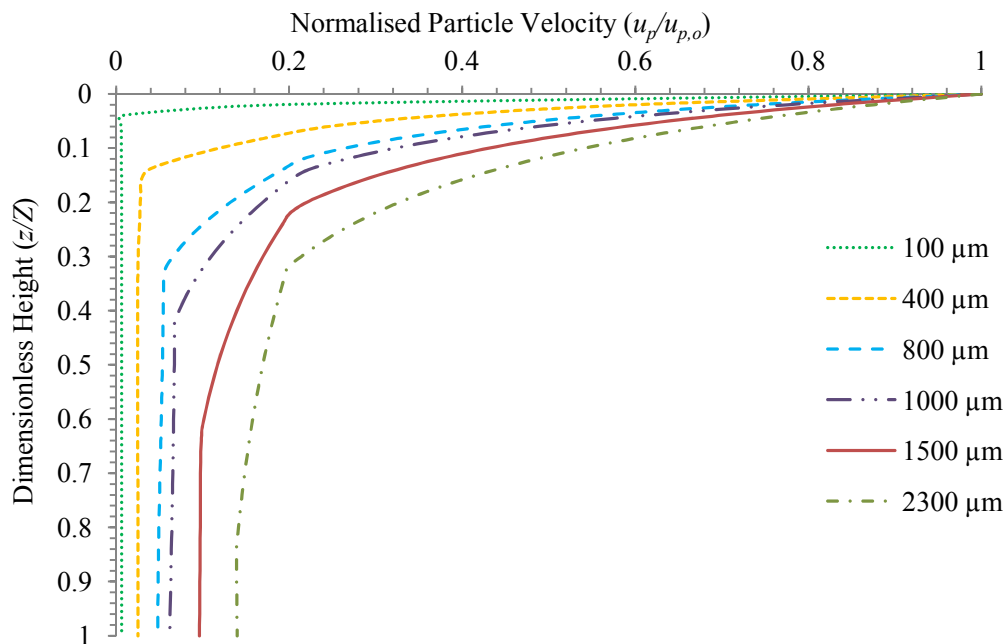


Figure – 5.8: Velocity profile of droplets/particles of different sizes.

Figure 5.9 is a plot of temperature profiles of selected particles sizes as well as for the gas along the dimensionless height. When the droplets are injected from the atomiser, the initial temperature of the slurry droplets is greater than the wet bulb temperature. At this stage, the evaporation occurring from the surface of the droplet is greater than the heat transfer to the droplets. Hence the temperature starts to drop down for all droplet

sizes. However, none of the droplets reaches an expected constant wet bulb temperature of 325 K. After a certain point, the temperature of the particles starts to rise rapidly. This is due to a crust formation at the droplet surface. This trend is observed for all droplet sizes. The crust formation occurs at a much shorter distance for smallest droplets compared to larger droplet sizes. Once a crust is formed, the rate of moisture loss from the droplet decreases, resulting in greater heat transfer to the droplet compared to heat released due to evaporation of moisture. The smallest particle size (100  $\mu\text{m}$ ) quickly reaches the gas temperature thereafter and continues to rise as the gas temperature increases towards the bottom of the tower. For 400  $\mu\text{m}$  and greater particle sizes, a constant temperature region at about 373 K occurs. This temperature corresponds to the boiling point of the slurry. Once the slurry reaches the boiling point, the rise in droplet temperature is dependent on the slurry boiling point. The boiling point starts to rise as the moisture fraction in the slurry decreases, because the equilibrium pressure of the moisture over the slurry is lowered by the presence of the solute. The slurry boiling point is a weak function of moisture content at high moisture fractions, but increases rapidly as the moisture reduces. The temperature of 400  $\mu\text{m}$  particles approaches the gas temperature as it moves downward. For the 800 to 1500  $\mu\text{m}$  particle size, the particles exit at slurry boiling point at the corresponding moisture content. For the largest particle size (2300  $\mu\text{m}$ ) the particle exits just below the boiling point. The gas temperature is highest at the bottom; the gas temperature reduces due to heat exchange with droplets/particles and exits from the top at a temperature of about 396 K which is greater than the initial slurry droplets temperature.

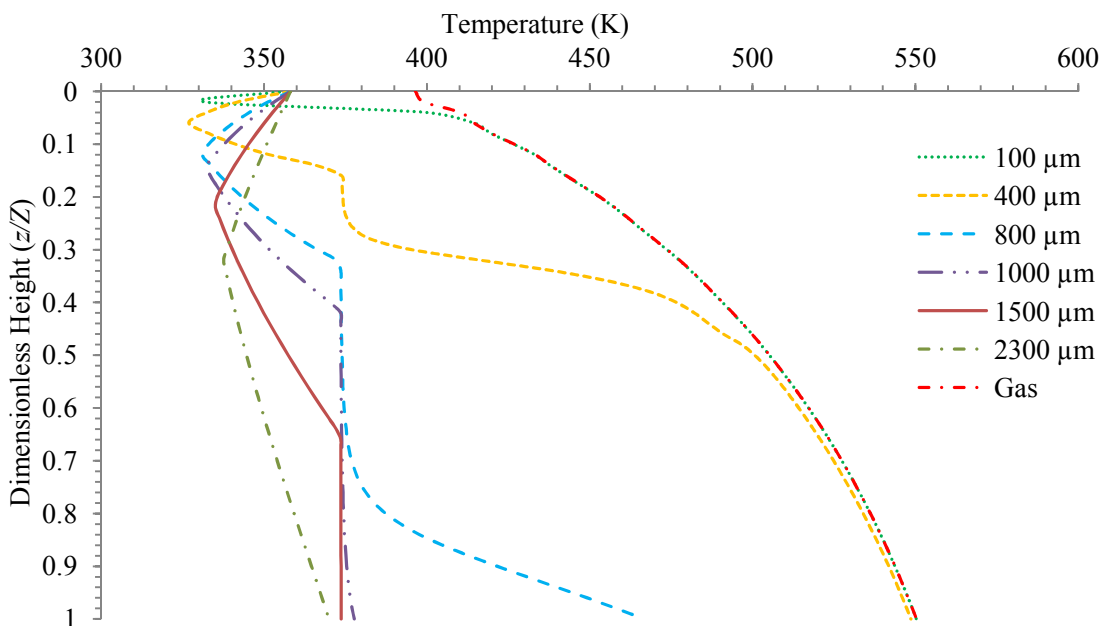


Figure – 5.9: Temperature profile of droplets/particles of different sizes.

Figure 5.10 is a plot of heat transfer coefficient of selected sizes along the dimensionless tower height. The heat transfer coefficient for all sizes is largest at the top and decreases along the tower height. The initial value of the heat transfer coefficient is the largest for the smallest droplet as it is inversely proportional to diameter. It decreases very rapidly along the height due to the rapid decrease in the velocity and eventually becomes constant as the minimum particle velocity is limited at the terminal falling velocity. Despite a rapid decrease in heat transfer coefficient for this size, it remains the highest compared to all larger sizes. The heat transfer coefficient is smallest for the largest size (2300  $\mu\text{m}$ ).

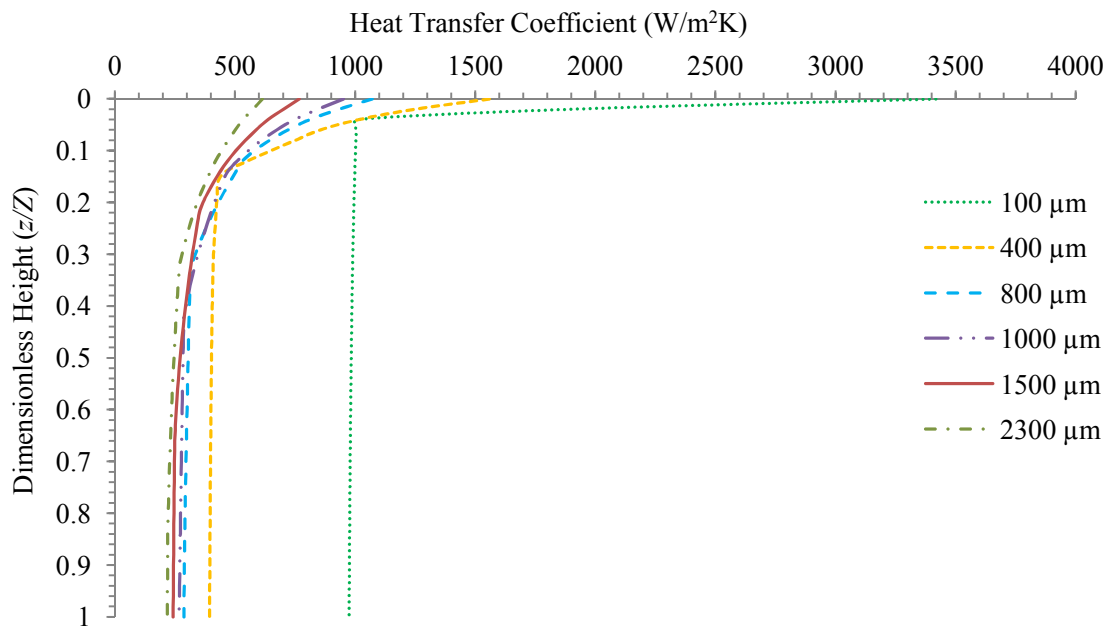


Figure – 5.10: Heat transfer coefficient profile of droplets/particles of different sizes.

Figure 5.11 is a plot of mass transfer coefficient of particles of different sizes. A similar trend occurs for the mass transfer coefficient profile along the dimensionless tower height for different sizes as for the heat transfer coefficient. Hence the same explanation applies to the mass transfer coefficient for the reduction in values along the tower height. Since the heat and mass transfer coefficients for smaller particles are greater and the residence times of smallest particles are also greater, therefore the smaller particles exit at much lower moisture contents compared to larger particles.

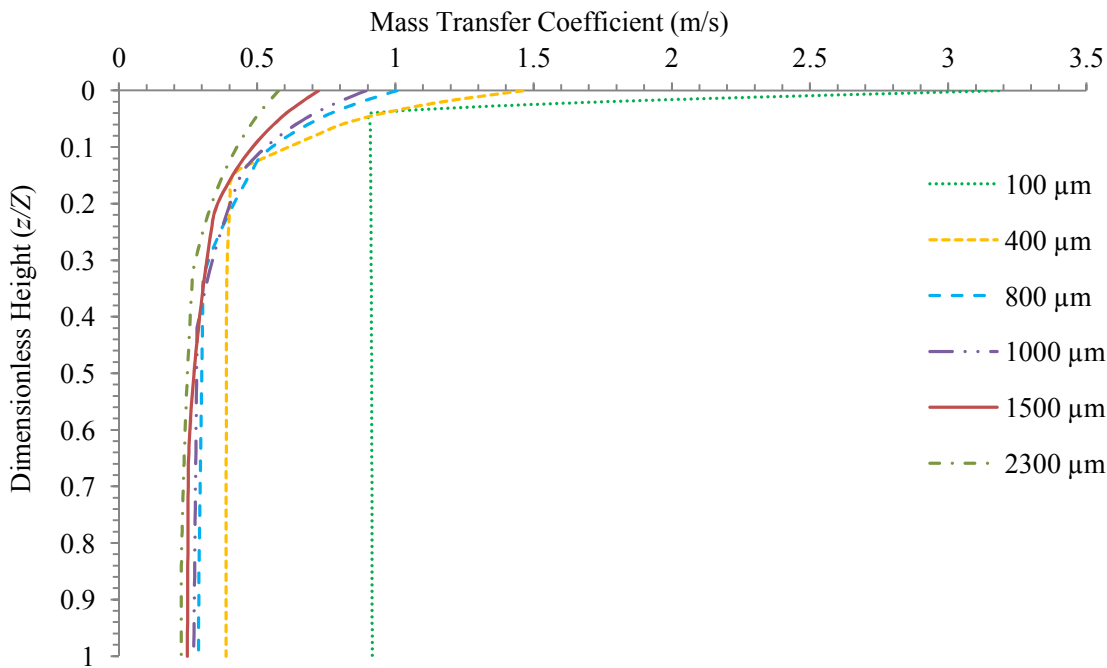


Figure – 5.11: Mass transfer coefficient profile of droplets/particles of different sizes.

Figure 5.12 is a plot of dimensionless moisture profiles ( $w/w_{l,o}$ ) of droplets/particles of selected sizes. The smaller particles sizes lose the moisture quicker than the larger particle sizes. This is due to the greater residence time and larger specific area of the smaller sizes. The particle sizes undergo four distinct slopes of the moisture-loss profiles, representing the three drying stages. These are more clearly visible in the moisture profiles of the medium size particles (400-800  $\mu\text{m}$ ). In the first stage, the moisture-loss slope along the height is almost linear, corresponding to the surface drying (first stage). The rate of moisture-loss then becomes slower. This corresponds to the diffusion controlled drying stage (second stage). The rate of moisture loss then increases again, corresponding to the third stage of drying when the temperature of particle reaches slurry boiling point. The rate of moisture-loss decreases as the particle moisture content approaches zero and the temperature approaches the gas temperature since the driving force in this stage is the temperature difference between the particle and the gas which becomes smaller. The particle sizes up to 400  $\mu\text{m}$  lose all the moisture before exiting from the tower. In reality, the moisture content is not expected to fall below the equilibrium moisture content at the exit condition.

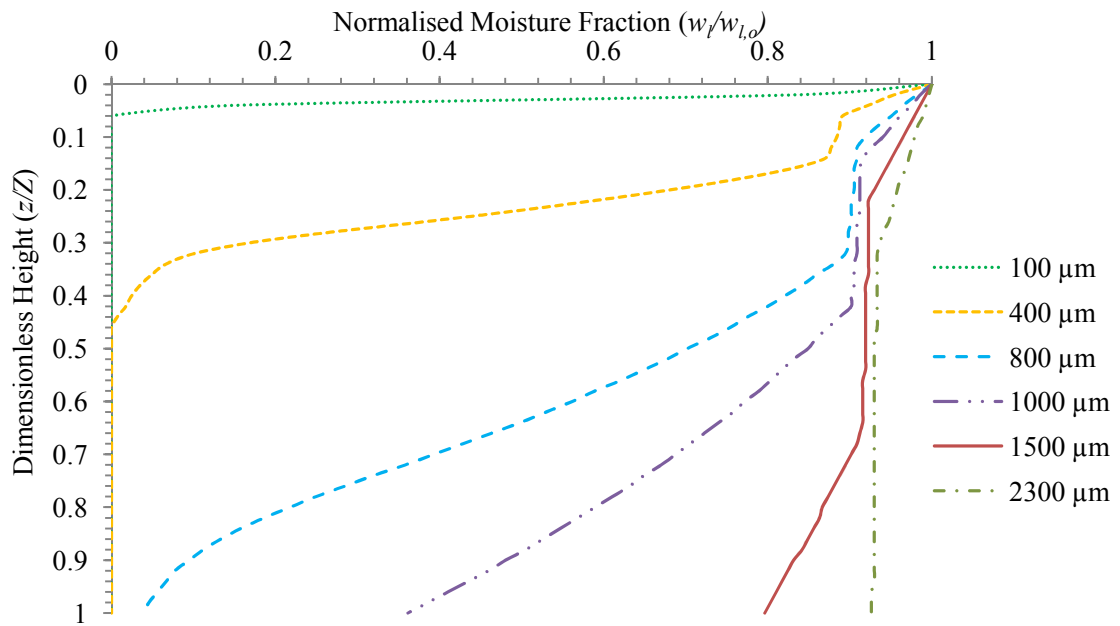


Figure – 5.12: Moisture profiles of droplets/particles of different sizes along the dimensionless tower height.

Figure 5.13 is a plot of drying rates of selected particle sizes along the dimensionless tower height. The horizontal axis is plotted on a logarithmic scale due to the orders of magnitude difference in the drying rate of particles of different sizes. The drying rate profiles correspond to the three stages of drying and are more clearly visible for larger particle sizes (400  $\mu\text{m}$  and above). For all the sizes, the drying rate is the highest in the beginning of the first stage of drying. The drying rate in the first stage falls quickly as the velocity of the injected droplets starts to reduce due to drag, this reduces the mass transfer coefficient and hence the drying rate. The drying rate in the second stage is independent of the surrounding conditions in the tower as it is internal moisture diffusion controlled, hence it is relatively uniform. The drying rate increases in the third stage due to the internal vapourisation of moisture that facilitates the transport of moisture to the surface, hence the heat transfer to the particle controls the rate of drying. In the third stage of drying, for larger particle sizes, sharp changes in the drying rate are observed, this occurs when particle temperature starts to rise more rapidly, resulting in a decrease in the heat transfer driving force (temperature difference between the gas and the particle), at some stage, the heat transfer to the particle becomes insufficient to maintain the particle temperature at its corresponding boiling point and therefore the drying rate fluctuates between the second and third stages.

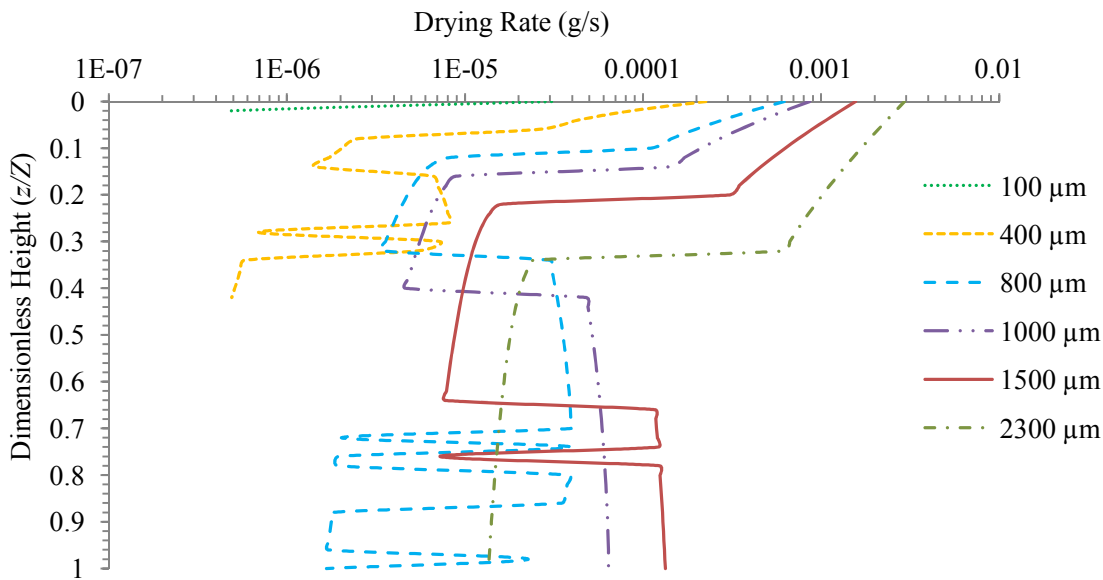


Figure – 5.13: Drying rate of droplets/particles of different sizes along the dimensionless tower height.

Figure 5.14 is a plot of particle temperature, the corresponding boiling and drying rate for a 400  $\mu\text{m}$  particle size, and gas temperature along the dimensionless tower height. The drying rate is highest initially when the droplet is injected and begins to decrease due to the fall in the particle velocity (which reduces the heat and mass transfer coefficients). The particle temperature becomes lower during this period. Once a crust is formed at the surface, a dramatic fall in the drying rate happens and a corresponding rise in temperature as most of the heat is used up in rising the particle temperature. This continues until the particle temperature is equal to the slurry boiling point ( $T_{boil}$ ). The drying rate increases rapidly at the slurry boiling point as the mass transfer from the particle is controlled by rate of heat transfer to the particle. The rate of heat transfer to the particle is dependent on the temperature difference between the particle and the gas. After a certain height, the temperature of the particle begins to rise as the moisture content in the particle reduces and the slurry boiling point increases. The equilibrium pressure of water vapours over the slurry is lowered as the slurry becomes thicker due to loss of moisture and results in a rise in slurry boiling point. The rise in slurry boiling point also results in rise in particle temperature. The rise in particle temperature results in a decrease in the heat transfer driving force ( $T_{gas} - T_p$ ) depicted in Figure 5.15. The rapid decrease in driving force results in a rapid decrease in the drying rate and the particle temperature reduces slightly below the slurry boiling temperature as sufficient heat is not transferred to the particle. The drying rate fluctuates between second and the third stage until the slurry boiling point corresponding to particle moisture content becomes greater than the gas temperature and the drying rate again becomes diffusion

rate controlled. After a certain dimensionless height all the moisture from the particle is removed and only sensible heat transfer takes place from the gas to the particle there onwards. At the exit, the particle temperature is very close to the gas temperature.

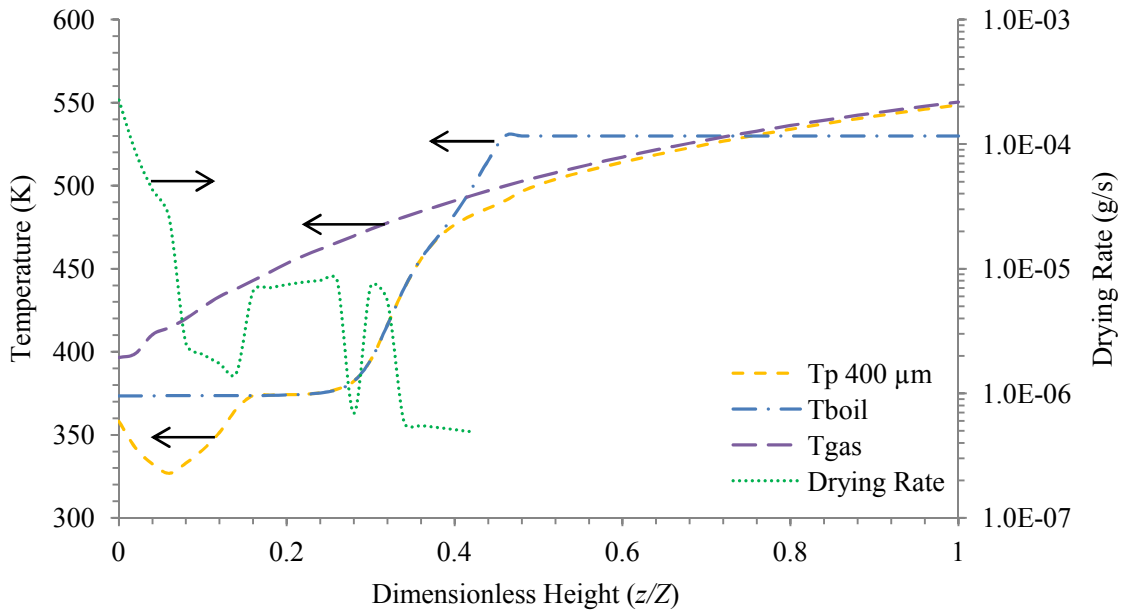


Figure – 5.14: Particle and gas temperatures, slurry boiling point and corresponding drying rate along the dimensionless height for a 400  $\mu\text{m}$  size particle.

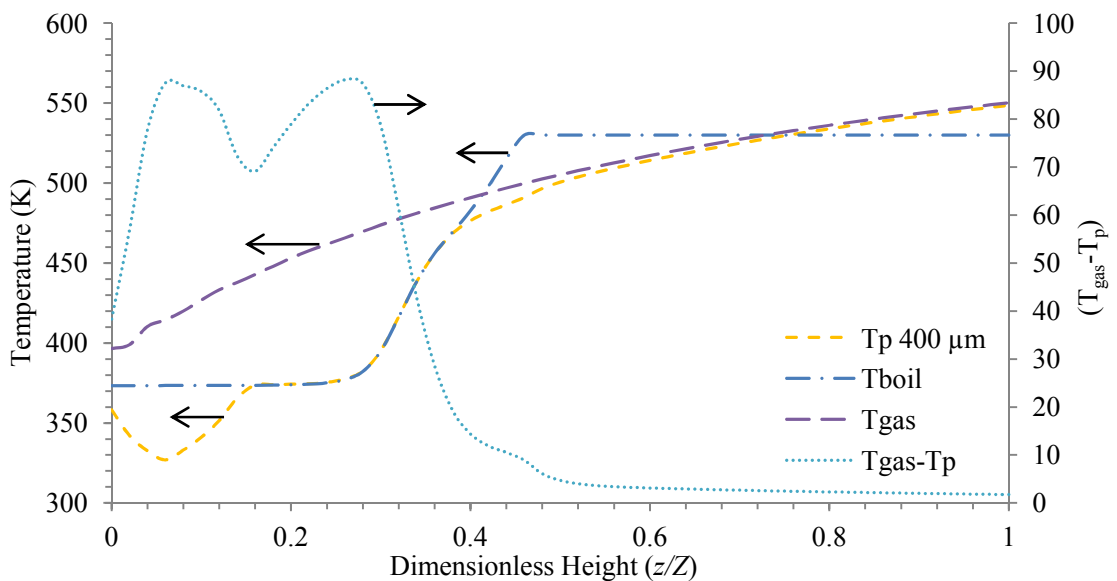


Figure – 5.15: Particle and gas temperatures, slurry boiling point and the temperature difference along the dimensionless height for a 400  $\mu\text{m}$  size particle.

Figure 5.16 is a plot of the density of the particles along the dimensionless tower height. The density plot is qualitatively similar to the moisture profiles of the particles (Figure 5.12) as the particles lose the moisture content, the density is decreased accordingly. A distinct feature in these profiles is a sudden change in the density of particles, for example a particle size of 400  $\mu\text{m}$  at a dimensionless height of about 0.2, the density

reduces very sharply. This is due to the expansion of particle in the third stage. The largest particle (2300  $\mu\text{m}$ ) does not undergo puffing as it exits from the tower in the second stage of drying.

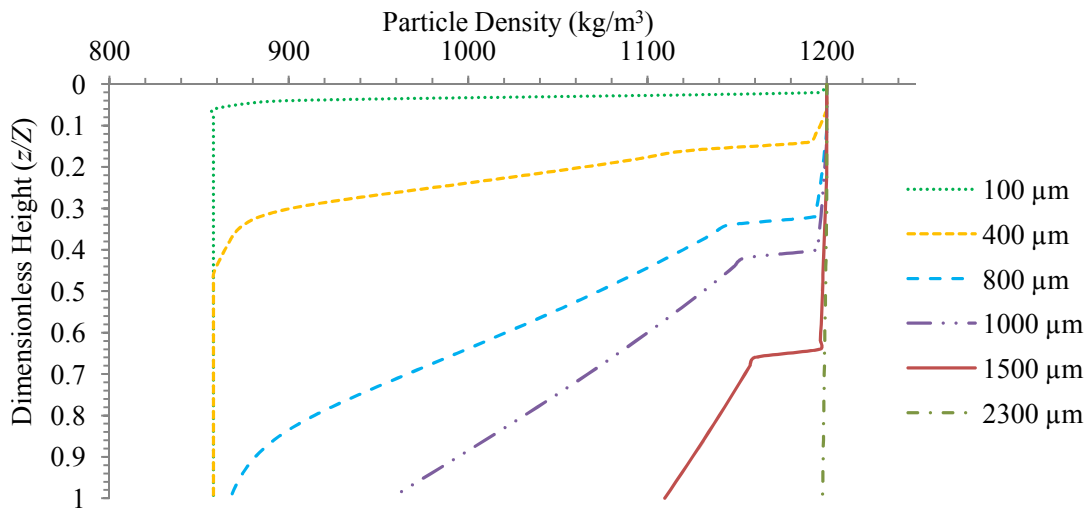


Figure – 5.16: Density of droplets/particles of different sizes along the dimensionless tower height.

Figure 5.17 is a plot of the specific heat of particles of different sizes along the dimensionless tower height. The specific heat of all particle sizes reduces along the tower height; the plots are qualitatively similar to the particle moisture fraction profiles. Since the specific heat of particles changes with moisture content.

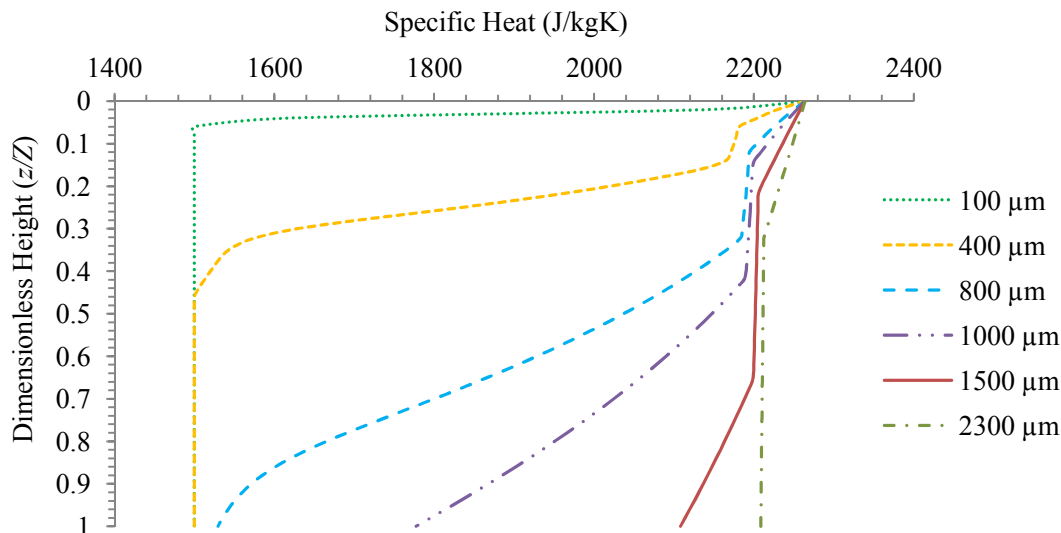


Figure – 5.17: Specific heat of droplets/particles of different sizes along the dimensionless tower height.

Figure 5.18 is a plot of the temperatures and normalised moisture contents of the particles at the exit of the spray drying tower. Smaller particles up to 700  $\mu\text{m}$  exit at

zero moisture content due to greater residence times and lower resistances to heat and mass transfer. The temperatures of these particles are also very high compared to larger particles (800  $\mu\text{m}$  and above). The larger particles have a higher moisture content and a considerably lower temperature at the exit due to shorter residence times and greater resistances to heat and mass transfer.

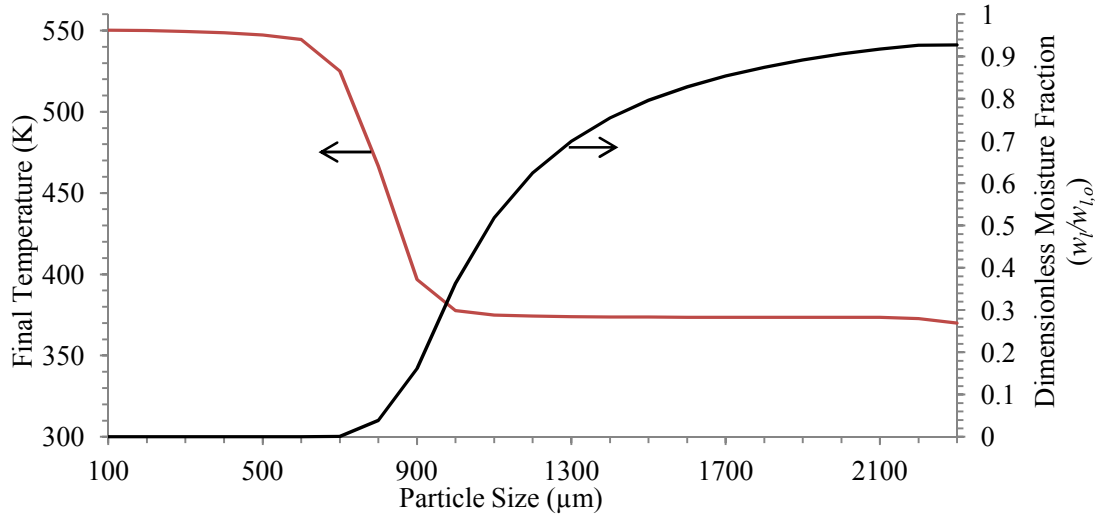


Figure – 5.18: Outlet temperatures and moisture contents as a function of size.

Figure 5.19 is a plot of gas velocity along the tower height normalised by the initial gas velocity which is the maximum. The gas velocity reduces due to a reduction in temperature as it goes up, which increases the gas density and hence the reduction in velocity. However the mass flow of the gas gets larger due to the increase in moisture content of the gas as it travels upwards, but the net effect is a decrease in gas velocity up the tower.

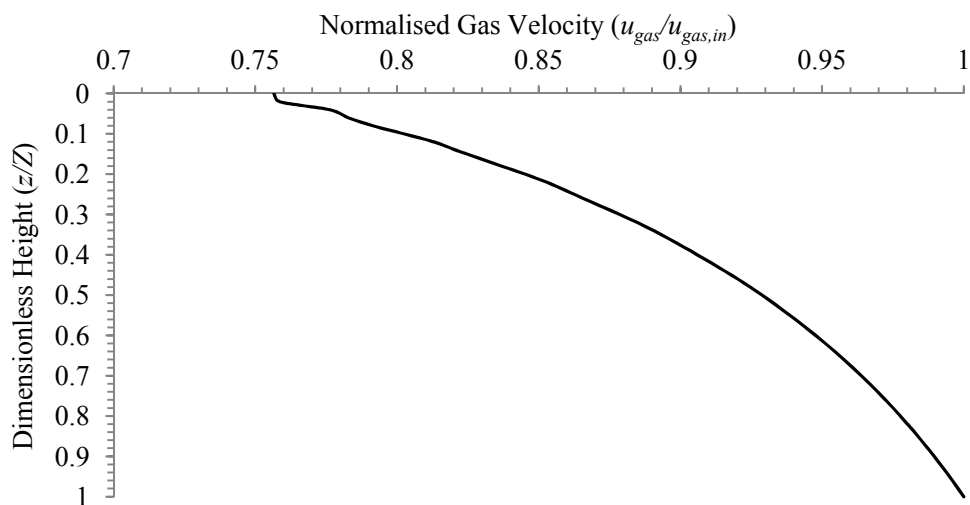


Figure – 5.19: Normalised gas velocity along the tower height.

Figure 5.20 is a plot of the heat fluxes through the insulated column wall to the surroundings along the dimensionless tower height. The negative sign indicates that the

heat is being lost from the tower to the surroundings. The heat flux is a maximum at the bottom of the tower due to increased velocity and higher temperature of the gas at the bottom of the tower. As the gas loses temperature and decreases in velocity, the heat flux also decreases. The predicted total heat loss through the column walls is 5.58 kW.

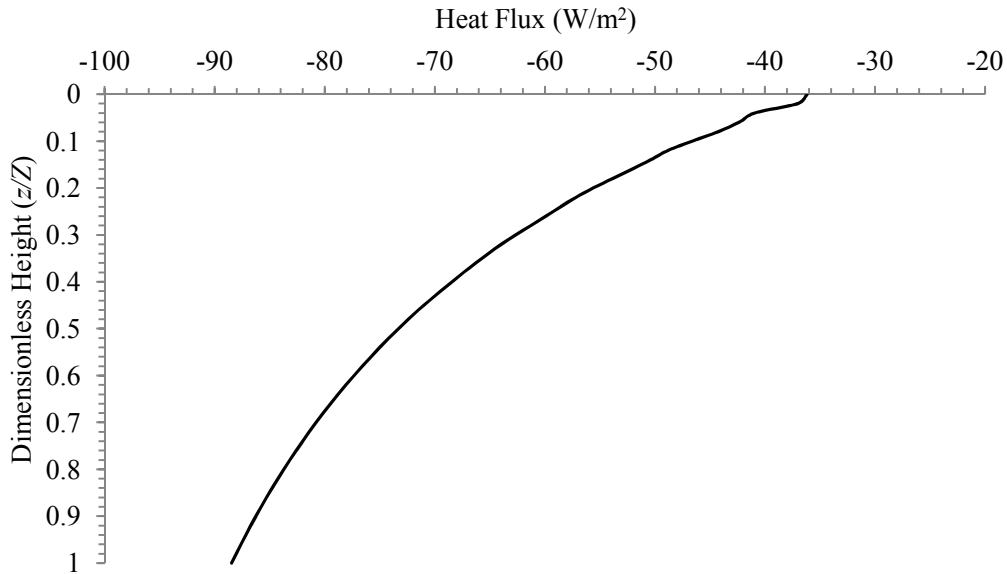


Figure – 5.20: Heat flux through the column wall v/s dimensionless height.

To evaluate the influence of rate of mass transfer from the surface of the droplet/particle on the heat transfer coefficient calculated using the Nusselt number correlation (given by equation (3.1)), the corrected Nusselt number is calculated using equation (3.12), based on which the corrected heat transfer coefficient is calculated. Figure 5.21 is a plot of heat transfer coefficient calculated using equation (3.1) compared with that calculated using the Nusselt number correction due to high surface mass transfer rate for a 500  $\mu\text{m}$  particle size along the dimensionless tower height. It is observed that the difference in the corrected heat transfer coefficient is negligibly small. Hence the rate of mass transfer from the droplet/particle surface is not sufficiently high to appreciably change the Nusselt number proposed by Ranz and Marshall (1952).

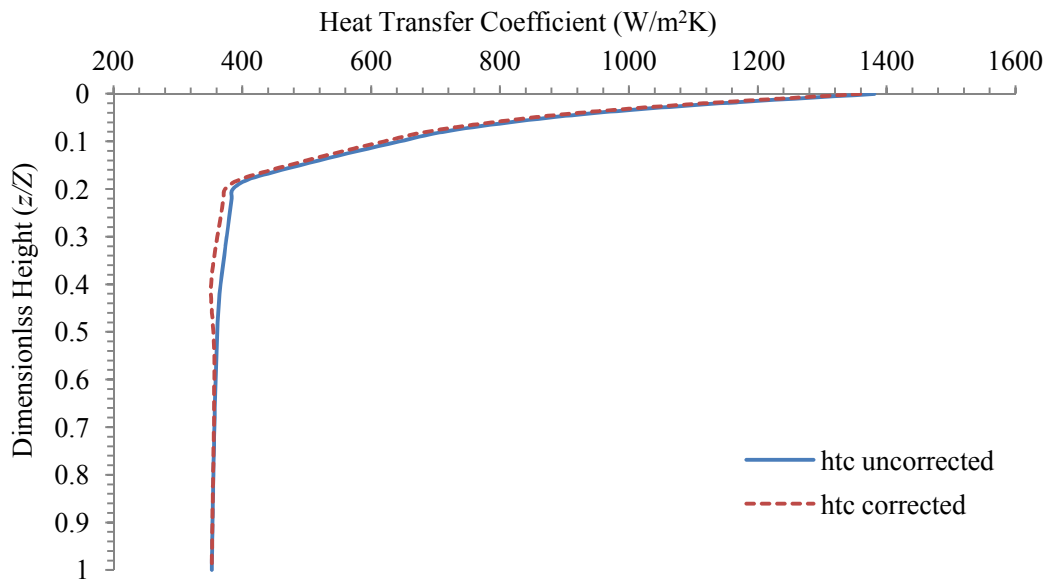


Figure – 5.21: Corrected heat transfer coefficient v/s dimensionless height.

The effect of mass transfer rate on the drag coefficient and hence the velocity profile of the droplet/particle was evaluated using equation (3.66). Figure 5.22 is a plot of velocity profile of a 500  $\mu\text{m}$  particle size along the dimensionless tower height calculated using the surface mass transfer corrected drag coefficient and compared with that calculated without the surface mass transfer correction. It is observed that the surface mass transfer correction in the drag coefficient does not appreciably change the velocity profile; hence its influence in changing the residence times of the droplets/particles is negligible.

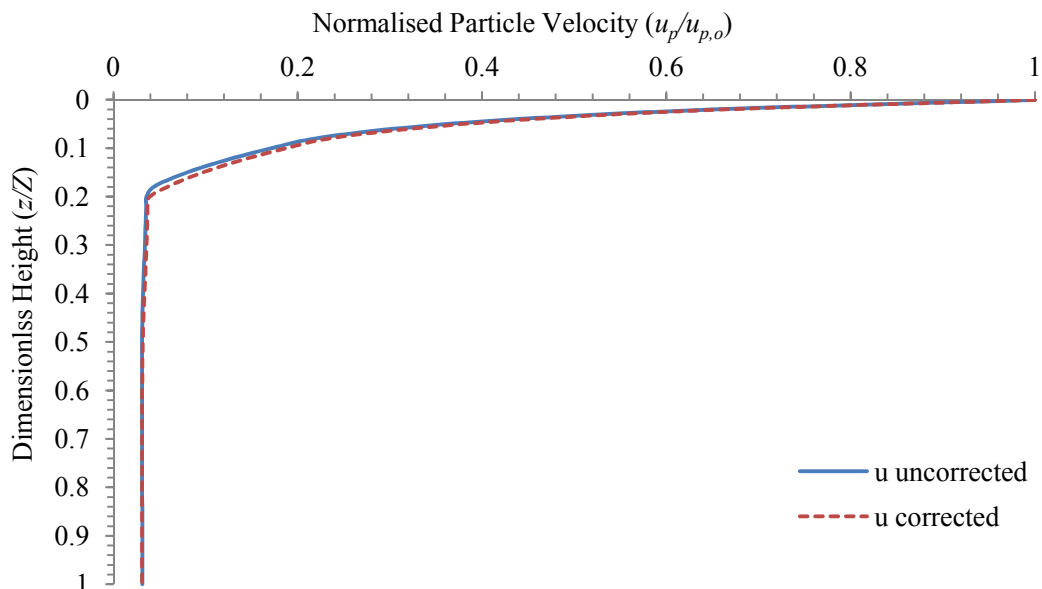


Figure – 5.22: Corrected particle velocity v/s dimensionless height.

Table 5.5 is a list of the predicted gas outlet temperature, the average particle outlet temperature and moisture content and the heat loss through the column wall with experimental data and with the differences.

Table – 5.5: Comparison of simulation results and pilot-plant data.

	Predicted	Experimental (Martin de Juan, 2011)	Difference
Gas outlet temperature (K)	396.4	367	29.4
Powder outlet temperature (K)	482.2	356	126.2
Dried powder moisture content %(w/w)	5.88	1.80	4.08
Heat loss though the tower (kW)	5.58	62.1	-56.5

The predicted and experimental data are not in good agreement and this is due to several factors. There is a difference of 126.2 K (35%) in the calculated and experimentally measured powder outlet temperatures. The measured outlet temperature of the powder is much less than the calculated value, because in the actual process, the dried powder comes into contact with an entrained cold air stream at the bottom exit of the spray tower and this will result in cooling of the powder. In addition, the measured temperature is not at the exit of the tower, but is obtained by a temperature probe installed on a belt conveyor at a few metres away from the location where the powder falls from the tower (see Figure 4.2). The temperature of the powder will be reduced significantly by this point. The model does not consider cooling of particles due to entrained air and cooling of particles when the powder falls on the belt conveyor.

The predicted moisture content is different from the measured value of the spray dried powder. This is primarily because of two reasons. Firstly, the assumption in the droplet drying model that drying continues to take place in the third stage of drying even at very low moisture content. In reality, the particles moisture content will not reduce below the equilibrium moisture condition at the exit gas condition; hence the actual moisture content will be greater. Secondly, the moisture content of the dried powder is measured from a sample which is first conveyed through the belt to the air lift and is then transported to the sampling section via an air lift. The dried powder in this route not only gets a reduction in temperature, but it also absorbs surrounding moisture content and begins to equilibrate with the new conditions. Hence the measured moisture content is expected to be greater than the predicted average powder moisture content. But in the current case, the measured moisture content is smaller than the predicted value. This could mainly be due to the use of the dried powder size distribution as the initial droplet size distribution.

The dried powder size distribution is expected to be greater than the initial droplet size distribution resulting from atomisation at the nozzle. As the droplets fall downwards, they collide with other droplets which may coalesce; similarly the wet particles may also collide to form agglomerates. Furthermore, the entrainment of deposits on the wall may also have a contribution in the increased mean particle size. Due to the increase in particle size and mass, the particles will fall down more quickly as it has been shown in Figure 5.7 that the larger particles have significantly smaller residence times, similarly, the larger particles exit at a much higher moisture content compared to the smaller particles. The heat and mass transfer coefficients of the larger particles are also significantly less than those of the smaller particles (Figures 5.10 and 5.11). These conditions favour more rapid evaporation of moisture from the smaller particles compared to the larger particles.

The predicted exhaust gas temperature is also higher than the measured value. The exhaust gas temperature indicates the amount of heat exchange taking place between the gas and the droplets/particles. In this case, the predicted exhaust gas temperature is 29 K greater than the measured temperature. Since the predicted particle exit moisture content is greater, hence the exhaust gas temperature is also greater. Furthermore, the heat loss predicted by the model is significantly smaller than the calculated heat loss (based on measured temperatures) taking place in the spray drying tower. The actual heat loss is calculated based on the measured values, although it also includes the associated measurement errors, but the difference in measured and predicted heat losses is not expected to be as high as 56.5 kW. There are several reasons for a higher heat loss taking place from the tower compared to the prediction. Firstly, the inlet gas temperature is measured in the inlet gas duct to the distribution ring. The distribution ring is fairly poorly insulated; hence a reduction in gas temperature will take place before the gas actually enters the tower. In addition to the heat loss through the insulated wall to the surroundings, there may be conduction through the body of the tower to the supporting structure. Furthermore, there may be air ingress through the inspection hatches into the tower, since the tower operates at slightly below atmospheric pressure, this entrained air will reduce the gas temperature. These factors will contribute to greater heat losses calculated via measured temperatures. Additionally, the measurement of exhaust gas temperature is taken at a few metres away from the exit, inside the gas duct by an unsheathed thermocouple; hence there may be some measurement error in the exhaust gas temperature. In the model, the heat loss from the

wall is allowed up to the height of nozzle location. Consideration of heat loss from the tower walls above the nozzle will reduce the difference between the measurement and prediction. The inside film coefficient ( $\alpha_D$ ) is calculated using the correlation applicable to fully developed flow, however, the flow inside the tower is a swirling flow induced due to tangential entry of the inlets. It is well known that the swirling gas flow significantly enhance the film coefficient (Razgaitis and Holman, 1976).

Other reasons for the differences between the measurements and the simulation results could be due to the simplifying assumptions in the model to predict the particle residence times including the limitation of minimum particle velocity to the terminal falling velocity, the use of smooth particle drag law, no particle deposition on the wall and no particle-particle interaction. The smaller particles will get entrained by the gas, in addition they may get caught up in the recirculating zones, and this will increase their residence times. The drag law which is used for the calculation of the drag force on the particles is valid for smooth spherical particles. However, the particles will undergo a change in shape due to drying as well as agglomeration. The irregular shaped particles may experience a larger drag force, and hence, a greater residence time, which is not accounted in the simulation. The wet particles may get deposited on the wall; the particles may retain at the wall for some time and lose moisture before the particles eventually get entrained back into the gas stream. The particle-particle interaction is also ignored in the simulation. The larger particles move faster compared to smaller particles, hence the movement of larger particles will be hindered by the slower moving particles and vice versa. These assumptions need to be relaxed for a better estimation of the particle residence times.

The particles are assumed to move only in the axial direction and the swirl component of the gas phase and the particles is ignored. Due to the presence of swirl, most of the particles move close to the wall hence a temperature gradient in the gas phase will be present along the cross-section, i.e., a high temperature gas in the central region and relatively lower temperature gas near the walls. Hence the plug-flow assumption may give overprediction of the spray drying tower performance. The correlations which are used to obtain the heat and mass transfer coefficients are applicable to the smooth spherical particles, the change in shape of the particles may also cause a deviation of the heat and mass transfer coefficients from the ones calculated using Ranz and Marshall (1952) correlations.

#### 5.5.4 Influence of Initial Droplet Size Distribution on the Simulation Results

In the Base Case, it is found that the size distribution of the droplets specified at the top inlet can have a significant impact on the spray dryer modelling results as the smaller particles dry more quickly and the larger particles take a longer time. In addition, the residence time of particles vary significantly with size. Therefore, to investigate the influence of initial size distribution specification on the plug-flow modelling results, two further simulation runs are carried out, hereafter referred to as plug-flow Case 1 and plug-flow Case 2. The two cases differ in the specification of initial droplet size distribution. In the plug-flow Case 1, the measured size distribution of the droplets (Martin de Juan, 2012) is used as the initial droplet size distribution. In the plug-flow Case 2, the measured size distribution of the dried powder (Martin de Juan, 2012) is specified as the initial droplet size distribution. The measured droplet size distribution data is fitted using a size constant ( $d_m$ ) of 325  $\mu\text{m}$  and a distribution parameter ( $u_s$ ) of 1.6. The measured powder size distribution was fitted using two Rosin-Rammler distributions for the entire range of sizes. For sizes up to 600  $\mu\text{m}$ ,  $d_m = 500 \mu\text{m}$  with  $u_s = 2.2$  was used and for sizes greater than 600  $\mu\text{m}$ ,  $d_m = 300 \mu\text{m}$  with  $u_s = 0.6$  gave the best fitting with measurements. Figure 5.23 is a plot of cumulative size distribution of droplets and particles, and the corresponding curve fits using a Rosin-Rammler distribution.

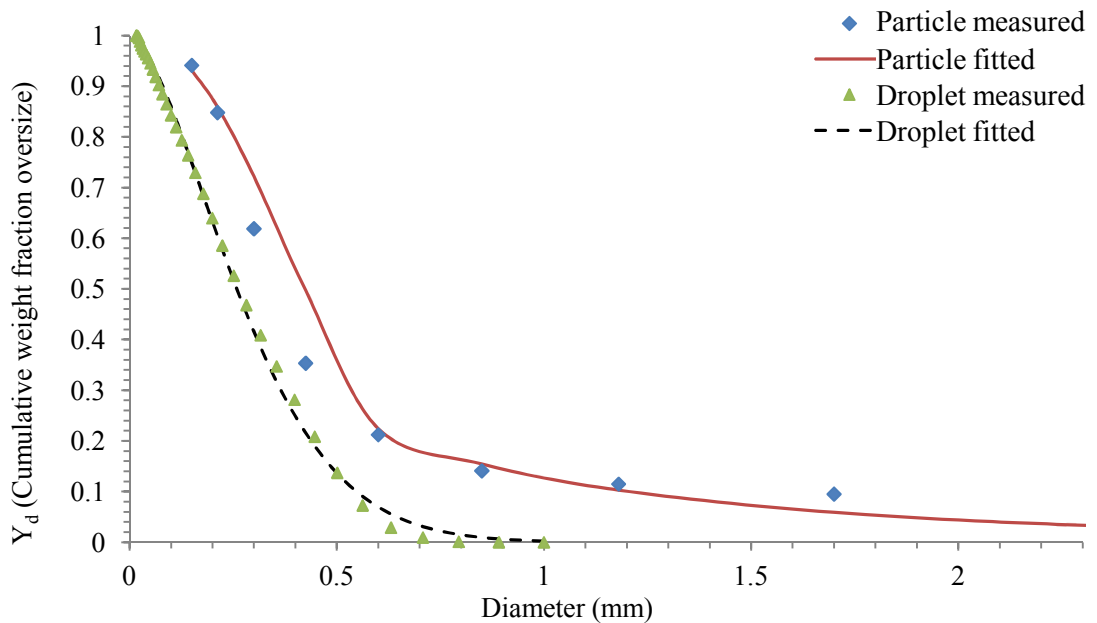


Figure – 5.23: Size distribution of atomised droplets and spray dried powder cumulative mass basis.

Table – 5.6: Input operating conditions (Martin de Juan, 2012).

Droplet Properties		
Slurry inlet temperature	365.5	K
Slurry mass flux	0.17	kg/m <sup>2</sup> s
Specific heat of dried particle	1500	J/kg K
Specific heat of solvent	4180	J/kg K
Specific heat of vapours	1900	J/kg K
Density of slurry	1566	kg/m <sup>3</sup>
Latent heat of vapourisation	2.26×10 <sup>6</sup>	J/kg
Diffusion coefficient of water in slurry	3.0×10 <sup>-11</sup>	m <sup>2</sup> /s
Diffusion coefficient of water vapour into gas	2.6×10 <sup>-5</sup>	m <sup>2</sup> /s
Gas Properties		
Hot gas temperature	559.5	K
Hot gas mass flux	0.76	kg/m <sup>2</sup> s
Gas pressure	101325	Pa
Gas thermal conductivity	0.03	W/mK
Entrained air mass flux	0.038	kg/m <sup>2</sup> s
Specific heat	1006	J/kg K
Ambient temperature	281	K
Column Wall		
Metal wall thickness	0.006	m
Metal wall thermal conductivity	18.8	W/mK
Insulation thickness	0.105	m
Insulation thermal conductivity	0.04	W/mK

The size distribution of the droplets varies from 20 µm to 1000 µm whereas the size distribution of the dried powder varies from 100 µm to about 2300 µm. The distribution range of dried powder as well as the final particle size of the dried powder is larger than the sizes of the initial droplets. The Sauter mean diameter ( $d_{32}$ ) of the measured droplets size distribution, shown in Figure 5.23, is calculated using equation (2.1) and the value is 198 µm. The  $d_{32}$  of the measured dried powder size distribution (see Figure 5.23) is 350 µm. If it is assumed that no coalescence, agglomeration and attrition takes place in the spray drying tower, then the following equation can be used to calculate the final mean particle size from the initial mean droplet size (Pinto *et al.*, 2014):

$$d_{32,p} = d_{32,d} \left( \frac{\rho_d (1 - w_{l,d})}{\rho_p (1 - w_{l,p})} \right)^{1/3} \quad (5.41)$$

Using the above equation,  $d_{32,p}$  of the particle is calculated to be 792  $\mu\text{m}$ , which is more than two times greater than the  $d_{32,p}$  value based on the measured powder size distribution. This indicates that the increase in the mean particle size is mainly due to coalescence and agglomeration.

For both simulation cases the operating conditions are listed in Table 5.6 (Martin de Juan, 2012), which are from an experimental run in the IPP spray drying tower. For the droplet size distribution case (plug-flow Case 1), the minimum droplet size is taken to be 50  $\mu\text{m}$  as the mass fraction of the droplets smaller than 50  $\mu\text{m}$  is less than 3%. The predicted overall enthalpy balance error for plug-flow Case 1 is 0.6%, whereas for plug-flow Case 2, it is 0.3%.

### 5.5.5 Solution Dependency on the Number of Increments

The solution was investigated for numerical accuracy by increasing the total number of increments ( $\Delta z$ ). Although this has been done in the Base Case, but the input operating conditions (gas and slurry mass flow and temperatures) are changed, therefore this investigation is carried out again. The particle size distribution was represented using 39 discrete sizes. In Table 5.7, the variations of the calculated values of the outlet mass weighted average particle temperature, moisture content and gas temperature as well as the inlet gas temperature are listed for total number of increments of 3580 and 7160. The simulation did not converge when the total number of increments was reduced below 3580. The sensitivity of the results on the number of grid size is very small. The grid size selected for all further simulations is 3580. The simulation run time for 3580 grids is about 1 minute on a desktop PC.

Table – 5.7: Solution dependency on the number of increments.

S. No.	Total number of increments	No. of iterations	Particle average outlet temperature (K)	Particle average moisture % (w/w)	Outlet gas temperature (K)
1	3580	7	525.31	1.08	378.28
2	7160	7	525.32	1.08	378.30

### 5.5.6 Solution Dependency on the Number of Discrete Sizes

Table 5.8 lists simulated values of the average particle outlet temperature and moisture content, and the gas outlet temperature for increasing the number of discrete sizes used for representing the size distribution from 20 to 77. By increasing the number of discrete sizes, a small increase in the average outlet moisture fraction is observed along with an increase in gas outlet temperature. The influence of number of discrete sizes on particle average outlet temperature is negligible. Overall, the influence of number of discrete sizes on the simulation results is not dramatically large. Hence any of the above listed size cuts can be used for the simulation run. In this study, total 39 discrete sizes are used to represent the droplet size distribution.

Table – 5.8: Solution dependency on the number of discrete sizes.

S. No.	Number of discrete sizes	Size cut ( $\mu\text{m}$ )	Particle average outlet temperature (K)	Particle average moisture content % (w/w)	Gas outlet temperature (K)	Simulation Time (s)
1	20	50	525.57	1.07	375.41	39
2	39	25	525.31	1.08	378.28	76
3	77	12.5	525.18	1.09	379.82	156

#### Plug-Flow Case 1:

Figure 5.24 is a plot of residence time of particles of different sizes. Smaller particles have larger residence times compared to larger particles and the decline in the residence time with increasing particle sizes is exponential. Larger particles show less sensitivity towards the decrease in residence time with increase in particle size compared to smaller particles. Similar trend is observed in the plot of residence time distribution of particles in the previous case (Figure 5.7).

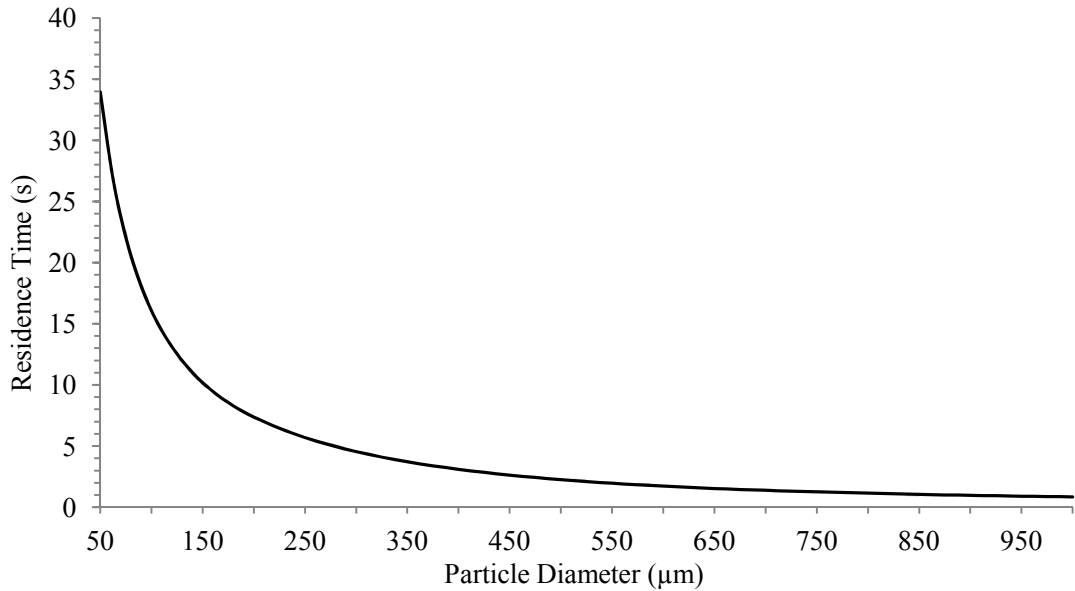


Figure – 5.24: Residence time of particles of different sizes for plug-flow Case 1.

Figure 5.25 is a plot of temperature profiles of the droplets/particles of different sizes as well as the gas temperature profile. The initial temperature of the slurry droplets is greater than the wet bulb temperature, which is found to be 322 K at the exit gas condition. Therefore the temperature of all the droplets initially falls as the droplets move downward. It is observed that none of the droplet sizes achieve a constant wet bulb temperature. After a certain height, the temperature of the particles starts to rise. This is due to the formation of a crust at the surface and the transformation from droplet to wet particle. At this stage, since the rate of moisture removal from the surface becomes dependent on the internal diffusion of moisture to the surface, this result in a decrease in the drying rate and hence most of the absorbed heat causes a rapid rise in the particle temperature. For smaller particles, the temperature quickly reaches the gas temperature and follows the gas temperature profile along the tower height afterwards. This is because smaller particles have a greater specific surface area, a smaller diffusion path and larger heat and mass transfer coefficients (as depicted in Figure 5.10 and 5.11 in the Base Case), resulting in greater heat and mass exchange rates. The temperature profiles of particle sizes of diameter 400 μm and greater remain fairly constant at about 373 K up to a certain height before they start to rise again. This temperature of 373 K corresponds to the slurry boiling temperature. Once the particles reach the slurry boiling point, the drying rate becomes dependent on the rate of heat transfer to the particles (third stage of drying). The slurry boiling point increases rapidly as the particles lose moisture content; therefore a sharp rise in the particle temperature is observed, which is more obvious for particle sizes up to 400 μm. The larger particles exit at lower temperatures, because the residence times of larger particles are shorter than the smaller

particles and the specific surface area is also smaller. The hot gas temperature is highest at the bottom of the tower and decreases rapidly as the gas flows towards the top due to heat exchange with the droplets/particles.

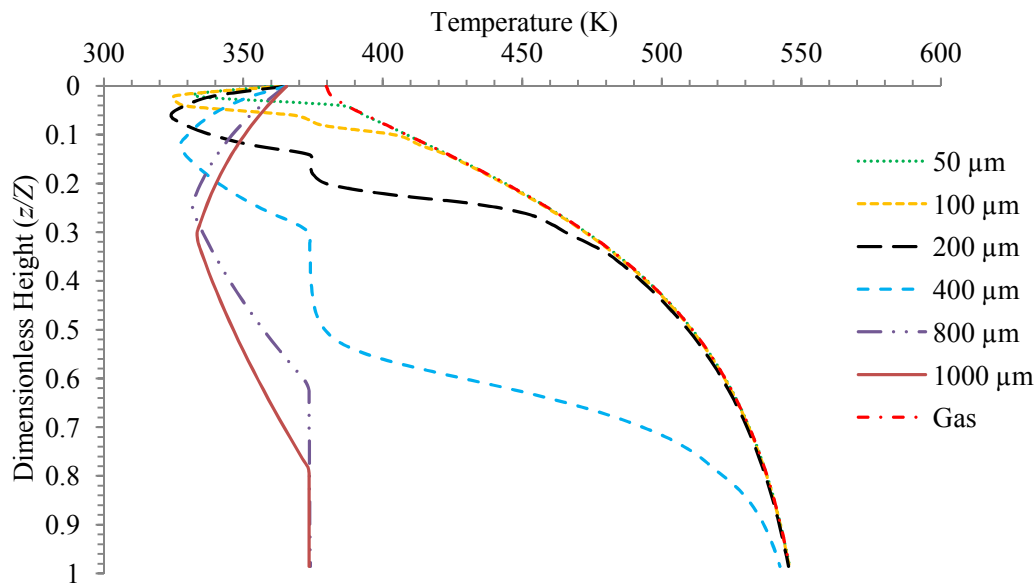


Figure – 5.25: Temperature profiles of droplets/particles and hot gas for plug-flow Case 1.

Figure 5.26 is a plot of temperature and moisture content of the particles at the exit of the spray drying tower. Smaller particles (up to 450  $\mu\text{m}$ ) have zero moisture content, because these particles have higher residence times and higher specific area, resulting in greater heat and mass transfer. The larger particles exit at a higher moisture content. Smaller particle sizes (up to 450  $\mu\text{m}$ ) exit at nearly a constant temperature. The moisture content of these particle sizes is also zero. Hence once the particles are completely dried, they quickly acquire the surrounding gas temperature. A sharp decrease in the temperature of the particles sizes ranging from 425  $\mu\text{m}$  to 650  $\mu\text{m}$  occurs. The exit moisture content in this range of particles has a sharp rise with an increase in particle size. Since the particles exit at the slurry boiling temperature (third stage of drying), in this stage, the boiling point of slurry is a function of moisture content. The slurry boiling point increases exponentially with a decrease in the moisture content as moisture becomes more bound. Hence a sharp decrease in temperature of the particles happens as the moisture content increases. The exit temperatures of particle sizes greater than 650  $\mu\text{m}$  are fairly constant as the slurry boiling point does not vary significantly at higher moisture content. These distributions are used to generate the weighted average values of temperature and moisture content.

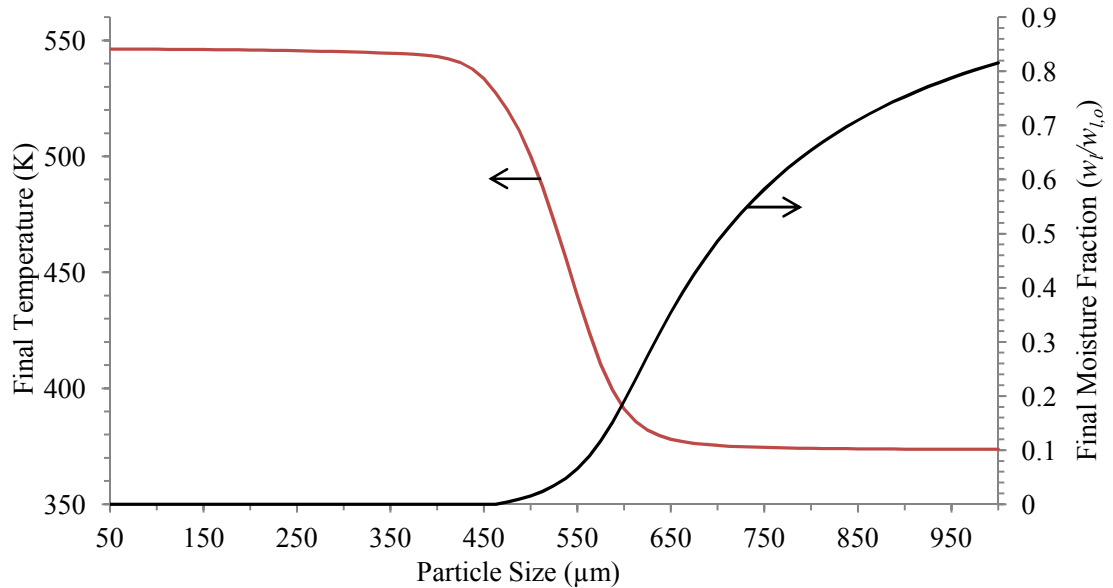


Figure – 5.26: Particle exit temperature and moisture content for plug-flow Case 1.

Plug-Flow Case 2:

Figure 5.27 is a plot of residence time of the range of particle sizes considered in this case. The plot is qualitatively similar to the previous cases with an exponential decrease in the residence time with an increase in particle sizes. The residence time becomes nearly uniform for very large particle sizes ( $> 1700 \mu\text{m}$ ).

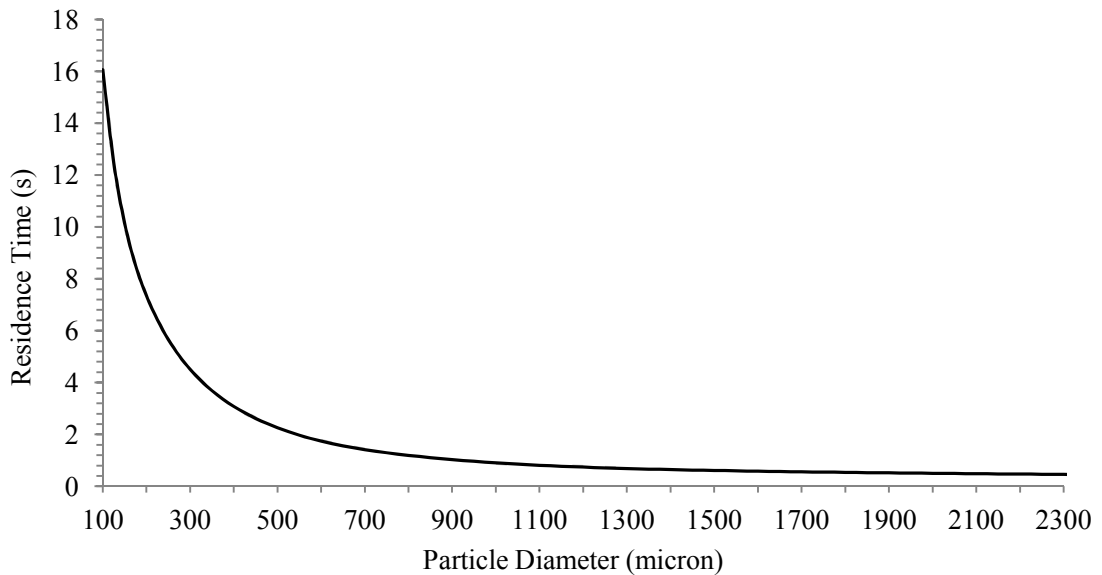


Figure – 5.27: Residence time of particles of different sizes for plug-flow Case 2.

Figure 5.28 is a plot of temperature profiles of the droplets/particles of selected sizes and the hot gas. The temperature profiles of the droplets/particles and the hot gas is qualitatively similar to that obtained from Case 1, however, the range of sizes is different. In the previous case, all the particles exited at the boiling point of the slurry.

While in this case, the larger particles exit at a temperature less than the slurry boiling point. This occurs for the 1500  $\mu\text{m}$  and 2300  $\mu\text{m}$  particle size profiles.

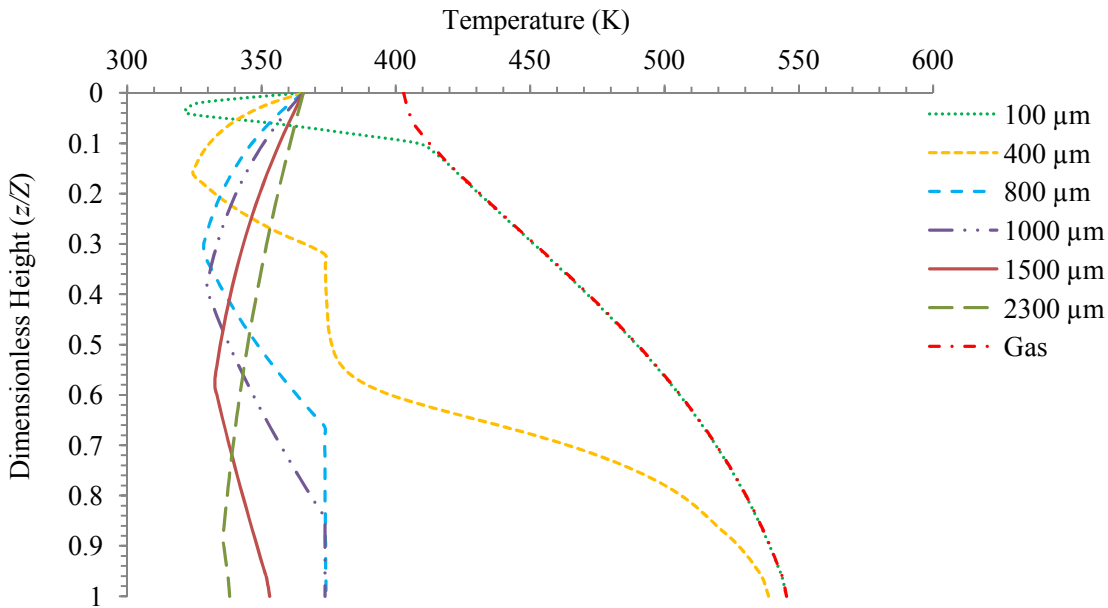


Figure – 5.28: Temperature profiles of droplets/particles and hot gas for plug-flow Case 2.

Figure 5.29 is a plot of exit temperature and moisture content of the particles as a function of size. The smaller particles (up to 450  $\mu\text{m}$ ) exit at an almost uniform temperature and the moisture content of these particles is also zero. The particle sizes in the range of 500  $\mu\text{m}$  to 650  $\mu\text{m}$  show a similar behaviour as in plug-flow Case 1, in which the greatest change in moisture content and exit temperature are observed with increasing particle sizes from 425  $\mu\text{m}$  to 650  $\mu\text{m}$ . The particle sizes in the range of 700  $\mu\text{m}$  to 1200  $\mu\text{m}$  exit at almost uniform temperature, because the slurry boiling temperature has a very small variation in this range of the moisture content. For the particle sizes greater than 1200  $\mu\text{m}$ , the temperature starts to fall and the moisture content is nearly uniform, because these particles exit in the second stage of drying, in which the drying rate is controlled by moisture diffusion to the surface. The temperature of these particles depends on how much exposure the particles have with the hot gas. For this range of particle sizes (1250  $\mu\text{m}$  to 2300  $\mu\text{m}$ ), since the larger particles have shorter residence times, hence the exit temperature is also lower compared to smaller particles.

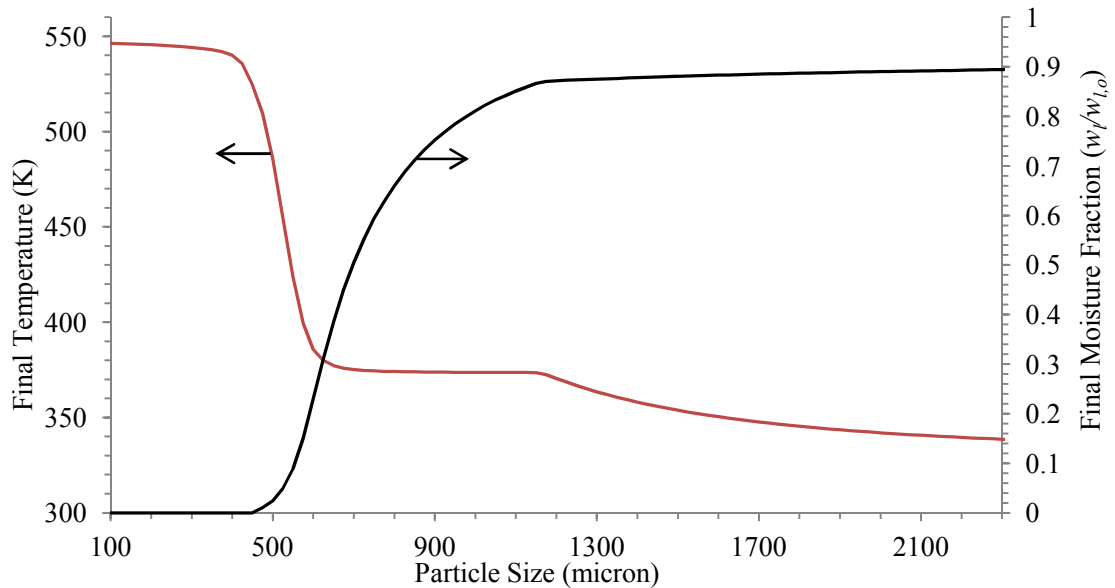


Figure – 5.29: Particle exit temperature and moisture content for plug-flow Case 2.

Figure 5.30 is a plot of heat fluxes through the insulated column wall to the surrounding v/s the dimensionless column height for both cases. The negative sign indicates that the heat is lost from the tower to the surrounding. The heat loss is greatest at the bottom of the tower because the temperature difference between the hot gas and the ambient is the largest, as the temperature of the hot gas is lowered; the heat loss also becomes relatively smaller. From the comparison of the two cases, it is found that, up to a dimensionless height of 0 - 0.1 from the top, the heat flux in plug-flow Case 1 is smaller, but it becomes greater after a dimensionless height of 0.1. Since most of the heat and mass exchange between the droplets and particles with the gas takes place in the top region of the tower in plug-flow Case 1 due to smaller droplets/particles having greater surface areas, allowing rapid evaporation of moisture. Hence the temperature of the gas is greater in the bottom region of the tower due to comparably less heat exchange as most of the heat is taken up in evaporating the moisture from the droplets/particles in the top region of the tower.

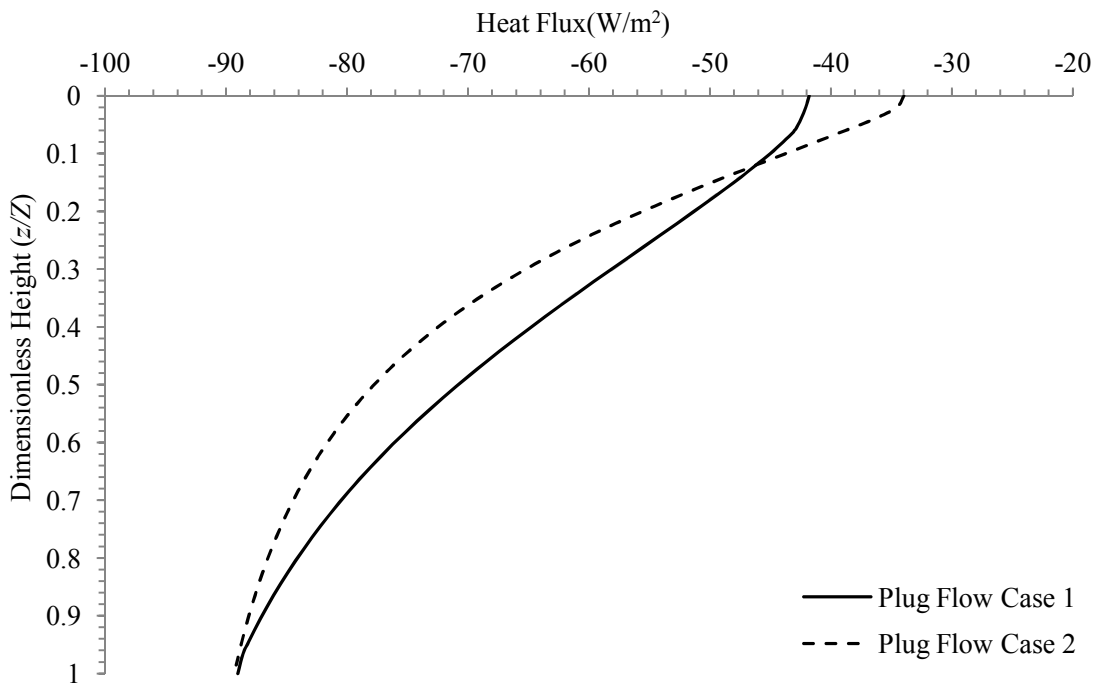


Figure – 5.30: Heat Flux through the column wall to the surrounding.

Table 5.9 lists the surface drying time and residence time of particles of different sizes. The surface drying time for smaller particles is very short compared to larger particles since the surface drying time is inversely proportional to the square of the mass transfer coefficient, which is greater for smaller particles. For larger particles, the residence time is only slightly greater than the surface drying time hence these particles exit soon after a crust is formed at the surface.

Table – 5.9: Surface drying time and residence time of different particle sizes.

Particle Size ( $\mu\text{m}$ )	Surface Drying Time (s)	Residence Time (s)
100	0.012	37.540
200	0.027	8.127
300	0.043	4.600
400	0.059	3.094
500	0.075	2.255
600	0.091	1.739
700	0.107	1.413
800	0.124	1.192
900	0.141	1.028
1000	0.157	0.906
1100	0.174	0.812
1200	0.191	0.741
1300	0.208	0.686
1400	0.224	0.644
1500	0.241	0.611
1600	0.258	0.583
1700	0.275	0.559
1800	0.292	0.538
1900	0.309	0.519
2000	0.326	0.502
2100	0.343	0.486
2200	0.360	0.471
2300	0.378	0.455

Table 5.10 lists the mass weighted average particle temperature and moisture content for the whole size distribution, the gas outlet temperature and heat loss for the plug-flow Case 1 and plug-flow Case 2 along with the measured values. The mass weighted average dried powder moisture content predicted by plug-flow Case 1 is smaller than plug-flow Case 2 and measurement. This is primarily because of the use of measured droplet size distribution as the initial droplet sizes in the simulation. As it has been shown earlier, the drying rates of the droplets/particles vary significantly with size.

Smaller droplets/particles lose the moisture content more quickly due to higher specific surface areas, smaller moisture diffusion paths and higher heat and mass transfer coefficients. In addition, the residence times of smaller particles are also greater. These are the primary reasons of overprediction of the drying of particles in plug-flow Case 1. In this case, since the dried particle average moisture content is smaller, hence the gas outlet temperature is also smaller.

In plug-flow Case 2, the measured dried powder size distribution is used to represent the initial droplet size distribution. This results in an underprediction of the drying of particles, since larger particles exchange less heat due to lower specific surface areas, larger moisture diffusion paths, smaller heat and mass transfer coefficients and smaller residence times. In the actual spray drying process, the size distribution of the particles continue to change with the tower height since the particles agglomerate as they fall down as a result of which the particle size distribution of dried powder is significantly greater than the initial droplet size distribution. These results suggest that the inclusion of agglomeration in the counter-current spray drying tower is important for a more reasonable prediction of the dried powder parameters. Large differences occur between the measured and predicted heat loss from the tower wall. Possible reasons for this large discrepancy in the measured and predicted heat losses have been given in the discussion on the results of the previous case. The possible reasons for the large discrepancy in the measured and predicted temperature are also explained in the previous case (Base Case).

Table – 5.10: Simulation results and measured data.

Parameter	Plug-Flow Case-1	Plug-Flow Case-2	Experiment (Martin de Juan, 2012)
Dried powder average moisture content % (w/w)	1.08	4.62	2.49
Powder average outlet temperature (K)	525.31	486.12	361.7
Gas outlet temperature (K)	378.28	402.92	382.3
Average particle density (kg/m <sup>3</sup> )	1134	1190	703
Heat Loss (kW)	3.42	3.26	21.43

## 5.6 Conclusions

A one-dimensional plug-flow model has been developed to simulate droplet/particle drying in a counter-current arrangement for gas and particle flow in a spray drying tower. The particles are assumed to be uniformly dispersed over the cross-section of the tower. The particles size strongly influences the temperature and moisture history of the particles as it affects the residence time of the particles and the surface area available for heat and mass transfer. Smaller droplets/particles have greater heat and mass transfer coefficients and larger residence times hence these particles exit at lower moisture content. The slurry inlet temperature is higher than the wet bulb temperature; therefore, the temperature of the droplets begins to fall. However, a constant wet bulb temperature is not reached since the solids content in the slurry is very high and a crust is formed before a constant wet bulb temperature could be reached. The crust formation of smaller particles occurs quicker. After the crust formation, the temperature of the particle begins to rise.

From a comparison of the simulation results of plug-flow Cases 1 and 2 with experimental data, it is found that the case with measured droplet size distribution overpredicts, while the case with dried powder size distribution underpredict the heat and mass exchange between the gas and the particles. The large difference in the results of the simulated cases indicate the importance of accurate initial size distribution of the droplets as well as inclusion of coalescence/agglomeration to allow for changes in droplet/particle diameters along the tower height. The large discrepancy in the predicted and measured powder outlet temperature and powder average moisture content is primarily due to the difference in the location of the predicted output value used for the comparison and the locations where the sample of powder for data measurement are taken. The temperature of the dried powder is expected to reduce significantly at the measured temperature location due to cooling effect with atmospheric gas. Similarly dried powder will approach equilibrium moisture condition under new temperature and surrounding moisture content. Hence there is a need for a more accurate data measurement from the tower for a more fair validation of the predictions.

This simple plug-flow model has an advantage of being computationally efficient compared to a more detailed modelling approach. Despite the simplifying assumptions made in the model, the quality of measured data and the complexity of the spray drying process, the model predicts similar trends to that of the measurements. The model can

be used to quickly estimate the performance of a counter-current spray drying tower with a low computing requirement (few minutes on a desktop computer) and can be a useful supplement in the determination of operating conditions for pilot-plant trials that would enable more extensive and accurate optimisation of the spray drying process.

## **6. SINGLE PHASE CFD MODELLING**

This chapter is divided into two sections, in the first section, single phase, three-dimensional CFD modelling of spray drying tower has been carried out to select a suitable mesh size and turbulence model for the prediction of air velocity profiles in the spray drying tower considering isothermal conditions, since the air velocity profiles have a significant influence on the droplet/particle trajectories, residence times and hence the drying rates. The predicted velocity profiles are compared with experimentally measured velocity profiles collected from the IPP spray drying tower. In the second section, non-isothermal single phase CFD modelling of a spray drying tower has been carried out to investigate the heat loss from the tower and to validate the predicted radial gas temperature profiles within the tower with measured gas temperatures.

### **6.1 Isothermal Single Phase CFD Modelling**

In this section, single phase, three-dimensional CFD simulations are carried out using steady state, isothermal and incompressible flow assumptions using commercial CFD software Fluent v.12 (Fluent, 2009) which uses the finite volume method to discretize the fluid flow equations given in Section 3.8, in the computational domain. The purpose of this study is to select a suitable mesh size and discretisation scheme as well as to select a turbulence model that gives the best validation with measured gas velocity profiles, which will then later be used to carry out multiphase CFD simulation of spray drying tower (Chapter 7). For this purpose, mesh independency test is carried out in Section 6.1.3 with different mesh to select an optimal mesh size with respect to accuracy as well as the computational time. The effect of convective discretisation scheme on the solution results is assessed in Section 6.1.4. The influence of steady and transient simulation conditions on the simulation results is investigated in Section 6.1.5. The influence of various turbulence models on the simulation results is assessed in Section 6.1.6. The effect of wall roughness on the predicted velocity profiles is assessed in Section 6.1.8 and the effect of pressure strain term in the predictability of the Reynolds stress turbulence is presented in Section 6.1.9. Conclusions of the investigations are given in Section 6.1.10.

### 6.1.1 Numerical Solution Method

The discretised equations are solved using the PISO (Issa, 1985) scheme for the pressure-velocity coupling and for pressure interpolation, PRESTO! (Patankar, 1980) scheme is used which is recommended for flows with swirl (Fluent, 2009). The simulations were initialised using the first-order upwind discretisation scheme, since the second-order scheme is less stable. In order to avoid divergence, the second-order scheme was selected after a few thousand iterations. The under-relaxation factors used in the simulation are listed in Table 6.1. The convergence criteria are specified as  $1 \times 10^{-4}$  for the continuity, momentum and the turbulence quantities.

Table – 6.1: Under relaxation factors

Pressure	Momentum	$k$	$\varepsilon$	$\mu_t$
0.3	0.5	0.8	0.8	0.5

### 6.1.2 Boundary Conditions

The air enters the tower at ambient temperature and is assumed to be moisture free. Due to the absence of measured mass flow distribution of air in each nozzle, the air flow is assumed to be distributed equally in each inlet nozzle. Some air gets entrained through the bottom outlet of the tower from where the particles exit due to lower pressure in the core region of the tower (see Figure 4.4 in Chapter 4). The amount of entrained air is assumed to be 5% of the mass flow of the air introduced through the inlet nozzles. The Reynolds number in the cylindrical region of the tower is of the order of  $2 \times 10^5$ . A summary of boundary conditions are listed in Table 6.2.

Table – 6.2: Boundary conditions used in isothermal simulation cases.

Parameter	Value	Boundary Condition Type
Inlet air mass flux	2.215 kg/m <sup>2</sup> s	Velocity Inlet
Entrained air mass flux	5% of inlet air	Velocity Inlet
Pressure at outlet face	-300 Pa	Pressure Outlet
Air density	1.25 kg/m <sup>3</sup>	--
Air viscosity	$1.78 \times 10^{-5}$ kg/ms	--

For the inlet turbulence boundary conditions, a turbulent intensity ( $I_t$ ) of 5% at the inlet face of the air inlet nozzle and the bottom outlet along with the hydraulic diameter ( $D_H$ ) is specified. This is used for the calculation of Reynolds stresses,  $k$  and  $\varepsilon$  at the boundaries using the following equations:

$$\begin{aligned}
 k &= \frac{3}{2} (U_{ref} I_t)^2 \\
 \varepsilon &= C_\mu^{3/4} \frac{k^{3/2}}{l} \\
 l &= 0.07 D_H \\
 \overline{u_i^2} = \overline{u_j^2} = \overline{u_k^2} &= 2/3 k \\
 \overline{u_i u_j} &= 0 \quad (i \neq j)
 \end{aligned} \tag{6.1}$$

The swirl is imparted due to the tangential entry of the air; therefore the initial turbulence condition in the air inlet nozzle is not likely to have significant influence on the swirling flow in the tower. The wall is considered to be smooth for the sensitivity studies carried out, including mesh independency test, selection of a suitable discretisation scheme and turbulence model. The influence of wall roughness on the simulation results is studied in Section 6.1.8. The no-slip boundary condition is applied at the wall. The modelling of flow near the wall is carried out using wall functions. The non-dimensional wall distance  $y^+$  was checked to ensure that it lies in the log-law of the wall region, which is required by the standard wall functions to be applicable in the near-wall region.

### 6.1.3 Mesh Independency Test

Before evaluating the effect of the turbulence model on the CFD modelling results, it is ensured that the results are essentially independent of the number of cells used in the computational domain. The standard  $k$ - $\varepsilon$  model is selected to perform the mesh independency tests with a second-order upwind convective discretisation scheme. Due to time constraint, the tests have been carried out using three different unstructured mesh sizes. The mesh type and the number of cells used in three different meshes are listed in Table 6.3. The mesh for the whole spray drying tower is shown in Figure 6.1 (a). Figure 6.1 (b) is the cross-sectional view of the three meshes in the cylindrical region of the tower. The degree of skewness is shown by colours. The yellow colour

indicates cells with a low skewness, while green colour indicates cells with a higher skewness. Highly skewed cells (skewness > 0.9) can cause the solution to diverge. Therefore it is ensured during meshing that the maximum skewness of the cells is less than 0.9.

Table – 6.3: Meshes used for grid independency test.

Mesh Name	Mesh Type	Number of Cells	Max. Skewness
Mesh 1	Tetrahedral cells	$1.3 \times 10^6$	0.79
Mesh 2	Primarily tetrahedral cells with refined mesh using prism cells near the wall in the cylindrical region.	$3 \times 10^6$	0.849
Mesh 3	Same as in Mesh 2	$4.8 \times 10^6$	0.83

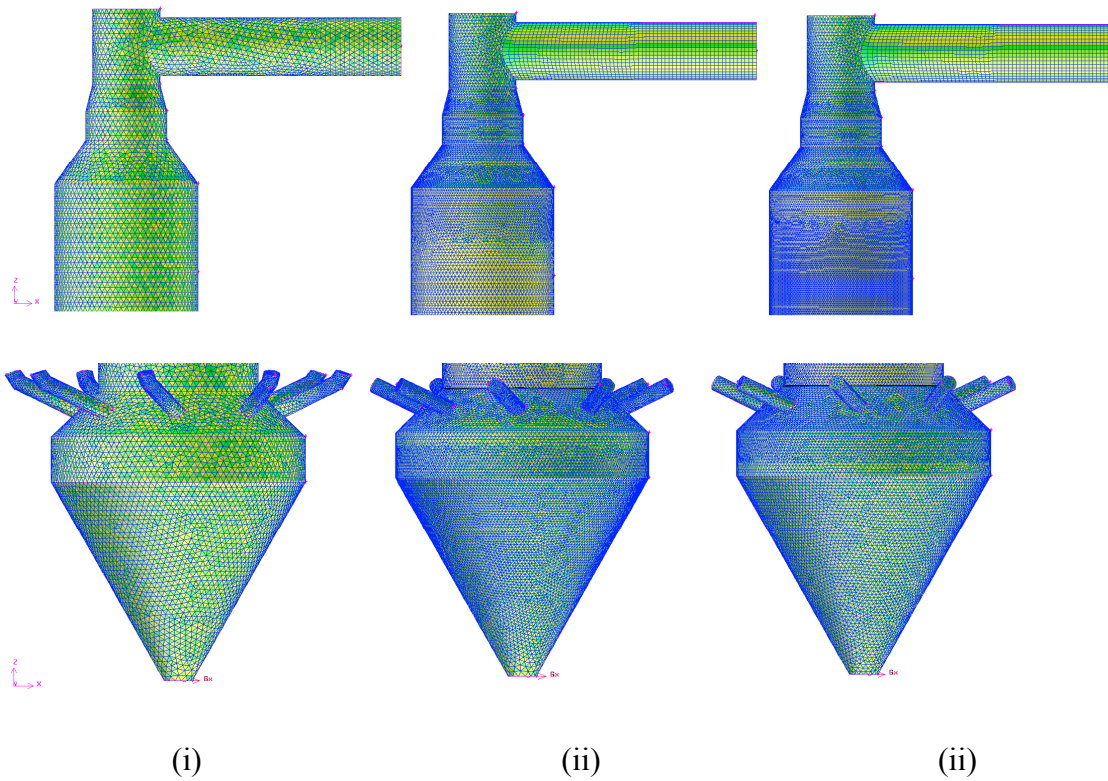


Figure – 6.1 (a): Meshing of spray drying tower: (i) Mesh-1, (ii) Mesh-2, (iii) Mesh-3.

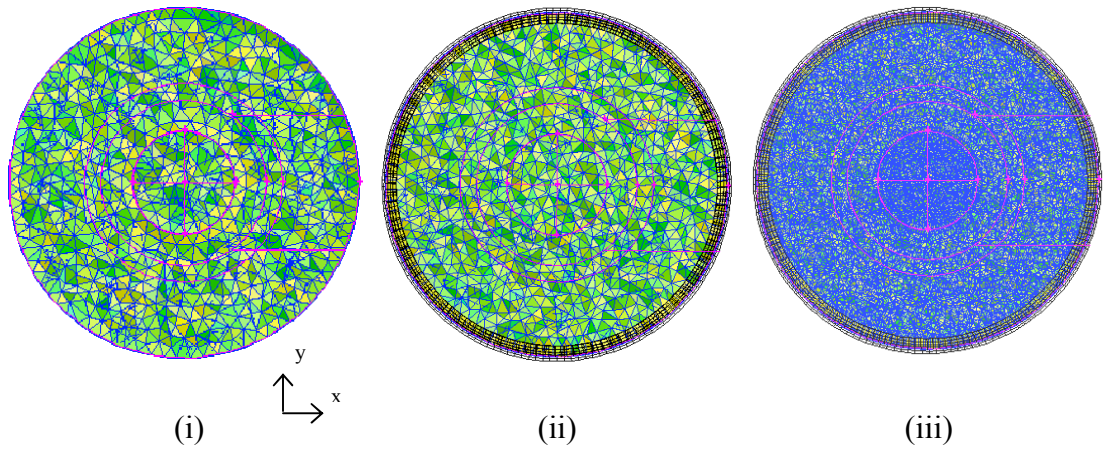


Figure – 6.1 (b): Cross-sectional view of the mesh: (a) Mesh 1, (b) Mesh 2, (c) Mesh 3.

Simulations were carried out using 2.9 GHz Intel quad core processor with 16 GB of RAM. The typical simulation time for Mesh 1 was 12 hrs, Mesh 2 was 27 hrs and Mesh 3 was 48 hours. Varied levels of convergence were achieved for the three mesh sizes based on monitoring of the residuals (defined as the imbalance in the computed variables summed over all the computational cells). The residuals of all three meshes did not converge to the required tolerance limit specified in Section 6.1.1. Figure 6.2 is a plot of residuals for the three meshes. For Mesh 1, the residual of continuity did not change after reaching  $5 \times 10^{-4}$ , while the residuals of momentum and turbulence equations were below the specified tolerance limit. The simulation was considered to be converged at this point. For Mesh 2, the residual of continuity was  $7 \times 10^{-4}$  while the residuals of momentum and turbulence were below the required tolerance limit. In Mesh 3, highest fluctuations in the residuals were observed and the residuals of continuity, momentum and turbulence equations were above the specified tolerance limits. A sharp peak observed in all three convergence residuals is due to shifting of the upwind discretisation scheme from the first-order to the second-order.

A comparison of the mean axial velocity profiles at different heights using three mesh sizes is given in Figure 6.3, all the reported values are taken along the x-axis of the tower (see Figure 6.1 (b)) at different dimensionless heights ( $z/Z$ ), with zero representing the bottom of the tower and 1 representing the top. From the plot of mean axial velocity profiles, it is observed that Mesh 3 has a slightly higher axial velocity in the central region of the tower compared to the Mesh 1 and Mesh 2. The variation of the axial velocity magnitude in all three meshes at all heights is very small with a maximum deviation of 0.3 m/s in the centreline. All three meshes produce qualitatively similar velocity profiles.

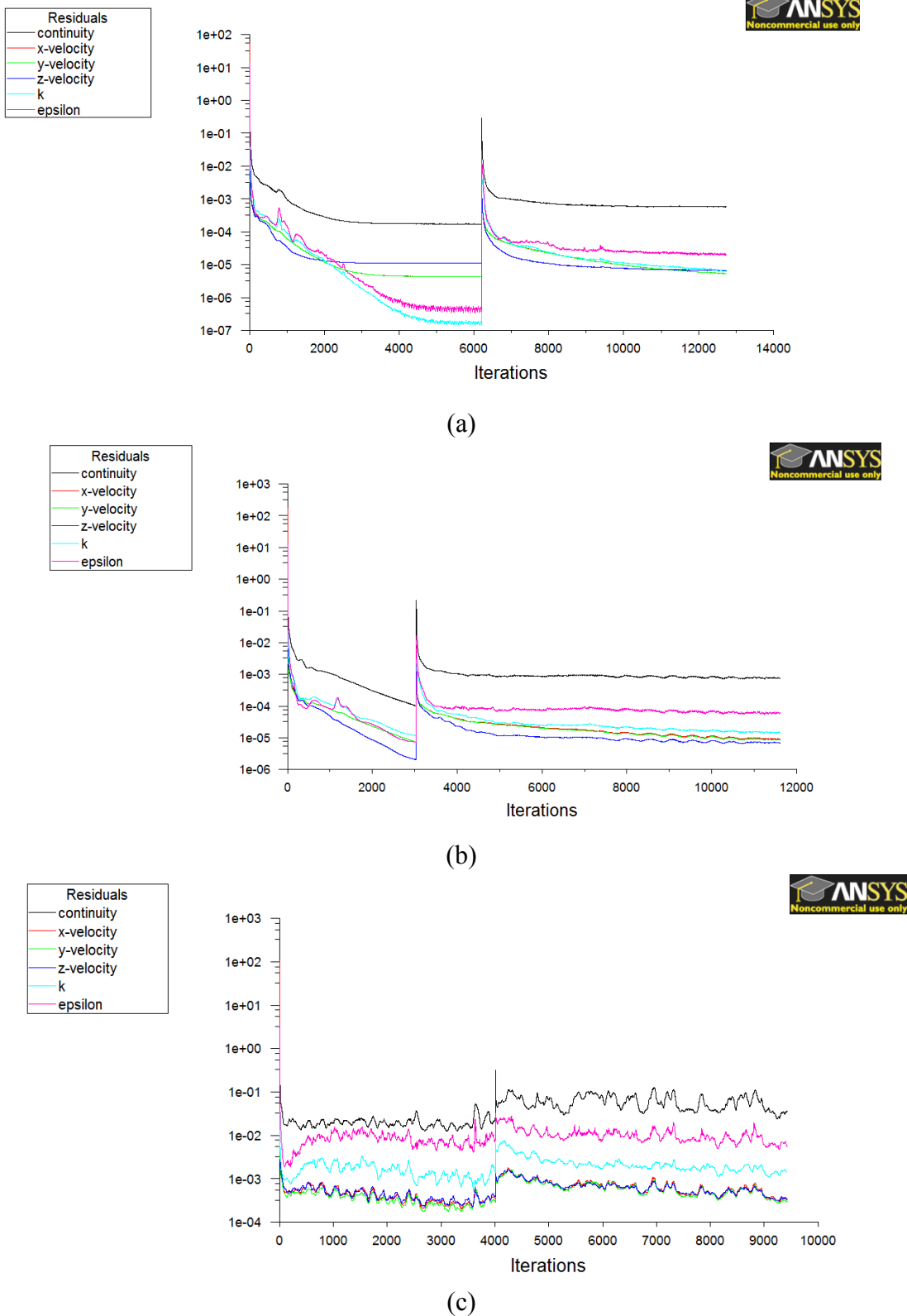


Figure – 6.2: Convergence residuals: (a) Mesh-1, (b) Mesh-2, (c) Mesh-3

A comparison of the mean tangential velocity profiles at different dimensionless heights ( $z/Z$ ) using the three mesh sizes is given in Figure 6.4. From the plot of tangential velocity profiles in Figure 6.4, it is observed that all three meshes produce qualitatively similar velocity profiles. Mesh 2 and Mesh 3 have refined mesh near the wall in the

cylindrical region. Mesh 3 gives higher velocity magnitude near the walls, with a maximum deviation of 16% compared to Mesh 1, also refined mesh near the wall (Mesh 2 and Mesh 3) results in a slight shift in the maximum tangential velocity towards the wall, which is not captured in Mesh 1. However, this requires significantly larger number of cells that increase the computational time by about 3 times. The level of convergence of Mesh 1 is also better compared to Mesh 2 and Mesh 3. Hence Mesh 1 is taken as the optimal mesh size with respect to accuracy as well as the computational time.

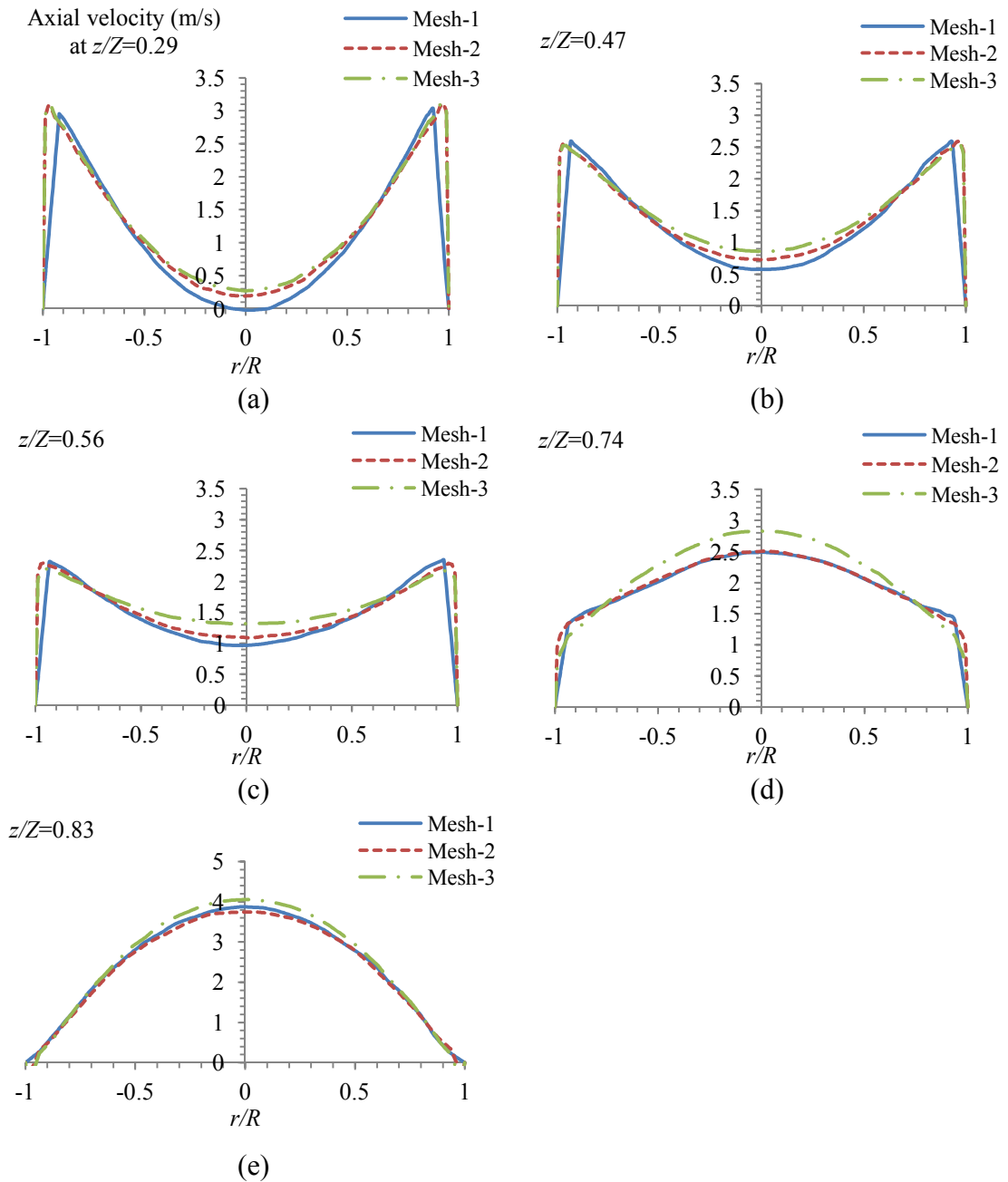


Figure – 6.3: Cross-sectional axial velocity profiles

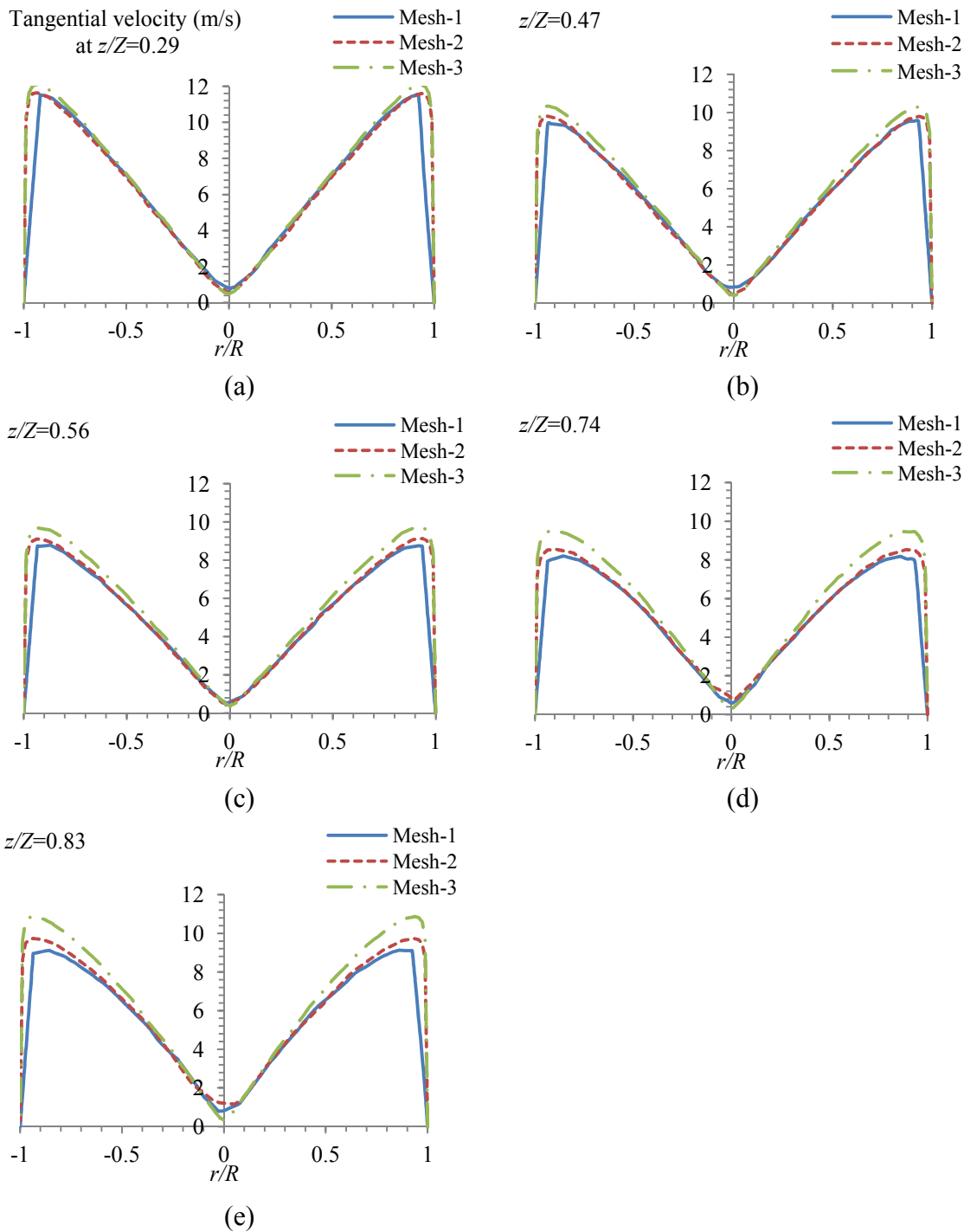


Figure – 6.4: Cross-sectional tangential velocity profiles

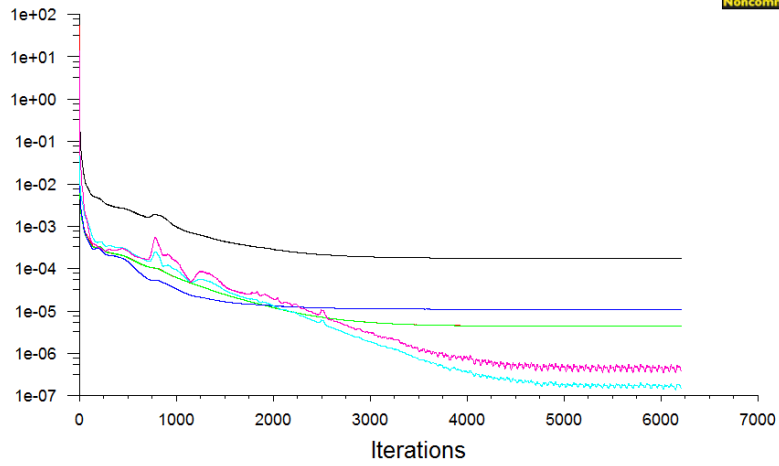
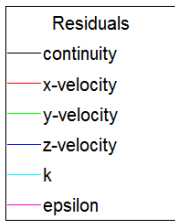
#### 6.1.4 Numerical Discretisation Scheme

The lower order discretisation schemes such as first-order upwind discretisation scheme and power law, for the convection terms of the governing equations are easier to converge because they are more stable but they have greater numerical diffusion errors compared to the higher order discretisation schemes. The higher order discretisation schemes are difficult to converge and slower in computation time compared to the lower order discretisation schemes, but they have lesser numerical diffusion error. Therefore

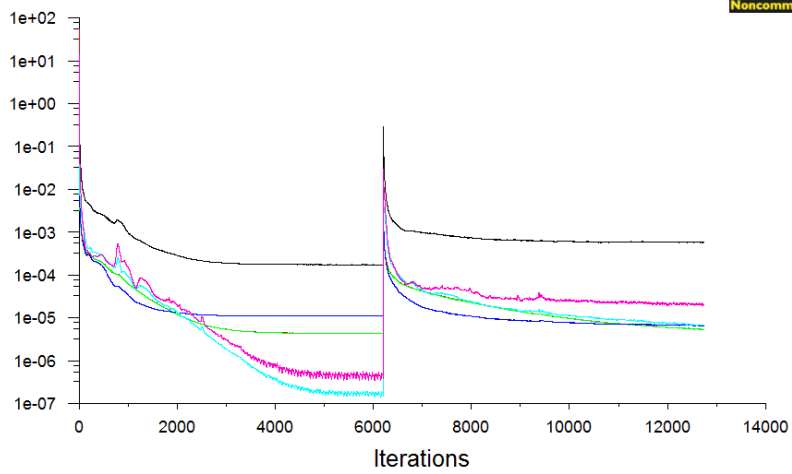
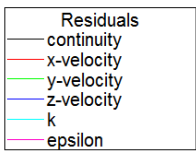
to select a suitable discretisation scheme with respect to stability, convergence and accuracy, CFD simulations have been carried out using Mesh 1 with the standard  $k-\epsilon$  turbulence model using the first-order upwind (FOU) (Versteeg and Malalasekera, 1995), second-order upwind (SOU) (Versteeg and Malalasekera, 1995) and quadratic upstream interpolation for convective kinetics (QUICK) (Leonard and Mokhtari, 1990) discretisation schemes. The boundary conditions and the convergence criteria are kept same as described in Section 6.1.1 and 6.1.2. For the cases in which SOU and QUICK schemes are used, the simulations were initialised with the converged solution utilising the FOU scheme as these discretisation schemes are less stable.

Figure 6.5 is a plot of the residuals for all three discretisation schemes. All the discretisation schemes did not show convergence to the required tolerance limit. The simulations were taken to be converged when the residuals of the continuity equation stopped changing with iterations. The residual of continuity in the FOU scheme did not change after a value of  $1.7 \times 10^{-4}$ , the residual of SOU and QUICK schemes stopped changing after  $5 \times 10^{-4}$ . A sharp peak in the cases utilising the SOU and QUICK schemes at about 6200 iterations is because these simulations are initialised from the FOU scheme at 6200 iterations. Total number of iterations required for FOU scheme is 6200 and for SOU and QUICK scheme is 12600.

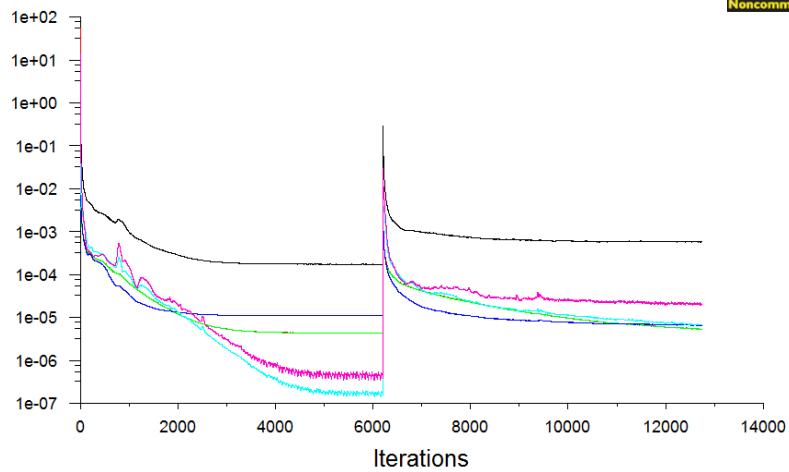
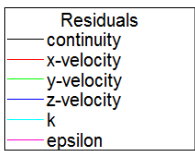
A comparison of the axial velocity profiles computed using these schemes at different heights is given in Figure 6.6. It is observed in Figure 6.6 that the FOU discretisation scheme produces flatter axial velocity profiles, more prominent at the top region of the tower, which is a result of a higher numerical diffusion error. The higher order schemes produce very similar velocity profiles. Hence both the SOU and QUICK discretisation schemes are acceptable discretisation schemes. The SOU discretisation scheme is selected because it is comparably more stable and computationally more efficient than the QUICK scheme.



(a)



(b)



(c)

Figure – 6.5: Convergence residuals for discretisation scheme. (a) FOU; (b) SOU; (c)

QUICK

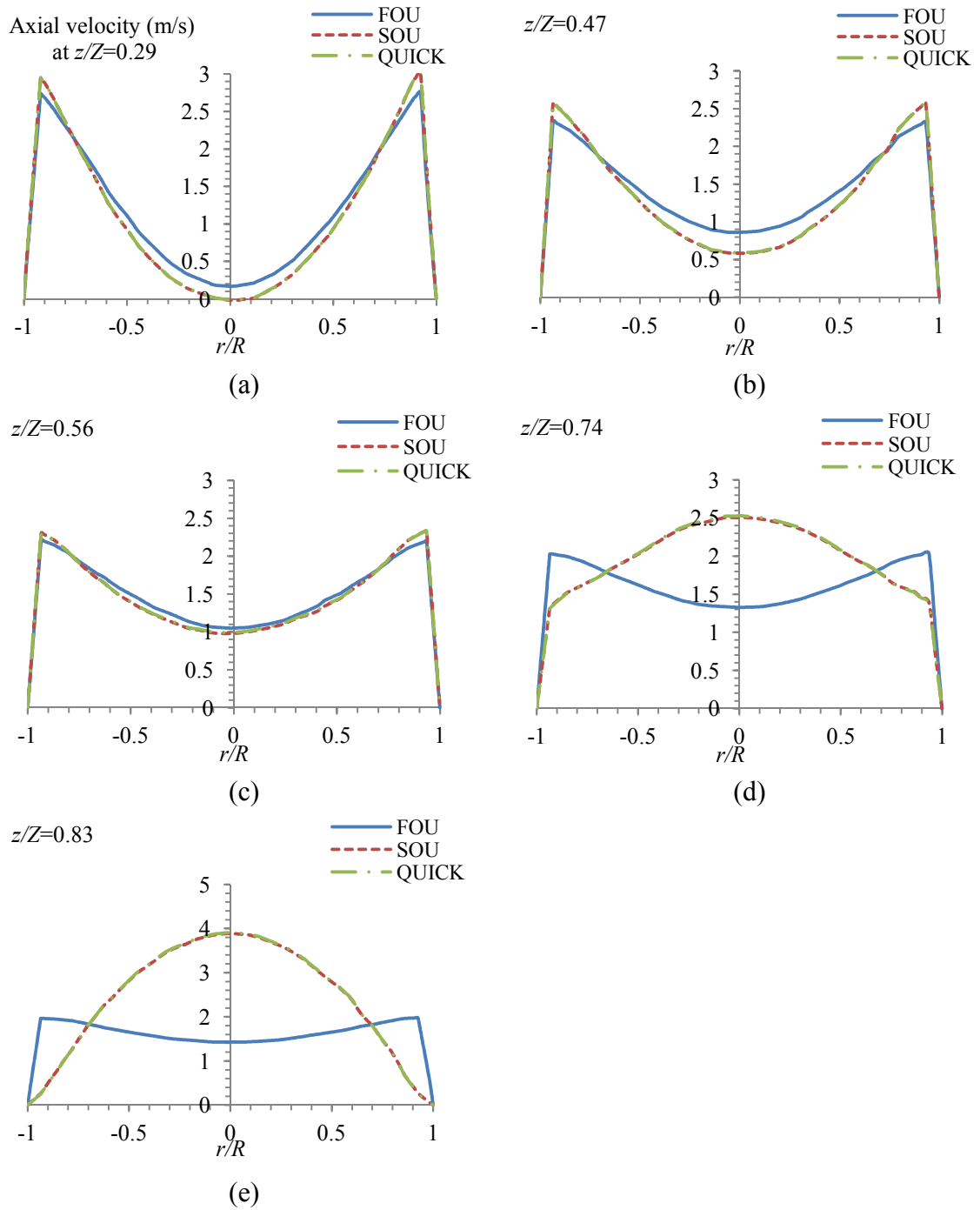


Figure – 6.6: Cross-sectional axial velocity profiles computed using different discretisation schemes

### 6.1.5 Transient vs Steady State

In the previous sections, the steady state assumption was used to carry out simulations. To check the assumption that the mean flow is time independent, transient simulations were carried out and the results were compared with the steady state simulations. The turbulence models used are the standard  $k-\epsilon$  turbulence and the RST model. In the transient simulation, the time step was set to be adaptive in which the size of the time step is selected based on the estimation of the truncation error associated with the time

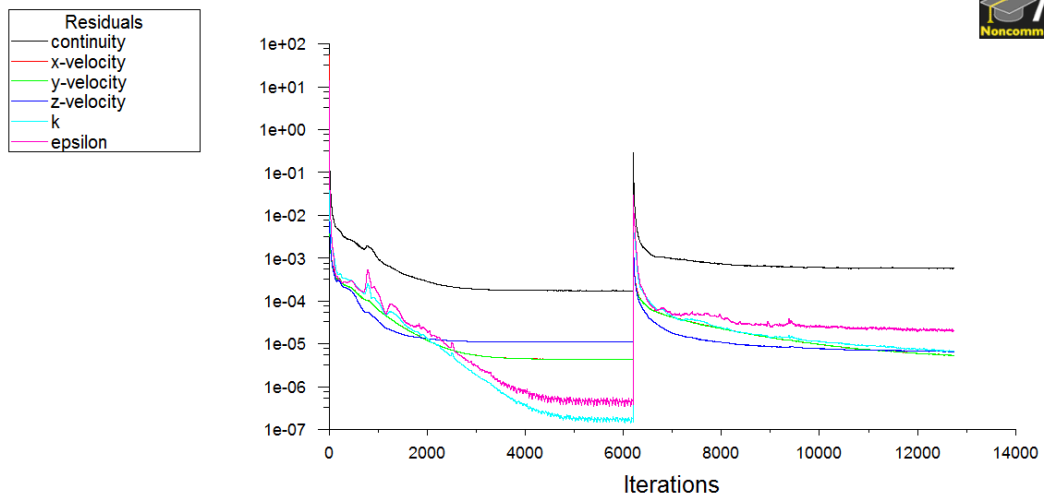
integration scheme (Fluent, 2009). The average residence time of the fluid in the spray tower (volume of the geometry/volumetric flow of air) is 13.5 s. The transient simulations were run for about 20 s of the flow time to ensure that it has reached a stable condition.

For the steady and transient simulations using the standard  $k$ - $\varepsilon$  turbulence model, the under-relaxation factors are specified in Table 6.1. For the RST model, the under-relaxation factors used are listed in Table 6.4. The LRR model (Launder *et al.*, 1975) is used for the pressure strain term. The convergence criteria for the simulations with both turbulence models are specified as  $1 \times 10^{-4}$  for the continuity, momentum and turbulence model equations. The SOU discretisation scheme is selected for both models. The boundary conditions used are specified in Section 6.1.2.

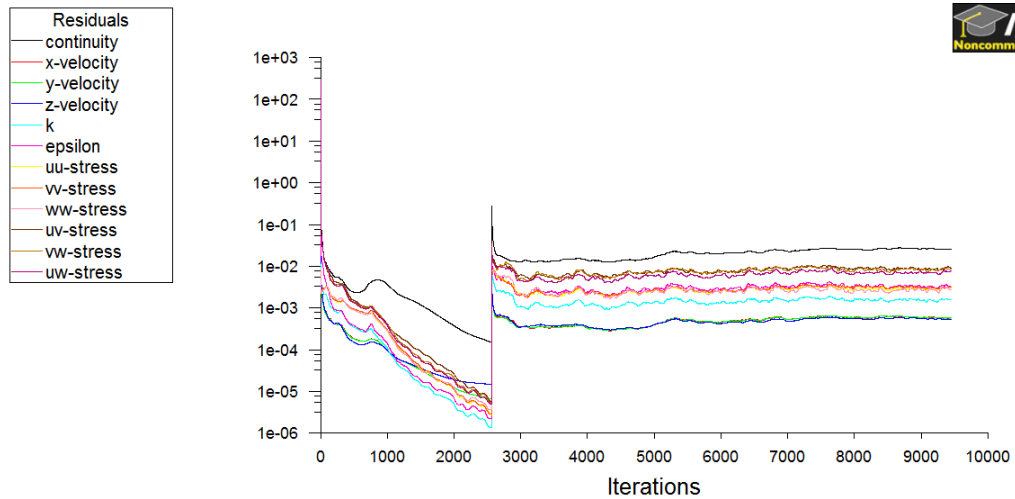
Table – 6.4: Under relaxation factors used with the RST turbulence model

Pressure	Momentum	$k$	$\varepsilon$	$\mu_t$	$\overline{u_i u_j}$
0.3	0.7	0.8	0.8	0.5	0.5

The simulations were initialised using the converged results obtained from the FOU scheme steady solution. For the steady state simulation using the standard  $k$ - $\varepsilon$  turbulence and the RST model the residuals did not converge to the required tolerance limits. The residuals of continuity in both models reached a constant value after certain number of iterations. The simulations were considered to be a converged solution at that point. Figure 6.7 is a plot of residuals for the steady state simulations for both the standard  $k$ - $\varepsilon$  turbulence and the RST model.



(a)



(b)

Figure – 6.7: Convergence residuals for steady state solution. (a) Standard  $k-\epsilon$  turbulence model; (b) RST model.

A comparison of the mean axial velocity profiles for the steady state and transient simulations computed using the standard  $k-\epsilon$  turbulence model is given in Figure 6.8. The mean axial velocity profiles are averaged over a period of the last 2.5 seconds in the transient simulation case. It is observed that both the steady and transient simulations show similar velocity profiles both qualitatively and quantitatively. Hence the mean axial velocity in the spray tower is steady.

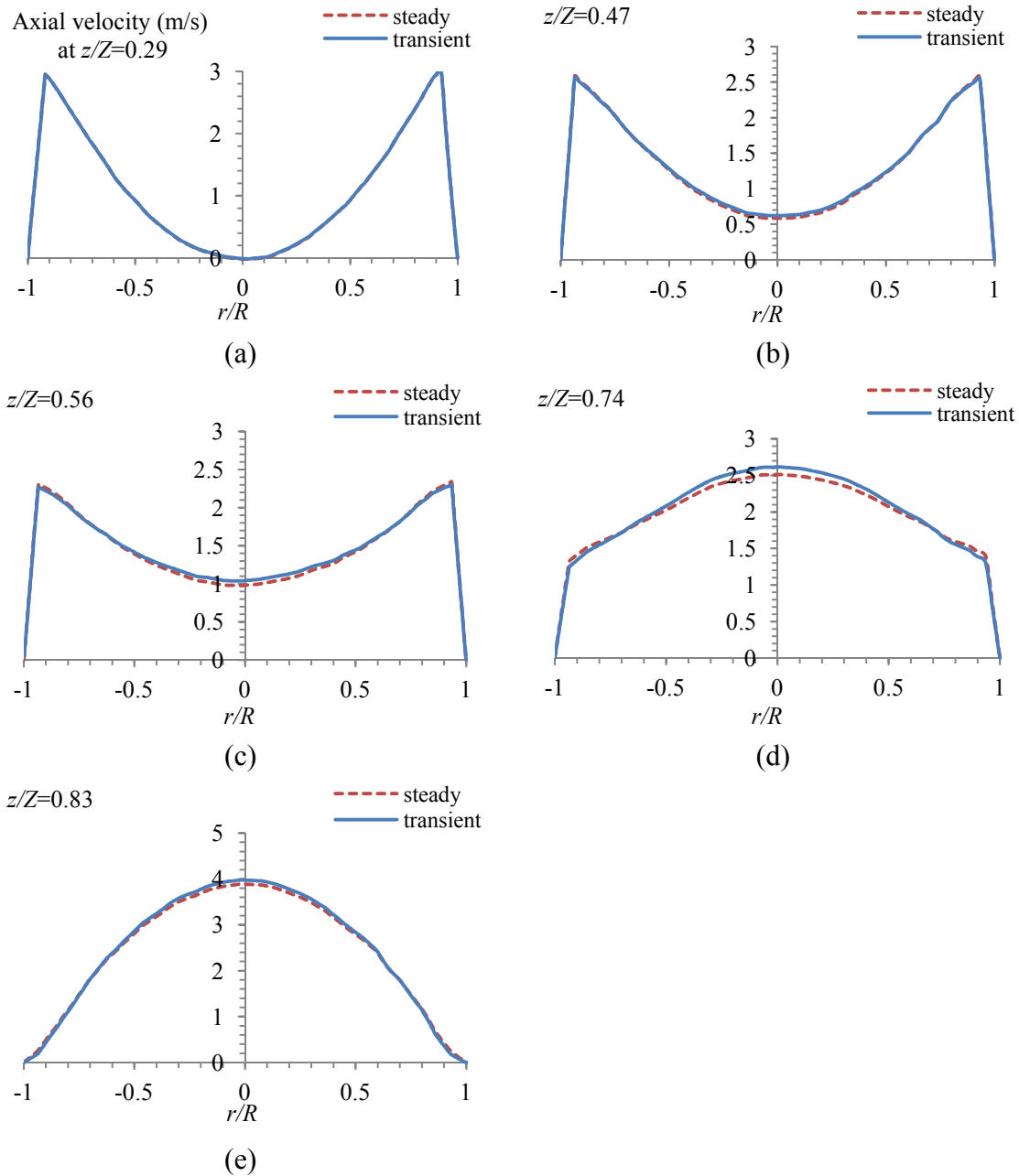


Figure – 6.8: Steady v/s transient simulation axial velocity comparison using standard  $k-\epsilon$  model.

A comparison of the mean tangential velocity profiles using the standard  $k-\epsilon$  model is given in Figure 6.9. The tangential velocity profiles computed using the steady and transient simulations also look similar both qualitatively and quantitatively at all the axial locations.

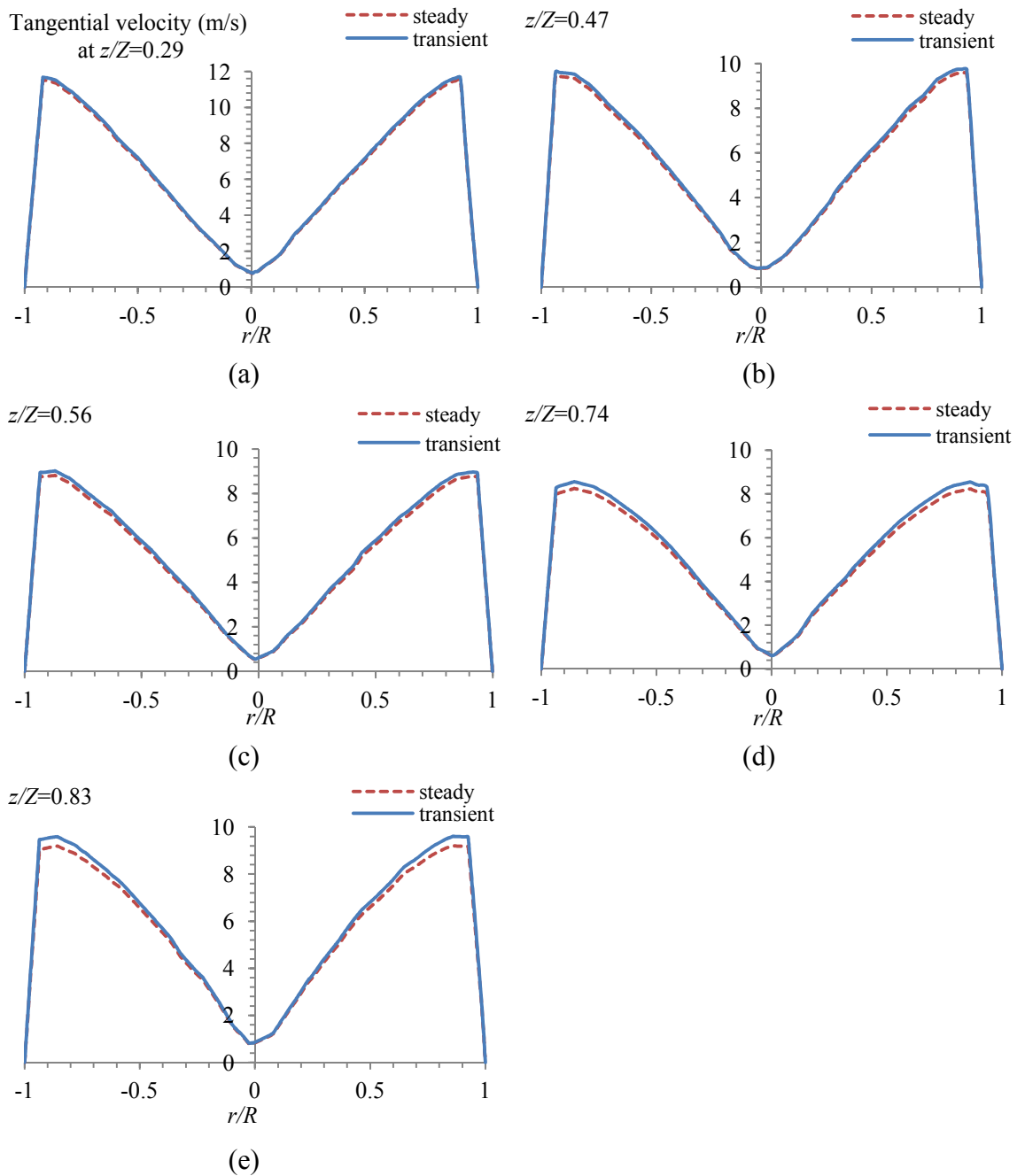


Figure – 6.9: Tangential velocity comparison for steady v/s transient case using standard  $k-\epsilon$  model.

A comparison of the steady state axial velocity with the time averaged axial velocity from the transient simulation carried out using the RST turbulence model is given in Figure 6.10. The average is taken over a period of the last 2.5 seconds of simulation. It is observed that the average profiles of the transient simulation match very well with the steady state simulation results at all the axial locations, which indicates that the flow profiles in the spray tower are not time dependent.

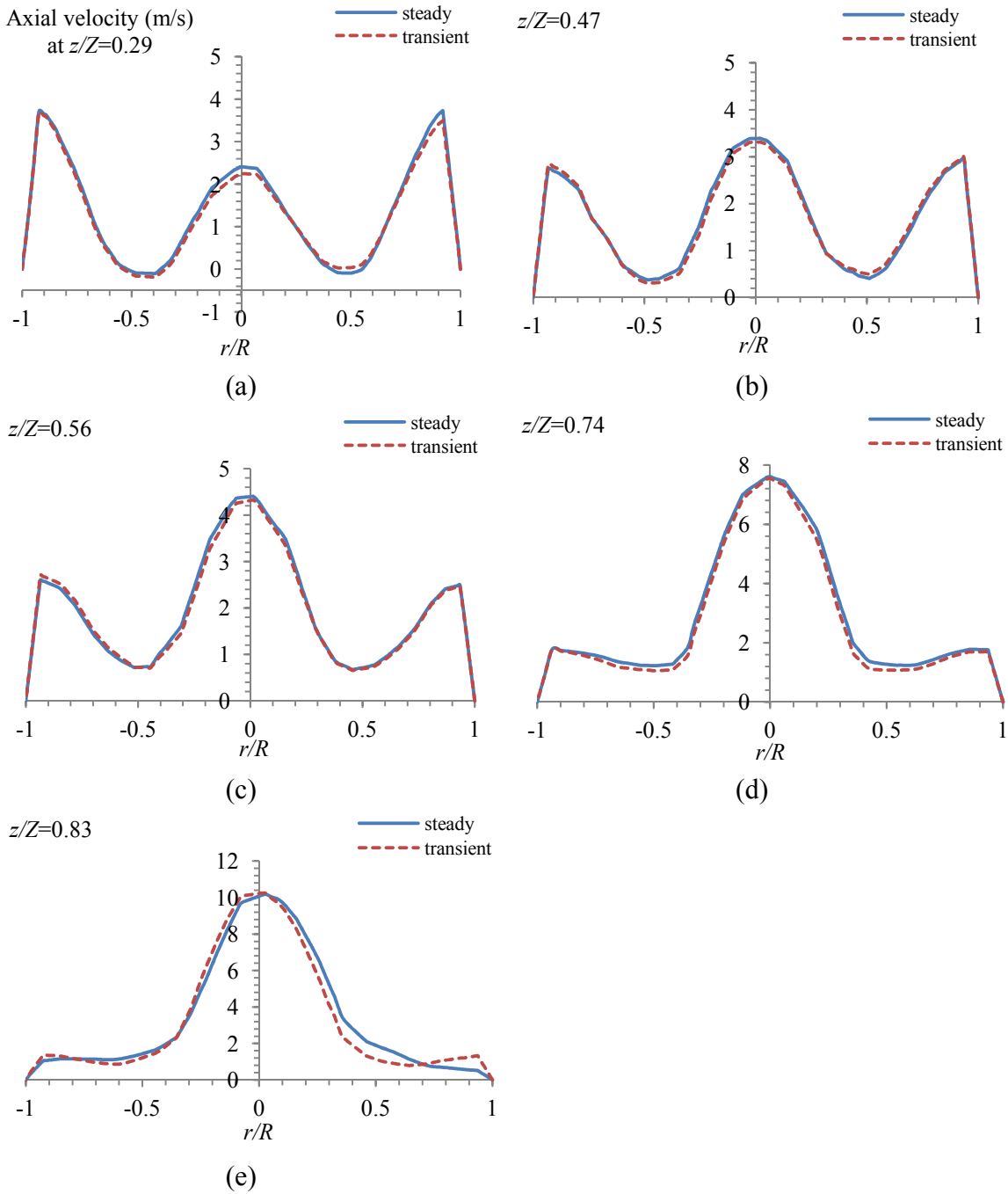


Figure – 6.10: Steady v/s transient simulation axial velocity comparison using the RST model.

A comparison of the tangential velocity profiles computed using the steady and transient simulations using the RST model is given in Figure 6.11. A good comparison between the steady and time-average tangential velocity profiles is observed at all the dimensionless heights. At  $z/Z = 0.83$  (Figure 6.11 (e)), a slight asymmetry is observed in the tangential velocity profile predicted by the steady state RST model but the difference is not significantly large. Hence the mean tangential component of velocity is also time independent.

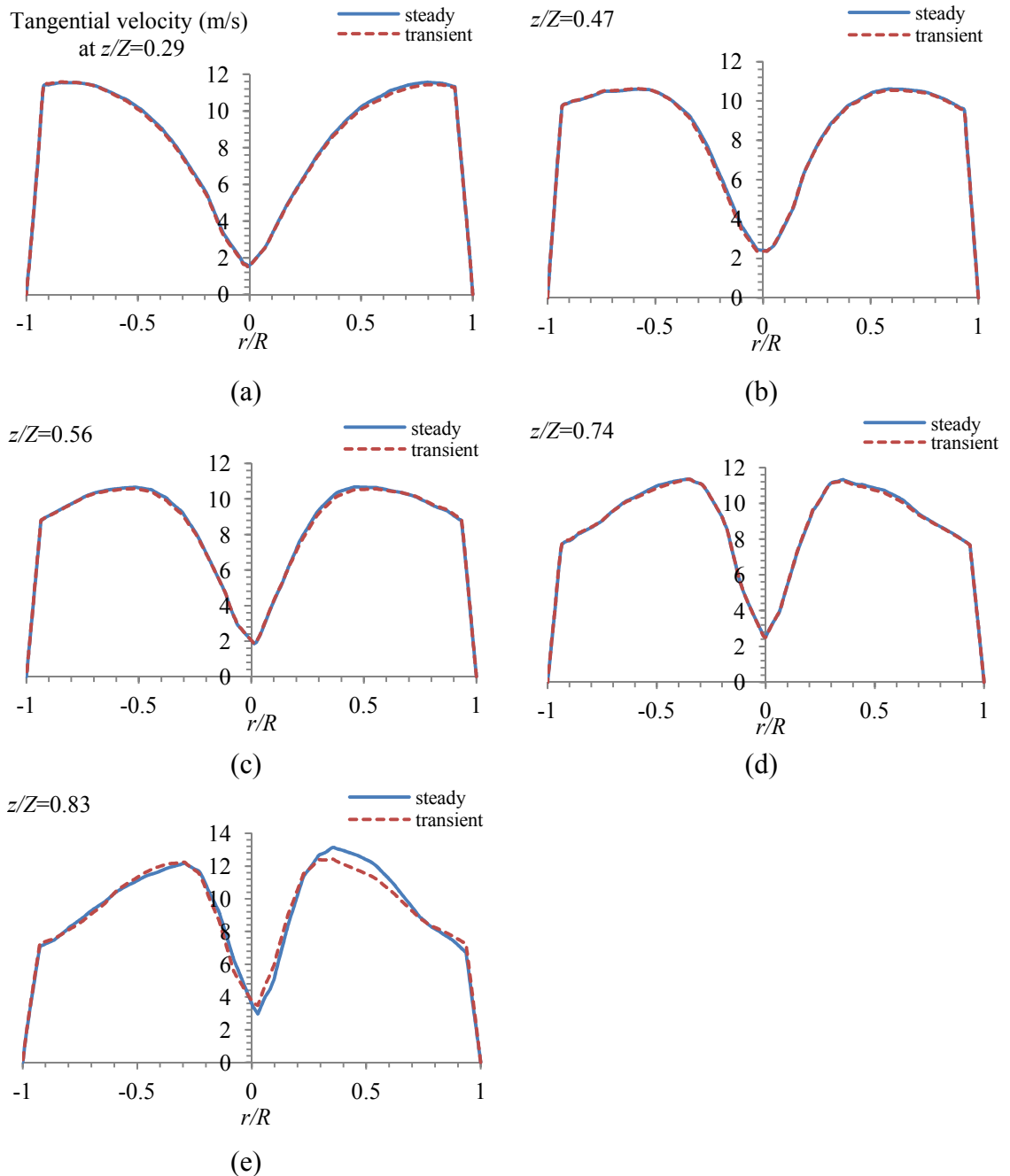


Figure – 6.11: Tangential velocity comparison for steady v/s transient case using RST model.

A comparison between the steady state and the transient simulation results show that the difference between the two are negligible, this confirms the findings of previous studies (Sharma, 1990; Harvie *et al.*, 2001; Wawrzyniak *et al.*, 2012a) that the flow patterns in the spray tower are stable at horizontal and radial angles of the air inlet nozzles in the range of  $20^\circ$  and  $30^\circ$ . A good agreement between the steady and transient simulation cases also confirms that the level of residuals taken as converged solution is sufficient for this study. The time required for running a transient simulation is typically 1 week, while the time required for running a steady state simulation is about 12 hours. Hence

the simulation can be run with the steady state approximation. The details of the differences observed in the predicted axial and tangential velocity profiles computed using the  $k-\varepsilon$  turbulence model and the RST model is given in the next section.

### **6.1.6 Selection of Turbulence Model**

To check the dependency of results on the turbulence models, the steady state results of the RST turbulence model are compared with the steady state results of the standard  $k-\varepsilon$ , RNG  $k-\varepsilon$  model, Realizable  $k-\varepsilon$  model and SST model. In the RST model, the linear pressure strain (LRR) model (Launder *et al.*, 1975) is used, which is defined in Section 3.10.5. The boundary conditions used are specified in Section 6.1.2. In each of the turbulence model, the SOU discretisation scheme is used. The simulations are started using the FOU discretisation scheme solution to avoid divergence, which was later changed to the SOU scheme. The mesh used for the comparison of turbulence models is Mesh 1. The convergence criteria, under-relaxation factors and the numerical method are kept the same as in the previous simulation cases. In all the simulations, the wall is assumed to be smooth. The simulation results are also compared with the experimental data taken by Francia (2011), the details about velocity measurements is given in Section 4.6.1.

A comparison of the mean axial velocity profiles computed using different turbulence models as well as with the experimental data (Francia, 2011) in the cylindrical section of the tower is given in Figure 6.12. It is observed that only the RST and the Realizable  $k-\varepsilon$  models are able to predict qualitatively the shape of the measured axial velocity profiles including a sharp rise in the velocity at the centreline. The rest of the turbulence models (based on eddy-viscosity concept) fail to correctly reproduce the measured velocity profiles at all measurement locations. The velocity profiles predicted by these models are nearly flat in the central region of the tower. However, the RST turbulence model overpredicts the axial velocity in the centreline while the Realizable  $k-\varepsilon$  gives underpredicts velocity at almost all axial locations. Measured negative velocities can be seen in the annular region of the tower in the bottom cylindrical section (at  $z/Z = 0.29$  and  $0.47$ ), which both the RST and the Realizable  $k-\varepsilon$  fail to correctly reproduce. In the top region of the tower (at  $z/Z = 0.74$  and  $0.83$ ), Figure 6.12 (d) and (e), the RST model gives a better qualitative agreement with measurements although the magnitude of velocity is overpredicted in the centreline. It can be concluded that the RST turbulence

model gives an overall best agreement in predicting the axial velocity profiles compared to the eddy-viscosity based turbulence models.

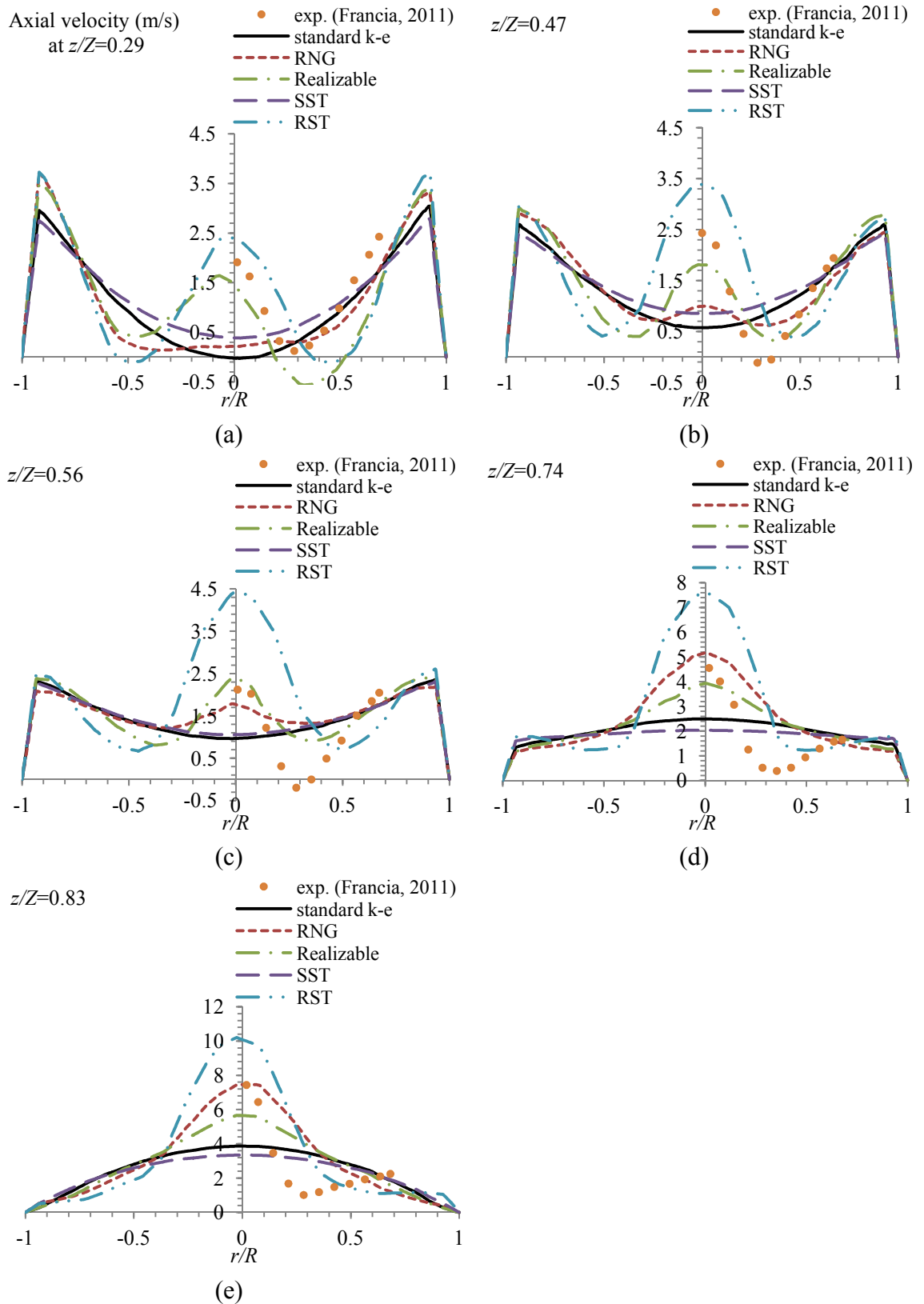


Figure – 6.12: Comparison of axial velocity profiles using different turbulence models and with experimental data by Francia (2011).

Figure 6.13 is a plot of mean tangential velocity profiles computed using different turbulence models and a comparison with experimental data at various measurement locations in the cylindrical region of the tower.

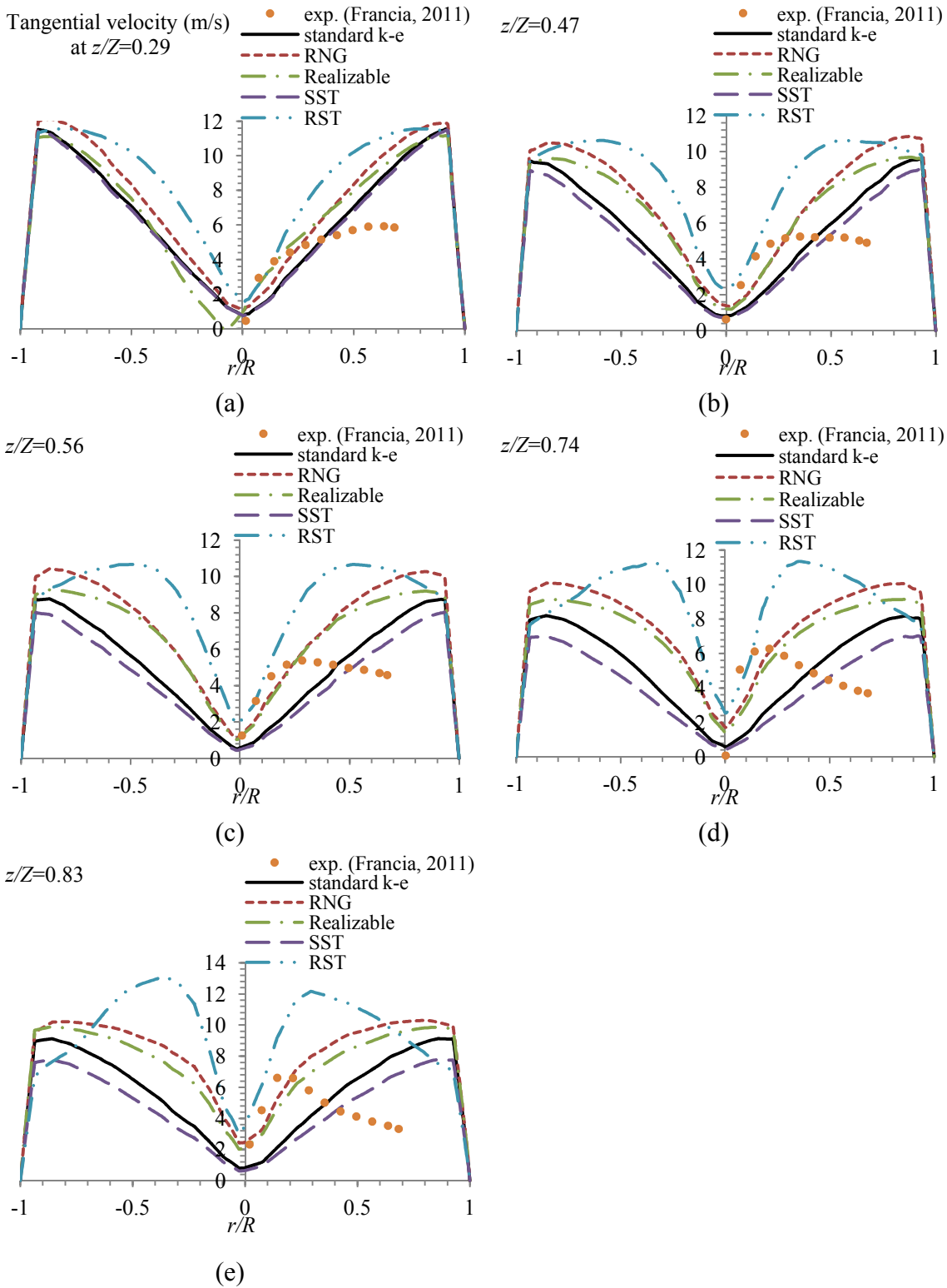


Figure – 6.13: Comparison of tangential velocity profiles computed using different turbulence models with experimental data by Francia (2011).

From the experimental data (Francia, 2011) in Figure 6.13, it is observed that the forced vortex transforms into a Rankine vortex after the first measurement location at  $z/Z = 0.29$ . This trend is only correctly predicted by the RST turbulence model. All other models predict a forced vortex profile at all measurement locations, including the Realizable  $k-\varepsilon$  model although this model gives a good qualitative comparison with the measured axial velocities at most of the tower height (Figure 6.12). The magnitude of the mean tangential velocity profiles predicted by all the turbulence models is about two times greater than the measured velocity magnitude. This could be explained by the fact that the tower wall contains highly uneven deposit layer of detergent powder. The presence of deposits on the wall will cause roughness at the surface which reduces the tangential momentum and hence the swirl intensity. As mentioned above, these simulations are carried out with smooth wall assumption; hence the predicted tangential velocity component is significantly higher than measurements. The effect of surface roughness is studied in Section 6.1.8.

A comparison of velocity profiles predicted by different turbulence models with experimentally measured mean axial and tangential velocity profiles show that only the RST turbulence model is able to predict correct qualitative behaviour, although the magnitude differ significantly for the tangential velocity profiles. The eddy-viscosity based turbulence models fail to correctly reproduce the measured velocity profiles. Hence the RST model has been selected for further investigation of air flow patterns in the spray drying tower.

### **6.1.7 Results and Discussion of the RST Model**

In Section 6.1.6, it is found that the RST model gives an overall better qualitative agreement. Hence in this section the results of the RST model are further discussed. Figure 6.14 is a plot of cross-sectional view of the contours of the magnitude of mean velocity components obtained from the RST model. The air entry nozzles are located at a dimensionless height of 0.13. The magnitude of mean velocity components is high in the annular region of the tower, both in the conical region as well as in the cylindrical region of the tower. A low velocity magnitude persists in the central region of the tower up to a dimensionless height ( $z/Z$ ) of 0.81. The radius of low velocity region becomes smaller as the air moves upwards in the cylindrical region. Above  $z/Z=0.81$ , the velocity in the centreline region starts to increase as the air passes through a narrow tube (vortex breaker) and eventually goes to the exhaust gas duct.

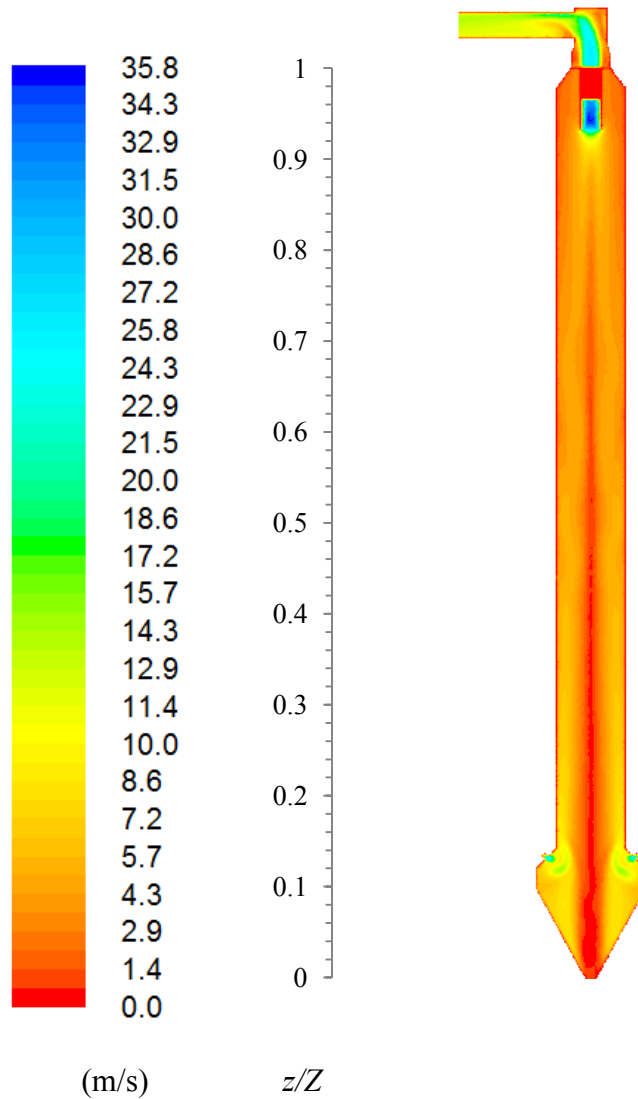


Figure – 6.14: Contours of magnitude of mean velocity components.

Figure 6.15 is a plot of path lines of air velocity magnitude coloured by the mean tangential velocity component (m/s) in the bottom conical section of the tower. It is observed that a low tangential velocity in the downward direction exists near the cone wall, while a high tangential velocity in the annular region and a low velocity in the central region of the tower exist. The flow reversal occurs near the bottom exit of the tower. This type of flow also exists in cyclone separators.

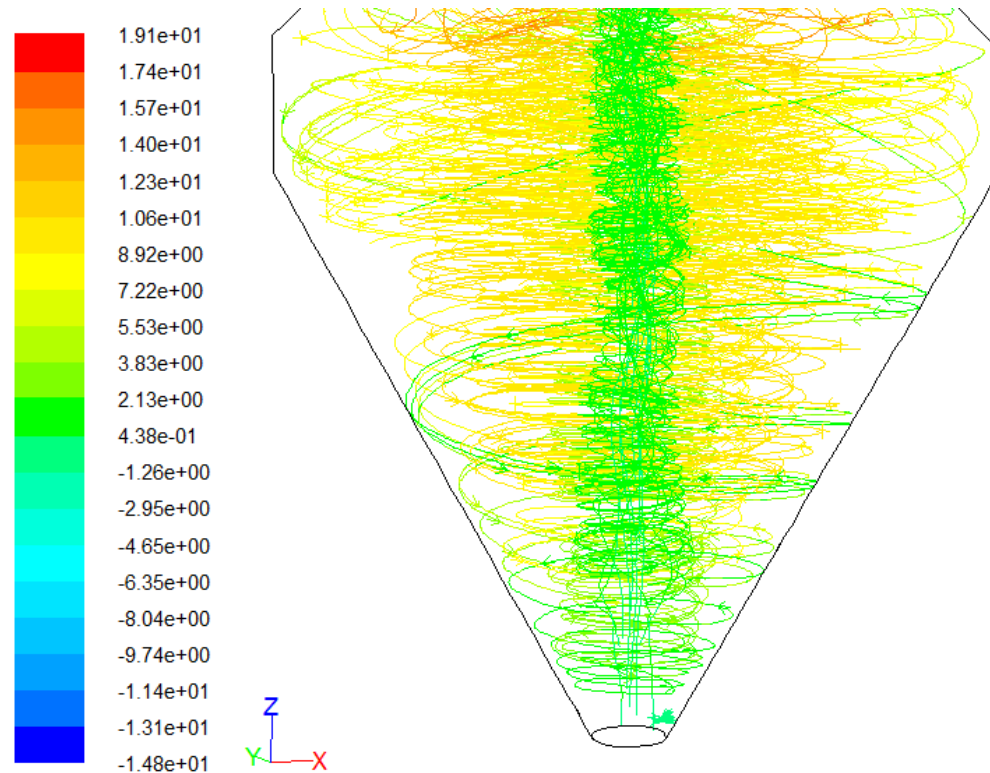


Figure – 6.15: Path lines of air velocity coloured by tangential velocity component (m/s) in the bottom conical region.

Figure 6.16 is a contour plot of the turbulent intensity defined as (Fluent, 2009):

$$I_t = \frac{\sqrt{\frac{1}{3}(\overline{u_i'^2} + \overline{u_j'^2} + \overline{u_k'^2})}}{\overline{U}} \times 100\% \quad (6.2)$$

It is observed that the turbulent intensity inside the tower is a maximum near the air inlet nozzles and at the bottom outlet. In the cylindrical region of the tower above the air inlet nozzle, the turbulent intensity is a maximum in the centreline and it decays along the height of the tower due to the decay in swirl as given in Figure 6.24. The flow becomes relatively more homogenous in the top cylindrical region ( $z/Z=0.7-0.8$ ) of the tower as the turbulence intensity becomes fairly uniform over the radius. The turbulence intensity is below 100% in the cylindrical region of the tower.

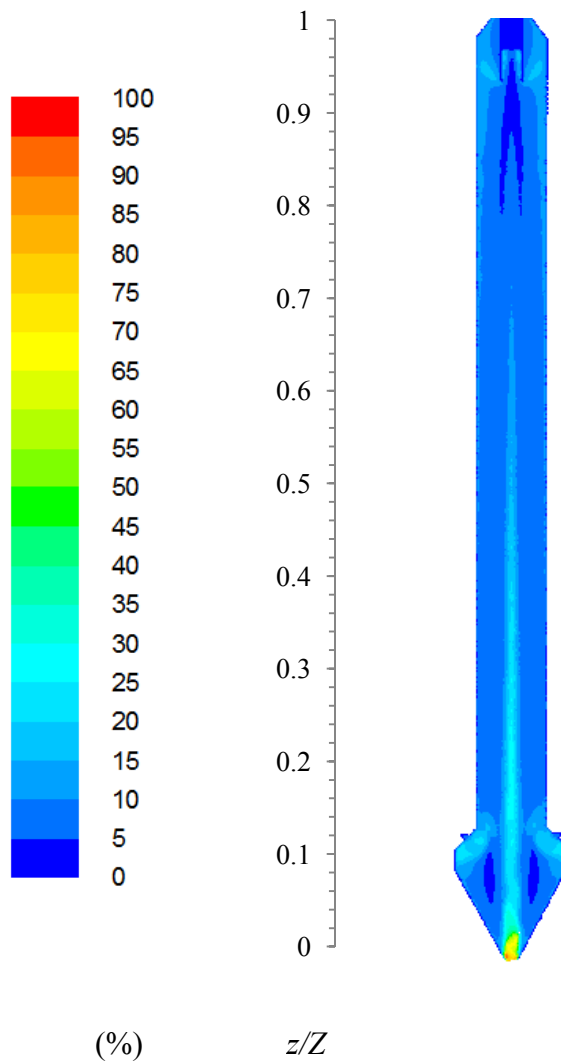


Figure – 6.16: Contour plot of turbulent intensity.

Figure 6.17 is a plot of the magnitude of the mean velocity components at different dimensionless heights over the cross-section of the tower cylindrical region, and at different times (taken at time intervals of 0.12s) obtained using the transient simulation using the RST model. From the plot it is observed that the predicted air flow is symmetrical throughout the tower height and the flow is not changing with time. The low velocity magnitude coincides with the centre of the tower at all reported times, indicating that vortex precision is not present in the predicted air flow.

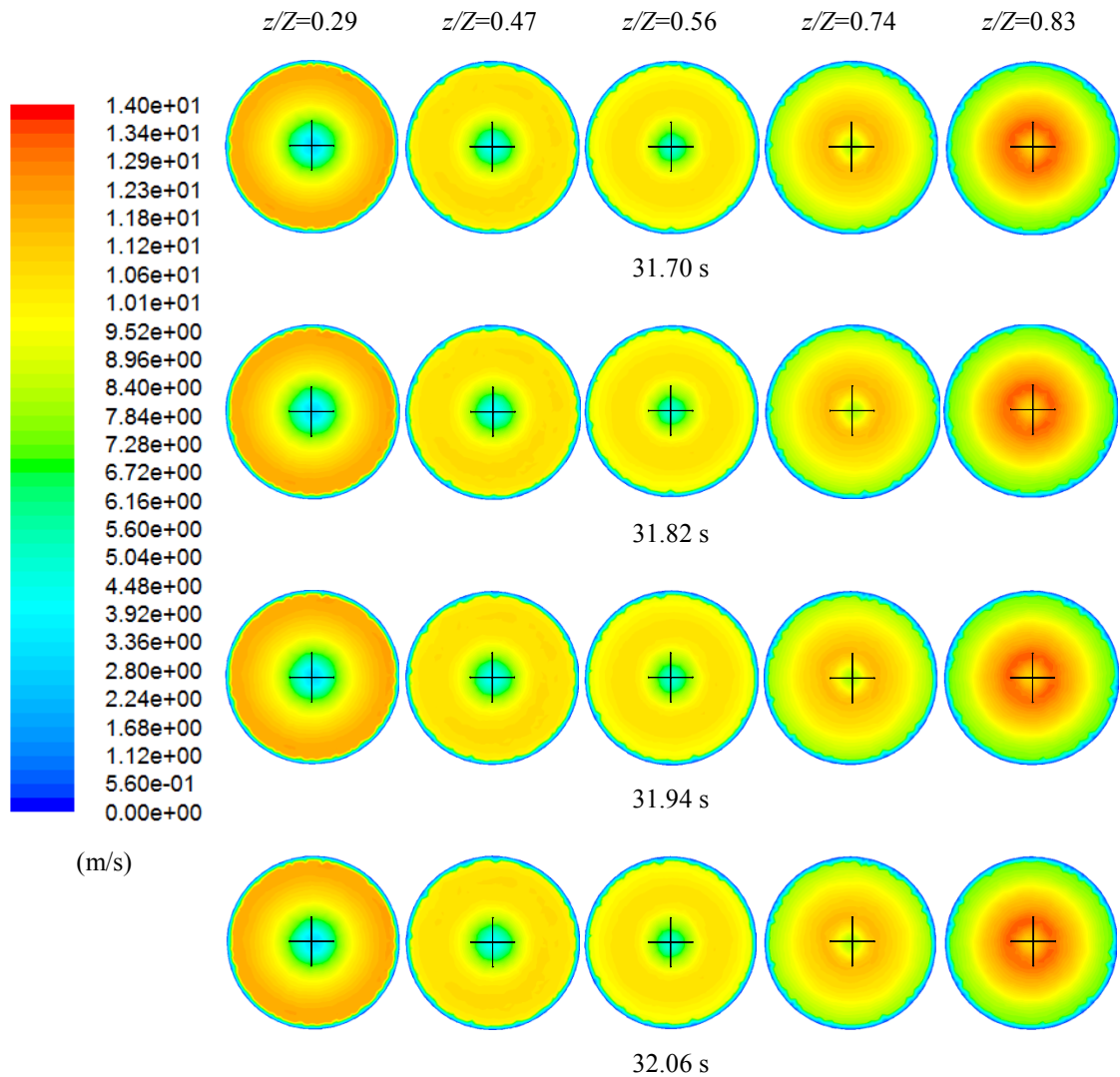


Figure – 6.17: Cross-sectional view of mean velocity magnitude contours at various dimensionless heights and at different times.

### 6.1.8 Effect of Surface Roughness

To include the effect of roughness produced on the tower wall surface due to the presence of deposits, a uniform roughness height is specified through the tower height (varying from 2 mm to 5 mm) and a roughness constant of  $C_s = 1.0$  is used. These are incorporated in the log-law of the wall for rough surfaces (equation (3.47)). The rest of the boundary conditions and numerical method are kept the same as specified in Sections 6.1.1 and 6.1.2. The modelling of pressure strain term is carried out using LRR model defined in Section 3.10.5.

Figure 6.18 is a plot of mean tangential velocity profiles at different dimensionless height. The y-velocity profiles obtained from Fluent were converted to tangential

velocity profiles using coordinate transformation. A comparison is made between the measured data by Francia (2011) and predicted values obtained from the LRR-RST model with clean wall ( $k_s = 0$  mm) and rough wall considering  $k_s = 2$  mm and 5 mm. It is observed that there is a significant improvement in the predicted mean tangential velocity profiles after including the effect of surface roughness in the simulation compared to the predictions of the clean surface in which the predicted mean tangential velocities were about two times greater than the measurements. From a comparison of predicted tangential velocity profiles obtained from all three simulation cases, it is observed that the magnitude of tangential velocity profile decreases with increasing roughness height at all measurement locations but qualitatively, all three cases give similar tangential velocity profiles. Hence the decay in the angular momentum of the air flow is greater with a higher value of roughness height. The case with a roughness height of 2 mm gives the closest prediction to the measured data while the case with clean wall assumption ( $k_s = 0$  mm) overpredicts the tangential velocity magnitude and a 5 mm roughness height assumption gives underprediction particularly in the magnitude of forced vortex at all measurement locations.

Figure 6.19 is a plot of mean axial velocity profiles at different dimensionless heights obtained using smooth and rough wall assumptions. It is observed that the wall roughness height influences the axial velocity profiles at all measured locations. The smooth wall predicts a greater velocity in the centreline compared to the simulation cases with rough wall assumption. Additionally, the axial velocity profile predicted using the smooth wall assumption shows negative axial velocity (recirculation zone) only at  $z/Z = 0.29$  (Figure 6.19 (a)). The radial location of the negative velocity is also not well predicted by the smooth wall assumption. The axial velocity profile predicted using 2 mm roughness height gives an overall better agreement in predicting the centreline velocity and the radial location of the recirculation zone at all measurement locations. The case with 5 mm roughness height gives an underprediction in the axial velocity at the centreline at all measurement locations.

The CFD simulation case with 2 mm roughness height gives the best agreement with the measured axial and tangential velocity profiles hence a roughness height of 2 mm is selected for further investigation.

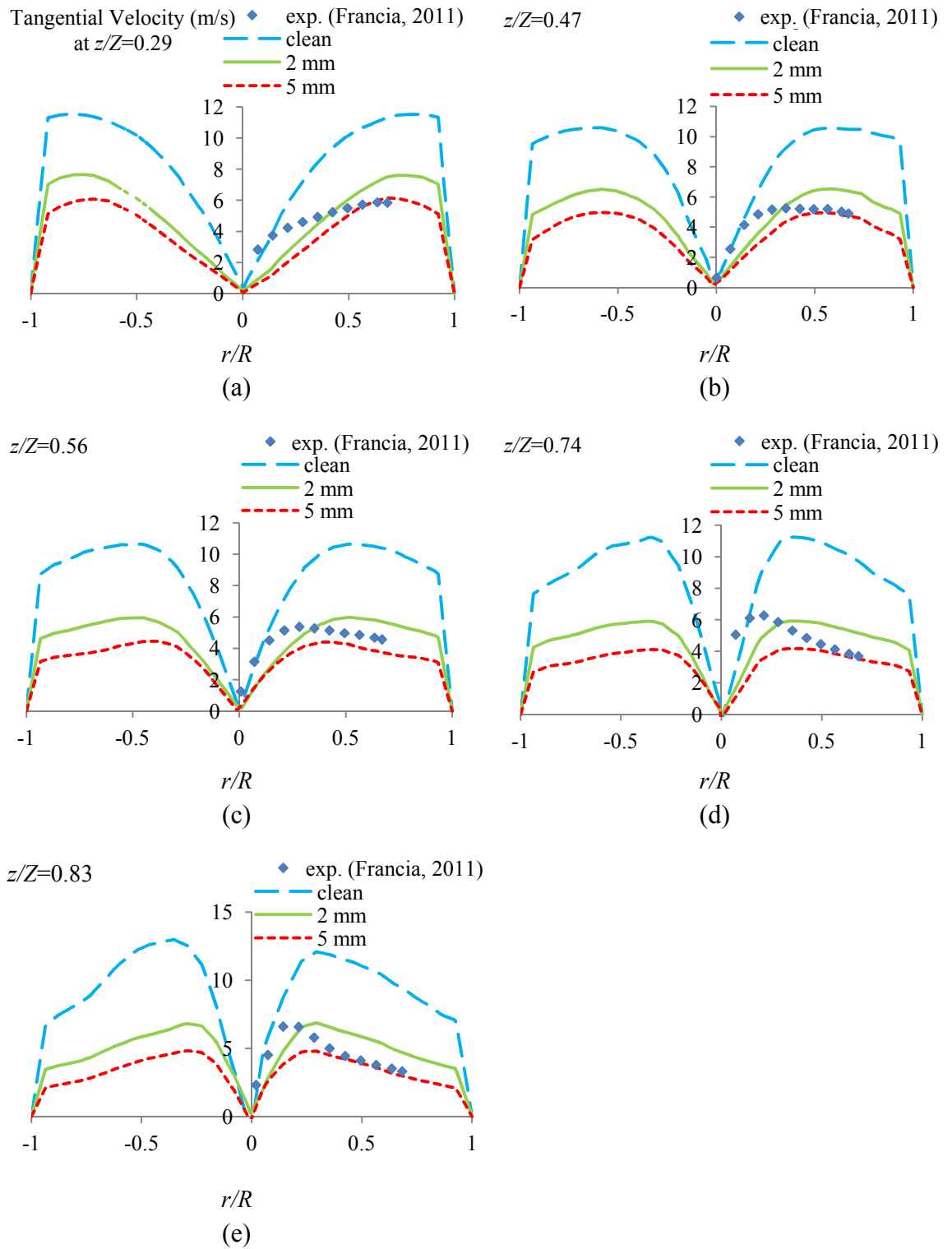


Figure – 6.18: Tangential velocity profiles predicted using smooth and rough wall assumption and a comparison with experimental data by Francia (2011).

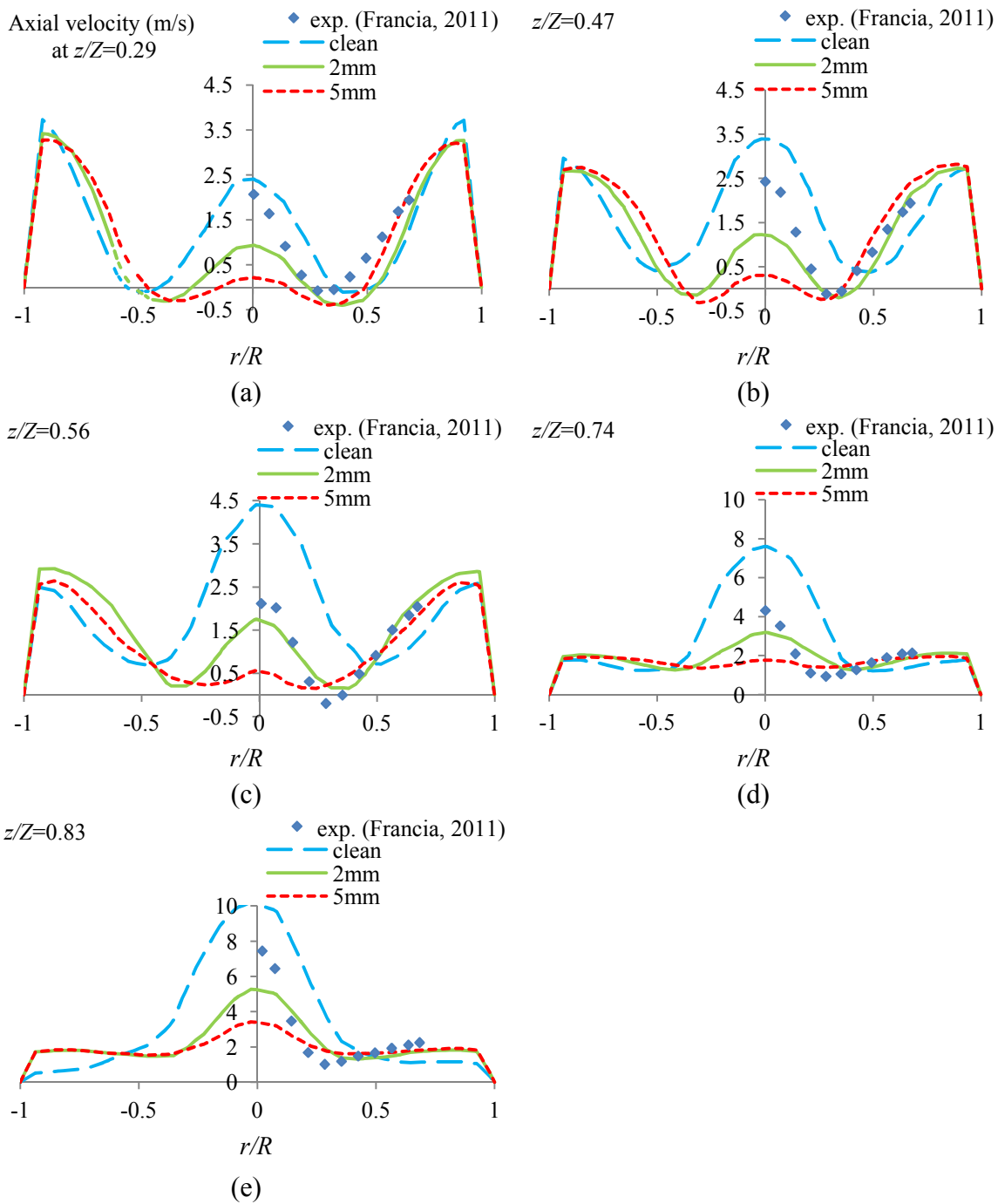


Figure – 6.19: Axial velocity profiles predicted using smooth and rough wall assumption and a comparison with experimental data by Francia (2011).

### 6.1.9 Effect of Pressure Strain Term in the RST Model Prediction and a Discussion of Final Results

As stated earlier in Section 3.10.5, the predictability of the RST model depends largely on the modelling of the pressure strain term. The simulations were carried out with two models of the pressure strain term, the LRR and the SSG models (see Section 3.10.5). For the RST model with the SSG pressure strain model, the steady state simulation diverged after a few iterations, so the simulation with this model was carried out using a

transient approach. The time step was set to be adaptive. The simulation was run for about 26 s, which is about twice the average residence time of the fluid in the tower. Figure 6.20 is a plot of the predicted mean axial velocity profiles along with experimental data at various axial locations in the cylindrical section of the spray tower.

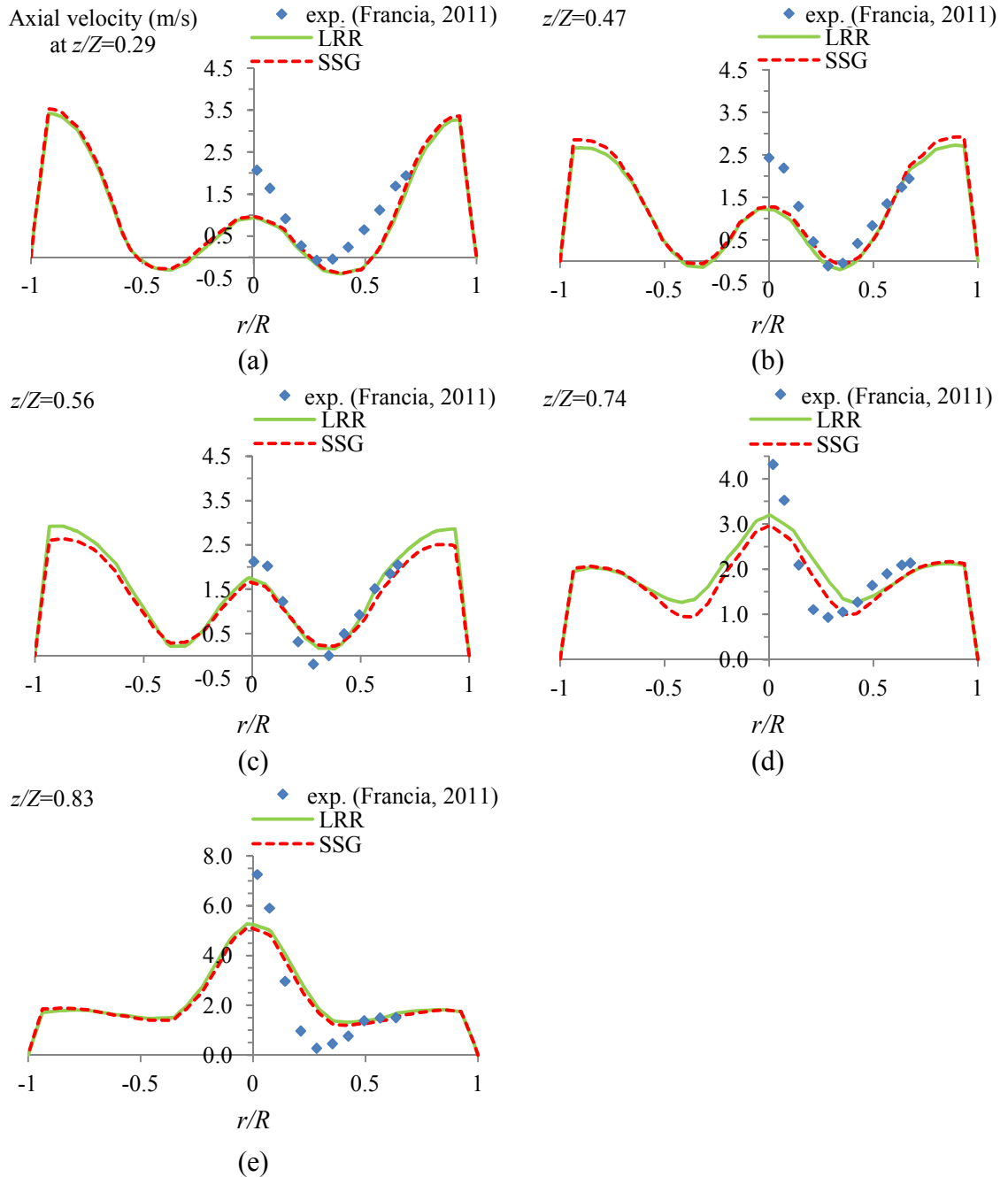


Figure – 6.20: Axial velocity profiles computed using LRR and SSG pressure strain models and a comparison with experimental data by Francia (2011).

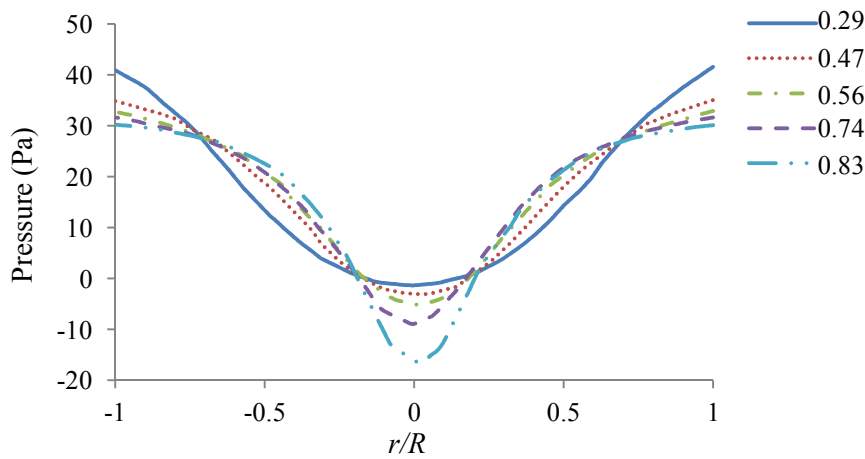


Figure – 6.21: Predicted pressure variation along the dimensionless radius at various dimensionless heights using the LRR-RST model.

From the plot of axial velocity profiles (Figure 6.20), it is observed that both the LRR and SSG pressure strain models used in the RST model give very similar prediction at all measurement locations. Both predict a peak velocity in the central region and a low velocity in the annular region at all measurement locations, which are validated using the measured data. A reverse flow is observed in the measured data in the annular region (at  $0.3 < r/R < 0.4$ ) of the tower in Figure 6.20 (a), (b) and (c). This is due to high tangential velocities in these regions, as depicted in Figure 6.22, which cause adverse pressure gradient (in the flow direction) in the annular region, resulting in the flow reversal. Figure 6.20 is a plot of the variation of pressure along the radius at these measurement locations predicted using the LRR-RST model. A low pressure zone exists in the centre of the tower, while a higher pressure near the wall. In the annular region, the pressure increases along the height which is responsible for the reverse flow.

One of the earliest observations of the reverse axial flow in highly swirling flows was reported by Nuttall (1953). Yajnik and Subbaiah (1973) carried out experimental investigation into confined swirling flows and observed a tendency of reversed axial flow in the annular region with increasing swirl number ( $\Omega$ ) from 0 to 0.15. Hence the flow in this region can be classified as highly swirling flow. The reverse flow can lead to an enhanced mixing of air and a smaller temperature gradient of air along the tower height in spray drying operations. This can result in an improved efficiency of the tower. Both models predict reverse flow at  $z/Z = 0.29$  ( $\Omega \approx 1.7$ ) and  $0.47$  ( $\Omega \approx 1.5$ ) as observed in Figure 6.20 (a) and (b). The length of this reverse flow zone is slightly underpredicted by both models since the measured data show negative axial velocities at  $z/Z = 0.56$  in Figure 6.20 (c) but the models predict positive velocity in the annular

region at this axial location. The flow becomes positive in the annular region in Figure 6.20 (d) and (e) due to the reduction of swirl velocity as the air goes up. An overall good agreement can be seen with the measured data at all measurement locations in the annular region. The predicted axial velocity profiles are axisymmetric at all measurement locations. The measured axial velocity at the axis of the tower starts to increase as the air flows upwards, due to the presence of a vortex finder at the top of the tower; hence more fluid has to pass through the central core region to satisfy the mass conservation. Both the LRR and SSG models predict this sharp rise in the axial velocity at the tower axis. Similar simulation results for the axial velocity profiles using a VLES approach have been reported by Harvie *et al.* (2001) at the top region for a laboratory-scale counter-current spray tower. As depicted in Figure 6.20, the peak velocity in the central region of the tower is underpredicted by both pressure strain models at all measurement locations, this could be due to the shortcomings of the RST model including isotropic eddy-viscosity assumption for turbulence dissipation rate and the modelling of pressure strain terms. However, an overall fair agreement with the measured data can be seen at all measurement locations despite the complexity of the flow.

The simulation results show the existence of a high axial velocity near the walls which is desirable because this results in an increased residence time of the particles going downwards and hence a more efficient drying operation. The quality of the predicted velocity profiles close to the wall could not be ascertained because of the lack of data due to inaccessibility of the sonic velocity anemometer probe near the wall. It should be noted that the experimental data (Francia, 2011) includes measurement errors related to the accuracy of the sonic velocity anemometer (1% RMS in speed and 1° in direction), error due to variation in the mass flow of air throughout the experiment resulting from the variability in the speed of the fan delivering the air to the tower. The errors in measurement of the sonic velocity anemometer position and alignment as well as disruption caused to the air flow due to the presence of anemometer. It should be noted that the sonic anemometer measures the velocity data between the transducer path length, which is not a point measurement, hence any sharp variation in velocity between the transducer cannot be measured, and the measured velocity is an average of the transducer path length.

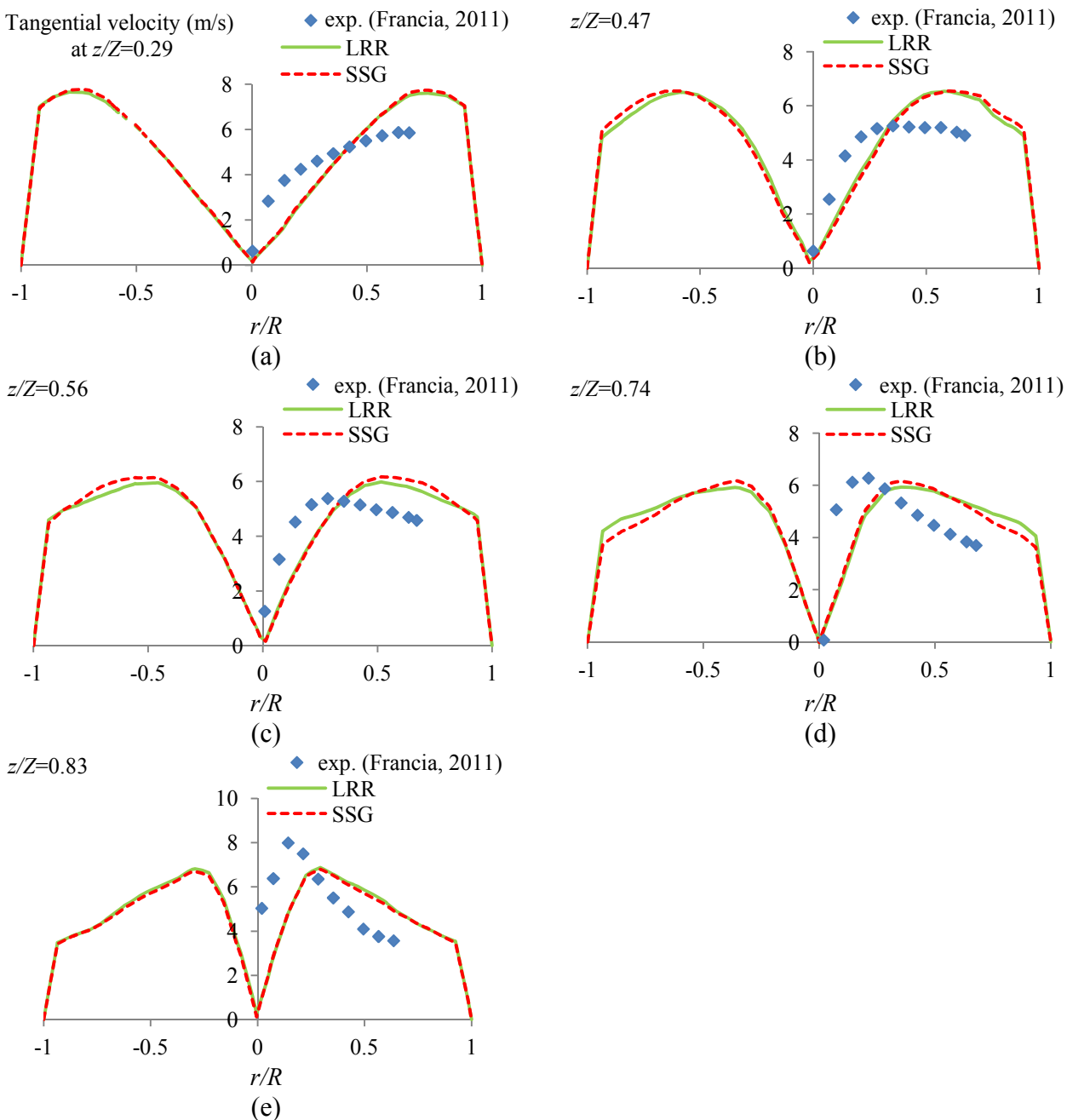


Figure – 6.22: Tangential velocity profiles computed using LRR and SSG pressure strain models and a comparison with experimental data by Francia (2011).

From the plot of mean tangential velocity profiles along the tower dimensionless height in Figure 6.22, it is observed that the forced vortex at the bottom of the tower (Figure 6.22 a) transforms into a combination of free and forced vortex as air goes at the top. Similar measurements and simulation results of the tangential velocity profiles have been reported by Bayly *et al.* (2004) in a laboratory-scale counter-current spray drying tower. The magnitude of the tangential velocity (measured and predicted) in the bottom region of the tower is about twice as large as the axial velocity component. Hence the tangential velocity is the dominant component in the spray tower. The peak velocity in the forced vortex moves towards the tower central axis as the air flows in the upward

direction as a consequence of the decay in swirl due to roughness, therefore the swirl number reduces (Figure 6.24). The prediction of radial location of transformation from the free vortex to the forced vortex by both the LRR and SSG models is similar. The predicted tangential velocity profiles show a fair agreement with the measured tangential velocity magnitude in the core region of the tower in Figure 6.22 c, d and e. However, some discrepancy exists between the predicted and measured radial locations of the free to forced vortex transformation regions. This may be attributed to a high degree of unevenness in the deposits layer (variation in deposit layer thickness) on the tower causing a highly non-uniform surface roughness and a reduction in the cross-sectional area of the tower, which is simplified to a uniform surface roughness with a constant height ( $k_s$ ) in the simulation using equation (3.47).

It is observed in Figures 6.20 and 6.22 that both the mean axial and tangential velocity profiles (measured and predicted) continue to change with the axial distance. Hence a fully developed flow is not achieved in the tower and the swirl flow persists throughout the height of the tower. A high tangential velocity exists in the near wall region which may be useful in reducing the level of deposition on the tower wall (Wawrzyniak *et al.*, 2012a). The swirling flow, in addition to improving heat and mass transfer, also adds centrifugal force to the particles as a result the particles falling down the tower will be more populated near the wall. Hence the wet particles with a tendency to stick may get deposited but the dried particles will cause attrition to the deposited layer. Thus equilibrium will be established between the deposition and re-entrainment of the particles.

Figure 6.23 is a plot of the measured and predicted mean radial velocity profiles at different measurement locations. The predicted radial velocity profiles are asymmetric around the axis in contrast to the axial and tangential velocity profiles which are fairly symmetric. It is observed that the magnitude of the measured radial velocity component is very small at all measurement locations compared to the axial and tangential velocity components. Hence a definite conclusion about the performance of the models in predicting the radial velocity profiles compared to the experimental data cannot be drawn.

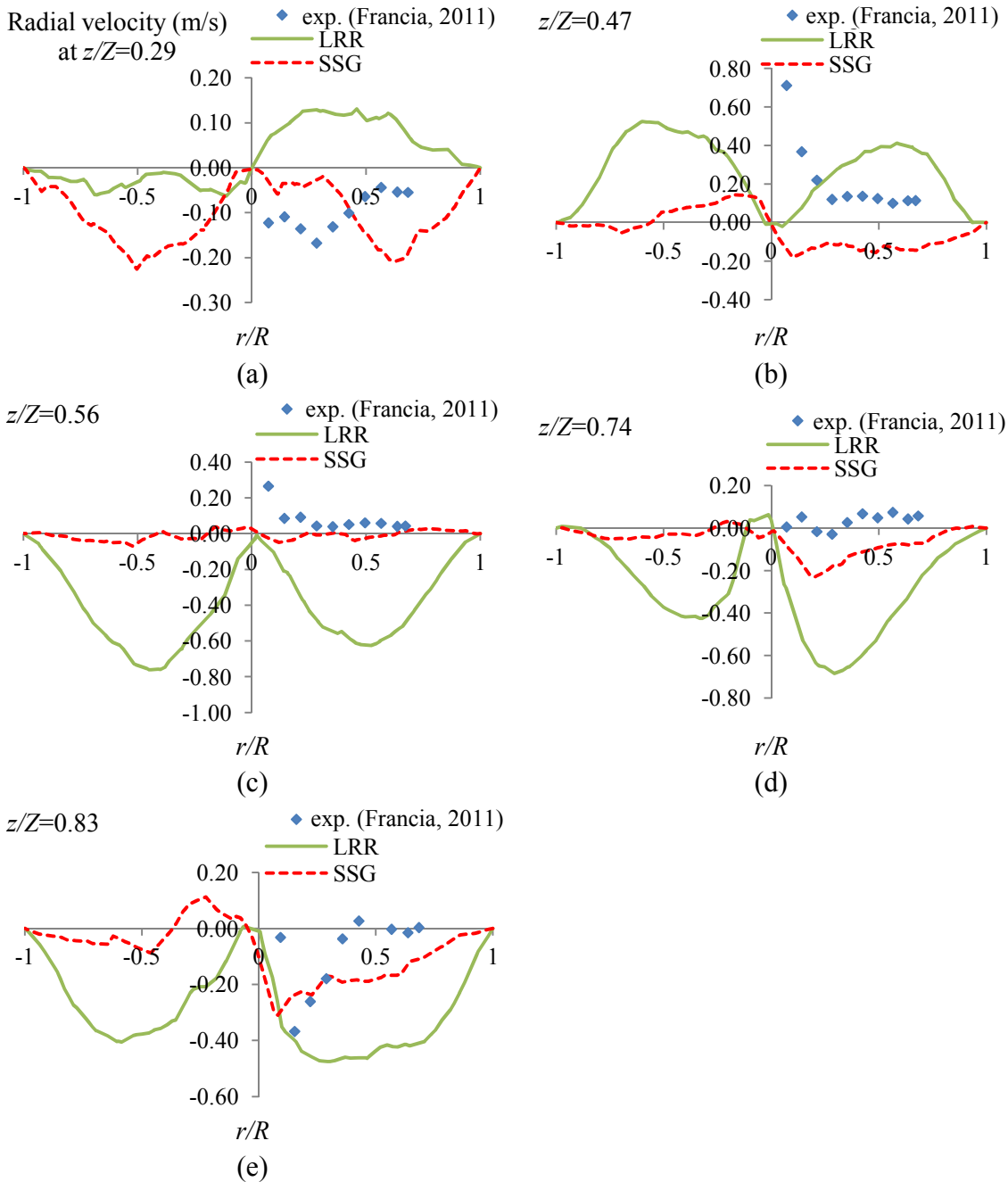


Figure – 6.23: Radial velocity profiles computed using LRR and SSG pressure strain models and a comparison with experimental data by Francia (2011).

Figure 6.24 is a plot of the predicted swirl number calculated from equation (3.73) using the predicted mean axial and tangential velocities as a function of the dimensionless height compared with the swirl number calculated using the measured velocities. It is observed that the swirl decays as the air flows to the top and both the pressure strain models predict a declining trend in the swirl as the air flow to the top; however the rate of decay in swirl intensity is slightly underpredicted by both CFD models (LRR 2mm and SSG 2mm). The initial swirl number in the case of smooth wall (LRR-clean) is about 3.4. A rapid decrease in the swirl number in this case is found after  $z/Z = 0.6$ , this

is due to contraction of the air flow towards the outlet as the air exits through a narrow tube hence more air passes through the central region of the tower and the swirl number may not be valid to represent intensity of swirl in a region very close to the exit. The case with 5 mm roughness height (LRR 5 mm) underpredicts the swirl number compared to the values based on the measured velocity data. In the experimental swirl number, due to the absence of measured axial velocity and tangential velocity components close to the wall, the measured profiles were extrapolated towards the wall, therefore, the swirl number based on experimental data contains errors due to extrapolation of axial and tangential velocity data towards the wall.

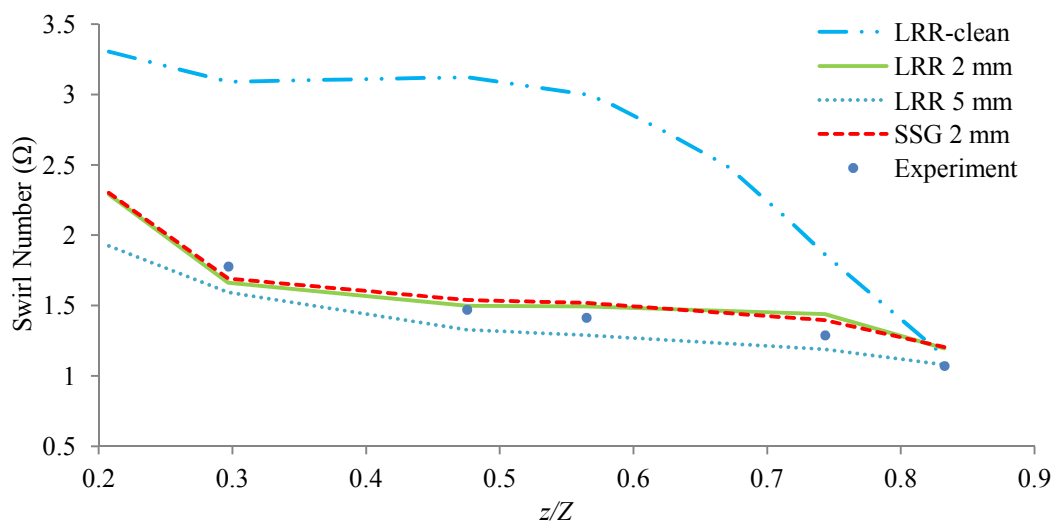


Figure – 6.24: Swirl number as a function of dimensionless height.

Figure 6.25 is a plot of turbulent intensity (%) (defined using equation 6.2) at various dimensionless heights in the cylindrical region of the tower, predicted using LRR-RST and SSG-RST turbulence models ( $k_s = 2$  mm). A comparison is made with the measured data by Francia (2011). In both measurements and experimental data, a decreasing trend with increasing height is observed. In the measurements and predictions, the turbulent intensity in the bottom region of the tower ( $z/Z = 0.29$  to  $0.56$ ) is highest near the centre and decreases away from the centre. At  $z/Z = 0.74$  and  $0.83$ , the measurements and the predictions give a relatively flat turbulence intensity profile. The decay in turbulence intensity with increasing height due to decay in swirl is well predicted by both turbulence models; the SSG-RST model however, gives a better prediction throughout the tower height.

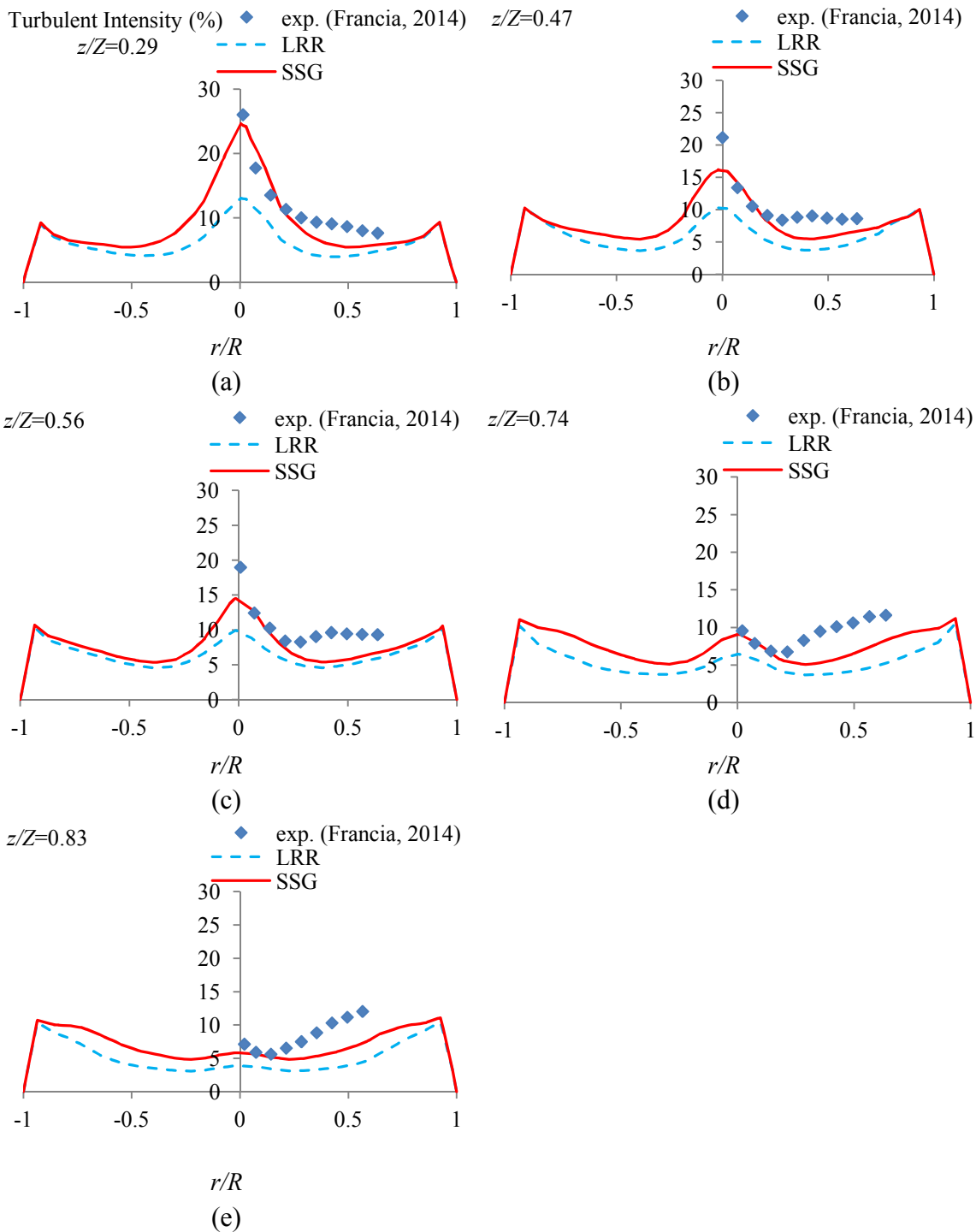


Figure – 6.25: Turbulent intensity computed using LRR and SSG pressure strain models and compared with measurements by Francia (2011).

Figure 6.26 is a plot of turbulent normal stresses, normalised by square of mean velocity at various dimensionless heights along the x-axis of the tower. U, V and W refer to the normalised axial, radial and tangential normal stresses respectively, which are obtained from the LRR-RST model (see Section 6.1.9). At  $z/Z = 0.29$ , all three normal stresses are isotropic in the central region of the tower up to a dimensional radius of 0.5,

after which the normal stresses start to become anisotropic. Similar pattern is observed at  $z/Z = 0.47$ , at this location, the maximum value of the normal stresses near the wall is relatively smaller. At  $z/Z = 0.56$ , the normal stresses are isotropic up to a dimensionless radius of 0.4, thereafter, the stresses start to become anisotropic. At  $z/Z = 0.74$  and 0.83, the maximum value of normal stresses near the wall is smaller and the difference between the normal stresses near the wall and at the centre is relatively smaller. At all the axial locations, the normal stress in the radial direction is the smallest in the annular region and greatest at the wall, while the axial normal stress is the maximum in the annular region followed by a sharp decline near the wall. The isotropy of normal stresses in the central region of the tower and highly anisotropic stresses in the near-wall region particularly in the bottom region of the tower is due to the presence of stronger swirl in the bottom region (see Figure 6.24). The presence of stronger swirl makes the normal stresses isotropic in the central region and highly anisotropic near the wall. As the swirl reduces as the air flows up the tower, the difference in the normal stresses at the central and the wall region also reduces. Hence the eddy viscosity based turbulence models using isotropic turbulence assumption are not valid for the modelling of flow encountered in the investigated counter-current spray drying tower.

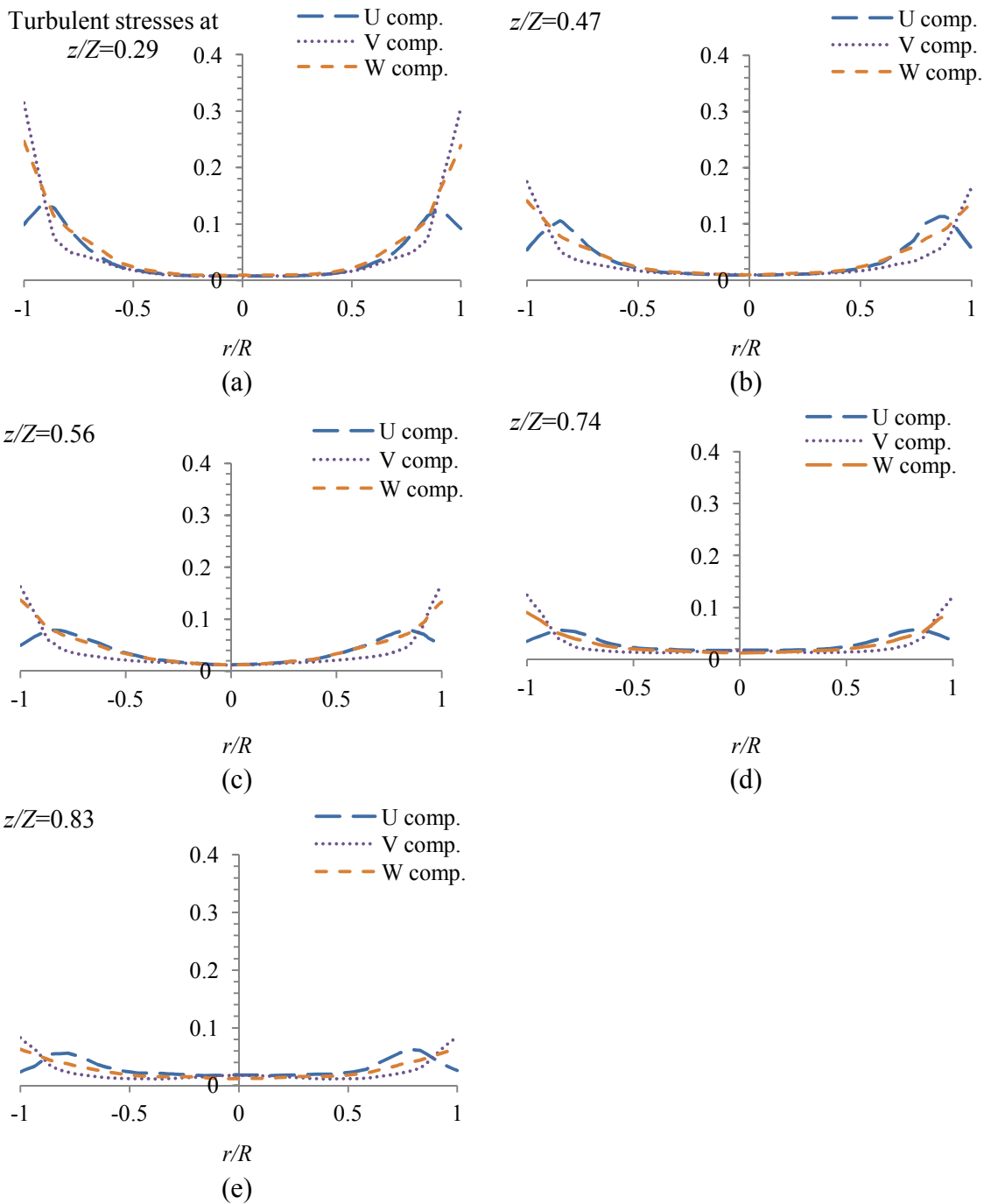


Figure – 6.26: Plots of normalised turbulent normal stresses computed using the LRR-RST model.

### 6.1.10 Conclusions

The basic features of the turbulent swirling air flow in a pilot-scale counter-current spray drying tower including the presence of a Rankine vortex in the tangential velocity profiles and reverse flow in the axial velocity profiles in the bottom cylindrical region of the tower is observed in the measurements made by Francia (2011). A quantitative validation of the CFD predictions using different turbulence models with the measured mean velocity components has been carried out. It has been found that for the given air

inlet nozzles configuration, the measured velocity profiles in the spray tower is stable and hence can be modelled using the steady state approximation. Only the RST models are able to reproduce the basic features of the air flow including a Rankine vortex in tangential velocity profile and reverse flow in the annular region in axial velocity profiles. The eddy-viscosity based turbulence models failed to reproduce these flow features and predicted a forced vortex in tangential velocity profile and a relatively flat axial velocity profiles.

It is found that the surface roughness on the wall due to the solid deposits plays a major role in the decay of swirl in the tower, which was verified by carrying out three simulation runs with different roughness heights specified in the modified log-law of the wall and the best agreement with experimental data was obtained with 2 mm roughness height specification. The predictions of both the LRR and SSG pressure strain models used in RST model are very similar in capturing the basic features of the flow and are in general good agreement with the measured velocity profiles. Both the LRR-RST and SSG-RST models have predicted the forced vortex in the bottom cylindrical region as well as the transformation of forced to Rankine vortex and the decay of swirl along the height of the tower with a reasonably good accuracy. A strong level of swirl persists throughout the tower, although it decays along the tower height. The axial and tangential velocity components are symmetrical and are the main velocity components in the spray tower.

## 6.2 CFD Modelling of Non-Isothermal Single Phase Flows

In this section, CFD modelling of single-phase, steady state, non-isothermal flows in the spray drying tower without the spray of slurry droplets has been carried out. The predicted gas temperature profiles inside the spray drying tower at various heights have been validated with two sets of experimental data measured by P&G (Martin de Juan, 2012; Ahmadian, 2013). In the first set of experimental data by Martin de Juan (2012), the predicted temperature profiles are compared with measured gas temperature profiles inside the spray tower to validate the CFD model predictions; in addition the heat loss from the tower is also investigated. The measured operating conditions of the spray tower for the first experimental data are given in Table 6.5. In the second set of experimental data by Ahmadian (2013), the role of wall roughness in influencing the temperature profiles inside the spray tower is investigated and compared with the measured gas temperature profiles. The details of temperature probe used for measurement of gas temperature inside the spray tower and experimental setup are given in Section 4.6.2 in Chapter 4.

Table – 6.5: Spray tower operating conditions for non-isothermal run (without slurry spray by Martin de Juan, 2012).

Parameter	Value
Inlet hot gas temperature	373 K
Outlet gas temperature	358 K
Ambient temperature	293 K
Mass flux of hot gas	1.0 kg/m <sup>2</sup> s
Pressure at the outlet	-300 Pa

### 6.2.1 Modelling of Heat Loss From the Wall

The heat loss from the tower wall to the surrounding is taken into account in the CFD simulation by considering radial conduction through the insulated wall. The inner surface of the wall contains a layer of deposits; the thermal resistance of the deposit layer is also taken into account by assuming it to be of uniform thickness throughout the

tower height. The conditions of the wall used for calculating the heat loss are given in Table 6.6.

Table – 6.6: Wall conditions for the calculation of heat loss.

Wall material	Stainless Steel 316
Insulation material	Glass Fibre
Wall thickness	6 mm (top), 8 mm (bottom)
Insulation thickness	105 mm
Thermal conductivity of metal wall	18.8 W/m K
Thermal conductivity of fibre glass insulation	0.04 W/m K
Deposit layer thickness	2 mm
Thermal conductivity of deposit	1.3 W/m K

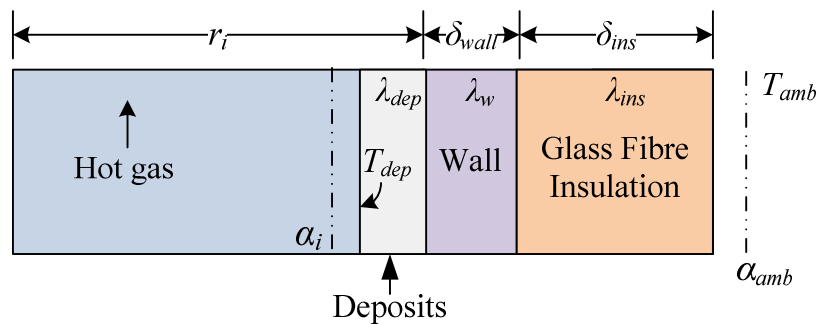


Figure – 6.27: Thermal resistances considered in the calculation of heat loss.

The heat flux from the tower is specified as a thermal boundary condition using Fluent UDF feature. The heat flux through the insulated tower wall (Figure 6.27) is given by:

$$\dot{q} = U(T_{dep} - T_{amb}) \quad (6.3)$$

where:

$\dot{q}$  is the heat flux,

$U$  is the overall heat transfer coefficient,

$T_{dep}$  is the temperature of the deposit layer inside surface, and

$T_{amb}$  is the ambient temperature,

The overall heat transfer coefficient ( $U$ ) is given by:

$$\frac{1}{U} = \frac{r_i \ln\left(\frac{r_i}{r_i - \delta_{dep}}\right)}{\lambda_{dep}} + \frac{r_i \ln\left(\frac{r_i + \delta_w}{r_i}\right)}{\lambda_w} + \frac{r_i \ln\left(\frac{r_i + \delta_w + \delta_{ins}}{r_i + \delta_w}\right)}{\lambda_{ins}} + \frac{r_i}{\alpha_{amb}(r_i + \delta_w + \delta_{ins})} \quad (6.4)$$

In equation (6.4), the overall heat transfer coefficient does not include the thermal resistance of the convective film along the inside surface of the deposit layer since the temperature at the surface of the deposits ( $T_{dep}$ ) is known as it is calculated using equation (3.51), which is the log-law representation of the thermal boundary layer. The value of outside film coefficient ( $\alpha_{amb}$ ) is taken to be a constant value of 14 W/m<sup>2</sup>K (Heggs, 2012).

## 6.2.2 Numerical Solution Method

Mesh 1 is used for all non-isothermal cases. The non-isothermal, turbulent and swirling drying gas flow is modelled using the Reynolds-averaged continuity, Navier-Stokes and energy equations (given in Section 3.9.1 and 3.10.8). The turbulence is modelled using the RST model (Section 3.10.5). The pressure strain term in the RST is modelled using the linear approximation by Launder *et al.* (1975). The choice of the turbulence model is based on the results of CFD simulations of isothermal (cold) gas flow in which the predictions of different turbulence models were compared with experimentally measured time-averaged axial and tangential velocity profiles at various axial locations in the tower (Section 6.1.9). The tower wall roughness due to deposit layer on the inner wall is taken into account by assuming a roughness height of  $k_s = 2.0$  mm and a roughness constant of  $C_s = 1.0$  (as in Section 6.1.9). For the heat transfer calculations, the energy transport equation is solved (equation 3.53). The turbulent diffusion flux in the energy transport equation is modelled using the gradient-diffusion approach (equation 3.54) with a value of 0.85 for the turbulent Prandtl number, which is the recommended value in Fluent (2009). Radiation heat transfer is not considered as this is a low temperature system.

For pressure-velocity coupling, the PISO scheme (Issa, 1985) has been used and for pressure interpolation, PRESTO! scheme (Patankar, 1980) is used which is recommended for flows with swirl (Fluent, 2009). The convective terms are discretized using the SOU scheme. The under-relaxation factor for the energy equation is specified as 1.0. The under-relation factors for all other equations are listed in Table 6.1. The convergence criteria are specified as  $1 \times 10^{-4}$  for the continuity, momentum and the turbulence quantities. The convergence criterion for energy equation is  $1 \times 10^{-6}$ .

### **6.2.3 Boundary Condition Specifications**

The concentrations of water vapour and CO<sub>2</sub> in the gas stream (resulting from the heating of air in a direct fired furnace) are small and hence neglected in the CFD simulation, hence the air is considered as the hot gas. The hot gas is injected into the tower through the tangential-entry gas inlet nozzles. For the hot gas inlet nozzles, the mass flow is specified as the inlet boundary condition. For the gas exhaust, a pressure boundary condition is specified. The specified temperature and mass flow of the hot gas inlet and the exhaust gas pressure are given in Table 6.5. Some cold air is entrained from the bottom of the spray drying tower due to below atmospheric pressure inside the tower. The exact amount of the cold air entrained in the tower is not known. This is assumed to be a certain percentage of the mass flow of the hot gas (listed in Table 6.7) and is used as the boundary condition to account for the cold air entrainment. The temperature of the cold air is considered to be the same as the temperature of the ambient air given in Table 6.5. Both streams are assumed to be moisture-free. Heat flux through the insulated tower wall is calculated using equation (6.3), which requires inside deposit surface temperature ( $T_{dep}$ ) and ambient temperature ( $T_{amb}$ ).  $T_{dep}$  is calculated using log-law of the wall for thermal boundary layer (equation 3.51). The gas density is considered a function of temperature and is calculated using the ideal gas law (equation 3.56). The gas viscosity and specific heat are considered to be constant with a value of  $1.79 \times 10^{-5}$  kg/ms and 1006.4 J/kgK, respectively.

### **6.2.4 Simulation Cases**

Four non-isothermal cases of CFD simulations are carried out for the input operating conditions given in Table 6.5. In Case 1, a fixed amount of cold air (5% of the hot gas flow) entrained from the bottom of the tower is specified. The thermal conductivity of the insulation is also specified as a fixed value of 0.04 W/mK. However, this resulted in a significantly smaller heat loss compared to the heat loss based on the measurement.

Therefore, three further simulation cases are carried out. In Case 2, the amount of cold entrained air is specified to be 10% of the hot gas mass flow. In Case 3, the thermal conductivity of the insulation is calculated on the basis of measured heat loss, which is then specified in the simulation for the calculation of heat loss. The cold air entrainment value is specified to be 10% of the hot gas mass flow. In Case 4, it is assumed that most of the heat loss occurs before the gas enters the tower via tangential entry inlets, i.e., the gas loses heat due to heat loss in the inlet gas duct (which supplies gas to the gas distribution ring) and in the gas distribution ring (which supplies gas to the hot gas inlet nozzles). A lower gas inlet temperature, assuming a temperature drop of 10°C is specified and the thermal conductivity of insulation and the cold air entrainment value is kept the same as in Case 1. The differences in the boundary conditions of all four simulation cases are listed in Table 6.7.

Table – 6.7: Boundary Conditions used in the simulation of Case 1 to 4.

Simulation Case	Specified hot gas temperature (K)	Specified cold air entrained mass flow	Wall heat flux condition
Case 1	373	5% of hot gas mass flow	Heat flux based on constant $\lambda_{ins}$ (0.04 W/mK)
Case 2	373	10% of hot mass flow	Same as in Case 1
Case 3	373	Same as in Case 2	Heat flux based on $\lambda_{ins,calc}$
Case 4	363	Same as in Case 1	Same as in Case 1

### 6.2.5 Simulation Convergence

The level of residuals for continuity, momentum and turbulence quantities (given in Section 6.2.2) did not reach the required level of convergence and became fairly stable after a few thousand iterations and the level of residuals for continuity, momentum and turbulence quantities is of the same order of magnitude as in the isothermal simulation case. Therefore, the mass weighted average axial and tangential velocities of the gas in the cylindrical region of the tower at two different heights were monitored. The solution was taken to be converged when the monitored weighted average velocities become stable and do not fluctuate significantly with iterations. Figure 6.28 is a plot of residuals

and Figure 6.29 is a plot of variation of monitored velocity components with iteration for non-isothermal Case 1.

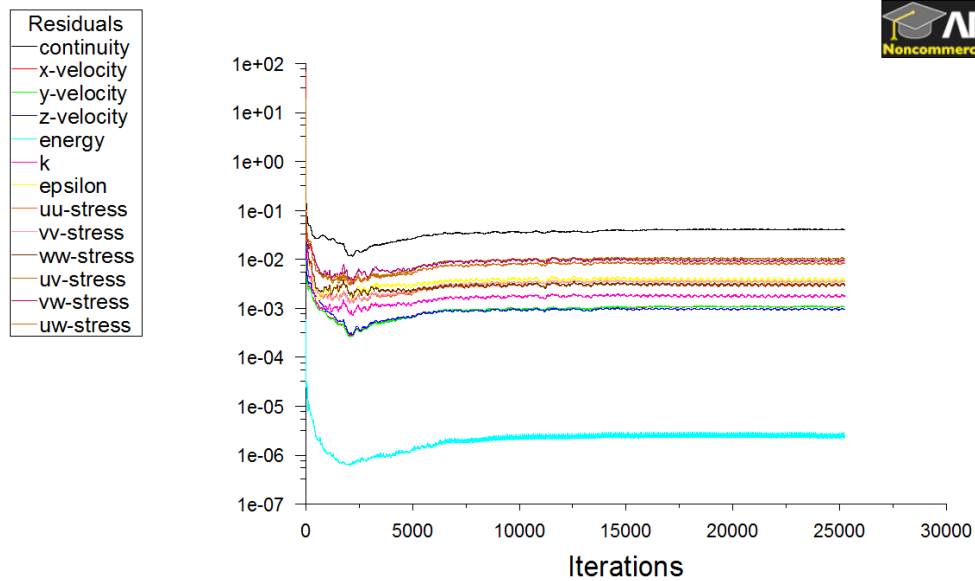


Figure – 6.28: Convergence residuals for non-isothermal Case 1.

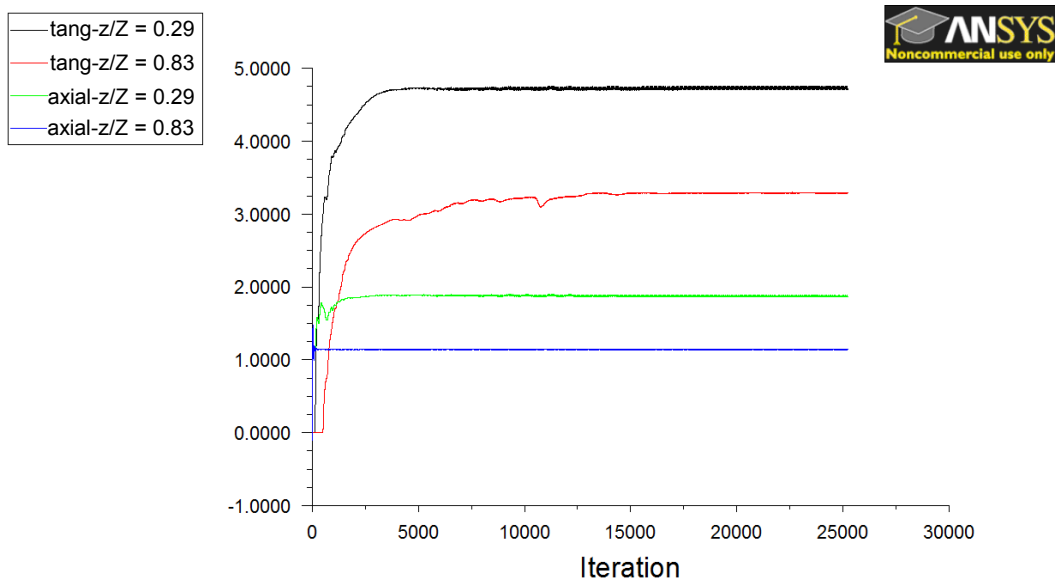


Figure – 6.29: Convergence history of weighted averaged axial and tangential velocities.

### 6.2.6 Simulation Results for Case 1

The measured temperatures at various dimensionless heights (Martin de Juan, 2012) with  $z/Z=0$  at the bottom outlet and  $z/Z=1$  at the top outlet of the spray tower (all measurements are taken in the cylindrical region of the tower) are compared with the predicted temperature profiles in Figure 6.30. The shape of the measured temperature profile varies from a bird-wing profile in the bottom region of the tower ( $z/Z=0.24$  to

0.60) to a nearly plug-flow profile in the central region at the top ( $z/Z=0.82$ ). Up to a dimensionless height of 0.60, a lower temperature in the central region of the tower is observed. This is due to the mixing of the hot gas with cold air entrained through the centrally located opening at the bottom of the tower for dried powder exit. A sharp decline in the temperature in both measurement and prediction can be observed near the wall at all measurement locations. This is due to heat loss through the wall. It is observed that the predicted temperatures in Case 1 are 10-15 K higher than the measured values. It may be due to the fact that the actual heat loss occurring through the insulation is greater than the calculated heat loss due to damaged insulation. It may also be due to incorrect specification of the amount of entrained cold air. The actual amount of entrained cold air may be higher which may reduce the temperature in the tower. For this experimental trial (Martin de Juan, 2012), the air mass flow entrained from the bottom of the tower was not measured, therefore a value of 5% of the hot gas mass flow is assumed. In the measured temperature profiles, it is observed that the lower temperature in the centreline region persists up to a dimensionless height of 0.60, but in the simulation, the lower centre line temperature can be seen only at  $z/Z = 0.24$ . The predicted temperature profiles are relatively flat compared to measurements in the central region of the tower for  $z/Z > 0.42$ , this indicates that the mixing of the hot gas and the cold entrained air is overpredicted by the simulation. The value of  $Pr_t$  used for turbulent mixing may also influence the gas temperature prediction which in this case is taken to be 0.85. The influence of this parameter in predicting the gas temperature profiles is given in Figure 6.38. The predicted temperature profiles show a sharp temperature decline near the wall at all dimensionless heights; however, the predicted near-wall temperature is 10-15 K greater.

The measured temperature profiles taken by Martin de Juan (2012) in Figure 6.30 were not corrected for measurement errors due to radiation losses. Therefore, corrections in the measured temperature profiles for radiation losses have been carried out in this study. The calculation procedure as well as the corrected temperature profiles is given in Appendix II. The corrections in the measured temperature are not significant (with a maximum difference of 0.4 K), hence the measured temperatures are used for the comparison with the predicted profiles.

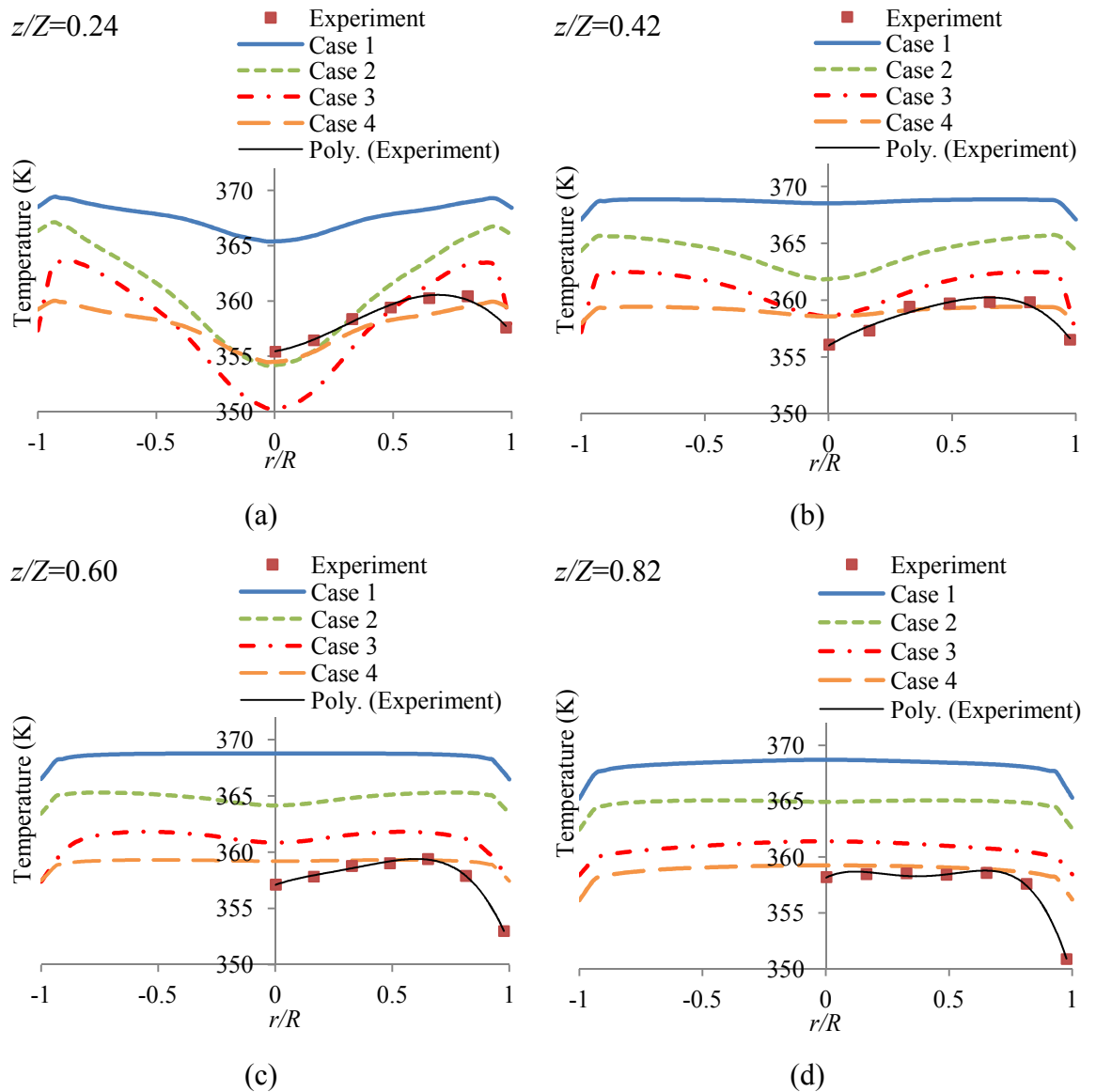


Figure – 6.30: Temperature profiles at different axial locations, a comparison of non-isothermal cases with experimental data.

Figure 6.31 is a contour plot of the predicted gas temperature inside the spray drying tower. The gas temperature is highest at the gas inlet nozzles. A minimum temperature at the bottom outlet can be seen due to the entrainment of cold air from the bottom exit of the spray drying tower. The cold air mixes with the hot gas as it travels upwards, due to which a lower temperature is observed in the centreline of the tower, eventually the gas temperature becomes fairly constant along the radius of the tower at  $z/Z = 0.35$ .

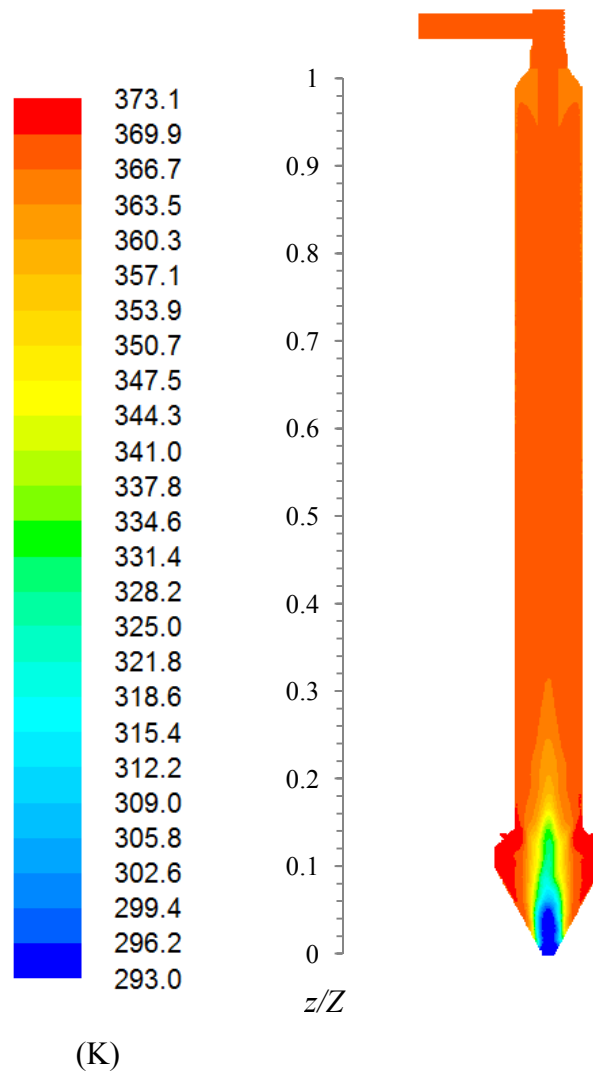


Figure – 6.31: Contours of the predicted gas temperature profiles inside the spray drying tower.

Figure 6.32 is a plot of the predicted axial velocity profiles at various dimensionless heights. Negative velocity is observed in the annular region in the bottom section of the tower (at  $z/Z = 0.24$  and  $0.42$ ). This negative velocity is also observed in the isothermal single phase simulation cases (Section 6.1.8) and is due to highly swirling flow in the bottom region of the spray tower. The annular recirculation region does not appear in the top section of the spray tower due to decay of swirl as the gas flows upwards and loses the tangential momentum due to friction and viscous losses. The magnitude of velocity in the centreline can be seen to increase with the axial distance. The axial velocity plots of isothermal single phase simulation cases are qualitatively similar to the non-isothermal simulation case.

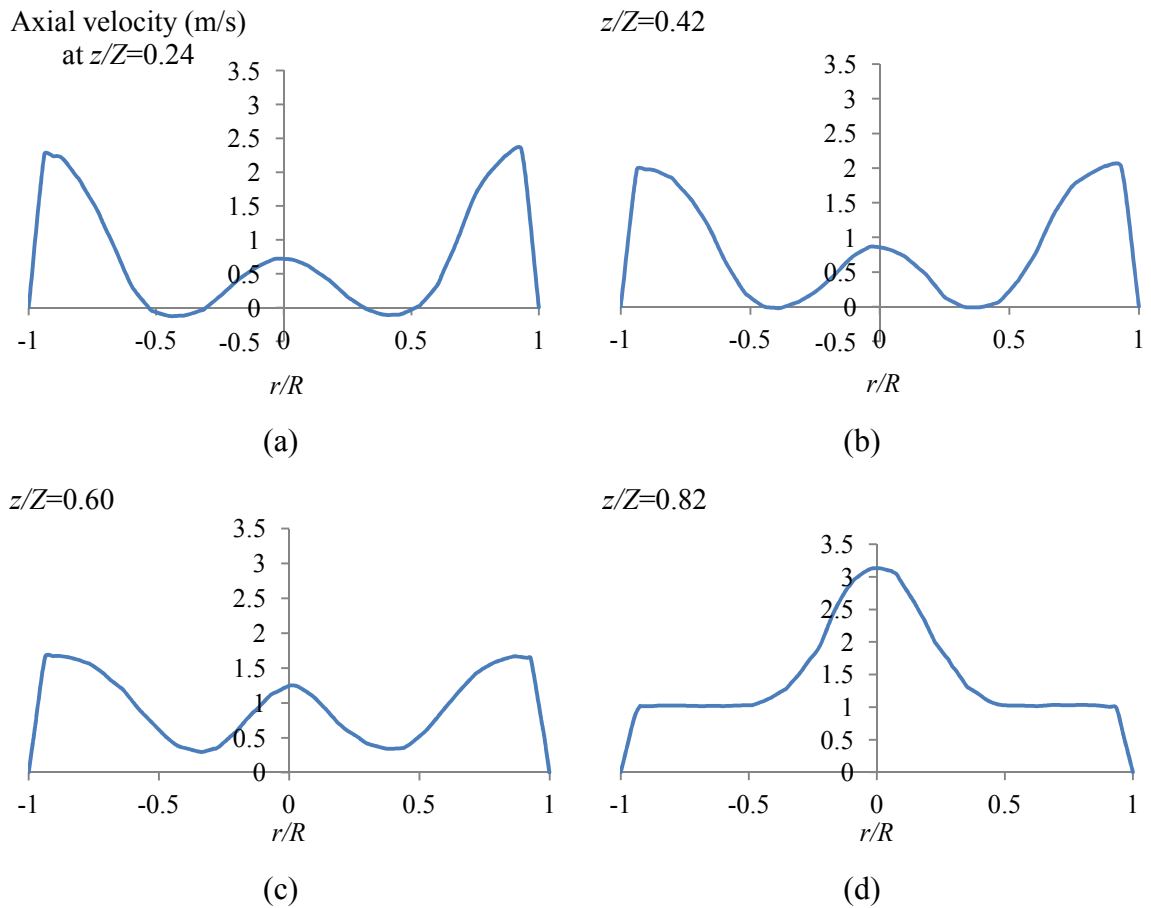


Figure – 6.32: Predicted axial velocity profiles at various axial locations (Case 1).

Figure 6.33 is a plot of mean tangential velocity profiles at different dimensionless heights. The tangential velocity profile in Figure 6.33 (a) resembles a forced vortex. Which is also observed in the isothermal single phase CFD cases (Section 6.1.8). The force vortex transforms into a Rankine vortex at  $z/Z = 0.42$  and above. The radial location of the transformation of forced to free vortex region becomes closer to the centreline as the gas flows upwards, which is also observed in the isothermal CFD simulation cases. The tangential velocity profiles in the non-isothermal CFD simulation case is qualitatively similar to the isothermal CFD simulation cases.

Figure 6.34 is a plot of the inside film coefficient (left) and the corresponding Nusselt number (right) for Case 1. The inside film coefficient is calculated in Fluent as post-processing using equation (3.52). The wall heat flux (in equation 3.52) is calculated using equation (6.3). The value given in the plot is averaged over the tower circumference. The inside film coefficient is a maximum at the tangential-entry inlets ( $z/Z = 0.13$ ) as the swirl is maximum at the inlets (Figure 6.36). The influence of swirl in increasing the surface heat transfer for air flow in a pipe was experimentally investigated by (Chang and Dhir, 1995). For a flow with a swirl number of 2.5, Chang

and Dhir (1995) found a 200% increase in surface Nusselt number compared to non-swirling air flow. In this case, the maximum swirl number is 2.5 (at  $z/Z = 0.13$ ) and the swirl number near the outlet ( $z/Z = 0.90$ ) is about 1.0 (Figure 6.36). The Nusselt number in this case is about 220% greater near the tangential-entry inlets compared to the Nusselt number near the gas outlet. The swirl increases the axial velocity profile close to the wall (due to radial pressure gradient resulting from centrifugal force due to swirl) which increases the convective heat transfer close to the wall surface, hence an increase in the heat transfer coefficient (Chang and Dhir, 1995). The inside film coefficient decreases as the gas flows upwards due to decrease in the swirl, resulting in a decrease the axial velocity close to the wall.

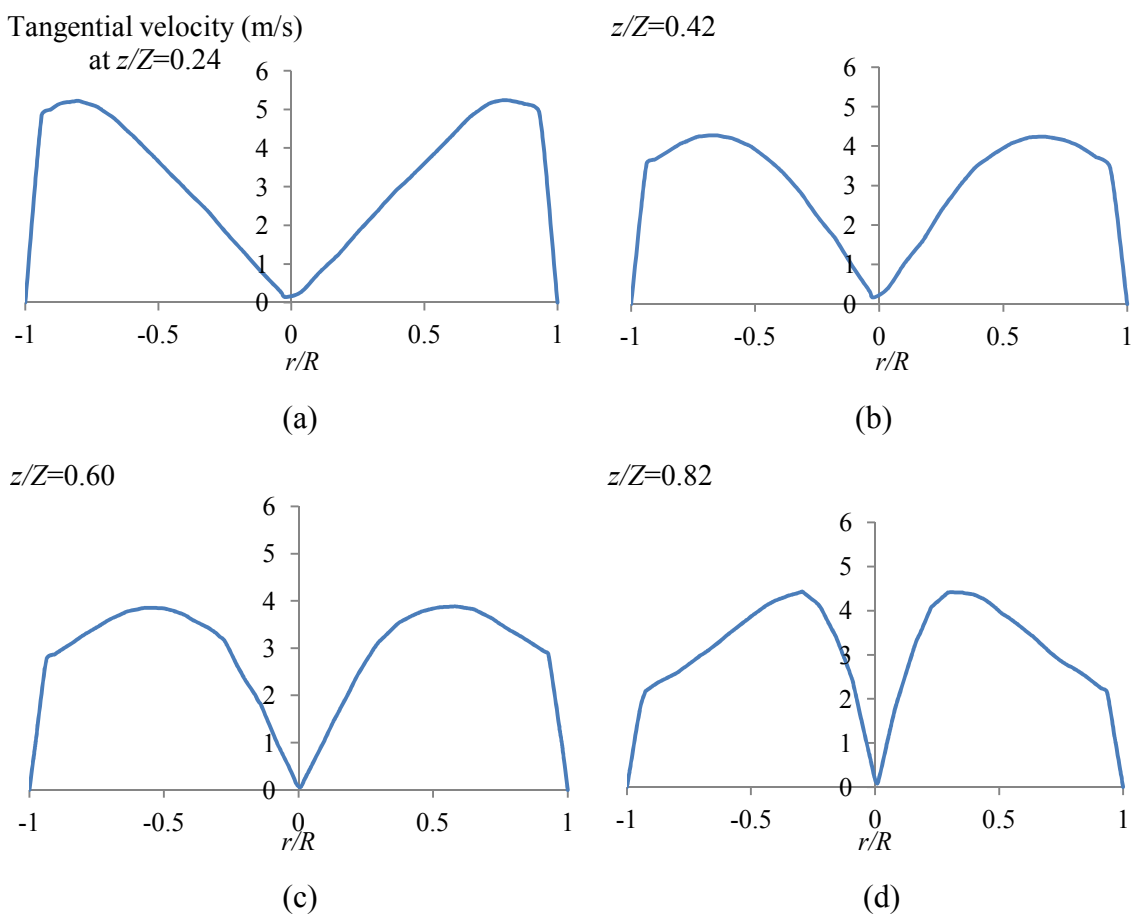


Figure – 6.33: Predicted tangential velocity profiles at various heights (Case 1).

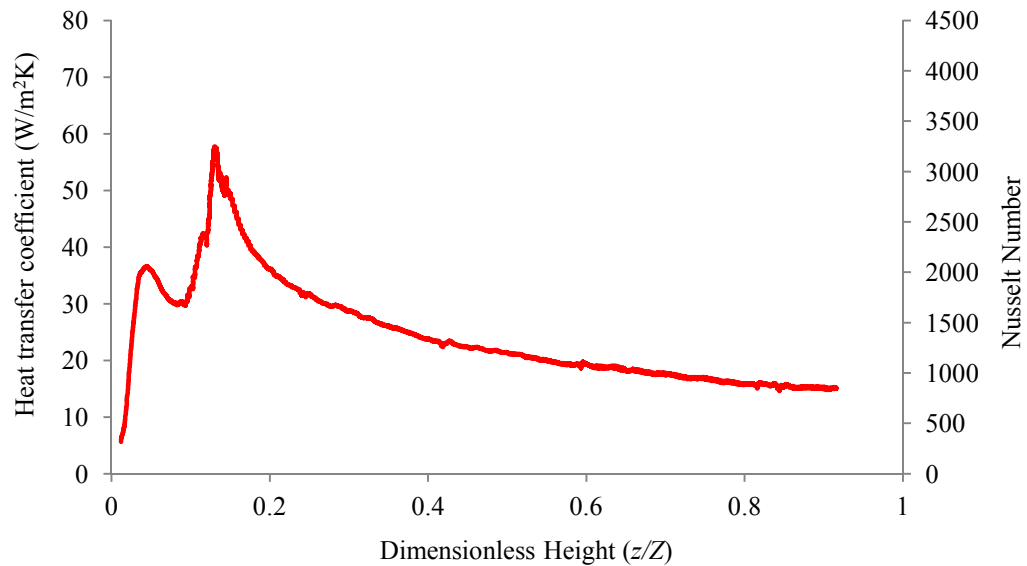


Figure – 6.34: Predicted inside film coefficient along the dimensionless height (Case 1).

### 6.2.7 Case 2

In Case 1, it was found that the predicted temperature is higher than the measured temperature at all measurement locations. The maximum temperature difference is between 10-15 K. The predicted temperature profiles in Case 1 are also relatively flat compared to the measured temperature profiles. One of the reasons for this may be due to the fact that the amount of cold air entrained is greater than that specified in the calculation. Therefore, in this case, the amount of cold air in the tower is increased to 10% of the hot gas mass flow. For the prediction of heat loss through the tower wall, the thermal conductivity of insulation is specified to be 0.04 W/mK (same as in Case 1). The predicted temperature profiles for Case 2 are depicted in Figure 6.30.

It is observed that by increasing the mass flow of cold air, the predicted gas temperature goes down. At the first measurement location Figure 6.30 (a), the predicted temperature in the central region is higher in Case 1 with 5% of mass flow of cold air, while in the case of 10% of mass flow, the temperature in the central region matches well with the measured value at  $r/R = 0$  to 0.3. However, the temperature near the wall is overpredicted in both cases, although in Case 2 the predicted temperature is relatively in better agreement with measurement. At the second measurement location Figure 6.30 (b), the wall temperature as well as the temperature in the central region of the tower is overpredicted in both 5% and 10% of the cold air flow rates. In contrast to a flat temperature profile in Case 1, the temperature profile predicted by Case 2 gives a bird wing profile similar to the measurement but the predicted temperature is greater by about 6 K. At the third measurement location (Figure 6.30 (c)), the predicted

temperature is greater near the wall as well as near the centreline. At the third and fourth measurement locations, the temperature is overpredicted by both cases. The predicted centreline temperature at these locations is greater, which shows that in the predicted gas temperatures, mixing of the cold air and the hot gas takes place more rapidly compared to the measurement. The predicted wall temperature is higher than the measured temperature at all measurement locations; this could be due to greater heat losses from the tower, and is underpredicted by the simulation. The temperature in the central region of the tower at  $z/Z = 0.42, 0.60$  and  $0.82$  is overpredicted by both simulation cases.

### 6.2.8 Case 3

In the previous two cases, it is found that the temperature at the wall is overpredicted by the model even when the mass flow of cold entrained air is 10% of the mass flow of hot gas. This indicates that the heat loss from the tower may be underpredicted by the simulation. In Case 3, the calculated value of the overall heat transfer coefficient using the measured temperatures (Martin de Juan, 2012) is specified in the CFD simulation.

### 6.2.9 Analysis of Experimental Data

The evaluation of the overall heat transfer coefficient based on measured temperatures requires calculation of the average gas temperature at the measured heights, which is calculated using two methods. In the first method, an area weighted average value of the measured gas temperature at the axial location is calculated from the integration of a polynomial curve fit equation of the experimental data. The average temperature is given by:

$$T_{avg} = \frac{2}{R^2} \int_0^R r T_{gas}(r) dr \quad (6.5)$$

The polynomial curve fits of the experimentally measured data are given by continuous lines in Figure 6.30. The curve fit equations and their respective  $R^2$  values for all measurement heights are given below:

For  $z/Z=0.24$ , the polynomial curve fit equation is:

$$T_{gas} = -24(r/R)^3 + 22.385(r/R)^2 + 3.3772(r/R) + 355.446 \quad (6.6)$$

The corresponding  $R^2$  value for the curve fit is 0.98.

For  $z/Z=0.42$  m height, the polynomial curve fit equation is:

$$T_{gas} = -24.79(r/R)^4 + 32.393(r/R)^3 - 20.885(r/R)^2 + 13.259(r/R) + 355.968 \quad (6.7)$$

The corresponding  $R^2$  value is 0.96.

For  $z/Z=0.60$  m, the curve fit equation is:

$$T_{gas} = -31.305(r/R)^3 + 27.878(r/R)^2 - 1.5844(r/R) + 357.246 \quad (6.8)$$

The corresponding  $R^2$  value is 0.98.

For  $z/Z=0.82$ , the curve fit equation is:

$$T_{gas} = -96.334(r/R)^4 + 146.36(r/R)^3 - 70.053(r/R)^2 + 11.151(r/R) + 358.133 \quad (6.9)$$

The corresponding  $R^2$  value is 0.99.

The heat flux at the wall (required for the calculation  $U$ ) is calculated using the following equation:

$$\dot{q} = -\lambda_{gas} \left. \frac{dT_{gas}}{dr} \right|_{r=R} = \alpha_i (T_{avg} - T_{dep}) \quad (6.10)$$

where  $\lambda_{gas}$  is the thermal conductivity of gas taken as a constant value of 0.03 W/mK for the range of gas temperatures in the experimental investigation. The temperature gradient in equation (6.10) is calculated by differentiating the polynomial curve fit equations (6.6, 6.7, 6.8 and 6.9) at  $r = R$ .

The overall heat transfer coefficient ( $U$ ) is then calculated using the following equation:

$$U = \frac{\dot{q}}{(T_{avg} - T_{amb})} \quad (6.11)$$

The inside film coefficient  $\alpha_i$  is calculated using equation (6.10).

Table 6.8 summarises the calculated heat flux values and the corresponding  $U$  values and insulation thermal conductivity ( $\lambda_{ins,calc}$ ) (calculated using equation (6.4)) based on the calculated  $U$  values (using equation 6.11).

Table – 6.8: Heat flux calculated using the first method

Dim. Height (z/Z)	$T_{avg}$ (K)	$T_{dep}$ (K)	$\left. \frac{dT_{gas}}{dr} \right _{r=R}$ (K/m)	$\dot{q}$ (W/m <sup>2</sup> )	$\alpha_i$ (W/m <sup>2</sup> K)	$U$ (W/m <sup>2</sup> K)	$\lambda_{ins,calc}$ (W/mK)
0.24	359.31	357.0	-35.18	1.05	0.45	0.015	0.0015
0.42	359.05	356.18	-35.87	1.07	0.37	0.016	0.0016
0.60	357.65	351.85	-59.95	1.80	0.31	0.027	0.0027
0.82	356.75	348.90	-106.85	3.20	0.40	0.050	0.0049

From the above table it is observed that the calculated value of  $\lambda_{ins,calc}$  is much smaller than the value of glass fibre insulation thermal conductivity reported in the literature (Kreith, 1973) is 0.04 W/mK, which is unrealistic, hence these values are not used for calculation of heat losses.

In another method, the mean axial velocity profiles obtained from non-isothermal Case 1 (Figure 6.32) and the measured temperature profiles are used to calculate the bulk (cup mixing) temperature (the difference in the axial velocity profiles obtained from Case 1 and Case 2 was negligible, resulting in a maximum difference in bulk temperature of 0.1 K). The bulk temperature is given by (Jawarneh, 2011):

$$T_b = \frac{\int_0^R r \bar{u}_{axial} T_{gas}(r) dr}{\int_0^R r \bar{u}_{axial} dr} \quad (6.12)$$

where

$T_b$  is the bulk temperature,

$r$  is the radial coordinate,

$R$  is the radius of the spray tower, and

$u_{axial}$  is the mean axial velocity of gas.

Equation (6.12) is solved by numerical integration with trapezoidal rule using the measured gas temperature (Martin de Juan, 2012) and the CFD predicted mean axial velocity at the corresponding radial location. The calculated  $T_b$  values at each measurement location are listed in Table 6.9. The tower is divided into four sections based on the measured temperature locations and the cup mixing temperature is then used to calculate the heat losses in each section of the spray drying tower using enthalpy balance equation given by:

$$\dot{Q} = \dot{m}_{gas} c_{p, gas} (T_{b,2} - T_{b,1}) \quad (6.13)$$

where:

$\dot{Q}$  is the heat loss from the tower,

$\dot{m}_{air}$  is the mass flow of gas,

$c_{p, gas}$  is the specific heat of gas, and

$T_b$  is the bulk temperature.

At the first measurement location ( $z/Z=0.24$ ), the change in temperature of the hot gas will take place not only due to heat losses, but also due to mixing with the entrained air which is at a room temperature. Assuming the entrained amount of cold air to be 10% of the hot gas mass flow, the amount of heat exchanged between the hot gas and cold entrained air is 15.8 kW. This amount of heat is subtracted from the heat loss obtained from equation (6.13) to get the actual amount of heat loss from the tower at the first measurement height.

From the calculated heat loss, the overall heat transfer coefficient ( $U$ ) is calculated using the following equation:

$$U = \frac{\dot{Q}}{A(T_{b,average} - T_{amb})} \quad (6.14)$$

where

$T_{b,average}$  is the average (arithmetic mean) of the bulk temperatures at two successive axial measurement locations.

The inside film coefficient ( $\alpha_i$ ) is calculated using the following equation:

$$\alpha_i = \frac{(T_b - T_{dep})}{\dot{q}} \quad (6.15)$$

where  $T_{dep}$  is the deposit surface temperature given in Table 6.8 and is calculated using the polynomial curve fit equations (6.6, 6.7, 6.8 and 6.9) by putting  $r/R=1$ .

The calculated value of  $U$  obtained from equation (6.14) is put into equation (6.4) and solved for the thermal conductivity of insulation  $\lambda_{ins,calc}$ . The calculated value of heat flux ( $\dot{q}$ ),  $U$  and  $\lambda_{ins,calc}$  is listed in Table 6.9. In non-isothermal Case 3, the calculated values of the insulation thermal conductivity listed in Table 6.9 are used to calculate the overall heat transfer coefficient ( $U$ ) in each section and specified in the CFD simulation using Fluent UDF feature. The heat flux from the tower is then calculated using equation (6.3).

Table – 6.9: Heat losses calculated using the second method

Dim. Height (z/Z)	$T_b$ (K)	$\dot{q}$ (W/m <sup>2</sup> )	$\dot{Q}$ (W)	$\alpha_i$ (W/m <sup>2</sup> K)	$U$ (W/m <sup>2</sup> K)	$\lambda_{ins,calc}$ (W/mK)
0.24	359.88	220.8	17400	76.7	3.311	0.414
0.42	359.39	55.2	1209	17.2	0.833	0.086
0.60	357.95	175.8	3604	28.8	2.710	0.325
0.82	357.71	22.43	599	2.5	0.347	0.035

The computed temperature profiles after including the estimated insulation thermal conductivity are depicted in Figure 6.30. It is observed that the computed temperature profiles are in a relatively better qualitative and quantitative agreement with

measurements at all axial locations compared to Case 1 and 2. The maximum error between the predicted temperature and the measurement in this case is 4 K at  $z/Z=0.24$ . The predicted near-wall temperature by Case 3 is in good agreement with the measured temperature at this height. At a dimensionless height of 0.42 to 0.82, Case 3 predicts a correct qualitative temperature prediction (a lower temperature at the centre and near the wall), however, the predicted gas temperature is greater.

Figure 6.35 is a plot of heat flux along the dimensionless tower height in the cylindrical region of the tower predicted for Case 1 and Case 3 and a comparison with the experimental data. The negative sign indicates that the heat is lost from the tower to the surrounding. From the plot it is observed that the heat flux calculated in Case 3 matches well with the experimental data because in this case, the thermal conductivity of the insulation was adjusted to match with the calculated heat loss based on measurements, whereas Case 1 gives a smaller heat flux and is fairly constant throughout the tower height.

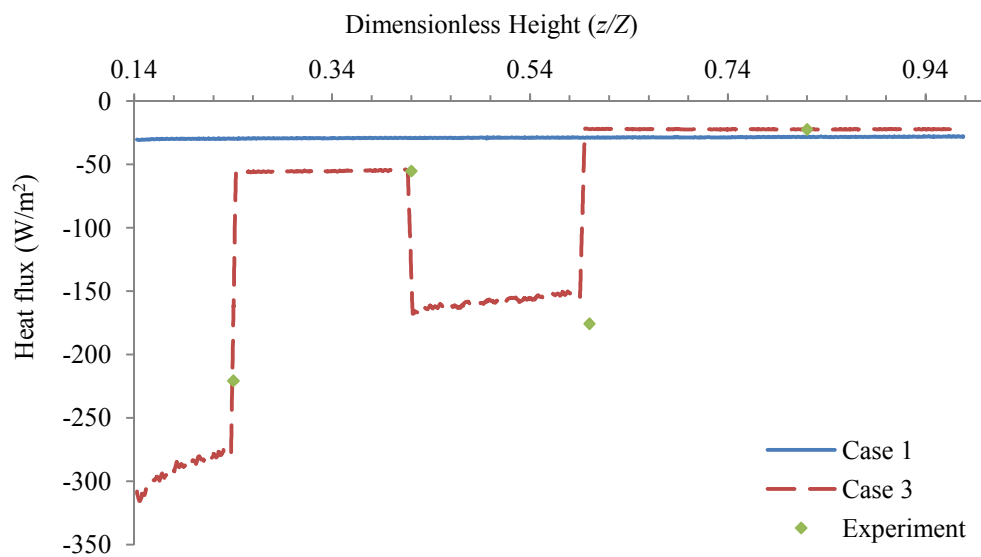


Figure – 6.35: Heat flux along the dimensionless tower height.

From the plots in Figures 6.34 and 6.35, it is observed that the insulation thermal resistance is the major resistance to heat transfer, as the major difference in Case 1 and Case 3 predicted heat flux is the value of insulation thermal conductivity. Although the inside film coefficient reduces by 300% along the tower height, but in Case 1, the heat flux is fairly constant throughout the tower height as depicted in Figure 6.35.

Figure 6.36 is a plot of inside convective film coefficient and swirl number along the dimensionless tower height for Case 3. The inside film coefficient decreases as the gas

moves upwards due to decrease in the swirl number along the tower height. A strong swirl causes a higher tangential and axial velocity close to the wall leading to a higher convective heat transfer rate, hence a large film coefficient. The CFD predicted inside film coefficient reduces by 300% due to decrease in swirl number. The strength of swirl reduces as the gas moves upwards due to viscous and frictional resistance. The dotted points represent the value of inside film coefficient based on measured temperatures, calculated using equation (6.15), which show a general declining trend up the tower height, although the values differ significantly at  $z/Z=0.24$  and at  $0.82$ . This is because the calculated values are based on the average of the heat flux in the entire section, and the deposit surface temperature ( $T_{dep}$ ) used in the calculation of  $\alpha_i$  is obtained from the extrapolation of values obtained from the polynomial curve fits to the measured temperature profile, assuming that the same declining trend (observed near the wall) continues up to the deposit surface.

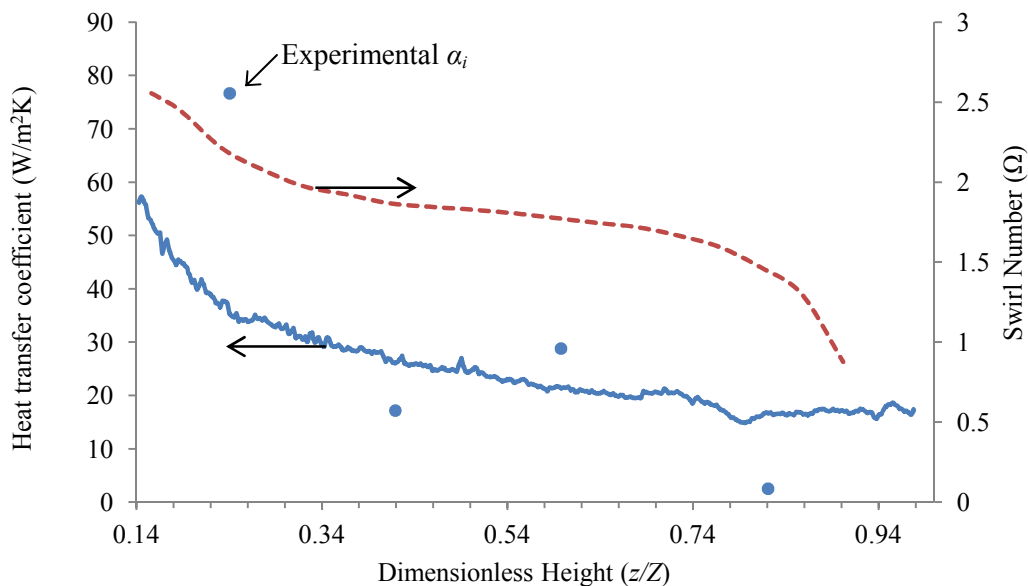


Figure – 6.36: Heat transfer coefficient and swirl number along the dimensionless tower height (Case 3).

#### 6.2.10 Case 4

In the simulation Case 4, it is assumed that most of the heat loss from the hot gas is occurring in the gas duct that supplies gas to the distribution ring around the spray drying tower as well as in the gas distribution ring. Therefore, a lower temperature is specified as the gas inlet temperature. The gas temperature at the inlets was not measured; hence an assumption was made that the gas loses its temperature by 10 K as it reaches the tangential-entry inlets. The specified hot gas inlet temperature in this case

is 353.15 K and the amount of cold air entrainment is taken to be 5% of the hot gas mass flow. For the calculation of heat loss through the wall, a constant value of thermal conductivity reported in the literature (Kreith, 1975) with a value of 0.04 W/mK is considered.

Figure 6.30 is a plot of temperature profiles predicted by Case 4. It is observed that Case 4 gives the best agreement with the experimental data at all the measured locations both in the central region of the tower as well as close to the wall. Therefore, most of the heat loss takes place before the gas actually enters the tower, i.e., in the inlet gas duct and in the distribution ring which supplies gas to the tangential-entry inlets. This indicates that the insulation in the duct and the distribution ring is severely damaged and requires replacement to prevent excessive heat loss in these regions. Another source of error could be due to the fact that the temperature measurement in the duct is taken at the centre, which may not represent the mean temperature of the gas as a non-uniform temperature profile may exist inside the inlet gas duct.

In all of the above four cases, the value of turbulent Prandtl number ( $Pr_t$ ) used to compute the turbulent heat flux, is taken to be 0.85, which is the default value in Fluent. The effect of  $Pr_t$  on the predicted temperature profiles is given in Figure 6.37, utilising Case 4 input conditions. The value of  $Pr_t$  is varied from 0.5 to 1.0. The predicted temperature profile becomes flatter as the value of  $Pr_t$  is decreased i.e., less than 1.0, in which case, turbulent heat diffusivity is greater than turbulent momentum diffusivity. The influence of  $Pr_t$  is more apparent in the bottom regions of the tower ( $z/Z = 0.24$  to 0.42). A default value of  $Pr_t = 0.85$  (used in all previous cases) gives the best predictions compared to experimental data in the bottom regions of the tower.

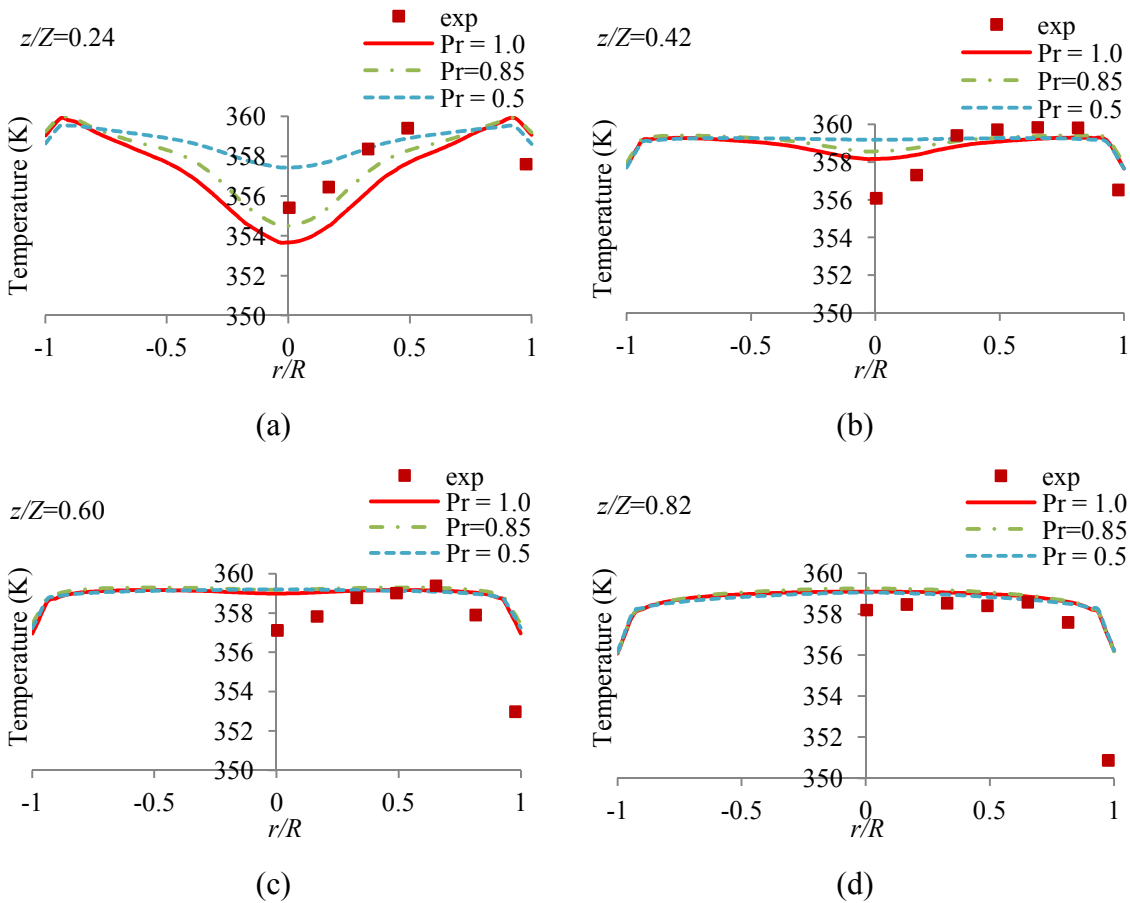


Figure – 6.37: The effect of turbulent Prandtl number in predicting temperature profiles (using Case 4 conditions).

Total heat loss from the tower wall is 4.1 kW in Case 1, 3.9 kW in Case 2, 15.1 kW in Case 3 and 3.5 kW in Case 4. The heat loss based on the experimental measurement of temperatures at the inlet gas duct and the exhaust gas temperature is 22.2 kW, which is 12% of the total heat input to the tower (taking entrained air mass flow to be 5% of the hot gas). Table 6.10 lists the measured and predicted exhaust gas temperatures from Cases 1 to 4. Case 4 gives the best agreement with measured exhaust gas temperature with a difference of 0.3 K.

Table – 6.10: A comparison of measured (Martin de Juan, 2012) and predicted exhaust gas temperatures.

Case	Exhaust Gas Temperature (K)
Case 1	368.1
Case 2	364.7
Case 3	360.6
Case 4	358.7
Measurement	358.4

From the previous four cases, it is evident that most of the heat loss occurs before the gas enters the spray drying tower; therefore it is important to measure the gas temperature at the inlet of the tangential-entry nozzles. A new experimental run was carried out by Ahmadian (2013) at P&G, in which the gas inlet temperature was measured at the tangential-entry inlets in addition to the temperature in the inlet gas duct. For the measurement of hot gas temperature at the tangential-entry nozzles, thermocouples were placed inside each of the inlet nozzles. By assuming equal mass flow distribution through each of the tangential-entry nozzles, the average inlet gas temperature entering the tower was calculated. In this experimental run, the amount of cold air entrained from the bottom of the tower was also measured by Ahmadian (2013) using a hot wire anemometer, which is found to be 4.3% of the mass flow of the hot gas. Hence the assumption of 5% of mass flow of hot gas used as entrained air used in the previous simulation cases (Case 1 and 4) was a reasonable approximation. The experimental conditions and the measured gas temperatures, and measured mass flux of entrained air are listed in Table 6.11.

Table – 6.11: Spray drying tower operating conditions under non-isothermal condition (Ahmadian, 2013).

Parameter	Value
Hot gas temperature at the duct	403.0 K
Average hot gas temperature at the tangential-entry nozzles	388.8 K
Exhaust gas temperature	381.2 K
Ambient temperature	299.5 K
Mass flux of hot gas	1.224 kg/m <sup>2</sup> s
Mass flux of entrained air	0.052 kg/m <sup>2</sup> s (4.3% of hot gas)
Pressure at the outlet	-25.0 Pa

For the new non-isothermal CFD simulation case, the operating conditions listed in Table 6.11 are used. From this table, it is observed that the actual gas temperature at the tangential-entry inlets is 14.2 K smaller than the gas temperature measured in the hot gas supply duct. The measured average hot gas temperature (Ahmadian, 2013) at the tangential-entry nozzles is used in the simulation cases as the hot gas inlet temperature. To evaluate the role of wall roughness in impacting the gas temperature profiles, three simulation cases have been carried out. In Case 5, 6 and 7, the influence of wall roughness is evaluated in predicting the gas temperature profiles. In Case 5, 6 and 7, a roughness height of 2 mm, 1 mm and 0.5 mm is specified respectively. To model heat loss from the wall, a constant thermal conductivity of 0.04 W/mK is specified throughout the tower height.  $Pr_t$  value of 0.85 is used in these simulation cases.

Figure 6.38 is a plot of measured temperature profiles (Ahmadian, 2013) and a comparison with temperature predictions from Case 5, 6 and 7 at various dimensionless heights, with 0 representing the tower bottom and 1 representing the tower top. From a comparison of measured temperatures in Figure 6.38 with Figure 6.30, it is observed that the measured temperature plots are qualitatively similar i.e., a lower temperature in the centreline in the bottom region of the tower, which becomes more like a plug-flow profile as the gas moves upwards. The presence of roughness at the wall contributes significantly on the decay of swirl in the tower, which influences both tangential and

axial velocity profiles hence the mixing of the cold (entrained) air and the hot gas. Similarly, the turbulence intensity in the central region of the tower decreases with an increase in swirl intensity but gets amplified in the near-wall region (Figure 6.25 in Section 6.1). This particularly influences the gas temperature profiles in the bottom region of the tower. At a dimensionless height of  $z/Z=0.22$ , the CFD simulation run with a roughness height of 2 mm gives a higher temperature in the central region, while 0.5 mm roughness height gives an underprediction. A roughness height of 1 mm gives a closer agreement with the measurement. Hence the mixing of the entrained air stream and the hot gas becomes more rapid (resulting in a flatter temperature profile) with decreasing swirl in the gas flow. At  $z/Z=0.45$ , 2 mm and 1 mm roughness height cases predict a relatively flat temperature profile in the central region while 0.5 mm predicts a slightly lower temperature in the central region but it is greater than the measured temperature. At  $z/Z=0.85$ , all the CFD simulation cases as well as measured data gives a flat temperature profile, however, the simulations overpredict the temperature by about 2 K. Overall, the simulation case with a roughness height of 1 mm gives the best agreement with experimental data.

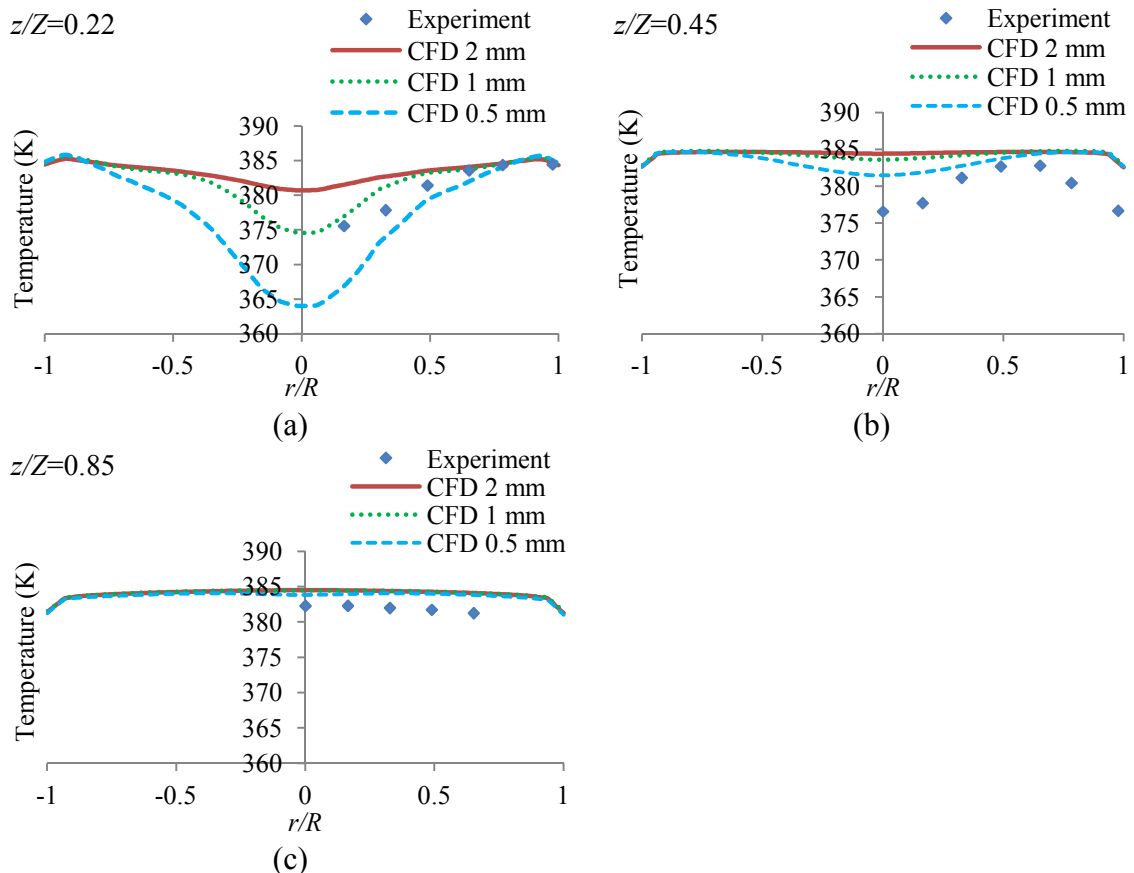


Figure – 6.38: Temperature profiles at different axial locations, a comparison of non-isothermal cases with different wall roughness with experimental data.

### **6.2.11 Conclusions**

CFD modelling work has been carried out to validate the predicted temperature profiles with available measurements for gas temperature within the spray drying tower and to study heat loss. In the first four non-isothermal simulate ion cases, different cold air entrainment rates, wall thermal conductivity and inlet gas temperatures were used to give the best prediction with the measured temperature profile. It was found that the case in which a lower inlet gas temperature was used gave the best prediction, while the other cases predicted a higher gas temperature compared to the measured temperatures. This implies that most of the heat loss takes place due to poor insulation in the inlet gas distribution duct and in the gas distribution ring that results in the lowering of the inlet gas temperature at the tangential-entry nozzles, which can be minimised by replacing the damaged insulation in the inlet gas duct and in the gas distribution ring. The discrepancy in using the measured inlet duct temperature could also be partly due to the fact that inside the duct, a single temperature measurement at the centre of the duct is made, which may not represent the true mean temperature of the gas flow in the duct. It is important to measure the gas temperature at the inlet of the tangential-entry nozzles, hence in the available data for the second experimental run, the measured temperature at the inlet of the tangential-entry nozzles was specified as the hot gas inlet temperature in the simulation and the effect of wall roughness on the predicted temperature profiles was evaluated. It was found that the wall roughness influences the gas temperature profiles particularly in the bottom region of the spray drying tower as mixing of cold (entrained) air with the hot gas is dependent on the gas velocity profiles and turbulence intensity, which are influenced by the wall roughness.

## **7. MULTIPHASE CFD MODELLING**

In this chapter, multiphase CFD modelling of spray drying tower is carried out considering isothermal (Section 7.1) and non-isothermal (Section 7.2) conditions. In the isothermal (constant temperature) CFD cases, only the influence of dried detergent particles on the gas phase (comprising air) velocity profiles and vice versa is assessed by considering momentum coupling between these two phases. The heat and mass transfer between the particles and the air is not considered. The effect of the number of particle trajectories on the air velocity profiles is also assessed and the resulting air velocities are compared with the single phase air velocity profiles (modelled previously in Section 6.1.9) to assess how the presence of particles influence the air velocity profiles. In Section 7.2, CFD simulations considering non-isothermal conditions are carried out to determine the gas flow and temperature profiles, the particle trajectories and drying behaviour of the droplets and particles in a complex three-dimensional swirling counter-current gas flow. The simulations consider coupled heat, mass and momentum transfer between the gas phase and the droplets/particles. The influence of particle-wall interaction, drag law and initial droplet size distribution specification on the model predictions is checked by carrying out various CFD simulation cases. A rough-wall collision model is developed and the influence of wall roughness on the particles post-collision trajectories and the heat and mass transfer is evaluated. The predictions are compared with the data collected from the IPP tower, which include measured output parameters (average powder moisture content, temperature and exhaust gas temperature) as well as the gas temperature profiles (wherever available) to assess the predictability of the CFD modelling approach in modelling the counter-current spray drying tower. The results of the plug-flow model (described in Chapter 5) are also compared with the CFD model to assess the validity of plug-flow approach in modelling the spray drying process.

### **7.1 Study of Particle Flow under Isothermal Flow Condition**

To assess the impact of particulate flow on the gas flow field, multiphase CFD simulation of the IPP tower is carried out considering isothermal flow (constant gas temperature) condition and dried particles are injected from the atomiser location. The simulation is two-way coupled in terms of momentum exchange between the dried particles and the air using the Eulerian-Lagrangian approach (described in Section 3.12), and the heat/mass transfer between these two phases is ignored.

### 7.1.1 Numerical Solution Method and Boundary Conditions

#### Continuous Phase

The continuous phase comprises air and the prediction of the air velocity profiles inside the spray drying tower is required so that the trajectories of the discrete phase can be calculated. The discretisation scheme for the continuous phase equations, pressure-velocity coupling and pressure interpolation schemes are kept the same as in the single phase isothermal CFD simulation run (given in Section 6.1.1). The turbulence modelling is carried out using the RST model with linear pressure strain term (LRR), as this gave the best agreement with the measured velocity profiles (Section 6.1.9). The modelling of flow near the wall is carried out using the standard wall functions. In order to take into account the effect of wall surface roughness due to the deposits on the air flow profiles, a roughness height of 2 mm is specified with a roughness constant of 1.0 in the log-law of the wall modified for roughness as this gave the best agreement with the measured velocity profiles (Section 6.1.8). For the gas phase boundary conditions, velocity inlet is specified as the boundary condition at the tangential-entry air inlets and at the entrained air inlet with the values given in Table 7.1. A pressure outlet boundary condition is specified at the air outlet with a value of -300 Pa pressure. The continuous phase is modelled using the steady state assumption.

#### Discrete Phase

For the modelling of the discrete phase (comprising dried detergent particles), a Lagrangian approach with steady state tracking is used. The discrete phase is represented by a number of parcels. Each parcel represents a fraction of the total mass flow of the discrete phase as explained in Section 3.12. The size distribution of dried powder measured using sieves by Martin de Juan (2011) is specified as the initial size distribution in this case. The measured size distribution of powder is fitted using the Rosin-Rammler distribution (Rosin and Rammler, 1933). The size distribution measurement and corresponding curve fit is given in Figure 5.5 (Section 5.5 of Chapter 5). The particles are injected at a dimensionless height of 0.8 in a hollow-cone pattern. The size distribution of powder ranges from 100  $\mu\text{m}$  to 2300  $\mu\text{m}$ . This range of particle sizes is represented using 23 diameters. The particle trajectories are calculated by solving the equation of motion of the particles (equation (3.57)) considering the gravitational, buoyancy and drag forces. The drag coefficient correlation proposed by Morsi and Alexander (1972) is used (equation (3.60)). The turbulence dispersion of

particles (i.e., the dispersion of particles due to the fluctuating velocity components) is considered in the simulation by using the Discrete Random Walk model (Fluent, 2009), described in Section 3.11.4, in which the parcel is tracked multiple times from the same injection location to get a statistically meaningful sample of the trajectory. In this case, the dispersed phase is tracked 3 times. 50 parcels are considered for each size considered. Hence the total number of parcels representing the discrete phase is 3450 ( $3 \times 50 \times 23$ ). To allow the simulation to be completed in a reasonable period of time, the maximum number of length steps allowed for each parcel trajectory is set to 50,000 corresponding to a maximum path length of 50 m. Any parcel trajectory that cannot exit from the computational domain within 50,000 length steps is eliminated from the parcel trajectory calculation and the next parcel is tracked.

The operating condition specifications for the discrete and continuous phases, required to run the simulation case are listed in Table 7.1. The inlet air mass flow is the same as specified in single phase CFD simulation cases in Chapter 6 (Table 6.2 in Section 6.1.2) and the amount of entrained air in this case is also assumed to be 5% of the inlet air mass flow.

Table – 7.1: Input parameters for studying particle flow under isothermal (constant temperature with no heat and mass transfer) condition.

Parameter	Value
Continuous Phase	
Inlet air mass flux	2.215 kg/m <sup>2</sup> s
Entrained air mass flux	0.010 kg/m <sup>2</sup> s (5%)
Air density	1.25 kg/m <sup>3</sup>
Air viscosity	$1.78 \times 10^{-5}$ kg/ms
Discrete Phase	
Particle mass flux	0.232 kg/m <sup>2</sup> s
Particle density	860 kg/m <sup>3</sup>
Spray cone half angle	20°
Particle initial velocity	65 m/s

In the simulation case (referred to as isothermal Case 1), the particle-wall interaction is modelled by specifying a restitution coefficient of 1.0 for both the normal and tangential components to the wall, which is a default value in Fluent. This corresponds to a

perfectly elastic collision with the wall. Hence particles will bounce off from the wall with the same velocity and angle as that of the impact.

### Simulation initialisation and convergence

The multiphase simulation was initialised using the converged solution of isothermal single phase CFD simulation run carried out using the RST model with linear pressure-strain term (Section 6.1.9), the particles are injected at about 50,000 iterations, therefore a peak is observed in the residuals at this point in the plot of residuals given in Figure 7.1. The discrete phase is tracked once after each continuous phase iteration, and the resulting continuous phase source term for the momentum exchange between the two phases (given by equation (3.70)) is updated with each iteration. The convergence criteria for the residuals were set to  $1 \times 10^{-4}$  for the continuity, momentum and turbulence stresses equations. The specified convergence criteria for the residuals could not be met during the simulation run due to the complexity of the air flow patterns and its interaction with the particles. During the multiphase simulation run the level of residuals for continuity, momentum and turbulence stresses were fluctuating in a similar order of magnitude as in the single phase flow (air-only case) simulation residuals. Hence this criterion could not be used as a check for simulation convergence.

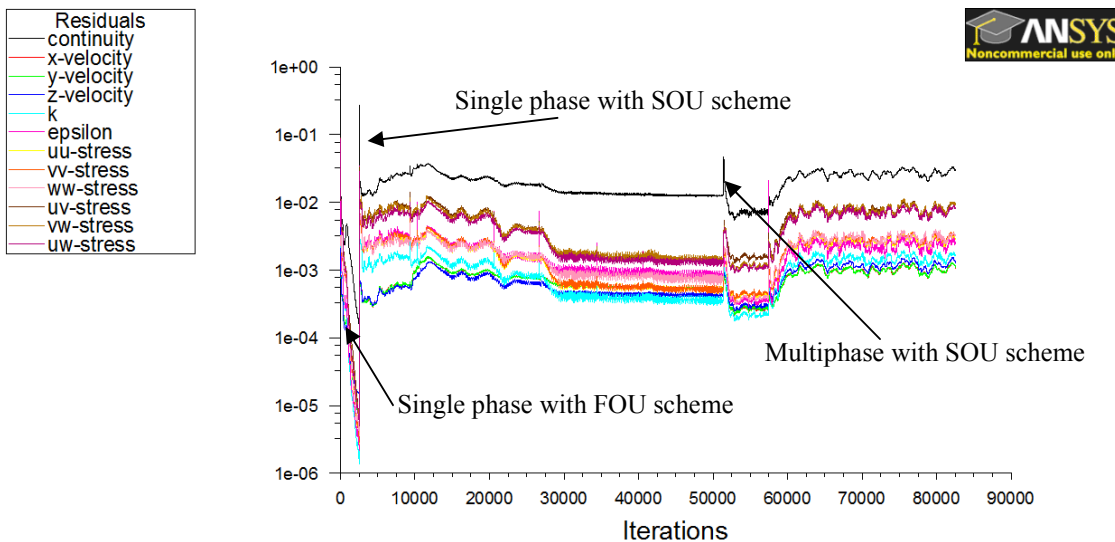


Figure – 7.1: Residuals of convergence for isothermal Case 1.

To ensure that the simulation has reached a steady solution, the area weighted average axial and tangential velocities of the air along the x-axis were monitored at two different heights during the iterations. When the values of these tangential and axial velocities showed fluctuations about a constant mean value, then the simulation was stopped and

the simulation was considered to be converged. Figure 7.2 is a plot of tangential and axial velocity profiles during the simulation run.

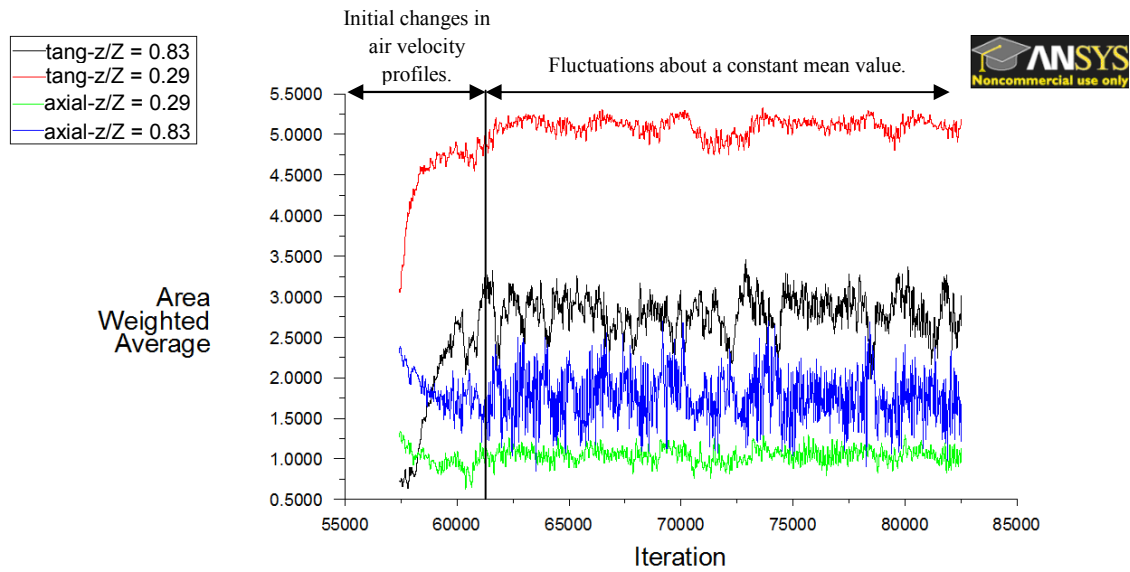


Figure – 7.2: Area weighted average tangential and axial velocity profiles during the simulation run for isothermal Case 1.

Figure 7.3 is a plot of particle trajectories of a selected number of tracks. In the plot of particle trajectories, it is observed that the particle sizes up to  $200\ \mu\text{m}$  get entrained by the gas from the top of the tower. The larger particles strike the wall after being injected into the spray tower and bounce back and reach the other side of the wall. These particles eventually reach the bottom conical region of the tower because of greater momentum compared to smaller particles (up to  $200\ \mu\text{m}$  sizes) and have less influence of drag force acting in the upward direction. As these particles come down the tower, they take up the swirling momentum of the air. The particles start swirling in the bottom conical region of the tower and do not come out from the bottom exit. These particles are swirling at a velocity sufficient to hold the particles in the conical region and the gravitational force acting in the downward direction is balanced by the normal contact force component acting in the upward direction arising from the swirling motion of particles and the drag force acting in the upward direction as depicted in Figure 7.4. This unrealistic behaviour of particles in the bottom conical region of the tower is due to the specification of perfectly elastic collision ( $C_r = 1.0$ ) between the wall and the particles, since the particles gain tangential momentum as they move down due to the momentum exchange with the swirling air flow, and do not lose this momentum upon collision with the wall.

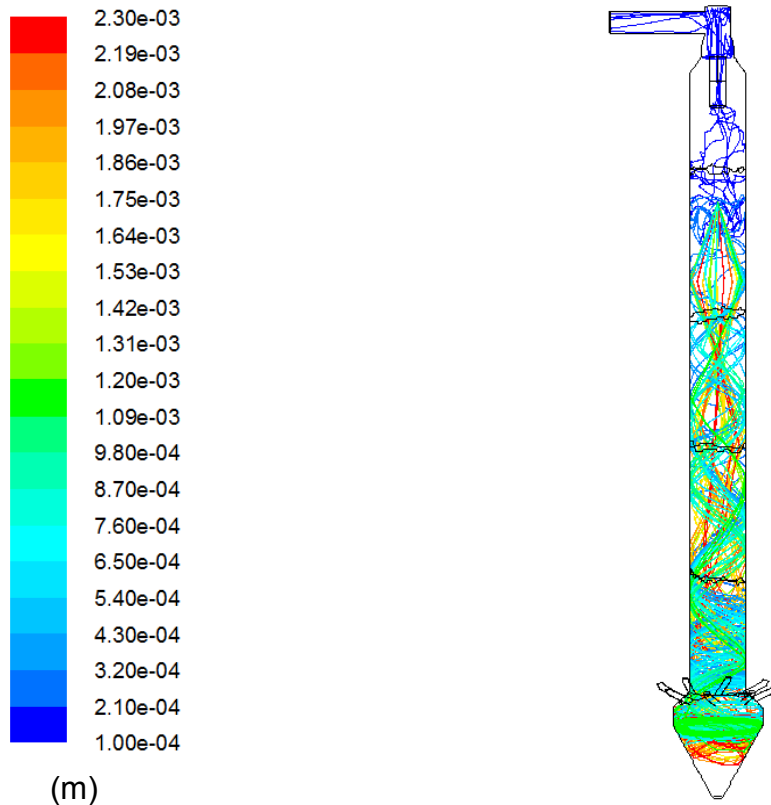


Figure – 7.3: Particle trajectories of different sizes in the spray drying tower coloured by diameter ( $C_r = 1.0$ ).

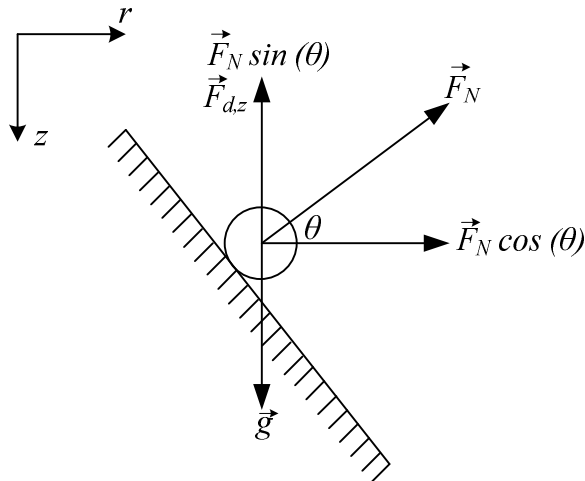


Figure – 7.4: Forces acting on a particle in the bottom conical region of the tower.

The above simulation case shows unrealistic particle behaviour since the particles do not come out from the bottom exit of the tower. To validate that this is due to the specification of elastic collision consideration between particle and wall, another simulation run is carried out (referred to as isothermal Case 2) with a wall restitution coefficient ( $C_r$ ) value of 0.4 for both normal and tangential components. This value of  $C_r$  is based on the measurement of restitution coefficient of spray dried detergent powder particles determined by Hassal (2011) in which a typical value obtained for

dried particles was 0.4. Figure 7.5 is a plot of particle trajectories coloured by particle diameter. It is observed that the larger particles exit from the bottom outlet of the tower. Since the particles in this case do not exhibit elastic collision, therefore a collision of particle with the wall results in loss of particle momentum, hence the swirling velocity of particles does not increase to a value such that the normal contact force component can be balanced by the gravitational force. Therefore particles in this case exit from the bottom outlet. At the end of each discrete phase iteration, typically 10-20 parcels out of 3450 parcels get entrapped into the recirculation zones in the tower and get eliminated from the calculation domain without exiting from the tower. The smaller particles (up to 200  $\mu\text{m}$ ) get entrained by the air and leave the tower from the top outlet as in the isothermal Case 1.

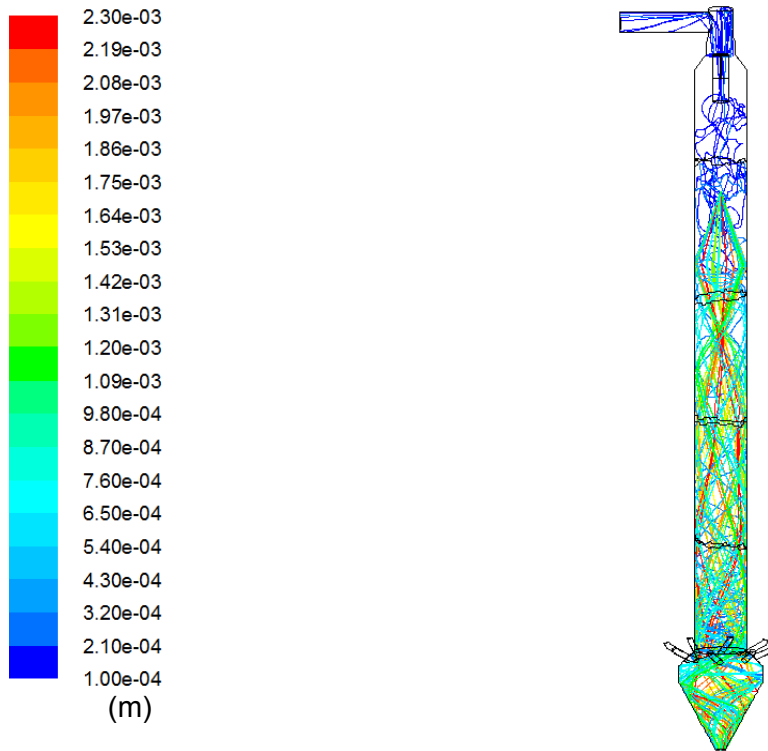


Figure – 7.5: Particle trajectories of different sizes coloured by diameter ( $C_r = 0.4$ ).

Figure 7.6 is a plot of axial velocity of the air at different dimensionless heights for this case. The air velocity profiles for the multiphase simulation case are compared with the single phase CFD simulation case (LRR-RST model) carried out in Section 6.1.9 (both cases have the same boundary condition specifications for the air mass flow). It is observed in Figure 7.6 that the particles have a significant impact on the axial velocity profiles along the tower height. Without the particles, at  $z/Z = 0.29, 0.47$  and  $0.56$ , the air flow very close to the wall is a maximum, and it is minimum in the annular region of the tower but in the presence of particles at all dimensionless heights, the peak value of

mean axial velocity shifts towards the annular region because the particles exert momentum on the air, additionally the axial velocity is lower in the centreline of the tower. At  $z/Z = 0.29$  and  $0.47$ , in the axial velocity profiles without particles, negative velocity is observed in the annular region (at  $r/R = 0.3$  to  $0.4$ ) as a consequence of strong swirl, this is not observed in the velocity profiles with particles. At  $z/Z = 0.74$  and  $0.83$ , without the particles, the maximum value of air velocity lies at the centreline, whereas in the presence of particles, it is minimum at the centreline at  $z/Z = 0.74$  and at  $z/Z = 0.83$ , the axial velocity profile in the presence of particles resembles closely to a parabolic velocity profile observed in pipe flow without swirl. This position is above the particle injection location. Hence the flow of particles is fairly dense to impact the axial velocity profiles of the air at all the reported locations.

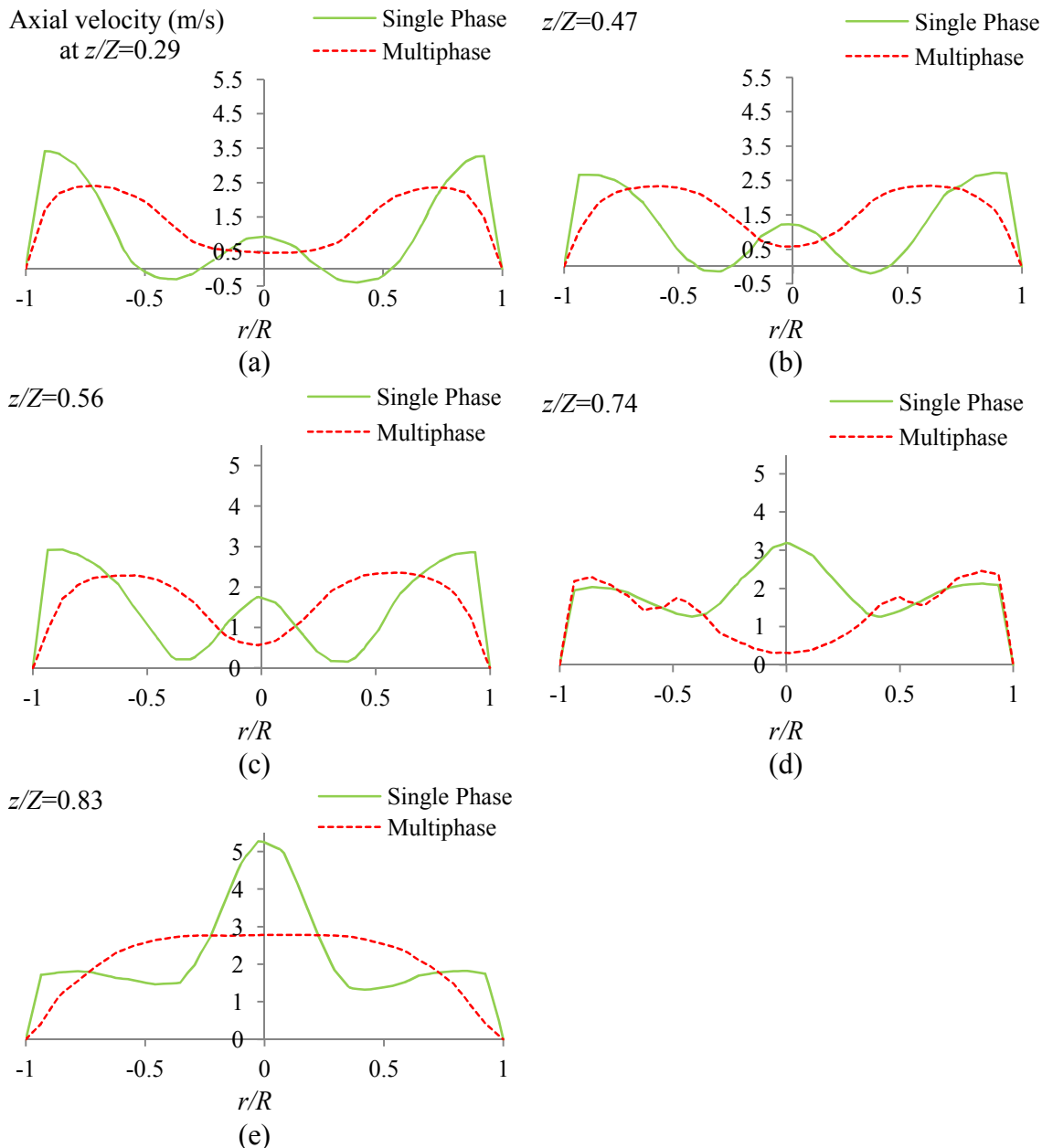


Figure – 7.6: Comparison of single phase and multiphase axial velocity profiles.

Figure 7.7 is a plot of mean tangential velocity profiles at different dimensionless heights for this case and a comparison is made with the single phase CFD simulation carried out in Section 6.1.9. It is observed at all the locations that the magnitude of tangential velocity is significantly reduced due to the presence of particles that take up the swirling momentum of the air. The tangential velocity of air with particles at  $z/Z = 0.29$  and  $0.47$  is about 2 times smaller than that without particles. As the air goes up in the presence of particles, the reduction in the tangential velocity occurs much faster. The particles are injected at  $z/Z = 0.8$ , therefore, at locations close to and above the nozzle (i.e.,  $z/Z = 0.74$  and  $0.83$ ), the tangential velocity is very close to zero because the swirling momentum is transferred to the particles. The Rankine vortex profile is also not observed at these locations.

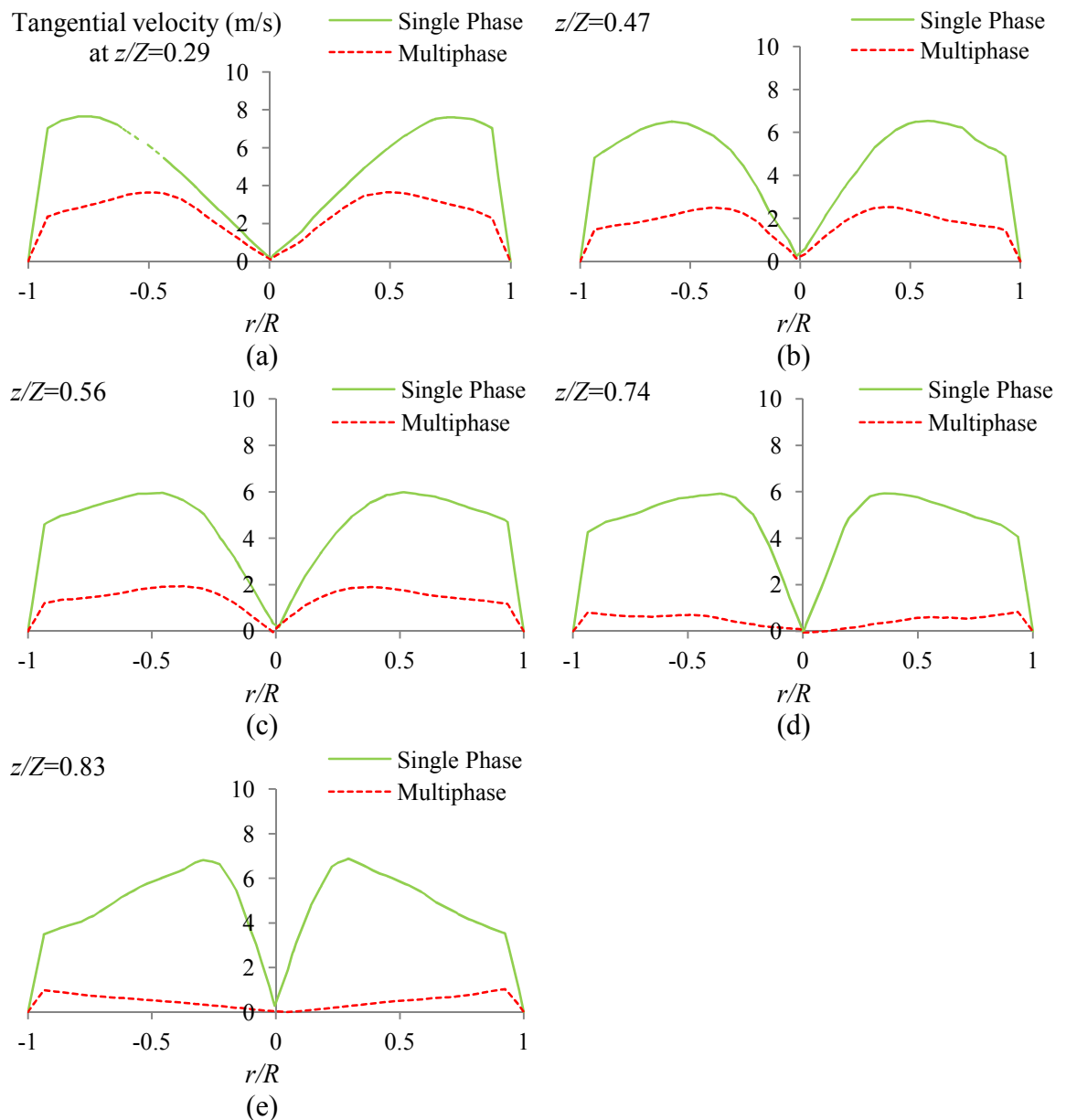


Figure – 7.7: Comparison of single phase and multiphase tangential velocity profiles.

Figure 7.8 is a plot of swirl number along the dimensionless tower height in the cylindrical region of the tower with 0 at the bottom and 1 at the top of the tower. The swirl number for this case is compared with the swirl number for the single phase CFD simulation run (LRR-RST model with  $k_s = 2$  mm). As observed in the tangential velocity profiles (Figure 7.7), the presence of particles lowers the tangential velocity and hence the swirl number is smaller, the decay in swirl number compared to the single phase simulation case is faster, because a significant amount of air tangential momentum is taken up by the particles as they move down in addition to the frictional resistance from the rough wall.

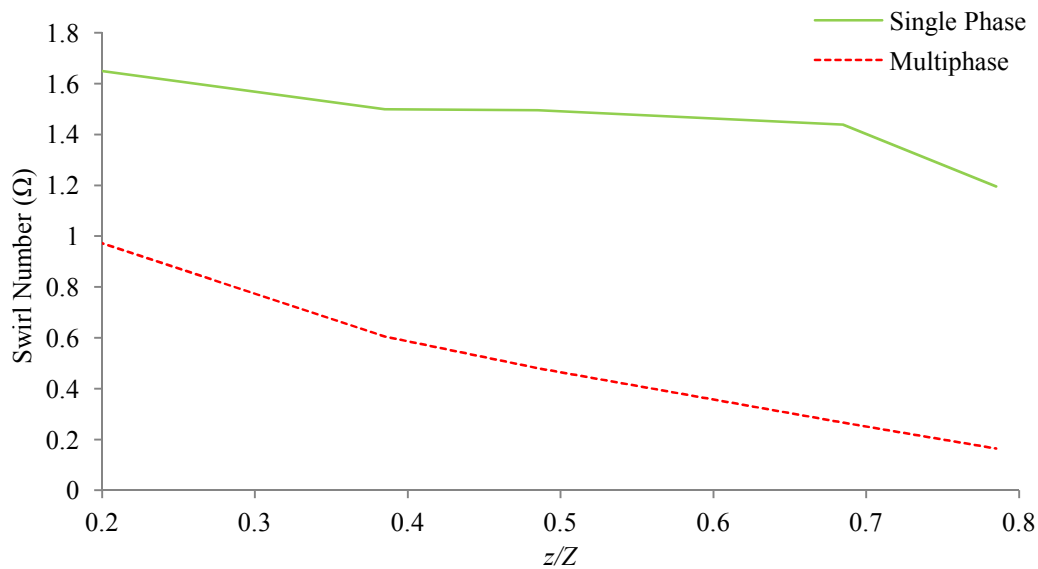


Figure – 7.8: Swirl number comparison along the tower height.

Figure 7.9 is a plot of air mean velocity magnitude. It is observed that the air mean velocity profiles are symmetrical along the tower height both above and below the particle injection location. Below the particle injection location, in the cylindrical region of the tower, a low air velocity magnitude is observed in the central region of the tower as well as along the wall. The velocity magnitude is higher in the annular region of the tower. A high velocity magnitude exists at the particle injection location, this indicates that the particles exert large momentum on the continuous phase near the injection location and change the air flow pattern in this region. The velocity magnitude is a maximum near the top outlet as the air passes through a narrow tube (vortex breaker) and eventually goes to the exhaust duct.

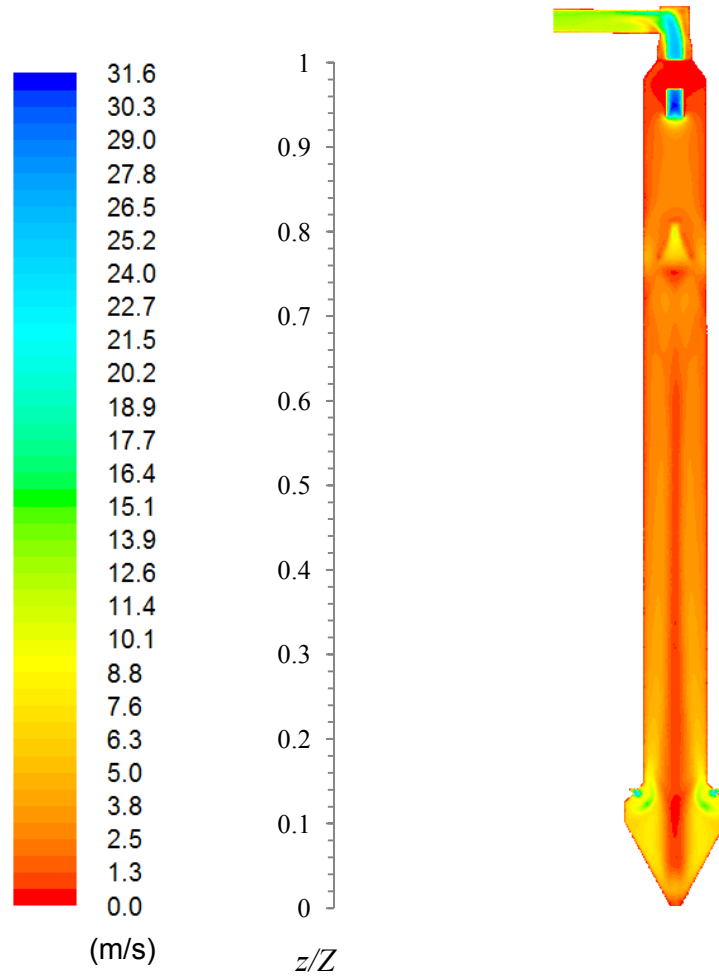


Figure – 7.9: Contour plot of air velocity magnitude.

Figure 7.10 is a vector plot of magnitude of mean air velocity close to the particle injection location. It is observed that the air gets entrained into the spray of particles due to a high momentum exerted by the particles on the air, and results in the formation of a jet of air in the downward direction. Recirculation zones are observed at the edges of the jet.

Figure 7.11 is a contour plot of air turbulence intensity (defined using equation 6.2) for the isothermal multiphase case compared with the single phase isothermal case. In the case of multiphase simulation, high turbulence intensity is observed near the particle injection location, this is caused by the recirculation of air due to high momentum exerted by the particles. The turbulence intensity above the particle injection location is greater compared to the turbulence intensity below the spray in the cylindrical section of the tower. Above the particle injection location, only smaller particles (up to  $300\ \mu\text{m}$ ) flow (Figure 7.5) and these particles may enhance the air flow turbulence. The swirl intensity above the particle injection location is also smaller which may also make the

flow more unstable and result in increased turbulence intensity. Overall, the turbulence intensity is increased in the presence of particles.

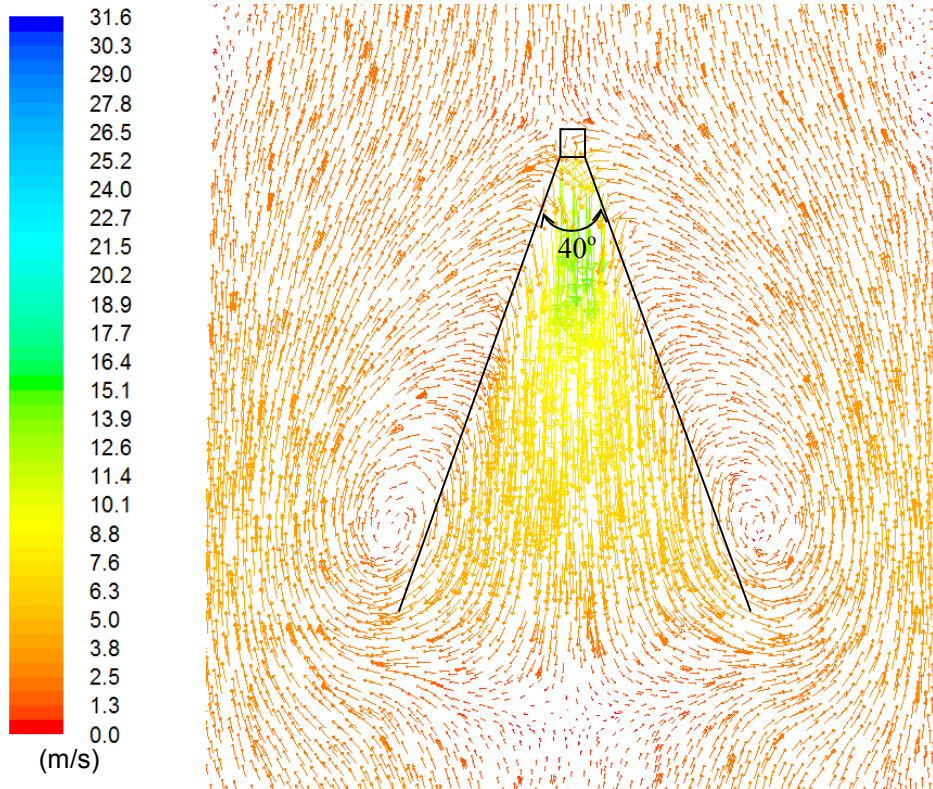


Figure – 7.10: Vector plot of air velocity magnitude near the nozzle.

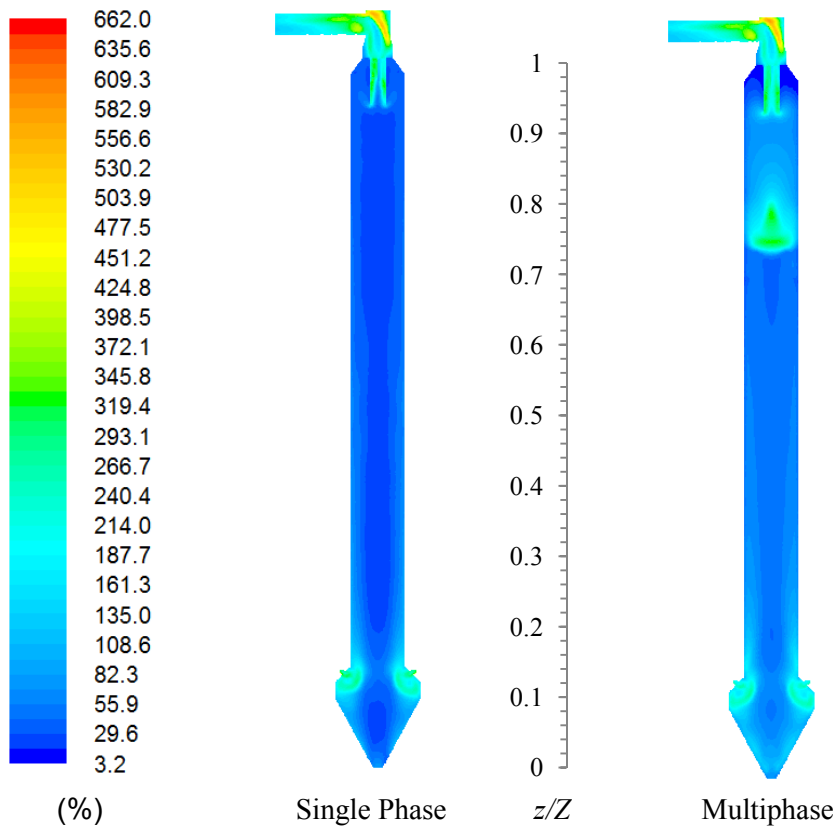


Figure – 7.11: Contour plot of turbulent intensity.

The effect of number of stochastic tracks for each parcel for tracking the dispersion of particles due to turbulence on the residence time of particles and on the velocity profiles of the continuous phase is checked by varying the number of stochastic parcel tracks from 1, 3 and 5. This also increased the total number of parcels tracked to 1150, 3450 to 5750 respectively and the computational time was also increased accordingly. Figure 7.12 is a comparison of the plot of average residence time of all the particles of a particular diameter collected from the bottom of the tower for the three cases.

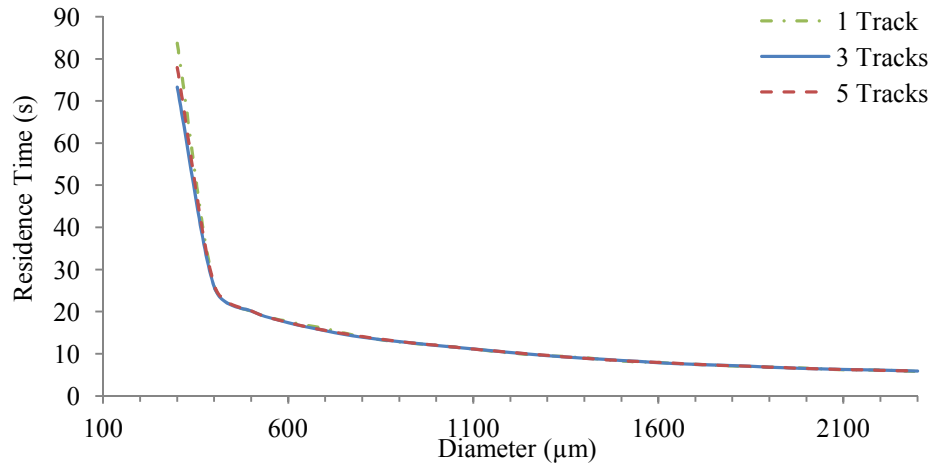


Figure – 7.12: Residence time of particles collected from the bottom of the tower.

In the plot of residence time of particles collected from the bottom of the tower, it is observed that the smaller particles have greater residence time compared to larger particles. The initial size range specified at the particle injection location is from 100  $\mu\text{m}$  to 2300  $\mu\text{m}$ . However, 100 and 200  $\mu\text{m}$  particles exit from the top of the tower because smaller particles get entrained by the air. The residence time of larger particle sizes (400  $\mu\text{m}$  and greater) in all three cases is very similar and is independent of the number of parcel tracks used for stochastic tracking. This is because the larger particles have greater momentum and show less influence of the effect of particle dispersion due to turbulence. For the case in which 1 parcel track is used for stochastic tracking, the residence time of the smallest particle that exits from the bottom, i.e., 300  $\mu\text{m}$  particle is slightly greater than the other two cases. Overall, the number of tries for stochastic tracking and hence the number of total tracks do not influence the residence time of particles collected from the bottom of the tower.

Figure 7.13 is a plot of size distribution of particles collected from the bottom of the tower for all three cases. It is observed that the size distribution of particles exiting from the tower bottom is similar in all the cases. Total mass flux of the particles injected was 0.232  $\text{kg}/\text{m}^2\text{s}$ . The particle mass flux collected from the bottom of the tower is 0.176

kg/m<sup>2</sup>s and the mass flux of particles entrained by the air is 0.051 kg/m<sup>2</sup>s. Hence a total of 0.227 kg/m<sup>2</sup>s of powder exits from the tower, while the remaining 0.005 kg/m<sup>2</sup>s of the powder mass flux gets entrapped in the spray drying tower and is unable to get out from the outlets within the maximum number of length steps specified for each parcel trajectory tracking. The entrapped particles form only 2.2% by mass of the total powder injected. Hence the specification of 50,000 steps for tracking parcel trajectories is satisfactory for a reasonable mass conservation of the discrete phase.

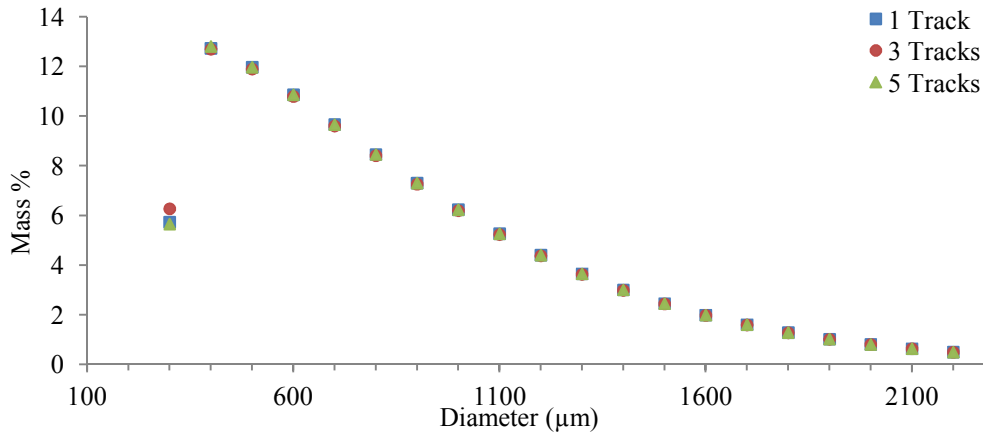


Figure – 7.13: Size distribution of particles collected from the bottom.

Figure 7.14 is a plot of size distribution of particles collected from the top of the tower. Particle sizes up to 300 μm get entrained by the gas and exit from the top of the tower. However, some of the 300 μm particles also exit from the bottom of the tower (Figure 7.13). The mass percentage of particles collected from the top is significantly different for the case in which 1 track is used, but in the case of 3 and 5 tracks, it is very similar. The size distribution of particles collected from the bottom of the tower is not significantly influenced by the number of tracks (Figure 7.13), but the smaller particles that exit from the top of the tower, show sensitivity towards this parameter, because smaller particles get more influenced by turbulence compared to the larger particles. Hence 3 stochastic parcel tracks are sufficient.

Figure 7.15 is a comparison of mean axial velocity profiles of the air for 1150, 3450 and 5750 parcel trajectories using 1, 3 and 5 tracks respectively for stochastic tracking at different dimensionless heights from bottom to top. It is observed that the axial velocities in the region below the nozzle (from  $z/Z=0.29$  to 0.56) are similar. The locations  $z/Z=0.74$  and 0.83 lie above the particle injection location. Above the particle injection location, smaller particles sizes (up to 300 μm) get entrained by the gas and show greater influence of turbulence on the trajectories, therefore, above the injection

location, the axial velocity profiles show a slight dependency of the number of tracks on the simulation results. However, the difference in the axial velocity profiles above the injection location is not significant.

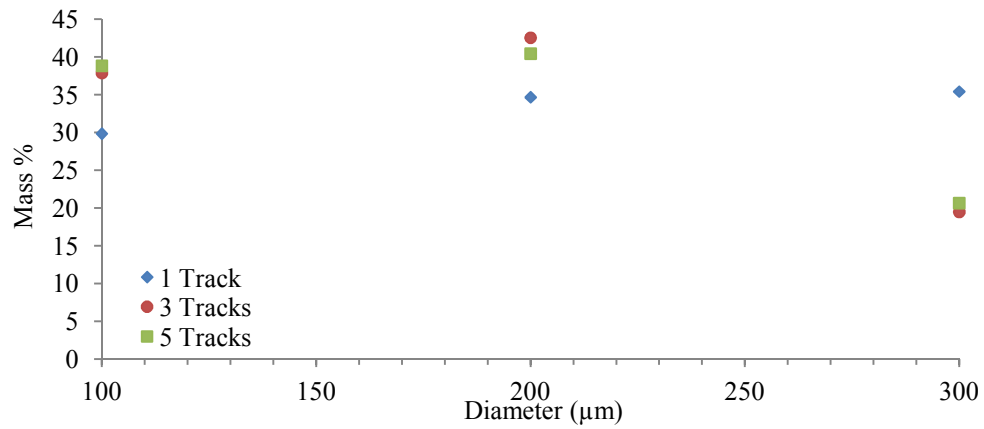


Figure – 7.14: Size distribution of particles collected from the top of the tower.

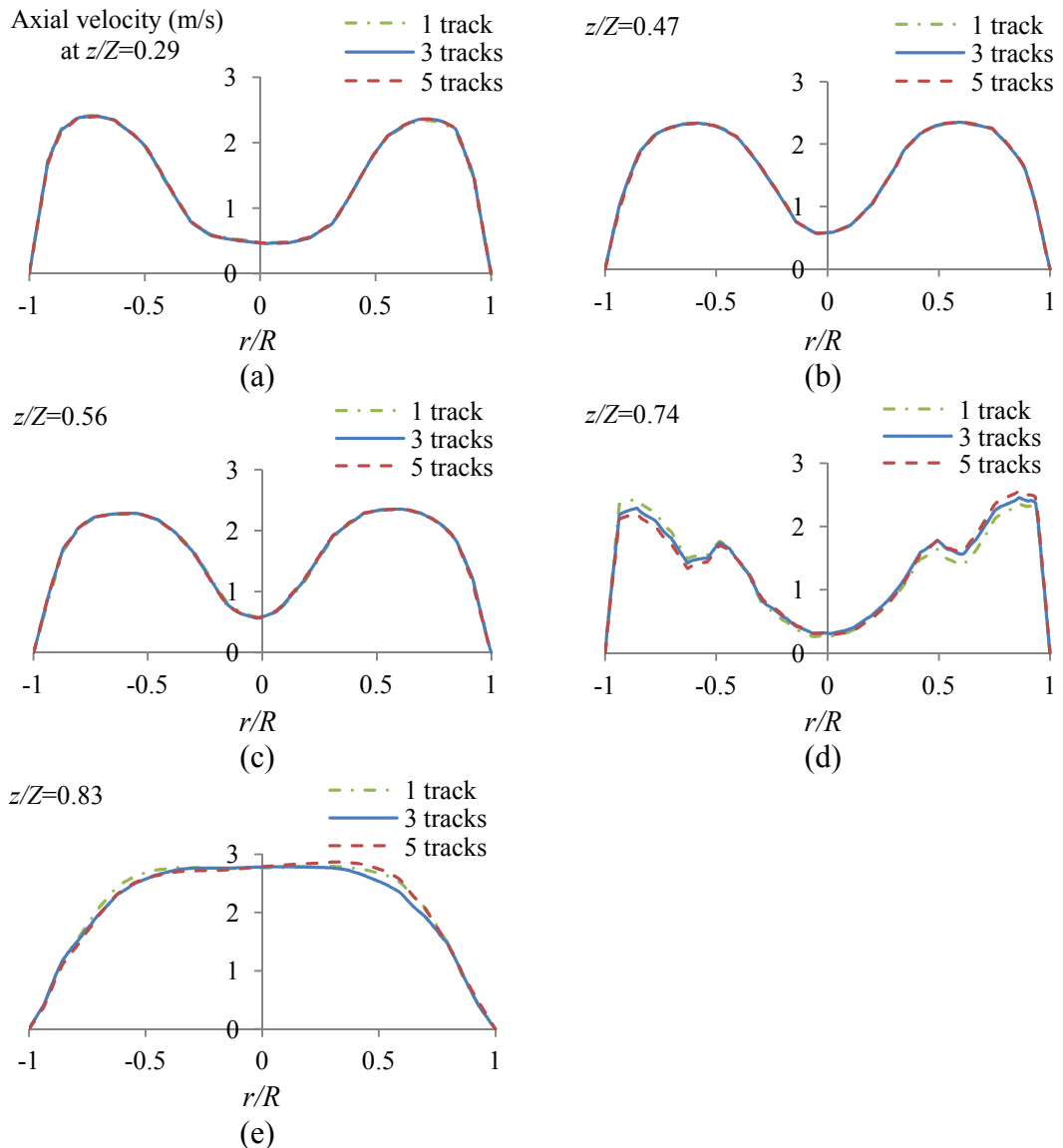


Figure – 7.15: Mean axial velocity profiles of the air at different heights.

### 7.1.2 Conclusions

Isothermal, multiphase CFD simulation of spray drying tower is carried out considering dried particles in the tower and momentum exchange between the particles and the air to study the impact of particles on the gas velocity profiles. It is found that the suitable convergence criteria are to monitor the weighted axial and tangential velocity components at different heights. The smaller particles (up to 300  $\mu\text{m}$ ) get entrained by the air and exit from the top of the tower while the larger particles ( $>300 \mu\text{m}$ ) in the case of elastic particle-wall collision keep rotating in the conical region and do not come out of the tower. Hence this condition cannot be used for particle-wall interaction. The restitution coefficient of 0.4 measured by Hassal (2011) was used in another simulation run, in which it is observed that all larger particles come out from the bottom exit of the tower. The axial and tangential velocities of the air in the multiphase simulation case are compared with single phase air velocity profiles. It is found that the presence of particles significantly impact the velocity profiles of the air. Hence two-way momentum coupling is required for the simulation of spray drying process. The influence of the number of parcel trajectories and the number of tracks (used for stochastic tracking) on the residence time of particles is also checked. It is found that 3450 parcels with 3 tracks for the stochastic tracking are sufficient for this investigation. Total 50,000 length steps per parcel is allowed in the computational domain before its trajectory is eliminated from the calculation if the parcel does not exit from the domain, which gives a discrete phase mass balance error of about 2%. In a comparison of turbulence intensity of the single phase non-isothermal case with multiphase case, it is found that the turbulence intensity is increased by the presence of particles due to the momentum exerted by the particles on the gas phase.

## **7.2 CFD Simulation of Spray Drying Process**

In this section, the assumption of isothermal flow condition is relaxed and the droplet/particle flow is studied by considering heat, mass and momentum transfer between the discrete phase (comprising droplets/particles) and the continuous phase (comprising gas). The gas phase is assumed to follow ideal gas law. The convergence criterion is kept the same as in the isothermal multiphase simulation run, additionally; the mass weighted average gas temperature at the exhaust is also monitored with iteration as this indicates the amount of heat exchange with the discrete phase and could be used to assess the level of convergence of the simulation run. For the gas phase, in addition to the continuity, momentum, Reynolds stresses, turbulence kinetic energy and turbulence dissipation rate, additional transport equations are also solved, i.e., the energy transport equation for the heat transfer between the discrete phase and the continuous phase and the species transport equation for the transport of species. Heat loss from the column to the surrounding atmosphere is also taken into account in the simulation by considering radial thermal conduction through the insulated wall with the inside of the wall containing a uniform 2 mm thick layer of the deposits. The modelling of heat loss through the wall is explained in Section 6.2.1. This is specified in the CFD simulation using Fluent UDF feature. The wall conditions used for the calculation of heat loss from the tower are given in Table 6.4 in Chapter 6. Heat transfer due to radiation is not considered in the simulation, both in the calculation of heat loss as well as in the calculation of heat transfer between the discrete and the continuous phases as this is a relatively low temperature system. Several cases are considered to assess the importance of modelling various interactions and specifications on the CFD modelling of spray drying towers. In Cases 1 and 2, the influence of particle-wall interaction on the particle trajectories and heat and mass transfer is evaluated. In Case 3, the effect of thermal boundary condition is evaluated. In Case 4, the influence of non-spherical particle drag law on the residence times is evaluated. In Cases 5 and 6, the influence of initial droplet size distribution on the overall heat and mass transfer is evaluated. In Case 7, a rough-wall collision model is applied to predict post particle-wall collision trajectories and its effect on heat and mass transfer. A summary of all the cases considered in this chapter is given in Table 7.2.

Table – 7.2: Summary of modelling conditions in the CFD simulation cases

Case Name	Input Operating Conditions	Particle-Wall Interaction	Heat Loss Modelling	Drag Law	Droplet Size Distribution
Case 1	Given in Table 7.4	Fixed $C_r$	Based on constant $\lambda_{ins}$ (0.04 W/mK)	Smooth spherical particles	Measured powder PSD (see Figure 5.5)
Case 2	Same as in Case 1	Linear function of $w_l$	Same as in Case 1	Same as in Case 1	Same as in Case 1
Case 3	Same as in Case 1	Same as in Case 2	Based on $\lambda_{ins,calc}$	Same as in Case 1	Same as in Case 1
Case 4	Same as in Case 1	Same as in Case 2	Same as in Case 3	Rough particle drag law	Same as in Case 1
Case 5	Given in Table 5.6	Same as in Case 2	Same as in Case 3	Droplet drag law and smooth spherical particle law	Given in Figure 5.23 (for droplets)
Case 6	Same as in Case 5	Same as in Case 2	Same as in Case 3	Same as in Case 5	Given in Figure 5.23 (for particles)
Case 7	Same as in Case 1	Rough particle-wall model	Same as in Case 1	Same as in Case 1	Same as in Case 1

### 7.2.1 Drying Gas Composition and its Physical Properties

The drying gas contains atmospheric air and combustion products including H<sub>2</sub>O vapours and CO<sub>2</sub> since the air is heated using a direct fired furnace using methane as the fuel. CO<sub>2</sub> is neglected in the drying gas stream since the mass fraction of CO<sub>2</sub> is very small (~0.01). The composition of the drying gas specified in the simulation is given in

Table 7.3. The density of the drying gas is considered to be a function of temperature and composition and is calculated using ideal gas law (equation (3.56)). The viscosity of the drying gas is considered as a linear function of temperature.

Table – 7.3: Specified composition of drying gas at the inlet of the spray tower

Species	Mass Fraction
H <sub>2</sub> O	0.0229
Air (O <sub>2</sub> + N <sub>2</sub> )	0.9771

### **7.2.2 Initial Size Distribution of Droplets**

The experimentally measured size distribution of the dried powder is specified as the initial size distribution of the droplets in Cases 1 to 4. Although the size distribution of the droplets in the spray is expected to be different from the size distribution of the dried product collected from the bottom due to coalescence, agglomeration and breakage of the droplets/particles, but these are not considered in the simulation due to complexities involved in modelling of coalescence, agglomeration and breakage. The size distribution measurement and corresponding curve fit is given in Figure 5.5 in Chapter 5. The sizes vary from 100 microns to 2360 microns. A total 23 discrete sizes are used to represent the droplets of varying sizes. Inter-particle collision is not considered in the simulation.

### **7.2.3 Initial Velocity of Droplets**

The droplets are injected using a hollow cone pressure nozzle atomiser (T3C). The initial velocity of the droplets is calculated using the equation (5.31). It is assumed that the droplets are formed immediately after the slurry exits from the nozzle, i.e. the formation of liquid sheet and its breakup into ligament is ignored. The initial velocity of all the droplets sizes is assumed to be the same. Other researchers (Sharma, 1990; Kieviet, 1997; Huang *et al.*, 2006) have also used equation (5.31) to calculate the initial velocity of the injected droplets from a pressure nozzle atomiser. Equation (5.31) requires the air core radius, which is taken from the data reported by Nelson and Stevens (1961), in which the variation of air-core radius with the spray cone angle is reported. The vendor-provided spray cone angle for T3C pressure nozzle atomiser for water at an operating pressure of 70 bar is 40° (full cone angle), which is used in all the simulation cases.

#### 7.2.4 Droplet Drying Kinetics

The semi-empirical droplet drying model by Hecht (2012) used in the plug-flow spray drying model described in Chapter 5 (equations (5.4), (5.13) and (5.14) for calculating drying rates in different drying stages) is also applied in the multiphase CFD simulations to model droplet drying kinetics. The source term for the enthalpy transport equation (3.53) for the gas phase comprises the heat transported to the droplets/particles which is given by equation (3.71). The source term for the species transport equation comprises moisture that is transported from the droplets/particles into the gas phase as vapours which is given by equation (3.72). The droplet drying model is incorporated into the CFD simulation using User-Defined Function (UDF).

Due to smaller cross-sectional area of the bottom outlet the volume fraction of particles in the cell becomes larger as the particles approach the outlet. A lower temperature of the continuous phase also exists at the bottom outlet due to cold air entrainment at the bottom exit. Hence a high mass fraction of the hot particles get exposed to a very low temperature as they approach the bottom outlet. This results in sudden cooling of the dried particles in this region. Therefore the source term for the heat transfer becomes very large and results in unrealistic temperature in the bottom cone region near the outlet, which causes the simulation to diverge. To overcome this problem, two conditions are imposed to allow the heat transfer to take place in this region. In the first condition, the heat transfer between the discrete and continuous phase is allowed only when the temperature difference between these two phases is less than 15 K. In the second condition, the heat transfer is allowed when the discrete phase volume fraction in the computational cell is less than 2%. The first condition is eventually removed as the particles cool down and gas temperature in this region rises so the temperature difference between the two phases becomes less than 15 K in the region where the solid volume fraction is less than 2%. However, in the computational cells with larger solid volume fraction ( $> 2\%$ ) no heat or mass transfer takes place, this condition exists in the cells very close to the bottom outlet since the area of the bottom outlet is smaller, and this does not have an appreciable impact on the predicted results. This is due to the limitation of the Lagrangian approach as it considers the discrete phase as a point source (occupying no volume) in a computational cell and hence not valid approach in the regions containing high volume fraction of the discrete phase in the computational cell.

### 7.2.5 Modelling of Particle-Wall Interaction and Particle Motion

In the previous isothermal simulation cases in Section 7.1, it was found that the particle-wall interaction greatly influences the particles trajectories. For the case in which elastic collision was assumed, the particles did not exit from the bottom outlet. Whereas for the case in which a lower value of restitution coefficient was used, larger particles (>200  $\mu\text{m}$ ) exited from the bottom. In this section, the particle-wall interaction is modelled using two cases. In Case 1, a constant value of 0.4 for the restitution coefficient for both tangential and normal components is used. The value of restitution coefficient is based on measurement of restitution coefficient of dried particles by Hassal (2011). In Case 2, the restitution coefficient is specified as a linear function of moisture content varying from 0 for droplets with an initial moisture content, to 0.4 for dried particles in the calculation of both tangential and normal restitution components. The linear relationship between the moisture content and the restitution coefficient is given by:

$$C_r = -0.4 \left( \frac{w_l}{w_{l,o}} \right) + 0.4 \quad (7.1)$$

For Case 2, in the bottom conical region of the tower, a constant restitution coefficient of 0.4 is specified regardless of the particle moisture content, since the wet particles will be carried away by the dried particles as all the particles slide down along the wall in the bottom conical region of the tower. Otherwise, the particles with high moisture content will become almost stationary at the conical wall and will not come out of the tower, which is unrealistic in a steady spray drying operation.

The motion of the droplets/particles, the drag force, the dispersion of particles due to turbulence is modelled in the same way as described in Section 7.1.1 for the discrete phase. Total number of parcel trajectories selected for the simulation run is 3750 with 3 tracks for stochastic tracking, which were found to be sufficient for the multiphase isothermal case in Section 7.1; similarly the maximum number of length steps allowed for each parcel tracking is set to 50,000.

### 7.2.6 Boundary Conditions

For both Case 1 and 2, the hot gas inlet nozzles, the mass flow is specified as the inlet boundary condition. For the gas exhaust, a pressure outlet boundary condition is

specified. The specified temperature and mass flow of the hot gas inlet and the exhaust gas pressure are given in Table 7.4. Some cold air is entrained from the bottom of the spray drying tower due to below atmospheric pressure inside the tower. The exact amount of the cold air entrained in the tower is not known. This is assumed to be 5% of the mass flow of the hot gas and is used as the boundary condition to account for the cold air entrainment, the same amount was assumed in the isothermal single phase simulation cases. The composition of the hot gas is listed in Table 7.3. The cold (entrained) air is assumed to be moisture-free. The initial conditions of the sprayed droplets are listed in Table 7.4. The slurry droplets physical properties are listed in Table 5.1.

**Table – 7.4: Initial and boundary condition specifications (Martin de Juan, 2011).**

Parameter	Value
Continuous Phase	
Drying gas mass flux	0.92 kg/m <sup>2</sup> s
Hot gas temperature	563 K
Entrained air mass flux	0.046 kg/m <sup>2</sup> s (5%)
Entrained air/ambient temperature	293 K
Air outlet pressure	-300 Pa
Drying gas density	Ideal gas law
Drying gas viscosity	Function of temperature
Discrete Phase	
Slurry mass flux	0.21 kg/m <sup>2</sup> s
Slurry temperature	361 K
Spray cone half angle	20°
Dimensionless height of the nozzle (z/Z)	0.67

### **7.2.7 Numerical Solution Method for the Continuous Phase**

The numerical solution method for the continuous phase is kept the same as in the non-isothermal simulation runs, specified in Section 6.2.2.

### **7.2.8 Convergence Criteria**

For all the multiphase simulation runs, initially, the single phase gas velocity profiles were allowed to reach a fairly converged state, after which the discrete phase was

introduced. The simulations were carried out using the under-relaxation factors listed in Table 7.5. The level of residuals specified for convergence is also given in Table 7.5. However, the level of residuals did not reach the required tolerance limit. The plot of residuals for simulation Case 1 is given in Figure 7.16 and that for Case 2 is given in Figure 7.17. Therefore, to ensure that the simulation has converged, the mass weighted exit gas temperature, which is a measure of the amount of heat exchange taking place between the discrete phase and the continuous phase was monitored with iteration, which is given in Figure 7.18 for Case 1 and Figure 7.19 for Case 2. The simulation runs were stopped when the exit gas temperature became fairly constant. Additionally, the area weighted averaged axial and tangential velocities were also monitored (Figure 7.20 for Case 1 and 7.21 for Case 2), which also become fairly stable at the end of the simulation run.

Table – 7.5: The under-relaxation factors used in the simulation and the level of residuals specified and at converged solution.

	Under-relaxation factor	Residual level specified
Pressure/Continuity	0.3	$1 \times 10^{-4}$
Momentum	0.7	$1 \times 10^{-4}$
Turbulent Viscosity	1	-
Species	0.7	$1 \times 10^{-4}$
Turbulent Kinetic Energy	0.8	$1 \times 10^{-4}$
Turbulent Dissipation Rate	0.8	$1 \times 10^{-4}$
Energy	0.7	$1 \times 10^{-6}$
Body Forces	1	-
Density	1	-
Reynolds Stresses	0.5	$1 \times 10^{-4}$
Discrete Phase	0.5	-

- Residuals
- continuity
- x-velocity
- y-velocity
- z-velocity
- energy
- k
- epsilon
- uu-stress
- vv-stress
- ww-stress
- uv-stress
- vw-stress
- uw-stress
- h2o

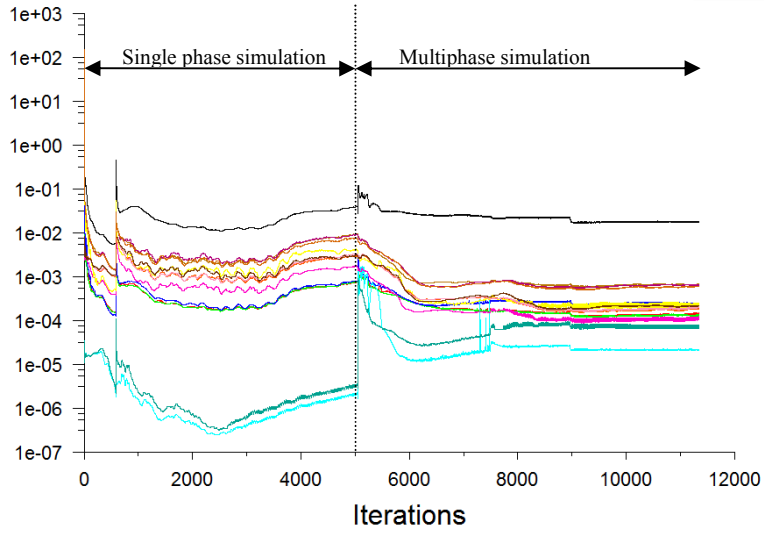


Figure – 7.16: Residuals for Case 1.

- Residuals
- continuity
- x-velocity
- y-velocity
- z-velocity
- energy
- k
- epsilon
- uu-stress
- vv-stress
- ww-stress
- uv-stress
- vw-stress
- uw-stress
- h2o

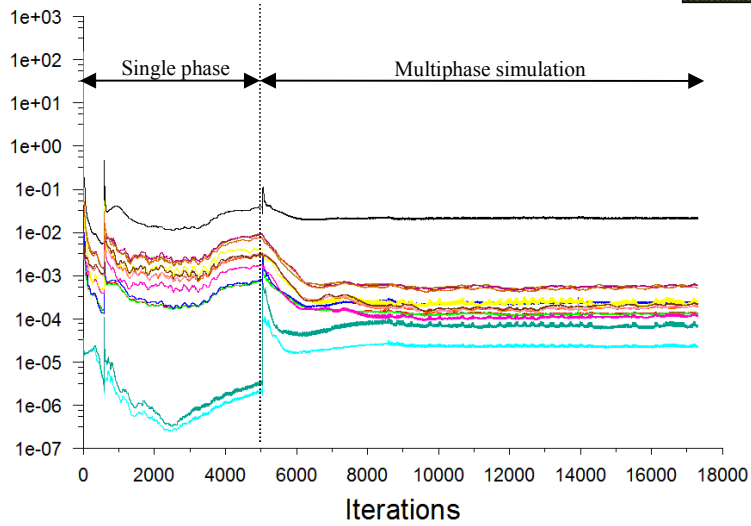


Figure – 7.17: Residuals for Case 2.

- exit-temperature

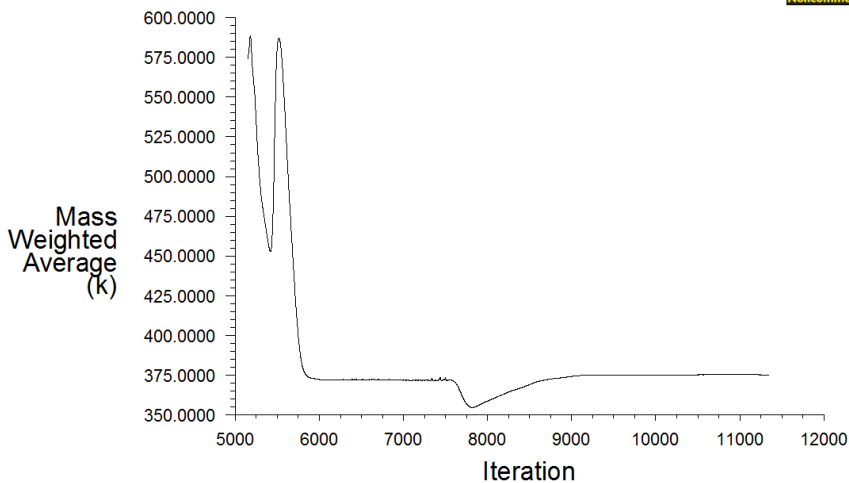


Figure – 7.18: Exhaust gas temperature v/s iteration for Case 1.

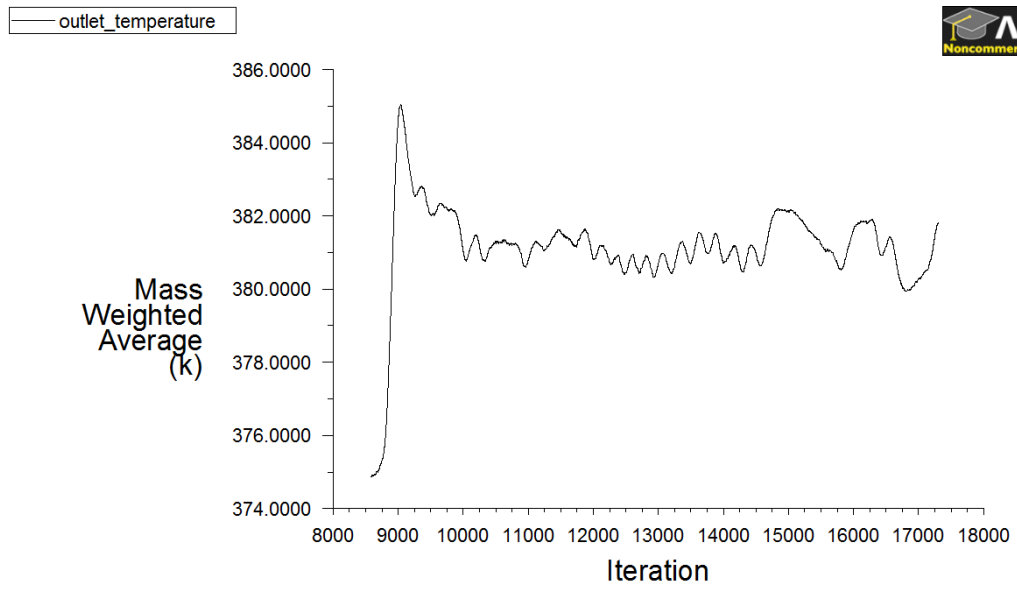


Figure – 7.19: Exhaust gas temperature vs iterations for Case 2.

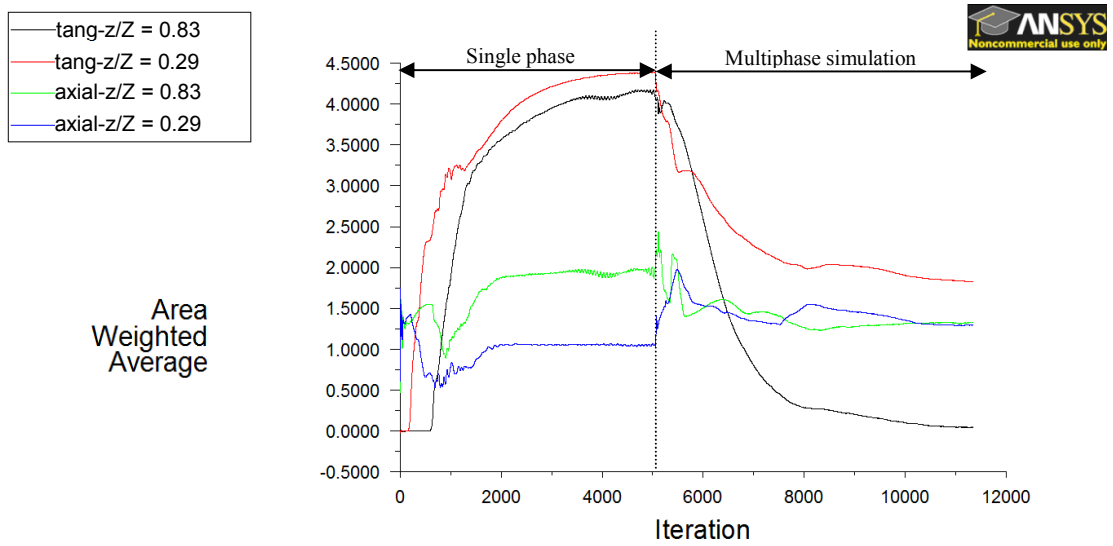


Figure – 7.20: Area weighted average axial and tangential velocities v/s iteration for Case 1.

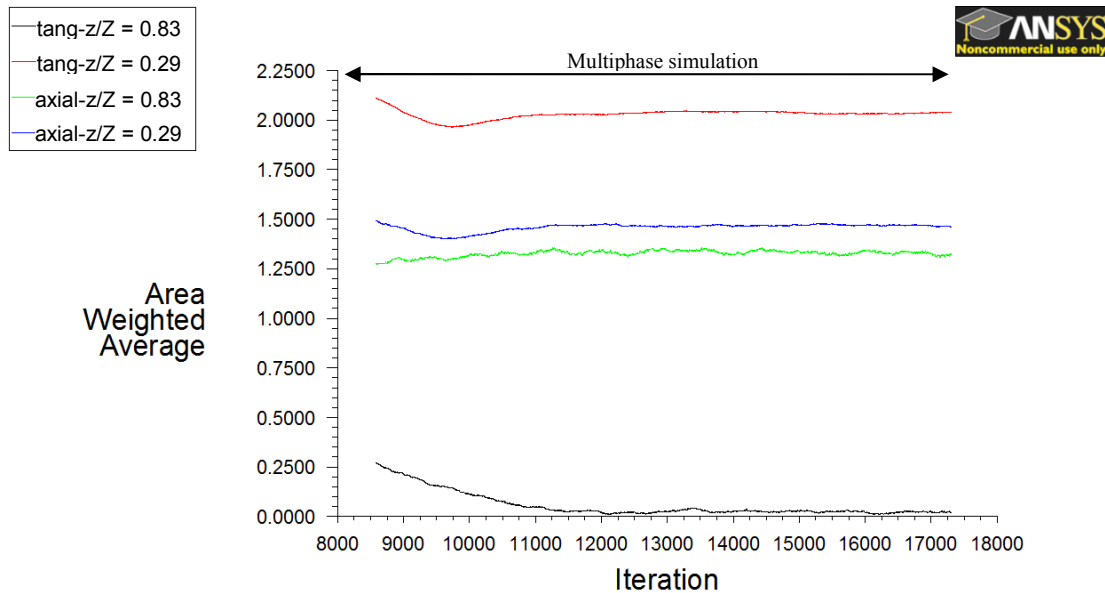


Figure – 7.21: Area weighted average axial and tangential velocity profiles for Case 2.

The overall heat and mass balance at the end of the simulation run was also checked to ensure that the mass and energy balance is satisfied up to a tolerance level. All the injected parcel trajectories were able to escape from the computational domain within the maximum allowed 50,000 length steps. The mass balance for the discrete phase for Case 1 and 2 is given in Table 7.6 and is reported in terms of mass flux i.e., the mass flow divided by the tower cross-sectional area for confidentiality reasons. For Case 1, the total mass balance error is  $4.7 \times 10^{-2}$  % and for Case 2, the mass balance error is -0.58%. The simulations typically took 4 days for the required convergence on a 2.8 GHz quad core processor.

Table – 7.6: Mass balance on the discrete phase.

	Case 1	Case 2
Mass flux of injected droplets ( $\text{kg}/\text{m}^2\text{s}$ )	0.2101	0.2101
Mass flux of powder collected from bottom ( $\text{kg}/\text{m}^2\text{s}$ )	-0.1374	-0.1404
Mass flux of powder entrained by gas ( $\text{kg}/\text{m}^2\text{s}$ )	-0.0171	-0.0164
Vapours evaporated from the discrete phase to gas ( $\text{kg}/\text{m}^2\text{s}$ )	-0.0555	-0.0544
Percentage mass imbalance (%)	$4.7 \times 10^{-2}$	-0.58

Table 7.7 lists the overall enthalpy balance on the tower for Case 1 and 2. The overall enthalpy balance is carried out considering the inlet and outlet streams for the continuous and discrete phase inside the spray drying tower as well as heat loss

(depicted in Figure 7.22). The enthalpy of inlet streams is taken as positive and the enthalpy of outlet streams is taken as negative. The overall enthalpy balance error is the difference of enthalpy in the inlet and outlet streams. The reported enthalpies in Table 7.7 are based on a reference temperature of 288.16 K.

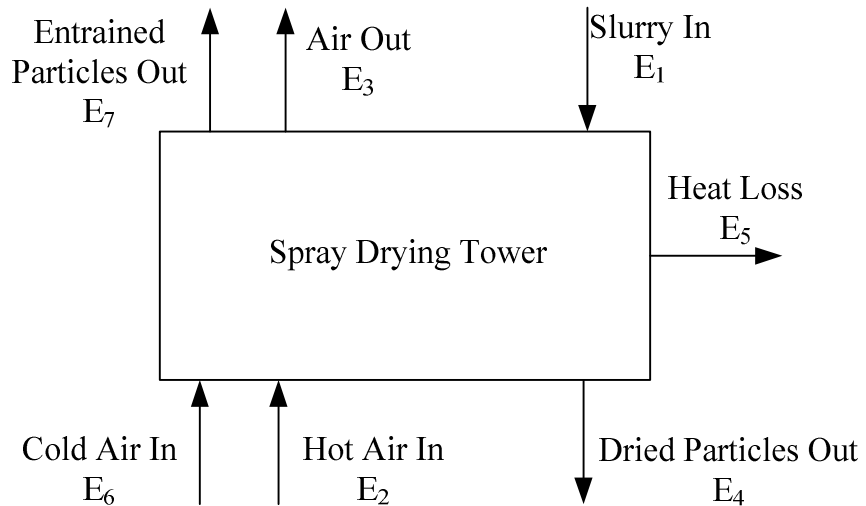


Figure – 7.22: Overall enthalpy balance schematic.

Table – 7.7: Overall enthalpy balance.

	Case 1	Case 2
Slurry inlet $E_1$ (W)	97218.8	97218.8
Hot gas inlet $E_2$ (W)	576581.4	576581.4
Gas outlet $E_3$ (W)	-533499.5	-542956.5
Dried particles outlet $E_4$ (W)	-129716.2	-125399.4
Heat loss $E_5$ (W)	-6600.0	-5430.0
Cold air inlet $E_6$ (W)	1241.3	1241.3
Entrained particles outlet $E_7$ (W)	-7801.3	-8490.3
Total enthalpy inlet ( $E_1+E_2+E_6$ )	675041.5	675041.5
Total enthalpy outlet ( $E_3+E_4+E_5+E_7$ )	-677617.0	-682276.3
Percentage Error (%)	-0.4	-1.07

The overall enthalpy balance error and mass balance error is acceptable in both cases considering the complexity of the process.

### 7.2.9 Simulation Results and Discussion

Figure 7.23 is a plot of a selected number of predicted trajectories of the droplets/particles in the tower, coloured by diameter obtained from Case 1 and 2. The droplets are injected using a hollow cone pressure nozzle atomiser at a dimensionless height of 0.67. The smaller droplets/particles (100  $\mu\text{m}$  and some 200  $\mu\text{m}$ ) are entrained by the gas and flow in the upward direction, whereas larger diameters droplets/particles ( $>100 \mu\text{m}$ ) reach the wall in both the cases. The particles are wet and when they hit the wall, they are more susceptible to deposit there. In Case 1, the droplets/particles trajectories are similar to those computed in Section 7.1 using  $C_r = 0.4$ . In Case 2, i.e.,  $C_r = f(w_l)$ , the particles move along the wall after they strike the wall. In this case, since the values of  $C_r$  are smaller than those of Case 1 (equation (7.1)), the particles lose most of their momentum upon collision with the wall. The smaller particles are observed to move downwards along the wall with a swirling motion as the swirl momentum of the gas is taken up by the particles as they move downwards. Hassal (2011) studied the concentration distribution of particles in the same tower using Particle Image Velocimetry (PIV) technique. The study showed a higher concentration of particles moving along the wall. Hence Case 2 provides relatively more realistic particle trajectories. In the isothermal Cases (Section 7.1), particle sizes up to 300  $\mu\text{m}$  were entrained because the air mass flow was greater and also due to the specification of dried particle density at the injection point, which is smaller than the droplet density.

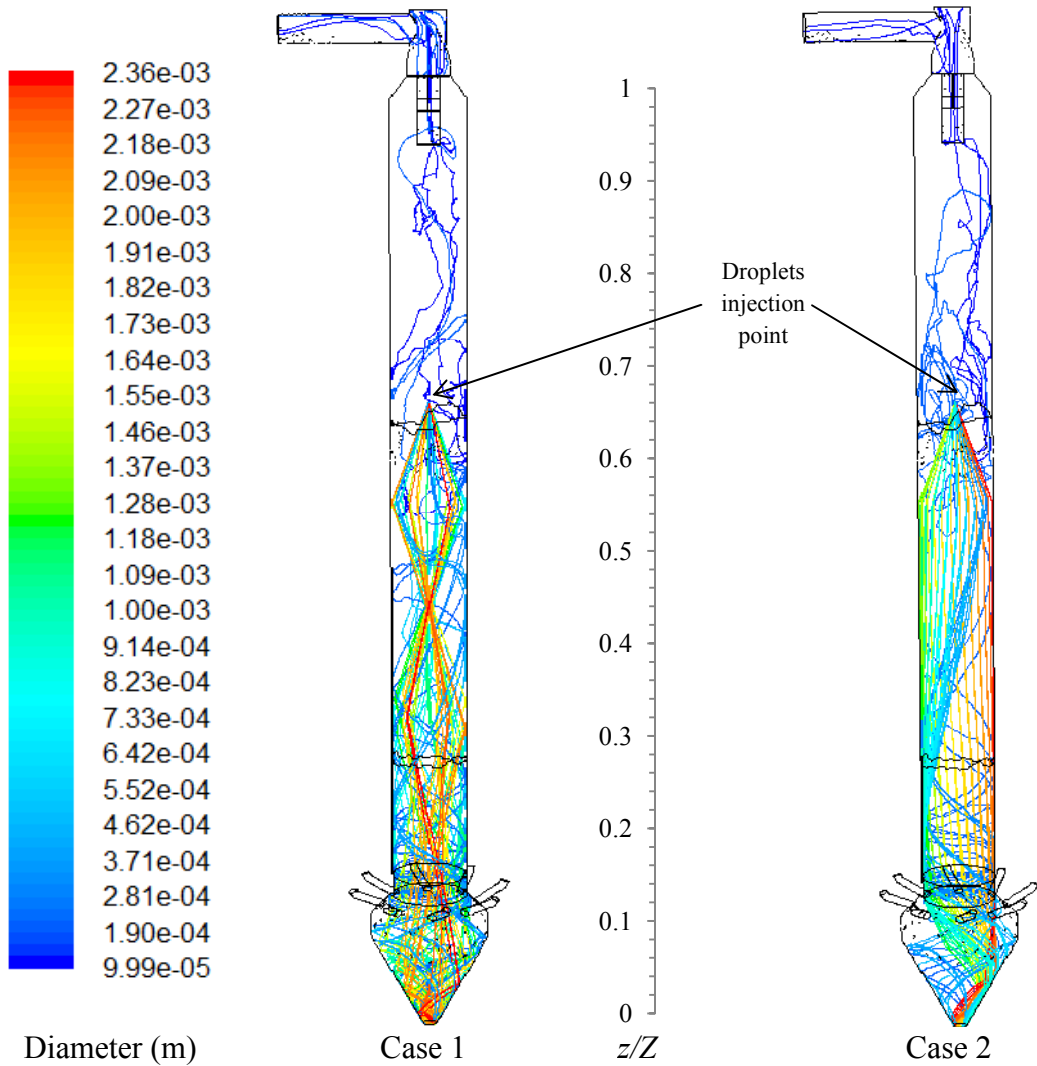


Figure – 7.23: Droplet/particle tracks coloured by diameter.

Figure 7.24 (a) is a plot of size distribution of particles collected from the bottom of the tower and Figure 7.24 (b) is the size distribution plot of particles that get entrained by the gas and exit from the top of the tower, which in both Case 1 and 2 were similar therefore only Case 2 results are plotted. It is observed that all  $100 \mu\text{m}$  particle sizes exit from the top of the tower. A fraction of  $194 \mu\text{m}$  particle sizes exit from the top and the remaining exits from the bottom of the tower. All particle sizes greater than  $194 \mu\text{m}$  diameter exit from the bottom of the tower. The entrained particles comprise mostly of  $100 \mu\text{m}$  particle sizes. A mass balance for the discrete phase along with the mass flow of particles that exit from the top and bottom of the tower for both Case 1 and 2 is given in Table 7.6.

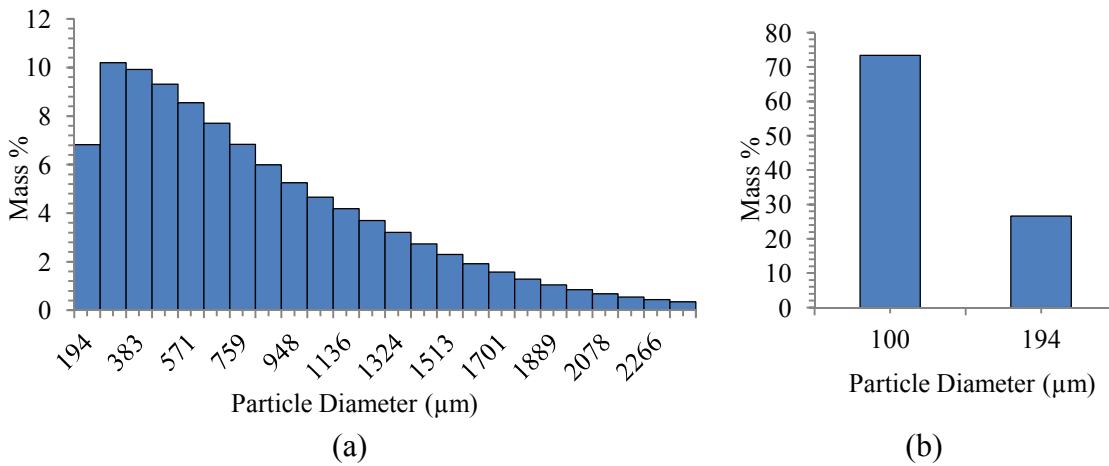


Figure – 7.24: Size distribution of particles exiting from the bottom (a) and top (b) of the tower (Case 2).

In Figure 7.25 a comparison of residence time is made between these two cases for particles of different sizes collected from the bottom of the tower. It is observed that the smaller particles have greater residence time compared to larger particles. In both cases, the residence time decreases rapidly with the increase in particle size up to 300 μm and then relatively slowly for larger particles. The plot does not contain residence time of 100 μm particles since all 100 μm particles get entrained by the gas and exit from the exhaust gas outlet at the top. The smaller particles lose their initial momentum quicker. The trajectories of the smaller particles also get more influenced by the turbulence and recirculating zones in the gas flow compared to the larger particles. From a comparison of the two cases, it is observed that the residence times in Case 2 are smaller for the particle sizes less than 500 μm, while they are greater for larger particles. The smaller particles (<500 μm) have a lower residence time in Case 2 compared to Case 1, since the gas velocity near the wall in Case 2 is smaller compared to Case 1. This is because all the particles in Case 2 start to move downwards close to the wall upon collision. The downward moving particles exert momentum on the gas flowing counter-current to the particles. This exchange of momentum causes the gas flow to become almost stationary near the wall. For sizes greater than 500 μm, the residence time becomes greater in Case 2, since larger particles have greater moisture and lose more momentum upon each collision with the wall, although the gas velocity near the wall is smaller. In Case 1 however, most of the particles after striking the wall bounce back towards the tower centre and do not move close to the wall over most of the tower height. Therefore a relatively higher gas velocity exists near the wall. Hence the smaller particle sizes in Case 2 reach the bottom outlet much quicker compared to those in Case 1. The larger particles in Case 1 have greater momentum because particles after striking the wall do

not lose most of the momentum (as they have higher restitution coefficient) and thus move faster, this results in a lower residence times of larger particles in Case 1.

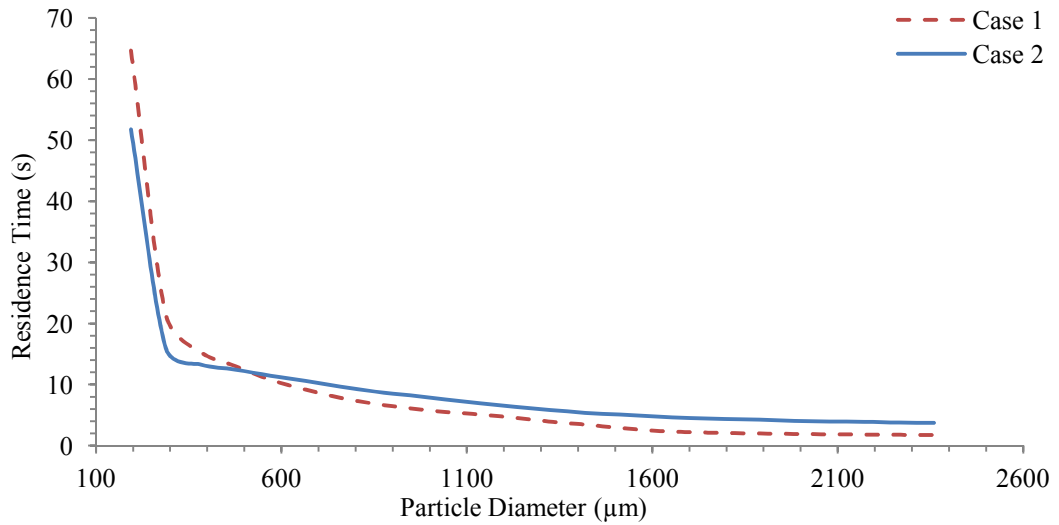


Figure – 7.25: Residence times of particles collected from the bottom outlet.

Figure 7.26 is a plot of velocity distribution of the gas phase coloured by gas velocity magnitude. Below the nozzle, a lower velocity near the wall and at the centre and a high velocity in the annular region are observed. The flow is symmetrical in the bottom region of the tower up to a dimensionless height of 0.5. The gas flow becomes asymmetric as it approaches the nozzle. This asymmetry persists in the top region of the tower above the nozzle. In Case 1, the low velocity zone in the centre of the tower below the nozzle (at  $z/Z = 0.45$ ) becomes wider, because the particles pass through the centre after bouncing from the wall. The flow of gas becomes almost stationary in this region due to the exchange of momentum between the two phases. In Case 2, the high velocity annular region becomes narrower with height, which eventually disappears at  $z/Z = 0.49$  and the velocity becomes more uniform over the cross-section except near the wall where the low velocity exists. At the top of the tower, the gas exits via a narrow tube with vortex breaker installed at the top of the tube. Due to smaller diameter of the tube the gas velocity increases sharply in the tube and in the exhaust gas header, a jet of gas can be seen which impinges to the wall of the header. The flow is symmetrical in the isothermal CFD simulation case (Figure 7.9), whereas, in the non-isothermal simulation cases, it is slightly asymmetric near the nozzle, primarily due to the temperature gradient near the nozzle as a consequence of the evaporation of droplets.

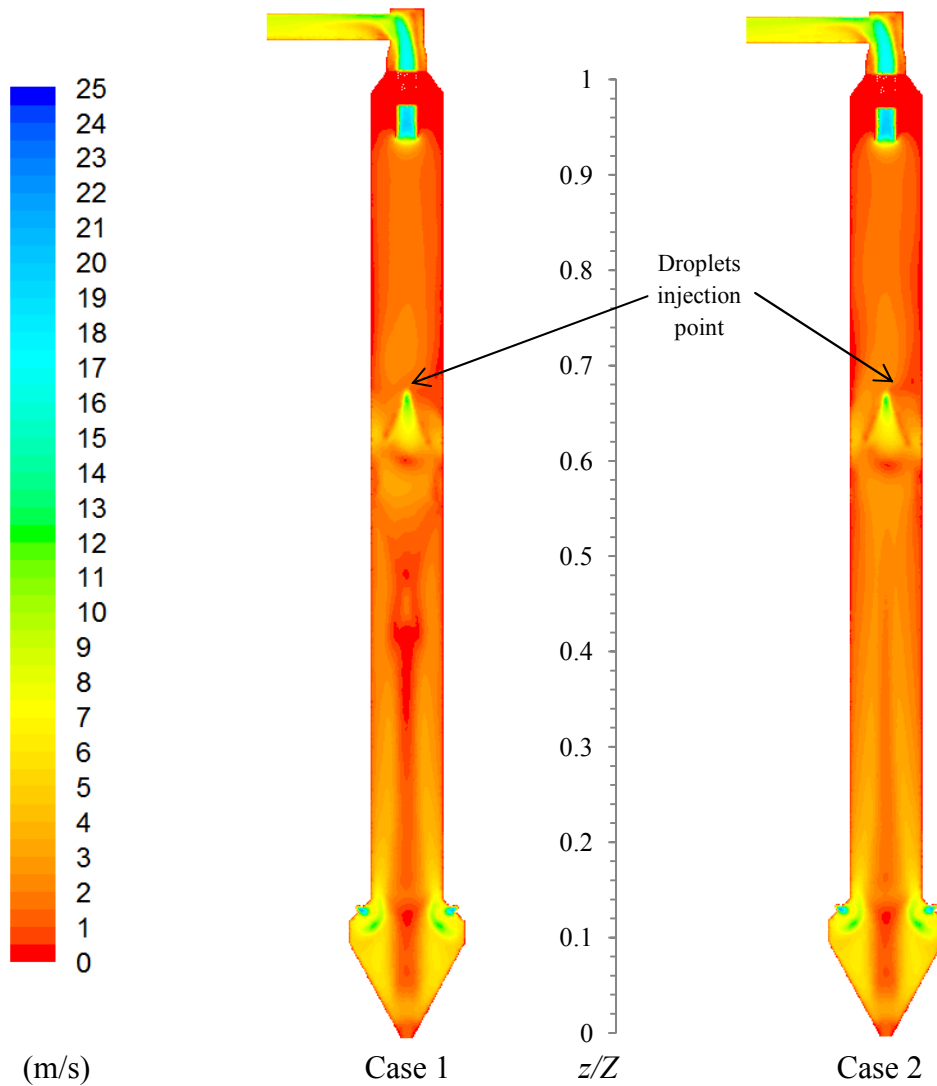


Figure – 7.26: Gas velocity distributions coloured by velocity magnitude.

Figure 7.27 is a vector plot of the gas flow pattern (coloured by magnitude of the velocity components) near the nozzle. The gas flow patterns near the nozzle are similar in both cases, therefore, only the flow patterns obtained from Case 1 are plotted. Just below the droplet injection point, a jet of gas can be seen. This is due to the exchange of momentum between the high velocity droplets and the gas resulting in the entrainment of the surrounding gas into the spray of droplets. At the outer edge of the spray, recirculation regions are established which are caused by the reversal of the direction of the gas flow. Figure 7.27 is very similar to Figure 7.10, in which no heat/mass exchange took place between the two phases except for the asymmetry of the flow above the nozzle in Figure 7.27. The evaporation of droplets does not significantly alter the gas flow patterns near the nozzle although some asymmetry is present due to evaporation of the droplets.

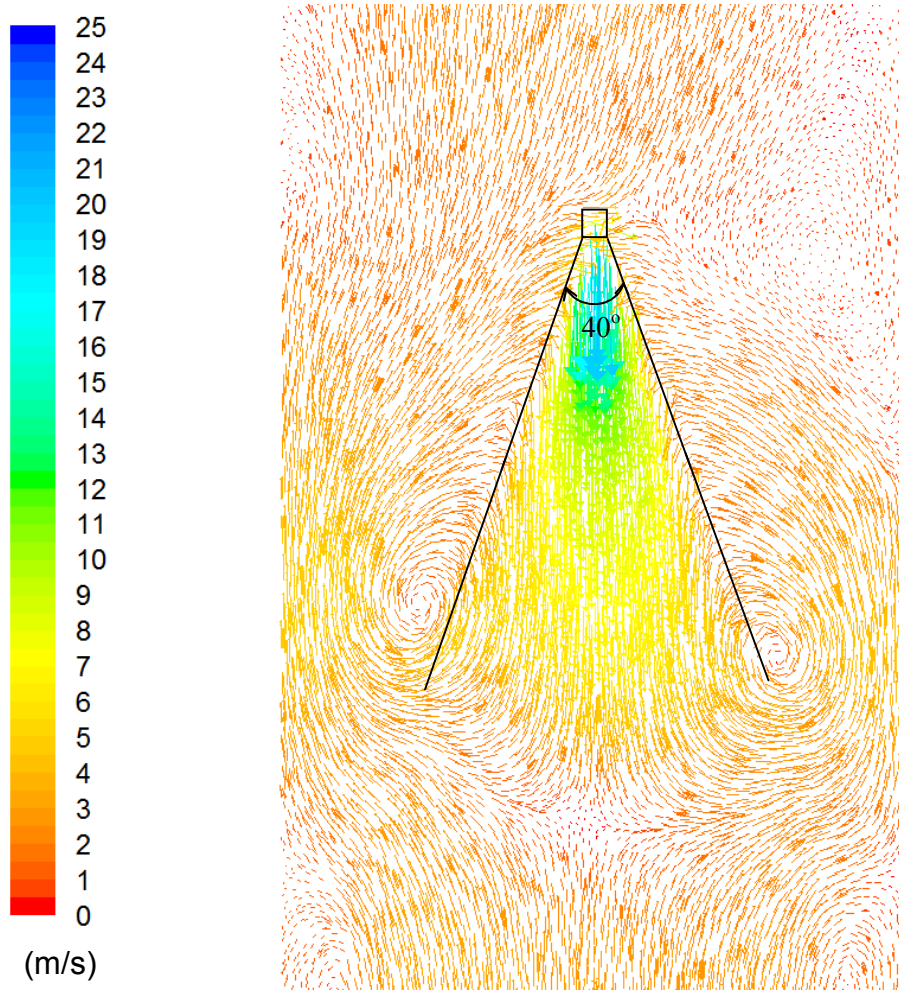


Figure – 7.27: Vector plot of air velocity magnitude near the nozzle.

Figure 7.28 is a plot of mean axial and tangential velocity profiles along the radius of the tower, calculated using Case 1 and 2 at various dimensionless heights. At  $z/Z = 0.2$ , the axial and tangential velocity profiles predicted using both cases are qualitatively similar. Since the particles in Case 1 pass through the centre of the tower after collision with the wall, therefore, the axial velocity near the centreline is slightly smaller compared to Case 2, consequently, the small change in the tangential velocity (Figure 7.28 (b)) is also reflected. The dimensionless height of  $z/Z = 0.5$  is close to the spray zone (nozzle is at  $z/Z = 0.67$ ), at this location, since the particles after collision with the wall move close to the wall in Case 2, therefore the axial velocity near the wall is smaller and it is higher at the centre and resembles a parabolic profile, whereas in Case 1, the velocity is maximum in the region close to the wall and minimum near the centreline due to momentum exerted by the particles as they pass through the centreline. The tangential velocity profile at this location is asymmetric particularly in Case 1. At a dimensionless height of  $z/Z = 0.78$  (above the nozzle), the axial velocity profiles in both

cases are parabolic. The tangential velocity in above the nozzle in both cases is very small as most of the angular momentum is transferred to the droplets/particles.

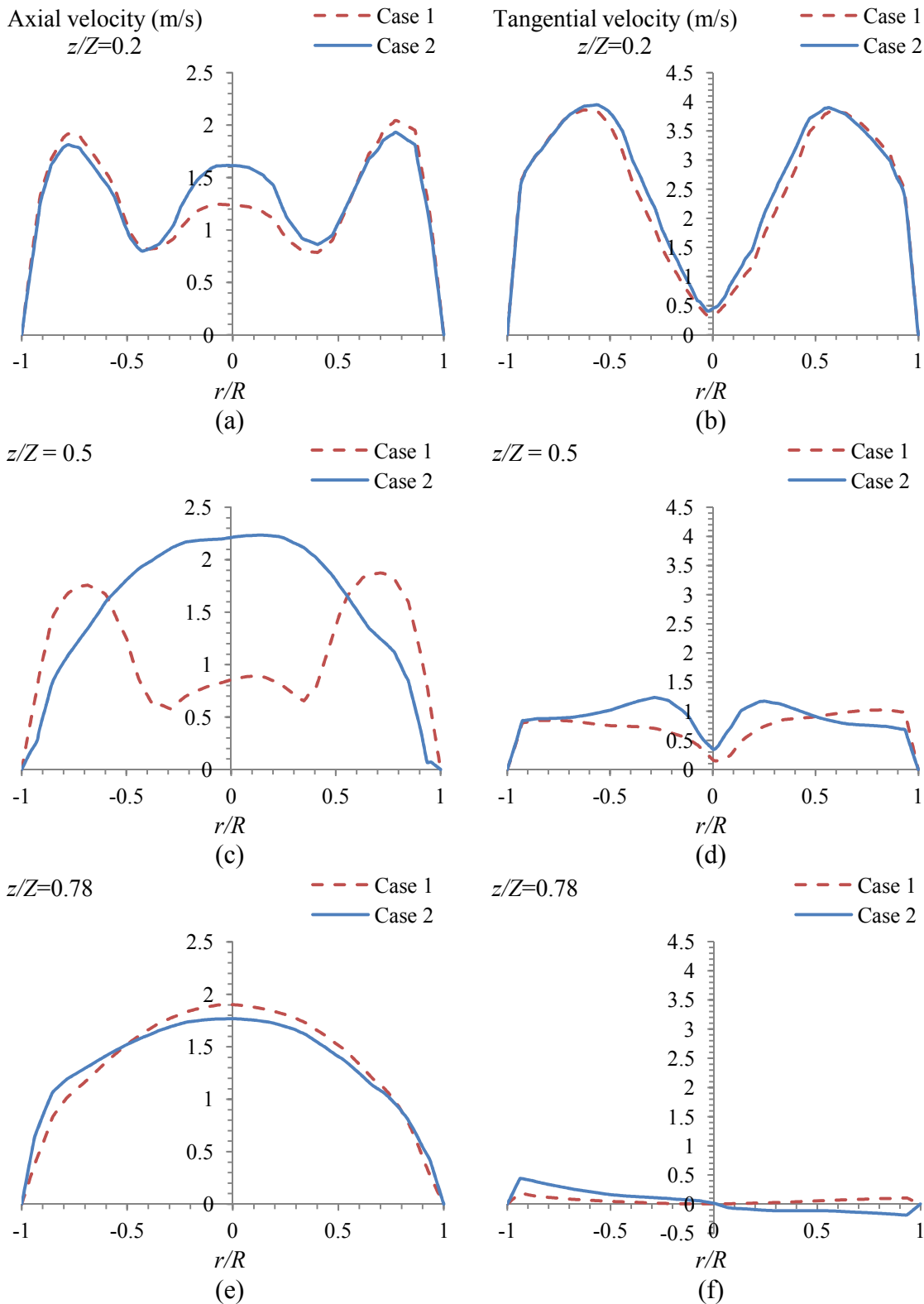


Figure – 7.28: Mean axial and tangential velocity profiles computed from Case 1 and 2.

Figure 7.29 is a plot of swirl number along the dimensionless tower height for Case 1 and 2. The spray nozzle is located at a dimensionless height of 0.67, below the spray

nozzle along the tower height, the swirl number is greater in Case 1 compared to Case 2, because in Case 1, the droplets/particles after collision with the wall do not flow close to the wall where the tangential velocity is maximum at most of the tower height, therefore the angular momentum exchange between the gas and the droplets/particles in Case 1 is not as rapid as in Case 2. Above  $z/Z = 0.67$ , the swirl number in both cases is close to zero as the swirling momentum is transferred to the droplets at this location. High swirl number along the tower height is desirable as it results in increased relative velocity between the droplets/particles and drying gas as well as increased turbulence intensity which favours higher heat and mass transfer rates.

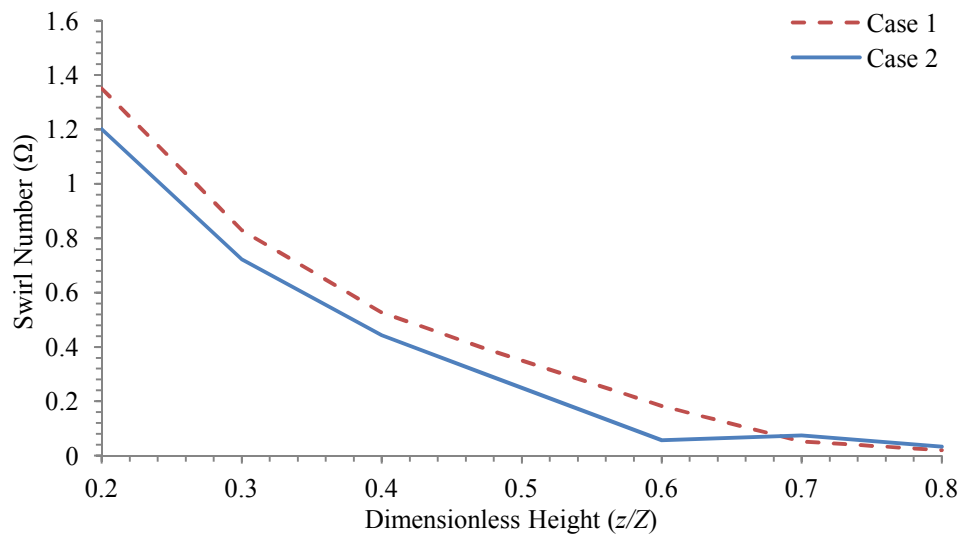


Figure – 7.29: Swirl number along the tower height.

Figure 7.30 is a plot of turbulent intensity of the gas phase defined using equation (6.2). The turbulence intensity is maximum in the spray region of the tower. The turbulence intensity below the nozzle is relatively smaller compared to the turbulence intensity above the nozzle. Therefore, the presence of smaller particles enhances turbulence. Furthermore, the swirl above the nozzle is smaller, due to which the flow is more unstable and more turbulent. High turbulence intensity can be seen at the exit header bent due to a sharp change in the flow direction. The turbulence intensity plots in both Case 1 and Case 2 are very similar except at  $z/Z = 0.4$  to  $0.5$ . This is due to the bouncing of larger particles in Case 1, which pass through this region after post-wall collision. This does not occur in Case 2, in which case all particle sizes move close to the wall after collision.

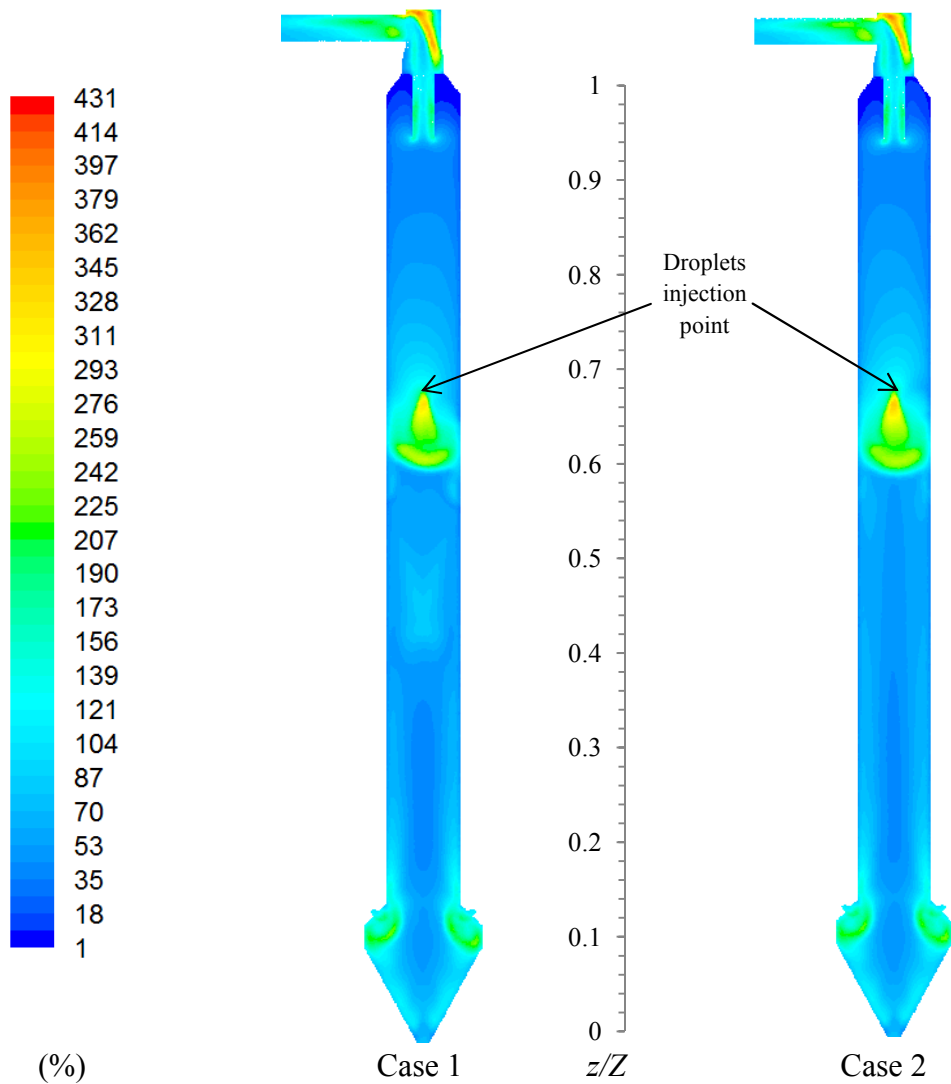


Figure – 7.30: Gas turbulence intensity distributions.

Figure 7.31 is a plot of discrete phase concentration in the bottom region of the tower. The discrete phase concentration was very similar for both cases, therefore, only for Case 2 is depicted. The discrete phase concentration is defined as the mass flow of particles per unit volume of a computational cell multiplied by the residence time of those particles. Hence the discrete phase concentration gives an indication of the solid loading/volume fraction of the discrete phase in the computational cells. In the bottom cylindrical region ( $z/Z = 0.15$  to  $0.21$ ), the discrete phase concentration is a maximum close to the wall as the particles move close to the wall. In the bottom conical region of the tower, the discrete phase concentration increases as the particles approach the bottom outlet due to a decrease in the cross-sectional area of the tower.

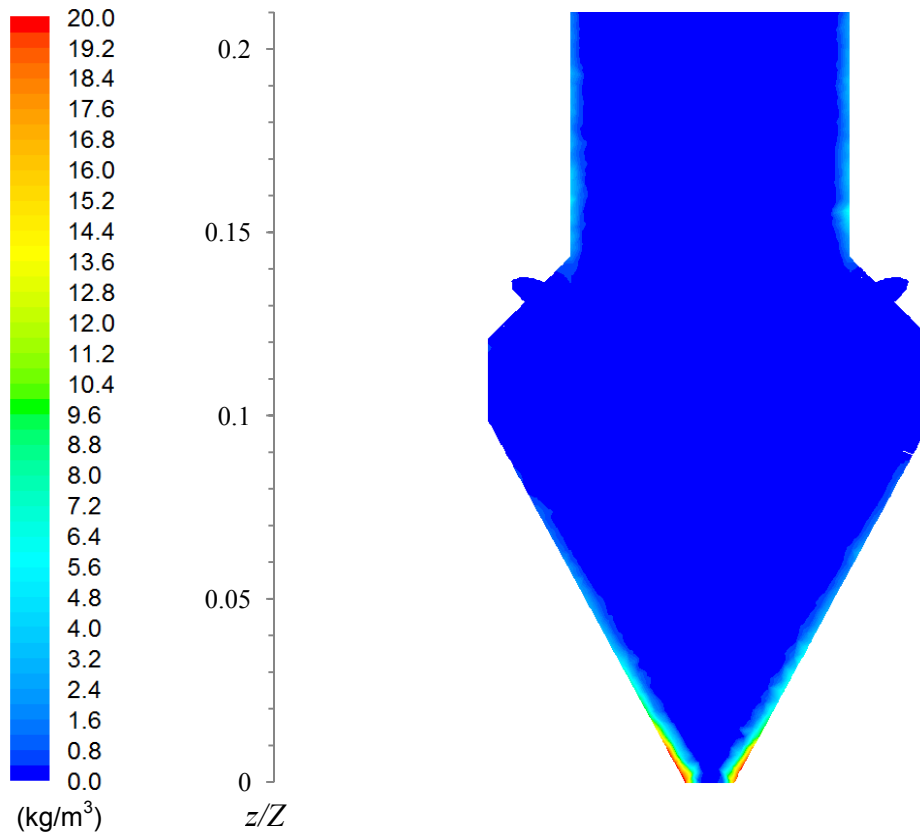


Figure – 7.31: Discrete phase concentration for Case 2.

Figure 7.32 is a plot of contours of the gas temperature and moisture fraction distributions. The gas temperature is higher at the bottom of the tower (at the tangential-entry inlets) and decreases as the heat exchange takes place between the two phases, similarly the water vapour fraction is the minimum at the inlets and increases due to inclusion of evaporated moisture from droplets and wet particles. A low gas temperature region in the spray zone is observed ( $z/Z = 0.61$  to  $0.7$ ). The mass fraction of water vapour is a maximum inside the spray region in both cases. This indicates that maximum evaporation is occurring inside the spray zone, because the droplets initially have free moisture at the surface and the velocity of the droplets is a maximum in the spray. This results in a high heat and mass transfer coefficient and therefore the evaporation rate is a maximum. The temperature of injected droplets is greater than the wet bulb temperature; therefore the droplets get cooled down due to rapid evaporation of moisture from their surface, resulting in cooling of the surrounding gas. Above the nozzle, the gas phase temperature and moisture content is fairly uniform indicating that very little evaporation is occurring. It is observed that the temperature and moisture profiles are significantly different between the two cases below the spray region ( $z/Z < 0.61$ ). In the central region of the tower below the nozzle (at  $z/Z = 0.4$  to  $0.5$ ), the temperature is lower in Case 1 compared to Case 2. Because in Case 1, the particles

after colliding with the wall bounce back with a higher velocity and pass through this region of the tower and exchange heat with the gas, resulting in an increase in the particle temperature and a decrease in the gas temperature. In Case 2, the gas temperature near the wall below the spray region is lower and the moisture fraction is higher as the particles flow close to the wall after the first impact with the wall. This results in heat/mass exchange between the two phases taking place near the wall. The exhaust gas temperature in Case 1 is 375.3 K, while that in Case 2 is 381.4 K. The exit gas temperature in Case 1 is smaller, hence there is greater heat exchange taking place between the two phases in Case 1. In Case 1, the particles bounce back from the wall and move through the central region of the tower, where the gas temperature is higher, therefore a greater amount of heat exchange take place between the gas and particles compared to Case 2 in which particle move along the wall and a relatively lower temperature difference persists between the two phase at most of the tower height.

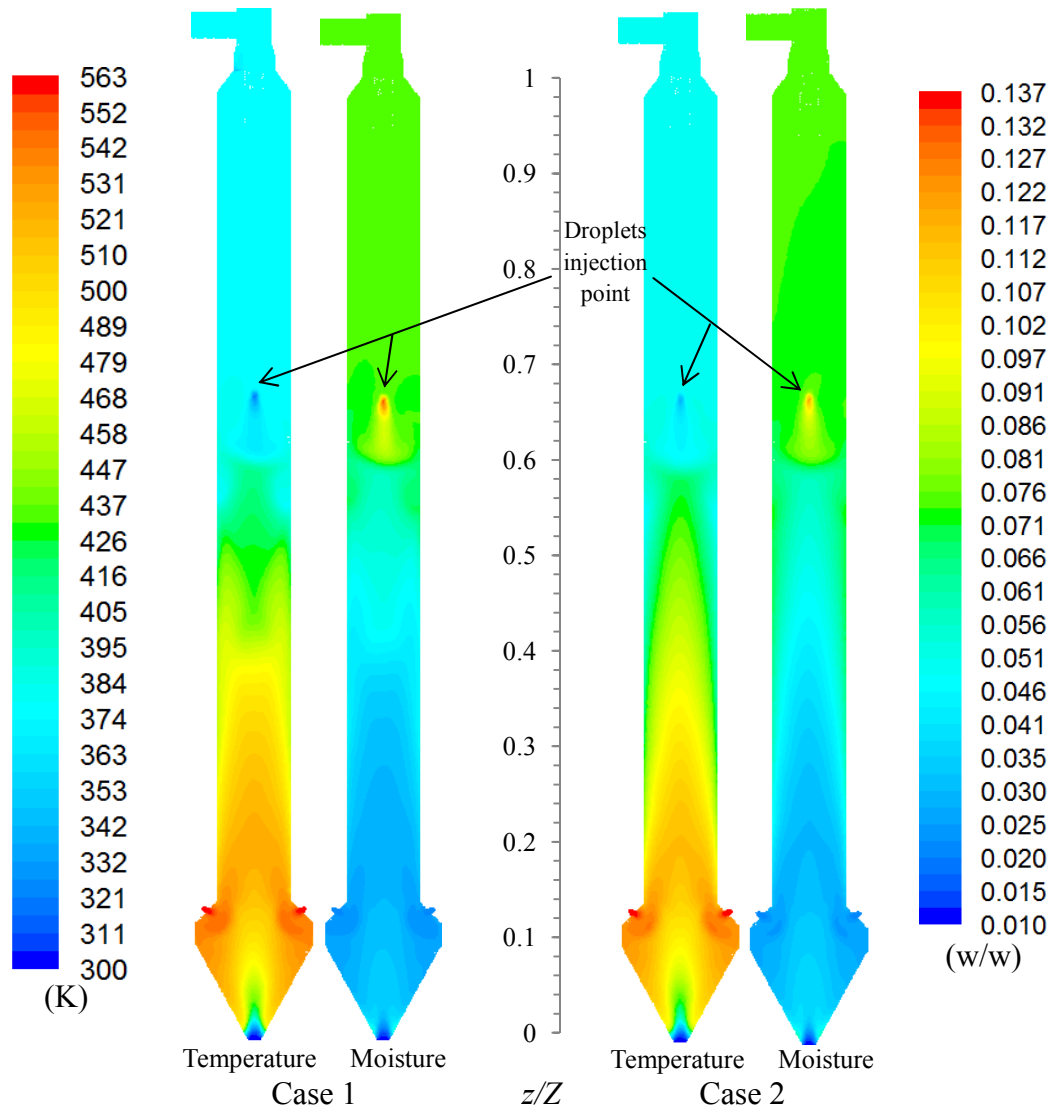


Figure – 7.32: Gas temperature and moisture distributions.

Figure 7.33 is a plot of heat flux through the cylindrical region of the tower along the dimensionless tower height. The negative value indicates that the heat is being lost through the column wall to the ambient. The spray nozzle is located at a dimensionless height of 0.67. Above the nozzle, the heat flux is fairly constant, since the gas temperature is fairly uniform above the nozzle (see Figure 7.32) whereas below the nozzle, at a dimensionless height of 0.67 to 0.55, the heat flux first increases and then decreases to a minimum value. This region corresponds to the spray zone in which the gas is entrained in the spray, due to the entrainment of gas, in the spray, the gas exhibits recirculation (Figure 7.27) and also, a relatively lower temperature exists in this zone due to evaporative cooling of the droplets. Below the dimensionless height of 0.55, the heat flux increase continuously. The fluctuations in the heat flux are due to collision of particles with the wall that results in change in the gas flow profiles close to the wall and hence the inside film coefficient. From a comparison of the heat flux profiles for both cases, it is observed that the heat flux above the nozzle for Case 1 is smaller and below the nozzle it is greater. Because above the nozzle, the gas temperature in Case 1 is smaller and below the nozzle, the near-wall gas temperature in Case 1 is greater (Figure 7.32), resulting in greater heat flux through the wall below the nozzle and lower heat flux above the nozzle. The total heat loss through the wall in Case 1 is 6.66 kW and in Case 2 is 5.43 kW.

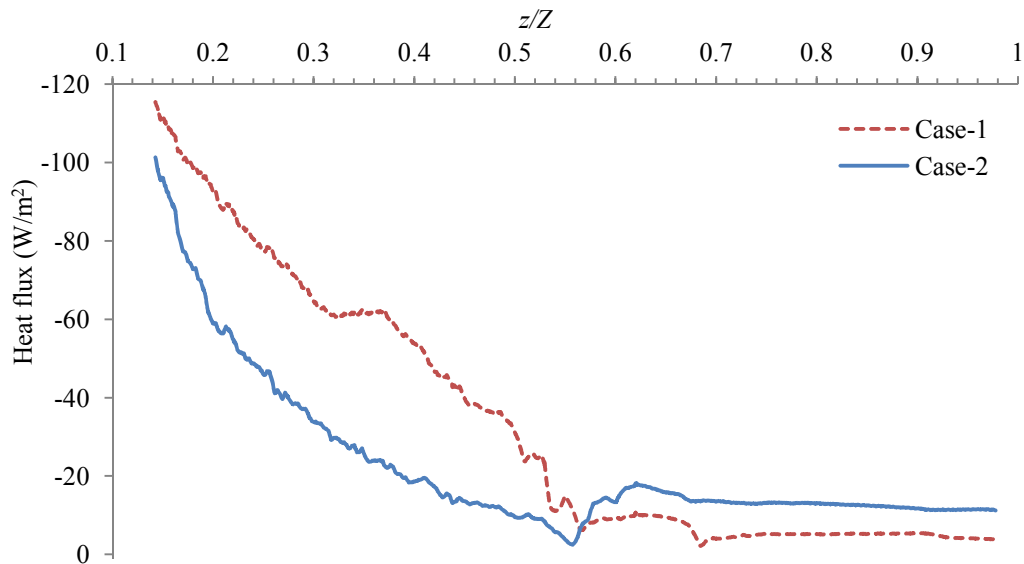


Figure – 7.33: Heat flux along the dimensionless tower height.

Figure 7.34 is a plot of temperature and normalised moisture fraction versus size of the particles that exit from the bottom outlet. In general, the temperature of smaller particles is greater compared to the larger particles. The moisture content of smaller particles

sizes is less than that of the larger sizes. The particles sizes up to 800  $\mu\text{m}$  exit at almost the same temperature because the exit moisture content of these particle sizes is zero. Once the particles are completely dried; further heat exchange with the gas results in change in particle temperature. Due to a high surface area and lower heat capacity of the small, dried particles, the particles exit at a temperature similar to the surrounding gas at the bottom outlet. A sharp decrease in the exit particle temperatures is observed for the particle sizes in the range of 900  $\mu\text{m}$  to 1200  $\mu\text{m}$ . This is because the particle drying rate in the third stage depends on the boiling point of the slurry which is a function of moisture content (equation 5.14). The slurry boiling point increases exponentially at lower moisture content. The exit moisture content of these particle sizes lie in that range of moisture content, hence a large difference in the exit temperatures in these particle sizes results with small changes in the exit moisture content. The exit temperature of particles greater than 1200  $\mu\text{m}$  is fairly uniform because these particles exit at a high moisture, the slurry boiling point is fairly constant in that range of moisture content.

From a comparison of particles exit temperatures and moisture contents of the two cases, it is observed that the temperatures of particles in Case 2 are smaller for particle size up to 1300  $\mu\text{m}$  and the moisture content is greater. Because the particles move close to the wall at most of the tower height, the temperature of the drying gas is lower near the wall hence the particles in this case exchange less heat and mass with the drying gas. The slurry boiling point at high moisture content does not show a large variation with moisture content hence the temperature of particles greater than 1300  $\mu\text{m}$  (having high moisture content) is the same in both cases even though the exit moisture content of particles in Case 2 is greater. In Case 1, the particles bounce back and get exposed to a higher temperature in the central region of the tower, this results in greater heat and mass exchange between the two phases and hence the particles sizes up to 1500  $\mu\text{m}$  have a higher exit temperature. The trend of smaller particles exiting at zero moisture content is unrealistic and is due to the assumption in the drying model that the particle drying continues to take place even at below the equilibrium moisture content. In reality, the particle drying will stop when it reaches the equilibrium moisture content with the surrounding gas. Therefore, another stage is required in the drying model in which the particles remain at equilibrium moisture content with the surrounding gas, which is not considered at this stage.

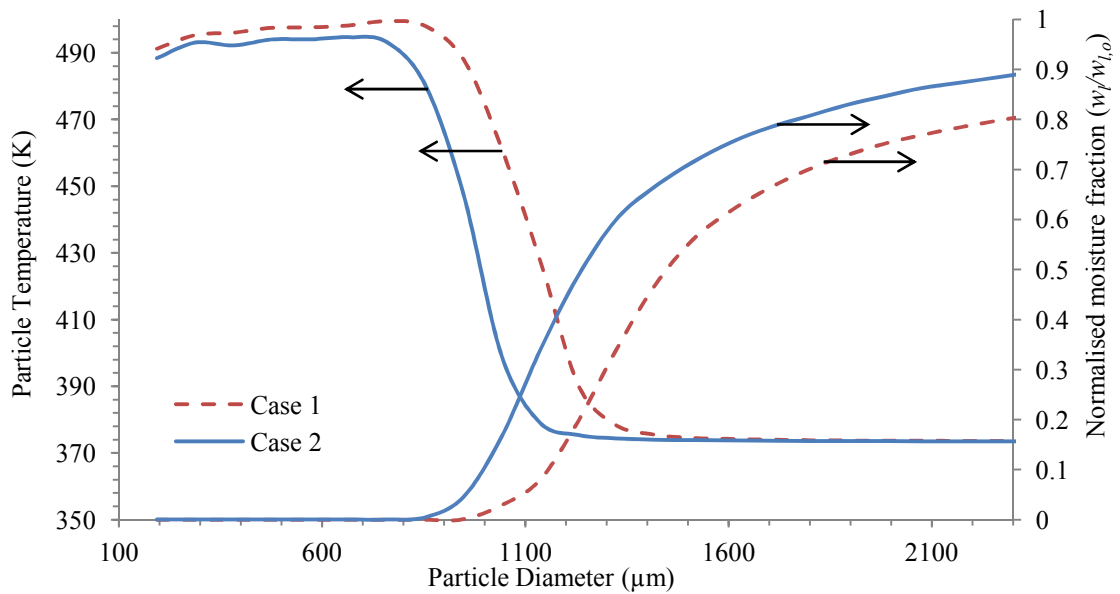


Figure – 7.34: Particle exit temperature and moisture content at the bottom outlet.

Figure 7.35 is a plot of density of particles that exit from the bottom of the tower. The density variation with particle size looks qualitatively similar to the moisture fraction profile (Figure 7.34), since the density of the particles vary with the moisture fraction.

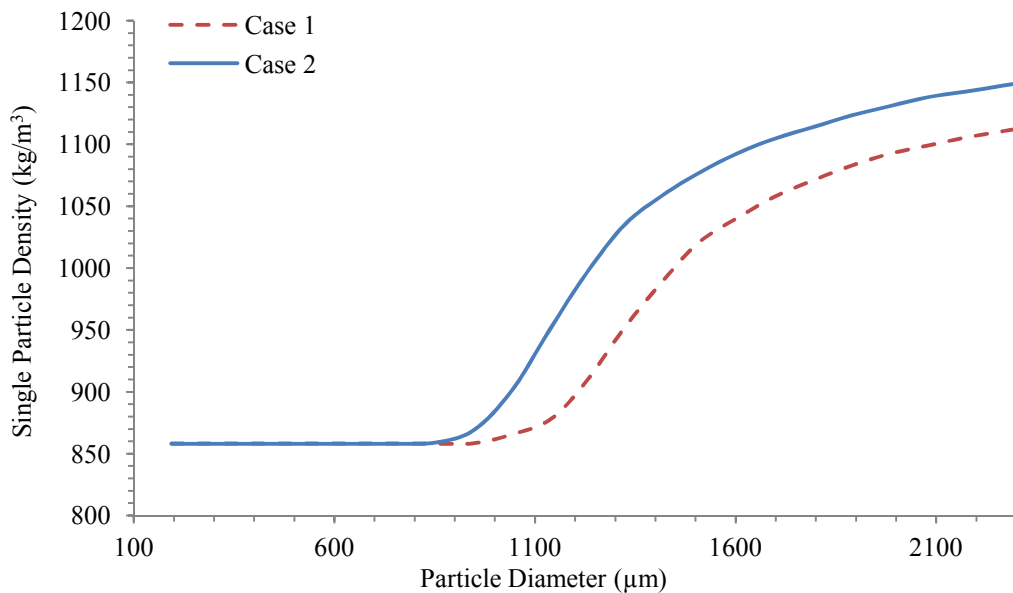


Figure – 7.35: Particle exit density at the bottom outlet.

Figure 7.36 is a plot of temperature profile of a 700  $\mu\text{m}$  particle size and dimensionless moisture fraction as a function of residence time inside the spray drying tower. The droplet temperature rises initially and keeps fairly constant at a temperature of 373 K up to about 4 seconds of its residence time. This corresponds to the slurry boiling point. The particle moisture continues to decrease with time. After about 4 seconds, the moisture becomes more bound and slurry boiling point increases exponentially with decrease in moisture content. Therefore the temperature of the particle rises rapidly. At

about 7 seconds all the moisture from the particle is removed and the particle exhibits a maximum temperature at this point. The maximum temperature is exhibited by the particle near the gas inlets, when the particle reaches the bottom conical region of the tower. Thereafter, it starts to cool down due to cold air entrainment from the bottom of the tower where the particles reaches the bottom exit of the tower.

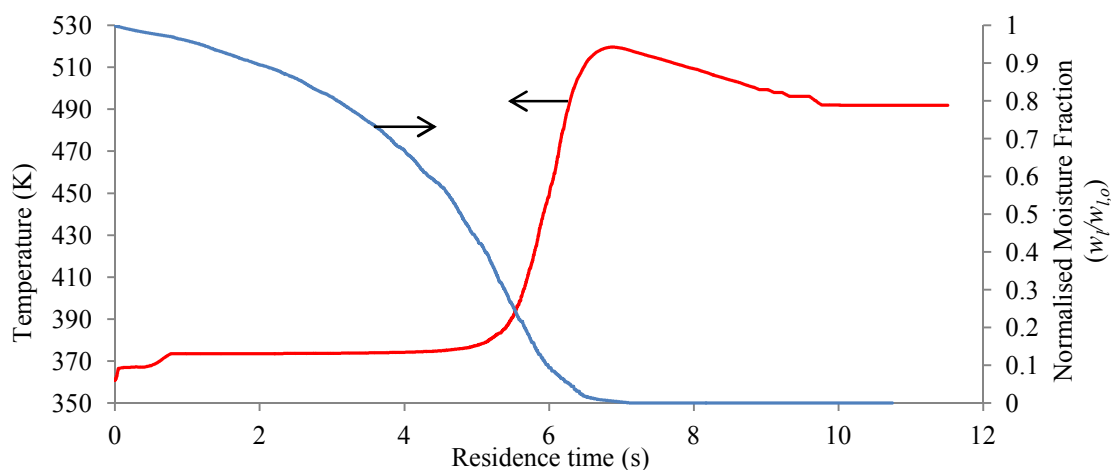


Figure – 7.36: Temperature profile and dimensionless moisture profile of a 700  $\mu\text{m}$  particle size.

In Cases 1 and 2, the thermal conductivity of the fibre glass insulation taken from the literature is used to model heat loss through the wall. However, in Section 6.2.8 it is shown that the effective thermal conductivity of the insulation, back calculated from the measured temperature data (in the absence of measured gas temperature at the tangential entry inlet) is significantly larger at various heights of the tower, resulting in greater heat loss. To assess the influence of heat losses from the wall on the simulation results, a simulation case with calculated effective thermal conductivity of the insulation is carried out, referred to as Case 3 and compared with Case 2. The input operating conditions for both gas and droplets/particles and convergence criteria are the same as in the previous two cases. The wall restitution coefficient is considered as a linear function of particle moisture content as in Case 2. Figure 7.37 is a plot of comparison of heat flux through the wall in Case 2 and Case 3.

In Figure 7.37, it is observed that the heat flux in Case 3 is significantly greater than the heat flux calculated in Case 2 especially in the bottom region of the tower due to the use of effective thermal conductivity of the insulation calculated in Section 6.2.8. Total heat loss from the wall in Case 3 is 35.2 kW. The exit particle average temperature, moisture content and exhaust gas temperature calculated for Case 3 and its comparison with other cases and experimental data (Martin de Juan, 2011) is given in Table 7.8.

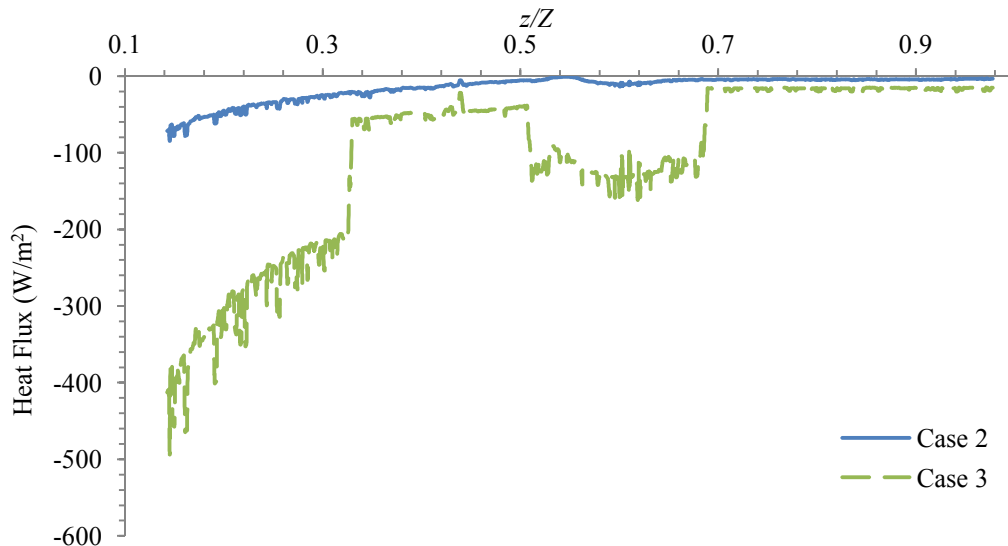


Figure – 7.37: Comparison of heat flux through the column wall.

### 7.2.10 Study of the Influence of Non-Spherical Drag Law

In the previous three cases, the drag law proposed by Morsi and Alexander (1972) has been used, which is applicable to smooth spherical particles. However, the particles undergo changes in shape due to agglomeration as well as morphological changes occurring during the drying of particles. The resulting particles are non-spherical in shape and the drag force acting on non-spherical bodies is expected to be greater. To assess the influence of drag law used for calculating drag force on particles residence times, a drag law for non-spherical particles proposed by Haider and Levenspiel (1989) is used for particles (equation 3.64). For the droplets, the drag law reported by Williams (1976) has been used, which was obtained for burning oil droplets (equation 3.61 and 3.62). The drag law is changed from  $C_D$  for droplets by Williams (1976) to  $C_D$  for non-spherical particles when a crust is formed at the surface of the droplet and it transforms into a wet particle. The drag laws were specified using Fluent user-defined function feature. This case is referred to as Case 4. The drag law for non-spherical particles depends on the value of sphericity (defined in Section 3.11.1), which is assumed to be a constant with a value of 0.8, corresponding to a cubical shape. The effect of different drag laws on the value of drag coefficient for a range of particle Reynolds numbers is depicted in Figure 7.38 using log-log scale. Up to a  $Re_p$  of 100, a linear decreasing trend is predicted by all three drag laws, after which the drag laws proposed by Haider and Levenspiel (1989) and Williams (1976) show a slight increasing trend with increasing  $Re_p$  but Morsi and Alexander (1972) correlation shows a decreasing trend with  $C_D$  reaching a plateau as  $Re_p$  approaches 10000. It is observed that at low  $Re_p$  (0.1-10), the

drag coefficient calculated by smooth and rough particle drag laws are very similar, but the one reported by Williams (1976) is smaller. At high  $Re_p$  ( $>100$ ), the drag coefficient proposed by Haider and Levenspiel (1989) and Williams (1976) give similar values.

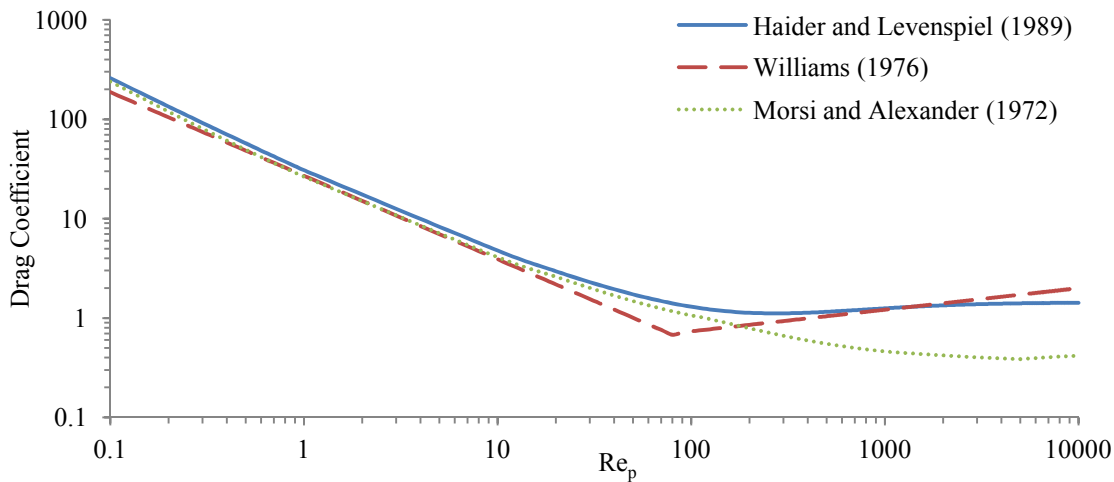


Figure – 7.38: Residence time of particles collected from the tower bottom.

The tower input operating conditions are kept the same as in the previous three cases. The wall restitution coefficient is considered as a function of moisture content (as in Case 2 and 3) and for the modelling of heat loss through the wall, modified insulation thermal conductivity is used, which is also used in Case 3.

Figure 7.39 is a plot of residence time of particles collected from the bottom of the tower obtained from simulation Case 4 and compared with simulation Case 3. All 100  $\mu\text{m}$  particles in both cases exit from the top of the tower due to entrainment by the gas hence the residence time of these particles is not shown. The residence time of the smallest particle size that exits from the tower (200  $\mu\text{m}$ ) is about 8 seconds greater in Case 4 in which non-spherical drag coefficient is used compared to Case 3. The residence times of larger particles ( $>200 \mu\text{m}$ ) are only slightly greater in Case 4. The residence time of particles greater than 1000  $\mu\text{m}$  is on average about 2 seconds greater in Case 4. The residence time of exiting particles is increased by the use of non-spherical drag law. The rough drag coefficient requires the value of sphericity, which is very difficult to predict because the particle will deviate from a perfect spherical shape due to complex interactions between particle-particles and particle-wall, resulting in breakage and agglomeration. Furthermore, during the drying process, the morphological changes that occur in particles may also cause particles to become non-spherical in shape. Therefore the sphericity of the particles is expected to change throughout the tower height. This is not accounted for in the model.

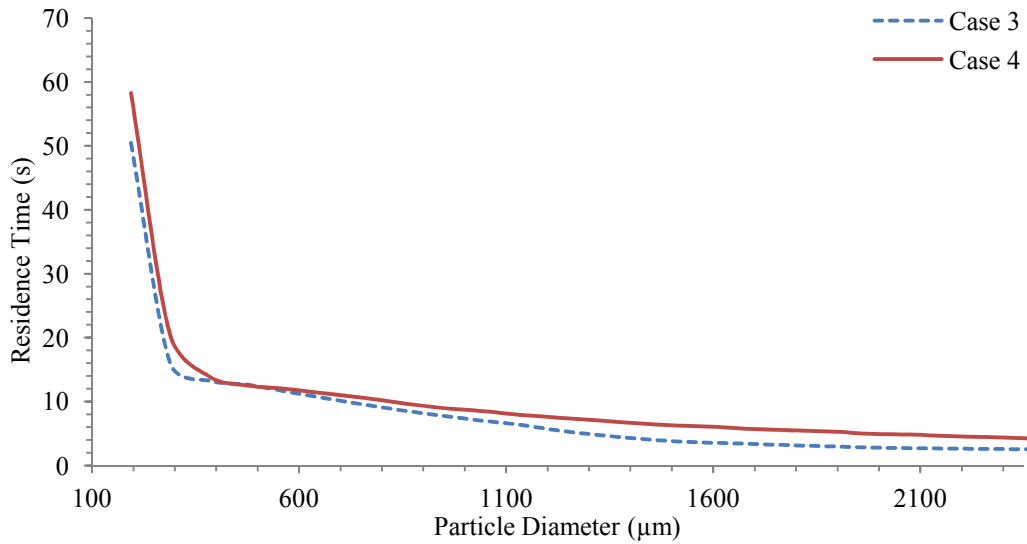


Figure – 7.39: Residence time of particles collected from the tower bottom.

A comparison of simulation results of Case 1, 2, 3, 4 and experimental data collected from the spray drying tower is presented in Table 7.8. From a comparison of Case 1 and 2, it is observed that Case 1 predicts greater heat/mass transfer between the two phases and hence smaller moisture content and smaller exhaust gas temperature. In Case 1, the particles come in contact with the hot gas in the central region of the tower when the particles bounce off from the wall and therefore exchange more heat. Hence the way particle-wall interaction is modelled influences the residence times and trajectories of the particles, which in turn affects the predicted dried powder average moisture content.

The dried particle average moisture content in Case 2 and Case 3 is very similar, however, the exhaust gas temperature in Case 3 is about 8 K smaller. This is due to greater heat loss from the wall in this case. The moisture content in Case 3 is slightly smaller due to greater heat loss from the wall causing a lower temperature close to the wall hence relatively less heat exchange takes place between the droplets/particles and drying gas, although the difference in the particle exit moisture of Case 2 and 3 is not significant. The average particle moisture content in Case 4 is 4% while in Case 3, it is 5%. The increase in residence time of particles (due to non-spherical drag law) has reduced the average particle moisture content, as the particles get more time in Case 4 to exchange heat with the drying gas. The heat loss in Case 4 is similar to the heat loss in Case 3 because in both cases, the effective thermal conductivity of insulation is used for the calculation of heat flux (calculated in Section 6.2.8 in Chapter 6). The exhaust gas temperature in Case 4 is the smallest. From a comparison of all the simulation cases with the experimental data, it is observed that the measured moisture content and outlet gas temperature is smaller compared to the simulation results. Hence the heat transfer

between the two phases is underpredicted by all the simulation cases. One of the reasons can be due to the use of dried powder particle size distribution (which is typically larger compared to the droplet size distribution) as the initial droplet size distribution. The other reason could be the underprediction of the residence time of the particles due to the assumption of smooth spherical particles. The shape of the particles is expected to change throughout the tower height due to drying and agglomeration.

Table – 7.8: Comparison of simulation results with experiment.

Parameter	Case 1	Case 2	Case 3	Case 4	Measured (Martin de Juan, 2011)
Particle weighted average moisture content, %	3.03	4.75	5.03	4.03	1.8
Particle weighted average temperature, K	468.2	456.2	446.6	442.3	356
Outlet gas temperature, K	375.3	381.4	373.2	372.2	367
Heat loss, kW	6.6	5.4	35.2	35.8	62.1

As discussed in Chapter 5, the outlet particle temperature is significantly higher compared to the measured temperature, because the temperature measurement is taken at the belt which is a few meters away from the location where the particles fall from the tower. The temperature of the particles is expected to fall down very quickly on contact with the cold air as the dried particles have a low heat capacity.

The heat loss calculated from the measured data is significantly greater than the predicted heat loss in Case 1 and Case 2. However in Case 3 and 4, the predicted heat loss is closer to the heat loss based on measured temperatures because an effective thermal conductivity was used, which was larger than the value reported in the literature for insulation thermal conductivity. The difference in the predicted heat loss and the heat loss based on the measurement is primarily due to the temperature measurement error at the inlet as it is found in Section 6.2.9 of Chapter 6 that the gas loses temperature in the duct and in the distribution ring that supplies hot gas to the tangential-entry inlets.

### **7.2.11 Study of the Influence of Initial Droplet Size Distribution**

In all four cases considered above, the measured powder size distribution was used as the initial droplet size distribution at the nozzle. In Chapter 5, it is found that the initial

droplet size distribution specification significantly influences the overall heat and mass transfer taking place between the gas phase and the droplets/particles. Therefore, two more CFD simulation runs are carried out (referred to as Case 5 and Case 6) to assess the influence of the initial droplet size distribution specification on the overall heat and mass transfer between the gas and the droplets/particles. In Case 5, the measured droplet size distribution is used as the initial droplet size distribution. In Case 6, the measured spray dried powder size distribution is used. The measured droplet and particle size distribution and the corresponding curve fits are depicted in Figure 5.23. The operating conditions used for both Case 5 and 6 are listed in Table 5.6 in Chapter 5. The droplets are sprayed at a dimensionless height of 0.4. The heat loss through the insulated wall is modelled considering the effective thermal conductivity of the insulation. The wall restitution coefficient is specified as a function of moisture content (equation 7.1). The drag coefficient correlation reported by Williams (1976) is used for droplets and for the particles the drag correlation proposed by Morsi and Alexander (1972) is used. The CFD numerical methodology, boundary condition type and convergence criteria are kept the same as in the previous simulation Cases 1 to 4 (given in Sections 7.2.6 and 7.2.7).

Table 7.9 lists mass balance of the discrete phase for Case 5 and 6. In Case 5, 58.4% of the total slurry mass is collected from the bottom of the tower while 13.6% of the inlet slurry mass gets entrained by the gas as fine powder. The remaining amount is the vapours evaporated from the discrete phase to the gas phase. In Case 6, 70.4 % of the mass of slurry exits from the bottom region of the tower while 4% of the powder gets entrained by the gas and the remaining amount is the evaporated vapours that exit with the gas. The overall enthalpy balance error for Case 5 is 0.07% and for Case 6, it is 1.5%.

Table – 7.9: Mass balance on the discrete phase.

Parameter	Case 5	Case 6
Mass flux of injected droplets (kg/m <sup>2</sup> s)	0.1669	0.1669
Mass flux of powder collected from bottom (kg/m <sup>2</sup> s)	-0.0930	-0.1175
Mass flux of powder entrained by gas (kg/m <sup>2</sup> s)	-0.0227	-0.0067
Vapours evaporated from the discrete phase to gas (kg/m <sup>2</sup> s)	-0.0453	-0.0416
Percentage mass imbalance (%)	3.53%	0.65%

Figure 7.40 is a plot of contours of gas temperature in the cylindrical region of the tower. The spray nozzle is located at a dimensionless height of 0.4. A low gas

temperature exits in the spray region in both Cases 5 and 6, due to rapid evaporation of moisture from the initial slurry droplets causing cooling of the surrounding gas (inlet slurry temperature is 365.5 K). The temperature in the bottom cylindrical region of the tower is highest and gets lowered as the gas moves upwards due to exchange of heat with the droplets/particles. In Case 5 (droplet PSD), the gas temperature at  $z/Z = 0.15$  is higher compared to Case 6 (particle PSD), and above the nozzle  $z/Z > 0.4$ , the gas temperature is relatively lower in Case 5. This is due to the specification of initial droplet size distribution in Case 5, resulting in a more rapid heat exchange between the two phases near the spray nozzle, hence the outlet gas temperature in Case 5 is lower than that in Case 6. Similarly, the gas temperature in Case 5 is higher in the bottom region ( $z/Z = 0.15$ ), because most of the heat exchange takes place close to the nozzle, hence when the particles reach the bottom region, only sensible heating is the dominant heat transfer mode for most of the particles, whereas in Case 6, since the sizes are larger, they fall down relatively quicker and much of the drying is taking place in the bottom cylindrical region of the tower, and this heat for drying is supplied by the gas, therefore, the gas temperature in the bottom region is smaller in Case 6 and the particles are less susceptible to thermal degradation.

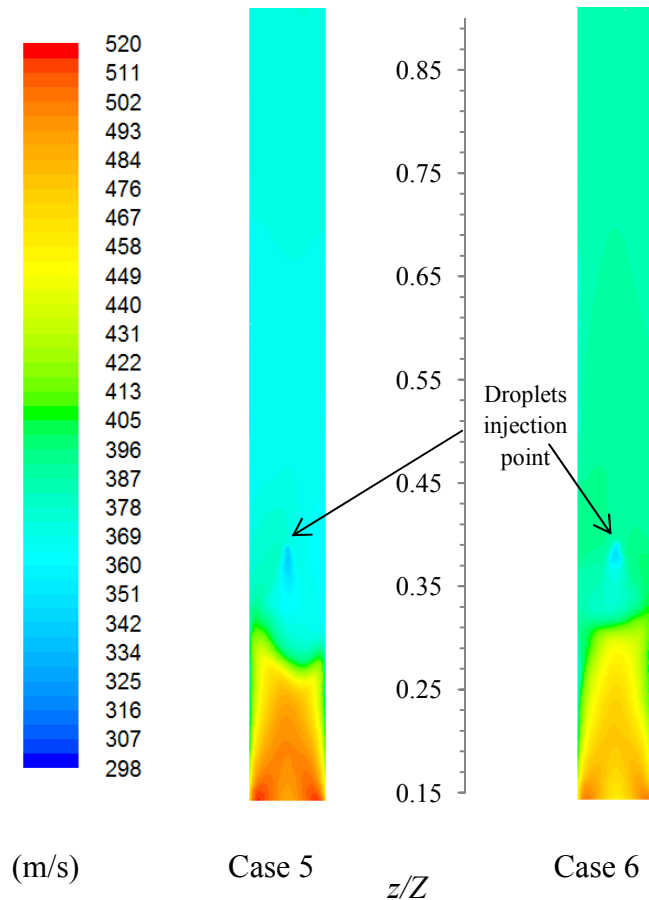


Figure – 7.40: Contours of gas temperature distribution.

Figure 7.41 is plot of measured time-averaged gas temperature profiles along the radius at two axial locations compared with predicted gas temperature profiles in Case 5 and Case 6. At a dimensionless height of 0.23 (below the spray nozzle), the measured temperature profiles represents a parabolic profile. The gas temperature is lower near the wall and higher near the centre. Above the spray nozzle ( $z/Z=0.41$ ), the measured temperature profile is relatively flat and resembles a plug-flow profile. It is observed that Case 2 (particle PSD) gives a closer comparison with measured temperature profile at both measurement locations. It should be noted that due to the presence of slurry spray, the droplets/particles were also deposited to the thermocouples (Figure 4.9 (c), (d) and (e) in Chapter 4), hence the measured temperatures also include associated errors due to the deposition of particles on the thermocouples.

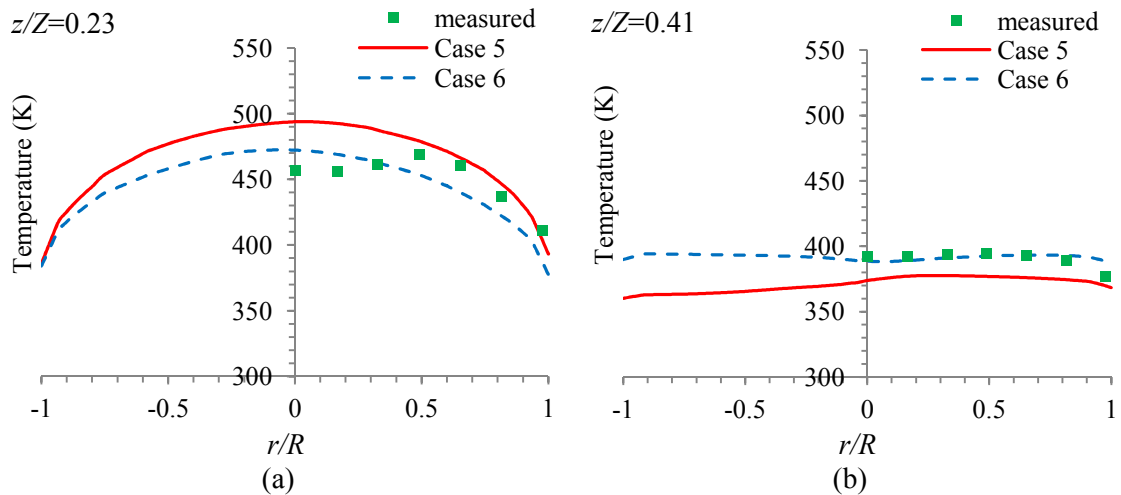


Figure – 7.41: Predicted gas temperature profiles compared with measurements by Martin de Juan (2012).

Figure 7.42 is a plot of residence time of particles of different sizes that exit from the bottom of the tower in CFD Case 5 and Case 6. The smaller particles have greater residence time compared to larger particles. The smaller particles (up to about 600  $\mu\text{m}$ ) show a greater decrease in the residence time with increasing particle size compared to larger particles. For particle sizes larger than 1000  $\mu\text{m}$  in CFD Case 5, the residence time does not change appreciably with increasing particle size. From a comparison of the residence time of both CFD Cases, it is observed that the predicted residence times for the common sizes is very similar in both cases, same observation applies to the plug-flow predicted residence times. It is observed that the predicted temperature profile (Figure 7.40 and 7.41) in CFD Case 5 has a greater temperature in the bottom cylindrical region, but it does not affect the predicted residence times appreciably when compared with the common particle sizes in Case 5 and 6. In Case 5, 150  $\mu\text{m}$  particle

sizes also exit from the tower bottom and have a much larger residence time compared to the larger particle sizes. In the plug-flow model, the entrainment of particles is not considered; therefore the residence time of particles sizes less than 150  $\mu\text{m}$  is also observed. The residence times of all particle sizes in the plug-flow cases are smaller than the residence times predicted by the CFD cases. The differences in the residence times are greatest for smaller particle sizes because smaller particles show greater influence of turbulent fluctuating velocities and smaller particles also get caught up in the recirculating regions of the gas flow which are not taken into account in the plug-flow model. Additionally, in the plug-flow model, the minimum velocity is set to the terminal falling velocity, but particles may exhibit velocity less than the terminal falling velocity therefore this limitation of the plug-flow model is also responsible for predicting shorter residence time of particles. However, both the plug-flow and CFD cases give qualitatively similar residence times, i.e., an exponentially decreasing trend in the residence times with increasing particle sizes.

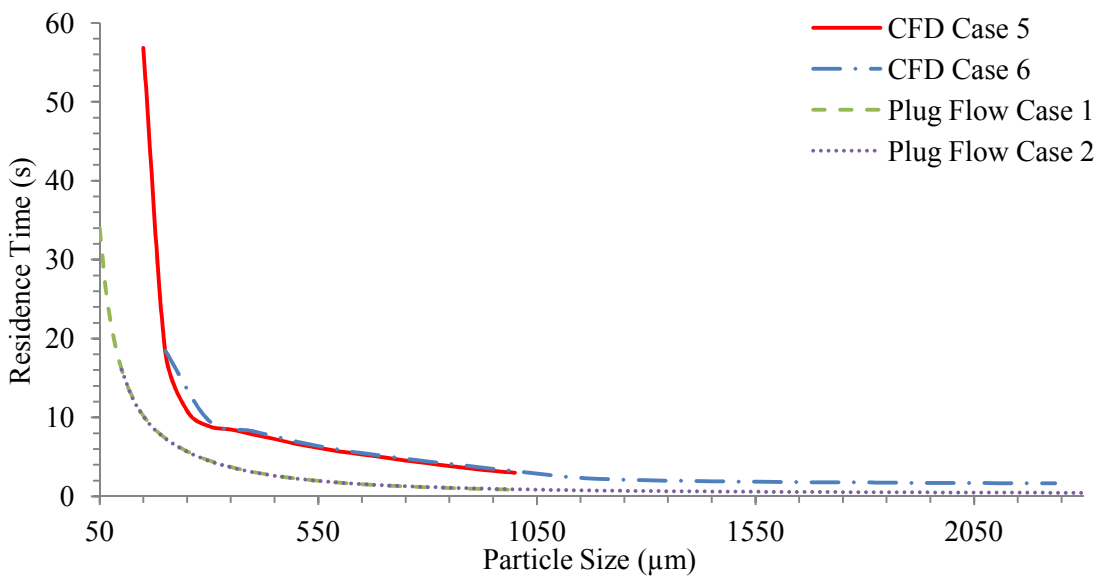


Figure – 7.42: Predicted residence times of different particle sizes.

Figure 7.43 is a plot of exit temperature and normalised moisture fraction of particles of different sizes at the tower bottom in both Cases 5 and 6. Particle size up to about 500  $\mu\text{m}$  exit at zero moisture content in both cases, while larger particles have greater moisture content with increasing size. This is because smaller particles have greater residence times compared to larger particles (Figure 7.42), additionally, smaller particles have greater heat and mass transfer rates due to greater specific area and hence lose moisture quicker. Similarly these particle sizes have the highest exit temperature as dried particles quickly acquire the surrounding gas temperature near the bottom exit.

The exit particle temperature of these sizes is greater in Case 5 because the gas temperature is greater at the bottom in Case 5 (Figure 7.40). A noticeable difference is observed in the predicted exit normalised moisture of particles in the range of 550 to 900  $\mu\text{m}$  in Case 5 and 6. Case 5 predicts a relatively smaller moisture content for these sizes, this is because in Case 5, the gas temperature in the bottom region of the tower is larger (Figure 7.40) as most of the drying in this case takes place near the nozzle. Therefore, the particles whose moisture content is above zero pass through higher temperature and lose moisture relatively quicker than Case 6. It is interesting to note that this gas temperature difference in both cases does not appreciably influence the exit particle residence times of the common sizes of Case 5 and 6 (Figure 7.42). Hence a higher gas temperature has a more dominant influence on the particles drying rates and less dominant influence on the residence times. In Case 6, for particle sizes greater than 1900  $\mu\text{m}$ , the exit temperature starts to reduce again, this is because these particles exit at a higher moisture content and their temperatures do not reach the slurry boiling point.

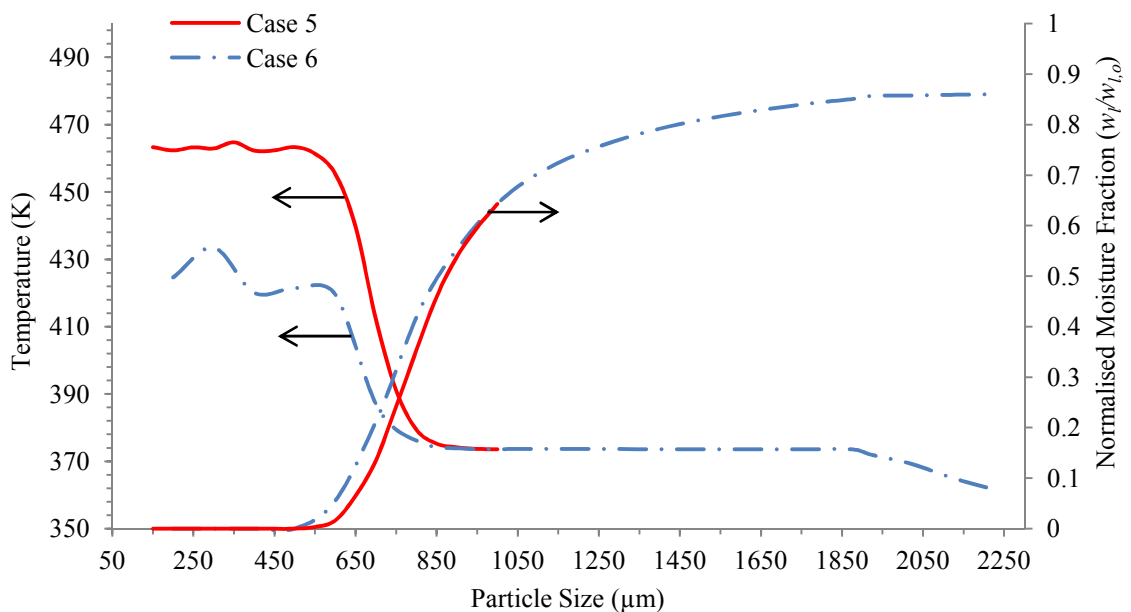


Figure – 7.43: Particle exit temperature and moisture content at the bottom outlet.

Table 7.10 lists a comparison of predicted dried powder parameters and exhaust gas temperature with the measured values. From a comparison of both simulation cases with experimental measurements by Martin de Juan (2012), it is found that the case with droplet size distribution (Case 5) overpredicts the overall heat and mass transfer between the discrete phase and the continuous phase as indicated by a lower gas temperature and dried powder moisture content. The case utilising measured powder size distribution (Case 6) underpredicts heat and mass transfer between the two phases as indicated by greater moisture content and a larger exhaust gas temperature. The same

trend is also observed in the plug-flow Case 1 and 2 and a discussion on the results is given in Section 5.5.6. It should be noted that the experimental data also include measurement errors as mentioned previously in Section 7.2.10.

Table – 7.10: Comparison of simulation results with experiment.

Parameter	Case 5 (Droplet PSD)	Case 6 (Powder PSD)	Measured (Martin de Juan, 2012)
Particle weighted average moisture content, %	0.51	4.39	2.49
Particle weighted average temperature, K	458.5	412.5	361.7
Average single particle density, kg/m <sup>3</sup>	1167	1228	703
Outlet gas temperature, K	374.6	385.19	382.3
Heat loss, kW	35.06	34.37	21.43

### **7.2.12 Modelling of Rough-Wall Collision Model**

From a comparison of CFD Cases 1 and 2, it is found that particle-wall interaction modelling impacts particle trajectories and residence times. In all the previous cases, the dispersion of particles due to rough surface resulting from wall deposits was not taken into account. In this section, a stochastic model for collision between the particle and the wall has been developed, that generates a surface roughness inclination angle at the point of particle-wall impact. The inclination angle of the rough wall surface is determined by assuming a Gaussian distribution with roughness surface inclination angle varying from  $-90^{\circ}$  to  $90^{\circ}$ . The probability of multiple particle rebound is evaluated and its effect on the particle trajectory is also calculated. The impacting particles are assumed to be smooth and spherical. The model is applied to the counter-current spray drying tower to predict post particle-wall collision trajectories considering a rough wall surface with a specified roughness height. Different particle-rough wall collision scenarios are depicted in Figure 7.44.



$$l_s = k_s \left( \frac{1}{\tan(|\theta_{w+}|)} + \frac{1}{\tan(|\theta_{w-}|)} \right) \quad (7.4)$$

In the following scenarios, only a single collision will take place between the particle and the wall:

1. If the particle hits the luff side and the particle-wall impact angle ( $\theta_{wp}$ ) is less than  $90^\circ$ .
2. If the particle hits the lee side and the particle rebound angle ( $\theta_{pr1}$ ) is greater than or equal to the roughness inclination angle of the luff side ( $|\theta_{w-}|$ ).
3. If the diameter of the particle is greater than  $l_s$ .

The particle post collision velocity components are determined by the normal and tangential restitution coefficients. The normal restitution coefficient is considered as a linear function of particle-wall impact angle obtained from the data given by Hassal (2011) who determined the restitution coefficients of dry detergent particles by impacting on a smooth steel wall at different impact angles. The normal restitution coefficient is given by:

$$C_{r,n} = -0.0033\theta_{wp} + 0.45 \quad (7.5)$$

The tangential restitution coefficient ( $C_{r,t}$ ) is considered as a linear function of moisture content (equation (7.1)).

To evaluate whether multiple particle rebound occurs, the post collision angle ( $\theta_{pr1}$ ) is required, which is calculated using the following equation:

$$\theta_{pr1} = \tan^{-1} \left( \frac{u_{pr,2}}{u_{pz,2}} \right) \quad (7.6)$$

The height of the particle-wall impact location is determined by stochastic approach, using the following equation:

$$h_1 = k_s \zeta' \quad (7.7)$$

where  $\zeta'$  is a uniformly distributed random number in the range 0 to 1.

The height traversed by the rebound particle at a distance  $l_p$  from the first impact location is calculated using the following equation:

$$h_2 = \left( \frac{h_1}{\tan(|\theta_{w+}|)} + \frac{k_s}{\tan(|\theta_{w-}|)} - d_p \right) \times \tan(\theta_{pr1}) \quad (7.7)$$

If the sum of  $h_1$  and  $h_2$  is less than the roughness height ( $k_s$ ), then the particle will rebound with the wall again. The post rebound velocity of the particle is then again calculated using the normal and tangential restitution coefficients given by equation (7.5) and (7.1) respectively. An algorithm for particle-rough wall collision model is depicted in Figure 7.45. The particle-rough wall collision has been applied to the modelling of spray drying process to predict post particle-wall collision trajectories. The model is incorporated in Fluent using user-defined functions. The value of roughness height ( $k_s$ ) is specified to be 2 mm.

### **7.2.13 Simulation Results With Rough Wall Collision Model**

The input operating conditions for the discrete and continuous phases are listed in Table 7.4. The wall heat flux is modelled in the same manner as in Case 2. The convergence criteria are kept the same as in the previous cases. The resulting particle trajectories of different sizes are given in Figure 7.46, which are coloured by particle diameter. From the plot of droplet/particle trajectories, it is observed that the larger particles after colliding with the wall move towards the centre of the wall until they reach the other side of the wall, while the smaller particles (up to 200  $\mu\text{m}$ ) get entrained by the gas. Particles greater than 200  $\mu\text{m}$  strike the wall and start to move close to the wall. In the trajectories of the largest particle sizes, the effect of wall roughness on rebound angle is not very significant, but it is more prominent for particles in the intermediate range (500  $\mu\text{m}$  to 2000  $\mu\text{m}$ ), in which a spread in the rebound angle is observed due to the stochastic treatment of roughness inclination angles.

65.6% of the slurry inlet mass exits from the tower bottom and 7.2% of the slurry mass exits as entrained powder and the remaining mass of the slurry is evaporated from the droplets/particles as water vapours.

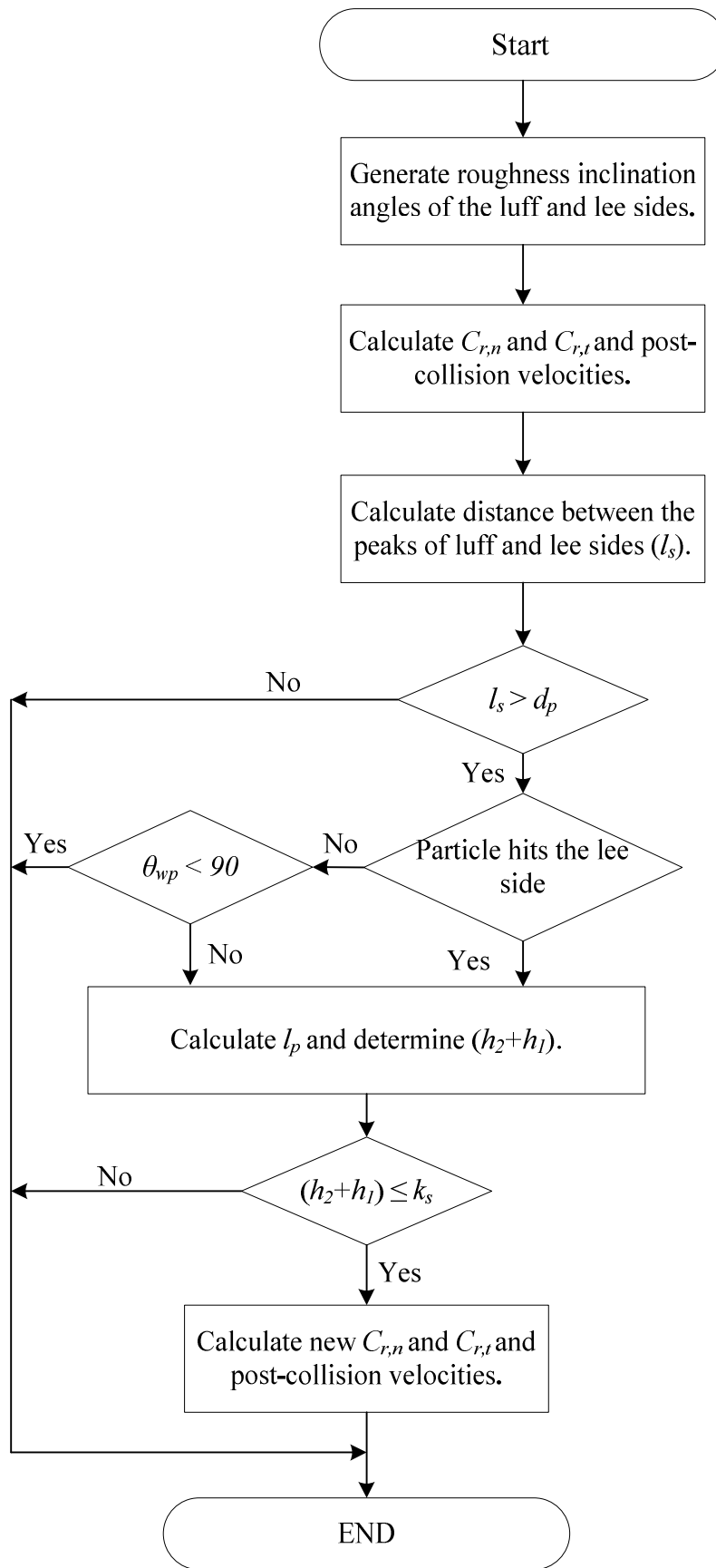


Figure – 7.45: Particle-rough wall collision model algorithm.

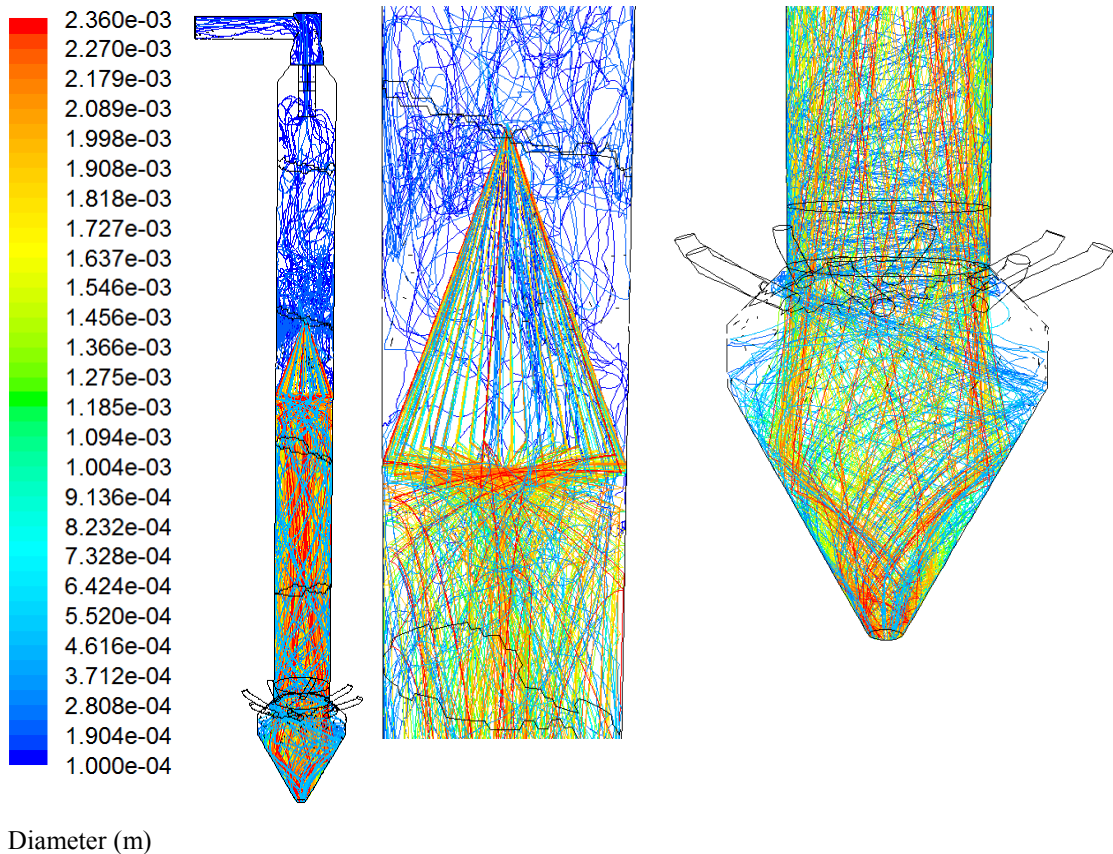


Figure – 7.46: Particle trajectories coloured by diameter.

Figure 7.47 is a plot of discrete phase concentration along the radius of the column. The droplets are sprayed at  $z/Z=0.67$ . At all dimensionless heights, the discrete phase concentration is highest close to the wall and smallest near the centre. At the closest location to the spray nozzle ( $z/Z=0.56$ ), the concentration of droplets/particles is more uniform along the radius compared to all other dimensionless heights. As the particles further move downward, the discrete phase concentration near the wall increases and near the centreline it decreases. This is due to the centrifugal action of the swirling gas flow that forces the particles to move towards the wall as they flow downwards. At  $z/Z = 0.38, 0.29$  and  $0.20$ , the concentration of particles near the centreline is zero.

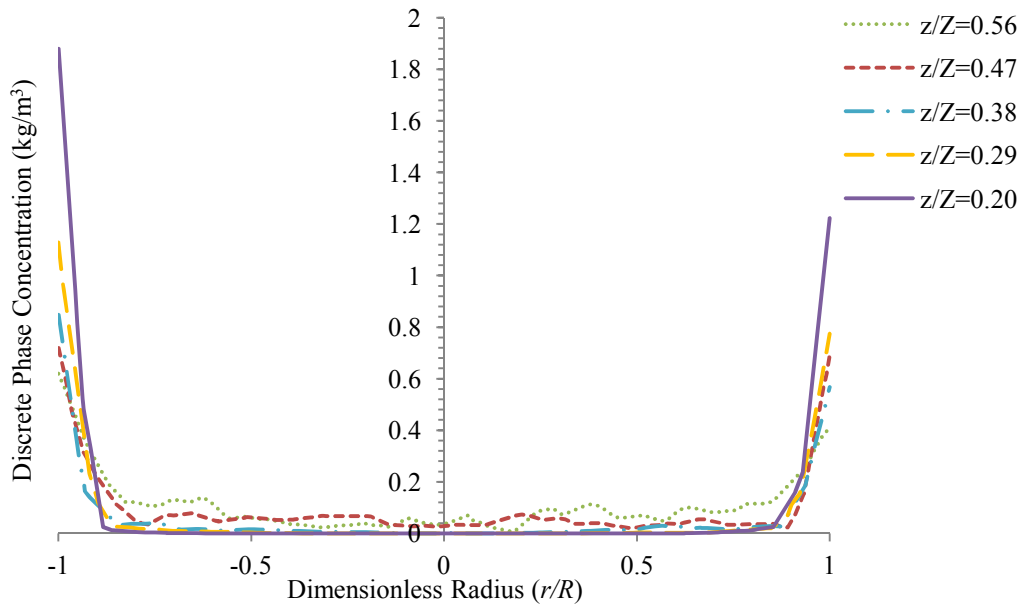


Figure – 7.47: Discrete phase concentration at different dimensionless heights.

In Figure 7.48, the trajectory of each particle size is plotted and the path lines are coloured by particle velocity. The smallest particle size (100  $\mu\text{m}$ ) escape from the top of the tower. Some of the 200  $\mu\text{m}$  particle sizes escape from top region while the others escape from the bottom of the tower. Particle sizes having a diameter of 300  $\mu\text{m}$  and above escape from the bottom region of the tower. Particle sizes of diameter 200  $\mu\text{m}$  and 300  $\mu\text{m}$  start to move towards the wall after the first impact with the wall, while the larger particle sizes 400  $\mu\text{m}$  and above bounce back from the wall after the first collision, since these particles have relatively greater momentum and have smaller influence of drag compared to particle sizes up to 300  $\mu\text{m}$ . From the post particle-wall collision trajectory, it is found that particle bounce off at different angles even of the same size, as the rough wall inclination is treated in a stochastic manner for each tracked parcel.

In Figure 7.49, the trajectories of particles of different sizes are plotted and are coloured by post-wall collision angle. It is observed that smaller particles (200  $\mu\text{m}$ ) bounce back from the wall at a higher angle as they swirl down the wall in the bottom cylindrical region of the tower. All particle sizes when they hit the wall from the injection location bounce back with different post-wall collision angles due to surface roughness at the wall treated stochastically for each particle-wall collision.

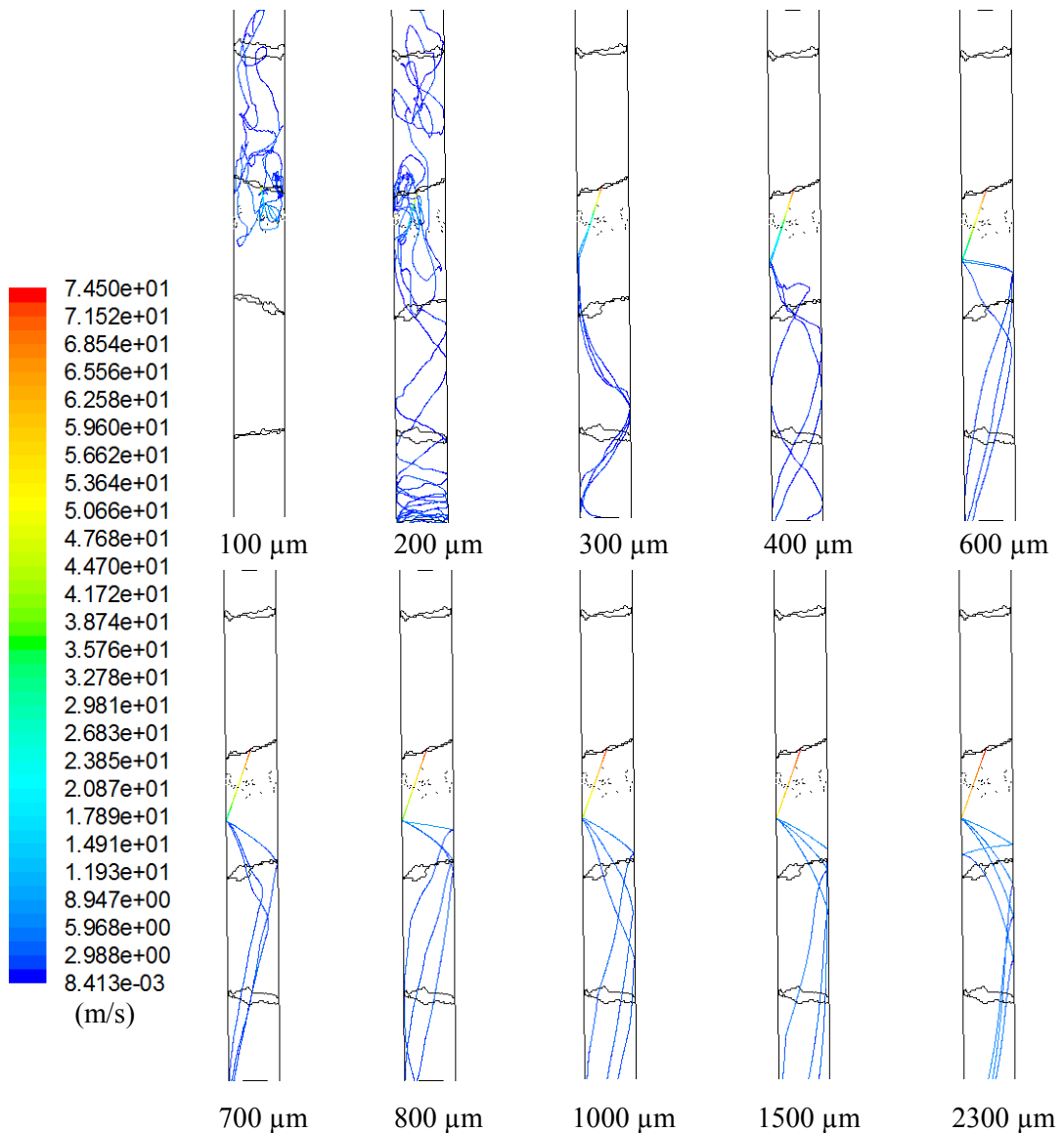


Figure – 7.48: Trajectories of particles of different sizes coloured by velocity.

Figure 7.50 is a plot of residence times of particles of different sizes that exit from the bottom of the tower. A comparison is made between Case 2 and Case 7, because in both cases, the same input conditions were used but the wall restitution coefficient in Case 2 was considered a linear function of moisture content for both normal and tangential components. It is interesting to note that the residence times of particles of different sizes in both cases are very similar. It may be due to the fact that the tangential restitution coefficient (used for computing velocity component parallel to the wall) in Case 7 is also modelled in the same way as in Case 2, i.e., a linear function of moisture content given by equation (7.1). In both cases, an exponential trend of decreasing residence time with increasing particle size is observed.

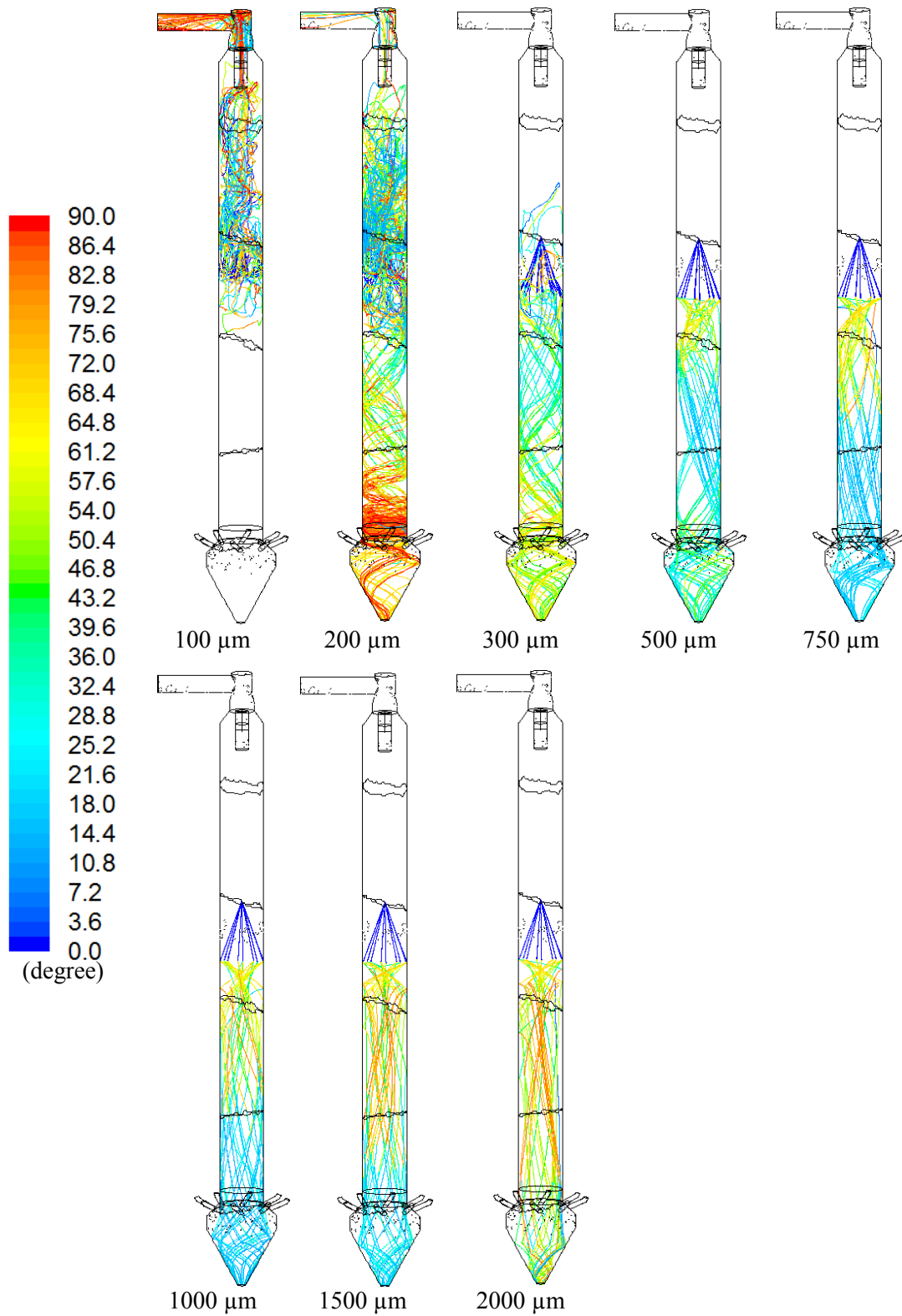


Figure – 7.49: Trajectories of particles of different sizes coloured by post-wall collision angles.

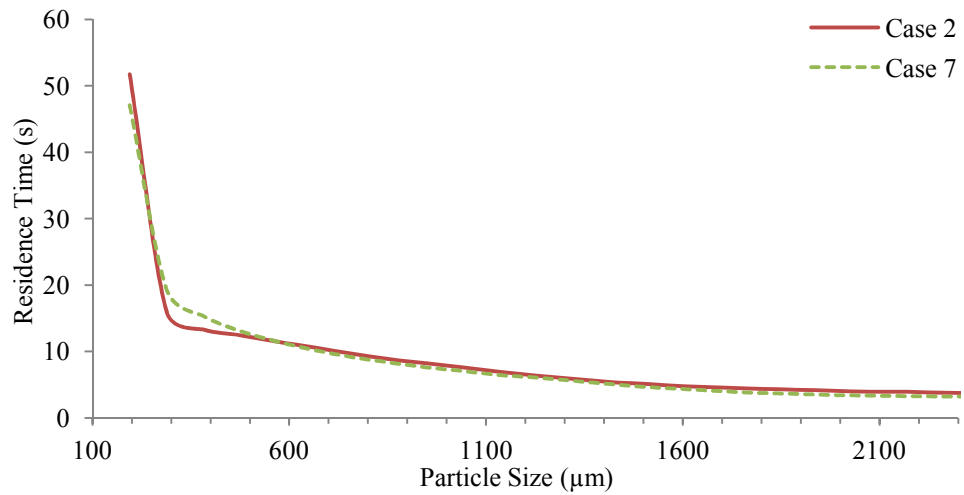


Figure – 7.50: Residence time of particles of different sizes.

Figure 7.51 is a plot of contours of gas temperature; a comparison is made with Case 2, in which the same thermal boundary condition was used as in Case 7 but the wall restitution coefficient was considered a linear function of moisture content for both the normal and tangential components. From a comparison of the gas temperature contours of both cases it is observed that in the bottom cylindrical region ( $z/Z = 0.16-0.5$ ) of the spray tower, a higher near-wall temperature exists in Case 7 compared to Case 2, this is due to the use of rough-wall surface modified restitution coefficient, in which the particles after striking the wall get more dispersed over the cross-section compared to Case 2, in which particles continue to move very close to the wall. Since the particles are more dispersed, therefore the temperature near the wall is relatively higher. The exhaust gas temperature in Case 7 is lower, because the particles are more dispersed and come in contact with higher gas temperature away from the wall, therefore more heat exchange takes place between the two phases, resulting in a lower gas temperature at the exit. The temperature near the tangential inlets ( $z/Z = 0.12$ ) of the tower in Case 7 is greater compared to Case 2, since most of the heat exchange between the two phases takes place in the top region of the tower, on the contrary, particles in Case 2 have a higher moisture when they reach the bottom region because they get exposed to a lower gas temperature in the top region and hence exchange relatively more heat with the drying gas in the bottom region, therefore in Case 2, the conical region has a lower temperature.

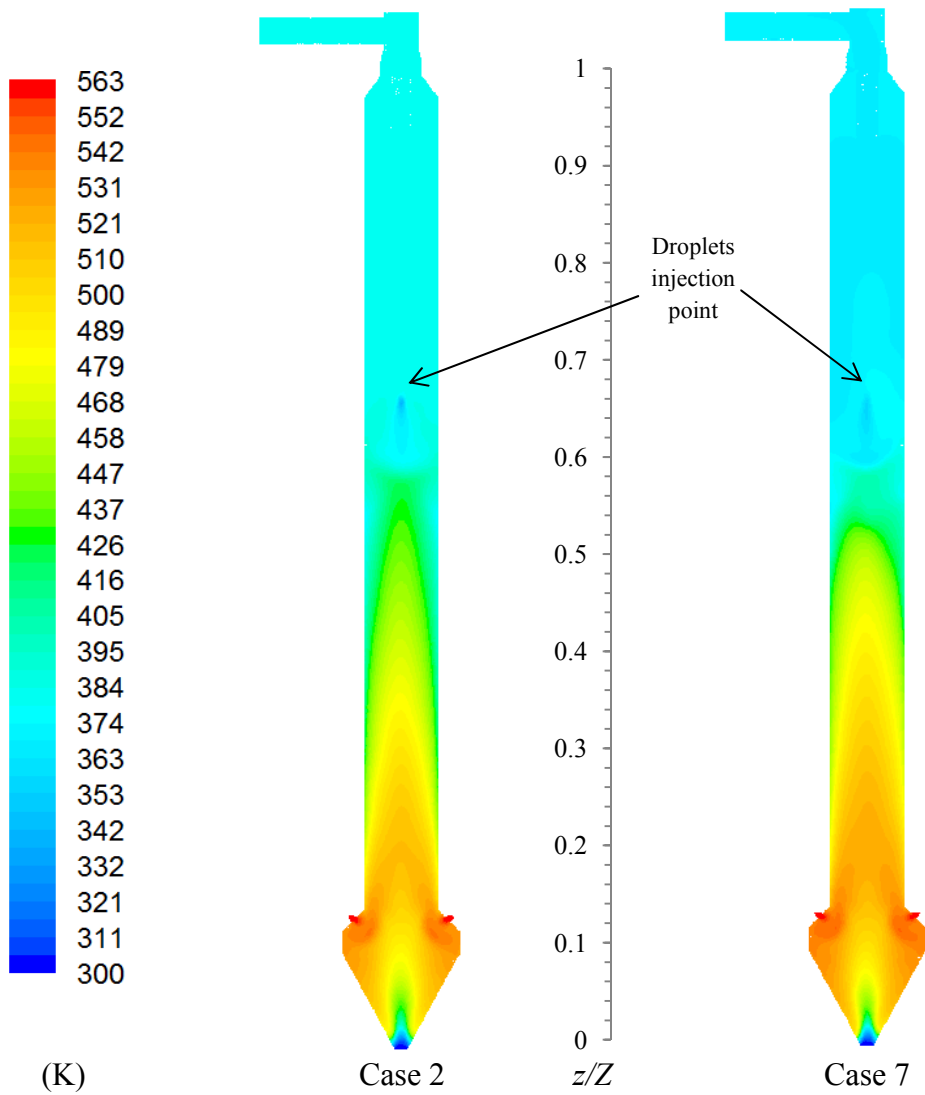


Figure – 7.51: Gas temperature distributions.

Figure 7.52 is a plot of temperature and normalised moisture fraction of particles that exit from the bottom outlet of the spray tower. A comparison is made between Case 2 and Case 7. In Case 7, the particles of sizes up to 1500  $\mu\text{m}$  exit at a higher temperature compared to Case 2 prediction. Because in Case 7, the particles get more dispersed over the cross-section of the tower as a result of particle-rough wall impact, therefore they exchange more heat in the cylindrical region of the tower and at the bottom, they have a lower moisture content and thus exit at a higher temperature compared to Case 2 in which particles remain closer to the wall as they fall down, where the temperature is lower and thus heat and mass transfer between the two phases is not as rapid, and when they reach the bottom conical region, the moisture in larger particles sizes ( $>900 \mu\text{m}$ ) is still evaporating resulting in cooling of the gas in the bottom conical region of the tower.

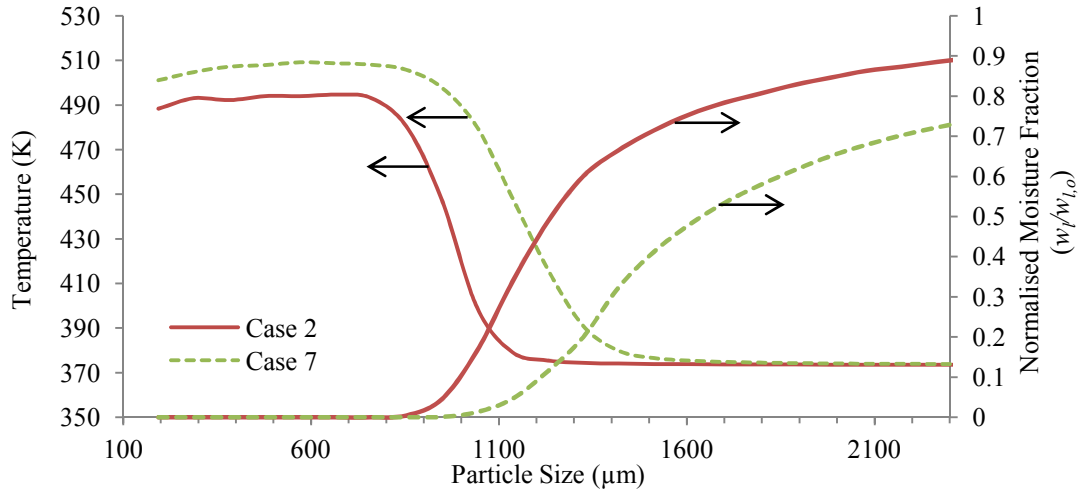


Figure – 7.52: Exit temperature and normalised moisture fraction of particles.

Table 7.11 lists a comparison of CFD simulation Cases 2 and 7 and measured data. It is observed that Case 7 gives a very close agreement with measured particle weighted average moisture content and outlet gas temperature compared to Case 2. The predicted weighted average particle outlet temperature in Case 7 is greater than in Case 2 as the particles in this case exit at a much lower moisture content and the gas temperature in the bottom conical region in Case 7 is also greater compared to Case 2 (Figure 7.51). The large difference between the heat loss based on measured values and that predicted by the simulation results is already explained in Section 5.5.3.

Table – 7.11: Comparison of CFD simulation results with experimental data.

Parameter	Case 2	Case 7	Measured (Martin de Juan, 2011)
Particle weighted average moisture content, %	4.75	2.19	1.8
Particle weighted average temperature, K	456.19	479.7	356
Outlet gas temperature, K	381.4	368.7	367
Heat loss, kW	5.4	5.91	62.1

#### **7.2.14 Conclusions**

Multiphase CFD modelling of spray drying process was carried out considering heat, mass and momentum transfer between the discrete phase and the continuous phase using steady state, Eulerian-Lagrangian approach. The droplet drying kinetics was modelled using a semi-empirical droplet drying model. It was found that the modelling

of particle-wall interaction is one of the critical factors, as it influences the particle trajectories and hence the heat and mass transfer between the two phases. A restitution coefficient which is a function of moisture content gives more realistic particle trajectories. The influence of non-spherical drag law on the particles residence time is also evaluated. It is found that the drag coefficient for non-spherical particle increases the particles residence time. But it is very difficult to calculate particle sphericity as it depends on a number of factors including the level of agglomeration, morphological changes during drying and temperature history of particles. Further simulation runs were carried out to assess the influence of initial droplet size distribution specification by specifying measured droplet size distribution as well as powder size distribution as the initial droplet sizes. This parameter significantly influences the simulation results as the smaller droplets sizes exchange more heat and mass and have greater residence time compared to larger particles. The larger particles have smaller heat and mass transfer rate and shorter residence time. It is found that in Case 5 (droplet PSD) that the gas temperature is higher in the bottom region of the tower, but this does not have a significant influence on the residence time of common particle sizes compared with Case 6 (powder PSD), however an appreciable difference in the exit particle moisture content is observed in common particle sizes between the two cases. Hence it can be concluded that the change in gas temperature has a stronger influence on the particle drying rate and less influence on the particle residence time. When the powder PSD is used (Case 6), then the final particle temperature is smaller for sizes exiting at zero moisture content, hence the possibility of thermal degradation is greater if a fine powder is produced compared to a coarser powder.

From a comparison of plug-flow modelling results with CFD it is found that the plug-flow model underpredicts the residence time of particles. This is primarily due to the assumption of terminal falling velocity of the particles as the minimum velocity, although both the plug-flow model and the CFD models predict the same trend of increasing residence time with decreasing particle size. A rough-wall particle collision model is developed based on stochastic approach to study the influence of wall surface roughness on the post-wall collision trajectories in CFD modelling. Wall roughness increases the dispersion of particles over the cross-section of the tower after particle-wall impact and this primarily increases the heat and mass transfer rate between the two phases because the particles get exposed to a higher gas temperature. This results in a lower exhaust gas temperature and a lower exit particle moisture content.

The present work emphasizes on the importance of inclusion of agglomeration in the CFD modelling of spray drying process for a more reliable prediction, additionally, the data used for CFD model validation should be measured at the same location. Furthermore, the effect of wall deposition and re-entrainment of particles upon wall collision should also be assessed by developing appropriate models for wall deposition and re-entrainment of deposits back into the gas flow.

## **8. MODELLING OF A SPRAY DRYING TOWER WITH TWO NOZZLES**

### **8.1 Introduction**

In Chapters 5 and 7, modelling of the IPP spray drying tower was carried out considering a single centrally located hollow-cone nozzle using plug-flow and CFD approaches respectively. The spraying of slurry using multiple nozzles at different heights is commonly practised in the commercial spray drying towers to increase the throughput without adversely affecting the level of agglomeration (Bayly, 2013). The IPP tower has multiple centrally located hollow-cone nozzles at different heights and sometimes the slurry is sprayed using two nozzles to evaluate its effect on the spray dried powder characteristics as it closely resembles the operating mode of the commercial spray drying towers. The mass flows of slurry and hot gas in this configuration are typically larger than those from a single nozzle. In this chapter, both plug-flow and CFD modelling have been carried out using two nozzles and the results are validated with experimental data collected from the IPP spray drying tower.

### **8.2 Plug-Flow Modelling with Two Nozzles**

A plug-flow modelling simulation run is carried out considering two centrally located nozzles located at different heights in the tower (listed in Table 8.1). To accommodate two nozzles in the simulation run, no changes in the plug-flow solution methodology were required. The set of equations described in Chapter 5 for the droplets/particles and the gas are also applicable to the two nozzle case. The solution algorithm was however modified to account for the second nozzle and changes were made in the MATLAB (2010) code to accommodate spray of droplets from another nozzle located at a specified height. The solution is initialised using estimated values of outlet gas temperature ( $T_{gas,out}$ ) and outlet gas mass flow. The polydispersed droplet/particle velocities, Reynolds numbers, drying rates, temperatures and moisture contents, sprayed from the first nozzle are calculated at each incremental height ( $\Delta z$ ) until the height of the tower reaches the second nozzle location where the polydispersed droplets injected from the second nozzle are also included into the heat and mass transfer calculations at each incremental height ( $\Delta z$ ) until they reach the bottom outlet of the tower. Figure 8.1 is the logic flow diagram of the algorithm for the numerical solution.

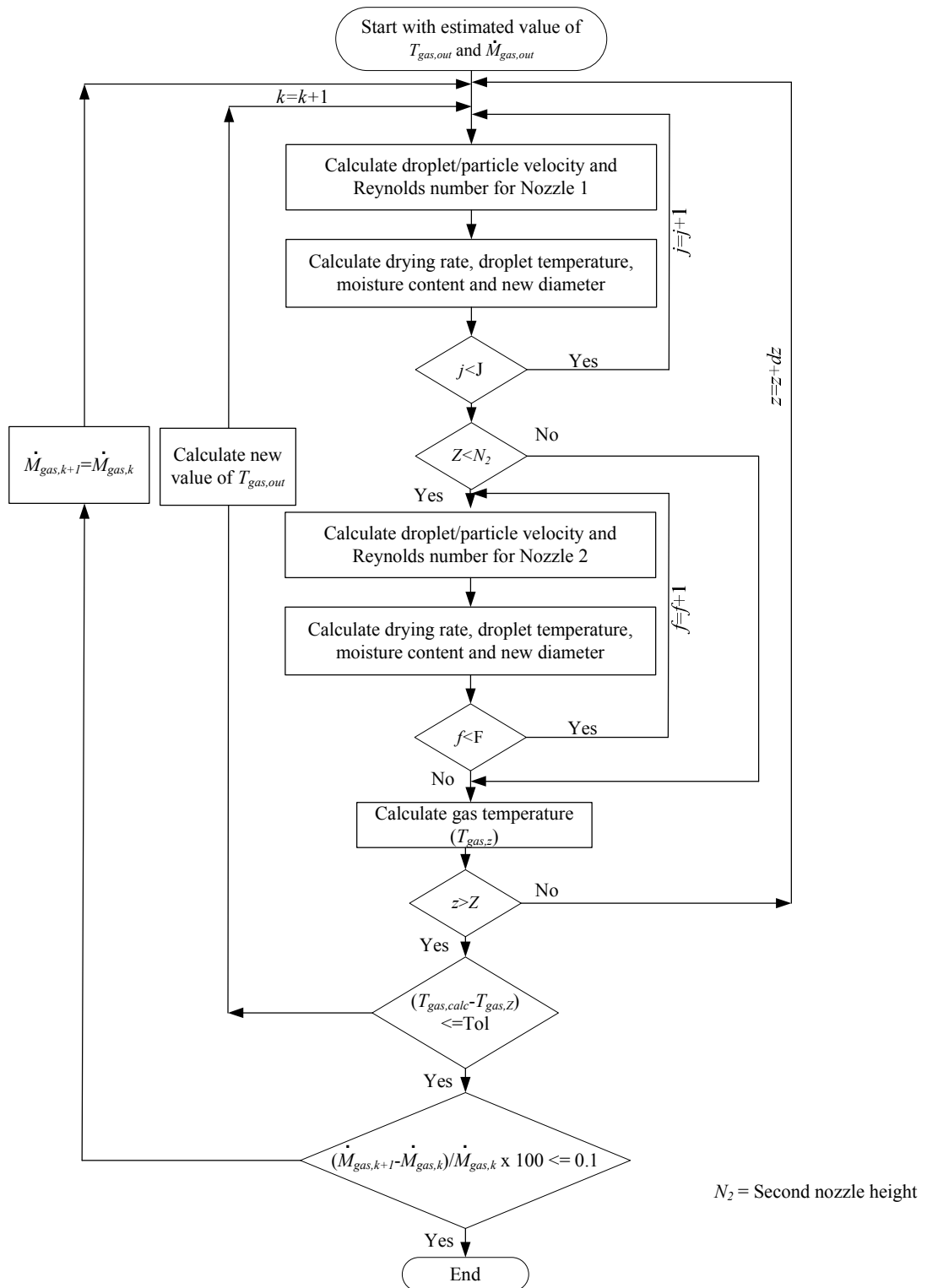


Figure – 8.1: Logic flow diagram of the algorithm for the plug-flow model with two nozzles.

Two cases are considered for this mode of operation of the tower, hereby referred to as plug-flow Case 3 and plug-flow Case 4. In plug-flow Case 3, the measured droplet size distribution is used as the initial droplet size distribution, whereas in plug-flow Case 4, the measured size distribution of the dried powder is used as the initial droplet size distribution. The measured droplet and particle size distributions and the corresponding

curve fits using a Rosin-Rammler distribution ( $d_m=245 \mu\text{m}$ ,  $u_s=1.4$  for droplets;  $d_m = 700 \mu\text{m}$ ,  $u_s = 1.8$  for particle sizes up to  $600 \mu\text{m}$ , and  $d_m = 1100 \mu\text{m}$  with  $u_s = 1.4$  for particle sizes greater than  $600 \mu\text{m}$ ) are given in Figure 8.2 (Martin de Juan, 2012). The input operating conditions listed in Table 8.1 were taken from the IPP spray drying tower run (Martin de Juan, 2012) carried out with two centrally located nozzles at different heights.

Table – 8.1: Input operating conditions for two nozzle configuration (Martin de Juan, 2012).

Droplet Properties		
Slurry inlet temperature	367.2	K
Slurry mass flux by each nozzles	0.164	kg/m <sup>2</sup> s
Specific heat of dried particle	1500	J/kg K
Specific heat of solvent	4180	J/kg K
Specific heat of vapours	1900	J/kg K
Density of slurry	1566	kg/m <sup>3</sup>
Latent heat of vapourisation	$2.26 \times 10^6$	J/kg
Diffusion coefficient of water in slurry	$3.0 \times 10^{-11}$	m <sup>2</sup> /s
Diffusion coefficient of water vapour into gas	$2.6 \times 10^{-5}$	m <sup>2</sup> /s
Spray Nozzle Position	Plug-Flow	CFD
Dimensionless height of nozzle 1	0	0.8
Dimensionless height of nozzle 2	0.5	0.4
Gas Properties		
Hot gas temperature	563.1	K
Hot gas mass flux	1.221	kg/m <sup>2</sup> s
Gas pressure	101325	Pa
Gas thermal conductivity	0.03	W/mK
Entrained air mass flux	0.061	kg/m <sup>2</sup> s
Specific heat	1006	J/kg K
Ambient temperature	282	K
Column Wall		
Metal wall thickness	0.006	m
Metal wall thermal conductivity	18.8	W/mK
Insulation thickness	0.105	m
Insulation thermal conductivity	0.04	W/mK

The first nozzle is located at a greater height compared to the plug-flow Case 1 and 2 (Chapter 5). The total number of increments used for this case is 7180; this corresponds to the same step size height ( $\Delta z$ ) as used in plug-flow Cases 1 and 2. The number of discrete sizes used for representation of the spray droplets of different sizes is 39 based on the sensitivity study in the plug-flow Case 1 in Chapter 5.

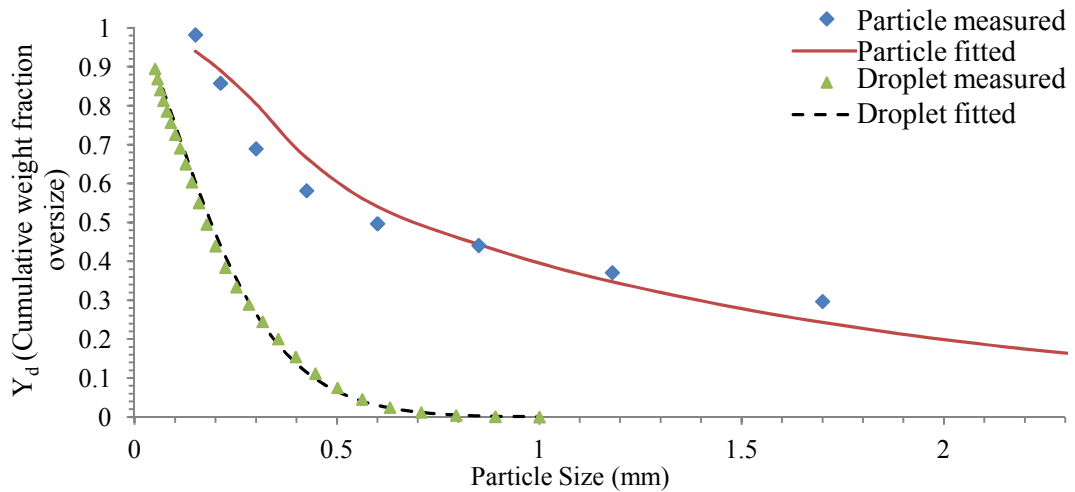


Figure – 8.2: Cumulative droplet and particle size distribution.

Figure 8.3 is a plot of residence time of particles of different sizes that exit from the bottom of the spray drying tower. The droplets are sprayed from nozzle 1 and nozzle 2 located at two different heights. The residence time of nozzle 2 particles is shorter because the nozzle is located at a lower height compared to nozzle 1, which is twice the height of nozzle 2. The qualitative trend is similar as that of single nozzle plug-flow cases, i.e., the smaller particles show a greater decline in residence time with an increase in size compared to larger particles ( $>600 \mu\text{m}$ ), which are almost insensitive to the particle size.

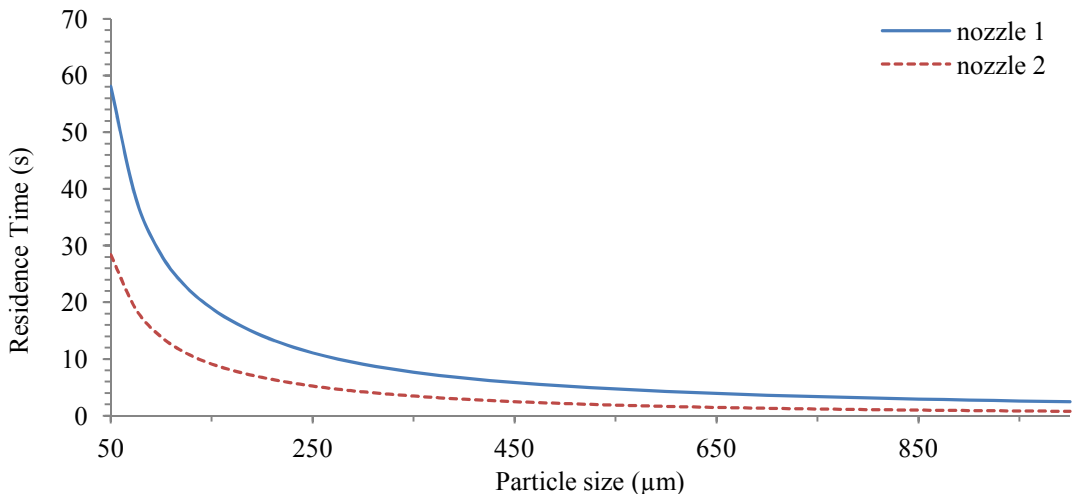


Figure – 8.3: Residence time of particles of different sizes for plug-flow Case 3.

Figure 8.4 is a plot of outlet temperature and normalised moisture content of particles of different sizes which are initially sprayed using nozzle 1 and 2. The particle sizes up to about 450  $\mu\text{m}$  exit at zero moisture content and the exit temperature is uniform for these particle sizes. The temperature drops rapidly and the moisture content increases for particle sizes greater than 450  $\mu\text{m}$ . For the nozzle which is located at a lower height (nozzle 2), the exit particle temperature is smaller and moisture content is greater because these particles have smaller residence times compared to the droplets injected from nozzle 1.

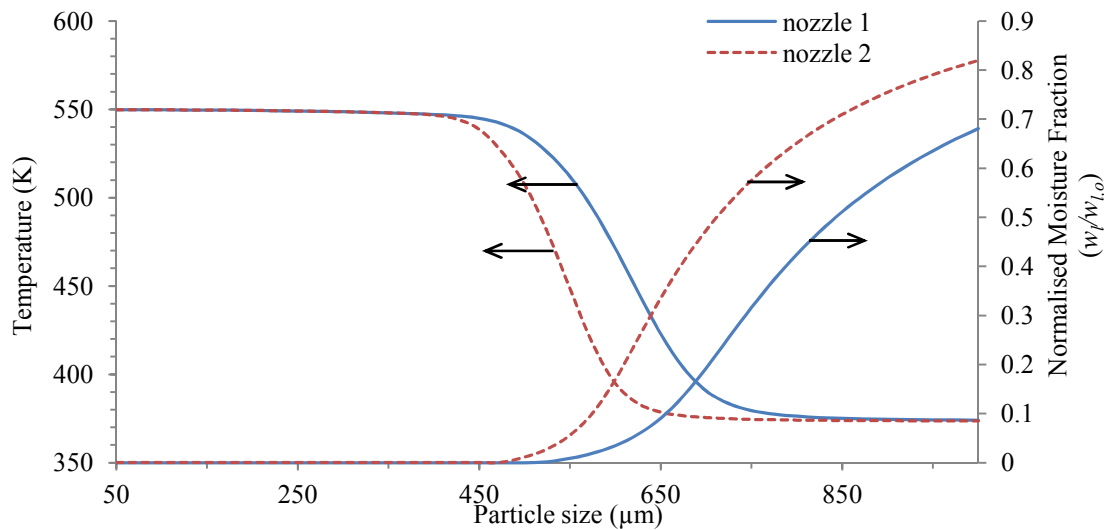


Figure – 8.4: Final temperature and moisture content of particles of different sizes for plug-flow Case 3.

Figure 8.5 is a plot of temperature profiles of the droplets/particles which are injected from nozzle 1 (at  $z/Z = 1$ ) in plug-flow Case 3. The temperature of initial slurry droplets is greater than the wet bulb temperature, therefore the temperature starts to fall rapidly for all droplet sizes. After a certain distance from the nozzle, the temperature starts to rise. This is due to crust formation on the surface causing a rise in temperature due to the lowering of the evaporation rate. Smaller droplets (50-100  $\mu\text{m}$ ) reach the gas temperature very quickly as they get dried quicker due to greater heat and mass transfer coefficients, smaller diffusion path and greater specific surface area. For larger particle sizes (>100  $\mu\text{m}$ ), there is a constant temperature region corresponding to about 373 K, this is the boiling point of the slurry. Once the particles reach the slurry boiling point, the drying rate becomes dependent on the rate of heat transfer to the particles (third stage of drying). The slurry boiling point varies strongly at lower moisture contents, therefore as the particles become more dry, the temperature starts to rise rapidly, which is observed in the temperature profile of particle sizes up to 400  $\mu\text{m}$ . The exit gas

temperature is lower than the initial slurry droplet temperature due to the use of two nozzles and nozzle 1 is located at a greater height compared to plug-flow Case 1 and 2, therefore the gas gets more time to exchange heat with the droplets and particles and evaporative cooling lowers the exit gas temperature to below the initial slurry droplet temperature.

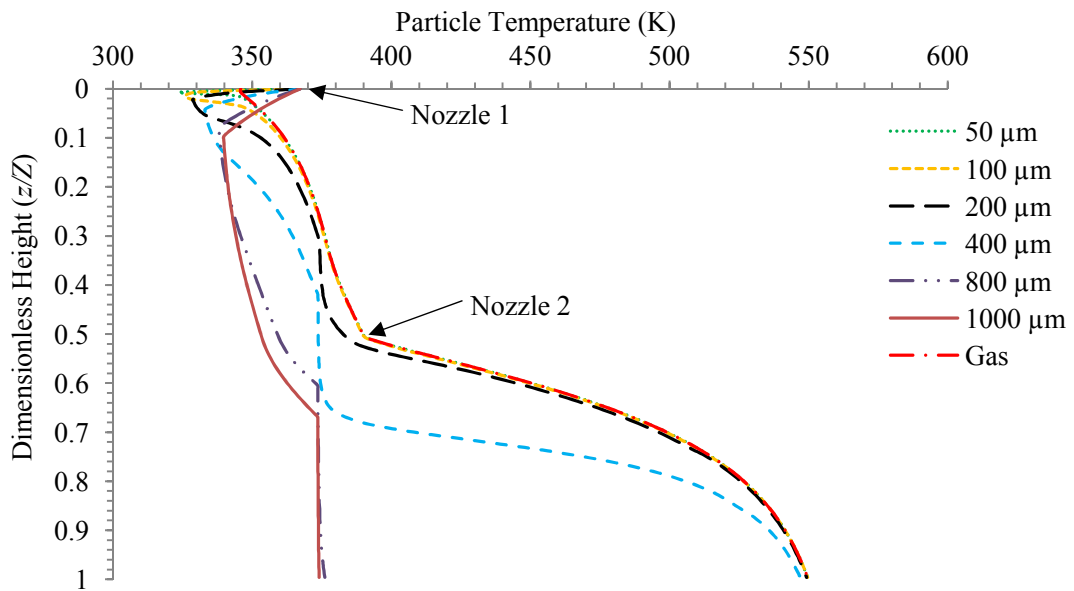


Figure – 8.5: Temperature profiles of gas and particles injected from nozzle 1.

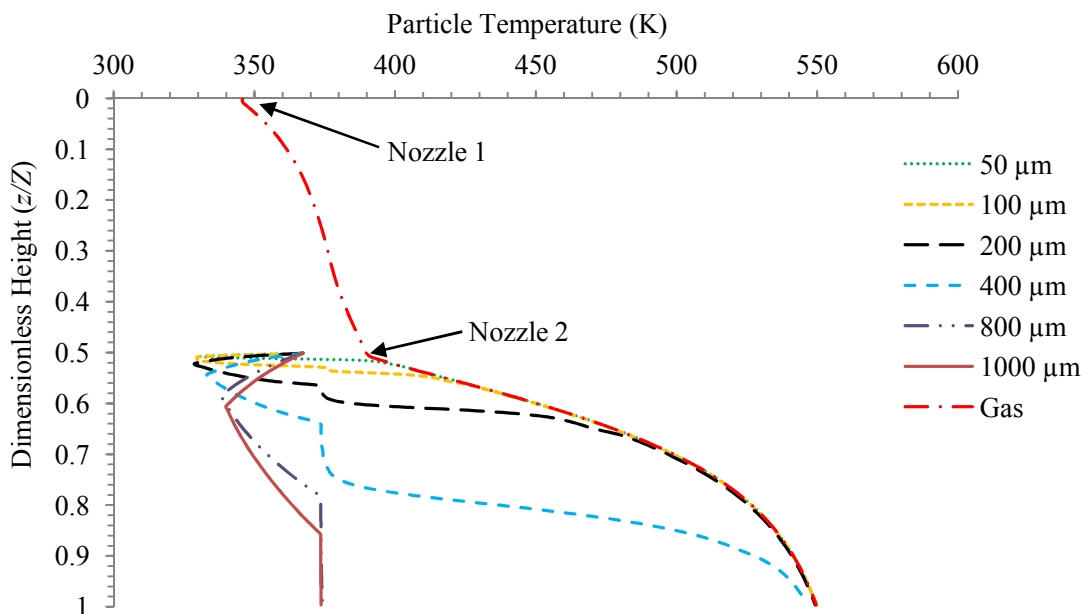


Figure – 8.6: Temperature profiles of gas and particles injected from nozzle 2.

Figure 8.6 is a plot of temperature profiles of droplet/particles injected using nozzle 2 in plug-flow Case 3, which is located at a lower height. All the droplets/particles exhibit similar behaviour as in Figure 8.5 but these droplets/particles get exposed to a higher gas temperature. Therefore the rise in temperature of particles is steeper. Consequently

the constant temperature region corresponding to slurry boiling point at high moisture content is observed to be shorter for 200  $\mu\text{m}$  and 400  $\mu\text{m}$  particles because the drying rate is faster for particles injected from nozzle 2.

The predicted temperature profiles in plug-flow Case 4 are qualitatively similar, and the discussions of Figures 8.5 and 8.6 are also applicable to this case, therefore they are not presented.

Figure 8.7 is a plot of residence time of different particle sizes obtained from plug-flow Case 4 simulation run. The residence time distribution plot is qualitatively similar to that in Figure 8.3 for plug-flow Case 3. In this case, the size distribution of droplets/particles ranges from 100 to 2300  $\mu\text{m}$ .

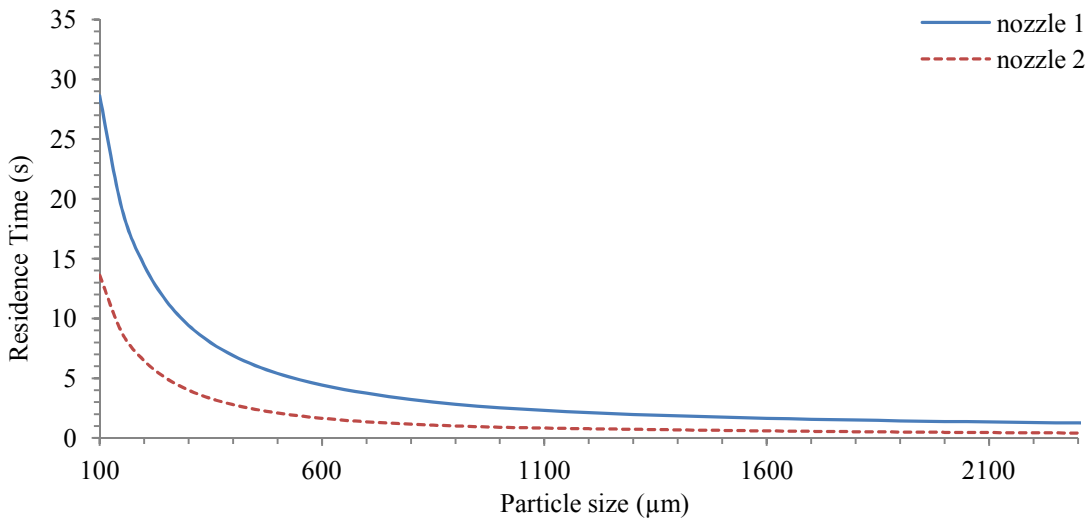


Figure – 8.7: Residence time of particles of different sizes for plug-flow Case 4.

### **8.3 CFD Modelling with Two Nozzles**

In this section, CFD simulation cases have been carried out to study the influence of slurry sprayed from two nozzles on the gas velocity and temperature profiles and how well the CFD model predicts the dried powder characteristics compared to experimental data in this mode of operation and how it compares with the results of the plug-flow model. The two cases considered are referred to as CFD Case 8 and CFD Case 9. In CFD Case 8, the measured initial droplet size distribution at each nozzle is used and in CFD Case 9, the measured dried powder size distribution is used, both fitted using Rosin-Rammler distribution given in Figure 8.2. The input operating conditions used in CFD Case 8 and 9 are listed in Table 8.1.

For the modelling of particle-wall collisions, a restitution coefficient varying as a linear function of moisture content (equation 7.1) is used. The modelling of heat loss is carried out in the same manner as in Cases 5 and 6 in Chapter 7. The convergence criteria used for the single nozzle cases carried out in Chapter 7 is also used to check the convergence of multiple nozzle cases. Table 8.2 shows the mass balance on the discrete phase (given in terms of mass flux due to confidentiality reasons) for Case 8 and Case 9 at the end of the simulation runs. 24% of the input slurry mass is entrained by the gas in Case 8, while in Case 9, it is only 5.2%. This is due to the use of a smaller size distribution in Case 8, therefore a larger mass of powder comprises smaller sizes, which gets entrained with the exhaust air. The overall enthalpy balance error is 2.1 % for CFD Case 8 and that for CFD Case 9 is 0.2%.

Table – 8.2: Mass balance on the discrete phase for CFD simulations.

Parameter	Case 8	Case 9
Mass flux of injected droplets (nozzle 1+ nozzle 2) (kg/m <sup>2</sup> s)	0.3282	0.3282
Mass flux of powder collected from bottom (kg/m <sup>2</sup> s)	0.1570	0.2359
Mass flux of powder entrained by gas (kg/m <sup>2</sup> s)	0.0797 (24%)	0.0173 (5.2%)
Vapours evaporated from the discrete phase to gas (kg/m <sup>2</sup> s)	0.0896	0.0770
Percentage mass imbalance of discrete phase	0.57%	-0.61%

Figure 8.8 is a plot of contours of gas velocity profile coloured by magnitude of mean velocity components for CFD Cases 8 and 9. A higher gas velocity can be seen at a dimensionless height of 0.82 and 0.4 at which the droplets are sprayed via hollow-cone nozzles. This is due to the entrainment of gas in the spray zone as a high momentum is exerted by the sprayed droplets. A lower gas velocity region exists close to the wall throughout the tower height in the cylindrical region of the tower. Below nozzle 2 at a dimensionless height of 0.4, the flow is symmetrical in the cylindrical region with a low gas velocity magnitude near the wall and in the central region of the tower and a higher velocity in the annular region of the tower. This is due to swirling gas flow below nozzle 2 (as given by a higher swirl number in Figure 8.9, below  $z/Z = 0.4$ ). Above nozzle 2 (at  $z/Z > 0.4$ ), the gas velocity is nearly plug-flow in the cylindrical region, but a low gas velocity region exists near the wall. The velocity magnitude in both cases is

very similar throughout the tower height. The overall velocity profiles in both cases are reasonably symmetrical.

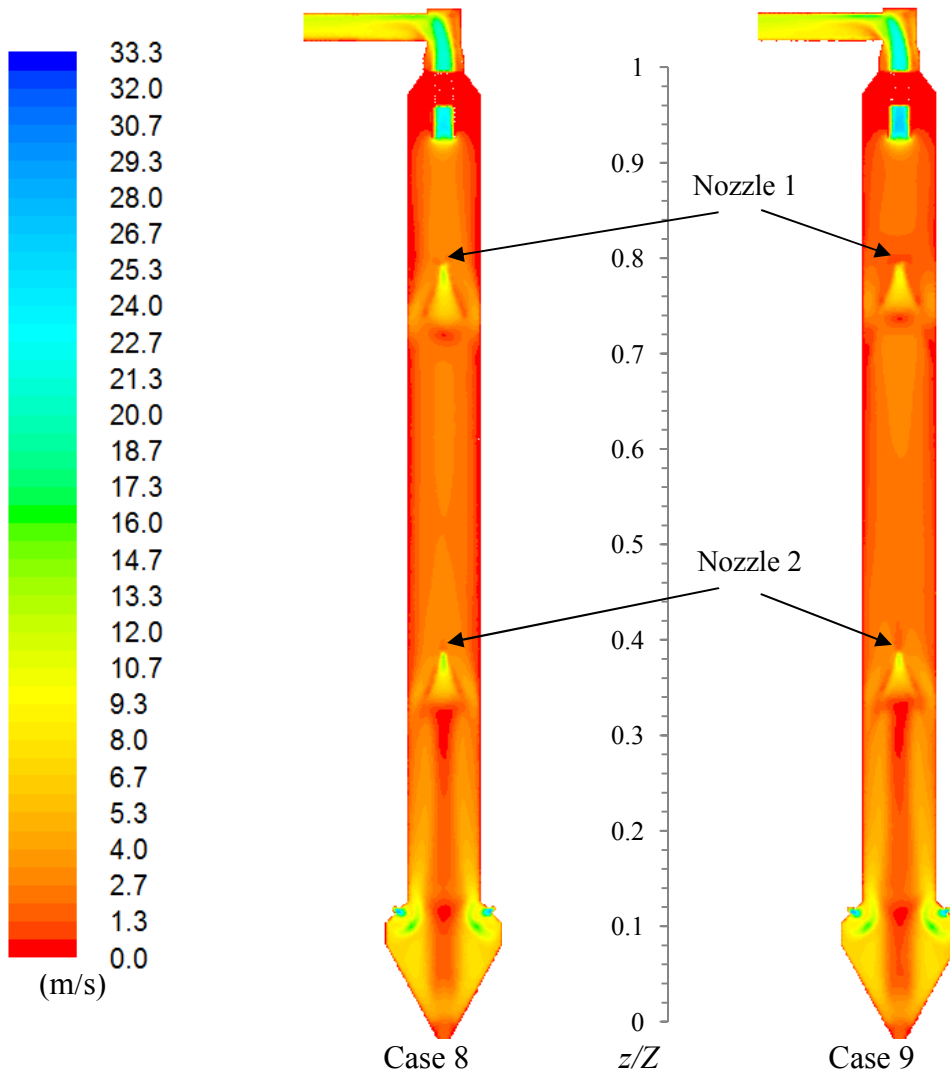


Figure – 8.8: Gas velocity distribution coloured by magnitude of velocity components.

Figure 8.9 is a plot of swirl number along the dimensionless tower height. The initial swirl number in Case 8 in the cylindrical region is about 1.6 which decreases sharply as the gas approaches the second nozzle located at  $z/Z = 0.4$ , above the second nozzle, the swirl number is less than 0.1, which approaches zero as the gas flows upwards, towards the first nozzle located at  $z/Z = 0.8$ , the gas loses all the swirl momentum at this location. In Case 9, the initial swirl number is about 1.8 and the decrease in swirl number in this case is relatively slower, hence a higher swirl strength exists in Case 9 even after the first nozzle (at  $z/Z = 0.4$ ). This is due to the fact that in Case 9 the distribution of droplets/particles comprises larger sizes compared to Case 8 and the larger sizes fall down faster (Figure 8.14) and have less time to exchange swirl momentum with the gas.

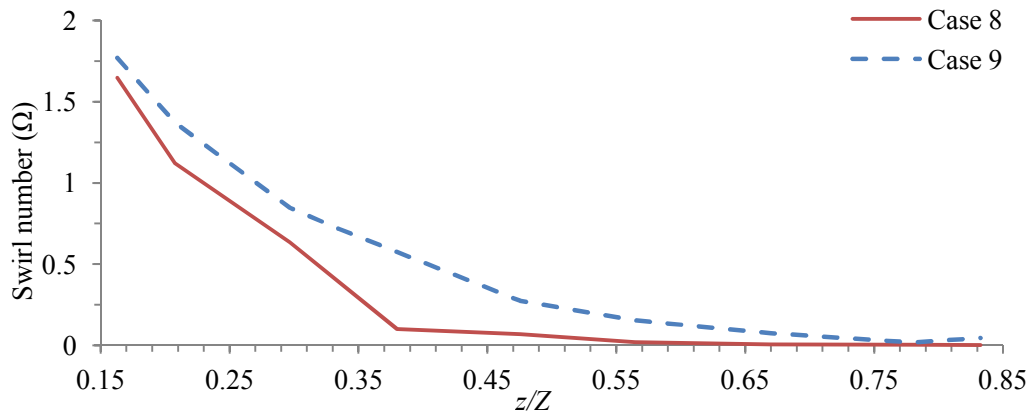


Figure – 8.9: Swirl number along the dimensionless tower height (Case 8).

Figure 8.10 is a plot of gas velocity vectors obtained from Case 8 near the top and bottom spray nozzles. In both cases the entrainment of gas inside the spray is observed due to the high momentum of the sprayed droplets moving in the downward direction, this causes a jet of gas to move in the downward direction. Around the edges of the spray in both spray nozzles, recirculation of the gas flow is observed due to reversal in the gas flow direction. The flow pattern in the top nozzle is asymmetric and a higher gas velocity is observed at the right side of the edge of the spray, whereas the gas flow in the bottom nozzle is more symmetrical with an even distribution of gas velocity around the spray, the gas has higher swirl momentum at the bottom, which could be responsible for a more even flow distribution around the bottom spray nozzle. Asymmetric gas flow around the nozzle is undesirable as this may lead to impingement of droplets onto the wall, causing excessive deposition, which could be minimised by decreasing the mass flow in the top nozzle.

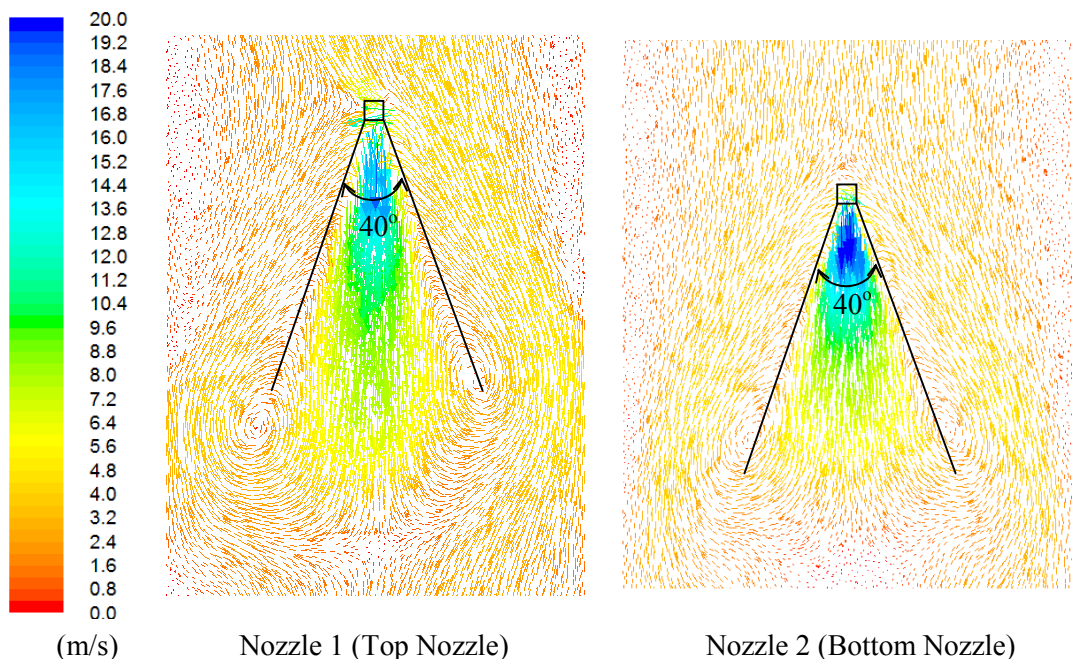


Figure – 8.10: Gas velocity vectors coloured by velocity magnitude (Case 8).

Figure 8.11 is a plot of the trajectories of droplets/particles of selected sizes sprayed from both top and bottom nozzles in Case 8 and 9. Smaller particles (up to 200  $\mu\text{m}$ ) get entrained by the gas in both cases from both the top and bottom nozzles. The larger particles exit from the bottom of the tower. The larger particles, after collision with the wall, start to move along the wall. The particles below the second (bottom) nozzle in both cases start to swirl as they flow downwards due to higher swirling gas flow below the bottom nozzle.

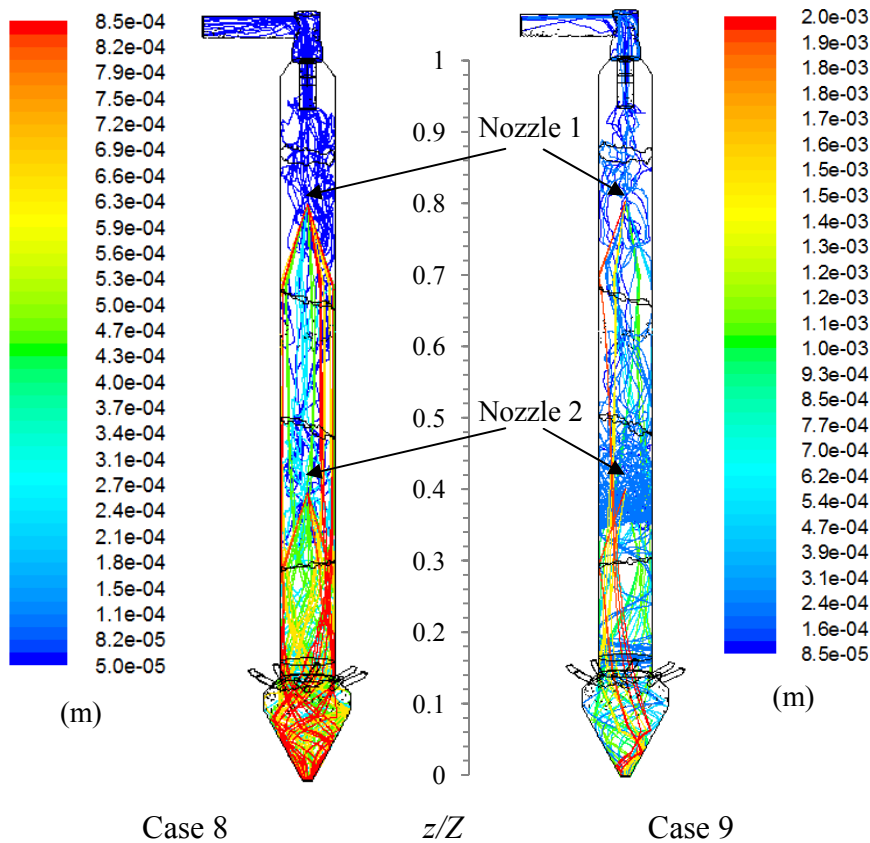


Figure – 8.11: Gas velocity distribution coloured by magnitude of velocity components.

Figure 8.12 is a plot of temperature distributions of the gas phase for CFD Cases 8 and 9. The overall temperature distributions in both cases are similar. The gas temperature in the spray zone of the nozzle located at a dimensionless height of 0.4 is lower compared to the surrounding gas temperature. This is due to rapid evaporation of moisture from the droplets causing cooling of the gas. Below the nozzle, at a dimensionless height 0.35, the gas temperature is lower near the wall as the particles move close to the wall. Above the nozzle ( $z/Z > 0.4$ ) the temperature is reasonably uniform. The gas temperature is further reduced above the nozzle at a dimensionless height of 0.81. The exhaust gas temperature in Case 8 is 351 K and that in Case 9 is 374

K. The exhaust gas temperature in Case 8 is lower due to the use of droplet size distribution at the exit of the spray nozzle, which comprises smaller sizes (50 to 1000  $\mu\text{m}$ ) compared to the powder size distribution (100 to 2300  $\mu\text{m}$ ) and the heat/mass transfer rates are more rapid, resulting in a lower exhaust gas temperature in Case 8.

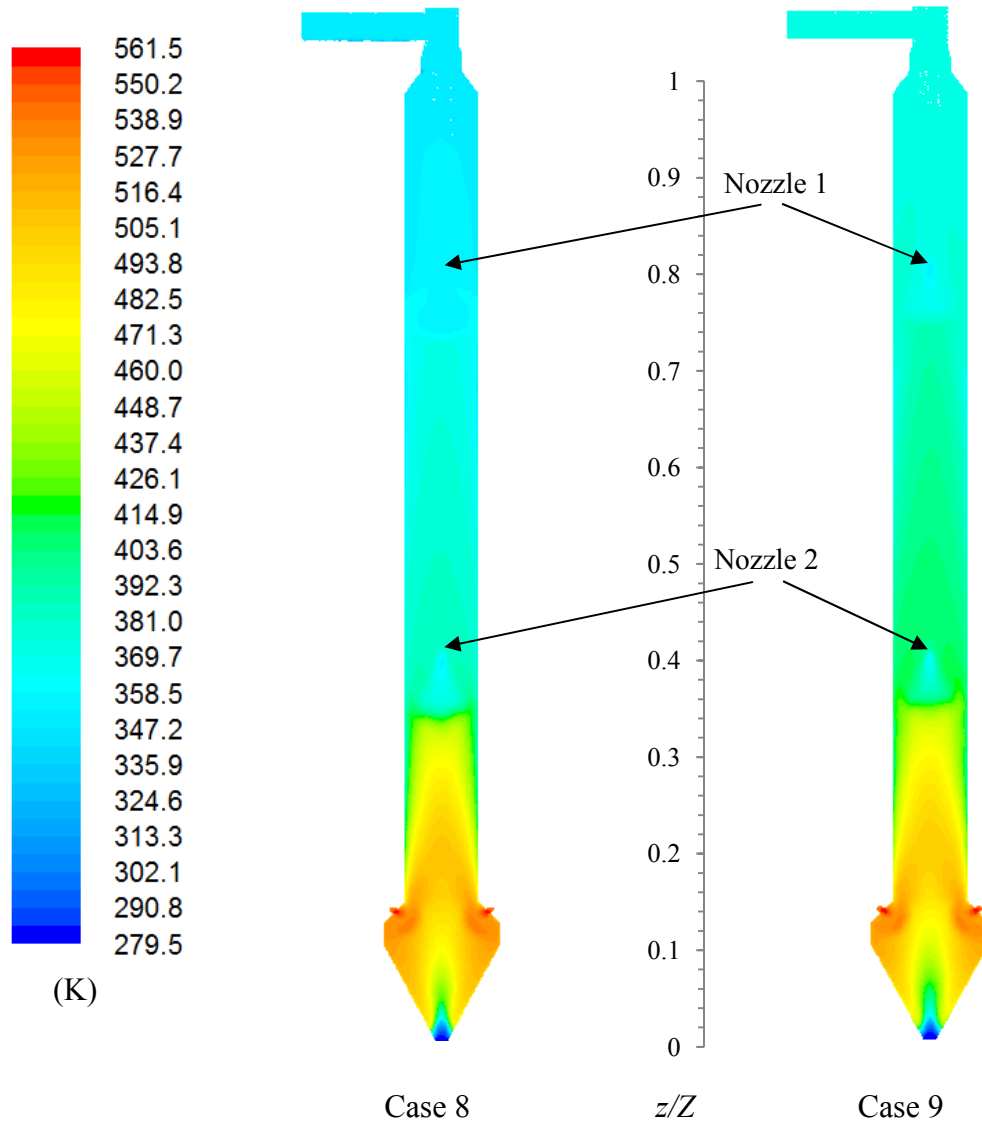


Figure – 8.12: Gas temperature distributions.

Figure 8.13 is a plot of radial temperature profiles for both CFD Cases 8 and 9 at 6 dimensionless heights in the cylindrical region of the tower. At a dimensionless height of 0.29 (Figure 8.13 (a)), the gas profile is parabolic for both cases. The gas temperature is lower close to the wall and higher in the central region of the tower. This location corresponds to a height below the second nozzle. At this location, the particles move close to the wall, therefore, the temperature close to the wall is smaller as the gas gets cooled down by exchanging heat with the particles. The calculated temperature in Case 9 is about 5 K greater than in Case 8 due to the use of particle size distribution. This trend is opposite to that found in temperature profiles for CFD simulation Case 5 and 6

carried out with a single nozzle in Chapter 7. CFD Case 5 (droplet size distribution specification) had a greater temperature in the bottom cylindrical region compared to Case 6 (particle size distribution specification). This opposite trend observed in Case 8 and 9 can be explained by the fact that below the top nozzle (nozzle 1), the temperature in Case 8 is smaller, hence less drying takes place with the use of the droplet size distribution, therefore greater drying is taking place below the bottom nozzle (nozzle 2), resulting in a lower gas temperature in Case 8 in the bottom cylindrical region. Figure 8.13 (b) represents the gas phase temperature within the spray zone of the second nozzle. In both cases at this location, a lower temperature in the central region is observed due to evaporative cooling of the sprayed droplets passing through this region causing the lowering of the gas temperature. The gas temperature is lower in Case 8 compared to Case 9 due to the use of the droplet size distribution comprising smaller sizes (50 to 1000  $\mu\text{m}$ ), and causing more rapid evaporation compared to Case 9 (sizes ranging from 100 to 2300  $\mu\text{m}$ ). At a dimensionless height of 0.56 and 0.67 (above the second spray nozzle), the gas temperature profile is relatively flat in both cases. The highest gas temperature is still at the centre of the tower. The lower wall temperature is due to heat loss through the tower wall and due to droplets/particles from the first nozzle moving close to the wall and exchange heat with the drying gas. The calculated gas temperature in Case 9 is about 20 K greater than in Case 8 at all three locations. The temperature reduces as the gas goes to the top in both cases due to the heat exchange with the droplets/particles. The dimensionless height of 0.78 (Figure 8.13 (e)) lies in the spray zone of the first nozzle. At this location, the temperature profile in Case 8 is qualitatively different from that of Case 9. In Case 8, a lower gas temperature near the walls and a higher gas temperature at the central region with slight asymmetry is observed. However, in Case 9, the temperature profile depicts a lower temperature at the centre with increasing temperature towards the wall due to evaporative cooling of the droplets as they pass through the central region after being injected. In Case 8, the gas is already at a low temperature, and therefore does not exhibit cooling in the central region. At a dimensionless height of 0.83 (just above the first nozzle), the temperature profile in Case 9 is fairly uniform while the temperature profile in Case 8 gives a lower temperature near the wall and a higher temperature in the central region of the tower, because the mass flow of powder entrained in Case 8 is greater than that in Case 9 (Table 8.2), hence relatively more heat exchange takes place in Case 8 above the nozzle, compared to Case 9, which changes the gas temperature profile in Case 8.

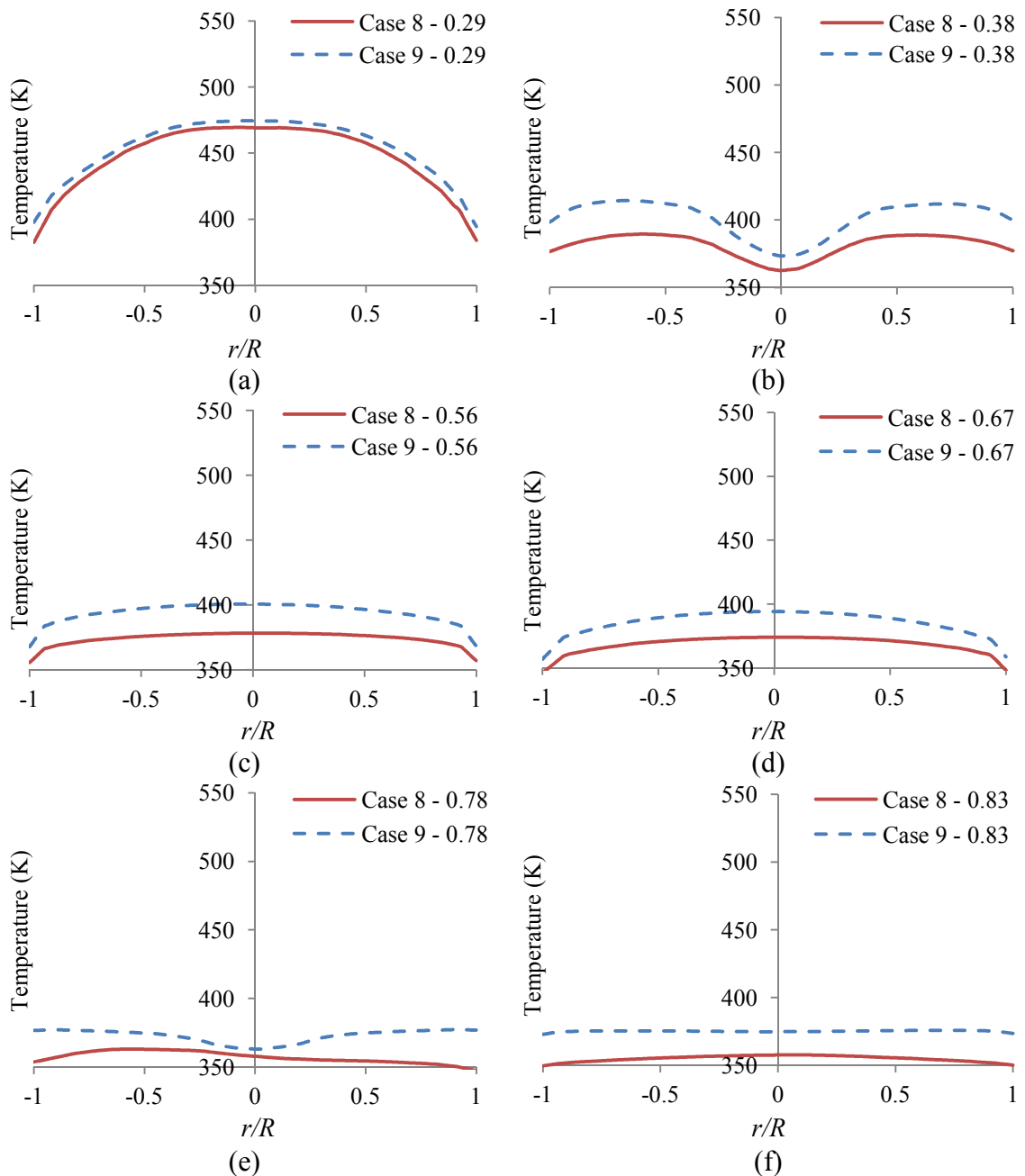


Figure – 8.13: Gas temperature profile comparison for Cases 8 and 9.

Figure 8.14 is a plot of near-wall gas temperature along the tower height. The near-wall gas temperature is not smooth along the tower height primarily due to the interaction of the gas with droplets/particles. The near-wall gas temperature is higher for Case 9 at most of the tower heights ( $z/Z = 0.15$  to  $1.0$ ) as explained above, but in the bottom conical region of the tower ( $z/Z = 0.1$  to  $0.15$ ), it is smaller in Case 9, since the larger particles evaporate in the bottom conical region of the tower in this case. It is due to this reason that the exit temperature of dried particles in Case 9 is smaller (Figure 8.16). From a comparison of near-wall temperature with single nozzle CFD Cases 5 and 6 carried out in Chapter 7 (Figure 7.40), it is found that in Case 8 (droplet size distribution), the near-wall temperature is lowered at most of the tower height by the use

of two nozzles, which in the case of single nozzle (Case 5 utilising droplet size distribution) was higher in the bottom cylindrical region compared to Case 6 (utilising particle size distribution), thus making the particles (especially the smaller sizes) more susceptible to thermal degradation. Hence by manipulating the slurry mass flow and spray nozzle arrangements, thermal degradation can be controlled.

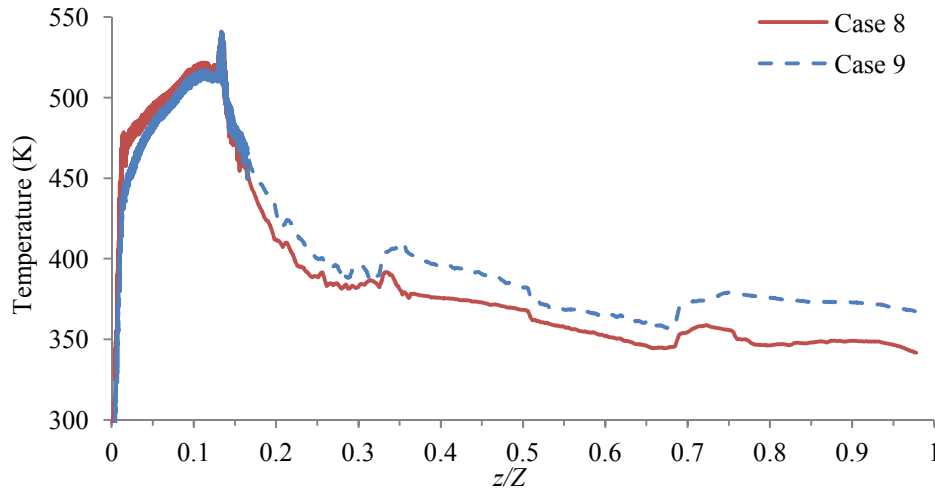


Figure – 8.14: Gas temperature near the wall along the dimensionless tower height.

Figure 8.15 is a plot of residence times of particle sizes exiting from the tower bottom, initially sprayed as droplets from nozzle 1 (top nozzle) and nozzle 2 (bottom nozzle) for CFD Case 8. The qualitative trend of decreasing residence times with increasing sizes is similar for both nozzles 1 and 2 and the residence times of particles initially injected from nozzle 1 (top nozzle) must travel a greater distance and hence have about twice as large residence times compared to those from nozzle 2 (bottom nozzle).

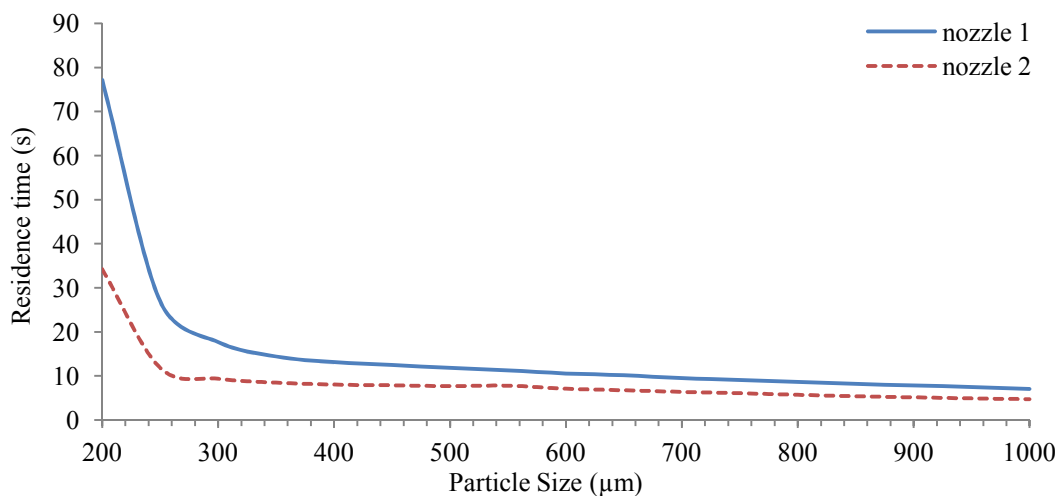


Figure – 8.15: Residence time of particles of different sizes for CFD Case 8.

The residence time distribution plot in Figure 8.16 is an average of the residence time of all the particles of a particular size at the bottom of the tower, which are initially sprayed as droplets from both nozzles. In CFD Case 8, the exit particle size distribution ranges from 200  $\mu\text{m}$  to 1000  $\mu\text{m}$  since the measured droplet size distribution is used as the initial condition, which varies from 50 to 1000  $\mu\text{m}$ . In both CFD Cases 8 and 9, the particle sizes up to 100  $\mu\text{m}$  get entrained by the gas and exit from the top of the tower, therefore the residence times of particle sizes less than 200  $\mu\text{m}$  are not present in this plot. Particle sizes up to 300  $\mu\text{m}$  show a sharper decline in residence times with increasing particle size compared to larger particle sizes in both cases. A similar trend was observed in the residence time distribution plots in the previous cases (in Chapter 7) in which the slurry was sprayed using a single nozzle. The residence times of particles in CFD Case 8 are lower than these for CFD Case 9. This may be due to the fact that the gas temperature is lower in CFD Case 8 at most of the tower height (Figures 8.12 and 8.13), which decreases the velocity of the gas due to an increase in gas density. The difference in the residence times of particles of larger sizes ( $>700 \mu\text{m}$ ) is smaller between CFD Cases 8 and 9, since the larger particles have a greater momentum hence they travel faster and are less sensitive to the changes in gas velocity due to the temperature differences in CFD Cases 8 and 9. The predicted residence times from the plug-flow Cases 3 and 4 are also plotted in Figure 8.16. The plug-flow model underpredicts the residence times for all particle sizes, although qualitatively the trend is similar. The underprediction by the plug-flow model is due to the fact that the minimum particle velocity is limited to the terminal falling velocity, additionally the particle-wall interactions are also not considered in the plug-flow model.

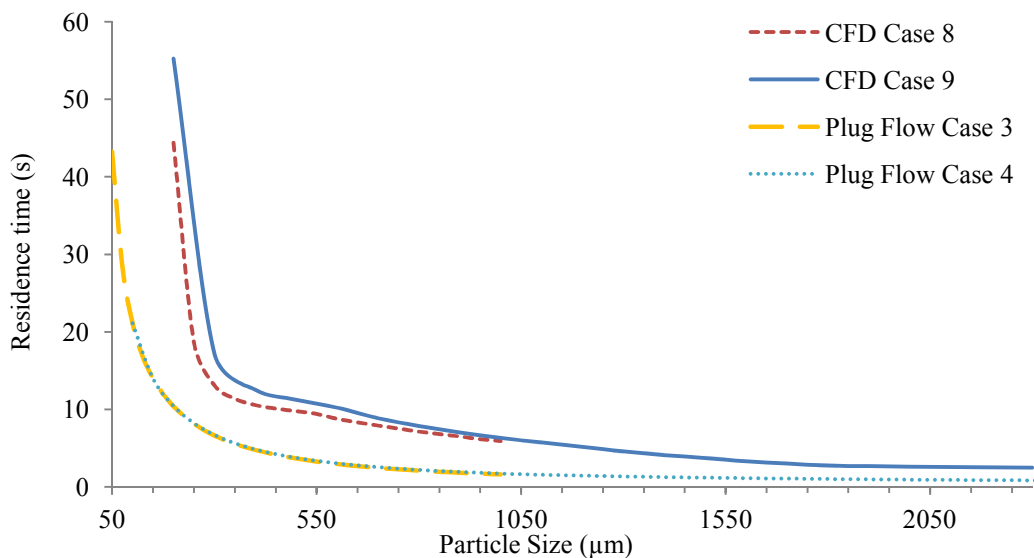


Figure – 8.16: Residence time of particles at the tower bottom.

Figure 8.17 is a plot of particles temperatures and normalised moisture fraction at the tower bottom exit as a function of size, which are initially sprayed from nozzles 1 and 2. It is found that the particles that are resulting from nozzle 1 (top nozzle) exit at relatively higher moisture fraction and consequently lower temperature for sizes  $> 700 \mu\text{m}$  compared to those from nozzle 2 (bottom nozzle) despite the fact that the particles from nozzle 1 travel a larger distance and have a greater residence time compared to those from nozzle 2. This unexpected trend is due to the fact that the droplets sprayed from the bottom nozzle exhibit a greater relative velocity between the gas and the droplets, resulting in a higher heat and mass transfer coefficient. Therefore, the droplets which are sprayed from the bottom nozzle in the first stage of drying lose the moisture quicker compared to those from the top nozzle (see Figure 8.18) and this causes the particles sprayed from the bottom nozzle to exit at lower moisture content. As observed in Figure 8.4, this trend is not captured by the plug-flow model.

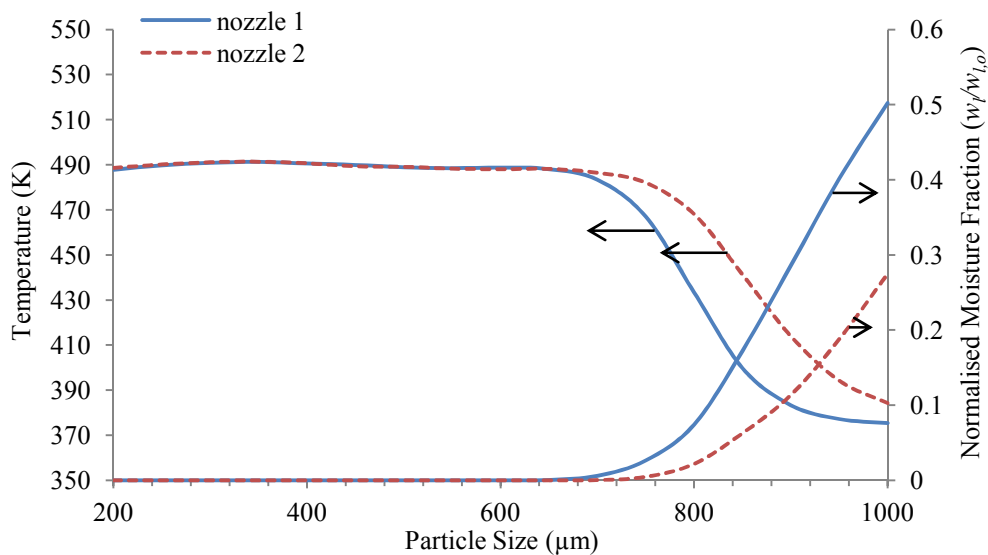


Figure – 8.17: Final temperature and moisture content of particles of different sizes for CFD Case 8.

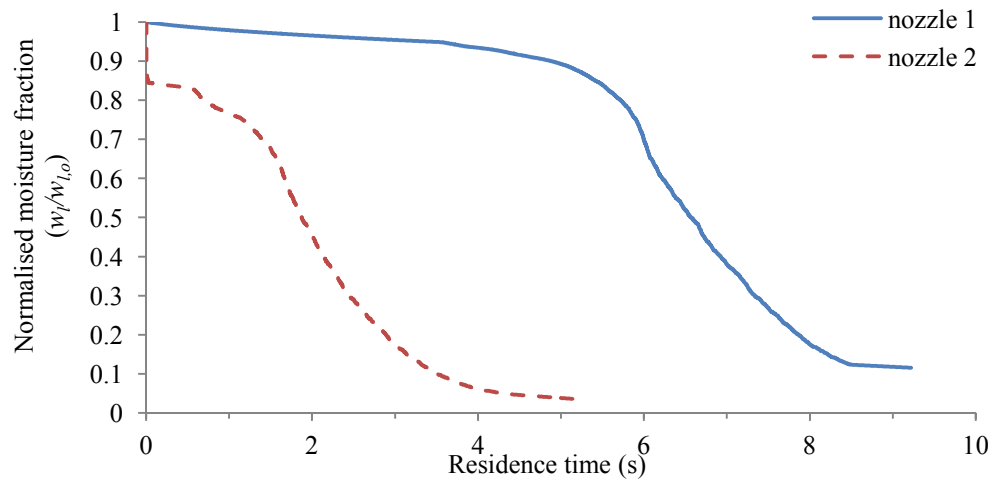


Figure – 8.18: Moisture fraction profile of 800  $\mu\text{m}$  particle size for Case 8.

Figure 8.19 is a plot of the temperature of particles of different sizes that exit from the tower bottom (sprayed from both nozzles). The exit particle temperatures for both CFD cases for the sizes up to 700  $\mu\text{m}$  are fairly uniform ( $\sim 490$  K for Case 8 and 470 K for Case 9). Particle sizes greater than 700  $\mu\text{m}$  in both CFD cases have a sharp decline in their temperatures as they exit with a greater moisture content (Figure 8.20). In CFD Case 9, particles greater than 1100  $\mu\text{m}$  exit at a uniform temperature of 373 K corresponding to the slurry boiling point at a high moisture content. In CFD Case 8, the exit temperature of particles up to 700  $\mu\text{m}$  is greater and for larger particles ( $>700$   $\mu\text{m}$ ) it is smaller compared to CFD Case 9 as the exit moisture of particle sizes  $>700$   $\mu\text{m}$  in CFD Case 8 is comparably greater and is explained below. A comparison of CFD predicted exit particle temperatures with plug-flow Cases 3 and 4 reveals that for smaller particles (up to 600  $\mu\text{m}$ ) the exit temperature is overpredicted by the plug-flow model, whereas for larger particles ( $>600$   $\mu\text{m}$ ) it is underpredicted by plug-flow model. This is mainly due to the small and dried particles (up to 500  $\mu\text{m}$ ) not coming into contact with entrained cold air at the bottom exit once all the moisture has been removed from them; hence a higher exit temperature is predicted by the plug-flow model. The larger particles ( $>600$   $\mu\text{m}$ ) which do not become completely dried (Figure 8.20) have a smaller residence time (Figure 8.16) compared to the CFD model, hence they exit at a lower temperature and consequently at a greater moisture fraction.

Figure 8.20 is a plot of average normalised moisture content of the particles at the bottom of the spray tower initially sprayed as droplets from both nozzles. Particle sizes up to about 700  $\mu\text{m}$  in both of the CFD cases exit at zero moisture content. Larger particles ( $>700$   $\mu\text{m}$ ) contain moisture which increases with increasing particle size. A comparison of both CFD cases shows that in Case 8, the particles  $> 700$   $\mu\text{m}$  exit at

greater moisture content compared to Case 9. It could be due to relatively shorter residence times of particles in CFD Case 8 (Figure 8.16) and due to a lower gas temperature in CFD Case 8 resulting in a smaller evaporation rate. A comparison of CFD and plug-flow predicted exit particle moisture profiles shows that the exit moisture predicted by the plug-flow models is greater for particle sizes larger than 500  $\mu\text{m}$  mainly due to shorter residence times predicted by the plug-flow model (Figure 8.16).

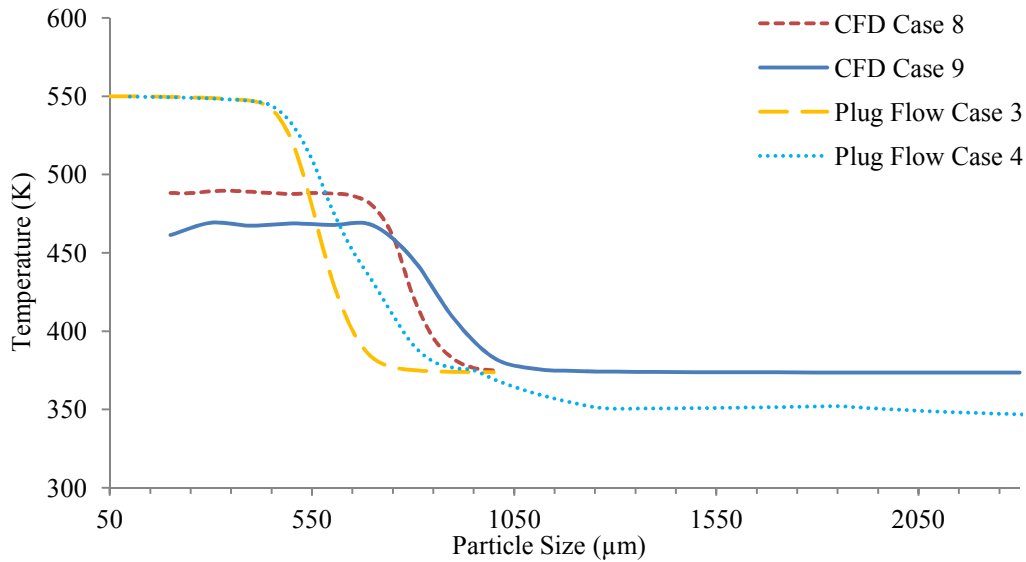


Figure – 8.19: Temperature of particles at the tower bottom.

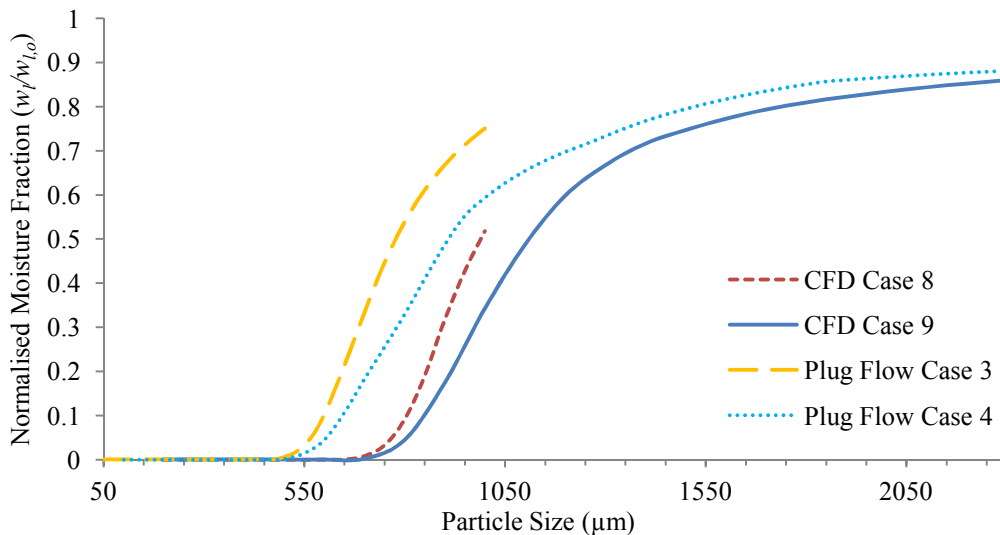


Figure – 8.20: Moisture of particles at the tower bottom.

Figure 8.21 is a plot of gas temperature profiles along the axial direction with  $z/Z = 0$  representing the tower bottom and 1 representing the tower top, predicted using the plug-flow and CFD cases. In the CFD cases, since a temperature gradient exists along the radius, therefore, the values of temperature reported are mass weighted average temperature over the cross-section. In the CFD cases, below a dimensionless height of

0.15, the temperature decreases, due to entrainment of cold air from the bottom, which is not considered in the plug-flow model, therefore this results in a greater particle outlet temperature prediction in the plug-flow cases (Table 8.3). The drop in gas temperature with increasing height up to the bottom nozzle location ( $z/Z = 0.4$ ) is sharper compared to the decline in temperature between the nozzle 1 and 2 in both the plug flow and CFD cases. In plug-flow Case 4, the gas temperature is significantly greater compared to CFD Case 9 (both using powder size distribution), since in the plug-flow model the residence times are underpredicted, resulting in less heat and mass transfer between the two phases. The predicted gas temperature below the nozzle 2 (bottom nozzle at  $z/Z = 0.4$ ) in plug-flow Case 3 is overpredicted compared to CFD Case 8 (droplet size distribution cases). However, above the nozzle 2 ( $z/Z > 0.4$ ), the gas temperature predictions in both cases are very similar.

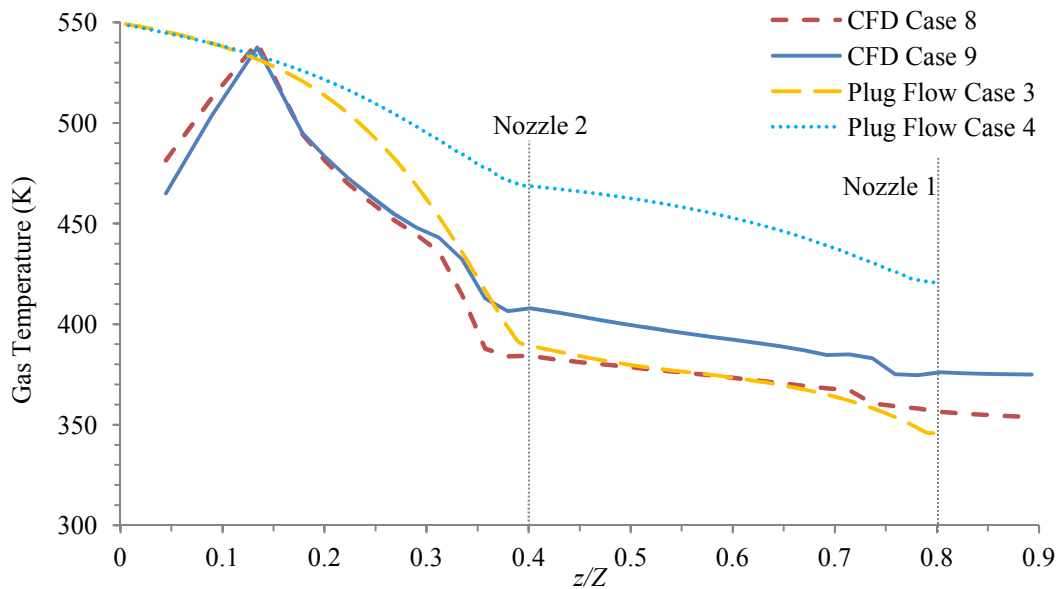


Figure – 8.21: Gas temperature profiles along the tower axis.

Table 8.3 is a list of parameters measured from the IPP spray tower and predicted from the plug-flow and CFD models. When the measured droplet size distribution is used to represent the size distribution at the nozzle exit, both plug-flow Case 3 and CFD Case 8 models underpredict the measured moisture content, the predicted outlet gas temperature is also lower compared to the measured temperature. When the measured powder size distribution is used to represent the size distribution at the nozzle, both plug-flow Case 4 and CFD Case 9 predict a higher moisture content compared to the measurement and the outlet gas temperature is higher compared to the measurement. The predicted particle temperatures are greater because the measured temperature is taken at the belt and the powder gets cooled down at this location. The predicted

average particle density is higher than the measurement due to the restriction of the particle inflation up to the initial particle size in the boiling stage of drying. These same trends were observed in plug-flow Cases 1 and 2 (Chapter 5) and CFD Cases 5 and 6 (Chapter 7). The reasons for this trend have been explained in the previous discussion on those results in Chapters 5 and 7. Hence the presence of two nozzles does not change the predictability trend in both plug-flow and in CFD modelling approaches. The value of heat loss based on measured data is significantly greater than the predicted values. It is mainly due to wrong location of inlet hot gas temperature measurement (i.e., in the inlet gas header), which is further exacerbated by the fact that a single measurement at the centre of the gas header was taken which may not represent the gas mean temperature. Hence more accurate data is required for a better validation.

Table – 8.3: Simulation results and experimental measurements.

Parameter	Plug-Flow Case 3	Plug-Flow Case 4	CFD Case 8	CFD Case 9	Measured (Martin de Juan, 2012)
Particle weighted average moisture content, %	0.88	9.35	0.19	7.70	5.03
Particle weighted average temperature, K	531.1	453.1	485.6	429.2	358.7
Average single particle density, kg/m <sup>3</sup>	1131.0	1279.1	1121.0	1201.9	703
Outlet gas temperature, K	345.8	420.8	351.1	374.1	366.9
Heat loss, kW	5.2	6.9	36.6	38.2	110.8

The results of plug-flow Case 3 and CFD Case 8 are very similar in terms of particle average moisture content and exhaust gas temperature, however the particle average outlet temperature is greater by about 45 K in plug-flow Case 3, mainly because in the plug-flow model, the particles do not cool down as they approach the bottom outlet, whereas in the CFD model, the particles get cooled down due to contact with entrained air from the bottom outlet. From a comparison of plug-flow Case 4 with CFD Case 9, it is found that the plug-flow model predicted particle average moisture content is greater than the CFD model and the predicted exhaust gas temperature is also greater. Additionally, the plug-flow model does not consider entrainment of particles, which in the CFD model is found to be 24% in Case 8 and 5.2% in Case 9 (Table 8.2). The

predicted average single particle density is very similar in all four simulated cases but greater than the measured value. The density is primarily affected by the amount of puffing, in the simulated cases, the maximum expansion of the particle due to puffing in the cases considered was allowed up to the point when it reaches the size equal to the initial diameter of the droplet. In the drying model, if the particle is allowed to increase further, then a more realistic density prediction could be obtained.

#### **8.4 Conclusions**

Modelling of the spray drying process has been carried out considering two nozzles at different heights using plug-flow and CFD approaches and validation is carried out with data collected from the IPP spray drying tower. In both modelling approaches, two cases are considered, i.e. the measured droplet size distribution and measured powder size distribution as the initial droplet size distribution at the nozzle. The overall trends of the results obtained considering two nozzles, i.e. the exhaust gas temperature, particle average temperature, moisture content and density are similar to those obtained from the single nozzle cases with both plug-flow and CFD approaches. However, in the CFD model, it is found that the droplets sprayed from the bottom nozzle are more dried at the bottom exit compared to that from the top nozzle, which is not captured by the plug-flow model. The gas flow around the top nozzle in CFD is asymmetric which can cause excessive deposition near the top nozzle, which could be minimised by decreasing the slurry mass flow in the top nozzle. The heat loss from the tower based on experimental data is somewhat unrealistic and emphasizes the need to take measurements of the inlet gas temperature at the tangential-entry inlets instead of the inlet gas duct and measurement of more reliable dried powder outlet parameters (temperature and moisture content).

## **9. ZONAL MODELLING OF SPRAY DRYING TOWER**

### **9.1 Introduction**

In the previous chapters, the modelling of the counter-current spray drying tower was carried out using a simplified one-dimensional plug-flow approach as well as using a three-dimensional CFD modelling approach. The plug-flow modelling approach predicted similar trends in the prediction of residence times, particle temperature and moisture content compared to the CFD model, however it underpredicted the residence times, and the predicted powder outlet moisture content was greater. In this chapter, a new approach for modelling of the spray drying process is used, which is aimed to give a closer prediction with the CFD model without requiring the need to have large computational resources and expertise, which are the draw backs of the CFD approach, to enable plant operators to get a quick estimation of the optimised operating conditions for the manufacture of powder with required characteristics.

### **9.2 Description of a Zonal Model**

The zonal modelling of spray drying tower has been carried out to predict dried powder characteristics using a simplified approach, using the results obtained from CFD simulation and in a computationally efficient manner. In the zonal model, the spray drying tower is divided into different zones and the heat, mass and momentum transfers between the gas phase and the droplets/particles takes place in each zone using either a plug-flow or a CSTR approach. The results of CFD simulation Case 2 modelled in Chapter 7 has been used as the basis for dividing the spray tower into different zones. Figure 9.1 is a schematic of the spray drying tower depicting different zones based on the CFD modelling results. The basis for division of each zone is given below. Figure 9.2 depicts the variables which are transferred from one zone to the other. The blue arrows represent the transfer of discrete phase variables and the black arrows represent the gas phase variables.

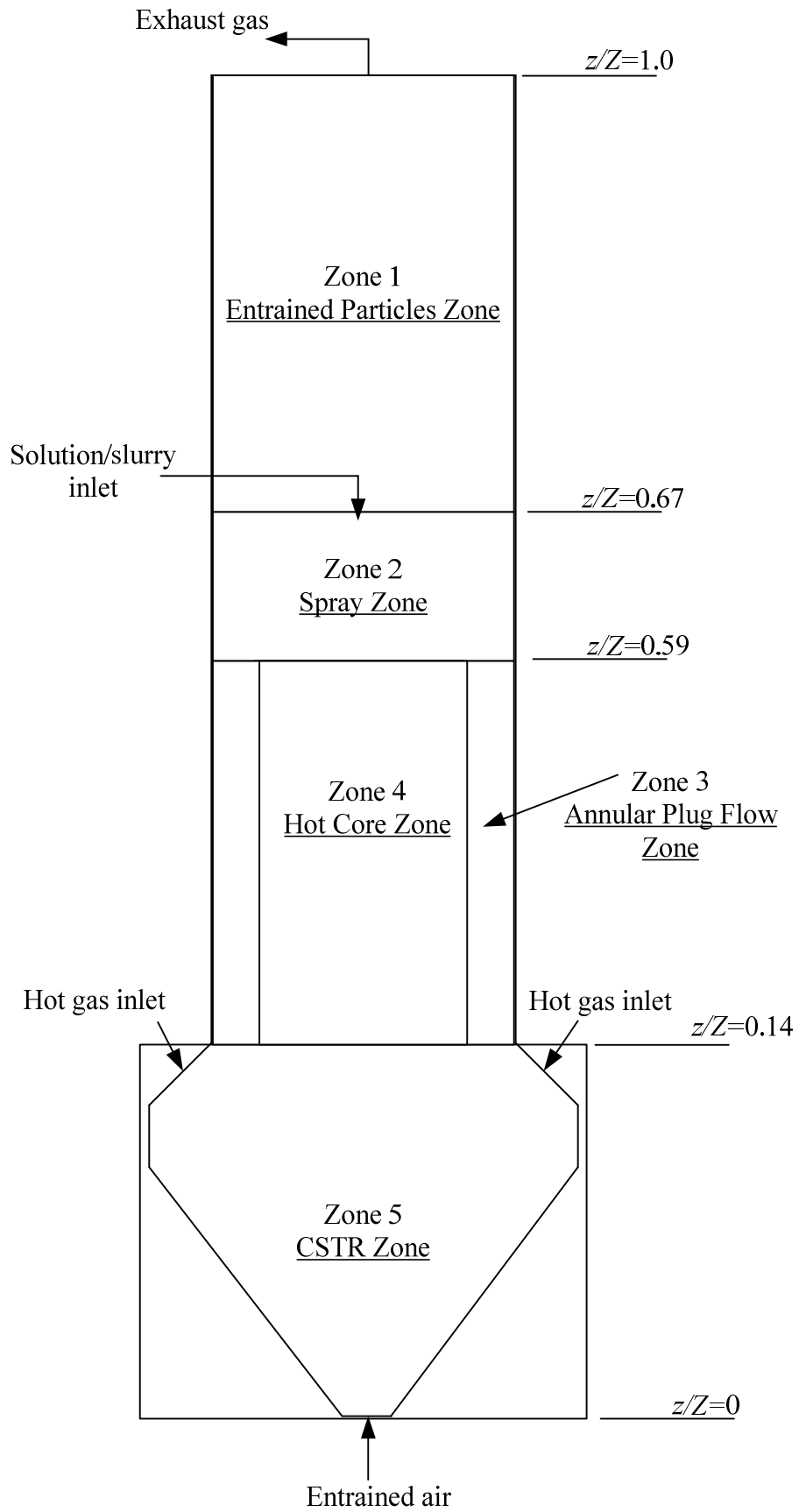


Figure – 9.1: Zones for numerical modelling of spray drying tower.



the gas flow. Figure 9.4 is a plot of the gas temperature in the centreline and near the wall along the dimensionless tower height. The nozzle is located at a dimensionless height of 0.67, above the nozzle, the temperature is fairly uniform both near the wall as well as in the centreline. The particle size range up to 200  $\mu\text{m}$  diameters get entrained by the gas (see Figure 7.24 in Chapter 7). The gas as well as the entrained particles exit from the top outlet of the spray drying tower. The droplets/particles above the nozzle are dispersed randomly as depicted in Figure 7.23, which causes non-smooth concentration distributions along the radius in Figure 9.5. Heat and mass transfer between the droplets/particle and the drying gas in this zone is modelled by using a CSTR approach. It is assumed that the entrained particles at the exit of the spray drying tower have the same temperature as that of the drying gas and the moisture content of the particles that exit from the top outlet of the spray drying tower is equal to zero. The heat and mass transfer between the gas phase and the droplets/particles as well as the heat losses from this zone is modelled by an overall energy balance.

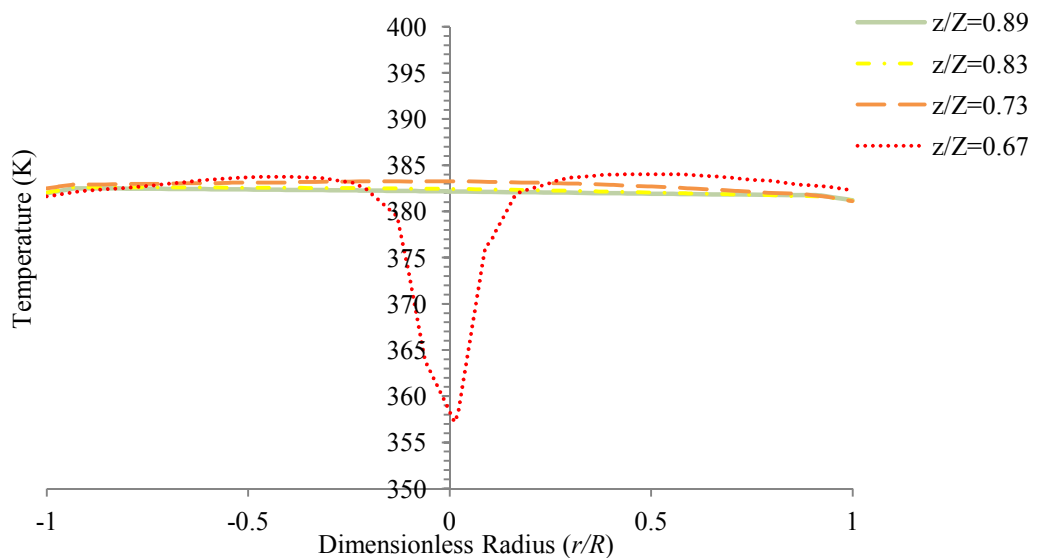


Figure – 9.3: Gas temperature profile along the above the spray nozzle.

The following assumptions are made for the overall energy balance:

1. A well-mixed (CSTR) approach is used for both particles as well as for the gas phase.
2. The particles exiting from Zone 1 have zero moisture content and the final temperature of the particles is taken to be equal to the exit gas temperature.
3. The exit gas temperature is taken from the CFD modelling result.
4. Particle size distribution in this zone is taken from the CFD modelling results.

- The initial moisture content of the particles that enter zone 1 is taken from zone 2 data, and requires an iterative solution.

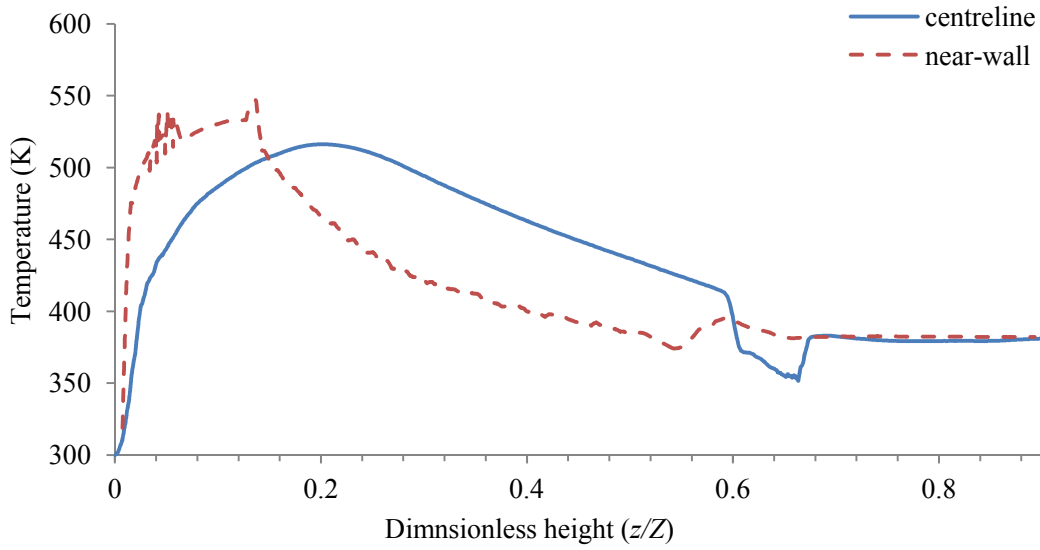


Figure – 9.4: Gas temperature in the centreline of the tower along the dimensionless height.

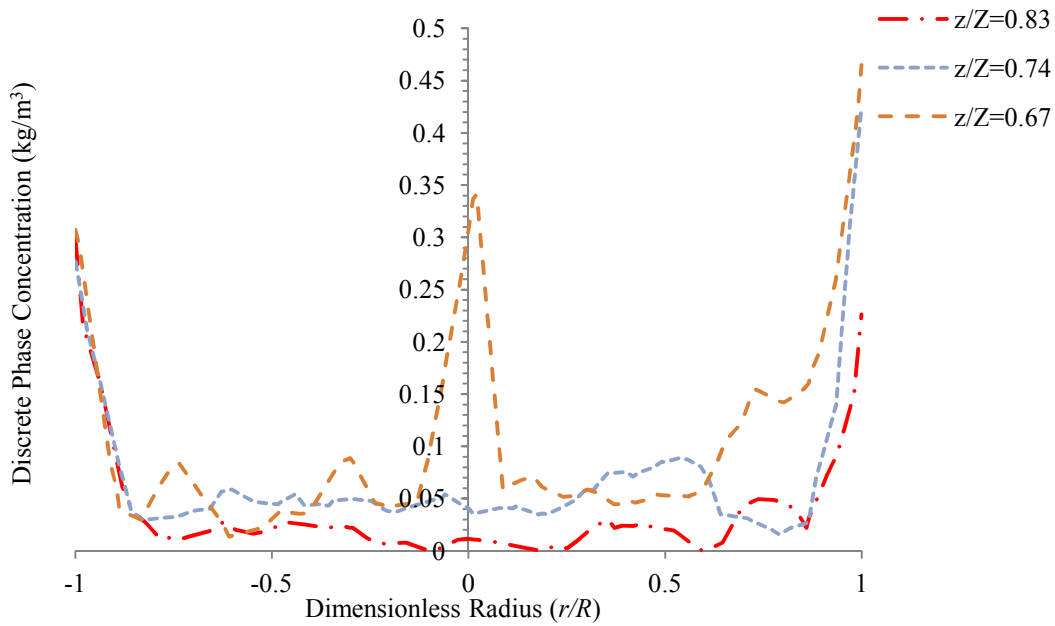


Figure – 9.5: Discrete phase concentration along the radius of the tower above the nozzle.

The gas temperature ( $T_{g,2 \rightarrow 1}$ ) at the interface of Zone 1 and Zone 2 is calculated using an overall energy balance, which gives the following equation:

$$\begin{aligned}
T_{g,2 \rightarrow 1} = & \left\{ \underbrace{\sum_{j=1}^J T_{p,j,2 \rightarrow 1} M_{p,j,2 \rightarrow 1} n_j c_{p,slurry}}_{\text{Total enthalpy of particles leaving Zone1}} - \underbrace{\sum_{j=1}^J T_{p,j,2 \rightarrow 1} M_{p,j,2 \rightarrow 1} n_j [(1 - w_{l,j,2 \rightarrow 1}) c_{p,slurry} + w_{l,j} c_{p,l}]}_{\text{Total enthalpy of droplets/particles entering Zone1}} \right. \\
& + \underbrace{\dot{M}_{g,1 \rightarrow 0} c_{p,g,1 \rightarrow 0} T_{g,1 \rightarrow 0}}_{\text{Enthalpy of gas leaving the tower}} + \underbrace{(\dot{M}_{g,1 \rightarrow 0} - \dot{M}_{g,2 \rightarrow 1}) (c_{p,vap} \times 373.15 + h_{fg} + c_{p,vap} (T_{g,1 \rightarrow 0} - 373.15))}_{\text{Enthalpy of vapours}} \\
& \left. + \underbrace{2\pi r_i H_1 U_1 (T_{g,1 \rightarrow 0} - T_{amb})}_{\text{Heat loss to the environment}} \right\} / (\dot{M}_{g,2 \rightarrow 1} c_{p,g,2 \rightarrow 1}) \quad (9.1)
\end{aligned}$$

The subscripts  $1 \rightarrow 2$  represent the variable at the interface of zone 1 and 2 and the subscripts  $1 \rightarrow 0$  represent the outlet value of variable exiting from zone 1. The exhaust gas temperature ( $T_{g,1 \rightarrow 0}$ ) and mass flow ( $\dot{M}_{g,1 \rightarrow 0}$ ) is obtained from CFD.

### 9.2.2 Zone 2 (Spray Zone)

The spray zone is the region where the droplets are injected into the spray drying tower using a hollow-cone pressure nozzle atomiser. The droplets have a high injection velocity at the nozzle tip which results in entrainment of the surrounding drying gas into the spray of droplets. Hence the droplets move in the downward direction in a complex gas flow patterns with part of the flow moving counter-current to the droplets while some of the gas gets entrained into the spray. The complex gas flow pattern in this zone are depicted in Figure 7.27. The temperature profiles along the radius of the tower in this zone is depicted in Figure 9.6. It is observed from Figure 9.6 that a complex radial variation of gas temperature exists in this zone. Near the nozzle location ( $z/Z = 0.67 - 0.65$ ), the gas temperature lowers down sharply in the centreline, due to rapid evaporation of droplets causing cooling of the gas. The drop in temperature flattens out away from the nozzle ( $z/Z = 0.63 - 0.61$ ), further away from the nozzle at  $z/Z = 0.59$ , the gas temperature is higher near the centre and lower near the wall. Figure 9.7 is a plot of normalised mass flow of the gas (based on inlet gas mass flow) in the spray zone. Near the centreline the flow is in the downward direction (negative), hence the gas flow is entrained by the gas whereas near the wall, the flow is positive hence moving counter-current to the droplets. At  $z/Z = 0.59$ , the gas flow is positive along the radius with but zero at the tower centreline hence the gas flow is not entrained at this location.

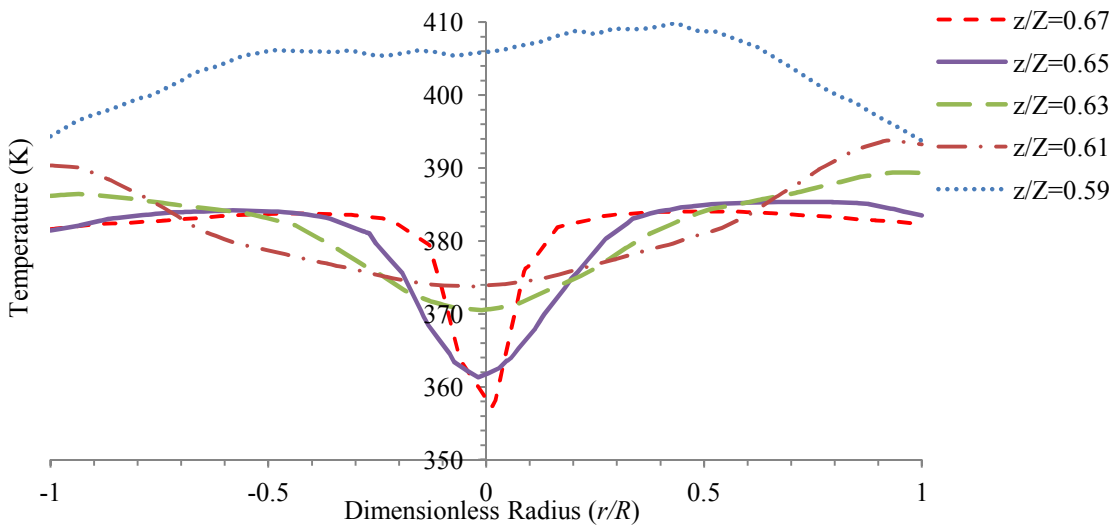


Figure – 9.6: Gas temperature along the radius of the tower in the spray zone.

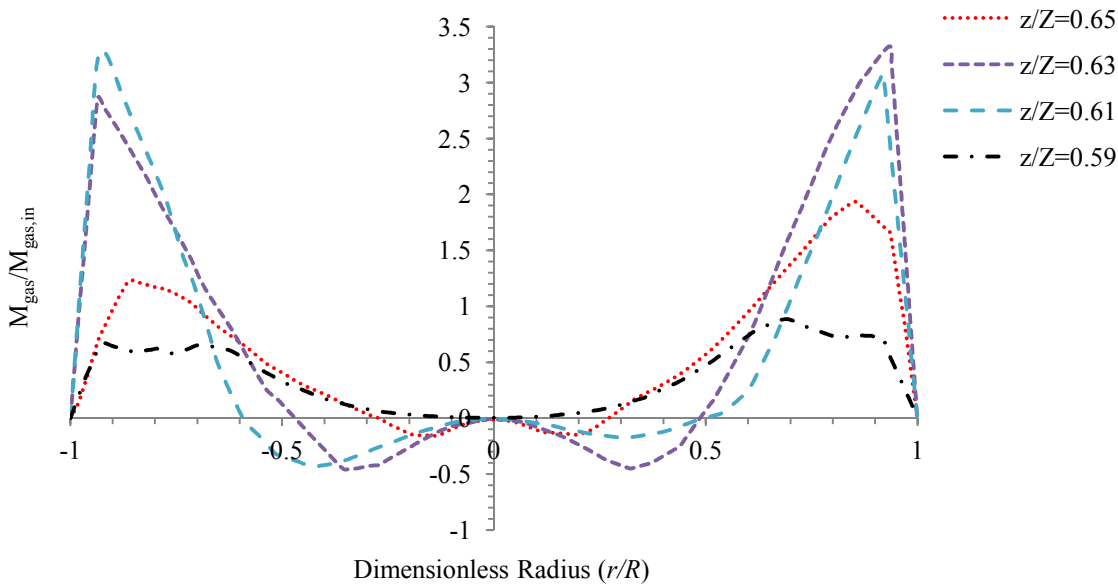


Figure – 9.7: Gas mass flow along the radius of the tower in the spray zone.

The smaller droplets/particles (up to 200  $\mu\text{m}$  diameters) in this zone start to get entrained by the gas flow moving in the upward direction at a certain distance below the nozzle, whereas the larger droplets/particles eventually hit the wall (see Figure 7.23 and 7.24). The main assumptions in this zone are as follows:

1. The gas phase as well as the droplets/particles are assumed to follow the plug-flow approach.
2. The calculation of particle sizes which get entrained by the gas phase is stopped once it reaches the terminal velocity or the specified height of this zone.
3. The minimum velocity of particles which are collected from the bottom exit of the tower is limited to the terminal falling velocity.

The temperature of the gas phase is calculated using the following equation:

$$\begin{aligned}
 \underbrace{\dot{M}_{g,2} c_{p,g,2} \frac{dT_{g,2}}{dz}}_{\text{Heat transfer from the air to the droplets}} = & \\
 \underbrace{\sum_{j=1}^J \alpha_j A_{p_j} (T_{p_j,2} - T_{g,2}) \cdot \frac{n_j}{\tilde{u}_{p,j}}}_{\text{Total heat input to the droplets by convection}} + \underbrace{\sum_{j=1}^J \left( \frac{dM_l}{dt} \right)_j c_{p,vap} (T_{p_j,2} - T_{g,2}) \cdot \frac{n_j}{\tilde{u}_{p,j}}}_{\text{Sensible heat to the evaporated vapours}} & \quad (9.2) \\
 + \underbrace{2\pi r_i U (T_{amb} - T_{g,2})}_{\text{Heat loss to the environment}} &
 \end{aligned}$$

The temperature of the droplets/particles is calculated using the following equation:

$$\underbrace{M_{p,2} c_{p,drop} \tilde{u}_p \frac{dT_{p,2}}{dz}}_{\text{Heat absorbed by the droplet/particle}} = \underbrace{\alpha_p A_p (T_{g,2} - T_{p,2})}_{\text{Heat input to the droplet/particle by convection}} + \underbrace{h_{fg} \frac{dM_l}{dt}}_{\text{Heat consumed in vapourizing the moisture}} \quad (9.3)$$

The drying rate of the droplets/particles is calculated using the semi-empirical droplet drying model described in Chapter 5, using equations (5.4), (5.13) and (5.14), representing the drying rates at different stages. The droplet/particle velocity is calculated by solving the equation of motion for the particles (equation 5.3) given in Chapter 5. The boundary conditions specifications for the solution of equation (9.2) and (9.3) are given below:

$$\dot{M}_{slurry,2}, w_{l,2}, u_{p,2}, T_{p,2}, T_g = T_{g,2 \rightarrow 1}, \dot{M}_{g,2} = \dot{M}_{g,2 \rightarrow 1}, PSD$$

### 9.2.3 Zone 3 (Annular Plug-Flow Zone) and Zone 4 (Hot Core Zone)

The annular plug-flow zone lies below the spray zone in the cylindrical region of the tower. This zone comprises the annular region close to the wall where the droplets/particles move downward and counter-current to the gas flow. The selection of this zone is based on the fact that the droplets/particles move close to the wall in the cylindrical region of the tower as observed in CFD Case 2 in Chapter 7. The particle concentration profiles in the cylindrical region of the tower, depicted in Figure 9.8 also disclose a high concentration of particles close to the wall. Therefore, the annular region of a dimensionless radius from 0.88 to 1.0 is considered in the annular plug-flow zone. The assumptions used in this zone are listed below:

1. Both the gas phase and the particle phase in this zone are modelled using the plug-flow assumption.

2. Only those droplets/particle sizes are considered in this zone which exit from the bottom of the tower (fines that exit from the tower top are excluded).
3. The minimum velocity of the droplets is set to the terminal falling velocity.

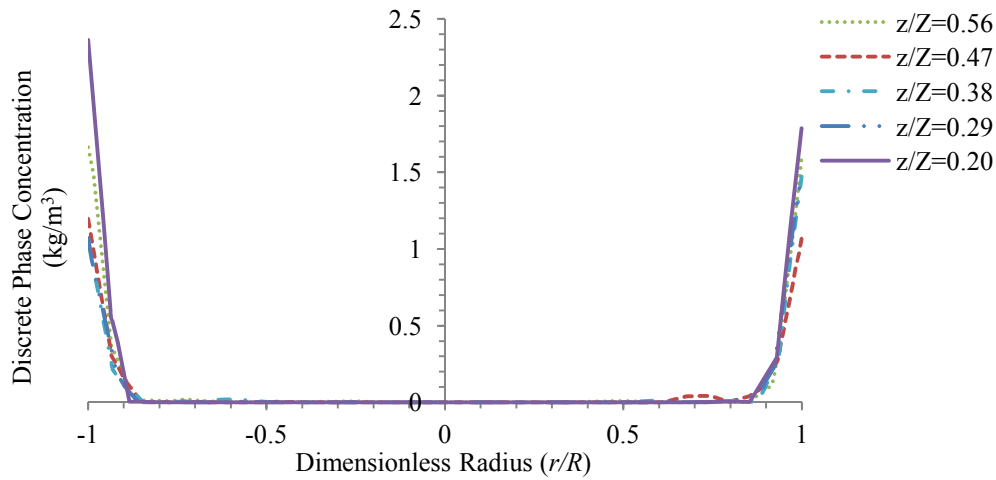


Figure – 9.8: Radial profiles of discrete phase concentration in the cylindrical region of the tower.

Figure 9.9 is a plot of radial temperature profiles of the gas phase along the dimensionless tower height obtained from the CFD analysis. The radial temperature profiles of the gas phase show a lower temperature in the annular region of the tower due to exchange of heat with the particles. The temperature in the core region of the tower decreases as the gas goes up due to mixing of the hot gas in the core region of the tower with gas in the annular region as well as thermal diffusion. Therefore the core region of the tower can be modelled as a separate zone, and the heat transfer between the core region and the annular region of the tower can be estimated by calculating the cup mixing temperature of both the annular region and the core region and calculating the heat transfer from the core to the annular region using the calculated cup mixing temperatures. Figure 9.10 is a plot of cup mixing temperature in the core, annular and for the entire cross section of the tower along the tower height within the cylindrical region of the tower with 0 representing the tower bottom and 1 representing the tower top. The solid lines represent the respective curve fits with  $R^2$  values greater than 0.99. The plots of cup mixing temperatures of the annular and core regions reveal that the annular temperature is smaller than the core temperature. The cup mixing temperature for the entire cross-section is close to the temperature of the core region of the tower.

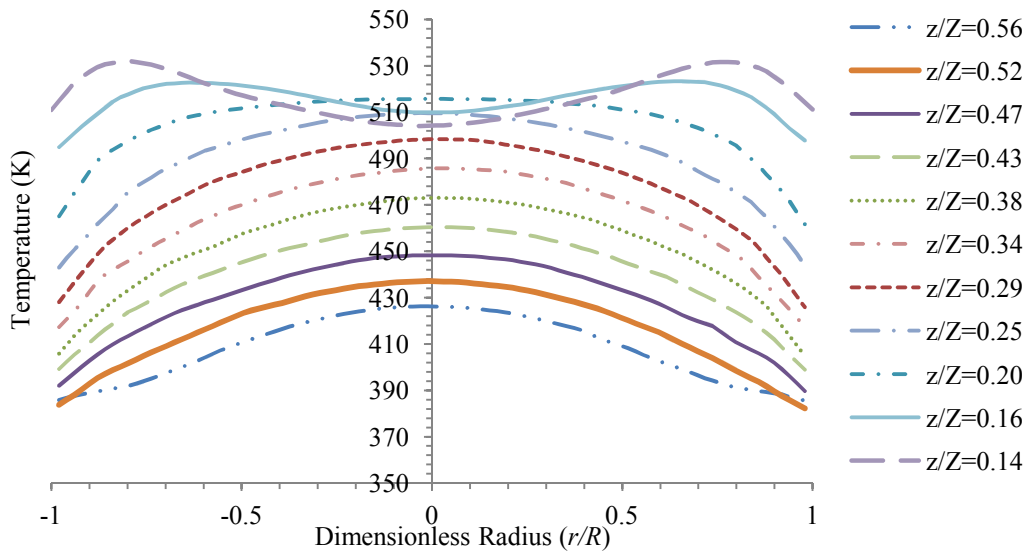


Figure – 9.9: Radial temperature profiles of gas in the cylindrical region of the tower.

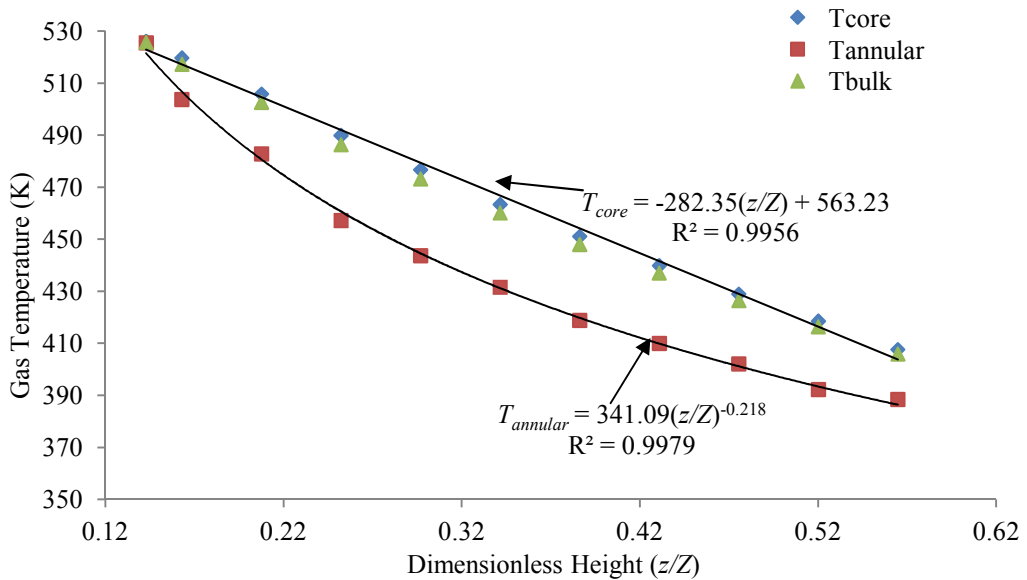


Figure – 9.10: Cup mixing temperature along the tower height in the cylindrical region of the tower.

Figure 9.11 is a plot of radial profile of the gas phase dimensionless mass flow (normalised by dividing with inlet gas flow) at different dimensionless heights. The mass flow is a minimum at the centre of the tower throughout the height, it increases away from the centre and reaches a maximum value at a certain location away from the wall and starts to decrease again close to the wall. The mass flow at  $z/Z = 0.56$  shows a downward flow of the gas near the wall due to high momentum exerted by the downward moving droplets/particles that result in reversal of the gas flow in this region. The plot indicates that the mass flow of the gas in the annular region of the tower is not a constant and varies along the height.

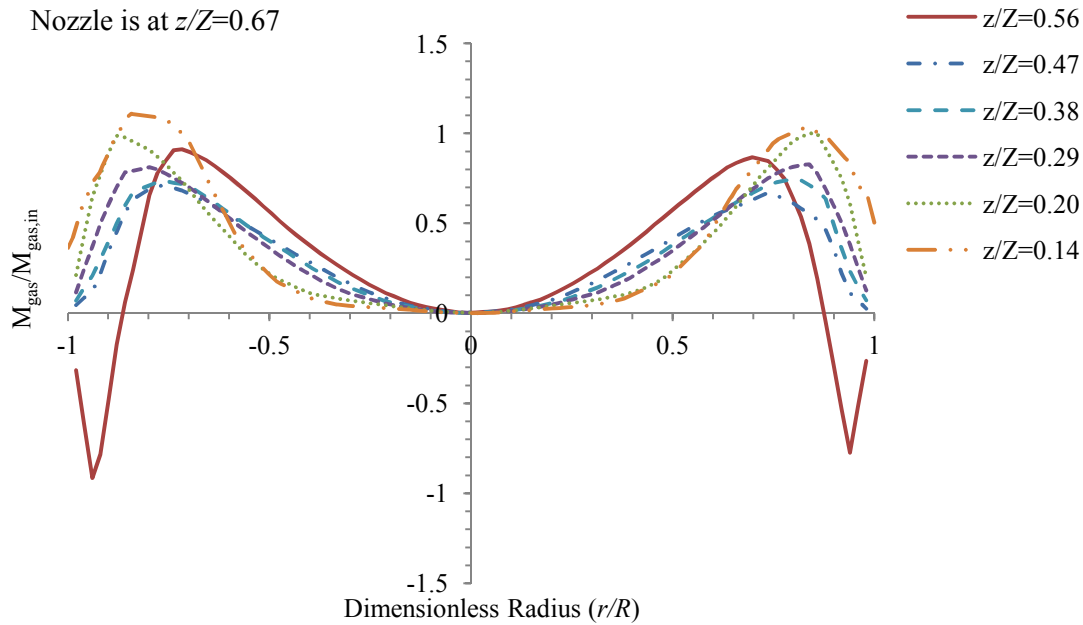


Figure – 9.11: Radial profile of gas mass flow at different heights.

The curve fit equations of gas temperature obtained from plots in Figure 9.10 are used in Zone 3 and Zone 4. Therefore the gas temperature is pre-specified along the height of the two zones (Zone 3 and 4), given by:

$$T_{annular} = 341.09(z/Z)^{-0.218} \quad (9.4)$$

$$T_{core} = -282.35(z/Z) + 563.23 \quad (9.5)$$

The gas temperature in the annular region can also be calculated using equation (9.6). The term  $\dot{q}_{3 \rightarrow 4}$  in equation (9.6) can be estimated using two methods, i.e., by calculating the heat transfer coefficient responsible for the transfer of heat from the core to the annular region of the tower or by using a curve fit equation for the heat flux obtained by calculating the heat transfer between zone 3 and 4 by analysing the CFD results. However this is left as a future work and the curve fit equations in Figure 9.10 are used for the determination of gas temperature.

$$\underbrace{\dot{M}_{g,3} c_{p,g,3} \frac{dT_{g,3}}{dz}}_{\text{Heat transfer from the air to the droplets}} = \underbrace{\sum_{j=1}^J \alpha_j A_{p_j} (T_{p_j,3} - T_{g,3}) \cdot \frac{n_j}{\tilde{u}_{p,j}}}_{\text{Total heat input to the droplets by convection}} + \underbrace{\sum_{j=1}^J \left( \frac{dM_l}{dt} \right)_j c_{p,vap} (T_{p_j,3} - T_{g,3}) \cdot \frac{n_j}{\tilde{u}_{p,j}}}_{\text{Sensible heat to the evaporated vapours}} \quad (9.6)$$

$$+ \underbrace{2\pi r_i U (T_{amb} - T_{g,3})}_{\text{Heat loss to the environment}} + \dot{q}_{3 \rightarrow 4}$$

The residence times of droplets/particles in the annular plug-flow zone (Zone 3) is taken from CFD Case 2 results in Chapter 7 and are listed in Table 9.1.

Table – 9.1: Residence time of particles in the cylindrical region of the tower.

Particle size ( $\mu\text{m}$ )	Residence time in cylindrical region (s)
200	4.1
300	4.8
500	4.6
1000	2.8
1500	1.5
2000	0.8

The data listed in Table 9.1 are used to estimate the best fit curve of residence times of particles v/s size in the cylindrical region of the tower, the residence time data and the corresponding curve fit equation is given in Figure 9.12.

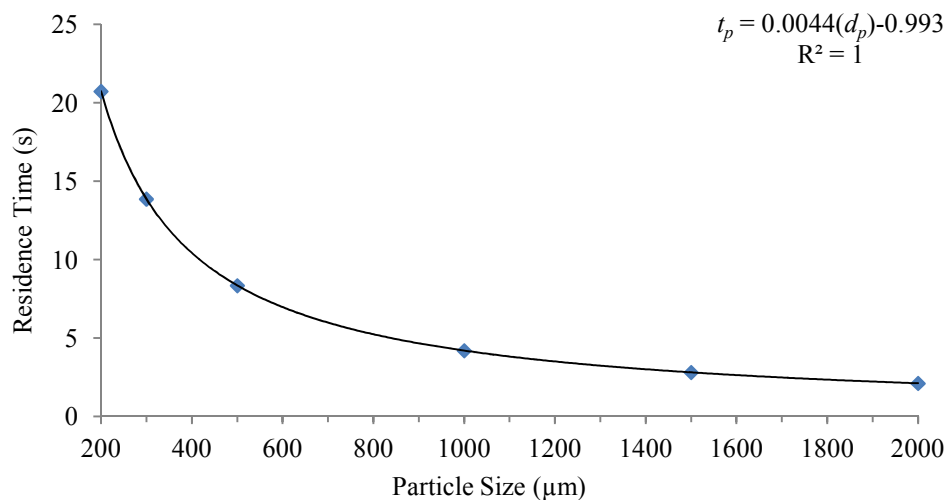


Figure – 9.12: Residence time of particles in the cylindrical region.

The drying rate of the droplets/particles is calculated using the semi-empirical droplet drying model described in Chapter 5, using equations (5.4), (5.13) and (5.14), representing the drying rates at different stages.

#### 9.2.4 **Zone 5 (CSTR Zone)**

The hot gas entry is via tangential-entry inlets hence a highly swirling gas flow exists in this conical region of the tower. The particles exchange heat with the gas phase in the conical region of the tower and exit from the bottom outlet of the tower. The gas phase in this zone is modelled as a well mixed region using CSTR approach, while the particles are modelled as plug-flow with the particles residence time specified from the CFD modelling results. The residence time of various particle sizes in the conical region of the tower obtained from CFD Case 2 results in Chapter 7 for different particle sizes is listed in Table 9.2. The data listed in Table 9.2 are then used to estimate the best fit curve of residence time of particle  $v/s$  particle size in the bottom conical region of the tower. The corresponding curve fit with an  $R^2$  value of 0.95 is depicted in Figure 9.13. The temperature of the gas phase in this zone is the average (mean) of the gas mass weighted inlet temperatures  $T_{hg,5}$ ,  $T_{cg,5}$  and the gas mass weighted temperatures at the interface of Zone 4-5 and Zone 3-5.

Table – 9.2: Residence time of particles in the conical region of the tower.

Particle size ( $\mu\text{m}$ )	Residence time in conical region (s)
200	4.1
300	4.8
500	4.6
1000	2.8
1500	1.5
2000	0.8

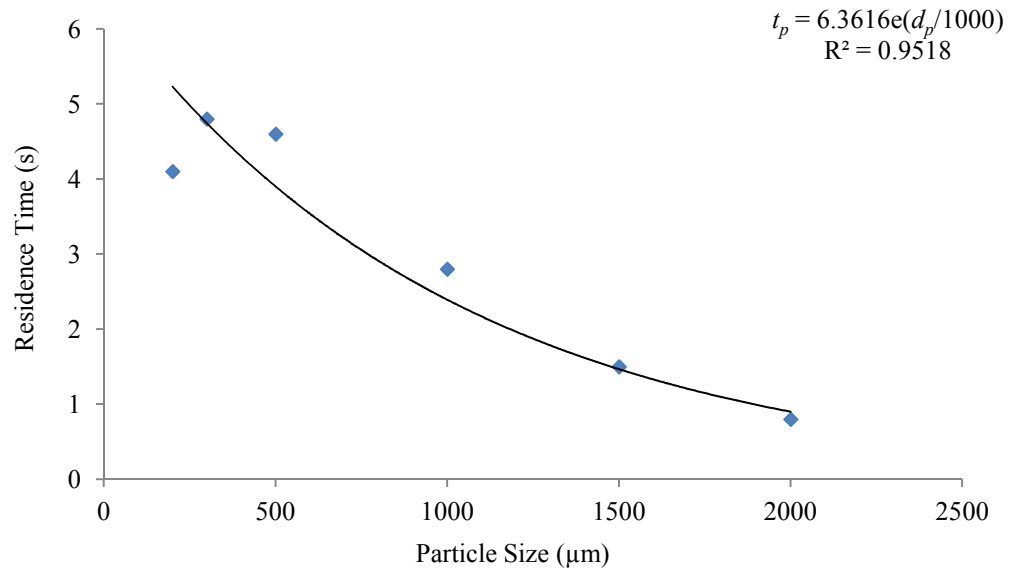


Figure – 9.13: Residence time of particles in the conical region of the tower.

The drying rate of the droplets/particles in this zone is calculated in the same manner as in Zone 3.

### **9.2.5 Solution Methodology**

The calculation is started from the top region of the tower. Using equation (9.1) the gas temperature at the interface of Zone 1 and 2 is calculated. Equation (9.1) requires temperature and moisture content of entrained droplets/particles at the interface of Zone 1 and 2, which is not known, therefore an iterative solution is required. For the first iteration, it is assumed that the entrained droplets/particles have the temperature and moisture content specified as the initial slurry (feed) condition. The calculated exhaust gas temperature at the interface of Zone 1 and 2 is used to solve Zone 2 using a plug-flow approach. In this zone, the calculation of particle sizes that get entrained (obtained from CFD) is stopped when the velocity of these particle sizes reaches the terminal velocity, and the final moisture content and temperature of these particles is used for the next iteration at the interface of Zone 1 and 2. The larger particles (particle sizes which exit from the bottom outlet) upon reaching terminal velocity are assumed to continue to fall with the same velocity in this zone. In Zone 3, heat exchange takes place only from the gas to the particles and the gas phase temperature obtained from CFD results as the curve fit equation for the gas temperature is specified as a function of height (Figure 9.10). The mass exchange between the droplets and particles and the gas is allowed to take place. The velocity of droplets/particles in Zone 3 is calculated from the residence time of particles in this section of the tower obtained from CFD (Figure 9.12). The gas phase in Zone 5 is solved as a CSTR while the particles are assumed to be plug-flow.

The exit mass flow of the gas is compared after each iteration. The solution is converged when the difference in the exit mass flow between the two successive iterations is less than the specified tolerance limit. The solution algorithm is depicted in Figure 9.14. The solution methodology is implemented in the computer software package MATLAB (2010).

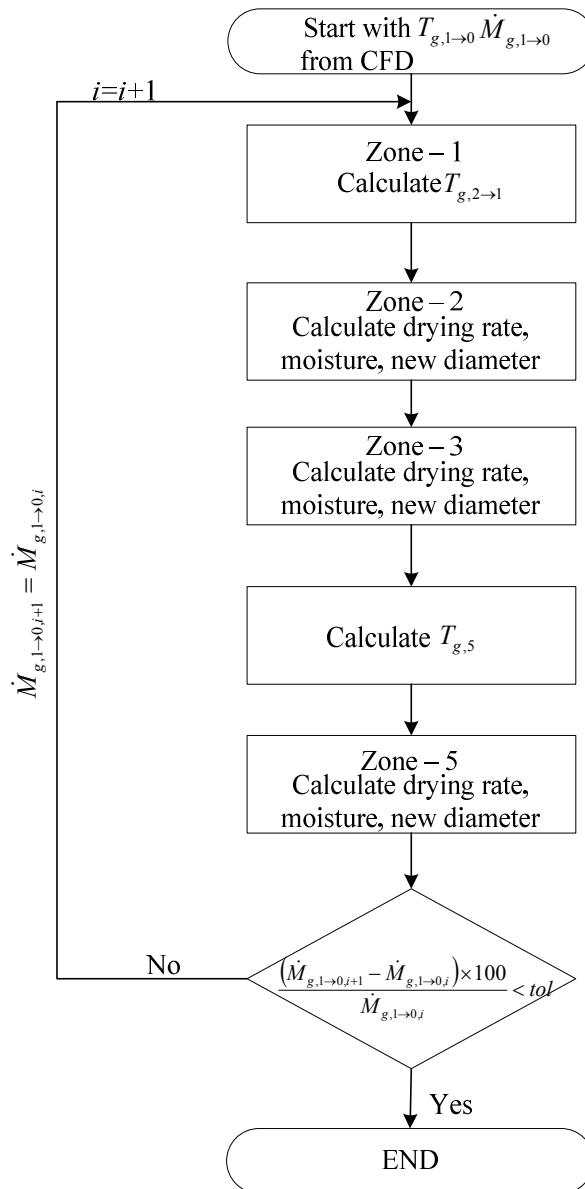


Figure – 9.14: Solution algorithm for zonal modelling.

Since the gas temperature in Zone 3 and Zone 4 is not calculated, therefore it is not a predictive model, and is hereby referred to as Zonal Model 1 (ZM 1) and is used as a concept to prove that this approach can be used to give results similar to the CFD model. In another approach, referred to as Zonal Model 2 (ZM 2), Zone 3 and Zone 4 are combined as a single plug-flow zone and the gas temperature is calculated in the same manner as in Zone 2, hence Zone 2, 3 and 4 are merged as a single plug-flow zone

in ZM 2. The solution methodology in ZM 2 is the same as in ZM 1. The results of both approaches are compared with CFD modelling results as well as with the plug-flow model.

### 9.2.6 Simulation Results

For the zonal modelling of spray drying tower, CFD simulation Base Case 2 results were used, therefore the tower is simulated using the operating conditions of this case, which are listed in Table 7.1 (Chapter 7). Most of the entrained powder predicted by the CFD model in Figure 7.24 comprises 100  $\mu\text{m}$  size, therefore only 100  $\mu\text{m}$  size is considered as the entrained particles in Zone 1 (Entrained Particles Zone) particle sizes greater than 100  $\mu\text{m}$  are allowed to exit from the tower bottom. For Zone 2, 3, and 5 (requiring plug-flow approach for the droplets/particles) the height of each of these zones is divided into a number of increments ( $\Delta z$ ). The size of the increments is based on the study of solution dependency on number of increments, carried out in Section 5.5.1 in Chapter 5. Two iterations were required to get the difference in the exit mass flow of the gas between the iterations to be less than the required tolerance limited, which was specified to be 0.5%. The time for convergence of solution was less than 1 minute.

Figure 9.15 is a plot of gas temperature profiles along the dimensionless height in different zones calculated using ZM 1 approach. Zone 1 is modelled as a CSTR therefore, its temperature is constant. The gas temperature in this zone is the lowest compared to all other zones as it lies above the nozzle and most of the heat exchange with droplets/particles takes place around and below the nozzle, therefore, the exiting gas temperature is the minimum. Zone 2 is modelled as plug-flow, therefore, the gas temperature decreases along the height due to exchange of heat with droplets in this zone. In Zone 3 and 4, the gas temperature is pre-specified using curve fit equations for gas temperatures, which show a decrease in temperature as the gas moves upwards. Zone 5 is modelled as a CSTR; therefore, gas temperature in this zone is constant. It has the highest temperature, since this lies at the tower bottom, near the hot gas inlets.

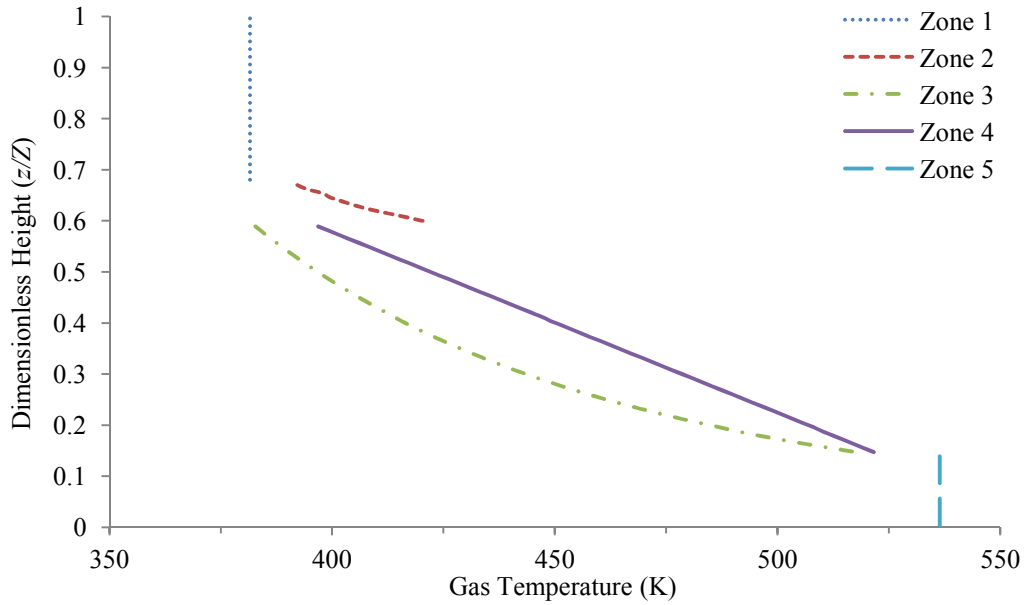


Figure – 9.15: Gas temperature profile along the dimensionless tower height in different zones using ZM 1 approach.

Figure 9.16 is a plot of gas temperature profiles along the dimensionless height in different zones of the tower obtained using ZM 2 approach. In this case, the gas temperatures at the interface of Zone 2 and Zone 3/4 overlap because the Zone 3/4 gas temperature is calculated using a plug-flow approach. It is observed that the gas temperature in Zone 3/4 using ZM 2 approach is greater compared to the curve fit gas temperatures in ZM 1 approach. The calculated gas temperature in Zone 5 using ZM 2 approach is also greater compared to that in ZM 1 approach.

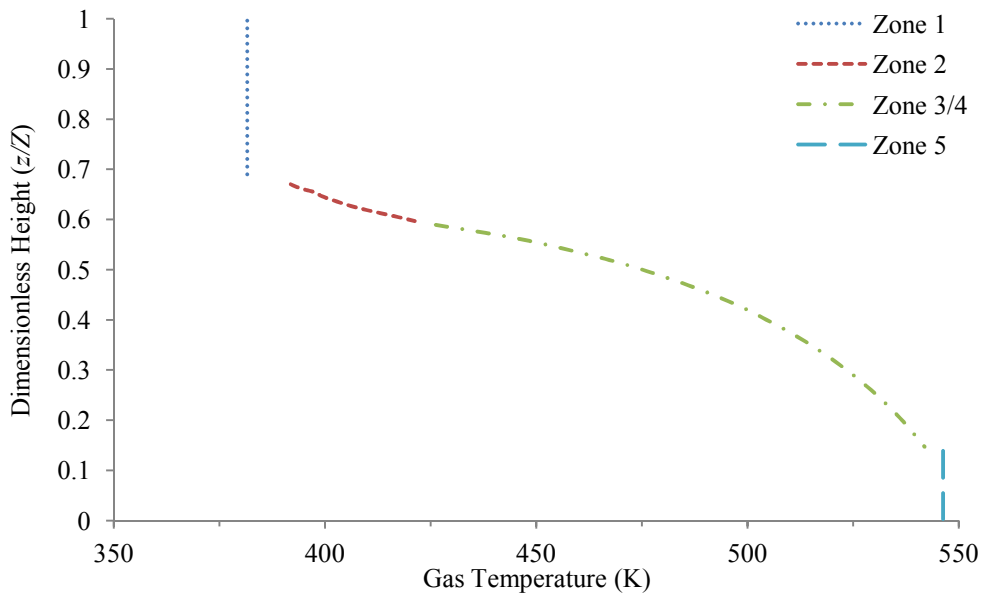


Figure – 9.16: Gas temperature profile along the dimensionless tower height in different zones using ZM 2 approach.

Figure 9.17 is a plot of temperature of particles that exit from the bottom of the tower obtained from CFD, zonal (ZM 1 and ZM 2) and plug-flow models for the same input conditions. The smaller particles exit at a higher temperature in all models, a sharp decrease in the exit temperature is observed in all the model results for particles of a certain size range. The larger particles exit at a fairly uniform temperature. Plug-flow model predicts the highest temperature for the smaller particles (up to 500  $\mu\text{m}$ ). A sharp decrease in exit particle temperature occurs for sizes in the range of 600 to 1000  $\mu\text{m}$  particle sizes. The exit temperature of particles greater than 1000  $\mu\text{m}$  is fairly constant and for sizes greater than 1400  $\mu\text{m}$ , it coincides with the results of CFD and zonal models. In ZM 1, the exit temperatures of particles up to 700  $\mu\text{m}$  is slightly smaller compared to the plug-flow model, since a CSTR approach is used to model the bottom region of the tower and has a lower gas temperature compared to the gas inlet temperature. A sharp decrease in exit particle temperature occurs for sizes in the range of 800 to 1200  $\mu\text{m}$ . The larger particles ( $>1200 \mu\text{m}$ ) exit at a constant temperature. The exit temperature of particle sizes in the range of 800 to 1200  $\mu\text{m}$  is larger compared to the plug-flow model because in the zonal model, residence times obtained from CFD are used, which are larger compared to the plug-flow predicted residence times (Figure 9.19). In ZM 2, the exit temperature of smaller particles ranging from 200 to 600  $\mu\text{m}$  exit at a higher temperature compared to ZM 1, primarily because Zone 3 and Zone 4 are merged as a single Zone and the resulting gas temperature is greater compared to the curve fitted gas temperature used in Zone 3 in ZM 1, but the residence times in both ZM 1 and ZM 2 are same. Hence ZM 2 predicts the highest exit particle temperatures for sizes in the range of 700 to 1400  $\mu\text{m}$  compared to all other models. The CFD model predicts the lowest exit particle temperature for sizes in the range of 200 to 700  $\mu\text{m}$ , because in the CFD model, the exiting particles come in contact with cold entrained air before they exit the tower and the smallest particles are more dried and have higher specific surface area therefore they quickly lose temperature upon contact with cold air. The exit particle temperature predicted by CFD for sizes in the range of 800 to 1100  $\mu\text{m}$  is higher than the plug-flow model and less than ZM 1 and ZM 2 models. The exit temperature of sizes greater than 1100  $\mu\text{m}$  is constant.

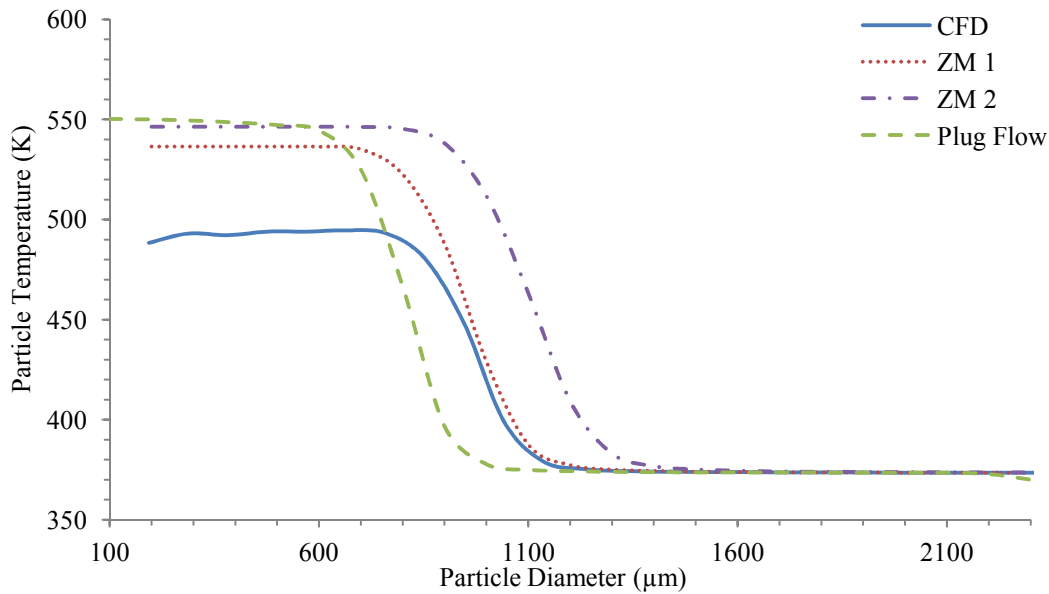


Figure – 9.17: Particle exit temperature obtained from different models.

Figure 9.18 is a plot of normalised moisture fraction of particles exiting from the tower bottom, obtained from CFD, zonal (ZM 1 and ZM 2) and Plug Flow models. The results of all the models are qualitatively similar, i.e., the smaller particles exit at zero moisture content while the larger particles exit at higher moisture content. In the plug-flow model, particle sizes up to 700  $\mu\text{m}$  exit at zero moisture content. While particle sizes greater than 700  $\mu\text{m}$  show increasing exit moisture content with increasing particle size. In both CFD and ZM 1 model predictions, the exiting moisture content of particle sizes up to 800  $\mu\text{m}$  is zero, while the larger particles show an increasing trend with increasing particle size. The ZM 2 model predicts the lowest exit moisture content of particles, because in ZM 2 model the temperature profiles in Zone 3 are calculated, which are greater than ZM 1 approach, therefore the particles get dried more quickly. The results of exit moisture content of the ZM 1 are very similar to that of CFD. Hence consideration of lower gas temperature in the annular region of the tower and good prediction of residence time are important factors necessary for a good agreement of particle exit moisture content with the CFD model.

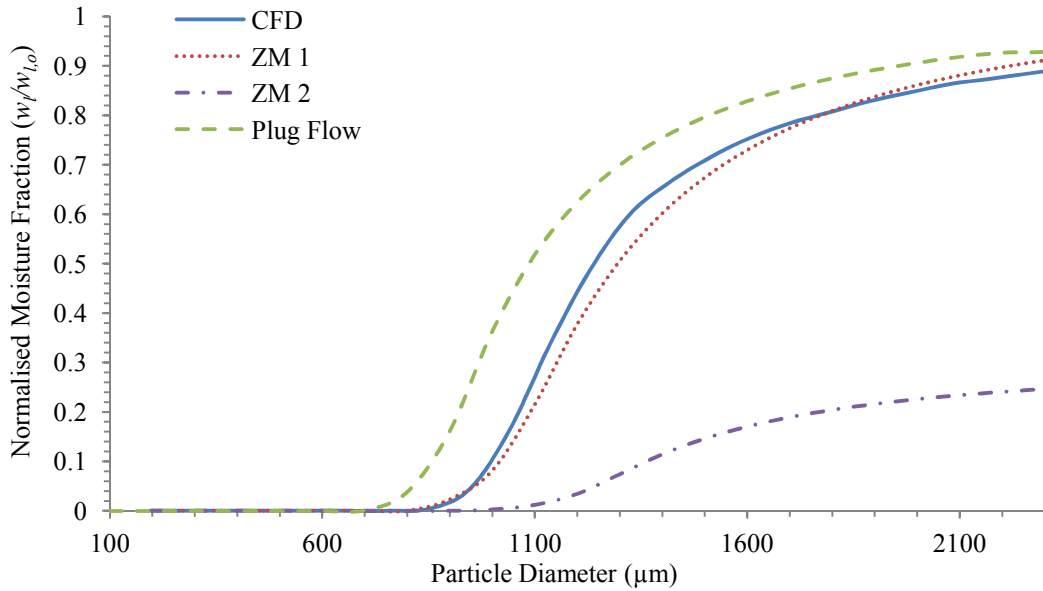


Figure – 9.18: Exit normalised moisture content of particles.

Figure 9.19 is a plot of the residence times of the exiting particles obtained from the CFD simulation, the zonal (ZM 1/ZM 2) and plug-flow modelling results. Qualitatively, the trend in the residence times of particles exiting from the tower bottom with changing particle sizes is very similar in all three approaches. The smaller particles take longer to exit from the tower bottom while the larger particles exit more quickly. From a comparison of the residence times of particles obtained from all the models, the plug-flow model predicts a shorter residence time for all particles sizes compared to the other two models. Because in the plug-flow model, particle-wall interaction as well as recirculation of the particles and entrainment are not considered. The CFD model predicts a very large residence time for the smallest particle size (200 μm), which exits from the tower bottom compared to the zonal models, because the smallest particle size in the CFD model is caught up in the recirculation regions close to the injection location, whereas in the zonal models (both ZM 1 and ZM 2), the residence time of droplets/particles in Zone 2 is calculated by solving the equation of motion. The residence times in the zonal models in Zone 3 and 5 are obtained from the CFD simulation. The residence times of larger particles (400 μm and greater) in the zonal models are very similar to that obtained from CFD simulation, because these particle sizes do not get caught up in the recirculation zones near the nozzle due to greater momentum.

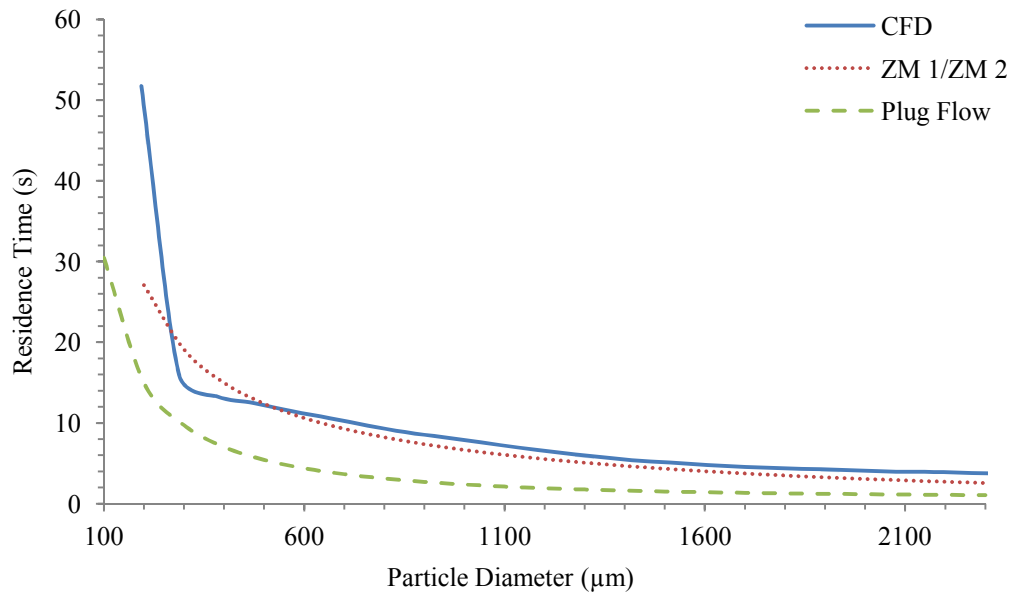


Figure – 9.19: Particles residence times obtained from different models.

The weighted average powder outlet parameters and tower heat loss obtained from CFD, zonal and plug-flow models are listed in Table 9.3. The weighted average temperature of the powder is smaller in the CFD model compared to all other models. The exit powder temperature predicted by the plug-flow and the ZM 1 is very similar. The exit powder temperature predicted by the ZM 2 is the highest. The weighted average powder moisture content is very similar in both the ZM 1 as well as in the CFD model, and is slightly higher in the plug-flow model. The heat loss predicted by CFD, ZM 1 and plug-flow models is very similar, but in ZM 2 it is slightly greater because in the annular region in ZM 2, the gas temperature is greater. Overall, the ZM 1 model gives a closer agreement with the CFD model compared to the plug-flow and the ZM 2 models. In the ZM 1, a lower gas temperature in the annular region (obtained from CFD) was imposed; hence consideration of lower gas temperature in the zonal model is necessary for a good agreement with the CFD model. Hence the prediction of exit temperature of the particles can be further improved by considering another zone below Zone 5, in which the particles get cooled down due to contact with entrained air.

Table – 9.3: Average results from the CFD, zonal and plug-flow models.

Parameter	CFD	Zonal (ZM 1)	Zonal (ZM 2)	Plug-Flow
Particle weighted average moisture content, %	4.75	4.31	2.82	5.88
Particle weighted average temperature, K	456.2	485.7	506.7	482.2
Heat loss, kW	5.4	5.6	7.0	5.5

### 9.3 Conclusions

Zonal modelling methodology comprising plug-flow and well mixed zones has been used to model the spray drying process in a counter-current spray drying tower. The basis of dividing the tower into different zones is obtained by interpolating the CFD modelling results. A comparison of the results of CFD, ZM 1, ZM 2 and plug-flow model is presented. All the models give the same qualitative trends when the exit particle moisture contents, temperatures and residence times are compared for different particle sizes. The ZM 1 model gives the closest agreement with the CFD modelling results compared to the plug-flow and ZM 2 models. Thus the present zonal modelling methodology can be used as an alternative to the CFD model to predict dried powder parameters as reliably as a CFD simulation. The results of ZM 1 and ZM 2 models vary significantly. The only difference in these two models is the consideration of lower temperatures near the wall in ZM 1 by imposing CFD predicted gas temperature profile, whereas in ZM 2, the gas temperature is constant over the entire cross-section of the tower and is calculated by solving heat and mass transfer between the droplets/particles and gas, in this case the modelled gas temperature in Zone 3 is found to be greater than the imposed gas temperature profile. Hence consideration of lower gas temperature in the cylindrical region of the tower is important for a closer agreement with the CFD model. The exit particle temperature prediction can be improved by considering another zone in which the exiting particles only exchange heat with the entrained air and get cooled down, which is left as a future work.

## **10. CONCLUSIONS AND RECOMMENDATIONS**

The conclusions drawn from the plug-flow, CFD and zonal modelling work on the IPP spray drying tower and the recommendations for the future work are given below.

### **10.1 Conclusions**

The modelling of the IPP spray drying tower was carried out considering plug-flow, CFD and zonal modelling approaches. All modelling approaches utilised a semi-empirical single droplet drying model (Hecht, 2012) to model the drying kinetics. All models considered droplets/particles of a range of sizes and variation of gas temperature along the tower height. In the plug-flow and CFD models, simulations were performed using different operating conditions obtained from the IPP tower runs using a single nozzle as well as two nozzles at different heights and the results were compared with the experimental data. The main conclusions drawn from the research work are given below:

#### **10.1.1 Plug-Flow Modelling**

1. Plug-flow modelling considering a single spray nozzle was carried out (Chapter 5) to evaluate the suitability of this approach in modelling the counter-current spray drying tower. An algorithm was developed to solve the model equations and it was implemented in the computer software package MATLAB (2010). In the plug-flow model, several simplifying assumptions were made to make it workable including limiting the final velocity of particles to the terminal falling velocity based on the stationary gas. The justification of this assumption was due to the fact that the particles move close to the wall where the gas velocity is very small and hence the particles fall according to the terminal falling velocity. This assumption had a direct influence on the residence time of particles. In the predicted residence times, it was found that the smaller particles have greater residence times and larger particles have shorter residence times (Figure 5.7). This is expected because smaller particles have lower weight hence less momentum and will have a greater influence of drag force. The trend of a decrease in the residence times of particles with increasing sizes is exponential.
2. It was found that the heat and mass transfer coefficients increased with decreasing droplet diameter; additionally, as the specific surface area of smaller particles was larger, the rate of heat and mass transfer was the highest for smaller particles

(Figures 5.10 and 5.11). Additionally the residence times of smaller particles were greater, hence the smaller particles exchanged more heat and mass with the gas compared to the larger particles.

3. Smaller particle sizes exited the tower at zero moisture content, which is unrealistic because the moisture content of the particles will not go down below the equilibrium moisture content at the surrounding gas conditions (Figure 5.18). This is due to the simplifying assumption in the droplet drying model (Hecht, 2012), which assumes that the drying process continues to take place even when particle moisture content falls below the equilibrium moisture content at surrounding gas conditions. Similarly, the larger particles that exited the bottom of the tower had a very high moisture content. This is also unrealistic, since the larger particles ( $>1000 \mu\text{m}$ ) in the simulation were considered to form and fall from the top of the tower (at the nozzle spray); however, these particles will be a result of coalescence and agglomeration below the nozzle spray. As the droplets/particles flow downwards they will become larger in size due to droplet-droplet, droplet-particle and particle-particle interactions resulting in coalescence and agglomeration. Hence by the time particles become very large they would lose much of the moisture content. Since coalescence and agglomeration processes were not considered in the model, therefore, these larger particles, having excessively high predicted moisture content acted to balance out the zero moisture content of the smaller particles in the average powder moisture content when compared with experimentally measured powder moisture fraction.
4. The measured outlet temperature of the powder was significantly less than the predicted value, because in the actual process, the dried powder comes into contact with an entrained cold air stream at the bottom exit of the tower and this will result in cooling of the powder. In addition, the powder temperature measurement is not taken at the exit of the tower, but is obtained by a temperature probe installed on a belt conveyor at a few metres away from the location where the powder falls from the tower (see Figure 4.2). The temperature of the powder is expected to reduce at this point. The model does not consider cooling of particles due to the entrained cold air and cooling of particles on the belt conveyor.
5. To find out the influence of the initial droplet size distribution on the modelling results, two more simulation cases were carried out. One case considered the measured droplet size distribution (plug-flow Case 1) and in the other case, the dried powder size distribution (plug-flow Case 2) was considered at the nozzle

spray. From a comparison of the predicted dried powder average moisture content with the measured data, it was found that the plug-flow Case 1 overpredicted, while the plug-flow Case 2 underpredicted the heat and mass transfer rates between the gas and particles. The large difference in the predicted dried powder moisture contents in these two simulated cases indicates the importance of accurate initial size distribution of the droplets as well as inclusion of coalescence/agglomeration to allow for changes in droplet/particle diameters along the tower height.

6. The plug-flow model was extended to accommodate two spray nozzles at different heights (Chapter 8) and a comparison was made with the experimental data. The trends of the results obtained (discussed above) considering two nozzles were similar to those obtained for a single nozzle.
7. The results of the plug-flow model were also compared with the CFD simulation results and it was found that this approach gave similar qualitative trends compared to the CFD model but underpredicted the residence times of particles primarily due to the limitation of particle falling velocity to its terminal velocity. The plug-flow model however has the advantage of being cheap in computational resources and can be used as an aid for quick estimation of optimised parameters for the IPP spray drying tower.

### **10.1.2 Single Phase CFD Modelling**

1. Before carrying out the CFD modelling of the detergent spray drying process it was necessary to ensure that the turbulence model successfully predicted the gas velocity profiles, because the particle trajectories and hence the residence time of particles depended on the predicted gas velocity profiles. Additionally it is important to ensure that the results are mesh independent. Therefore a single phase, CFD simulation of the IPP tower was carried out under isothermal conditions to study the sensitivity of predicted air velocity profiles on the mesh size. After selection of a suitable mesh size, the predicted mean axial, radial and tangential velocity profiles were compared with measured velocity profiles at various axial locations using various turbulence models. It was found that the LRR-RST model gave the best agreement with the experimental data. The mean tangential velocity component was found to be the major velocity component followed by the mean axial velocity component.

2. The IPP tower typically contains a layer of deposited particles on the wall that increases the wall surface roughness. It was found that the wall surface roughness significantly affected the strength of swirl (Figure 6.24) and consequently the tangential (Figure 6.18) and axial (Figure 6.19) velocity profiles as the air went up the tower. Therefore it is important to include wall surface roughness in modelling this spray drying tower.
3. From a comparison of the steady state and transient simulation results (Section 6.1.5), it was found that the mean air velocity profiles in the spray tower are stable and hence can be modelled using a steady state assumption.
4. A comparison of the predicted and measured air turbulent intensities was made (Figure 6.25); the LRR-RST model gave a better prediction of the measured turbulence intensity in the top cylindrical region of the tower as compared to the SSG-RST model.
5. Single phase non-isothermal CFD modelling of the IPP tower was carried out to validate the gas temperature predictions with measurements and to evaluate the heat loss from the tower (Section 6.2). In the experimental run, the inlet hot gas temperature measurement was taken at the inlet gas duct that supplies hot gas to the distribution ring. It was found that a significant drop in the gas temperature occurred between the inlet of the gas duct and the gas inlet nozzles mounted at the gas distribution ring. When this drop in temperature was taken into account the predicted gas temperature profiles inside the tower at various axial locations agreed well with the measured temperatures (Figure 6.30).
6. It was found that the internal film heat transfer coefficient at the tower wall decreased as the swirl intensity decreased (Figure 6.36). The overall decrease in the inside film coefficient was about 220%.
7. It was found that the wall surface roughness boundary condition affected the predicted gas temperature profiles inside the spray drying tower, particularly in the bottom cylindrical region as the mixing of the hot gas and cold entrained air was affected by the strength of swirl in the tower (Figure 6.38).

### **10.1.3 Multiphase CFD Modelling**

1. Isothermal, momentum-coupled multiphase CFD simulation of gas-particles flows in the spray drying tower was carried out using the Eulerian-Lagrangian approach. For the case in which a restitution coefficient of 1.0 was used, it was found that the larger particles ( $>200\ \mu\text{m}$ ) did not exit from the bottom of the tower (Figure

- 7.3). This was because of the use of elastic collision of particles with the wall. These particles gained angular momentum as they fell down and by the time particles reached the conical section of the tower, the angular momentum was high enough, so that on collision with the inclined wall they experienced an upward normal contact force component high enough to balance the gravitational force. Therefore, a lower value of the coefficient of restitution, 0.4 (based on the measured value for dried powder by Hassal (2011)), was used. In this case, the larger particles exited from the bottom of the tower (Figure 7.5).
2. The presence of particles significantly influenced the gas flow profiles. The swirl in the gas flow decayed faster (Figure 7.8), consequently, the axial (Figure 7.6) and tangential (Figure 7.7) velocities of the air also changed significantly compared to the corresponding single phase as the particles exchanged momentum with the gas phase. Hence the momentum coupling between the particles and the gas phase is important for this process.
  3. Multiphase CFD simulations of the detergent spray drying process were carried out considering heat, mass and momentum transfer between the gas phase and the discrete phase (comprising droplets and particles) using the Eulerian-Lagrangian approach. It was found that the smaller particles (up to 200  $\mu\text{m}$ ) were entrained by the upward flowing gas and they exited from the top of the tower with the exhaust gas, while the larger particles exited from the bottom (Figure 7.24). It was also found that the way the particle-wall interaction was modelled significantly altered the particle trajectories. The case in which a constant value of the restitution coefficient was used (a value of 0.4), the predicted particle trajectories showed an unrealistic behaviour of bouncing off from the wall (Figure 7.23). When the restitution coefficient was considered as a linear function of the particle moisture content (ranging from 0 for initial slurry droplets to 0.4 for dried particles), the particle trajectories were more realistic as confirmed by the visual inspection of particles in the pilot-scale spray tower. It is therefore important to include the particle-wall interaction as a function of moisture content. Due to the unavailability of data, it was assumed to be a linear relationship between the moisture content and the restitution coefficient. However, in reality it may be non-linear and in addition to the moisture content, the restitution coefficient can also vary with particle size, shape, impact angle, impact velocity and the wall roughness.

4. A rough-wall particle collision model was developed based on a stochastic approach (Section 7.2.12) to study the influence of wall surface roughness on the post-wall collision trajectories in multiphase, non-isothermal CFD modelling of the spray drying process in the IPP tower. The dispersion of particles increased over the cross-section of the tower due to the wall roughness. This resulted in a greater heat and mass exchange between the droplets/particles and the drying gas as the gas temperature was higher in the central region of the tower (Table 7.11).
5. The influence of non-spherical drag law on the particles residence times was checked (Section 7.2.10) by assuming a constant value of the sphericity to define the particle shape (assuming it to be cubical) and it was found that this increased the residence time of particles. But the particle sphericity depends on a number of factors including the degree of agglomeration, morphological changes during drying and breakage of particles and will continue to change as the particles fall down the tower, which were not considered due to the complexities involved in modelling these processes.
6. The influence of initial droplet size distribution specification on the simulation results was checked by using the measured droplet size distribution and the measured powder size distribution (Section 7.2.11). For the case in which droplet size distribution was used (CFD Case 5 in Chapter 7), the average dried powder moisture content was overpredicted and that for the powder size distribution (Case 6 in Chapter 7) was underpredicted compared to measured data (Table 7.10). Hence it is important to include coalescence and agglomeration in the model for a better prediction of the dried powder characteristics. For the common particle sizes in both cases, the difference in the residence times is negligible (Figure 7.42), but the exit powder moisture content is appreciably different (Figure 7.43). The use of different initial droplet size distributions primarily influenced the gas temperature profiles (Figure 7.40 and Figure 7.41). Hence the change in gas temperature has a stronger influence on particle drying rate than its residence time.
7. The residence times predicted by the CFD model were compared with the plug-flow predictions (Figure 7.42) and it was found that both gave a similar exponential decreasing trend with increasing particle size; however, the plug-flow model underpredicted the residence times.
8. The results of different CFD modelling cases were compared with the experimental data (Table 7.8, 7.10, and 7.11) and a reasonably good agreement

was observed when the restitution coefficient was considered a function of moisture content and when the rough wall collision model was used for predicting post-particle wall collision trajectories.

9. CFD modelling of the IPP tower was carried out considering two nozzles. The gas flow around the top nozzle was fairly asymmetric while at the bottom nozzle it was symmetrical, which is believed to be due to higher swirl in the bottom region of the tower and lower swirl at the top. Uneven distribution of gas flow around the nozzle may cause excessive deposition, which may be minimised by reducing the mass flow of slurry at the top nozzle. The overall trends of the results obtained considering two nozzles were similar to those obtained from the single nozzle cases when compared with measurements (Table 8.3).
10. CFD is a useful modelling tool which provides detailed information about the gas flow and temperature profiles and droplets/particles trajectories and can be used to tackle spray tower operational and product quality issues such as wall deposition and thermal degradation.

#### **10.1.4 Zonal Modelling**

1. A zonal modelling strategy was developed to enable predictions of the dried powder characteristics in the IPP tower as reliably as the CFD model but requiring much less computational time. The gas flow profiles and droplet/particle trajectories obtained from the multiphase CFD model were used to divide the tower into five zones. In each zone (see Figure 9.1), a CSTR or a plug-flow modelling methodology was used.
2. Two cases of zonal modelling were considered, referred to as ZM 1 and ZM 2. In ZM 1, the gas temperature profiles obtained from the CFD simulation were imposed in Zone 3 (Annular Zone) and Zone 4 (Hot Core Zone). In ZM 2, Zone 3 and 4 were merged into a single plug-flow zone and the gas temperature was calculated based on heat exchange with the droplets along the length of the tower. In ZM 1, the gas temperature in the annular zone was lower compared to that in ZM 2. The ZM 1 case gave a very close prediction of the exit particle moisture content compared with the CFD modelling results and hence it is a valid approach for dividing the tower into different zones. The ZM 2 model predicted a much lower exit particle moisture content due to a higher gas temperature in the whole region. Hence the consideration of a lower gas temperature in the annular region of the tower is important for a reliable prediction using the zonal model. The exit

particle temperature for particles having a moisture content greater than zero in the ZM 1 model matched well with the CFD model, but the temperature of particles exiting at zero moisture content was higher in both zonal models as compared to the CFD model, because the cooling of particles due to entrained air was not considered.

3. From a comparison of plug-flow and zonal models with the CFD model, it was found that the ZM 1 model gave a closer agreement with the CFD predicted exit particle moisture content (Figure 9.18). Hence the proposed zonal modelling methodology (ZM 1) can be applied to model spray drying process in a computationally efficiently manner.

### **10.1.5 Summary of Modelling Approaches**

1. The simple plug-flow model has the advantage of being cheap in computational resources and can be used to determine the influence of various operating parameters (gas mass flow, gas temperature, slurry mass flow, initial slurry moisture content and slurry temperature) on the product quality attributes and hence to select optimised parameters for the spray drying tower.
2. The more detailed CFD modelling approach provides information about the gas velocity profiles, temperature profiles, particle trajectories and can be used to tackle operational and product quality issues such as wall deposition and thermal degradation. The influence of changes in the design of the tower for optimised operation can also be assessed more comprehensively using CFD.
3. The zonal modelling approach can be used to predict the influence of changes in operating parameters on the dried product characteristics as reliably as the CFD model, but it is currently not a fully predictable model as it requires residence time distribution of particles and gas temperature profiles from the CFD model.

### **10.2 Recommendations for Future Work**

Based on the plug-flow, CFD and zonal modelling results and their comparison with the measured data in the IPP tower, the following recommendations are made for future work to improve the quality of model predictions:

1. In the CFD model, the restitution coefficient should be considered as a function of the particle impact velocity, size, impact angle and other particle characteristics, the wall surface roughness and structure in addition to the moisture content of

particles. In this study a linear function of moisture was assumed in the absence of any experimental data. The restitution coefficient may in fact not vary linearly with moisture content and an experimental investigation for the determination of restitution coefficient with varying moisture content should be carried out. Similarly the effect of impact angle and impact velocity should also be studied and then incorporated in the CFD model.

2. The importance of particle-particle interaction in changing the residence times should be evaluated as the larger particles fall down quicker and smaller particles move at a lower velocity, and the particles are more densely populated near the wall hence the larger particles will collide with slower moving smaller particles and get decelerated and vice versa. This can be studied by carrying out isothermal, coupled CFD-DEM simulation.
3. The residence times predicted by the models should be validated with the measured residence times of particles of different sizes in the IPP tower.
4. Particle-particle collision will result in agglomeration provided that the colliding particles are sufficiently wet. Therefore the conditions for agglomeration of wet particles should be determined experimentally and an agglomeration model should be developed based on experimental data and included in the CFD model as it has been found in both the plug-flow and CFD simulation results that the inclusion of the coalescence and agglomeration processes can make a significant improvement in the model predictions.
5. The influence of the particle-wall interactions resulting in the deposition of particles on the wall and re-entrainment of deposited particles should be explored, as the deposited material will have a greater residence time and will continue to exchange heat/mass with the drying gas before it eventually gets entrained back into the gas flow. The size of the re-entrained particles may also be different from the size of the deposited particles. This process may be equally responsible for the change in size of the particles as is the coalescence/agglomeration.
6. The drying gas inlet temperature measurement was taken at the inlet of the duct that supplies gas to the distribution ring to which the inlet nozzles are mounted for all multiphase CFD cases. This region of the tower is poorly insulated; therefore, the actual temperature of the gas at the inlet of the spray drying tower is lower. This affects the tower heat loss calculations using the measured temperature at the inlet of the gas supply duct. This may also influence the heat and mass transfer rate between the two phases in the tower as a higher gas temperature will result in

a more rapid drying of particles and vice versa. Therefore, the inlet hot gas temperature measurement in the IPP tower should be taken by shielded thermocouples inside the tangential inlet nozzles.

7. There is a need for more accurate data of powder outlet parameters used for the validation of modelling results. The temperature measurement should be taken at the bottom section of the tower before the bottom bent header (see Figure 4.2). The sample for moisture measurement should also be taken at that point.
8. The cold air entrained from the bottom outlet of the tower should also be measured and the measured entrained air value should be used in the multiphase CFD model.
9. It should be ensured that the IPP tower walls are as clean as possible when experimental trials are carried out for data collection for the purpose of validation, as the deposit layer thickness and the wall roughness can significantly alter the gas velocity profiles.
10. In the droplet drying model, the drying continues to take place in the third stage even at a very low moisture content. The drying is expected to proceed at a very slow rate as the particle moisture content reaches the equilibrium moisture content. To prevent the particles moisture content from getting below the equilibrium moisture content with the surrounding gas a fourth stage is required in which the particles remain at the equilibrium moisture. This requires a water isotherm in the detergent at the exit temperature which should also be determined experimentally and a fourth stage should be included in the droplet drying model.
11. The spray drying models predictions depend on the reliability of the single droplet drying model. Therefore single droplet drying experiments for the detergent slurry droplet should be carried out under conditions identical to those encountered in the spray drying tower and the results of the semi-empirical droplet drying model should be validated with the experimental data.
12. The drag law used for the calculation of drag coefficient was applicable to smooth spherical particles. However, the particles undergo changes in shape due to agglomeration as well as morphological changes during drying and it may be necessary to take into account the change in the shape of particles as shown by the use of drag law for non-spherical particles (in Case 4, Chapter 7), which increased the residence time of particles. Similarly, the correlations used for the heat and mass transfer coefficient were applicable to spherical droplets/particles. The effect

of non-spherical shape on heat and mass transfer coefficients should also be evaluated.

13. As the droplets/particles are more concentrated near the wall, the effect of higher concentration of the discrete phase on the heat and mass transfer rates of individual droplets/particles should be evaluated.
14. In the zonal modelling approach (ZM 1), the gas temperature profile obtained from the CFD simulation was used in the annular zone (Zone 3) to prove that the suggested zoning methodology is able to predict the dried powder characteristics close to the CFD results. However, this was not a fully predictive model, as it requires a temperature profile obtained from CFD predictions for every new set of spray tower operating conditions in the annular (Zone 3) and core zone (Zone 4). To improve the predictability of the model, the modelling of exchange of heat and mass between Zone 3 and Zone 4 is required.
15. An additional zone should be added to the zonal model at the bottom outlet of the tower to allow for cooling of the dried particles with the entrained cold air and equilibration of the moisture content with the air conditions, to get a better agreement of the predicted particle temperatures between the zonal and CFD models, and measurements.

## REFERENCES

- Ade-John, A. O. and Jeffreys, G. V. (1978). Flow visualization and residence time studies in a spray drier. *Trans IChemE*, **vol. 56**, pp. 33-42.
- Ahmadian, H. (2012). Personal communication, P&G Newcastle Technical Centres, UK.
- Ahmadian, H. (2013). Personal communication, P&G Newcastle Technical Centres, UK.
- Al-Mansour, H. E., Al-Busairi, B. H. and Baker, C. G. J. (2011) Energy consumption of a pilot-scale spray dryer. *Drying Technology*, **vol. 29**, pp. 1901-1910.
- Al-Mubarak, A., Belkharchouche, M., Al-Hayan, M. and Husain, A. (2010). Mechanisms of single droplet drying. *Kuwait J. Sci. Eng.*, **vol. 37**, pp. 161-179.
- Amador, C. (2011). Personal communication, P&G Newcastle Technical Centres, UK.
- Anandharamakrishnan, C., Gimbin, J., Stapley, A. G. F. and Rilley, C. D. (2010). A study of particle histories during spray drying using computational fluid dynamic simulations. *Drying Technology*, **vol. 28**, pp. 566-576.
- Arnanson, G. and Crowe, C. T. (1980). Assessment of numerical models for spray drying. *Drying 1980 – Proceedings of the 2<sup>nd</sup> international drying symposium (IDS 1980)*, **vol. 2**, pp. 410-416.
- Arpagaus, C. (2012). A laboratory scale spray dryer to produce nanoparticles. *Drying Technology*, **vol. 30**, pp. 1113-1121.
- Audu, T. O. K. and Jeffreys, G. V. (1975). The drying of drops of particulate slurries. *Trans IChemE*, **vol. 53**, pp. 165-172.
- Bahu, E. R. (1992). Spray Drying – Maturity or Opportunities? *Drying'92, part - A*, pp. 74-91.
- Baker, C. G. J. and McKenzie, K. A. (2005). Energy consumption of industrial spray dryers. *Drying Technology*, **vol. 23**, pp. 365-386.
- Bakker, A. 2002. *Computational Fluid Mixing*. NH, USA: Fluent Inc.

- Bayly, A. E., Smith, D. J., Robets, S. N., Yord, D. W. and Capeci, S. (2009). Chapter 19: Detergent Processing in Handbook of Detergents/Part F: Production. Taylor & Francis, pp. 323-363.
- Bayly, A. E., Jukes, P., Groombridge, M. and McNally, C. (2004). Airflow patterns in a counter-current spray drying tower – simulation and measurement. *Proceedings of the 14th International Drying Symposium*, 2004, Sao Paulo, 22-25 August, **vol. B**, pp. 775-781.
- Bayly, A. E. (2013). Personal communication, University of Leeds, UK.
- Bentley, E. F. and Waddill, H. G. (1973). Detergent slurry compositions. U. S. Patent 3755203, filed Apr. 29, 1971, issued Aug. 28, 1973.
- Booyani, P., Bhandari, B. and Howes, T. (2004). Stickiness measurement techniques for food powders: a review. *Powder Technology*, **vol. 145**, pp. 34-46.
- Cal, K. and Sollohub, K. (2009). Spray Drying Technique. I: Hardware and Process Parameters. *J. Pharm. Sci.*, **vol. 99** (2), pp. 575-586.
- Cebeci, T. and Bradshaw, P. 1977. *Momentum Transfer in Boundary Layers*. McGraw-Hill, London.
- Chaloud, J. H., Martin, J.B. and Baker, J. S. (1957). Fundamentals of spray-drying detergents. *Chem. Eng. Prog.*, **vol. 53**, no. 12, pp. 593-596.
- Charlesworth, D. H. and Marshall, W. R. (1960). Evaporation from drops containing dissolved solids. *AIChE J.*, **vol. 6**, pp. 9 - 23.
- Chang, F. and Dhir, V. K. (1994). Turbulent flow field in tangentially injected swirl flows in tubes. *Int. J. Heat and Fluid Flow*, **vol. 15** (5), pp. 346-357.
- Chang, F. and Dhir, V. K. (1995). Mechanisms of heat transfer enhancement and slow decay of swirl in tubes using tangential injection. *Int. J. Heat and Fluid Flow*, **vol. 16** (2), pp. 78–87.
- Chen, J. C. and Lin, C. A. (1999). Computations of strongly swirling flows with second-moment closures. *Int. J. Numer. Meth. Fluids*, **vol. 30**, pp. 493-508.

- Chen, X. D. and Lin, S. X. Q. (2004). The reaction engineering approach to modelling drying of milk droplets. *Proceedings of the 14th International Drying Symposium*, 2004, Sao Paulo, 22-25 August, **vol. C**, pp. 1644-1651.
- Chen, X. D. and Lin, S. X. Q. (2005). Air drying of milk droplet under constant and time dependent conditions. *AIChE J.*, **vol. 51**, No. 6, pp. 1790-1799.
- Chen, X. D. and Xie, G. Z. (1997). Fingerprints of the drying behaviour of particulate or thin layer food materials established using a reaction engineering model. *Trans IChemE*, **vol. 75** (c), pp. 213-222.
- Chen, X. D., Pirini, W. and Ozilgen, M. (2001). The reaction engineering approach to modelling drying of thin layer of pulped Kiwifruit flesh under conditions of small Biot numbers. *Chem. Eng. Proc.*, **vol. 40**, pp. 311-320.
- Cheong, H. W., Jeffreys, G. V. and Mumford, C. J. (1986). A receding interface model for the drying of slurry droplets. *AIChE J.*, **vol. 32**, pp. 1334 - 1346.
- Choudhury, D. (1993). *Introduction to the renormalization group method and turbulence modelling*. Fluent Inc. Technical Memorandum TM-107, Lebanon NH 03766, USA.
- Chu, J. C., Stout, L. E. and Busche, R. M. (1951). Spray drying of santomerse. *Chem. Eng. Prog.*, **vol. 47**, pp. 29-38.
- Crank, J. (1975). *The Mathematics of Diffusion*. Oxford: Clarendon Press, second edn.
- Crowe, C. T. (1980). Modeling spray-air contact in spray-drying systems. *Advances in drying*, **vol. 1**, pp. 63-99.
- Crowe, C. T. (1983). Droplet-gas interaction in counter-current spray dryers. *Drying Technology*, **vol. 1**, pp. 35-56.
- Crowe, C. T., Sommerfeld, M and Tsuji, Y. (1998). *Multiphase flows with droplets and particles*. London: CRC Press.
- Crowe, C. T., Sharma, M. P. and Stock, D. E. (1977). The Particle-Source-In Cell (PSI-CELL) Model for gas-droplet flows. *J. Fluids Eng.*, **vol. 99** (2), pp. 325-332.

- Dalmaz, N., Ozbelge, H. O., Eraslan, A. N. and Uludag, Y. (2007). Heat and Mass Transfer Mechanisms in Drying of a Suspension Droplet: A New Computational Model. *Drying Technology*, **vol. 25** (2), pp. 391-400.
- Davidson, A. (2011). Personal communication, P&G Newcastle Technical Centres, UK.
- Djurdjevic, D. (2010). Personal communication, P&G Newcastle Technical Centres, UK.
- Dlouhy, J. and Gauvin, W. H. (1960). Heat and mass transfer in spray drying. *AIChE J.*, **vol. 6** (1), pp. 29-34.
- Effting, C., Folgueras, M. V., Guths, Saulo, Alarcon, O. E. (2010). Microstructural characterization of ceramic floor tiles with the incorporation of wastes from ceramic tile industries. *Materials Research*, **vol. 13** (3), pp. 319-323.
- Eisenklam, P., Arunachalam, S. A. and Wetson, J. A. (1967). Evaporation rate and drag resistance of burning drops. *11<sup>th</sup> International Symposium on Combustion*, Pittsburgh, pp. 715-728.
- Elperin, T. and Krasovitov, B. (1995). Evaporation of liquid droplets containing small solid particles. *Int. J. Heat Mass Tran.*, **vol. 38** (12), pp. 2259-2617.
- Escue, A. and Cui, J. (2010). Comparison of turbulence models in simulating swirling pipe flows. *App. Math. Modelling*, **vol. 34**, pp. 2840-2849.
- Farid, M. (2003). A new approach to modeling of single droplet drying. *Chem Eng. Sci.*, **vol. 58**, pp. 2985-2993.
- First Research (2008). First Research Report on Soap and Detergent Manufacture: Industry Profile.
- Fletcher, D., Guo, B., Harvie, D., Langrish, T., Nidjam, T. and Williams, J. (2003). What is important in the simulation of spray dryer performance and how do current CFD models perform? *Third international conference on CFD in Minerals and Process Industries CSIRO*, Melbourne, Australia, pp. 357-363.
- Fluent User's guide. (2009). *Ansys Inc.*
- Francia, V. (2011). Personal communication, University of Birmingham, UK.

- Francia, V., Martin, L., Bayly, A. E. and Simmons, M. (2013). The role of wall friction in the development, decay, and breakage of an air turbulent confined vortex. *8<sup>th</sup> International Conference on Multiphase Flow ICMF 2013*, Jeju, Korea.
- Furuta, T., Tsujimoto, S., Okazaki, M. and Toei, R. (1983). Effect of drying on retention of ethanol in maltodextrin solution during drying of a single droplet. *Drying Technology*, **vol. 3**, pp. 311-327.
- Fyhr, C. and Kemp, I. C. (1998). Comparison of different drying kinetics models for single particles. *Drying Technology*, **vol. 16** (7), pp. 1339-1369.
- Gambit, version 2.4, <http://www.ansys.com>
- Gauvin, W. H., Katta, S. and Knelman, F. H. (1975). Drop trajectory predictions and their importance in the design of spray dryers. *Int. J. Multiphas. Flow*, **vol. 1**, pp. 793-816.
- German, A. E. and Mahmud, T. (2005). Modelling of non-premixed swirl burner flows using a Reynolds-stress turbulence closure. *Fuel*, **vol. 84**, pp. 583-594.
- Gibson, M. M. and Launder, B. E. (1978). Ground effects on Pressure fluctuations in the atmospheric boundary layers. *J. Fluid Mech.*, **vol. 86**, part 3, pp. 491-511.
- Griffith, J. D., Bayly, A. E. and Johns, M L. (2008). Magnetic resonance studies of detergent drop drying. *Chem. Eng. Sci.*, **vol. 63**, pp. 3449-3456.
- Griffith, J. D. (2008). The drying and absorption properties of surfactant granules. Ph.D. Thesis, *University of Cambridge*, UK.
- Haider, A. and Levenspiel, O. (1989). Drag coefficient and terminal velocity of spherical and nonspherical particles. *Powder Technology*, **vol. 58**, pp. 63-70.
- Handscomb, C. S., Kraft, M. and Bayly, A. E. (2009a). A new model for the drying of droplets containing suspended solids. *Chem. Eng. Sci.*, **vol. 64**, pp. 628-637.
- Handscomb, C. S., Kraft, M. and Bayly, A. E. (2009b). A new model for the drying of droplets containing suspended solids after shell formation. *Chem. Eng. Sci.*, **vol. 64**, pp. 228-246.
- Hanus, M. J. and Langrish, T. A. G. (2007). Resuspension of wall deposits in spray dryers. *Journal of Zhejiang University Science A*, **vol. 8** (11), pp. 1762-1774.

- Harvie, D. J. E., Langrish, T. A. G. and Fletcher, D. F. (2001). Numerical simulations of gas-flow patterns within a tall-form spray dryer. *Trans IChemE*, **vol. 79**, part A, pp. 235-248.
- Harvie, D. J. E., Langrish, T. A. G. and Fletcher, D. F. (2002). A computational fluid dynamics study of a tall-form spray dryer. *Trans IChemE*, **vol. 80**, part C, pp. 163-174.
- Hassal, G. J. (2011). Wall build-up in spray dryers. Ph.D. Thesis, *University of Birmingham*, UK.
- Hassan, H. M. and Mumford, C. J. (1993). Mechanisms of drying of skin forming materials. 1. Droplets of materials which gelatinised at high temperature. *Drying Technology*, **vol. 11**, pp. 1730-1750.
- Hecht, J. P. (2012). Personal Communication, P&G Technical Centres, UK.
- Hecht, J. P. and King C. J. (2000a). Spray Drying: Influence of Developing Drop Morphology on Drying Rates and Retention of Volatile Substances. 1: Single-Drop Experiments. *Ind. Eng. Chem.*, **vol. 39**, pp. 1756-1765.
- Hecht, J. P. and King, C. J. (2000b). Spray Drying: Influence of Developing Drop Morphology on Drying Rates and Retention of Volatile Substances. 2: Modeling. *Ind. Eng. Chem.*, **vol. 39**, pp. 1766-1774.
- Heggs, P. J. (2012). Personal communication, University of Leeds, UK.
- Hoekstra, A. J., Derksen, J. J. and Van Den Akker, H. E. A. (1999). An experimental and numerical study of turbulent swirling flow in gas cyclones. *Chem. Eng. Sci.*, **vol. 54**, pp. 2055-2065.
- Hogg, S. and Leschziner, M. A. (1989). Computation of highly swirling confined flow with a Reynolds-stress turbulence model. *AIAA J.*, **vol. 27**, pp. 57-67.
- Huang, L., Kumar, K. and Mujumdar, A. S. (2003a). A parametric study of gas flow patterns and drying performance of co-current spray dryer: results of a computational fluid dynamics study. *Drying Technology*, **vol. 21** (6), pp. 957-978.
- Huang, L., Kumar, K. and Mujumdar, A. S. (2003b). Use of computational fluid dynamics to evaluate alternate spray dryer chamber configurations. *Drying Technology*, **vol. 21** (3), pp. 385-412.

- Huang, L., Passos, M. L., Kumar, K. and Mujumdar, A. S. (2004a). A three-dimensional simulation of a spray dryer with a rotary atomizer. *Drying 2004 – Proceedings of the 14th international drying symposium (IDS 2004)*, **vol. A**, pp. 319-325.
- Huang, L., Kumar, K. and Mujumdar, A. S. (2004b). Computational fluid dynamic simulation of droplet drying in a spray dryer. *Drying 2004 – Proceedings of the 14th international drying symposium (IDS 2004)*, **vol. A**, pp. 326-332.
- Huang, L. X., Kumar, K. and Mujumdar, A. S. (2006). A comparative study of a spray dryer with rotary disc atomizer and pressure nozzle using computational fluid dynamic simulations. *Chem. Engg. Proc.*, **vol. 45**, pp. 461-470.
- Huber, N. and Sommerfeld, M. (1998). Modelling and numerical calculation of dilute-phase pneumatic conveying in pipe systems. *Powder Technology*, **vol. 99**, pp. 90-101.
- Huntington, D. H. (2004). The influence of the spray drying process on product properties. *Drying Technology*, **vol. 22**, pp. 1261-1287.
- Issa, R. I. (1985). Solution of the implicitly discretised fluid flow equations by operator splitting. *J. Comp. Phy.*, **vol. 62**, pp. 40-65.
- Jakirlić, S., Hanjalić, K. and Tropea, C. (2002). Modeling rotating and swirling turbulent flows: A Prepetual Challenge. *AIAA J.*, **vol. 40**, no. 10, pp. 1984-1996.
- Jamaledine, T. J. and Ray, M. B. (2010). Application of computational fluid dynamics for simulation of drying processes: A review. *Drying Technology*, **vol. 28**, pp. 120-154.
- Jannot, Y., Talla, A., Nganhou, J and Puiggali, J. R. (2004). Modeling of banana convective drying by the drying characteristic curve (DCC) method. *Drying Technology*, **vol. 22** (8), pp. 1949-1968.
- Javed, K. H., Mahmud, T. and Purba, E. (2006). Enhancement of mass transfer in a spray tower using swirling gas flow. *Trans IChemE*, **vol. 84** (A6), part A, pp. 33-42.
- Jawarneh, A. M. (2011). Heat transfer enhancement in a narrow concentric annulus in decaying swirl flow. *Heat Transfer Research*, **vol. 42** (3), pp. 199-216.

- Jin, Y and Chen, X. D. (2009). Numerical study of the drying process of different sized particles in an industrial-scale spray dryer. *Drying Technology*, **vol. 27** (3), pp. 371-381.
- Jin, Y and Chen, X. D. (2010). A fundamental model of particle deposition incorporated in CFD simulations of an industrial milk spray dryer. *Drying Technology*, **vol. 28** (8), pp. 960-971.
- Jones, W. P. and Pascau, A. (1989). Calculation of confined swirling flows with a second moment closure. *J. Fluids Eng.*, **vol. 111** (3), pp. 248-255.
- Kadja, M. and Bergeles, G. (2003). Modelling of slurry droplet drying. *Appl. Thermal Eng.*, **vol. 23**, pp. 829-844.
- Katta, S. and Gauvin, W. H. (1975). Some fundamental aspects of spray drying. *AIChE J.*, **vol. 21**, pp. 143-152.
- Kaya, F., Karagoz, U. and Avci, A. (2011). Effects of surface roughness on the performance of tangential inlet cyclone separators. *Aerosol Sci. Tech.*, **vol. 45**, pp. 988-995.
- Key, R. B. and Pham, Q. T. (1976). Behaviour of spray dryers with nozzle atomisers. *The Chemical Engineer*, 311, pp. 516-521.
- Key, R. B., 1978. *Introduction to industrial drying operations*. Pergamon Press, Oxford.
- Khan, A., Sen, D., Kothalkar, P., Sapra, B. K., Mazumder, S. and Mayya, Y. S. (2012). Design and performance of spray dryer to realize evaporation-induced self-assembly of nanoparticles. *Drying Technology*, **vol. 30**, pp. 679-686.
- Kieviet, F. G. (1997). Modelling quality in spray drying. Ph.D. Thesis, *Eindhoven University of Technology*, The Netherlands.
- Kioth, O. (1991). Experimental study of turbulent swirling flow in a straight pipe. *J. Fluid Mech.*, **vol. 225**, pp. 445-479.
- Ko, J., Zahrai, S. and Macchion, O. (2006). Numerical modeling of highly swirling flows in a through-flow cylindrical hydrocyclone. *AIChE J.*, **vol. 52**, no. 10, pp. 3334-3344.

- Kota, K. and Langrish, T. (2007). Prediction of Deposition Patterns in a Pilot-Scale Spray Dryer Using Computational Fluid Dynamics (CFD) Simulations. *Chemical Product and Process Modeling*, **vol. 2**, Iss. 3, Article 26.
- Kreith, F. (1973). *Principles of heat transfer*. Singapore: Intext Press, third edn.
- Kuriakose, R. and Anandharamakrishnan, C. (2010). Computational fluid dynamics (CFD) applications in spray drying of food products. *Trends Food Sci. Tech.*, **vol. 21**, pp. 383-398.
- Langrish, T. A. G. (2007). New engineered particles from spray dryers: Research needs in spray drying. *Drying Technology*, **vol. 25** (6), pp. 971-983.
- Langrish, T. A. G. and Fletcher, D. F. (2001). Spray drying of food ingredients and applications of CFD in spray drying. *Chem. Eng. Proc.*, **vol. 40**, pp. 345-354.
- Langrish, T. A. G. and Fletcher, D. F. (2003): Prospects for the Modelling and Design of Spray Dryers in the 21st Century. *Drying Technology*, **vol. 21** (2), pp. 197-215.
- Langrish, T. A. G. and Kockel, T. K. (2001). The assessment of characteristic drying curve for milk powder for use in computational fluid dynamics modelling. *Chem. Eng. J.*, **vol. 84**, pp. 69-74.
- Langrish, T. A. G. and Zbicinski, I. (1994). The effects of air inlet geometry and spray cone angle on the wall deposition rate in spray dryers. *Trans IChemE*, **vol. 72** (A), pp. 420-430.
- Langrish, T. A. G., Oakley, D. E., Keey, R. B., Bahu, R. E. and Hutchinson, C. A. (1993). Time-dependent flow patterns in spray dryers. *TransIChemE*, **vol. 71** (A), pp. 355-360.
- Langrish, T. A. G., Williams, J. and Fletcher, D. F. (2004). Simulation of the effects of inlet swirl on gas flow patterns in a pilot-scale spray dryer. *Trans IChemE*, **vol. 82** (A7), pp. 821-833.
- Launder, B. E. (1989). Second moment closure and its use in modelling turbulent industrial flows. *Int. J. Numer. Meth. Fl.*, **vol. 9**, pp. 963-985.
- Launder, B. E. and Spalding, D. B. (1972). *Lectures in mathematical modelling of turbulence*. Academic Press, London.

- Launder, B. E. and Spalding, D. B. (1974). The numerical computation of turbulent flows. *Comput. Method. Appl. M.*, **vol. 3**, pp. 269-289.
- Launder, B. E., Reece, G. J. and Rodi, W. (1975). Progress in the development of a Reynolds-stress turbulence closure. *J. Fluid Mech.*, **vol. 68**, part 3, pp. 537-566.
- Lebarbier, C., Kockel, T. K., Fletcher, D. F. and Langrish, T. A. G. (2001). Experimental measurement and numerical simulation of the effect of swirl on flow stability in spray dryers. *Trans IChemE*, **vol. 79** (A), pp. 260-268.
- Leonard, B. P. and Mokhtari, S. (1990). Ultra-sharp non-oscillatory convection schemes for high-speed steady multidimensional flow. NASA TM 1-2568 (ICOMP-90-12), *NASA Lewis Research Center*.
- Leschziner, M. A. (1990). Modelling engineering flows with Reynolds stress turbulence closure. *J. Wind Eng. Ind. Aerod.*, **vol. 35**, pp. 21-47.
- Leschziner, M. A. and Kobayashi, T. (1988), Second-moment closures for recirculating and strongly swirling flows: Part 2. Applications. *Seisan-Kenkyu*, **vol. 40**, Institute of Industrial Science, University of Tokyo, pp. 261-268.
- Li, X. and Zbicinski, I. (2005). A sensitivity study on CFD modelling of cocurrent spray-drying process. *Drying Technology*, **vol. 23** (8), pp. 1681-1691.
- Lien, F. S. and Leschziner, M. A. (1994). Assessment of turbulence-transport models including non-linear RNG eddy viscosity formulation and second-moment closure for flow over a backward-facing step. *Computers Fluids*, **vol. 23** (8), pp. 983-1004.
- Lin, S. X. Q. and Chen, X. D. (2002). Improving the glass-filament method for accurate measurement of drying kinetics of liquid droplets. *Trans IChemE*, **vol. 80** (A), pp. 401-410.
- Lin, S. X. Q. and Chen, X. D. (2004). Changes in milk droplet diameter during drying under constant drying conditions investigated using the glass-filament method. *Trans IChemE*, **vol. 82** (C), pp. 213-218.
- Lin, S. X. Q. and Chen, X. D. (2006). A Model for Drying of an Aqueous Lactose Droplet Using the Reaction Engineering Approach. *Drying Technology*, **vol. 24** (11), pp. 1329-1334.

- Lin, S. X. Q. and Chen, X. D. (2007). The reaction engineering approach to modelling the cream and whey protein concentrate droplet drying. *Chem. Eng. and Proc.*, **vol. 46**, pp. 437-443.
- Lin, J. C. and Gentry, J. W. (2003). Spray Drying Drop Morphology: Experimental Study. *Aerosol Sci. Tech.*, **vol. 37**, pp. 15-32.
- Livesley, D. M., Oakley, D. E., Gillespie, R. F., Ranpuria, C. K., Taylor, T., Wood, W. and Yeoman, M. L. (1992). *Development and validation of a computational model for spray-gas mixing in spray dryers*. Drying '92, Ed. Mujumdar, A. S., pp. 407-416, New York: Hemisphere Publishing Corp.
- Lu, P. and Semiao, V. (2003). A new Second moment closure approach for turbulent swirling confined flows. *Int. J. Numer. Meth. Fl.*, **vol. 41**, pp. 133-150.
- Lu, Y., Esposito, E. and Ekkad, S.V. (2008). Predictions of Flow and Heat Transfer in Low Emission Combustors. *Heat Trans. Engg.*, **vol. 29** (4), pp. 375-384.
- Malvern. (2013). <http://www.malvern.com/common/downloads/MRK690.pdf>, Accessed: 15-05-2013.
- Manning, W. P. and Gauvin, W. H. (1960). Heat and mass transfer to decelerating finely atomised sprays. *AIChE J.*, **vol. 6** (2), pp. 184-190.
- Marshall, W. R. and Seltzer, E. (1950a). Principles of spray drying: Part I – Fundamentals of spray-dryer operation. *Chem. Eng. Prog.*, **vol. 46**, pp. 501-508.
- Marshall, W. R. and Seltzer, E. (1950b). Principles of spray drying: Part II – Elements of spray-dryer design. *Chem. Eng. Prog.*, **vol. 46**, pp. 575-584.
- Martin de Juan, L. (2011). Personal Communication, P&G Newcastle Technical Centres, UK.
- Martin de Juan, L. (2012). Personal Communication, P&G Newcastle Technical Centres, UK.
- Masters, K. (1972). *Spray Drying: An introduction to Principles, Operational Practice and Applications*. London: Leonard Hill Books.
- Masters, K. (1985). *Spray Drying Handbook*. London: Leonard Hill Books.

- Masters, K. (1995). Scale-up of spray dryers. *Drying Technology*, **vol. 12** (1-2), pp. 235-257.
- Masters, K. (1968). Successful application of spray drying is due in part to much improved knowledge and control of drop atomization, spray/air contact, and drop evaporation. *Ind. Eng. Chem.*, **vol. 60** (10), pp. 53-63.
- Masters, K. (2004). Current market driven spray drying development activities. *Drying Technology*, **vol. 22** (6), pp. 1351-1370.
- Masters, K. and Masters, S. G. (2006). Hygienic design requirements for spray drying operations. *Drying Technology*, **vol. 24**, pp. 685-693.
- Masuda, H. and Matsusaka, S. Particle deposition and reentrainment. In *Powder Technology Handbook*, 2<sup>nd</sup> ed. Gotoh, K., Masuda, H., Higashitani, K. Eds. Marcel Dekker, New York, NY, 143, 1997.
- MATLAB v. 7.10. The MathWorks Inc., 2010.
- Menter, F. R. (1994). Two-equation eddy-viscosity turbulence models for engineering applications. *AIAA J.*, **vol. 32** (8), pp. 1598-1605.
- Mezhericher, M., Levy, A. and Borde, I. (2007). Theoretical Drying Model of Single Droplets Containing Insoluble or Dissolved Solids. *Drying Technology*, **vol. 25**, pp. 1035-1042.
- Mezhericher, M., Levy, A. and Borde, I. (2008a). Heat and mass transfer of single droplet/wet particle drying. *Chem. Eng. Sci.*, **vol. 63**, pp. 12-23.
- Mezhericher, M., Levy, A. and Borde, I. (2008b). Droplet-Droplet Interactions in Spray Drying by Using 2D Computational Fluid Dynamics. *Drying Technology*, **vol. 26**, pp. 265- 282.
- Mezhericher, M., Levy, A. and Borde, I. (2009). Modeling of Droplet Drying in Spray Chambers Using 2D and 3D Computational Fluid Dynamics. *Drying Technology*, **vol. 27**, pp. 359-370.
- Mezhericher, M., Levy, A. and Borde, I. (2010a). Spray drying modelling based on advanced droplet drying kinetics. *Chem. Eng. Proc.*, **vol. 49**, pp. 1205–1213.

- Mezhericher, M., Levy, A. and Borde, I. (2010b). Theoretical Models of Single Droplet Drying Kinetics: A Review. *Drying Technology*, **vol. 28**, pp. 278-293.
- Mezhericher, M., Levy, A. and Borde, I. (2012a). Probabilistic hard-sphere model of binary particle-particle interactions in multiphase flow of spray dryers. *Int. J. Multiphas. Flow*, **vol. 43**, pp. 22-38.
- Mezhericher, M., Levy, A. and Borde, I. (2012b). Three-dimensional spray drying model based on comprehensive formulation of drying kinetics. *Drying Technology*, **vol. 30**, pp. 1256-1273.
- Micromeritics. (2013). <http://www.micromeritics.com/pressroom/press-release-list/geopyc-1360-press-release.aspx>, Accessed: 10-05-2013.
- Montazer-Rahmati, M. M. and Ghafele-Bashi, S. H. (2007). Improved Differential Modeling and Performance Simulation of Slurry Spray Dryers as Verified by Industrial Data. *Drying Technology*, **vol. 25** (9), pp. 1451-1462.
- Morsi, S. A. and Alexander, A. J. (1972). An investigation of particle trajectories in two-phase flow systems. *J. Fluid Mech.*, **vol. 55** (2), pp. 193-208.
- Mujumdar, A.S. (1987). *Handbook of Industrial Drying*. New York: Marcel Dekker
- Nath, S. and Satpathy, G. R. (1998). A systematic approach for investigation of spray drying processes. *Drying Technology*, **vol. 16** (6), pp. 1173-1193.
- Nelson, P. A. and Stevens, W. F. (1961). Size distribution of droplets from centrifugal spray nozzles. *AICHE J.*, **vol. 7**(1), pp. 80-86.
- Nešić, S. and Vodnik, J. (1991). Kinetics of droplet evaporation. *Chem. Eng. Sci.*, **vol. 46**, pp. 527-537.
- NIIR (2013). *Handbook on soaps, detergents and acid slurry*. Asia Pacific, 3<sup>rd</sup> Edn.
- Nijdam, J. J., Guo, B., Fletcher, D. F. and Langrish, T. A. G. (2003). Lagrangian and Eulerian models for simulating turbulent dispersion and agglomeration for droplets within a spray. *Third international conference on CFD in minerals and process industries*, pp. 377-382.
- Nikjooy, M. and Mongia, H. C. (1991). A second-order modelling study of confined swirling flow. *Int. J. Heat and Fluid Flow*, **vol. 12**, No. 1, pp. 12-19.

- Norton, T. and Sun, D. W. (2006). Computational Fluid Dynamics (CFD) – an effective and efficient design and analysis tool for the food industry: A review. *Trends Food Sci. Tech.*, **vol. 17**, pp. 600-620.
- Nuttal, J. B. (1953). Axial flow in a vortex. *Nature*, **vol. 172**, pp. 528-583.
- Oakley, D. E. (1994). Scale-up of spray dryers with the aid of computational fluid dynamics. *Drying Technology*, **vol. 12** (1-2), pp. 217-233.
- Oakley, D. E. (1997). Produce uniform particles by spray drying. *Chem. Eng. Prog.*, **vol. 93**, no. 10, pp. 48-54.
- Oakley, D. E. (2004). Spray Dryer Modeling in Theory and Practice. *Drying Technology*, **vol. 22** (6), pp. 1371-1402.
- Oakley, D. E. and Bahu, R. E. (1993). Computational modelling of spray dryers. *European symposium on Computer Aided Process Engineering-2*, pp. 493-498.
- Ozmen, L. and Langrish, T.A.G. (2003). An experimental investigation of the wall deposition of milk powder in pilot-scale spray dryer. *Drying Technology*, **vol. 21** (7), pp. 1253-1272.
- Ozmen, L. and Langrish, T.A.G. (2005). An experimental investigation into wall deposition of milk powder in spray dryers. *Developments in Chemical Engineering and Minerals Processing*, **vol. 13**(1-2), pp. 91-108.
- Papageorgakis, G. C. and Assanis, D. N. (1999). Comparison of linear and nonlinear RNG-based k-epsilon models for incompressible turbulent flows. *Numerical Heat Transfer, Part B: Fundamentals: An International Journal of Computation and Methodology*, **vol. 35** (1), pp. 1-22.
- Paris, J.R., Ross, P.N., Dastur, S.P. and Morris, R.L. (1971). Modeling of the Air Flow pattern in a Countercurrent Spray-Drying Tower. *Ind. Eng. Process Des. Develop.*, **vol. 10**, pp. 157-164.
- Parti, M. and Palancz, B. (1974). Mathematical model for spray drying. *Chem. Eng. Sci.*, **vol. 29**, pp. 355-362.
- Patankar, S.V. (1980). *Numerical heat transfer and fluid flow*. Hemisphere, Washington.

- Patel, K. C. and Chen, X. D. (2005). Prediction of spray-dried product quality using two simple drying kinetics models. *J. Food Process Eng.*, **vol. 28**, pp. 567-594.
- Patel, R. P., Patel, M. P. and Suthar, A. M. (2009). Spray drying technology: an overview. *Indian J. Sci. Technol.*, **vol. 2**, pp. 44-47.
- Perry, R.H. and Green, D.W. (1997). *Perry's Chemical Engineer's Handbook*. New York, McGraw-Hill, Seventh Edn.
- Pettyjohn, E. S. and Christiansen, E. B. (1948). Effect of particle shape on free-settling rates of isometric particles. *Chem. Eng. Prog.*, **vol. 44**, pp. 157-172.
- Peyret, R. (1996). *Handbook of computational fluid mechanics*. Elsevier Sci. and Tech.
- Piatowski, M. and Zbicinski, I. (2007). Analysis of the mechanism of counter-current spray drying. *Transp. Porous Med.*, **vol. 66**, pp. 89-101.
- Pinto, M., Kemp, I, Bermingham, S., Hartwig, T. and Bisten, A. (2014). Development of an axisymmetric population balance model for spray drying and validation against experimental data and CFD simulations. *Chem. Eng. Res. Des.*, In Press, Available Online December 2013, <http://dx.doi.org/10.1016/j.cherd.2013.12.019>
- Place, G., Ridgway, K. and Danckwerts, P. V. (1959). Investigation of air-flow in a spray-drier by tracer and model techniques. *Trans IChemE*, **vol. 37**, pp. 268-276.
- Putranto, A. and Chen, X. D. (2012). Roasting of barley and coffee modeled using the lumped-reaction engineering approach (L-REA). *Drying Technology*, **vol. 30**, pp. 475-483.
- Rahse, W. and Dicoi, O. (2001). Spray drying in the detergent industry. In: *Proceedings of Spray Drying Conference '01*. Dortmund, Germany.
- Ranz, W. E. and Marshall, W. R. (1952). Evaporation from drops. *Chem. Eng. Prog.*, **vol. 48**, pp. 141-146; 173-180.
- Razgaitis, R. and Holman, J. P. (1976). A survey of heat transfer in confined swirling flows. Future energy production systems: *Heat and mass transfer processes*, **vol. 2**, Hemisphere Publishing Corp., pp. 831-866.

- Reay, D. (1988). Fluid flow, residence time simulation and energy efficiency in industrial dryers. *Proceedings of the sixth international drying symposium IDS*, France, pp. KL. 1 – KL. 8.
- Rosin, P. and Rammler, E. (1933). The Laws Governing the Fineness of Powdered Coal. *Journal of the Institute of Fuel*, **vol. 7**, pp. 29-36.
- Rudolf, P., Hudec, M., Zubik, P. and Štefan, D. (2012). Experimental measurement and numerical modelling of cavitating flow in converging-diverging nozzle. *EPJ Web of conferences*, **vol. 25**, DOI: 10.1051/epjconf/20122501081.
- Sadripour, M., Rahimi, A. and Hatamipour, M. S. (2012). Experimental study and CFD modeling of wall deposition in a spray dryer. *Drying Technology*, **vol. 30** (6), pp. 574-582.
- Saleh, S. N. (2010). CFD simulations of a co-current spray dryer. *WASET*, **vol. 62**, pp. 772-777.
- Sano, Y. and Keey, R. B. (1982). The drying of a spherical particle containing colloidal material into a hollow sphere. *Chem. Eng. Sci.*, **vol. 37**, pp. 881-889.
- Schlichting, H., 1979. *Boundary Layer Theory*, McGraw Hill, Seventh edn., London.
- Shamami, K. K. and Birouk, M. (2008). Assessment of the Performances of RANS Models for simulating swirling flows in a can-combustor. *The Open Aerospace Engg J.*, **vol. 1**, pp. 8-27.
- Sharma, S. (1990). Spray dryer simulation and air flow pattern studies, Ph.D. Thesis, *The University of Aston*, Birmingham, UK.
- Shih, T. H., Liou, W. W., Shabbir, A., Yang, Z. and Zhu. J. (1995). A new  $k-\epsilon$  model eddy-viscosity model for high Reynolds number turbulent flows. *Comput. Fluids*, **vol. 24** (3), pp. 227-238.
- Shoukry, E. and Shemllt, L. W. (1985). Mass Transfer Enhancement in Swirling Annular Pipe Flow. *Ind. Eng. Chem. Proc. D. D.*, **vol. 24**, pp. 53-56.
- Sommerfeld, M. (1992). Modelling of particle-wall collisions in confined gas-particle flows. *Int. J. Multiphas. Flow*, **vol. 18** (6), pp. 905-926.

- Sommerfeld, M. (2001). Validation of a stochastic Lagrangian modeling approach for inter-particle collisions in homogeneous isotropic turbulence. *Int. J. Multiphas. Flow*, **vol. 27**, pp.1829-1858.
- Sommerfeld, M. and Huber, N. (1999). Experimental analysis and modelling of particle-wall collisions. *Int. J. Multiphas. Flow*, **vol. 25**, pp. 1457-1489.
- Southwell, D. B. and Langrish, T. A. G. (2001). The effect of swirl on flow stability in spray dryers. *Trans IChemE*, **vol. 79** (A), pp. 222-234.
- Southwell, D. B., Langrish, T. A. G. and Fletcher, D. F. (1999). Process intensification in spray dryers by turbulence enhancement. *Trans IChemE*, **vol. 77**, Part A, pp. 189-205.
- Spalding, D. B. (1953). Burning of fuel droplets. *Fourth International Symposium on combustion*, pp. 847-864.
- Speziale, C. G., Sarkar, S. and Gatski, T. B. (1991). Modelling the pressure-strain correlation of turbulence: an invariant dynamical systems approach. *J. Fluid Mech.*, **vol. 227**, pp. 245-272.
- Straatsma, J., Houwelingen, G. V., Steenbergen, A. E. and Jong, P. D. (1999). Spray drying of food products: 1. Simulation model. *J. Food Engng.*, **vol. 42**, pp. 67-72.
- Sunkel, J. M. and King, C. J. (1993). Influence of the development of particle morphology upon rates of loss of volatile solutes during drying of drops. *Ind. Eng. Chem. Res.*, **vol. 32**, pp. 2357-2364.
- Talbi, K., Nemouchi, Z., Donnot, A. and Belghar, N. (2011). An experimental study and a numerical simulation of the turbulent flow under the vortex finder of a cyclone separator. *J. App. Fluid Mech.*, **vol. 4**, no. 1, pp. 69-75.
- Topar, J. (1980). Mathematical model of spray drying reckoning with droplet size distribution. *Drying'80: Proceedings of the second international drying symposium*, **vol. 2**, pp. 405-409.
- Trommelen, A. M. and Crosby, E. J. (1970). Evaporation and Drying of drops in superheated vapours. *AIChE J.*, **vol. 16** (5), pp. 857-867.
- Vehring, R. (2008). Pharmaceutical particle engineering via spray drying. *Pharmaceut. Res.*, **vol. 25** (5), pp. 999-1022.

- Verdurmen, R. E. M., Menn, P., Ritzert, J., Blei, S., Nhumaio, G. C. S., Sonne Sørensen, T., Gunsing, M., Straatsma, J., Verschueren, M., Sibeijn, M., Schulte, G., Fritsching, U., Bauckhage, K., Tropea, C., Sommerfeld, M., Watkins, P., Yule, A. J., and Schønfeldt, H. (2004). Simulation of Agglomeration in Spray Drying Installations: The EDECAD Project. *Drying Technology*, **vol. 22** (6), pp. 1403-1461.
- Versteeg, H. K. and Malalasekera, W. (1995). *An Introduction to Computational Fluid Dynamics*. Longman Scientific and Technical, Harlow.
- Vicente, J., Pinto, J., Menezes, J. and Gaspar, F. (2013). Fundamental analysis of particle formation in spray drying. *Powder Technology*, **vol. 247**, pp. 1-7.
- Viegas, J. R., Rubesin, M. W. and Hortsman, C. C. (1985). On the use of wall functions as boundary conditions for two-dimensional separated compressible flows. *Technical Report AIAA-85-0180*, AIAA, 23rd Aerospace Sciences Meeting, Reno, Nevada.
- Wadell, H. (1934). The coefficient of resistance as a function of Reynolds number for solids of various shapes. *J. Franklin Institute*, **vol. 217** (4), pp. 459-490.
- Walton, D. E. (2000). The morphology of spray dried particles: A qualitative view. *Drying Technology*, **vol. 18** (9), pp. 1943-1986.
- Walton, D. E. and Mumford, C. J. (1999a). Spray Dried Products – Characterization of particle morphology. *Trans IChemE*, **vol. 77** (A), pp. 21-38.
- Walton, D. E. and Mumford, C. J. (1999b). The morphology of spray-dried particles: The effect of process variables upon morphology of spray-dried particles. *Trans IChemE*, **vol. 77** (A), pp. 442-460.
- Wawrzyniak, P., Podyma, M., Zbicinski, I., Bartczak, Z. and Rabaeva, J. (2012a). Modeling of Air Flow in an Industrial Countercurrent Spray-Drying Tower. *Drying Technology*, **vol. 30**, pp. 217-224.
- Wawrzyniak, P., Podyma, M., Zbicinski, I., Bartczak, Z., Polanczyk, A. and Rabaeva, J. (2012b). Model of heat and mass transfer in an industrial counter-current spray-drying tower. *Drying Technology*, **vol. 30**, pp. 1274-1282.

- Williams, A. (1976). Fundamentals of oil combustion. *Prog. Energy Combust. Sci.*, **vol. 2**, pp. 167-179.
- Woo, M. W., Che, L. M., Daud, W. R. W., Mujumdar, A. S. and Chen, X. D. (2012). Highly swirling transient flows in spray dryers and consequent effect on modelling of particle deposition. *Chem. Eng. Res. Des.*, **vol. 90**, pp. 336-345.
- Woo, M. W., Daud, W. R. W., Mujumdar, A. S., Talib, M. Z. M., Hua, W. Z. and Tasirin, S. M. (2008a). Comparative study of droplet drying models for CFD modelling. *Chem. Eng. Res. Des.*, **vol. 86**, pp. 1038-1048.
- Woo, M. W., Daud, W. R. W., Tasirin, S. M. and Talib, M. Z. M. (2008b). Effect of wall surface properties at different drying kinetics on the deposition problem in spray drying. *Drying Technology*, **vol. 26**, pp. 15-26.
- Xia, J. L., Yadigaroglu, G., Liu, Y. S., Schmidli, J. and Smith, B. L. (1998). Numerical and experimental study of swirling flow in a model combustor. *Int. J. Heat Mass Tran.*, **vol. 41**, no. 11, pp. 1485-1497.
- Xin, H. L. and Mujumdar, A.S. (2009). *Spray drying and its application in food processing*. In: *Innovation in food engineering*. pp. 303-329, CRC Press.
- Yajnik, K.S. and Subbaiah, M.V. (1973). Experiments on swirling turbulent flows. *J. Fluid Mech.*, **vol. 60** (4), pp. 665-687.
- Yamamoto, S. and Sano, Y. (1994). Drying of carbohydrate and protein solutions. *Drying Technology*, **vol. 12** (5), pp. 1069-1080.
- Yaras, M. I. and Grosvenor, A.D. (2003). Evaluation of one- and two-equation low-Re turbulence models. Part I – Axisymmetric separating and swirling flows. *Int. J. Numer. Meth. Fluids*, **vol. 42**, pp. 1293–1319.
- Younis, B. A., Weigand, B. and Vogler, A. D. (2009). Prediction of momentum and scalar transport in turbulent swirling flows with an objective Reynolds-stress transport closure. *Heat Mass Transfer*, **vol. 45**, pp. 1271–1283.
- Zbicinski, I. (1995). Development and experimental verification of momentum, heat and mass transfer model in spray drying. *The Chem. Eng. J.*, **vol. 58**, pp. 123-133.
- Zbicinski, I and Li, X. (2006). Conditions for accurate CFD modeling of spray-drying process. *Drying Technology*, **vol. 24**, pp. 1109-1114.

- Zbicinski, I. and Piatkowski, M. (2009). Continuous and discrete phase behavior in countercurrent spray drying process. *Drying Technology*, **vol. 27**, pp. 1353-1362.
- Zbicinski, I. and Zietara, R. (2004). CFD model of counter-current spray drying process. *Proceedings of the 14th International Drying Symposium*, 2004, Sao Paulo, 22-25 August, **vol. A**, pp. 169-176.
- Zbicinski, I., Piatkowski, M. and Strumillo, C. (2004). Experimental analysis of the mechanism of counter-current spray drying process. *Proceedings of the 14th International Drying Symposium*, 2004, Sao Paulo, 22-25 August, **vol. A**, pp. 161-168.

**APPENDIX – I**

## Mass and Energy Balance in a Spray Drying Tower

### 1. Overall Mass Balance on an element of unit volume in a Spray Tower

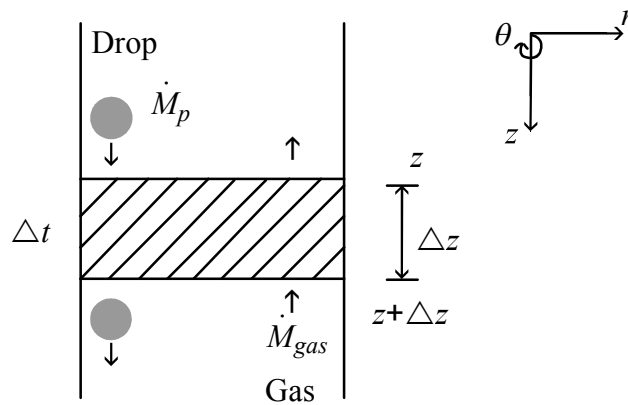


Figure – A1.1.1: Overall mass balance on an element of unit volume in a spray tower.

It is assumed that the mass of solid in the droplet/particle remains constant. The change in total mass of the droplets/particles  $\dot{M}_p$  takes place due to change in mass of the solvent which evaporates into the gas. One dimensional flow of gas and particles is considered. Radial and tangential velocity is assumed to be zero (Figure A1.1.1).

Rate of mass input to the control volume:  $\dot{M}_p|_z \Delta t + \dot{M}_{gas}|_{z+\Delta z} \Delta t$

Rate of mass output from the control volume:  $\dot{M}_p|_{z+\Delta z} \Delta t + \dot{M}_{gas}|_z \Delta t$

By Taylor series:

$$\dot{M}_p|_{z+\Delta z} \cong \dot{M}_p|_z + \Delta z \left. \frac{d\dot{M}_p}{dz} \right|_z + \text{Higher Order Differentials} \quad (\text{A1.1.1})$$

Similarly for the gas, according to Taylor series expansion:

$$\dot{M}_{gas}|_z \cong \dot{M}_{gas}|_{z+\Delta z} - \Delta z \left. \frac{d\dot{M}_{gas}}{dz} \right|_{z+\Delta z} + \text{Higher Order Differentials} \quad (\text{A1.1.2})$$

Accumulation of mass in the control volume is zero, as the process is a steady state process. So, Input = Output

Higher order differentials in equation (A1.1.1) and (A1.1.2) can be neglected. A mass balance on control volume gives:

$$\dot{M}_p|_z \Delta t + \dot{M}_{gas}|_{z+\Delta z} \Delta t = \dot{M}_p|_{z+\Delta z} \Delta t + \Delta z \left. \frac{d\dot{M}_p}{dz} \right|_z \Delta t + \dot{M}_{gas}|_z \Delta t - \Delta z \left. \frac{d\dot{M}_{gas}}{dz} \right|_{z+\Delta z} \Delta t \quad (\text{A1.1.3})$$

Therefore we have:

$$\left. \frac{d\dot{M}_p}{dz} \right|_z - \left. \frac{d\dot{M}_{gas}}{dz} \right|_{z+\Delta z} = 0 \quad (\text{A1.1.4})$$

Let  $\Delta z$  approaches zero, equation (A1.1.4) becomes:

$$\frac{d\dot{M}_p}{dz} - \frac{d\dot{M}_{gas}}{dz} = 0 \quad 0 \leq z \leq H_2 \quad (\text{A1.1.5})$$

Equation (A1.1.5) is the general equation for mass balance over a control volume in a spray tower. Equation (A1.1.5) is applicable to any control volume within the spray tower ranging in the following limits:

$$t \geq 0 \quad \left\{ \begin{array}{l} z = 0 \quad \dot{M}_p \text{ is specified} \\ z = H_1 \quad \dot{M}_{gas,h} \text{ is specified} \\ z = H_2 \quad \dot{M}_{air,c} \text{ is specified} \end{array} \right.$$

## 2. Change in Concentration of a Single Droplet/Particle in a Control Volume

It is assumed that the droplet is perfectly spherical throughout the control volume and mass of solute/solid remains constant in the droplet. The change in concentration of solvent in a single particle is given by following differential equation:

$$\frac{\partial C_{l,p}}{\partial t} = \frac{D}{r^2} \frac{\partial}{\partial r} \left( r^2 \frac{\partial C_{l,p}}{\partial r} \right) \quad (\text{A1.2.1})$$

Following initial and boundary conditions are applicable to equation (A1.2.1)

Initial condition:

$$\text{For } t < 0 \quad C_l = C_{l,p}(r) \quad 0 \leq r \leq r_p \quad (\text{A1.2.2})$$

Boundary Condition:

For  $t \geq 0$

$$\text{At } r=0, \quad \frac{\partial C_{l,p}}{\partial r} = 0 \quad (\text{A1.2.3})$$

$$\text{At } r=r_p, \quad -D \left( \frac{\partial C_{l,p}}{\partial r} \right) = k(C_{l,p} - C_{l,gas}) \quad (\text{A1.2.4})$$

Introducing an average solvent concentration in the particle defined as follows:

$$\tilde{C}_{l,p} = \frac{\int_0^{r_p} 4\pi r^2 C_{l,p} dr}{\int_0^{r_p} 4\pi r^2 dr} \quad (\text{A1.2.5})$$

where  $\tilde{C}_{l,p}$  is the mean concentration of solvent in the particle. Equation (A1.2.5) can be written as:

$$\tilde{C}_{l,p} = \frac{3}{r_p^3} \int_0^{r_p} r^2 C_{l,p} dr \quad (\text{A1.2.6})$$

Equation (A1.2.1) can be integrated with respect to  $r$  as limit  $r$  from 0 to  $r_p$ :

$$\int_0^{r_p} r^2 \frac{\partial C_{l,p}}{\partial t} dr = \int_0^{r_p} D \frac{\partial}{\partial r} \left( r^2 \frac{\partial C_{l,p}}{\partial r} \right) dr \quad (\text{A1.2.7})$$

Rearranging the first term of equation (A1.2.7) to give:

$$\frac{\partial}{\partial t} \int_0^{r_p} r^2 C_{l,p} dr = \int_0^{r_p} D \frac{\partial}{\partial r} \left( r^2 \frac{\partial C_{l,p}}{\partial r} \right) dr \quad (\text{A1.2.8})$$

Putting equation (A1.2.6) in equation (A1.2.8) and integrating the term on the r.h.s of the equation results in the following:

$$\frac{r_p^3}{3} \frac{\partial \tilde{C}_{l,p}}{\partial t} = D \left[ r_p^2 \frac{\partial C_{l,p}}{\partial r} \Big|_{r_p} - r^2 \frac{\partial C_{l,p}}{\partial r} \Big|_0 \right] \quad (\text{A1.2.9})$$

Insertion of boundary conditions equation (A1.2.3) and (A1.2.4) into equation (A1.2.9) results in the following equation:

$$\frac{\partial \tilde{C}_{l,p}}{\partial t} = -\frac{3k_c}{r_p} \left( C_{l,p} \Big|_{r_p} - C_{l,gas} \right) \quad (\text{A1.2.10})$$

Mass of the droplet/particle is given as:

$$M_p = M_{solvent} + M_{solute} \quad (\text{A1.2.11})$$

where  $M_{solute}$  remains constant. Differentiating equation (A1.2.11) with respect to time:

$$\frac{dM_p}{dt} = \frac{dM_{solvent}}{dt} \quad (\text{A1.2.12})$$

Concentration of solvent in a particle is given by:

$$\tilde{C}_{l,p} = \frac{M_{solvent}}{V_{particle}} \quad (\text{A1.2.13})$$

where  $V_{particle}$  is the volume of particle given by:

$$V_{particle} = \frac{4\pi r_p^3}{3} \quad (\text{A1.2.14})$$

Equation (A1.2.14) can be put into equation (A1.2.13) to give:

$$\tilde{C}_{l,p} = \frac{3M_{solvent}}{4\pi r_p^3} \quad (\text{A1.2.15})$$

Equation (A1.2.15) can be differentiated with respect to time ( $t$ ) to give:

$$\frac{d\tilde{C}_{l,p}}{dt} = \frac{3}{4\pi r_p^3} \frac{dM_{solvent}}{dt} \quad (\text{A1.2.16})$$

Equation (A1.2.16) can be put into equation (A1.2.10) to give:

$$\frac{dM_p}{dt} = -4\pi r_p^2 k_c \left( C_{l,p} \Big|_{r_p} - C_{l,gas} \right) \quad (\text{A1.2.17})$$

Equation (A1.2.17) gives change in mass of the particle in the first stage of drying process. Equation (A1.2.17) can be written in terms of particle residence time as:

$$\frac{dM_p}{dz} = \frac{-4\pi r_p^2 k_c}{\tilde{u}_p} \left( C_{l,p} \Big|_{r_p} - C_{l,gas} \right) \quad (\text{A1.2.18})$$

Equation (A1.2.18) is the general equation for change in mass of the particle in a control volume due to evaporation of solvent from the surface of the particle. From equation (A1.1.5) in section 1, we have:

$$\frac{d\dot{M}_p}{dz} = \frac{d\dot{M}_{gas}}{dz} \quad (\text{A1.2.19})$$

where  $\dot{M}_p$  and  $\dot{M}_{gas}$  are the total change in mass of the droplet/particle and the gas in a control volume respectively. Hence for total change in mass of the gas in a control volume, equation (A1.2.18) can be written as:

$$\frac{d\dot{M}_{gas}}{dz} = \frac{-n4\pi r_p^2 k_c}{\tilde{u}_p} \left( C_{l,p} \Big|_{r_p} - C_{l,gas} \right) \quad (\text{A1.2.20})$$

where  $n$  is the total number of droplets/particles in a control volume.

### 3. Overall Energy Balance on an Element of Unit Volume in a Spray Tower

Overall energy balance can be carried out by assuming the control volume to be adiabatic. It is also assumed that the gas is perfectly mixed over the cross section, but there is no longitudinal mixing.

Rate of energy input to the control volume:  $\dot{M}_p h_p \Big|_z \Delta t + \dot{M}_{gas} h_g \Big|_{z+\Delta z} \Delta t$

Rate of energy output from the control volume:  $\dot{M}_p h_p \Big|_{z+\Delta z} \Delta t + \dot{M}_{gas} h_g \Big|_z \Delta t$

By Taylor series:

$$\dot{M}_p h_p \Big|_{z+\Delta z} \cong \dot{M}_p h_p \Big|_z + \Delta z \frac{d(\dot{M}_p h_p)}{dz} \Big|_z + \text{Higher Order Differentials}$$

Similarly for the gas, according to Taylor series expansion:

$$\dot{M}_{gas} h_g \Big|_z \cong \dot{M}_{gas} h_g \Big|_{z+\Delta z} - \Delta z \frac{d(\dot{M}_{gas} h_g)}{dz} \Big|_{z+\Delta z} + \text{Higher Order Differentials}$$

Input = Output

$$\begin{aligned} \dot{M}_p h_p \Big|_z \Delta t + \dot{M}_{gas} h_g \Big|_{z+\Delta z} \Delta t = \\ \dot{M}_p h_p \Big|_z \Delta t + \Delta z \frac{d(\dot{M}_p h_p)}{dz} \Big|_z \Delta t + \dot{M}_{gas} h_g \Big|_{z+\Delta z} \Delta t - \Delta z \frac{d(\dot{M}_{gas} h_g)}{dz} \Big|_{z+\Delta z} \Delta t \end{aligned} \quad (\text{A1.3.1})$$

Equation (A1.3.1) can be written as:

$$\frac{d(\dot{M}_p h_p)}{dz} \Big|_z - \frac{d(\dot{M}_{gas} h_g)}{dz} \Big|_{z+\Delta z} = 0 \quad 0 \leq z \leq H_2 \quad (\text{A1.3.2})$$

Equation (A1.3.2) is the general equation for overall energy balance on the control volume in a spray tower.

#### 4. Energy Balance on a Single Droplet/Particle

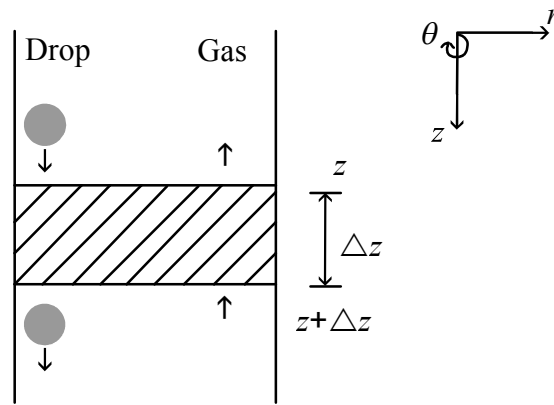


Figure – A1.4.1: Energy balance on a single droplet/particle.

Enthalpy balance about the droplet/particle can be carried out by assuming the temperature of the droplet/particle to remain uniform at any given location  $z$  and assuming the control volume to be adiabatic. It is also assumed that the gas is perfectly mixed along the cross section, but there is no longitudinal mixing. Droplet collision with the walls and with other droplets is also neglected and one dimensional flow of the droplets/particles and the gas is assumed (Figure A1.4.1).

$$M_p h_p \Big|_{z+\Delta z} - M_p h_p \Big|_z = \dot{Q}_{in} \frac{\Delta z}{\tilde{u}_p} \quad (\text{A1.4.1})$$

where  $M_p$  is the mass,  $H_p$  is the enthalpy and  $\tilde{u}_p$  is the average velocity of droplet/particle respectively.  $\dot{Q}_{in}$  is the rate of heat transfer from the gas to a single droplet/particle.

Equation (A1.4.1) is divided by  $\Delta z$  and multiplied by  $\tilde{u}_p$  to give the following:

$$\left( \frac{M_p h_p \Big|_{z+\Delta z} - M_p h_p \Big|_z}{\Delta z} \right) \tilde{u}_p = \dot{Q}_{in} \quad (\text{A1.4.2})$$

The heat flow into the droplet is as follows:

$$\dot{Q}_{in} = \alpha_p A_p (T_{gas} - T_p \Big|_z) \quad (\text{A1.4.3})$$

where  $T_{gas}$  is the temperature of gas,  $A_p$  and  $T_p$  are the area and temperature of the droplet/particle respectively.

Hence combination of equations (A1.4.2) and (A1.4.3) results in the following relationship:

$$\left( \frac{M_p h_p|_{z+\Delta z} - M_p h_p|_z}{\Delta z} \right) \tilde{u}_p = \alpha_p A_p|_z (T_{gas}|_z - T_p|_z) \quad (\text{A1.4.4})$$

In equation (A1.4.4) limit can be taken as  $\Delta z$  approaches zero:

$$\lim_{\Delta z \rightarrow 0} \left( \frac{M_p h_p|_{z+\Delta z} - M_p h_p|_z}{\Delta z} \right) \tilde{u}_p = \alpha_p A_p|_z (T_{gas}|_z - T_p|_z) \quad (\text{A1.4.5})$$

$$\tilde{u}_p \frac{d(M_p h_p)}{dz} = \alpha A_p (T_{gas} - T_p) \quad (\text{A1.4.6})$$

$$\tilde{u}_p h_p \frac{dM_p}{dz} + \tilde{u}_p M_p \frac{dh_p}{dz} = \alpha_p A_p (T_{gas} - T_p) \quad (\text{A1.4.7})$$

$$dh_p = d(c_{p,drop} T_p) \quad (\text{A1.4.8})$$

Putting equation (A1.4.8) in (A1.4.7):

$$\tilde{u}_p h_p \frac{dM_p}{dz} + \tilde{u}_p M_p \frac{d(c_{p,drop} T_p)}{dz} = \alpha_p A_p (T_{gas} - T_p) \quad (\text{A1.4.9})$$

Equation (A1.4.9) is the general equation for calculating temperature at any location along  $z$ .

Assuming  $c_{p,drop}$  to remain constant, equation (A1.4.9) can be written as:

$$\tilde{u}_p M_p c_{p,drop} \frac{dT_p}{dz} = \alpha_p A_p (T_{gas} - T_p) - \tilde{u}_p h_p \frac{dM_p}{dz} \quad (\text{A1.4.10})$$

Equation (A1.4.10) is the final equation for temperature of droplet at any location along  $z$  with constant  $c_p$ .

## 5. Energy Balance on the Gas Phase

$$\dot{M}_{gas} h_g \Big|_{z+\Delta z} - \dot{M}_{gas} h_g \Big|_z = \dot{Q}_{out} \frac{\Delta z}{\tilde{u}_p} n \quad (A1.5.1)$$

where  $n$  is the number of particles in a control volume,  $\dot{M}_{gas}$ ,  $h_g$  and  $h_{vap}$  is the mass flow rate, enthalpy of the gas and enthalpy of vapours respectively.  $\dot{Q}_{out}$  is the amount of heat transferred by the gas to a single droplet and to the evaporated vapours.

$$\dot{Q}_{out} = -\dot{Q}_{in} = \alpha_p A_p \Big|_z (T_p \Big|_z - T_{gas} \Big|_z) - h_{vap} \left( \frac{dm_l}{dt} \Big|_z \right) \quad (A1.5.2)$$

Equation (A1.5.2) can be put into (A1.5.1) and dividing by  $\frac{\tilde{u}_p}{\Delta z}$  to give:

$$\left( \frac{\dot{M}_{gas} h_g \Big|_{z+\Delta z} - \dot{M}_{gas} h_g \Big|_z}{\Delta z} \right) \tilde{u}_p = n \alpha_p A_p \Big|_z (T_p \Big|_z - T_{gas} \Big|_z) - n h_{vap} \left( \frac{dm_l}{dt} \Big|_z \right) \quad (A1.5.3)$$

In equation (A1.5.3) limit can be taken as  $\Delta z$  approaches zero:

$$\lim_{\Delta z \rightarrow 0} \left( \frac{\dot{M}_{gas} h_g \Big|_{z+\Delta z} - \dot{M}_{gas} h_g \Big|_z}{\Delta z} \right) \tilde{u}_p = n \alpha_p A_p \Big|_z (T_p \Big|_z - T_{gas} \Big|_z) - n h_{vap} \left( \frac{dm_l}{dt} \Big|_z \right) \quad (A1.5.4)$$

$$\tilde{u}_p \frac{d(\dot{M}_{gas} h_g)}{dz} = n \alpha_p A_p (T_p - T_{gas}) - n h_{vap} \left( \frac{dm_l}{dt} \right) \quad (A1.5.5)$$

$$\tilde{u}_p h_g \frac{d\dot{M}_{gas}}{dz} + \tilde{u}_p \dot{M}_{gas} \frac{dh_g}{dz} = n \alpha_p A_p (T_p - T_{gas}) - n h_{vap} \left( \frac{dm_l}{dt} \right) \quad (A1.5.6)$$

$$dh_g = d(c_{p,gas} T_{gas}) \quad (A1.5.7)$$

Putting (A1.5.7) in (A1.5.6):

$$\tilde{u}_p h_g \frac{d\dot{M}_{gas}}{dz} + \tilde{u}_p \dot{M}_{gas} \frac{d(c_{p,gas} T_{gas})}{dz} = n \alpha_p A_p (T_p - T_{gas}) - n h_{vap} \left( \frac{dm_l}{dt} \right) \quad (A1.5.8)$$

The change in gas mass flow is given by equation (A1.5.9) and is due to the evaporation of vapours from the droplets/particles:

$$\frac{d\dot{M}_{gas}}{dz} = -n \frac{1}{\tilde{u}_p} \left( \frac{dm_l}{dt} \right) \quad (A1.5.9)$$

$$-nh_g \left( \frac{dm_l}{dt} \right) + \tilde{u}_p \dot{M}_{gas} \frac{d(c_{p,gas} T_{gas})}{dz} = n\alpha_p A_p (T_p - T_{gas}) - nh_{vap} \left( \frac{dm_l}{dt} \right) \quad (\text{A1.5.10})$$

Rearranging the above equation:

$$\tilde{u}_p \dot{M}_{gas} \frac{d(c_{p,gas} T_{gas})}{dz} = n\alpha_p A_p (T_p - T_{gas}) - nh_{vap} \left( \frac{dm_l}{dt} \right) + nh_g \left( \frac{dm_l}{dt} \right) \quad (\text{A1.5.11})$$

$$\tilde{u}_p \dot{M}_{gas} \frac{d(c_{p,gas} T_{gas})}{dz} = n\alpha_p A_p (T_p - T_{gas}) - n \left( \frac{dm_l}{dt} \right) (h_{vap} - h_g) \quad (\text{A1.5.12})$$

Assuming specific heat of the gas to be same as that of the evaporated vapours, we get:

$$\tilde{u}_p \dot{M}_{gas} \frac{d(c_{p,gas} T_{gas})}{dz} = n\alpha_p A_p (T_p - T_{gas}) - n c_{p,vap} (T_p - T_g) \left( \frac{dm_l}{dt} \right) \quad (\text{A1.5.13})$$

Equation (A1.5.13) is the general equation for the calculation of gas temperature profile along the height of column.

## 6. Change in a Single Droplet/Particle Temperature

It is assumed that the droplet/particle is perfectly spherical throughout the control volume. The change in temperature of a single droplet is given by the following differential equation:

$$\rho_p \tilde{c}_p \frac{\partial T_p}{\partial t} = \frac{\lambda_p}{r^2} \left( \frac{\partial}{\partial r} \left( r^2 \frac{\partial T}{\partial r} \right) \right) \quad (\text{A1.6.1})$$

Equation (A1.6.1) can be written as:

$$r^2 \rho_p \tilde{c}_p \left( \frac{\partial T_p}{\partial t} \right) = \lambda_p \left( \frac{\partial}{\partial r} \left( r^2 \frac{\partial T}{\partial r} \right) \right) \quad (\text{A1.6.2})$$

Following initial and boundary conditions are applicable to equation (A1.6.2);

Initial condition:

$$\text{For } t < 0 \quad T_p = T_p(r) \quad 0 \leq r \leq r_p \quad (\text{A1.6.3})$$

Boundary Condition:

For  $t \geq 0$

$$\text{At } r=0, \quad \frac{\partial T_p}{\partial r} = 0 \quad (\text{A1.6.4})$$

$$\text{At } r=r_p, \quad -\lambda_p \frac{\partial T_p}{\partial r} = \alpha_p (T_p|_r - T_{gas}) + h_{fg} \times k_c (C_{l,p}|_{r_p} - C_{l,gas}) \quad (\text{A1.6.5})$$

Introducing an average temperature in the particle defined as follows:

$$\tilde{T}_p = \frac{\int_0^{r_p} 4\pi r^2 T_p dr}{\int_0^{r_p} 4\pi r^2 dr} \quad (\text{A1.6.6})$$

where  $\tilde{T}_p$  is the mean temperature of the particle. Equation (A1.6.6) can be written as:

$$\tilde{T}_p = \frac{3}{r_p^3} \int_0^{r_p} r^2 T_p dr \quad (\text{A1.6.7})$$

Equation (A1.6.2) can be integrated with respect to  $r$  as limit  $r$  from 0 to  $r_p$ :

$$\rho_p \tilde{c}_p \int_0^{r_p} r^2 \frac{\partial T_p}{\partial t} dr = \lambda_p \int_0^{r_p} \frac{\partial}{\partial r} \left( r^2 \frac{\partial T_p}{\partial r} \right) dr \quad (\text{A1.6.8})$$

Rearranging the first term of equation (A1.6.8) to give:

$$\rho_p \tilde{c}_p \frac{\partial}{\partial t} \int_0^{r_p} r^2 T_p dr = \lambda_p \int_0^{r_p} \frac{\partial}{\partial r} \left( r^2 \frac{\partial T_p}{\partial r} \right) dr \quad (\text{A1.6.9})$$

Putting equation (A1.6.7) in equation (A1.6.9) and integrating the term on r.h.s of the equation results in the following:

$$\rho_p \tilde{c}_p \frac{r_p^3}{3} \frac{\partial \tilde{T}_p}{\partial t} = \lambda_p \left[ r_p^2 \frac{\partial T_p}{\partial r} \Big|_{r_p} - r^2 \frac{\partial T_p}{\partial r} \Big|_0 \right] \quad (\text{A1.6.10})$$

Insertion of boundary conditions equation (A1.6.4) and (A1.6.5) into equation (A1.6.10) results in the following equation:

$$\rho_p \tilde{c}_p \frac{r_p^3}{3} \frac{d\tilde{T}_p}{dt} = -r_p^2 \alpha_p \left( T_p \Big|_{r_p} - T_{gas} \right) - r_p^2 h_{fg} \left( k_c \left( C_{l,p} \Big|_{r_p} - C_{l,gas} \right) \right) \quad (\text{A1.6.11})$$

Equation (A1.6.11) can be written as:

$$\tilde{c}_p \frac{d\tilde{T}_p}{dt} = -\frac{3\alpha_p}{\rho_p r_p} \left( T_p \Big|_{r_p} - T_{gas} \right) - \frac{3h_{fg}}{\rho_p r_p} \left( k_c \left( C_{l,p} \Big|_{r_p} - C_{l,gas} \right) \right) \quad (\text{A1.6.12})$$

Density of the particle is given by:

$$\rho_p = \frac{M_p}{V_{particle}} \quad (\text{A1.6.13})$$

where  $V_{particle}$  is the volume of a single particle given by following equation:

$$V_{particle} = \frac{4\pi r_p^3}{3} \quad (\text{A6.14})$$

Equation (A1.6.14) can be put into equation (A1.6.12) to give:

$$M_p \tilde{c}_p \frac{d\tilde{T}_p}{dt} = -4\pi r_p^2 \alpha_p \left( T_p \Big|_{r_p} - T_{gas} \right) - 4\pi r_p^2 h_{fg} \left( C_{l,p} \Big|_{r_p} - C_{l,gas} \right) \quad (\text{A1.6.15})$$

Equation (A1.6.15) gives change in temperature of the particle in the first stage of drying process. Equation (A1.6.15) can be written in terms of particle residence time as:

$$M_p \tilde{c}_p \frac{d\tilde{T}_p}{dz} = \frac{-4\pi r_p^2 \alpha_p}{\tilde{u}_p} \left( T_p|_{r_p} - T_{gas} \right) - \frac{4\pi r_p^2 h_{fg}}{\tilde{u}_p} \left( C_{l,p}|_{r_p} - C_{l,gas} \right) \quad (\text{A1.6.16})$$

Equation (A1.6.16) is the general equation for change in temperature of the particle in a control volume.

However, the average and surface temperatures are not known in equation (A1.6.16) and so it is assumed that they are equal for this version of the model. Hence equation (A1.6.16) becomes:

$$M_p \tilde{c}_p \frac{d\tilde{T}_p}{dz} = \frac{-4\pi r_p^2 \alpha_p}{\tilde{u}_p} (\tilde{T}_p - T_{gas}) - \frac{4\pi r_p^2 h_{fg}}{\tilde{u}_p} (C_{l,p}|_{r_p} - C_{l,gas}) \quad (\text{A1.6.17})$$

## 7. Momentum Balance on a Single Droplet/Particle

For momentum balance on a single droplet/particle, the forces that are considered include the gravitational force, the buoyancy force and the drag force (Figure A1.7.1).

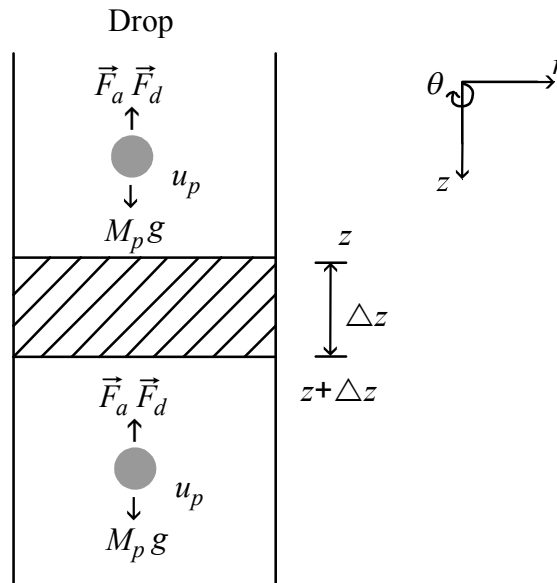


Figure – A1.7.1: Momentum balance on a single droplet/particle.

$$M_p \tilde{u}_p u_p \Big|_{z+\Delta z} - M_p \tilde{u}_p u_p \Big|_z = M_p g \Delta z + \vec{F}_a \Delta z + \vec{F}_d \Delta z \quad (\text{A1.7.1})$$

Equation (A1.7.1) can be divided by  $\Delta z$  to give:

$$\frac{M_p \tilde{u}_p u_p \Big|_{z+\Delta z} - M_p \tilde{u}_p u_p \Big|_z}{\Delta z} = M_p g + \vec{F}_a + \vec{F}_d \quad (\text{A1.7.2})$$

In equation (A1.7.2), limit can be taken as  $\Delta z$  approaches zero:

$$\lim_{\Delta z \rightarrow 0} \left( \frac{M_p \tilde{u}_p u_p \Big|_{z+\Delta z} - M_p \tilde{u}_p u_p \Big|_z}{\Delta z} \right) = M_p g + \vec{F}_a + \vec{F}_d \quad (\text{A1.7.3})$$

$$M_p \tilde{u}_p \frac{du_p}{dz} = M_p g + \vec{F}_a + \vec{F}_d \quad (\text{A1.7.4})$$

Equation (A1.7.4) is the equation for momentum balance on the droplet.

**APPENDIX – II**

Measured Temperature Corrections for Radiation Loss

## 1. Corrections for Gas Temperature Measured at Inlet Gas Duct

The inlet gas duct has a single centrally located *k-type* thermocouple that measures the gas temperature supplied to the gas distribution ring. The gas temperature measured by the thermocouple is corrected for radiation loss. The dimensions of the inlet gas duct and the insulation thickness is given in Table A2.1.1.

Table – A2.1.1: Data used for calculation of corrected gas temperature at inlet gas duct.

Thermocouple diameter $d_T$	0.006 m
Thermocouple material	SS 316
Thermocouple emissivity $\varepsilon_m$	0.85
Diameter of inlet gas duct $d_i$	0.6 m
Area of inlet gas duct $A_i$	0.36 m <sup>2</sup>
Inlet gas mass flux $m_{gas}$	0.92 kg/m <sup>2</sup> s (based on tower cross-section)
Inlet gas viscosity $\mu_{gas}$	2.676×10 <sup>-5</sup> kg/ms
Inlet gas density $\rho_{gas}$	0.65 kg/m <sup>3</sup>
Inlet gas thermal conductivity $\lambda_{gas}$	0.043 W/mK
Inlet gas specific heat $c_{p,gas}$	1047 J/kgK
Measured temperature $T_{gas}$	563 K
Ambient temperature $T_{amb}$	293 K
Thickness of metal wall $\delta_w$	0.008 m
Thickness of insulation $\delta_{ins}$	0.075 m
Thermal conductivity of metal wall $\lambda_w$	18.8 W/m <sup>2</sup> K
Thermal conductivity of insulation $\lambda_{ins}$	0.04 W/m <sup>2</sup> K
Stefan-Boltzman constant $\sigma$	5.670 W/m <sup>2</sup> K <sup>4</sup>

The surface heat transfer coefficient for the thermocouple ( $\alpha_T$ ) is calculated using the following correlation (Kreith, 1973):

$$\frac{\alpha_T d_T}{\lambda_{gas}} = 1.1C \left( \frac{\rho_{gas} v d_i}{\mu_{gas}} \right)^n \text{Pr}_{gas}^{0.31} \quad (\text{A2.1.1})$$

The Reynolds number inside the duct is:  $1.29 \times 10^5$

The Reynolds number ( $\text{Re}_T$ ) for the thermocouple is 1174.

For this  $\text{Re}_T$  the value of constants C and n in equation (A2.1.1) is 0.615 and 0.466 respectively (Source: Kreith, 1973).

Putting the values given in equation (A2.1.1) gives:

$$\alpha_T = 11428 \text{ W/m}^2\text{K}$$

The inside film coefficient in the duct ( $\alpha_D$ ) is given by:

$$\alpha_D = \frac{0.023 c_{p, gas} G}{Pr^{2/3} Re^{0.2} \left( \frac{\mu_{gas,w}}{\mu_{gas,b}} \right)^{0.14}} \quad (\text{A2.1.2})$$

Assuming  $\frac{\mu_{gas,w}}{\mu_{gas,b}}$  to be equal to unity and putting the values in equation (A2.1.2) gives:

$$\alpha_D = 17.63 \text{ W/m}^2\text{K}$$

The overall heat transfer coefficient ( $U$ ) based on a circular pipe with equivalent hydraulic diameter is given by:

$$\frac{1}{U} = \frac{d_o}{\alpha_i d_i} + \frac{d_o}{2\pi\lambda_w} \ln\left(\frac{d_i + 2\delta_w}{d_i}\right) + \frac{d_o}{2\pi\lambda_{ins}} \ln\left(\frac{d_i + 2\delta_w + 2\delta_{ins}}{d_i + 2\delta_w}\right) + \frac{1}{\alpha_{amb}} \quad (\text{A2.1.3})$$

$\alpha_{amb}$  (convective film coefficient for the outside surface) is taken to be  $14 \text{ W/m}^2\text{K}$  which combines convection and radiation. This gives the following overall heat transfer coefficient:

$$U = 0.44 \text{ W/m}^2\text{K}$$

Assuming that the heat absorbed by the thermocouple via convection is lost via radiation only, the energy balance for the thermocouple can be written as:

$$\alpha_T (T_{gas} - T_T) = \varepsilon_m \sigma (T_T^4 - T_w^4) \quad (\text{A2.1.4})$$

Rearranging equation (A2.1.4) in terms of  $T_{gas}$  gives:

$$T_{gas} = \frac{\varepsilon_m \sigma}{\alpha_T} (T_T^4 - T_w^4) + T_T \quad (\text{A2.1.5})$$

The wall temperature ( $T_w$ ) can be calculated using the following equation:

$$\dot{Q} = A_i \alpha_D (T_{gas} - T_w) \quad (A2.1.6)$$

$\dot{Q}$  in equation (A2.1.6) is calculated using the following equation:

$$\dot{Q} = UA_o (T_{gas} - T_{amb}) \quad (A2.1.7)$$

The wall temperature ( $T_w$ ) and fluid temperatures are not known, hence the set of equations (A2.1.5), (A2.1.6) and (A2.1.7) solved iteratively. Initially the value of  $T_{gas}$  is assumed to be equal to  $T_T$ , from which the heat flux is evaluated using equation (A2.1.6). The wall temperature is computed using equation (A2.1.7) and the new fluid temperature is calculated using equation (A2.1.5). The initial guessed value of  $T_{gas}$  is compared with the calculated value using equation (A2.1.5). If the difference is greater than 0.1 K, the calculated value of  $T_{gas}$  is used as the new guessed value for the calculation of  $T_w$  in equation (A2.1.6). The iterations are continued until the difference in guessed and calculated  $T_{gas}$  values is less than 0.1 K. A program is written in MATLAB (2010) for this purpose.

The value of  $T_{gas}$  is found to be 565.7 K. The fluid temperature measured by the thermocouple is 563.15 K. The difference between the thermocouple measurement and the fluid temperature ( $T_{gas}$ ) is **2.55 K**.

## 2. Corrections for Gas Temperature Measured at Exhaust Gas Duct

The exhaust gas duct has a single centrally located *k-type* thermocouple that measures the exhaust gas temperature. The gas temperature measured by the thermocouple is corrected for radiation loss. The dimensions of the exhaust gas duct and the insulation thickness is given in Table A2.2.2.

Table – A2.2.2: Data used for calculation of corrected gas temperature at exhaust gas duct.

Thermocouple diameter $d_T$	0.006 m
Thermocouple material	SS 316
Thermocouple emissivity $\varepsilon_m$	0.85
Area of the gas duct $A_i$	0.33 m <sup>2</sup>
Exhaust gas mass flux $m_i$	1.006 kg/m <sup>2</sup> s (based on tower cross-section)
Gas viscosity $\mu_{gas}$	1.72×10 <sup>-5</sup> kg/ms
Gas density $\rho_{gas}$	0.88 kg/m <sup>3</sup>
Gas thermal conductivity $\lambda_{gas}$	0.045 W/mK
Gas specific heat $c_{p,gas}$	1072 J/kgK
Measured temperature $T_{gas}$	367 K
Ambient temperature $T_{amb}$	293 K
Thickness of metal wall $\delta_w$	0.006 m
Thickness of insulation $\delta_{ins}$	0.105 m
Thermal conductivity of metal wall $\lambda_w$	18.8 W/m <sup>2</sup> K
Thermal conductivity of insulation $\lambda_{ins}$	0.04 W/m <sup>2</sup> K
Stefan-Boltzman constant $\sigma$	5.670 W/m <sup>2</sup> K <sup>4</sup>

The equations and calculation procedure is the same as in the case of temperature correction for inlet gas duct. The difference in measured and corrected exhaust gas temperature is **0.09 K**.

### 3. Corrections for Gas Temperatures Measured Inside the Spray Drying Tower

The temperature profiles measured inside the spray drying tower are corrected to account for radiation losses. The wall temperature in this case is estimated by extrapolation of the polynomial curve fits to the measured temperature profiles (given by equations 6.6, 6.7, 6.8 and 6.9) up to the wall (given in Figure 6.30). Therefore, iterative procedure was not required. For the calculation of convective film coefficients for the thermocouples, the magnitude of the velocity components obtained from Fluent for non-isothermal simulation Case 1 (Section 6.2.6) were used. Equation A2.1.5 was applied to calculate the corrected temperature. Figure A2.2.1 depicts the corrected and measured temperature profiles.

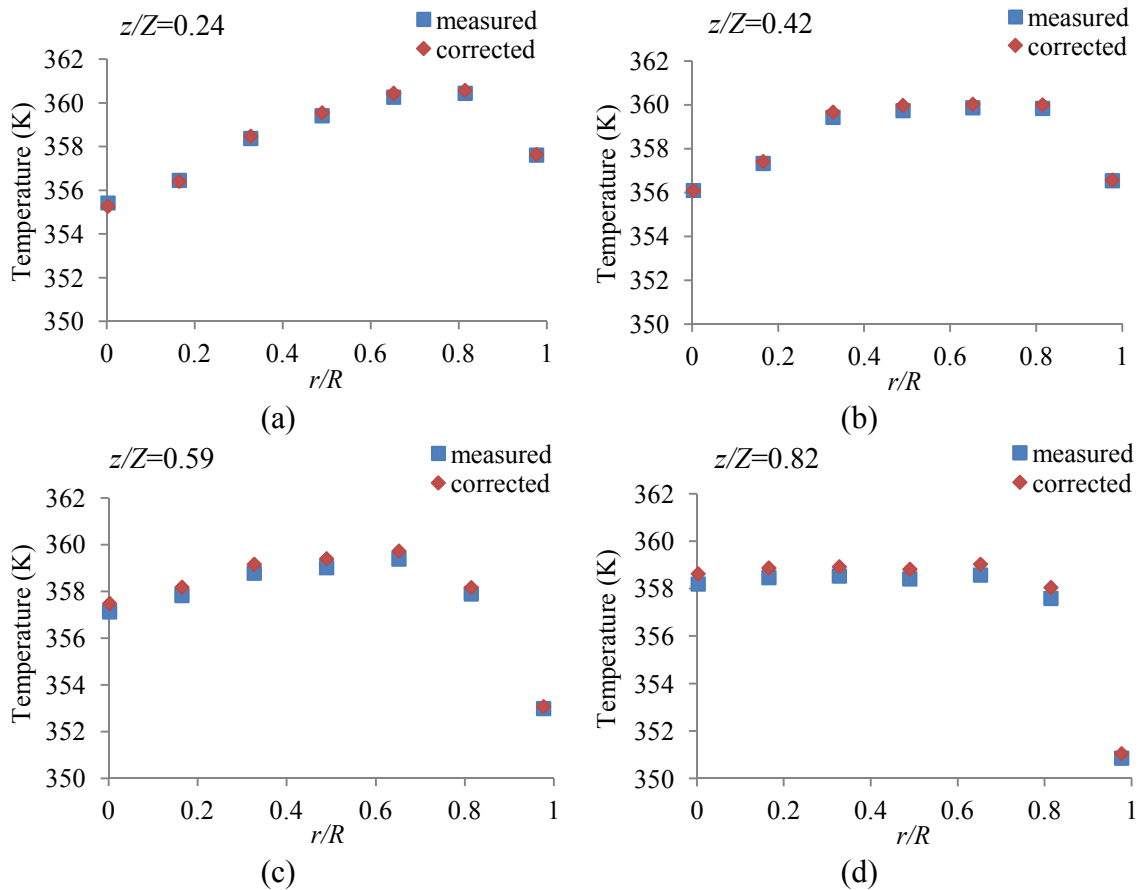


Figure – A2.2.1: Measured and corrected gas temperatures inside the spray drying tower.

**APPENDIX – III**

Publications Arising from this Thesis

## **1. Papers in Referred Journals**

The first author is highlighted in bold.

1. **Ali, M.**, Mahmud, T., Heggs, P. J., Ghadiri, M., Djurdjevic, D., Ahmadian, H., Juan, L. M., Amador, C. and Bayly, A. (2014). A one-dimensional plug-flow model of a counter-current spray drying tower. *Chem. Eng. Res. Des.*, vol. (92), pp. 826-841.
2. **Ali, M.**, Mahmud, T., Heggs, P. J., Ghadiri, M., Francia, V., Ahmadian, H., Martin de Juan, L., Djurdjevic, D. and Bayly, A. CFD modelling and validation of air velocity profiles in a counter-current spray drying tower, In Preparation.
3. **Ali, M.**, Mahmud, T., Heggs, P. J., Ghadiri, M., Davidson, A., Ahmadian, H., Martin de Juan, L., Djurdjevic, D. and Bayly, A. Investigation of heat losses from a pilot-scale counter-current spray drying tower. In Preparation.
4. **Ali, M.**, Mahmud, T., Heggs, P. J., Ghadiri, M., Ahmadian, H., Martin de Juan, L., Djurdjevic, D. and Bayly, A. Study of the influence of restitution coefficient on the modelling of a counter-current spray drying tower using CFD. In Preparation.
5. **Ali, M.**, Mahmud, T., Heggs, P. J., Ghadiri, M., Ahmadian, H., Martin de Juan, L., Djurdjevic, D. and Bayly, A. Study of the influence of initial size distribution on the spray drying process in a counter-current spray drying tower using CFD. In Preparation.
6. **Ali, M.**, Mahmud, T., Heggs, P. J., Ghadiri, M., Ahmadian, H., Martin de Juan, L., Djurdjevic, D. and Bayly, A. A stochastic particle-wall collision model applied to Eulerian-Lagrangian simulation of a spray drying tower. In Preparation.

## **2. Peer-Reviewed Conference Papers**

The first author is highlighted in bold.

1. **Ali, M.**, Mahmud, T., Heggs, P. J., Ghadiri, M., Bayly, A., Ahmadian, H., Martin de Juan, L. and Djurdjevic, D. Particle flow patterns in spray drying towers. To be presented in *13<sup>th</sup> International Conference on Multiphase Flow in Industrial Plants*, 17-19 September 2014, Sestri Levante, Italy.
2. **Ali, M.**, Mahmud, T., Heggs, P. J., Ghadiri, M., Bayly, A., Ahmadian, H., Martin de Juan, L. and Djurdjevic, D. CFD simulation of a counter-current spray drying tower with stochastic treatment of particle-wall collision. *7th World Congress on Particle Technology*, 19-22 May 2014, Beijing, China.

3. **Ali, M.**, Mahmud, T., Heggs, P. J., Ghadiri, M., Davidson, A., Ahmadian, H., Martin de Juan, L., Djurdjevic, D. and Bayly, A. Heat losses from a pilot-scale counter-current spray drying tower. *13th UK Heat Transfer Conference UKHTC2013*, 2-3 Sept. 2013, Imperial College London, UK.
4. **Ali, M.**, Mahmud, T., Heggs, P. J., Ghadiri, M., Francia, V., Ahmadian, H., Martin de Juan, L., Djurdjevic, D. and Bayly, A. CFD modelling of a counter-current spray drying tower. *8th International Conference on Multiphase Flow ICMF 2013*, 26-31 May 2013, Jeju, South Korea.

### **3. Oral Presentations**

The presenter and the first author is highlighted in bold.

1. **Ali, M.**, Mahmud, T., Heggs, P. J., **Ghadiri, M.**, Bayly, A., Ahmadian, H., Martin de Juan, L. and Djurdjevic, D. Particle flow patterns in spray drying towers. To be presented in *13th International Conference on Multiphase Flow in Industrial Plants*, 17-19 September 2014, Sestri Levante, Italy.
2. **Ali, M.**, **Mahmud, T.**, Heggs, P. J., Ghadiri, M., Bayly, A., Ahmadian, H., Martin de Juan, L. and Djurdjevic, D. CFD simulation of a counter-current spray drying tower with stochastic treatment of particle-wall collision. *7<sup>th</sup> World Congress on Particle Technology*, 19-22 May 2014, Beijing, China.
3. **Ali, M.**, Mahmud, T., Heggs, P. J., Ghadiri, M., Davidson, A., Ahmadian, H., Martin de Juan, L., Djurdjevic, D. and Bayly, A. Heat losses from a pilot-scale counter-current spray drying tower. *13<sup>th</sup> UK Heat Transfer Conference UKHTC2013*, 2-3 Sept. 2013, Imperial College London, UK.
4. **Ali, M.**, Mahmud, T., Heggs, P. J., Ghadiri, M., Francia, V., Ahmadian, H., Martin de Juan, L., Djurdjevic, D. and Bayly, A. CFD modelling of a counter-current spray drying tower. *8<sup>th</sup> International Conference on Multiphase Flow ICMF 2013*, 26-31 May 2013, Jeju, South Korea.
5. **Ali, M.**, Mahmud, T., Heggs, P. J., Ghadiri, M., Djurdjevic, D. and Bayly, A. Modelling drying of slurry droplets in a counter-current spray drying tower. *8<sup>th</sup> European Congress of Chemical Engineering*, 25-29 September 2011, Berlin, Germany.
6. **Ali, M.**, Mahmud, T., Heggs, P. J., Ghadiri, M., Djurdjevic, D. and Bayly, A. Numerical modelling of a counter-current spray drying tower. *Computer Aided Process Engineering Forum CAPE 2011*: 21-22 March 2011, Bradford, UK.